

**Stochastic Modeling and Simulation of Multiphase Reacting
Turbulent Flows with Complex Chemistry**

by

Peyman Givi, Cyrus K. Madnia and Dale B. Taulbee
Department of Mechanical and Aerospace Engineering
State University of New York at Buffalo
Buffalo, NY 14260-4400

**Final Report
for Grant N00014-94-1-0667**

March 1998

DISTRIBUTION STATEMENT A
Approved for public release
Distribution Unlimited



19980417 123

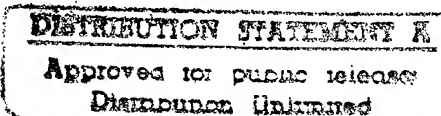
DTIC QUALITY INSPECTED

Prepared for
Dr. Gabriel D. Roy
OFFICE OF NAVAL RESEARCH
Mechanics and Energy Conversion Division
800 North Quincy Street
Arlington, VA 22217-5000

REPORT DOCUMENTATION PAGE

Form Approved
OMB No. 0704-0188

Public reporting burden for this collection of information is estimated to average 1 hour per response, including the time for reviewing instructions, searching existing data sources, gathering and maintaining the data needed, and completing and reviewing the collection of information. Send comments regarding this burden estimate or any other aspect of this collection of information, including suggestions for reducing this burden, to Washington Headquarters Services, Directorate for Information Operations and Reports, 1215 Jefferson Davis Highway, Suite 1204, Arlington, VA 22202-4302, and to the Office of Management and Budget, Paperwork Reduction Project (0704-0188), Washington, DC 20503.

1. AGENCY USE ONLY (Leave Blank)	2. REPORT DATE	3. REPORT TYPE AND DATES COVERED	
	March 1998	Final Report April 1994 - May 1998	
4. TITLE AND SUBTITLE Stochastic Modeling and Simulation of Multiphase Reacting Turbulent Flows with Complex Chemistry			5. FUNDING NUMBERS G N00014-94-1-0667
6. AUTHORS Peyman Givi, Cyrus K. Madnia, Dale B. Taulbee			
7. PERFORMING ORGANIZATION NAME(S) AND ADDRESS(ES) Department of Mechanical & Aerospace Engineering State University of New York at Buffalo Buffalo, New York 14260-4400			8. PERFORMING ORGANIZATION REPORT NUMBER
9. SPONSORING / MONITORING AGENCY NAME(S) AND ADDRESS(ES) Office of Naval Research 800 N. Quincy Street Arlington, VA 22217-5000			10. SPONSORING / MONITORING AGENCY REPORT NUMBER
11. SUPPLEMENTARY NOTES			
12a. DISTRIBUTION / AVAILABILITY STATEMENT  Approved for public release Distribution Unlimited		12b. DISTRIBUTION CODE	
13. ABSTRACT (Maximum 200 words) Two physical phenomena have been the primary subject of investigation: (1) multiphase transport in turbulence, (2) realistic chemistry in large scale numerical simulation of turbulent combustion. In addition, two other phenomena have also been considered: (3) scalar mixing in turbulence, and (4) magnetohydrodynamic turbulence. This Final Report provides a summary of our accomplishments in research on each of the above four problems.			
14. SUBJECT TERMS Multiphase transport, turbulent combustion, turbulence modeling, numerical simulation.		15. NUMBER OF PAGES 302	16. PRICE CODE
17. SECURITY CLASSIFICATION OF REPORT unclassified	18. SECURITY CLASSIFICATION OF THIS PAGE unclassified	19. SECURITY CLASSIFICATION OF ABSTRACT unclassified	20. LIMITATION OF ABSTRACT UL

NSN 7540-01-280-5500

Standard Form 298 (Rev. 2-89)
Prescribed by ANSI Std. Z39-1
298-102

Contents

1	Summary of Achievements	1
2	Collaborators	7
2.1	Postdoctoral Fellow	7
2.2	Graduate Students	7
2.3	High School Students	7
3	Honors, Awards and Promotions	8
4	Publications	9
4.1	Journal Papers and Book Chapters	9
4.2	Books Edited	9
4.3	Conference Papers	10
5	Public Lectures	12

Stochastic Modeling and Simulation of Multiphase Reacting Turbulent Flows with Complex Chemistry

Peyman Givi, Cyrus K. Madnia and Dale B. Taulbee
Department of Mechanical and Aerospace Engineering
State University of New York at Buffalo
Buffalo, NY 14260-4400

Abstract

Two physical phenomena have been the primary subject of investigation: (1) multiphase transport in turbulence, (2) realistic chemistry in large scale numerical simulation of turbulent combustion. In addition, two other phenomena have also been considered: (3) scalar mixing in turbulence, and (4) magnetohydrodynamic turbulence. This Final Report provides a summary of our accomplishments in research on each of the above four problems. This work is sponsored by the Office of Naval Research (ONR), Grant N00014-94-1-0667. Dr. Gabriel D. Roy is the Technical Monitor.

1 Summary of Achievements

This work deals with statistical-stochastic modeling and numerical simulation of complex turbulent flows. The terminology "complex" refers to issues which, if resolved, extend the boundaries of applicability of current modeling and simulation schemes for analytical analysis of turbulent flows. Two phenomena have been the primary subjects of investigation: (1) multiphase transport in turbulent flows, and (2) inclusion of realistic chemistry in turbulent combustion simulations. In addition, two other phenomena have also been considered: (3) scalar mixing in turbulence, and (4) magnetohydrodynamic turbulence. We do not imply these are the only unresolved issues in turbulence research; there are numerous other physical phenomena requiring further investigations. Neither do we suggest that the extent of progress on the issues considered here is insufficient. On the contrary, within the past

decade significant contributions have been made in each of the constituting elements of this research.

In the course of this research, we have been fortunate to make significant progress in each of the problems considered. Appendix I through Appendix X provide a very detailed description of our achievements in each of the constituents of our research. These achievements are summarized below:

Dispersion and polydispersity of droplets in stationary isotropic turbulence: In this part of our work, a rather detailed parametric study is conducted of dispersion and polydispersity of liquid drops in stationary isotropic turbulence via direct numerical simulation (DNS). Both non-evaporating and evaporating drops are simulated; in the latter both constant and variable rates of evaporation are considered. The simulations of non-evaporating drops are used to validate the numerical methodology and to assess the effects of the particle time constant and the drift velocity on the particle velocity autocorrelation, turbulence intensity and diffusivity. The simulated results are also used to appraise the performance of some of the available theoretical models for particle dispersion in stationary isotropic turbulence. The effects of the initial drop time constant, the initial evaporation rate, and the drop Schmidt number on the probability density function (PDF) of the drop size are studied. It is found that, after an initial transient period the PDF of the drop size becomes nearly Gaussian. However, the PDF deviates from Gaussian as the mean drop time constant becomes very small. The extent of this deviation depends on the evaporation rate. The effect of the initial spray size on the PDF is also studied and it is shown that as the spray size increases, the interaction between the spray and large scale turbulence structures influences the PDF. The effect of the initial size distribution on the PDF is also investigated by varying the initial standard deviation. Both Gaussian and double-delta initial drop size PDFs are considered. In the latter it is shown that a transition to Gaussian is possible provided that the initial mean drop time constant is large and/or the initial standard deviation of the drop diameter is small. *Please see Appendix I for a complete description of this work.*

Stochastic simulations of particle-laden isotropic turbulent flows: In this part of our work, stochastic simulations are performed of dispersion and polydispersity of particles in isotropic incompressible turbulence. The mass loading of the particles is assumed to be small; thus the effects of particles on the turbulence is neglected (one-way coupling). A stochastic model, based on the idea of “time series analysis,” is used to generate the fluid velocity at the particle location. The results of the simulations are used to assess

the performance of the stochastic model via comparisons made with analytical and DNS results. The model captures most of the trends reported in theory and DNS. However, the continuity effect associated with the crossing trajectories effect is not captured. Also, the peaking in the variation of the particle asymptotic diffusivity coefficient with the particle time constant is not observed in the stochastic simulations. For evaporating particles, the stochastic model predicts thinner PDFs for the particle diameter as compared to those generated by DNS. The stochastic model is then implemented to investigate the effects of the gravity on the evaporation. Several important features are observed in the results. The depletion rate increases with the increase of the drift velocity at short and intermediate times, and shows the opposite trend at long times. The standard deviation and skewness of the PDF of the particle diameter indicate peak values in their variations with the drift velocity. The dispersion of the evaporating particles is decreased with respect to that of the non-evaporating particles at small drift velocities. An opposite trend is observed at large drift velocities. The effects of the initial evaporation rate and the particle Schmidt number on the evaporation of particles in the gravity environment are also studied with the stochastic model. *Please see Appendix II for a complete description of this work.*

Algebraic Reynolds-stress and void-fraction flux models for two-phase turbulent flows: In this work, general “algebraic” closures are derived for the Reynolds stresses and the fluxes of the void fraction in the Reynolds averaged transport equations of two-phase turbulent flows. These closures are obtained from the hierarchy of second-order moment closures and are favored over conventional models based on the “Boussinesq” type approximations and linear gradient diffusion models. With a liberal use of the Cayley-Hamilton theorem, “explicit” solutions of the algebraic equations are obtained for the Reynolds stresses of both the carrier and the dispersed phases, and the turbulent fluxes of the void fraction. The solutions for the Reynolds stresses compare well with available DNS data of particle-laden homogeneous turbulent shear flows. By manipulating the explicit algebraic solutions, relations are provided for the “effective” turbulent diffusivities of the Reynolds stresses and the void fraction flux. These relations are utilized in the parabolic (thin layer) formulation of two-phase turbulent shear flows. The predicted results for a particle-laden axisymmetric jet show encouraging agreements with available laboratory data. *Please see Appendices III, IV for a complete description of this work.*

Large and direct numerical simulation of a methane jet flame: In this work, we make use of the “filtered mass density function” (FMDF) for large eddy simulation of a jet flame involving methane fuel. The flame chemistry is modeled via several “realistic” kinetics

models. The FMDF represents the single point joint probability density function of the subgrid scale (SGS) scalar quantities and is obtained by solution of its modeled transport equation. In this equation, the chemical reactions appear in closed form but the influences of scalar mixing and convection within the subgrid are modeled. The stochastic differential equations (SDEs) which yield statistically equivalent results to that of the FMDF transport equation are derived and are solved via a Lagrangian Monte Carlo scheme. The consistency, convergence, and accuracy of FMDF and the Monte Carlo solution of its equivalent SDEs are assessed via comparison with data generated by DNS and with experimental data. *Please see Appendix V for a complete description of this work.*

Structure of homogeneous non-helical magnetohydrodynamic turbulence: Results are obtained from three dimensional DNS of non-helical magnetohydrodynamic (MHD) turbulence for both stationary isotropic and homogeneous shear flow configurations with zero mean induction and unity magnetic Prandtl number. Small scale dynamo action is observed in both flows, and stationary values for the ratio of magnetic to kinetic energy are shown to scale nearly linearly with the Taylor microscale Reynolds numbers above a critical value of $Re_\lambda \approx 30$. The presence of the magnetic field has the effect of decreasing the kinetic energy of the flow, while simultaneously increasing the Taylor microscale Reynolds number due to enlargement of the hydrodynamic length scales. For shear flows, both the velocity and the magnetic fields become increasingly anisotropic with increasing initial magnetic field strength. The kinetic energy spectra show a relative increase in high wavenumber energy in the presence of a magnetic field. The magnetic field is found to portray an intermittent behavior, with peak values of the flatness near the critical Reynolds number. The magnetic field of both flows is organized in the form of “flux tubes” and magnetic “sheets.” These regions of large magnetic field strength show a small correlation with moderate vorticity regions, while the electric current structures are correlated with large amplitude strain regions of the turbulence. Some of the characteristics of small scale MHD turbulence are explained via the “structural” description of turbulence. *Please see Appendix VI for a complete description of this work.*

Non-Gaussian scalar statistics in homogeneous turbulence: Results are obtained from numerical simulations of passive scalar mixing in homogeneous, incompressible turbulent flows. These results are generated via the Linear Eddy Model (LEM) and DNS of turbulent flows under a variety of mixing conditions. The nature of mixing and its response to the turbulence field is examined and the single-point PDF of the scalar amplitude and the PDFs of the scalar spatial-derivatives are constructed. It is shown that both Gaussian and

exponential scalar PDFs emerge depending on the parameters of the simulations and the initial conditions of the scalar field. Aided by the analyses of data, several reasons are identified for the non-Gaussian behavior of the scalar amplitude. In particular, two mechanisms are identified for causing exponential PDF: (1) A non-uniform action of advection on the large and the small scalar scales, (2) the nonlinear interaction of the scalar and the velocity fluctuations at small scales. In the absence of a constant nonzero mean scalar gradient, the behavior of the scalar PDF is very sensitive to the initial conditions. In the presence of this gradient, an exponential PDF is not sustained regardless of initial conditions. The numerical results pertaining to the small scale intermittency (non-Gaussian scalar derivatives) are in accord with laboratory experimental results. The statistics of the scalar derivatives and those of the velocity-scalar fluctuations are also in accord with laboratory measured results.

Please see Appendix VII for a complete description of this work.

Conditional expected dissipation & diffusion in turbulent scalar mixing and re-action: Analytical expressions are obtained for the conditional expected dissipation and the conditional expected diffusion of a passive scalar contaminant in homogeneous turbulent flows by means of several turbulence closures. It is shown that if the single-point PDF of the scalar is represented by the family of Exponential distributions, the conditional expected dissipation varies significantly depending on the exponent of the PDF. However, the conditional expected diffusion remains identical. For those members with tails broader than Gaussian, the conditional expected dissipation is concave up and for tails narrower than Gaussian it is concave down. This is proved mathematically without resorting to asymptotic analysis (of the final stages of mixing) as conducted previously. For all cases, the conditional expected diffusion adopts a linear profile consistent with the linear mean square estimation (LMSE) theory. The similarity of the conditional diffusion field is explained in the context of the “lamellar” theory of turbulent mixing. The mathematical results are in accord with previous results generated by DNS and are further validated here by comparison with data obtained via the LEM. It is suggested that the behavior of the conditional expected diffusion at the scalar bound has a significant influence on the evolution of the PDF. *Please see Appendices VIII and IX for a complete description of this work.*

Inter-layer diffusion model of scalar mixing in homogeneous turbulence: A field-parameterized model termed the *Inter-Layer Diffusion Model* (ILDM) is developed and is implemented for the probabilistic description of scalar mixing in homogeneous turbulent flows. The essential element of the model is based on the lamellar theory of mixing in the context developed by Kerstein and proposes that there are two coupled mechanisms by which

the mixing process is described. These mechanisms are due to: (1) local events and (2) integrated global events. The mathematical formalities by which the closure is invoked are described and it is shown that the conditional expected diffusion of the scalar field depicted by the model depends more directly on the local events. With the manipulation of each of these two mechanisms, several families of scalar probability density functions (PDFs) are generated. These families include some of the distributions generated by other mixing closures. The similarity of local events imply the similarity of the conditional expected diffusion as generated via these models. The global events manifest themselves by the evolution of the conditional expected dissipation, and also the boundedness of the composition domain. While the PDFs generated in this way are very different, their applications for modeling of mixing limited reactions do not yield significantly different results. *Please see Appendix IX and for a complete description of this work.*

2 Collaborators

We are very grateful to benefit from participation of excellent junior collaborators in this research. The names and the current affiliations of these collaborators are provided below.

2.1 Postdoctoral Fellow

Dr. Farzad Mashayek (June 1994-August 1997). Current Position: Assistant Professor of Mechanical Engineering, The University of Hawaii at Manoa, Honolulu, HI.

2.2 Graduate Students

Dr. Virgil Adumitroaie. Ph.D. in Mechanical Engineering (1997). Dissertation: Quasi-Explicit Algebraic Turbulence Closures in Compressible Reacting Flows, Current Position: Research Scientist, CFD Research, Inc., Huntsville, AL.

Mr. Sean C. Garrick. M.S. in Mechanical Engineering (1994). Thesis: Affordable Computation of Turbulent Reactive Flows by Large Eddy Simulations. Current Position: Ph.D. candidate, SUNY at Buffalo.

Dr. Farhad A. Jaber. Ph.D. in Mechanical Engineering (1996). Dissertation: Mathematical Modeling and Computational Analysis of Turbulent Mixing and Reacting Systems, Current Position: Research Scientist, SUNY at Buffalo.

Dr. Sunil James. Ph.D. in Mechanical Engineering (1998). Dissertation: Realistic Chemistry in Large Scale Numerical Simulations of Methane Diffusion Flames, Current Position: Senior Project Engineer, Allison Engine Company, Indianapolis, IN.

Dr. Richard S. Miller. Ph.D. in Mechanical Engineering (1995). Dissertation: Passive Scalar, Magnetic Field, and Solid Particle Transport in Homogeneous Turbulence. Current Position: Research Scientist, Jet Propulsion Laboratory, California Institute of Technology, Pasadena, CA.

2.3 High School Students

Kristen M. Cassetta (1996-1997), Williamsville North High School, Amherst, NY.

Christopher R. MacKes (1996-1997), Williamsville North High School, Amherst, NY.

Matthew K. Marshall (1996-1997), Tonawanda High School, Tonawanda, NY.

3 Honors, Awards and Promotions

The following awards and honors were received by the researchers supported by this grant:

Paper entitled "Structure of a Turbulent Reacting Mixing Layer," (by R.S. Miller, C.K. Madnia and P. Givi, *Combustion Science and Technology*, 99, 1-36, 1994) selected for inclusion in the book *ONR Investing in the Future 1946-1996*, pp. 581-617, in celebration of the 50th Anniversary of the Office of Naval Research, Washington, DC, May 1996.

P. Givi, Invited to offer a short course at the "J.M. Burgerscentrum Summerschool on Reacting Flows: Flames, Chemical Reactors, and the Atmosphere," Delft University of Technology, Delft, Netherlands, August 25-29, 1997

P. Givi, Appointed Associate Editor, *AIAA Journal*, term: 1998-2000.

P. Givi, Appointed, Editorial Board of *Progress in Energy and Combustion Science*, 1996-present.

P. Givi, Invited Lecturer on "University Perspectives" at ICASE/LaRC Industry Roundtable, Williamsburg, VA, October 3-4, 1994.

P. Givi, Promoted to Professor, Department of Mechanical and Aerospace Engineering, State University of New York at Buffalo, Buffalo, NY, September 1993.

C.K. Madnia, Received CAREER Award, National Science Foundation (1996-2000).

S.C. Garrick, Received ONR/HBECC (Office of Naval Research/Historically Black Engineering College's Committee) Faculty Fellowship Award (1995-1998).

R.S. Miller, winner of *Abe M. Zarem Award for Distinguished Achievement in Aeronautics*. The Abe Zarem Medallion was awarded to Mr. Miller at the AIAA Aerospace Sciences Meeting in Reno, NV in January 1994.

S.C. Garrick, First Prize winner at the Graduate Technical Paper Competition of AIAA Northeast Regional Student Conference, Clarkson University, Potsdam, NY. Title of paper: "Large Eddy Simulation of Turbulent Reactive Flows," April 1994.

R.S. Miller, winner of *ICAS McCarthy Award* of the International Council of the Aeronautical Sciences (ICAS). This award is in relation to Mr. Miller's Invited ICAS Paper and Lecture: "The Manifestation of Eddy Shocklets and Laminar Diffusion Flamelets in a Shear Layer." The Award was presented to Mr. Miller at the 19th Congress of ICAS held at Anaheim, CA in September 1994. Mr. Miller was ranked First in a group of 28 contestants representing 11 countries with leading aerospace programs.

4 Publications

All of the following publications resulted from the work performed with the support of this Grant. In the list below, invited publications are identified by a •. The support of ONR is acknowledged in all of the following publications. This list does not include papers currently under review, or papers published under our AASERT Grant.

4.1 Journal Papers and Book Chapters

F. Mashayek, F.A. Jaberi, R.S. Miller, and P. Givi, "Dispersion and Polydispersity of Liquid Drops in Stationary Isotropic Turbulence," *International Journal of Multiphase Flow*, **23**(2), 337-355, 1997.

• F. Mashayek, D.B. Taulbee and P. Givi, "Modeling and Simulation of Two-Phase Turbulent Flow," Chapter 8 in *Propulsion Combustion: Fuels to Emissions*, pp. 241-2890, Editor: Gabriel D. Roy, Taylor & Francis, Washington, D.C., 1997.

F. Mashayek, D.B. Taulbee and P. Givi, "Statistical Modeling and Direct Simulation of Two-Phase Turbulent Flows," Chapter in *Advanced Computation & Analysis of Combustion*, pp. 161-174, Editors: G.D. Roy, S.M. Frolov and P. Givi, ENAS Publishers, Moscow, Russia, 1997.

F.A. Jaberi, R.S. Miller, C.K. Madnia and P. Givi, "Non-Gaussian Scalar Statistics in Homogeneous Turbulence," *Journal of Fluid Mechanics*, **313**, 241-282, 1996.

F.A. Jaberi, R.S. Miller and P. Givi, "Conditional Statistics in Turbulent Scalar Mixing and Reaction," *AICHE Journal*, **42**(4), 1149-1152, 1996.

R.S. Miller, F. Mashayek, V. Adumitroaie, and P. Givi, "Structure of Homogeneous Non-Helical Magnetohydrodynamic Turbulence," *Physics of Plasmas*, **3**(9), 3304-3317, 1996.

F.A. Jaberi, R.S. Miller and P. Givi, "Conditional Expected Dissipation & Diffusion in Turbulent Scalar Mixing and Reaction," in *Transport Phenomena in Combustion*, pp. 885-896, Editor: S.H. Chan, Taylor & Francis, Washington, D.C., 1996.

F.A. Jaberi and P. Givi, "Inter-Layer Diffusion Model of Scalar Mixing in Homogeneous Turbulence," *Combustion Science and Technology*, **104**(4-6), 249-272, 1995.

• F.A. Jaberi and P. Givi, "The Lamellar Description of Mixing in Turbulent Flows," Chapter in *Transition, Turbulence and Combustion*, pp. 265-274, Editors: M.Y. Hussaini, T.B. Gatski and T.L. Jackson, Kluwer Academic Publishers, Boston, MA, 1994.

4.2 Books Edited

G.D. Roy, S.M. Frolov and P. Givi, Editors: *Advanced Computation & Analysis of Combustion*, ENAS Publishers, Moscow, Russia, 592 pp., ISBN 5-89055-006-3, 1997.

G.D. Roy and P. Givi, Editors: *Proceedings of the Seventh ONR Propulsion Meeting*, Buffalo, NY, August 29-31, 1994.

4.3 Conference Papers

D.B. Taulbee, F. Mashayek, P. Givi and C. Barre, "Simulation and Reynolds Stress Modeling of Particle-Laden Turbulent Shear Flows," *Proceedings of Eleventh Symposium on Turbulent Shear Flows*, pp. 24.17-24.22, Grenoble, France, September 8-10, 1997.

D.B. Taulbee, F. Mashayek, and P. Givi, "Direct Numerical Simulation and Reynolds Stress Modeling of Particle-Laden Homogeneous Turbulent Shear Flows," *Bulletin of the American Physical Society*, **41**(9) pp. 1784-1785, 49th Annual Meeting of the Division of Fluid Dynamics of the American Physical Society, Syracuse, NY, November 24-26, 1996.

F. Mashayek, and P. Givi, "Direct Numerical Simulation of Evaporating Droplet Dispersion in Low Mach Number Shear Turbulence" *Bulletin of the American Physical Society*, **41**(9) pp. 1766-1767, 49th Annual Meeting of the Division of Fluid Dynamics of the American Physical Society, Syracuse, NY, November 24-26, 1996.

S. James and P. Givi, "Direct Numerical Simulation of Methane Oxidation in a Nonpremixed Plane Jet Flame," *Bulletin of the American Physical Society*, **41**(9) p. 1747, 49th Annual Meeting of the Division of Fluid Dynamics of the American Physical Society, Syracuse, NY, November 24-26, 1996.

R.S. Miller, F.A. Jaber and P. Givi, "Modeling and Simulation of Conditional Scalar Statistics in Turbulent Mixing and Reaction," *Proceedings of Tenth Symposium on Turbulent Shear Flows*, pp. 16.25-16.30, University Park, PA, August 14-16, 1995.

F.A. Jaber, R.S. Miller, C.K. Madnia and P. Givi, "Non-Gaussian Scalar Statistics in Homogeneous Turbulence," *Proceedings of Tenth Symposium on Turbulent Shear Flows*, pp. 31.13-31.18, University Park, PA, August 14-16, 1995

R.S. Miller, F. Mashayek, V. Adumitroaie, and P. Givi, "Structure of Isotropic and Homogeneous Shear Magnetohydrodynamic Turbulence," *Bulletin of the American Physical Society*, **40**(12) p. 1917, 48th Annual Meeting of the Division of Fluid Dynamics of the American Physical Society, Irvine, CA, November 19-21, 1995.

D.B. Taulbee, F. Mashayek, and P. Givi, "Explicit Algebraic Stress and Flux Models for Turbulent Particle-Laden Flows," *Bulletin of the American Physical Society*, **40**(12) p. 1993, 48th Annual Meeting of the Division of Fluid Dynamics of the American Physical Society, Irvine, CA, November 19-21, 1995.

F.A. Jaber, R.S. Miller and P. Givi, "Conditional Expectations in Turbulent Scalar Mixing and Reaction," *Proceedings of the 28th Fall Technical Meeting of the Combustion Institute, Eastern States Section*, in *Chemical and Physical Processes in Combustion*, pp. 401-404, Clearwater Beach, FL, December 4-7, 1994.

S.C. Garrick, R.S. Miller, and P. Givi, "Large Eddy Simulation of Reacting Turbulent Flows,"

Proceedings of the 28th Fall Technical Meeting of the Combustion Institute, Eastern States Section, in *Chemical and Physical Processes in Combustion*, pp. 393-396, Clearwater Beach, FL, December 4-7, 1994.

F.A. Jaber, R.S. Miller and P. Givi, "Conditional Statistics in Turbulent Scalar Mixing and Reaction," *Bulletin of the American Physical Society*, **29**(9) p. 1845, 47th Annual Meeting of the Division of Fluid Dynamics of the American Physical Society, Atlanta, GA, November 20-22, 1994.

F.A. Jaber and P. Givi, "Inter-Layer Diffusion Model of Scalar Mixing in Homogeneous turbulence," *Bulletin of the American Physical Society*, **38**(12) p. 2229, 46th Annual Meeting of the Division of Fluid Dynamics of the American Physical Society, Albuquerque, NM, November 21-23, 1993.

5 Public Lectures

The lectures and seminars listed below are based on the work sponsored by this Grant. All invited lectures are identified by •

“Quantitative Visualization of Turbulent Reacting Flows in Propulsion Systems,” Tenth ONR Propulsion Meeting, Monterey, CA, October 9, 1997.

Modeling and Simulation of Complex Reacting Flows, Tenth ONR Propulsion Meeting, Monterey, CA, October 8, 1997.

• Short course offered at the “J.M. Burgerscentrum Summerschool on Reacting Flows: Flames, Chemical Reactors, and the Atmosphere,” Delft University of Technology, Delft, Netherlands, August 25-29, 1997

“Statistical Modeling and Direct Simulation of Two-Phase Turbulent Flows,” International Colloquium on Advanced Computation and Analysis of Combustion, Moscow, Russia, May 12, 1997.

• “Model Free Simulations of Turbulent Reacting Flows,” Thermo and Fluid Dynamics Department, Chalmers University of Technology, Göteborg, Sweden, October 24, 1996.

“Modeling and Simulation of Complex Reacting Turbulent Flows,” Ninth ONR Propulsion Meeting, Washington, DC, September 9, 1996.

• “Stochastic Large Eddy Simulation of Turbulent Reactive Flows,” Structural, Geotechnical and Earthquake Engineering Seminar, Department of Civil Engineering, SUNY at Buffalo, Buffalo, NY, May 3, 1996.

• “PDF Methods for LES of Turbulent Reacting Flows,” Sibley School of Mechanical and Aerospace Engineering, Cornell University, Ithaca, NY, March 12, 1996.

• “A Simple but Reliable Recipe for Modeling of Plug Flow Reactors and Batch Mixers,” Department of Mechanical Engineering, New Jersey Institute of Technology, Newark, NJ, December 13, 1995.

• “LES-PDF of Turbulent Reacting Flows by a Lagrangian Monte Carlo Scheme,” School of Mechanical Engineering, Purdue University, West Lafayette, IN, October 31, 1995.

• “Modeling and Simulation of Turbulent Reacting Flows,” Department of Electrical and Computer Engineering and Department of Chemical Engineering, Kansas State University, Manhattan, KS, October 30, 1995.

• “Modeling and Simulation of Turbulent Reacting Flows,” Department of Chemical Engineering, Iowa State University, Ames, IA, October 27, 1995.

“Computational Tools for Propulsion Research,” A Presentation for AFOSR Management visit to NASA Langley Research Center, Hampton, VA, October 18, 1995.

“Modeling and Simulation of Complex Reacting Turbulent Flows,” Eight ONR Propulsion Meeting, La Jolla, CA, October 13, 1995.

• "Binary Scalar Mixing and Reaction in Homogeneous Turbulence," Department of Applied Mechanics and Engineering Science, University of California at San Diego, La Jolla, CA, October 10, 1995.

"Modeling and Simulation of Conditional Scalar Statistics in Turbulent Mixing and Reaction," 10th Symposium on Turbulent Shear Flows, University Park, PA, August 15, 1995.

"Progress Report on RANS and LES of High-Speed Reacting Turbulent Flows," Hypersonic Airbreathing Propulsion Branch, NASA Langley Research Center, Hampton, VA, August 1, 1995.

"Conditional Expected Dissipation & Diffusion in Turbulent Scalar Mixing and Reaction," 8th International Symposium on Transport Phenomena in Combustion, San Francisco, CA, July 17, 1995.

• "Binary Scalar Mixing and Reaction in Homogeneous Turbulence," Sibley School of Mechanical and Aerospace Engineering, Cornell University, Ithaca, NY, February 28, 1995.

• "Progress in Modeling and Simulation of Binary Scalar Mixing and Reaction in Turbulent Flows," Fall Seminar Series, Department of Mechanical, Aerospace and Nuclear Engineering, The University of Virginia, Charlottesville, VA, December 15, 1994.

"Conditional Statistics in Turbulent Scalar Mixing and Reaction," 47th Annual Meeting of the Division of Fluid Dynamics of the American Physical Society, Atlanta, GA, November 20, 1994.

• "Relevance of Basic Research in Applied Processes in Turbulent Combustion Systems," ICASE/LaRC Industry Roundtable, Williamsburg, VA, October 4, 1994.

"Stochastic Modeling and Simulation of Complex Reacting Turbulent Flows," Seventh ONR Propulsion Meeting, Buffalo, NY, August 29, 1994.

APPENDIX I

Dispersion and Polydispersity of Droplets in Stationary Isotropic Turbulence



Pergamon

Int. J. Multiphase Flow Vol. 23, No. 2, pp. 337-355, 1997
© 1997 Elsevier Science Ltd
Printed in Great Britain. All rights reserved
0301-9322/97 \$17.00 + 0.00
PII: S0301-9322(96)00065-1

DISPERSION AND POLYDISPERSITY OF DROPLETS IN STATIONARY ISOTROPIC TURBULENCE

F. MASHAYEK, F. A. JABERI, R. S. MILLER and P. GIVI

Department of Mechanical and Aerospace Engineering, State University of New York at Buffalo, Buffalo,
NY 14260-4400, U.S.A.

(Received 12 July 1995; in revised form 22 August 1996)

Abstract—A detailed parametric study is conducted of dispersion and polydispersity of liquid drops in stationary isotropic turbulence via direct numerical simulation. It is assumed that the flow is very dilute so that the effect of particles on the carrier fluid is negligible (one-way coupling). Both non-evaporating and evaporating drops are simulated; in the latter both constant and variable rates of evaporation are considered. The simulations of non-evaporating drops are used to validate the numerical methodology and to assess the effects of the particle time constant and the drift velocity on the particle velocity autocorrelation, turbulence intensity and diffusivity. The simulated results are also used to appraise the performance of some of the available theoretical models for particle dispersion in stationary isotropic turbulence. The effects of the initial drop time constant, the initial evaporation rate, and the drop Schmidt number on the probability density function (pdf) of the drop size are studied. It is found that, after an initial transient period the pdf of the drop size becomes nearly Gaussian. However, the pdf deviates from Gaussian as the mean drop time constant becomes very small. The extent of this deviation depends on the evaporation rate. The effect of the initial spray size on the pdf is also studied and it is shown that as the spray size increases, the interaction between the spray and large scale turbulence structures influences the pdf. The effect of the initial size distribution on the pdf is also investigated by varying the initial standard deviation. Both Gaussian and double-delta initial drop size pdfs are considered. In the latter it is shown that a transition to Gaussian is possible provided that the initial mean drop time constant is large and/or the initial standard deviation of the drop diameter is small. © 1997 Elsevier Science Ltd. All rights reserved.

Key Words: direct numerical simulation, isotropic turbulence, particle dispersion, polydispersity, evaporating drops, drop size distribution

1. INTRODUCTION

Dispersion of heavy particles in turbulent flows has been the subject of numerous investigations in recent years due to its applications in various aspects of technology (Eaton and Fessler 1994; McLaughlin 1994). One of the early theoretical studies of particle dispersion in turbulence is due to Tchen (1947) who derives relations for the particle diffusion coefficient under the assumption that the particle's neighbouring fluid does not change in the course of its motion. Yudine (1959) clarifies the consequences of this assumption by analyzing the motion of heavy particles in the presence of gravity and shows that as the heavy particle is transported under the influence of the external body force, its trajectory crosses that of the neighbouring fluid particle which is not affected by the gravity. This is referred to as the "crossing trajectories effect". Csanady (1963) points out the "continuity effect" which is associated with the crossing trajectories effect in the presence of gravity, and results in the reduction of the velocity autocorrelation in directions normal to the gravity direction in comparison to that in the gravity direction. Further relations for the velocity autocorrelation, the diffusion coefficient and the turbulence intensity of particle loaded turbulent flows are obtained by assuming either the fluid velocity autocorrelation along the particle trajectory (Reeks 1971; Pismen and Nir 1978) or the fluid spectral density function (Mei *et al.* 1991).

Experimental studies of particle dispersion in turbulent flow are pioneered by Snyder and Lumley (1971) who investigate dispersion characteristics of solid particles. They find that the particle inertia decreases its turbulence intensity in comparison to the fluid turbulence intensity. Wells and Stock (1983) study the effects of crossing trajectories in a homogeneous decaying turbulent flow. Using an electric field, they succeed to eliminate or enhance the effects of gravity, and indicate that the long time asymptotic particle diffusion coefficient is primarily affected by the drift velocity and that

the particle time constant is mostly effective in modifying the particle turbulence intensity. The experimental and numerical results of Wen *et al.* (1992) in shear flows show that particles with large response times are centrifuged toward the outer edges of the vortex structures resulting in higher particle diffusivity coefficients.

Experimental studies of evaporating drops are somewhat limited in comparison to those of solid particle dispersion. Previous studies have been mostly directed to assess the performance of turbulence models in multiphase flows. Shearer *et al.* (1979) conduct experiments on axisymmetric particle-laden jet flows to appraise the performance of a locally homogeneous flow model for evaporating sprays. A somewhat similar experiment is conducted by Solomon *et al.* (1984) with different loading ratios. Further laboratory and numerical experiments are conducted by Nguyen *et al.* (1991) who investigate the effects of the interactions among the drops on the drag force and the evaporation rate.

The important role of the small scales of the carrier phase in the dynamics of heavy particles has motivated the use of direct numerical simulation (DNS). The implementation of DNS in two-phase flows is pioneered by Riley and Patterson (1974) to investigate particle dispersion in decaying isotropic turbulence. Using a low resolution simulation (32³ grid points) and a relatively small number of particles (432), they find that an increase of the particle inertia increases the velocity autocorrelation. McLaughlin (1989) simulates particle deposition in a channel flow and shows the tendency of particles to accumulate in the viscous sublayer. Squires and Eaton (1990, 1991a, 1991b) simulate both stationary and decaying turbulence fields with one- and two-way coupling. The results show the increase of the eddy diffusivity of heavy particles over that of the fluid particle for cases with one-way coupling. In the cases with two-way coupling they find that the fraction of energy at high wavenumbers of the spatial energy spectrum of turbulence increases relative to that at low wavenumbers as the mass loading ratio is increased. They also find that large particles tend to collect preferentially in regions of low vorticity and high strain. This is also true for the cases with one-way coupling. Elghobashi and Truesdell (1992, 1993); Truesdell and Elghobashi (1994) conduct similar studies. They consider the full equation for the particle motion and show that the Stokes drag is of primary importance for large density ratios. In the presence of both gravity and two-way coupling they show that energy is transferred from the gravity direction to other directions by the pressure-strain correlation. The settling velocity of heavy particles in isotropic turbulence is studied by Wang and Maxey (1993) for different particle time constants and drift velocities. The results show an increase of the settling velocity for all cases. The maximum increase in settling velocity is obtained when both the particle time constant and the drift velocity are comparable to the Kolmogorov scales.

This paper deals with the problem of dispersion and polydispersity of evaporating drops in an isotropic turbulent flow via DNS. The DNS generated data are statistically analyzed to extract important physical information pertaining to turbulent dispersion of evaporating drops. While the polydispersity phenomenon caused by evaporation is the primary subject of this study, some issues pertaining to dispersion of nonevaporating drops (solid particles) are also considered. In this consideration, a detailed parametric study is conducted and the results are comparatively assessed via existing analytical, experimental and, if applicable, DNS results. This assessment is very useful for validations of our computational methodology and for the parameterization in the evaporating drops simulations. In section 2 the problem formulation and numerical technique are described, in section 3 the DNS results are analyzed: the summary along with concluding remarks are furnished in section 4.

2. PROBLEM FORMULATION AND NUMERICAL TECHNIQUE

Since this is the first attempt in DNS of the evaporating drop dispersion in turbulent flows, the problem is formulated based on models and correlations which are well established. The implementation of these models requires several simplifying assumptions: these are discussed in this section within the framework of the mathematical formulation. We consider motion of spherical particles in an incompressible and isotropic turbulent flow. It is assumed that the dispersed phase is very dilute, thus the effect of particles on the carrier fluid is negligible. The momentum equation for each particle is considered in the Lagrangian frame of reference. In general, this equation

contains the Stokes drag, the Basset force, the force due to fluid pressure gradient, the inertia force of added mass, and gravity (Maxey and Riley 1983). However, the results of several previous studies, e.g. Elghobashi and Truesdell (1992), indicate that if the ratio of the density of the particle to the density of the carrier fluid is large, the Stokes drag and the gravity forces are dominant and the other forces can be assumed negligible. With this assumption the momentum equation for a single particle is expressed as:

$$\frac{dv}{dt} = \frac{18\mu}{\rho_p d_p^2} (\mathbf{u} - \mathbf{v}) + g\mathbf{e}, \quad [1]$$

$$\frac{d\mathbf{X}}{dt} = \mathbf{v}, \quad [2]$$

where \mathbf{u} and \mathbf{v} (boldface indicates vector) denote the fluid velocity at the particle location and the particle velocity, respectively; t is time, \mathbf{X} is the center position of the particle, \mathbf{e} is the unit vector in the gravity direction, g is the gravity constant; ρ_p and d_p denote the particle density and diameter, respectively; and μ is the fluid viscosity. All of the variables are normalized by reference scales of length, L_0 , velocity, U_0 , and density, ρ_0 . The length scale is conveniently chosen such that the normalized size of the simulation box is 2π and the velocity scale is found from the box Reynolds number, $Re_0 = (\rho_0 U_0 L_0 / \mu)$. The fluid density is used as the scale for density.

In the simulations of non-evaporating (solid sphere) particles, the particle diameter remains constant. For the evaporating particles, the rate of diameter reduction is modeled by the d^2 -law (Strehlow 1985):

$$d_p^2 = d_{p0}^2 - \kappa t, \quad [3]$$

where d_{p0} is the initial diameter of the particle and the depletion rate is given by $\kappa = 8\Gamma \ln(1 + B_M) C_{Re}$, where Γ is the mass diffusivity coefficient and B_M is the transfer number (Spalding 1953). The parameter C_{Re} is a correction factor to account for the convective effects (Ranz and Marshall 1952):

$$C_{Re} = 1 + 0.3 Re_p^{0.5} Sc_p^{0.333}, \quad [4]$$

with Re_p and Sc_p representing the particle Reynolds and Schmidt numbers, respectively. It is assumed that the flow is isothermal and that evaporation is due to a constant temperature difference between the drop and the fluid. This model is in accord with that of several laboratory experiments (e.g. Shearer *et al.* 1979). In a dilute flow, the ratio of the mass of the particle to the mass of the carrier fluid is very small and it is assumed that all the particles are in contact with the carrier fluid during evaporation. Therefore, the variation of κ is only due to C_{Re} . The "particle time constant" (τ_p) is defined by:

$$\tau_p(t) = \frac{\rho_p d_p^2}{18\mu} = \tau_{p0} - \tau_e t, \quad [5]$$

where $\tau_{p0} = (\rho_p d_{p0}^2 / 18\mu)$ denotes the initial particle time constant, and:

$$\tau_e = C_{Re} \tau_{e0}, \quad \tau_{e0} = \frac{4\rho_p \Gamma}{9\mu} \ln(1 + B_M). \quad [6]$$

By introducing a drift velocity, $v_{dr} = \tau_{p0} g$, [1] is expressed as:

$$\frac{dv}{dt} = \frac{1}{\tau_p} (\mathbf{u} - \mathbf{v}) + \frac{1}{\tau_{p0}} v_{dr} \mathbf{e}. \quad [7]$$

The particle Reynolds number is defined as: $Re_p = (\rho_f d_p |\mathbf{u} - \mathbf{v}|) / \mu$ with ρ_f denoting the carrier fluid density. Following Wang and Maxey (1993) the Reynolds number is related to the Kolmogorov time (τ_k) and velocity (v_k) scales with $v = \tau_k v_k$, where $v = \mu / \rho_f$ is the fluid kinematic viscosity:

$$Re_p = \left(\frac{18\tau_p}{v\rho_p/\rho_f} \right)^{1/2} |\mathbf{u} - \mathbf{v}| = 4.243 \left(\frac{\rho_f}{\rho_p} \right)^{1/2} \left(\frac{\tau_p}{\tau_k} \right)^{1/2} \frac{|\mathbf{u} - \mathbf{v}|}{v_k}. \quad [8]$$

The density ratio is kept constant ($\rho_f/\rho_p = 10^{-3}$) in all the simulations.

With the assumption of dilute particles, the Eulerian equations governing the carrier gas transport are solved independently to determine the u -field. With the assumptions of incompressible, isothermal flows this field influences dispersion, but not the other way around (i.e. one-way coupling). Also, the possible corrections to the convective effects in the drop evaporation due to flow unsteadiness, and the modifications of the drag force due to drop evaporation are not considered. The DNS of the carrier fluid is based on a spectral collocation scheme involving Fourier basis functions (Givi and Madnia 1993). The turbulent flow is assumed isotropic with triply periodic boundary conditions, and is forced at low wavenumbers to maintain a stationary (non-decaying) turbulent field (Givi 1989). Equations [1] and [2] are integrated in time using a second order accurate Runge-Kutta numerical scheme. The fluid velocity at the particle location is evaluated by a fourth order accurate Lagrange four point interpolation scheme.

3. RESULTS

Table 1 provides a listing of the flow parameters considered in the simulations. In this table, Re_λ is the flow Reynolds number based on the Taylor length scale (λ) and the root mean square of the flow velocity (u'), k_{\max} denotes the highest resolved wavenumber after dealiasing, η represents the Kolmogorov length scale, u' is the root mean square of fluctuating velocity, and l is the integral length scale determined from the energy spectrum $E(k)$:

$$l = \frac{\pi}{2u'^2} \int_0^\infty \frac{E(k)}{k} dk.$$

The parameters listed in table 1 are used in the simulations of both non-evaporating and evaporating drops. All the simulations are performed on 64^3 collocation points. In order to determine the appropriate number of particles, some preliminary simulations are conducted with 16^3 , 21^3 , and 25^3 particles. In agreement with the results of similar tests performed by Elghobashi and Truesdell (1992) it is found that 21^3 particles provide sufficient accuracy. In the simulations of the non-evaporating and constant rate evaporating particles, 21^3 particles are tracked. In the simulations of variable rate evaporating particles 25^3 particles are considered. In the discussion below $\langle\langle \cdot \rangle\rangle$ and $\langle \cdot \rangle$ denote the Lagrangian and Eulerian average values, respectively. The time averaged quantity is denoted by an overbar. In the presentation of the results, time is normalized with the eddy turn over time, $l u'$.

3.1. Dispersion of non-evaporating particles

The purpose of simulations considered in this subsection is threefold: (1) to validate our present computational methodology by comparison with previous DNS results, (2) to appraise the performance of some of the recent models via comparative assessment with present DNS results, and (3) to identify the range of parameters in the evaporating drop simulations (discussed below) and to compare present results with those in the presence of evaporation.

In the simulations here, the particles are initially distributed uniformly within the box and are released with the same velocity as that of the local fluid particle. In order to obtain stationary conditions, the particles are allowed to interact with the flow for more than three eddy turnover times before data are extracted for statistical analysis. A measure of stationarity is the temporal variation of $\langle\langle Re_p \rangle\rangle$ as shown in figure 1 for four different τ_p values with zero gravity. This figure shows that a nearly stationary level is reached after an initial steep increase with a noticeable overshoot for cases with $\tau_p > \tau_\lambda$. The magnitude of $\langle\langle Re_p \rangle\rangle$ at the stationary condition increases with the increase of τ_p due to the larger slip velocity experienced by heavier particles.

Table 1. Flow parameters used in the simulations

Re	ηk_{\max}	τ_λ	v_λ	u'	l
41	1.41	8.229	5.72×10^{-4}	0.019	1.068

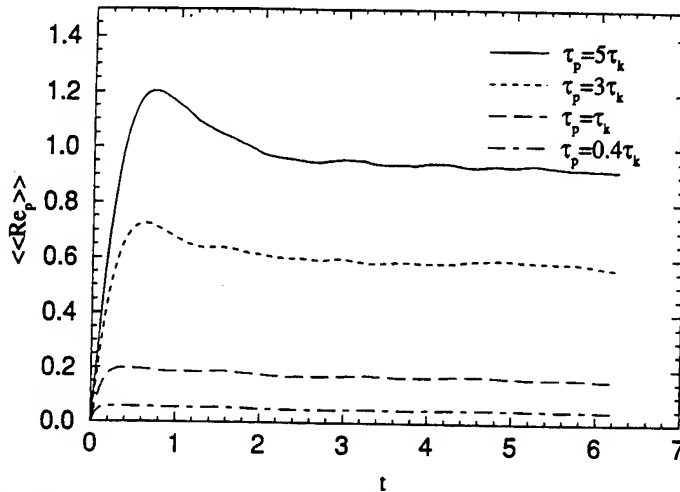


Figure 1. Temporal variation of $\langle\langle Re_p \rangle\rangle$ for different values of the particle time constant.

It is useful to consider the Fourier transform of [7] (Chao 1964). This transform in time for $\mathbf{w} = \mathbf{v} - v_{dr}\mathbf{e}$ yields:

$$\frac{E_p^p(\omega)}{E_u^f(\omega)} = \frac{1}{1 + \tau_p^2 \omega^2}, \quad [9]$$

where the spectral density function of the fluid velocity evaluated on the particle trajectory is $E_u^f(\omega) = \langle\langle \hat{u}_i(\omega) \hat{u}_j^*(\omega) \rangle\rangle$ ($\hat{\cdot}$ indicates the variable in the Fourier space, $*$ denotes complex conjugate, and ω is the frequency), and $E_p^p(\omega) = \langle\langle \hat{w}_i(\omega) \hat{w}_j^*(\omega) \rangle\rangle$ is the spectral density function of the particle velocity. The decrease of the ratio of $E_p^p(\omega)$ to $E_u^f(\omega)$ with the increase of τ_p indicates that heavy particles have a less tendency to adjust to the flow fluctuations. Equations [9] also shows that $E_p^p(\omega)$ deviates more from $E_u^f(\omega)$ as ω increases. Therefore, the ability of the heavy particle to follow the fluid fluctuations decreases at high frequencies.

Mei *et al.* (1991) obtain a solution for the particle turbulence intensity $\langle\langle w^2 \rangle\rangle$, and the particle diffusion coefficient, ϵ^p , by assuming the form of the spectral density function as proposed by Kraichnan (1970). They consider contributions of all the forces acting on the particle but suggest that only the Stokes drag and the Basset forces need to be retained. Their final results for cases in which the Basset force is neglected, are compared with our DNS data as will be presented below. However, it should be mentioned that although Mei *et al.* (1991) consider a wide range of τ_p and v_{dr} values, our DNS results indicate (not shown) that for $\tau_p > 5\tau_k$ and $v_{dr} > 5v_k$ the particle Reynolds number becomes considerably larger than unity and is beyond the range of validity of the Stokes drag. Therefore, we limit our parameter range to $\tau_p \leq 5\tau_k$ and $v_{dr} \leq 5v_k$.

Figure 2 shows the particle velocity autocorrelation for four particle time constants at different drift velocities. The autocorrelation of the fluid particle ($\tau_p = 0$) is also shown for comparison. The velocity autocorrelation is defined as:

$$R_{xx}^p(t) = \frac{\langle\langle w_x(0)w_x(t) \rangle\rangle}{\langle\langle w_x^2(0) \rangle\rangle} \quad \alpha = 1, 2, 3 \quad [10]$$

where α refers to the coordinate direction (with no summation over repeated Greek indices). In order to reduce the effect of anisotropy, the autocorrelations are calculated by averaging over the three directions. These averaged autocorrelations are denoted by R^p (no subscripts). In cases with a non-zero drift velocity, three different simulations are performed for each case (using the same velocity field for the fluid) with the gravity direction changing for each simulation. Therefore, the velocity autocorrelation in the gravity direction is evaluated by averaging over the three gravity directions, and those in no-gravity directions are averaged over six other directions considered in three simulations. Inspection of figure 2 reveals that variations of the particle velocity autocorrelation with the particle time constant and the drift velocity are in accord with previous observations (e.g. Csanady 1963; Wells and Stock 1983).

The variations of the particle turbulence intensity $\langle\langle w^2 \rangle\rangle$ (normalized by the fluid turbulence intensity $\langle u^2 \rangle$) due to the particle time constant and the drift velocity are shown in figure 3 and are compared with theoretical results of Mei *et al.* (1991). The temporal averages are evaluated by data sampling over more than three eddy turnover times. This figure indicates that, as the particle time constant is increased the particle turbulence intensity is reduced. In other words, the increase of the particle time constant decreases the drop tendency to follow the fluid motion. As τ_p is decreased, $\langle\langle w^2 \rangle\rangle/\langle u^2 \rangle$ approaches unity. This is expected since $w_i = u_i$ for $\tau_p = 0$. Although we have not performed simulations with $\tau_p < 0.4\tau_k$, the results suggest the existence of a plateau for $r_{dr} = 0$ near $\tau_p = 0$. This is also observed in the results of Mei *et al.* (1991).

Comparing the values of $\langle\langle w^2 \rangle\rangle/\langle u^2 \rangle$ in the no-gravity direction for $r_{dr} = v_k$ and $r_{dr} = 5v_k$ with those obtained for $r_{dr} = 0$ indicates the decrease of the particle turbulence intensity with the increase of gravity. Particles moving in the presence of a gravity field have a shorter time to interact with the instantaneous surrounding fluid particles in comparison with the particles moving in the zero

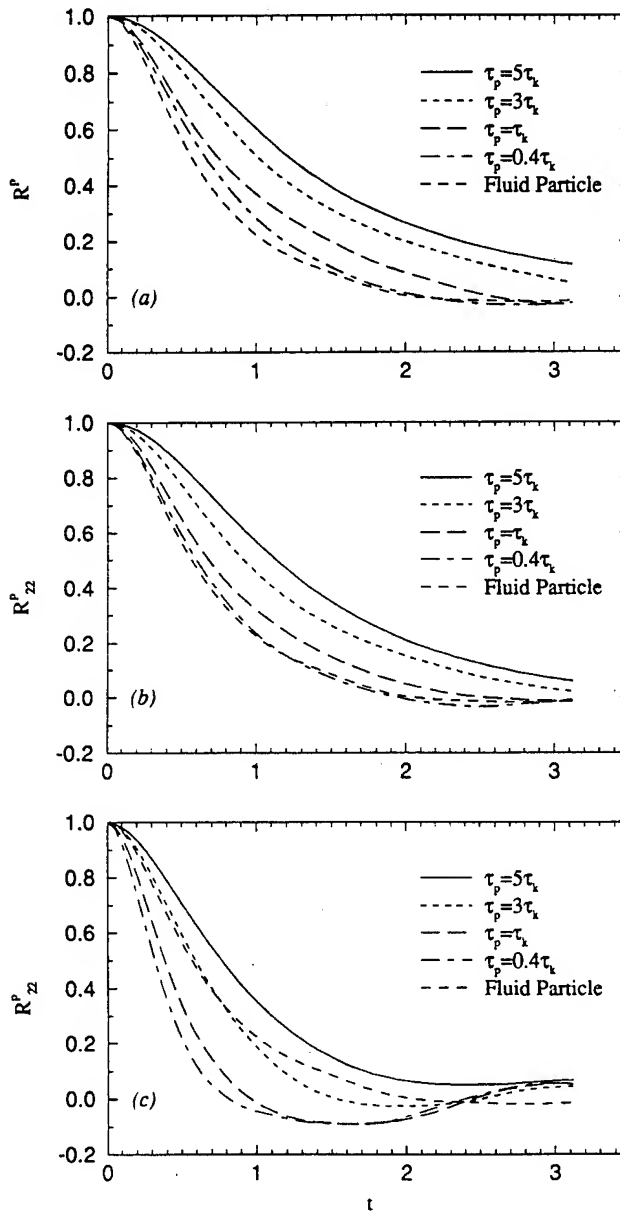


Figure 2. Particle velocity autocorrelations in the direction normal to the gravity direction. (a) $r_{dr} = 0$, (b) $r_{dr} = v_k$, and (c) $r_{dr} = 5v_k$.

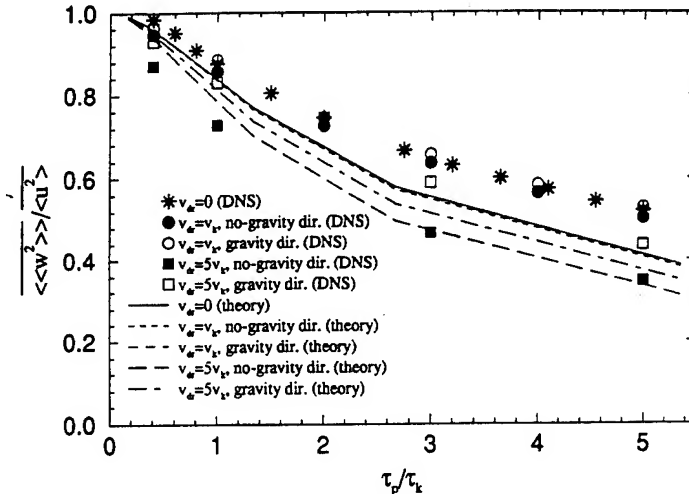


Figure 3. Variation of the particle turbulence intensity normalized with the fluid turbulence intensity with particle time constant.

gravity environment. However, as the particle time constant approaches zero, $\langle\langle w^2 \rangle\rangle / \langle u^2 \rangle$ approaches unity for all the v_{dr} values. This is due to the increase of particles' tendency to follow the fluid particle motion as the particle time constant is decreased. Figure 3 also shows that at a given particle time constant the turbulence intensity of the particle in the gravity direction is larger than that in the direction normal to the gravity direction.

Of central importance in the study of turbulent particle dispersion is the particle diffusion coefficient defined as (Hinze 1975):

$$\epsilon_{xz}^p(t) = \frac{1}{2} \frac{d}{dt} \langle\langle X_z^2(t) \rangle\rangle \quad z = 1, 2, 3. \quad [11]$$

For stationary particles, this coefficient is related to the velocity autocorrelation by:

$$\epsilon_{zz}^p(t) = \langle\langle w_z^2(0) \rangle\rangle \int_0^t R_{zz}^p(\tau) d\tau = \int_0^t \langle\langle w_z(0) w_z(\tau) \rangle\rangle d\tau. \quad [12]$$

The fluid particle diffusion coefficient ϵ_{zz}^f , is defined similarly by replacing w_z with u_z in [12]. Figure 4 shows the variations of the "asymptotic diffusion coefficient", $\epsilon^p(\infty)$ with the particle time constant and the drift velocity. Equation [12] is used for the determination of ϵ^p and the results are averaged in the three directions. Several observations are made from this figure: (i) in the absence of gravity ($v_{dr} = 0$) a peak is observed near $\tau_p = \tau_k$. The DNS results of Squires and Eaton (1991a) in stationary turbulence also show a similar behavior. However, this is in contrast to the analytical results of Pismen and Nir (1978) and Mei *et al.* (1991) which show a monotonic variation for $\epsilon^p(\infty)$ with τ_p . Squires and Eaton (1991a) attribute the difference between the analytical and DNS results to the sensitivity of the numerical results to the sample of large scale motions in forced turbulence; (ii) the increase of the drift velocity decreases the particle diffusion coefficient in both parallel and normal directions to the gravity direction. This behavior is also predicted by the models of Csanady (1963) and Mei *et al.* (1991); (iii) the diffusion coefficients are larger in the gravity direction than those in the direction normal to the gravity direction; however, the difference decreases with the increase of τ_p ; (iv) in agreement with the experimental results of Wells and Stock (1983) the asymptotic diffusion coefficients are more sensitive to the drift velocity than to the particle time constant.

Figure 4 also indicates that as the particle time constant approaches zero, for a constant drift velocity, the particle diffusion coefficient does not equate that of the massless fluid particle. This is in contrast to the behavior of the particle turbulence intensity which approaches the fluid turbulence intensity as $\tau_p \rightarrow 0$ (cf. figure 3). A decrease of the particle time constant, while the magnitude of the drift velocity is kept fixed, corresponds to an increase of the gravity coefficient.

Very small particles have small relative velocities and are capable of responding to local fluid fluctuations instantaneously. This results in the adjustment of the particle turbulence intensity to that of the fluid. However, since the effect of gravity on the carrier phase is neglected, by having a finite drift velocity the particles move quickly through the vortical structures. This decreases the particle velocity autocorrelation and therefore the diffusion coefficient.

3.2. Polydispersity of evaporating particles

One of the major differences between non-evaporating and evaporating particle dispersion phenomena is the lack of a stationary condition in the latter. When evaporating, the magnitude of τ_p continuously decreases with time; thus the momentum transfer between the particle and the surrounding fluid is in a transient condition. At a constant gravity level, the problem of evaporating particle dispersion is parametrized by: the initial particle time constant (τ_{p0}), the initial rate of evaporation (τ_{e0}), and the particle Schmidt number (Sc_p). In addition, due to the intrinsic non-stationary nature of the problem, the effects of initial conditions should also be considered. In the following simulations, the largest evaporation rate is chosen such that the velocity autocorrelation becomes close to zero by the time $\tau_p = 0.1\tau_{p0}$ (about 3.1 eddy turnover times). Very low τ_p values are not considered to avoid excessive computational requirements for particle tracking. Therefore, we set $\tau_{e0} = 0.9\tau_{ec}/3.1 = 0.29\tau_{ec}$ where τ_{ec} is introduced to relate the evaporation rate to the initial particle time constant.

First, we consider cases with constant rate of evaporation in which the decay of τ_p is the same for all particles. These cases are exemplified by neglecting the nonlinear term in [4], i.e. $C_{Re} = 1$. Figure 5 shows the velocity autocorrelation for evaporating particles. The autocorrelation of non-evaporating particles ($\tau_{ec} = 0$) is also presented for comparison. The initial position and velocity of the particles are taken from the simulations of nonevaporating particles at the same particle time constant. Therefore, the particles are stationary at time $t = 0$ before the onset of

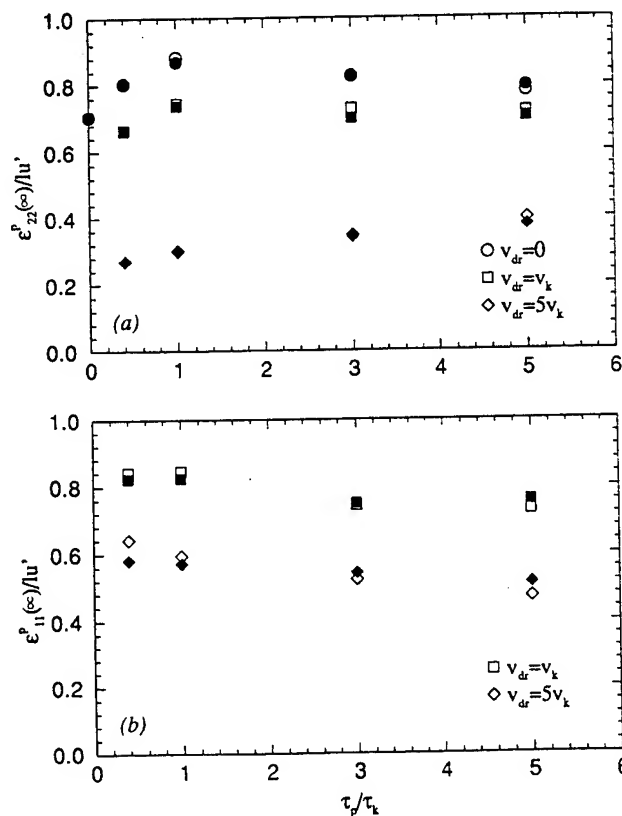


Figure 4. Variation of the diffusion coefficient for the heavy particle (hollow symbols) and the surrounding fluid particle (solid symbols) with the particle time constant: (a) in the direction normal to the gravity direction. (b) in the gravity direction.

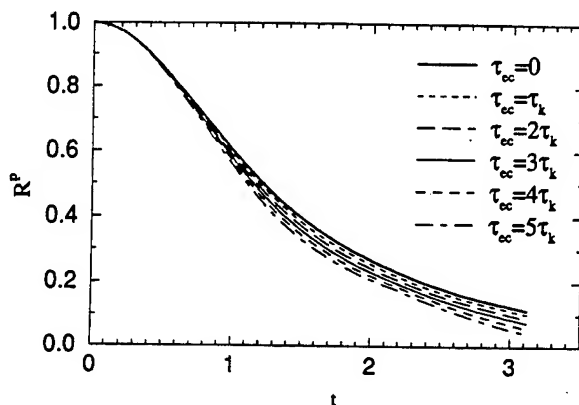


Figure 5. The velocity autocorrelation for the heavy particle at various evaporation rates for $\tau_{p0} = 5\tau_k$.

evaporation. The initial particle time constant is $\tau_{p0} = 5\tau_k$, and with a rate of evaporation of $\tau_{ec} = 5\tau_k$ the magnitude of τ_p is reduced to $0.5\tau_k$ by the end of the simulation. As expected, a decrease of the particle time constant results in the decrease of its velocity autocorrelation; the larger the evaporation rate the smaller the velocity autocorrelation at all times.

An important issue to address at this point is the speed of adjustment of the velocity of the evaporating particle to that of its surrounding fluid. As indicated in figure 1 when particles are released with a zero velocity relative to the fluid, there is a time delay before the average particle Reynolds number reaches a stationary value. Therefore, a comparison of the magnitude of $\langle\langle Re_p \rangle\rangle$ of the evaporating particle with those of the stationary non-evaporating particle at the same τ_p provides a reasonable indication of the speed of momentum adjustment. For the highest evaporation rate ($\tau_{ec} = 5\tau_k$) shown in figure 5, $\langle\langle Re_p \rangle\rangle$ ($\tau_p = 3\tau_k$) = 0.585 and $\langle\langle Re_p \rangle\rangle$ ($\tau_p = \tau_k$) = 0.173. These values are very close to those for stationary non-evaporating particles at the same particle time constant (0.589 and 0.172, respectively). This suggests that evaporating particles adjust quickly to their new conditions.

For a constant particle Schmidt number, the rate of evaporation becomes dependent on the magnitude of the particle Reynolds number and is different for each particle. Therefore, even with an identical initial τ_p value, the evaporation process results in polydispersity of drops. The remainder of this section is devoted to the study of the properties of the drop size distributions for different values of the particle time constant, the evaporation rate, and various initial conditions.

Figure 6 shows the temporal evolutions of the probability density function (pdf) of the variable $\tau_p^{1/2}$ (proportional to the particle diameter). In this simulation, $\tau_{p0} = 5\tau_k$, $\tau_{ec} = 5\tau_k$, and $Sc_p = 1.0$.

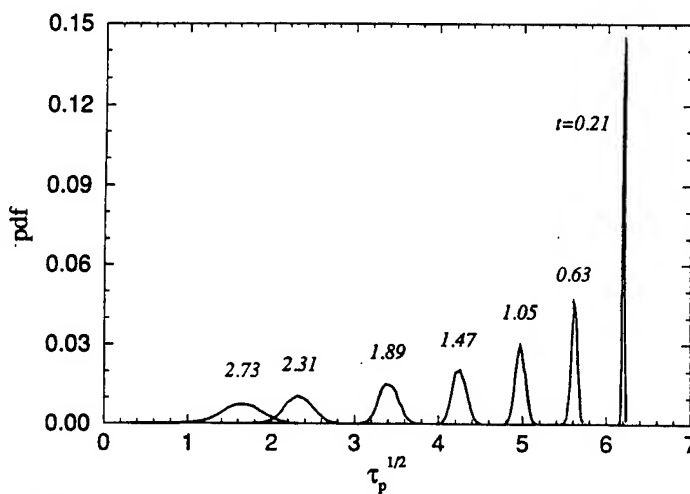


Figure 6. Pdfs of $\tau_p^{1/2}$ at different times for $\tau_{p0} = 5\tau_k$, $\tau_{ec} = 5\tau_k$, and $Sc_p = 1$.

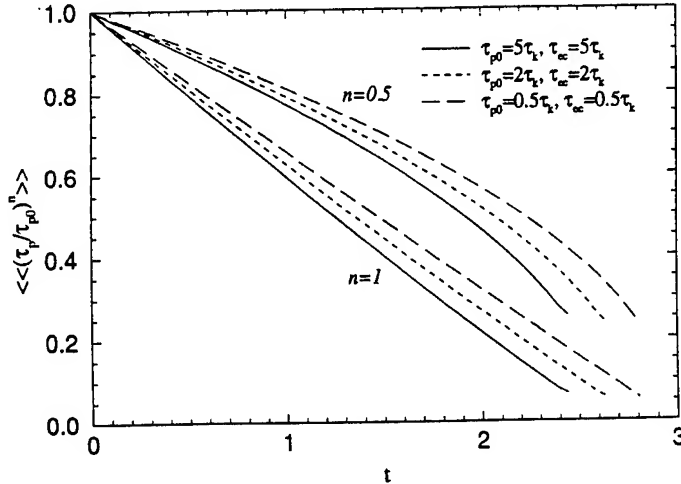


Figure 7. Temporal variations of $\langle\langle \tau_p / \tau_{p0} \rangle\rangle$ and $\langle\langle (\tau_p / \tau_{p0})^{1/2} \rangle\rangle$ for different initial particle time constants and evaporation rates.

The particles start to evaporate from a stationary condition at time $t = 0$, when the pdf is a delta function. At longer times the mean shifts towards smaller $\tau_p^{1/2}$ values due to reduction of the particle size. The variations of $\langle\langle (\tau_p / \tau_{p0})^{1/2} \rangle\rangle$ and $\langle\langle \tau_p / \tau_{p0} \rangle\rangle$ are shown in figure 7 for simulations in which three different groups of particles are considered; $\tau_{p0} = 5\tau_k$, $2\tau_k$, and $0.5\tau_k$ with corresponding initial evaporation rates of $\tau_{e0} = 5\tau_k$, $2\tau_k$, and $0.5\tau_k$, respectively. Equation [5] indicates that for a constant rate of evaporation, τ_p decreases linearly with time. When the evaporation rate is variable, a deviation from the linear behavior is expected. However, figure 7 shows that for the cases considered here the deviation is relatively small. This is mainly due to the one-way coupling assumption. Obviously, larger particles show a more nonlinear behavior than the smaller ones due to their larger Re_p values. The magnitude of the particle diameter decreases nonlinearly from the beginning and the rate of nonlinearity increases with time. This is easily explained by comparing the rate of change of τ_p and $\tau_p^{1/2}$. For a constant rate of change of τ_p (which is a reasonable assumption for the cases considered here), $d(\tau_p^{1/2})/dt \sim \text{constant}/\tau_p^{1/2}$. Therefore, the rate of the diameter decrease becomes larger as the size of the particle is reduced. Notice that although the initial evaporation rate for each group has been chosen proportional to its initial particle time constant, the curves of $\langle\langle (\tau_p / \tau_{p0})^{1/2} \rangle\rangle$ and $\langle\langle \tau_p / \tau_{p0} \rangle\rangle$ for different groups of particles are not identical. This is due to the nonlinear variation of Re_p with τ_p as observed in figure 1. When τ_p is increased by a factor of 10, the corresponding $\langle\langle Re_p \rangle\rangle$ is increased by a factor of about 15.

Shortly after the onset of evaporation, a wide range of droplet sizes is observed. In figure 8 the pdfs of $\tau_p^{1/2}$ are considered at an intermediate time ($t = 1$) and are shown to be close to Gaussian for all the cases. In figure 9 the temporal variations of the skewness and the kurtosis of the pdfs for the three cases are considered. At short times the pdfs are skewed towards the smaller sizes while at intermediate times they become more symmetric. Although the differences in Re_p for the particles is responsible for the generation of size distribution at each time, the mechanism which results in variation of Re_p is different at short and at long times. At short times, the diameters of all the particles are approximately the same and the changes in Re_p are due to the differences in the spatial locations of the particles. At long times, the differences in Re_p are also dependent on the size variations. In general, at intermediate times the pdf of the particle size is approximately Gaussian. However, the larger the initial particle time constant, the closer the pdf is to Gaussian. This is evident from figure 9 that shows larger deviations from Gaussian skewness and kurtosis values as the initial size of the particles is decreased. Larger particles with $\tau_{p0} = 5\tau_k$ and $2\tau_k$ attain pdfs with slightly positive skewness after about one eddy turnover time. The skewness of the particles with $\tau_{p0} = 0.5\tau_k$ remains negative for the entire simulation. In general, for large particles, after an initial transient time which depends on the particle size the pdfs become very close to Gaussian. But near the end of the simulations again the pdfs start to deviate from Gaussian. In fact, when the skewness and the kurtosis of different cases are plotted versus the instantaneous

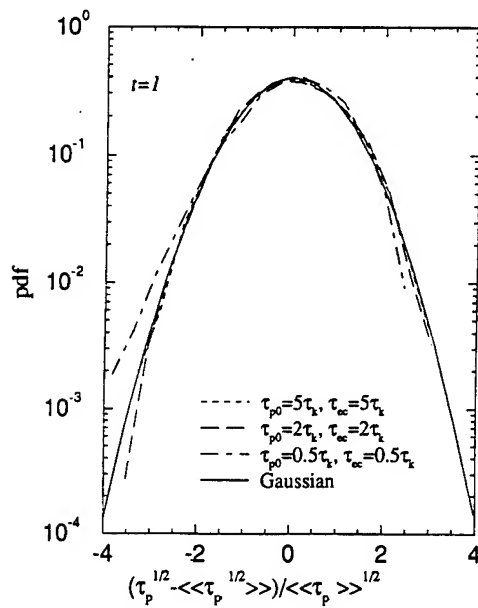


Figure 8. Normalized pdfs of $\tau_p^{1/2}$ for different particle time constants and evaporation rates at $t = 1$.

mean particle time constant, the pdfs become more non-Gaussian as $\langle\langle\tau_p\rangle\rangle$ becomes smaller than τ_k . This is due to nonlinearity of the rate of decrease of $\tau_p^{1/2}$ at small particle time constants. As indicated above, as the size of the drop decreases, the rate of change of its diameter increases and figure 7 shows that this effect is more pronounced when the drop time constant is small. Therefore, the diameters of the smaller drops decrease faster than the diameters of the larger drops and the pdf becomes skewed towards smaller diameter values.

We now consider the pdfs of particles with different initial evaporation rates. In figure 10 the temporal variations of the skewness and kurtosis for particles with $\tau_{p0} = 5\tau_k$ and initial evaporation rates of $\tau_{ee} = 5\tau_k$, $2.5\tau_k$, τ_k , and $0.4\tau_k$ are presented. The initial condition for these particles is different than those considered earlier. At $t = 0$ the particles are released with a zero velocity relative to the local fluid particle. An initial transient time is needed before the particles attain momentum equilibrium with the flow. Figure 10 indicates that this initial transient time appears independent of the rate of evaporation and is about the same as that required by the non-evaporating particles with $\tau_p = 5\tau_k$ to reach the stationary condition (cf. figure 1). After the momentum equilibrium is reached, the pdfs of $\tau_p^{1/2}$ tend to become Gaussian. Towards the end of the simulation, the pdfs for cases with higher evaporation rates ($\tau_{ee} = 5\tau_k$ and $2.5\tau_k$) become

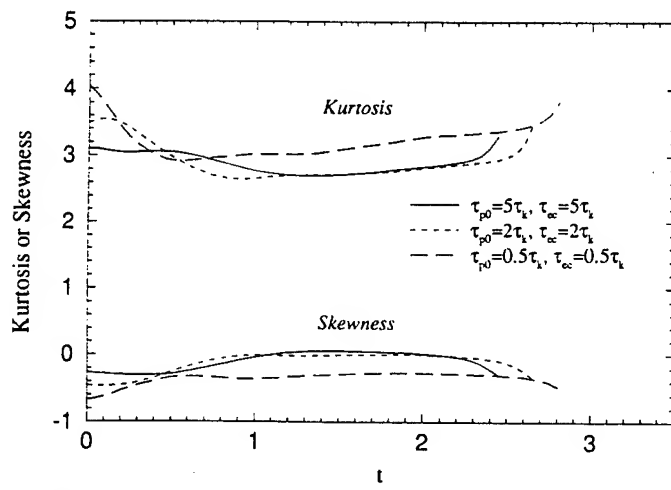


Figure 9. Temporal variations of the kurtosis and skewness of $\tau_p^{1/2}$.

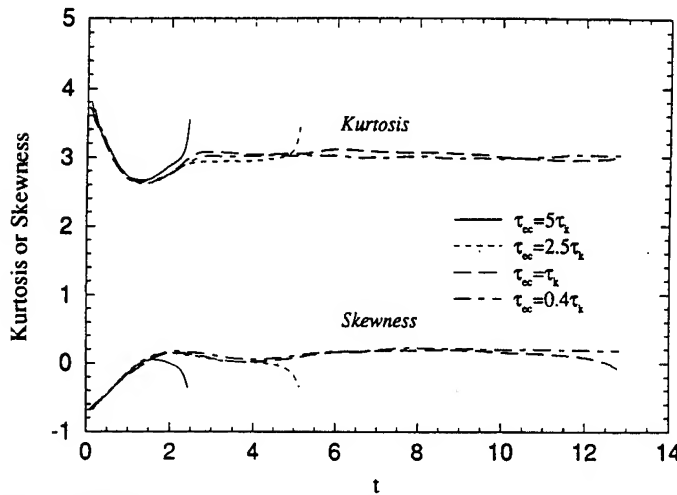


Figure 10. Temporal variation of the kurtosis and skewness of $\tau_p^{1/2}$ for an initial particle time constant $\tau_{p0} = 5\tau_k$ at different evaporation rates.

strongly non-Gaussian. However, as the evaporation rate decreases the pdfs tend to remain Gaussian. This is due to the smaller $\tau_p^{1/2}$ variances for cases with smaller evaporation rates. Therefore, as the evaporation rate is decreased a "narrower" pdf is obtained and the difference between the diameters of different drops is decreased. This, in turn, diminishes the effect of the nonlinearity of the rate of change of diameter which tends to skew the pdfs.

Effect of particle Schmidt number. The magnitude of the particle Schmidt number influences the rate of evaporation as indicated by [4]. Figure 11 shows the temporal variation of the Lagrangian average of the nonlinear part of [4] for two different particle time constants and three Sc_p values. Two different initial conditions are considered: stationary (solid symbols) and non-stationary (hollow symbols). In non-stationary cases, the initial particle velocity is zero relative to the local fluid; therefore, the initial value of $\langle\langle C_{Re} - 1 \rangle\rangle$ is zero. After an initial increase, this value starts to decrease due to the decrease of the particle size and consequently the decrease of the particle Reynolds number. The comparison of the results in the stationary and the non-stationary cases at the same $Sc_p = 1$ reveals that for large particles, the value of $\langle\langle C_{Re} - 1 \rangle\rangle$ in the non-stationary case overshoots that in the stationary case. This is due to the variation of Re_p in time which experiences an overshoot before it reaches a stationary value (figure 1). For small particles Re_p does not overshoot, and neither does $\langle\langle C_{Re} - 1 \rangle\rangle$. In general, the increase of Sc_p enhances the contribution of the nonlinear part of [4]; however, for the cases considered here with Sc_p as large as 5 this contribution is always less than 50% of the constant evaporation rate ($\langle\langle C_{Re} - 1 \rangle\rangle < 0.5$).

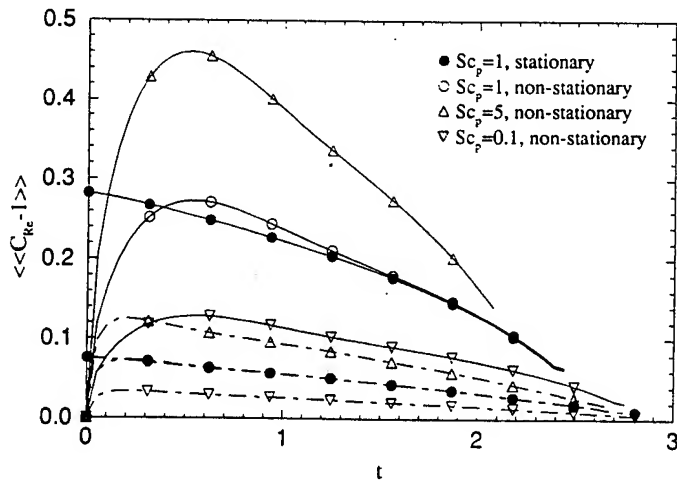
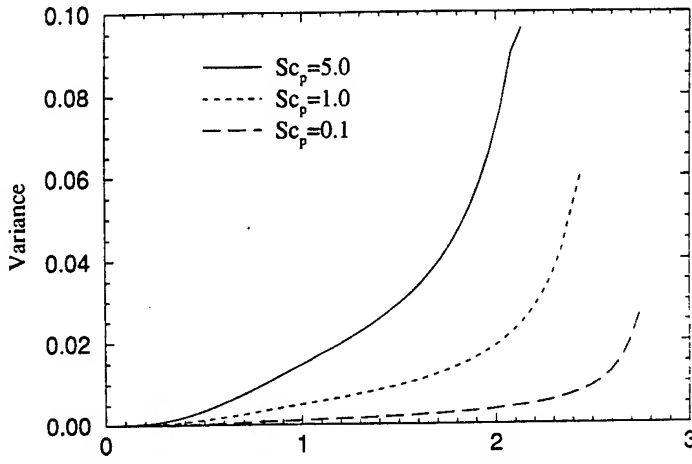


Figure 11. Variation of $\langle\langle C_{Re} - 1 \rangle\rangle$ with time. (—) $\tau_{p0} = 5\tau_k$, $\tau_{ev} = 5\tau_k$; (----) $\tau_{p0} = 0.5\tau_k$, $\tau_{ev} = 0.5\tau_k$.

Figure 12. Temporal variations of the variance of $\tau_p^{1/2}$. $\tau_{p0} = 5\tau_k$, $\tau_{ee} = \tau_k$.

In figure 12 the temporal evolution of the variance of $\tau_p^{1/2}$ is shown for three different particle Schmidt numbers. The initial particle time constant is $\tau_{p0} = 5\tau_k$ for all cases. As the particle Schmidt number increases the variance also increases. This means that at larger Sc_p , a wider range of particle sizes are present. At $Sc_p = 5\tau_k$ the difference between the maximum and the minimum values at the end of the simulation is about 0.41 while the corresponding difference for $Sc_p = 0.1$ is about 0.24. Therefore, while the minimum value of $(\tau_p/\tau_{p0})^{1/2}$ at the end of the simulation is the same for both cases, the case with the higher Sc_p value contains a higher number of larger particles. This is due to the fact that the increase of Sc_p enhances the effect of Re_p on evaporation. The skewness of the particle distribution towards smaller particles is also evident by comparing the distance from the mean value to the minimum and the maximum value at all times. Examination of the temporal variations of the skewness of $\tau_p^{1/2}$ revealed that, in all the cases, the skewness takes negative values at small times and then increases with time. For large τ_{p0} values, the skewness reaches small positive values for intermediate times. But it decreases and takes negative values close to the end of the simulation when τ_p values for most of the particles become small. Particles with smaller τ_{p0} values, have negative skewness during the entire simulation. In general, the effect of the particle time constant is more significant than the particle Schmidt number on the skewness of the particle sizes.

Effect of spray size. In many practical applications the size of the spray is smaller than the characteristic size of the flow. As the spray evolves with flow, dispersion of the particles is strongly affected by the interactions between the spray and the carrier fluid. It is expected that the size of the spray relative to the characteristic length scale of turbulence plays an important role on dispersion. In the case of evaporating particles this becomes even more important since the size distribution is also directly affected by the interaction between the droplets and the flow at different scales. In this subsection we investigate the effect of the relative size of the spray on the particle size distribution. We initialize the problem by randomly distributing the particles inside a cubic box which is located at the center of the computational box. All particles have the same size and a zero velocity relative to the local fluid element at $t = 0$. The length of one side of the particle-containing box is denoted by S and indicates the spray size.

First we consider a case with initial spray size $S_w/l = 0.28$. In figure 13 the variations of the kurtosis and skewness of $\tau_p^{1/2}$ are shown for two different initial particle time constants. On the same figures the temporal variations of the spray size are also shown. This size is determined by the dimension of the smallest box containing all of the particles at any time. Figure 13 reveals that the kurtosis and skewness of the particle size are very different from those corresponding to Gaussian. In contrast to the cases discussed earlier, the skewness is positive throughout the simulation. For both of the particle time constants considered, the growth of the spray size is nearly linear in time. This can be interpreted as a constant diffusion velocity which is about the same in both cases. The normalized spray size increases from its initial value to a final value corresponding to the ratio of the computational box to the integral length scale.

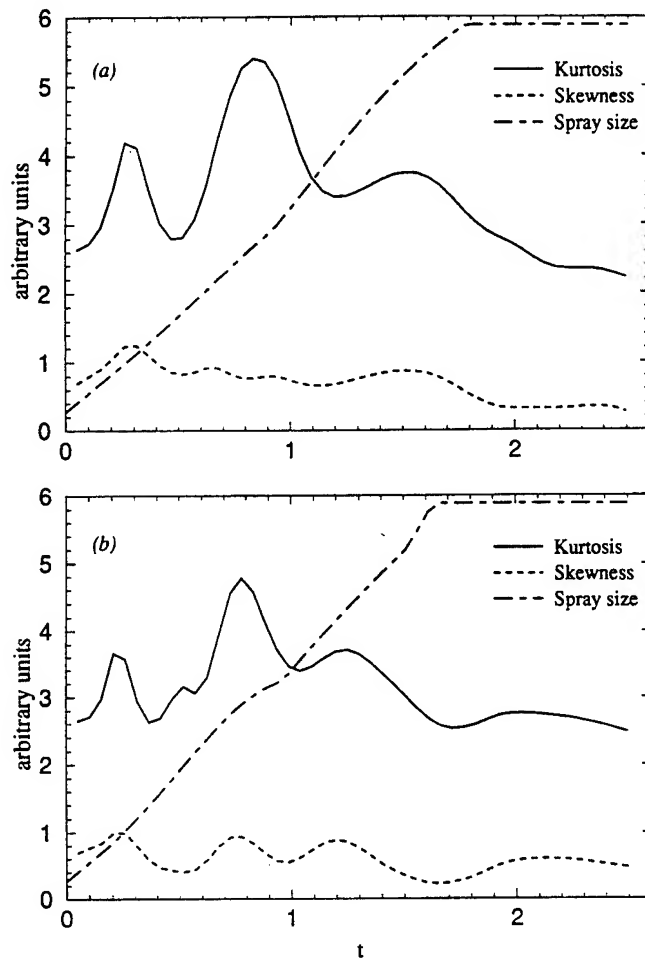


Figure 13. Temporal variations of the kurtosis and skewness of $\tau_p^{1/2}$, and spray size for $Sc_p = 1$ and $S_0/l = 0.28$. (a) $\tau_{p0} = 5\tau_k$ and $\tau_{ec} = 5\tau_k$. (b) $\tau_{p0} = 0.5\tau_k$ and $\tau_{ec} = 0.5\tau_k$.

Next, we consider cases with different S_0/l values. Examination of the temporal variations of the kurtosis and skewness of $\tau_p^{1/2}$ for cases with different S_0 and τ_{p0} values revealed that as the initial spray size is increased, the oscillations in the skewness and the kurtosis diminish and the values

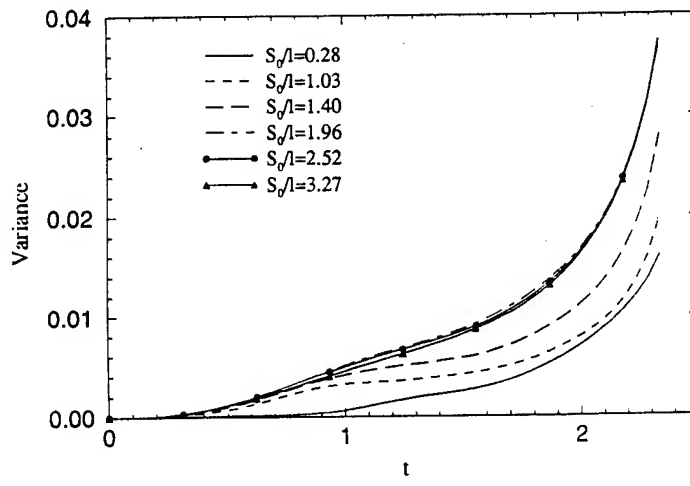


Figure 14. Temporal variation of the variance of $\tau_p^{1/2}$ for different initial spray sizes. $\tau_{p0} = 5\tau_k$, $\tau_{ec} = 5\tau_k$ and $Sc_p = 1$.

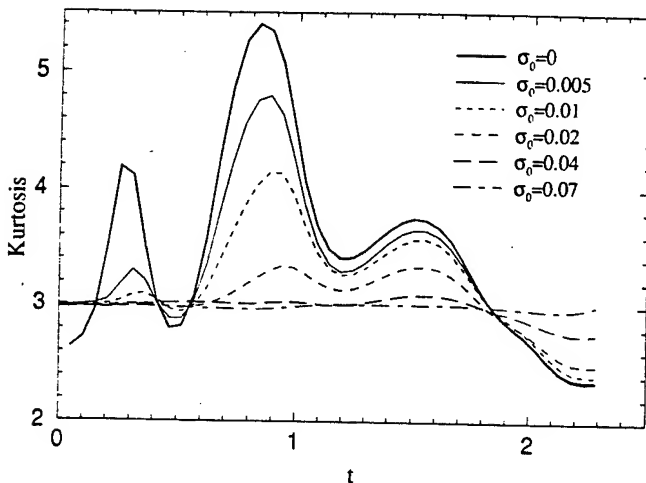


Figure 15. Temporal variation of the kurtosis of $\tau_p^{1/2}$ for different values of the initial standard deviation.
 $\tau_{p0} = 5\tau_k$, $\tau_{ee} = 5\tau_k$ and $S_0/l = 0.28$.

approach those corresponding to the Gaussian distribution. Figure 14 shows the time variation of the variance of $\tau_p^{1/2}$ for several values of S_0/l . The initial particle time constant and the evaporation rate are $\tau_{p0} = 5\tau_k$ and $\tau_{ee} = 5\tau_k$, respectively. As the initial spray size is increased, the instantaneous rate of variance increase approaches an asymptotic value corresponding to the case with $S_0/l = 1.96$. This implies that if the initial spray size is larger than about twice the integral length scale, the effect of the spray size on the variance is negligible. In general, three distinct regions are observed on the curves shown in figure 14. The first region corresponds to initial times $0 < t < 0.3$ during which the rate of variance growth is very small. Since particles are released with zero relative velocity, they have the same initial Re_p values and consequently the same initial evaporation rate. Therefore, at initial times the variance remains close to zero. As the particle Reynolds number increases, the particles experience different evaporation rates and the variance starts to increase. Figure 11 shows that the time interval $0 < t < 0.3$ corresponds to the period during which $\langle\langle C_{Re} \rangle\rangle$ adopts large values. At large particle Reynolds numbers, in the second region of the curves of figure 14 ($0.3 < t < 2$), the variance grows with a larger rate. The third region ($t > 2$) is marked by the largest rate of variance growth. This is explained by considering figure 7 which shows that the rate of reduction of $\tau_p^{1/2}$ increases at large times when the size of the particles is small.

Effect of the initial particle size distribution. The observed deviations of the particle size pdfs from the Gaussian for small S_0/l values motivate the analysis of cases with initial Gaussian diameter pdfs. These cases are characterized by the initial standard deviation of $\tau_p^{1/2}$ denoted by σ_0 . The cases considered in previous subsections refer to $\sigma_0 = 0$. The velocity and the position of the particles are initialized randomly similar to previous cases. The size of each particle is selected randomly from a Gaussian seed with specified values for the mean and the standard deviation. In order to prevent very small and very large particle time constants, the standard deviations considered are relatively small.

Figure 15 shows the kurtosis of $\tau_p^{1/2}$ for cases with several values of the initial standard deviation. The initial mean particle time constant is $\langle\langle \tau_{p0} \rangle\rangle = 5\tau_k$. The case with the smallest initial spray size ($S_0/l = 0.28$) is considered as the pdfs for this case deviate more from Gaussian; therefore, the effects of the initial size distribution are amplified. As expected, by increasing the initial standard deviation, the pdf becomes closer to Gaussian. For the range of $\langle\langle \tau_{p0} \rangle\rangle$ and S_0/l values considered here, a nearly perfect Gaussian pdf is achieved when the initial standard deviation is $\sigma_0 = 0.07$. The effect of the initial standard deviation is more pronounced at early times. An interesting feature observed in figure 15 is the similarity of the oscillations of the kurtosis curves for different cases. This verifies our previous observation in that these oscillations are due to interactions between the particles and the large structures of the flow. Since the initial spray size is identical, a similar oscillation pattern is experienced in all the cases.

Next, we consider the effect of the initial spray size for a constant initial standard deviation of

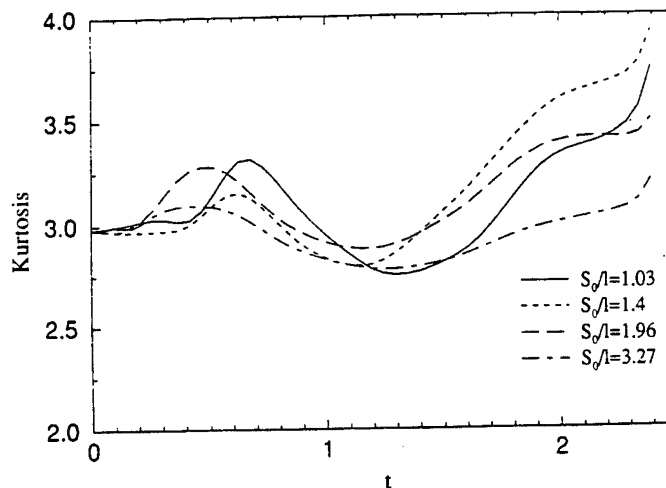


Figure 16. Temporal variation of the kurtosis of $\tau_p^{1/2}$ for different initial spray sizes. $\tau_{p0} = 5\tau_k$, $\tau_{ee} = 5\tau_k$ and $\sigma_0 = 0.02$.

$\sigma_0 = 0.02$. Figure 16 shows the temporal variation of the kurtosis of $\tau_p^{1/2}$. Similarly to the cases with $\sigma_0 = 0$, the pdf becomes more Gaussian as the initial spray size increases. Contrary to the cases with the same S_0/l , the kurtosis curves of figure 16 are not similar. The time of the occurrence of the first peak is decreased as the initial spray size is increased. This again is due to the interaction of the spray with the larger scales of the flow as the spray size increases. The examination of the variance of $\tau_p^{1/2}$ (not shown) for different cases indicated that the variance curves collapse for $S_0/l \geq 1.4$ when $\sigma_0 = 0.02$ in contrast to $S_0/l \geq 1.96$ when $\sigma_0 = 0$.

Finally, for completion, several cases are considered with initially non-Gaussian drop size distributions. For these cases, the initial distribution consists of two distinct uniform-size groups of drops (the initial pdf of $\tau_p^{1/2}$ is a double delta). The drops are initially injected into the flow with zero velocity relative to the local fluid and $Sc_p = 1$. Figure 17 shows the temporal evolution of the pdf of $\tau_p^{1/2}$ for a case with $\langle\langle\tau_{p0}\rangle\rangle = 5\tau_k$ and $\sigma_0 = 0.128$. As indicated in the figure, by the time $t = 0.52$ the two initially segregated branches of the pdf start to merge resulting in the increase of the $\tau_p^{1/2}$ kurtosis (figure 18). At $t \approx 2.35$ the double-hump pdf evolves into a single peak one; at the final time ($t = 2.62$), the pdf is close to Gaussian. However, it is also possible that with a large initial separation between the drop time constants (large σ_0) a single-hump pdf is not attained during the evaporation period. Figure 18 shows that as $\langle\langle\tau_{p0}\rangle\rangle$ is increased, for the same σ_0 , the kurtosis of $\tau_p^{1/2}$ deviates less from that of Gaussian. Inspection of the pdf evolution for the case with $\langle\langle\tau_{p0}\rangle\rangle = 1$

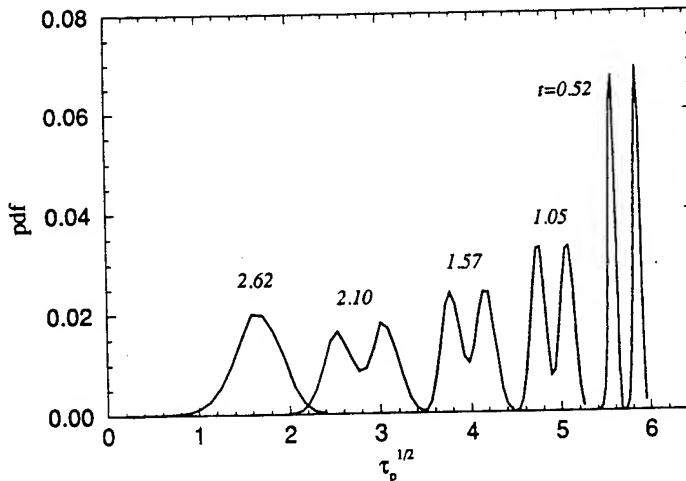


Figure 17. Pdfs of $\tau_p^{1/2}$ at different times. The initial pdf is double delta with drop time constants at $4.8\tau_k$ and $5.2\tau_k$. $\tau_{ee} = 5\tau_k$ and $Sc_p = 1$.

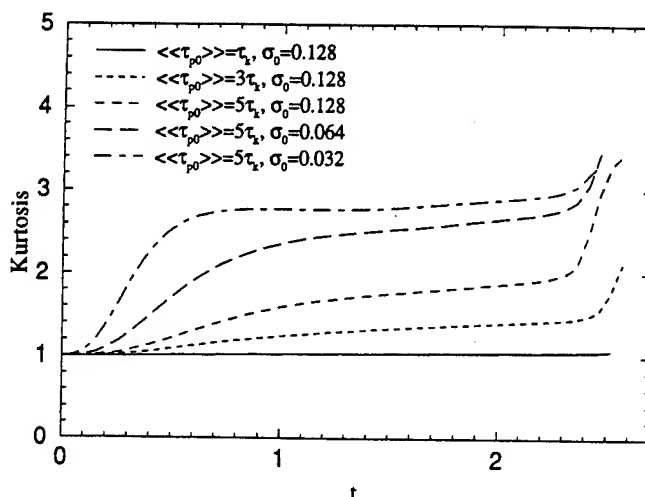


Figure 18. Temporal variation of the kurtosis of $\tau_p^{1/2}$ for different initial mean drop time constants and initial standard deviations.

(not shown) indicates the persistence of the double-hump pdf throughout the simulation. The effect of the variation of the initial standard deviation on the kurtosis is also shown in figure 18 for pdfs with $\langle\langle \tau_{p0} \rangle\rangle = 5\tau_k$. As expected, the evolution from a double-hump pdf into one with a single-hump is expedited with the decrease of σ_0 .

Based on these results, it is concluded that the evolution of the pdf is very sensitive to several parameters, especially $\langle\langle \tau_{p0} \rangle\rangle$, τ_{ee} , σ_0 , and S_0/l . Based on the magnitudes of these parameters and the initial form of the pdf, several asymptotic ($\langle\langle \tau_p \rangle\rangle \rightarrow 0$) forms of the pdf are produced. It would be instructive to suggest a dynamic (or Langevin) equation governing the evolution of the dispersed phase pdfs in a carrier gas with a Gaussian velocity field. This equation must include the parameters identified here as model input. Construction of such a stochastic model is currently underway; the DNS results produced here are very useful in appraising the performance of such models.

4. SUMMARY AND CONCLUDING REMARKS

Results obtained by direct numerical simulation (DNS) are used to investigate dispersion of both non-evaporating and evaporating particles in dilute stationary isotropic incompressible turbulent flow. The evaporating case is considered with both constant and variable rates of evaporation. In the simulations of non-evaporating particles, the effects of the particle time constant and the drift velocity on the particle autocorrelation, turbulence intensity and diffusivity are investigated. In agreement with the results of previous studies, it is found that the increase of the particle time constant results in the increase of the particle velocity autocorrelation and the decrease of its turbulence intensity. There is good agreement between the DNS results and the model of Mei *et al.* (1991) for the ratio of the particle turbulence intensity to the carrier fluid turbulence intensity, in the absence of gravity. But the agreement diminishes as the value of the drift velocity is increased. The particle turbulent diffusivity is rather insensitive to the changes in the particle time constant in accord with the experiment of Wells and Stock (1983). However, the present results exhibit a peak value in the variation of the particle turbulence diffusivity with the particle time constant. In the absence of gravity, the peak value occurs for particle time constants comparable to the Kolmogorov time scale. In the presence of gravity, the peak value for the particle diffusivity is observed in the direction normal to the gravity direction. The value of the particle time constant at which the peak value occurs depends on the magnitude of the drift velocity. No apparent peak value is observed for the particle diffusivity in the gravity direction. In general, the particle diffusivity is very sensitive to the drift velocity.

The effects of the constant rate evaporation on the particle velocity autocorrelation are studied for different initial particle time constants. The results show a decrease of the particle velocity autocorrelation with the increase of the evaporation rate for all the values of the initial particle

time constant. Variable rate evaporation results in polydispersity of drops. The effects of the initial drop time constant, the initial evaporation rate, and the drop Schmidt number on the probability density function (pdf) of the drop size are studied. Both cases with initially stationary and non-stationary particle velocities are considered. For cases with initially identical particle sizes it is found that after an initial transient period, the pdf of the particle size becomes Gaussian. The behavior of the pdf at long times depends on the particle size and the evaporation rate. In general, when the mean particle time constant becomes smaller than the Kolmogorov time scale, the pdf of the particle size starts to deviate from Gaussian. The extent of this deviation decreases with the decrease of the evaporation rate. The simulated results with different particle Schmidt numbers indicate an increase of the variance of $t_p^{1/2}$ with the increase of the Schmidt number. Also, the results show that the particle time constant is more influential than the particle Schmidt number in affecting the skewness of the particle sizes.

The effects of the initial spray size on the distribution of the particle size are also studied. The results indicate significant deviations from Gaussian when the initial spray size is smaller than the flow integral length scale. The spray size displays a linear temporal growth which is indicative of a constant rate of diffusion. This rate appears to be approximately the same for all the cases considered here. In addition to the initially identical particle sizes, several cases are considered in which the initial sizes of the particles are selected from a Gaussian seed. For an initial constant spray size (0.28 times the flow integral scale) it is shown that a nearly perfect Gaussian behavior is achieved when the standard deviation of the initial particle size distribution is 0.07. This value changes with the initial mean particle time constant and the initial spray size. For an initial double-delta pdf of the drop size it is shown that a transition to Gaussian pdf is possible provided that the initial mean drop time constant is large and/or the initial standard deviation is small.

At this point it is emphasized that the results presented here are based on simulations with several assumptions and simplifications as stated in section 2. These were necessary to make the problem computationally tractable with available resources. Some of these assumptions can be relaxed with improved computational capabilities. Future work is recommended in DNS of evaporating drop dispersion with two-way coupling, inclusion of compressibility effects, and modification of some of the coupling relations. It is also recommended to perform simulations with larger resolutions/realizations with data analysis coupled with consideration of preferential distribution of particles. The results generated thus far elucidate many important issues in regard to complex physics of drop dispersion in turbulent flows. These results motivate further extensions and utilizations of DNS for the analysis of more complex multiphase turbulent reacting flow systems.

Acknowledgements—We are grateful to Professor R. Mei for providing the data used in figure 3. This work is sponsored by the U.S. Office of Naval Research under Grant N00014-94-10667. Computational resources are provided by the SEAS Computing Center at SUNY—Buffalo and by the NCSA Facilities at the University of Illinois at Urbana—Champaign.

REFERENCES

- Chao, B. T. (1964) Turbulent transport behavior of small particles in dilute suspension. *Osterreichisches Ingenieur-Archiv*. **18**, 7–21.
- Csanady, G. T. (1963) Turbulent diffusion of heavy particles in the atmosphere. *J. Atmos. Sci.* **20**, 201–208.
- Eaton, J. K. and Fessler, J. R. (1994) Preferential concentration of particles by turbulence. *Int. J. Multiphase Flow Suppl.* **20**, 169–209.
- Elghobashi, S. and Truesdell, G. C. (1992) Direct simulation of particle dispersion in a decaying isotropic turbulence. *J. Fluid Mech.* **242**, 655–700.
- Elghobashi, S. and Truesdell, G. C. (1993) On the two-way interaction between homogeneous turbulence and dispersed solid particles. I: Turbulence modification. *Phys. Fluids* **5**, 1790–1801.
- Givi, P. (1989) Model free simulations of turbulent reactive flows. *Prog. Energy Combust. Sci.* **15**, 1–107.
- Givi, P. and Madnia, C. K. (1993) Spectral methods in combustion. In *Numerical Modeling in*

Combustion, ed. by T. J. Chung, Chapter 8, pp. 409–452. Taylor and Francis, Washington, D.C.

Hinze, J. O. (1975) *Turbulence*. McGraw-Hill Book Company, New York.

Kraichnan, R. H. (1970) Diffusion by a random velocity field. *Phys. Fluids* **13**, 22–31.

Maxey, M. R. and Riley, J. J. (1983) Equation of motion for a small rigid sphere in a nonuniform flow. *Phys. Fluids* **26**, 883–889.

McLaughlin, J. B. (1989) Aerosol particle deposition in numerically simulated channel flow. *Phys. Fluids* **1**, 1211–1224.

McLaughlin, J. B. (1994) Numerical computation of particles–turbulence interaction. *Int. J. Multiphase Flow Suppl.* **20**, 211–232.

Mei, R., Adrian, R. J. and Hanratty, T. J. (1991) Particle dispersion in isotropic turbulence under Stokes drag and basset force with gravitational settling. *J. Fluid Mech.* **225**, 481–495.

Nguyen, Q-V., Rangel, R. H. and Dunn-Rankin, D. (1991) Measurement and prediction of trajectories and collision of droplets. *Int. J. Multiphase Flow* **17**, 159–177.

Pismen, L. M. and Nir, A. (1978) On the motion of suspended particles in stationary homogeneous turbulence. *J. Fluid Mech.* **84**, 193–206.

Ranz, W. E. and Marshall, W. R. (1952) Evaporation from drops. *Chem. Engng Prog.* **48**, 141–173.

Reeks, M. W. (1971) On the dispersion of small particles suspended in an isotropic turbulent fluid. *J. Fluid Mech.* **83**, 529–546.

Riley, J. J. and Patterson, G. S. (1974) Diffusion experiments with numerically integrated isotropic turbulence. *Phys. Fluids* **17**, 292–297.

Shearer, A. J., Tamura, H. and Faeth, G. M. (1979) Evaluation of locally homogeneous flow model of spray evaporation. *J. Energy* **3**, 271–278.

Snyder, W. H. and Lumley, J. L. (1971) Some measurements of particle velocity autocorrelation functions in a turbulent flow. *J. Fluid Mech.* **48**, 41–47.

Solomon, A. S. P., Shuen, J-S., Zhang, Q-F. and Faeth, G. M. (1984) A theoretical and experimental study of turbulent evaporating sprays. NASA CR 174760.

Spalding, D. B. (1953) The combustion of liquid fuels. In *Proceedings of 4th Symp. (Int.) on Combustion*, pp. 847–864. The Combustion Institute, Baltimore, MD.

Squires, K. D. and Eaton, J. K. (1990) Particle response and turbulence modification in isotropic turbulence. *Phys. Fluids* **2**, 1191–1203.

Squires, K. D. and Eaton, J. K. (1991a) Measurements of particle dispersion obtained from direct numerical simulations of isotropic turbulence. *J. Fluid Mech.* **226**, 1–35.

Squires, K. D. and Eaton, J. K. (1991b) Preferential concentration of particles by turbulence. *Phys. Fluids* **3**, 1169–1178.

Strehlow, R. A. (1985) *Combustion Fundamentals*. McGraw-Hill, New York.

Tchen, C. M. (1947) Turbulent reacting flows. Ph.D. thesis. Delft University, The Hague.

Truesdell, G. C. and Elghobashi, S. (1994) On the two-way interaction between homogeneous turbulence and dispersed solid particles. II: Particle dispersion. *Phys. Fluids* **6**, 1790–1801.

Wang, L-P. and Maxey, M. R. (1993) Settling velocity and concentration distribution of heavy particles in isotropic turbulence. *J. Fluid Mech.* **256**, 27–68.

Wells, M. R. and Stock, D. E. (1983) The effects of crossing trajectories on the dispersion of particles in a turbulent flow. *J. Fluid Mech.* **136**, 31–62.

Wen, F., Kamalu, N., Chung, J. N., Crowe, C. T., and Troutt, T. R. (1992) Particle dispersion by vortex structures in plane mixing layers. *J. Fluids Eng.* **114**, 657–666.

Yudine, M. I. (1959) Physical considerations on heavy-particle diffusion. *Adv. Geophys.* **6**, 185–191.

Zhou, L. X. (1993) *Theory and Numerical Modeling of Turbulent Gas–Particle Flows and Combustion*. CRC Press, FL, USA.

APPENDIX II

Stochastic Simulations of Particle-Laden Isotropic Turbulent Flows

Stochastic Simulations of Particle-Laden Isotropic Turbulent Flow

F. Mashayek and P. Givi

Department of Mechanical and Aerospace Engineering
State University of New York at Buffalo
Buffalo, NY 14260-4400

Abstract

Numerical simulations are performed of dispersion and polydispersity of particles in isotropic incompressible turbulence. The mass loading of the particles is assumed to be small; thus the effects of particles on turbulence is neglected (one-way coupling). The stochastic model of Lu (1995) is employed to simulate the carrier phase. The results of the simulations are compared with direct numerical simulation (DNS) data of Mashayek *et al.* (1997) and theoretical results of Mei *et al.* (1991). The stochastic model predicts most of the trends as portrayed by DNS and theory. However, the continuity effect associated with the crossing trajectories effect is not captured. Also, the peaking in the variation of the particle asymptotic diffusivity coefficient with the particle time constant is not observed. For evaporating particles, the stochastic model predicts thinner probability density functions (pdfs) for the particle diameter as compared to DNS generated pdfs. The model is implemented to investigate the effects of gravity on evaporation. It is shown that the depletion rate increases with increase of the drift velocity at short and intermediate times, but an opposite trend is observed at long times. The standard deviation and skewness of the particle diameter indicate peak values in their variations with the drift velocity. Dispersion of evaporating particles decreases with respect to that of non-evaporating particles at small drift velocities; an opposite trend is observed at large drift velocities. The effects of the initial evaporation rate and the particle Schmidt number on the evaporation in the gravity environment are also studied.

1 Introduction

In stochastic modeling of particle-laden flows, an ensemble of physical particles is considered in conjunction with some assumptions pertaining to the turbulent flow field. The particles

can be considered as "Monte Carlo" computational elements which are expected to portray the physics of turbulent dispersion in a statistical manner. In this way, the flow field is not exactly calculated; rather its stochastic "realizations" are attempted. One of the early stochastic models of turbulent dispersion is due to Gosman and Ioannides (1981). In this model, the turbulence is assumed to be isotropic and to have a Gaussian pdf with the variance of $2k/3$, where k is the turbulence kinetic energy. The fluctuating fluid velocity along the particle trajectory is randomly sampled from the Gaussian pdf and the particle is allowed to interact with an eddy over a time interval which is the minimum of two time scales: the turbulent eddy life-time, and the residence time of the particle within the eddy. This model was also implemented by Shuen *et al.* (1983); Solomon *et al.* (1984); Shuen *et al.* (1985) to predict particle-laden jets, and by Graham and James (1996) who discuss the effects of the model parameters and the initial conditions.

The model of Gosman and Ioannides (1981) does not account for the temporal correlations and directional anisotropies associated with turbulent flows. This could result in some inaccuracies in capturing some of the well-established features of dispersion, such as the crossing trajectories effect. An improved model is proposed by Ormancey and Martinon (1984) which accommodates for both the temporal and the spatial structures of turbulence. In this model, the trajectories of massless fluid particles are constructed by integrating their Lagrangian equations. Associated with each fluid particle is a "fluid domain" centered at the fluid particle location. A heavy particle can follow a fluid domain or can move from one fluid domain to another, accounting for the effect of crossing trajectories. Within the fluid domain, the fluid velocity fluctuation at the particle location is taken from a random sample with specified one- and two-point correlations. A particle remains within one fluid domain as long as its distance from the fluid particle is smaller than some pre-defined length, or until the turbulent structure around the fluid particle is vanished by exceeding the random life-time of the fluid domain. The sizes and life-times of fluid domains are determined by length and time scales of turbulence. Similar models are proposed by Berlemont *et al.* (1990); Berlemont *et al.* (1991); Zhou and Leschziner (1991). Parthasarathy and Faeth (1990) use a stochastic model to predict dispersion of particles in self-generated homogeneous turbulence. This model is based on the idea of time series analysis of Box and Jenkins (1976) to satisfy the mean and fluctuating velocities and Lagrangian time correlations of the velocity fluctuations. Parthasarathy and Faeth (1990) report good agreement between the model

predictions and experimental data.

In this work, we consider the stochastic model proposed by Lu (1995). This model, similarly to that of Ormancey and Martinon (1984), accounts for the temporal and spatial correlations. However, instead of constructing the trajectories of fluid particles through the correlations at several time steps, only the correlation between two successive time steps is considered. As a result, the implementation of the model is somewhat easier and requires less bookkeeping efforts. Also, by using the Eulerian (as opposed to the Lagrangian) autocorrelation, the model is capable of producing the same trend for the variation of the particle diffusivity coefficient as those predicted by theory (*e.g.* Pismen and Nir (1978)). Lu (1995) reports good agreements between the model predictions and experimental data of Snyder and Lumley (1971). Here, we assess the performance of the model via comparisons with DNS data of Mashayek *et al.* (1997) and theoretical results of Mei *et al.* (1991) in isotropic incompressible particle-laden turbulent flows. The model is also implemented to investigate the effects of gravity on polydispersity of evaporating particles. The stochastic model is briefly described in §2, following the problem formulation. The model predictions are compared with the results of DNS and theory in §§3 and 4, respectively. In §5 the effects of gravity on evaporation is analyzed followed by the summary and concluding remarks in §6.

2 Formulation

We consider the motion of spherical particles in an incompressible and isotropic turbulent flow. It is assumed that the dispersed phase is very dilute, thus the effect of particles on the carrier fluid is negligible. The momentum equation for each particle is considered in the Lagrangian frame of reference. In general, this equation contains the Stokes drag, the Basset force, the force due to fluid pressure gradient, the inertia force of added mass, and the gravity (Maxey and Riley, 1983). However, if the ratio of the density of the particle to the density of the carrier fluid is large, the inertia, the Stokes drag, and the gravity forces are dominant and the other forces can be assumed negligible. With this assumption the

governing equations for a single particle are expressed as

$$\frac{d\mathbf{v}}{dt} = \frac{18\mu}{\rho_p d_p^2} (\mathbf{u} - \mathbf{v}) + g\mathbf{e}, \quad (1)$$

$$\frac{d\mathbf{X}}{dt} = \mathbf{v}, \quad (2)$$

where \mathbf{u} and \mathbf{v} (boldface indicates vector) denote the fluid velocity at the particle location and the particle velocity, respectively; t is time, \mathbf{X} is the center position of the particle, \mathbf{e} is the unit vector in the gravity direction, g is the gravity constant; ρ_p and d_p denote the particle density and diameter, respectively; and μ is the fluid viscosity. All the variables are normalized by reference scales of length, L_0 , velocity, U_0 , and density, ρ_0 .

In the simulations of non-evaporating (solid) particles, the particle diameter remains constant. For evaporating particles, the rate of diameter reduction is modeled by the d^2 -law (Strehlow, 1985)

$$d_p^2 = d_{p0}^2 - kt, \quad (3)$$

where d_{p0} is the initial diameter of the particle and the depletion rate is given by: $k = 8\Gamma \ln(1 + B_M) C_{Re}$, where Γ is the mass diffusivity coefficient and B_M is the transfer number (Spalding, 1953). The parameter $C_{Re} = 1 + 0.3 Re_p^{0.5} Sc_p^{0.33}$ is a correction factor to account for the convective effects (Ranz and Marshall, 1952) with Re_p and Sc_p representing the particle Reynolds and Schmidt numbers, respectively. The flow is assumed isothermal and evaporation is due to a constant temperature difference between the drop and the fluid. This model is in accord with that of several laboratory experiments (e.g. Shearer *et al.* (1979)). In a dilute flow, the ratio of the mass of the particle to the mass of the carrier fluid is very small and it is assumed that the particles are in contact with the carrier fluid during evaporation. Therefore, the transfer number B_M is the same for all the particles, and the variation of k is only due to the parameter C_{Re} . A relation for the "particle time constant" (τ_p) is obtained from Eq. (3)

$$\tau_p(t) = \frac{\rho_p d_p^2}{18\mu} = \tau_{p0} - \tau_e t, \quad (4)$$

where $\tau_{p0} = \frac{\rho_p d_{p0}^2}{18\mu}$ denotes the initial particle time constant, and

$$\tau_e = \tau_{e0} C_{Re}, \quad \tau_{e0} = \frac{4\rho_p \Gamma}{9\mu} \ln(1 + B_M). \quad (5)$$

For convenience, the largest evaporation rate is chosen such that the particle velocity autocorrelation approaches zero by the time $\tau_p = 0.1\tau_{p0}$ (about 3.1 eddy turnover times). Therefore: $\tau_{e0} = \frac{0.9\tau_{ec}}{3.1} = 0.29\tau_{ec}$ where τ_{ec} is introduced to relate the evaporation rate to the initial particle time constant. By introducing a drift velocity, $v_{dr} = \tau_{p0} g$, Eq. (1) is expressed as

$$\frac{d\mathbf{v}}{dt} = \frac{1}{\tau_p}(\mathbf{u} - \mathbf{v}) + \frac{1}{\tau_{p0}} v_{dr} \mathbf{e}. \quad (6)$$

The particle Reynolds number is defined as: $Re_p = \frac{\rho_f d_p |\mathbf{u} - \mathbf{v}|}{\mu}$ with ρ_f denoting the carrier fluid density. Following Wang and Maxey (1993) the Reynolds number is related to the flow Kolmogorov time scale (τ_k) and velocity scale (v_k) with $\nu = \tau_k v_k^2$, where $\nu = \mu/\rho_f$ is the fluid kinematic viscosity

$$Re_p = \left(\frac{18\tau_p}{\nu \rho_p / \rho_f} \right)^{1/2} |\mathbf{u} - \mathbf{v}| = 4.243 \left(\frac{\rho_f}{\rho_p} \right)^{1/2} \left(\frac{\tau_p}{\tau_k} \right)^{1/2} \frac{|\mathbf{u} - \mathbf{v}|}{v_k}. \quad (7)$$

For large particle Reynolds numbers a “modified” Stokes drag relation must be used. The modification is in the form of an empirical correction factor which is multiplied by the Stokes drag relation. The empirical correction factor is described as a function of the particle Reynolds number ($f(Re_p)$) and can be easily implemented in Eq. (6) by replacing τ_p with a modified particle time constant, $\tau_p^* = \frac{\tau_p}{f(Re_p)}$. A variety of relations for $f(Re_p)$ is available (Clift *et al.*, 1978), here we use

$$f(Re_p) = 1 + 0.15 Re_p^{0.687}. \quad (8)$$

The particles can be tracked in the Lagrangian frame by integrating Eqs. (6) and (2) provided that the fluid velocity at the particle location is known. Here, we use the stochastic model proposed by Lu (1995) to simulate the fluid velocity. The rudiments of the model are taken from the methodology of time series analysis (Box and Jenkins, 1976). Let the coordinate system move with the mean velocity; thus, only the fluctuating velocities are considered.

The particle position, $X_i(0)$, $i = 1, 2, 3$, and velocity, $v_i(X_i(0), 0)$, are given at the starting time $t = 0$. The initial fluid velocity, $u_i(X_i(0), 0)$, at the particle location is obtained from a random Gaussian seed with the standard deviation u' (assumed to be known *a priori*). Then, the particles are moved to their new positions, $X_i(\Delta t)$ (Δt is the time increment), using a second order Runge-Kutta method. In order to advance the calculations for the next time step, the fluid velocity, $u_i(X_i(\Delta t), \Delta t)$, at the new particle location must be found. By the time particles arrive at their new locations, the fluid velocity at the old particle location changes to $u_i(X_i(0), \Delta t)$. To relate the old and the new fluid velocities at $X_i(0)$, the Eulerian velocity autocorrelation

$$F_{\alpha\alpha}(\Delta t) = \frac{\langle w_\alpha(X_\alpha(0), 0) w_\alpha(X_\alpha(0), \Delta t) \rangle}{\langle w_\alpha(X_\alpha(0), 0) w_\alpha(X_\alpha(0), 0) \rangle}, \quad \alpha = 1, 2, 3 \quad (9)$$

(with no summation over repeated Greek indices) is used, where $w_i = u_i/u'$ is the normalized velocity and $\langle \rangle$ indicates the ensemble average. It is also necessary to account for the spatial separation between the fluid particle and the heavy particle locations through the Eulerian spatial correlation

$$G_{\alpha\alpha}(\Delta s) = \frac{\langle w_\alpha(X_\alpha(0), \Delta t) w_\alpha(X_\alpha(\Delta t), \Delta t) \rangle}{\langle w_\alpha(X_\alpha(0), \Delta t) w_\alpha(X_\alpha(0), \Delta t) \rangle}, \quad \alpha = 1, 2, 3 \quad (10)$$

where $\Delta s = |\mathbf{X}(\Delta t) - \mathbf{X}(0)|$ is the distance between the old and the new particle locations. To use Eq. (10), it is necessary to re-orient the coordinate system such that one of the axis coincides with $\mathbf{X}(\Delta t) - \mathbf{X}(0)$.

By defining autoregressive processes (Box and Jenkins, 1976) (in time) for $w_i(X_i(0), 0)$ and $w_i(X_i(0), \Delta t)$, and (in space) for $w_i(X_i(0), \Delta t)$ and $w_i(X_i(\Delta t), \Delta t)$, with some algebraic manipulations, Lu (1995) obtains:

$$w_\alpha(X_\alpha(\Delta t), \Delta t) = a_\alpha b_\alpha w_\alpha(X_\alpha(0), 0) + \gamma_\alpha, \quad \alpha = 1, 2, 3 \quad (11)$$

where $a_\alpha = F_{\alpha\alpha}(\Delta t)$, $b_\alpha = G_{\alpha\alpha}(\Delta t)$, and γ_α is a Wiener process which is determined by its variance, $\sigma_{\gamma\alpha} = \sqrt{1 - a_\alpha^2 b_\alpha^2}$. Once the fluid velocity at the new particle location is determined using Eq. (11), the steps described above are repeated and the particle trajectory is constructed.

The following relations are used for the Eulerian temporal and spatial correlations (Lu, 1995): $F_{\alpha\alpha}(\Delta t) = \exp(-\Delta t/\tau_E)$, $G_{11}(\Delta s) = \exp(-\Delta s/\Lambda_1)$, $G_{22}(\Delta s) = G_{33}(\Delta s) = \exp(-\Delta s/\Lambda_2)$, where τ_E is the Eulerian integral time scale and Λ_1 and Λ_2 are the Eulerian integral length scale in the longitudinal and transverse directions, respectively. In isotropic incompressible flows, these are estimated by:

$$\tau_L = C_1 \frac{(u')^2}{\epsilon}, \quad \tau_E = \frac{\tau_L}{C_2}, \quad \Lambda_1 = 2\Lambda_2 = C_3 \tau_L u',$$

where τ_L is the Lagrangian integral time scale, ϵ is the dissipation rate, and $C_1 = 0.212$, $C_2 = 0.73$, $C_3 = 2.778$. The values used for C_1 and C_3 are the same as those suggested by Lu (1995). The value of C_2 is larger than that used by Lu (1995), and is the upper limit found in the literature (Hinze, 1975), but provides better agreements with the results of theory and DNS. With this formulation, the values of the fluid turbulence intensity and dissipation rate of the turbulent kinetic energy are model inputs. The values $u' = 0.0185$ and $\epsilon = 3.987 \times 10^{-6}$ are taken from DNS of Mashayek *et al.* (1997). In the presentation of results, the particle variables are normalized by fluid variables. The optimized computational time step for each case depends on the parameter values as considered. In all cases, 25^3 particles are tracked.

3 Model assessment via comparison with DNS

Recently, Mashayek *et al.* (1997) have performed extensive DNS to investigate dispersion (and polydispersity) of solid (and evaporating) particles in stationary isotropic incompressible turbulence. This configuration provides an ideal setting for the assessment of the stochastic model. In this section, the DNS results of Mashayek *et al.* (1997) are used for this assessment. In doing so, the primary consideration is to re-scale the DNS generated time and velocity scales to those of stochastic simulations via (Elghobashi and Truesdell, 1992): $\left(\frac{\tau_p}{\tau_E}\right)_{\text{DNS}} = \left(\frac{\tau_p}{\tau_E}\right)_{\text{STH}}$ and $\left(\frac{\tau_g}{\tau_E}\right)_{\text{DNS}} = \left(\frac{\tau_g}{\tau_E}\right)_{\text{STH}}$, where $\tau_g = d_p/v_{dr}$ is the drift timescale. The reasoning for considering the fluid eddy turnover time for scaling is discussed by Elghobashi and Truesdell (1992). This adjustment is necessary as the stochastic model, by nature, is designed for Reynolds numbers higher than those attainable by DNS.

3.1 Dispersion of solid particles

First, we consider dispersion of solid (nonevaporating) particles. In Fig. 1 the particle velocity autocorrelation coefficients,

$$R_{\alpha\alpha}^p(t) = \frac{\langle v_\alpha(0)v_\alpha(t) \rangle}{\langle v_\alpha^2(0) \rangle}, \quad \alpha = 1, 2, 3. \quad (12)$$

as generated by DNS are compared with those by stochastic simulations (indicated by "STH") for various particle time constants. For direct comparisons with DNS results, the particle time constant and the drift velocity are expressed in terms of the Kolmogorov time and velocity scales, respectively. In the absence of gravity, Fig. 1a shows that the agreement between the particle velocity autocorrelations is very good for large particles. However, as the particle time constant is decreased, the results of stochastic simulations deviate from DNS results. At very small particle time constant ($\tau_p = 0.4\tau_k$) the stochastic model underestimates DNS results at short times and overestimates them at longer times. The agreement is weaker in the presence of gravity (Fig. 1b for $v_{dr} = 5v_k$) and significant deviations are observed for all particle time constants. It appears that the stochastic model does not predict the negative loops in the particle velocity autocorrelation curve. These loops are due to the continuity effect (Csanady, 1963) associated with the crossing trajectories effect. Therefore, while the effects of crossing trajectories are portrayed (as witnessed by the decrease of the particle velocity autocorrelation coefficient with the increase of the drift velocity), the continuity effects are not captured by the model.

The particle turbulence intensities calculated from the stochastic model are compared against DNS data for a variety of particle time constants and drift velocities in Fig. 2. These quantities are time averaged (indicated by an overbar) over more than three eddy turnover times in both simulations. As expected, with the increase of the particle's inertia, its tendency to follow turbulent fluctuations is diminished and the particle turbulence intensity is decreased. Also, the increase of the drift velocity results in the decrease of the particle turbulence intensity due to the crossing trajectories effect. The general trends shown in Fig. 2 have been observed by others (see e.g. Snyder and Lumley (1971); Wells and Stock (1983); Mei *et al.* (1991)). Figure 2 indicates that the agreement between the model predictions and DNS results is good in both of the directions parallel and normal to the gravity direction.

No apparent preference towards either small or large particles is observed. This is interesting as the scaling between the two simulations is based on the large scale eddy turnover time and the smaller particle time constants are of the order of the Kolmogorov time scale. Also, the good agreement observed in the presence of gravity indicates that the incapability of the stochastic model to account for the continuity effects does not affect the calculation of the particle turbulence intensity.

Figure 3 presents the asymptotic particle turbulence diffusivity coefficient, $\epsilon^p = D^p(t \rightarrow \infty)$, in both the presence and the absence of gravity. In accord with DNS, the particle diffusivity coefficient, $D^p(t) = \frac{1}{3}[D_{11}^p(t) + D_{22}^p(t) + D_{33}^p(t)]$, is determined by (Hinze, 1975)

$$D_{\alpha\alpha}^p(t) = \langle v_\alpha^2(0) \rangle \int_0^t R_{\alpha\alpha}^p(\tau) d\tau = \int_0^t \langle v_\alpha(0)v_\alpha(\tau) \rangle d\tau \quad \alpha = 1, 2, 3. \quad (13)$$

The results (not shown) for the diffusivity coefficients of the fluid particle surrounding the heavy particle exhibit similar trends as those observed in Fig. 3. The asymptotic values are calculated based on a “finite” time (about 3.5 eddy turnover times) in both DNS and stochastic simulations. The results in Fig. 3 show that, contrary to the particle turbulence intensity, the asymptotic particle diffusivity coefficients are predicted with some deviations from those calculated by DNS. The extent of deviation is increased as the particle time constant is decreased. This is not an artifact of using a finite time to calculate the asymptotic values, as with the decrease of the particle time constant the velocity autocorrelation approaches zero in a shorter time. Therefore, the asymptotic values are reached in a shorter time and smaller deviations are expected at smaller particle time constants. Figure 3 shows that the general trends in the variations of the particle diffusivity coefficient with the drift velocity are captured by the stochastic model. However, the model does not predict the peak value in the variation of the particle diffusivity coefficient with the particle time constant. The peak value in DNS occurs for particle time constants of the order of the Kolmogorov time scale and is due to the increase of the effects of the preferential collection of particles in high strain regions of the flow at these small particle time constants. This suggests that this model can be more safely used for particle time constants of the order of the larger time scales of the flow.

3.2 Polydispersity of evaporating particles

When the particles evaporate, their interaction with the carrier fluid results in a distribution of particle sizes. This is the case even if initially all the particles are of the same size. Since the evaporation rate is strongly controlled by the instantaneous particle Reynolds number, it is instructive to first consider the temporal variations of the particle Reynolds number for nonevaporating particles at different particle time constants. Figure 4 provides a comparison between the particle Reynolds number calculated using the stochastic model with those from DNS. By examining this figure it is realized that: (i) the initial time required by the particles to reach the stationary condition is much shorter in the stochastic simulations. (ii) For large particles, an overshoot is observed in the temporal variations of the particle Reynolds number, the extent of which is increased with the increase of the particle time constant. The stochastic model predicts a much smaller overshoot at the same particle time constant. (iii) The stationary values of the particle Reynolds number predicted by the stochastic model are larger than those via DNS. More importantly, the deviation observed between the stationary values depends on the particle time constant; the smaller the particle time constant the larger the deviation.

The influences of physics as itemized by (i)-(iii) are discussed by considering the temporal variations of the mean and higher order moments of $\tau_p^{1/2}$. This parameter is chosen since it is proportional to the particle diameter. First, we consider the temporal variations of the mean, the minimum, and the maximum values of $(\tau_p/\tau_{p0})^{1/2}$ for a case with $\tau_{p0} = 5\tau_k$, $\tau_{ec} = 5\tau_k$, and $Sc_p = 5$. The particles are initially injected into the flow with identical sizes and with the same velocity as that of their surrounding fluid elements. The particles are allowed to evaporate until the diameter of the smallest particle reaches 5% of its initial value at which time the simulation is terminated. Very small sizes are not considered to avoid the excessive computational requirements for particle tracking. Figure 5 shows that the stochastic model predicts the mean diameter value very closely to DNS, specially during short and intermediate times. However, the minimum and maximum particle sizes predicted by the model deviate from those calculated by DNS. This can be explained by considering the variation of the particle Reynolds number with the particle time constant in Fig. 4. When the particle time constant varies from $0.4\tau_k$ to $5\tau_k$ the stationary values of the particle Reynolds number is increased by a factor of ~ 19 in DNS and ~ 8.3 in the stochastic

simulations. Therefore, for the same size distribution, DNS predicts a much wider variation of the particle Reynolds number. Consequently, the variations of the evaporation rate is larger in DNS and a broader size distribution is resulted. This also explains the sharper decrease of the minimum particle diameter at long times in DNS. It is noted that for a constant rate of change of τ_p (which is a reasonable assumption for the case considered here), $\frac{d}{dt}(\tau_p^{1/2}) \sim \frac{\text{constant}}{\tau_p^{1/2}}$. Therefore, the rate of the diameter decrease becomes larger as the size of the particle is reduced.

Based on the discussion above, it is expected that the stochastic model predicts a narrower (thinner) size distribution than does DNS. This is evident in Fig. 6 which portrays the temporal variations of the standard deviation (σ) of $\tau_p^{1/2}$ for several Sc_p values. This figure shows that the stochastic model significantly underpredicts the standard deviation at intermediate and long times, although it is capable of predicting the right trend of variation with the particle Schmidt number. Three different regions are distinguished for each of the curves. The first region, for short times ($t/\tau_E < 0.2$), corresponds to the interval that the particle velocity is nonstationary. This period is characterized by small rates of growth of the standard deviations of $\tau_p^{1/2}$ as the particles are initially released with the same velocity as that of the surrounding fluid and the particle Reynolds number takes small values. Since the stochastic model predicts a larger variation of Re_p with the particle time constant in this nonstationary period (cf. Fig. 4), the standard deviations are higher in stochastic simulations during the initial short times – this is verified by considering the values near $t = 0$. In the second region ($0.2 < t/\tau_E < 2$), the particle Reynolds number adopts large values and the standard deviation increases more rapidly. In this region, the stochastic model underpredicts the DNS results as the model yields a smaller variation for the particle Reynolds number with the particle time constant. The third region ($t/\tau_E > 2$) is specified by the largest growth rates for the standard deviation. It is clearly seen in Fig. 6 that the model does not predict growth rates as large as those in DNS. This can be explained by the same argument provided earlier to explain the variations of the particle diameter at final times.

Figure 7 shows the temporal variations of the skewness and kurtosis of $\tau_p^{1/2}$ for particles with $\tau_{p0} = 5\tau_k$ and $Sc_p = 1$ at two initial evaporation rates $\tau_{ec} = 5\tau_k$ and $\tau_{ec} = \tau_k$. The particles have initially zero velocity relative to the surrounding fluid; therefore, there is an initial time for the skewness and the kurtosis to reach stationary levels. In DNS, this time

is about $2.5\tau_E$ which is about the same time required by nonevaporating particles to reach a stationary state (Fig. 4). The corresponding initial time in the stochastic simulations is about one eddy turnover time. As a result, the short time variations of both the skewness and the kurtosis are very different in DNS and stochastic simulations. At long times, for the case with smaller evaporation rate, the prediction of the stochastic model for the kurtosis is in good agreement with DNS results. However, the stochastic model underestimates the skewness values; it predicts a negative skewness throughout the duration of evaporation.

In general, the stochastic model predicts a narrower pdf of the droplet size than that obtained by DNS. This has a major impact on the evolution of the pdf when there is an initial size separation between the particles. In order to elaborate on this issue, we consider cases in which the initial particle size distribution consists of two distinct uniform-size groups of particles (i.e. the pdf of $\tau_p^{1/2}$ is double delta). In all of the cases, the particles are initially injected into the flow with a zero velocity relative to the local fluid, $\langle \tau_{p0} \rangle = 5\tau_k$, and $Sc_p = 1$. Figure 8 shows the temporal evolution of the kurtosis of $\tau_p^{1/2}$ for cases with different initial standard deviations. After the onset of evaporation, there is a time delay before the two initially segregated branches of the pdf merge, resulting in the increase of the kurtosis. Figure 8 indicates that this initial time delay depends on the initial separation between the two groups of particle sizes. As expected, the increase of this separation (the increase of σ_0) delays the merging. The stochastic model predicts a slower merging for all of the cases. This is due to the fact that the pdfs of each group of particles are predicted to be narrower (at any instant of time) in comparison to DNS.

4 Comparison with theory

Mei *et al.* (1991) obtain a solution for the particle turbulence intensity and diffusion coefficient by assuming the form of the spectral density function as proposed by Kraichnan (1970). They consider contributions of all the forces acting on the particle but show that only the Stokes drag and the Basset forces need to be retained. In this section, their final results for cases in which the Basset force is neglected, are compared with those predicted by the stochastic model.

The variations of the particle turbulence intensity with the particle time constant and the drift velocity are shown in Fig. 9. This figure indicates that the predictions via the stochastic model are in good agreements with those based on the theory for wide ranges of the particle time constant and the drift velocity. The stochastic model underestimates the results via the theory slightly in the absence of gravity while overpredicting these results at large drift velocity. The agreement between the two results diminishes with the decrease of the particle time constant. These trends are observed in both of the directions normal (Fig. 9a) and parallel (Fig. 9b) to the gravity direction. However, it must be emphasized that the predictions of the stochastic model is very sensitive to the magnitude of C_2 ; values smaller than 0.73 were found to produce larger deviations from the theory.

In Fig. 10, comparisons are made between the predictions via the model and the theory for the asymptotic particle diffusivity coefficient at different drift velocities. The particle diffusivity coefficient is evaluated from (Hinze, 1975)

$$D_{\alpha\alpha}^p(t) = \frac{1}{2} \frac{d}{dt} \langle X_\alpha^2(t) \rangle \quad \alpha = 1, 2, 3. \quad (14)$$

The overall agreement is good. The stochastic model is capable of predicting the variations of the particle diffusivity coefficient with the drift velocity and with the particle time constant. In both the gravity and no-gravity directions, ϵ^p increases with the increase of the particle time constant when the drift velocity is small. The increase of the drift velocity tends to diminish the variations of ϵ^p with the particle time constant; an effect observed more strongly in the direction normal to the gravity direction.

As pointed out by Lu (1995), some of the earlier stochastic models do not correctly predict the increase of the long time particle diffusivity coefficient with the increase of the particle time constant. This is, mainly, due to the use of the "Lagrangian" autocorrelation. In order to show this, we also consider a Lagrangian stochastic model proposed by Lu *et al.* (1993). The results of the simulations are presented in Fig. 11 and indicate a decreasing trend for the long time particle diffusivity coefficient at zero gravity. The variations of ϵ^p at higher drift velocity values are, however, predicted correctly. In both the gravity and no-gravity directions the particle diffusivity coefficient becomes rather insensitive to the variations of the particle time constant. It must be added here that the parameter C_2 does not appear in

$\frac{\tau_p}{\tau_E}$	$\frac{v_{dr}}{u'}$	$\langle Re_p \rangle$	$\frac{\langle v_m^2 \rangle - \langle v_{um}^2 \rangle}{\langle v_{um}^2 \rangle} \times 100$	$\frac{\langle \epsilon_m^p \rangle - \langle \epsilon_{um}^p \rangle}{\langle \epsilon_{um}^p \rangle} \times 100$
0.1	0	0.22	0.8	0.0
0.4	0	0.69	4.4	0.7
1.6	0	1.86	16.0	1.4
8.0	0	4.83	42.0	2.0
0.1	2	0.72	2.6	2.3
0.4	2	1.40	10.4	4.9
1.6	2	2.83	30.7	6.0
8.0	2	6.21	76.5	13.5
0.1	5	1.62	6.3	7.8
0.4	5	2.90	24.0	11.0
1.6	5	5.24	67.7	19.4
8.0	5	10.19	153.2	32.8

Table 1: Effects of the modified Stokes drag on the particle turbulence intensity and diffusivity. Subscripts “m” and “um” refer to the calculations based on the modified and unmodified (Stokes) drag, respectively. The particle intensity and diffusivity coefficient in cases with non-zero drift velocity belong to the gravity direction.

the Lagrangian model. However, the values of the particle diffusivity coefficient are indirectly dependent on C_2 as it relates τ_p to the “variable β ” as used by Mei *et al.* (1991). Of course, C_2 only affects the magnitude of the particle diffusivity coefficient and does not change the decreasing trend observed at zero gravity.

The results presented in Figs. 9-11 are based on the assumption of Stokes drag with no modification for large particle Reynolds numbers. This assumption is necessary for comparison with the theoretical results of Mei *et al.* (1991) which are also based on the same assumption. However, in several of the cases the particle Reynolds number significantly exceeds unity. This will affect the particle intensity and diffusivity coefficient. In order to quantify these effects, in table 1 the percentage relative differences between the results obtained with a modified drag relation (Eq. (8)) and those presented earlier based on the Stokes drag are provided. As expected, the particle Reynolds number increases with the increase of the particle time constant and/or the drift velocity, resulting in larger deviations for the particle intensity and diffusivity coefficient at larger τ_p and v_{dr} values. It is noted that the particle diffusivity coefficient is predicted with a much smaller error than that associated with the particle intensity. This behavior is mostly due to the higher sensitivity of the particle intensity to the particle time constant. Regardless of the magnitude of the drift velocity, the

particle intensity and diffusivity are predicted with comparable errors when the value of the particle time constant is small ($\tau_p = 0.1\tau_E$).

5 Effects of gravity on evaporation

We now consider the effects of gravity on polydispersity of evaporating particles. In all the simulations considered in this section, the initial value of the particle time constant is fixed at $\tau_{p0} = 10\tau_k$, and a modified drag coefficient (Eq. (8)) is used.

Figure 12 portrays the effects of gravity and evaporation on the velocity autocorrelation coefficient of both the heavy particle and its surrounding fluid particle (indicated by superscript "fp"). In Fig. 12a the velocity autocorrelations are given for nonevaporating particles at different drift velocities. As has been shown in previous studies (Wells and Stock, 1983; Mashayek *et al.*, 1997) the increase of the drift velocity decreases the velocity autocorrelation of both the particle and its surrounding fluid due to the effect of crossing trajectories. Figure 12b indicates that evaporation also results in a decrease of the particle velocity autocorrelation. This is due to the decrease of the particle size with evaporation. However, evaporation has virtually no effect on the velocity autocorrelation of the fluid. Therefore, the evaporating particle does not change its surrounding fluid as frequently as does the nonevaporating particle in a gravity environment.

The effects of gravity on the rate of evaporation are realized from Fig. 13 by considering the temporal variations of $-\frac{d(\langle \tau_p \rangle / \tau_{p0})}{dt}$ which is proportional to the depletion rate (k , Eq. (3)). When the nonlinear term in C_{Re} is zero (the case with $Sc_p = 0$ in Fig. 13), the evaporation rate is constant as expected. The inclusion of the nonlinear term increases the rate of evaporation. However, for all of the drift velocities, the rate of evaporation decreases nonlinearly in time due to the decrease of the particle size and, consequently, the particle Reynolds number. For short and intermediate times, the evaporation rate increases with the drift velocity as the particle Reynolds number is increased with the increase of the drift velocity. The larger evaporation rate at higher drift velocity results in a faster decrease of the particle size. As a result, a decreasing trend is observed for the variation of the evaporation

rate with the drift velocity at long times.

An interesting behavior is observed in the variations of the standard deviation of $\tau_p^{1/2}$ with the increase of the drift velocity. Figure 14a shows that by increasing the drift velocity from zero to $2v_k$, the standard deviation increases at all times. However, further increase of the drift velocity results in an opposite trend. At large drift velocities the particle Reynolds number takes large values. This has the effect of diminishing the relative differences in the Reynolds number of different particles and results in a narrower $\tau_p^{1/2}$ pdf. A similar behavior is observed for the skewness of $\tau_p^{1/2}$ in Fig. 14b which shows that skewness is largest at $v_{dr} = 5v_k$. Also, the increase of the drift velocity results in skewness of $\tau_p^{1/2}$ towards larger particles. Therefore, with the increase of the drift velocity, first the pdfs become wider and more skewed towards large particles. Further increase of the drift velocity results in an opposite trend.

When the rate of evaporation is decreased to $\tau_{ec} = 1$, Fig. 15 shows that the variations of the standard deviation and skewness of $\tau_p^{1/2}$ with the drift velocity change significantly. A monotonic decrease of the standard deviation with the increase of the drift velocity is observed at intermediate times. The skewness approaches near zero values for all drift velocities, before it sharply decreases (Fig. 15b). An examination of the standard deviation and skewness of $\tau_p^{1/2}$ for cases with $Sc_p = 5$ revealed no significant difference in their variations with the drift velocity when compared to those with $Sc_p = 1$.

Figure 16 shows the temporal variation of the dispersion $\langle [X_\alpha(t) - X_\alpha(t = 0)]^2 \rangle$. This figure indicates that dispersion decreases with the increase of the drift velocity in both of the directions parallel and normal to the gravity direction. Comparisons with the results of nonevaporating particles in Fig. 16 reveal that evaporation tends to decrease dispersion in low gravity environment and to increase it at higher drift velocities. This behavior is observed in both directions. It is also noted that the difference between the results under evaporating and nonevaporating conditions increases with time for all the drift velocities except $v_{dr} = 2v_k$ for which dispersion shows no apparent sensitivity to evaporation.

The temporal variations of dispersion for a case with $Sc_p = 5$ are shown in Fig. 17. Other parameters are the same as those considered for cases in Fig. 16. A comparison of these two figures reveals that the increase of the particle Schmidt number does not affect dispersion

in the direction normal to the gravity direction. However, significant changes are observed in the gravity direction. The effects of the particle Schmidt number on dispersion in the gravity direction is enhanced by increasing the drift velocity. It is also noted that similarly to the cases with $Sc_p = 1$, the case with $v_{dr} = 2v_k$ remains unaffected by evaporation.

6 Summary and concluding remarks

Results are presented of stochastic simulations of dispersion and polydispersity of particles in isotropic turbulent flows via the stochastic model proposed by Lu (1995). All of the empirical relations and the model's constant values are set the same as those suggested by Lu (1995). However, a value larger than that suggested for the ratio of the Lagrangian and Eulerian integral time scales was necessary.

The predicted results via the model are compared with the results based on DNS (Mashayek *et al.*, 1997) and theory (Mei *et al.*, 1991). The stochastic model based on the Eulerian autocorrelation correctly predicts most of the trends observed by theory and DNS. When the model is constructed with a Lagrangian autocorrelation, the particle asymptotic diffusivity coefficient decreases with the increase of the particle time constant, in the absence of gravity. This trend is opposite of that predicted by the theory. A comparison of the particle velocity autocorrelation coefficients simulated by the Eulerian stochastic model with those by DNS indicates that the continuity effect (associated with the crossing trajectories effect) is not captured. Also, the peaking for the variation of the particle asymptotic diffusivity coefficient with the particle time constant as observed in DNS is not predicted. When compared with DNS results, the model predictions exhibit better agreements for large particle time constants. The stochastic model is also used to quantify the effects of a modified drag relation on the particle turbulence intensity and the asymptotic diffusivity coefficient. The results suggest that the particle turbulence intensity is more sensitive to the drag calculations than is the particle diffusivity coefficient.

For evaporating particles, the stochastic model predicts thinner particle diameter pdfs than does DNS. This is mainly due to differences in the magnitudes of the particle Reynolds number in the two simulations. The higher order statistics of the particle size are calculated

by the stochastic model and reasonable agreements are found with DNS. The model is also used to investigate the effects of gravity on evaporation. The depletion rate indicates an increasing trend with the increase of the drift velocity at small and intermediate evaporation times; an opposite trend is observed at long times. Furthermore, the variations of the standard deviation and the skewness of $\tau_p^{1/2}$ with the drift velocity is not monotone. For small drift velocities, the standard deviation and the skewness increase with the increase of the drift velocity; an opposite trend is observed for large drift velocities.

At this point, it is important to note that the configuration of isotropic turbulence as considered here is much simpler than that in practical flow configurations. Therefore, weaker agreements between stochastic and DNS/experimental results are expected when the model is implemented in inhomogeneous flows especially those with large strain rates. Also, with extension and implementation of stochastic models to complex flows the problem associated with the (non)universality of the empirical constants must be resolved. Another important issue pertains to the number of particles for statistical sampling. Based on our experience, typically as many as 15,000 particles are necessary for reliable statistics. This could be a major restriction as in most of the reported applications of stochastic models to spatially inhomogeneous flows the total number of particles is significantly lower.

Acknowledgment:

We are grateful to Dr. Q. Q. Lu for insightful discussions and to Professor R. Mei for providing the data used in §3. This work is part of an effort sponsored by the U.S. Office of Naval Research under Grant N00014-94-10667. Computational resources are provided by the SEAS Computing Center at SUNY-Buffalo and by the NCSA facilities at the University of Illinois at Urbana-Champaign.

References

Berlemont, A., Desjonquieres, P., and Goussebet, G. (1990). Particle Lagrangian simulation in turbulent flows. *Int. J. Multiphase Flow* **16**, 19–34.

Berlemont, A., Grancher, M-S., and Gousebet, G. (1991). On the Lagrangian simulation of turbulence influence on droplet evaporation. *Int. J. Heat Mass Transfer* **34**, 2805–2812.

Box, G. E. P. and Jenkins, G. M. (1976). *Time Series Analysis*. Holden-Day, Oakland, CA.

Clift, R., Grace, J. R., and Weber, M. E. (1978). *Bubbles, Drops, and Particles*. Academic Press, New York, NY.

Csanady, G. T. (1963). Turbulent diffusion of heavy particles in the atmosphere. *J. Atmos. Sci.* **20**, 201–208.

Elghobashi, S. and Truesdell, G. C. (1992). Direct simulation of particle dispersion in a decaying isotropic turbulence. *J. Fluid Mech.* **242**, 655–700.

Gosman, A. D. and Ioannides, E. (1981). Aspects of computer simulation of liquid-fuelled combustors. AIAA Paper 81-0323.

Graham, D.I. and James, P.W. (1996). Turbulent dispersion of particles using eddy interaction models. *Int. J. Multiphase Flow* **22**, 157–175.

Hinze, J. O. (1975). *Turbulence*. McGraw Hill Book Company, New York, NY.

Kraichnan, R. H. (1970). Diffusion by a random velocity field. *Phys. Fluids* **13**, 22–31.

Lu, Q. Q., Fontaine, J. R., and Aubertin, G. (1993). A Lagrangian model for solid particles in turbulent flows. *Int. J. Multiphase Flow* **19**, 347–367.

Lu, Q. Q. (1995). An approach to modeling particle motion in turbulent flows—I. Homogeneous, isotropic turbulence. *Atmospheric Environment* **29**, 423–436.

Mashayek, F., Jaberi, F.A., Miller, R.S., and Givi, P. (1997). Dispersion and polydispersity of droplets in stationary isotropic turbulence. *Int. J. Multiphase Flow* **23**, 337–355.

Maxey, M. R. and Riley, J. J. (1983). Equation of motion for a small rigid sphere in a nonuniform flow. *Phys. Fluids* **26**, 883–889.

Mei, R., Adrian, R. J., and Hanratty, T. J. (1991). Particle dispersion in isotropic turbulence under Stokes drag and basset force with gravitational settling. *J. Fluid Mech.* **225**, 481–495.

Ormancey, A. and Martinon, J. (1984). Prediction of particle dispersion in turbulent flows. *PhysicoChemical Hydrodynamics* **5**, 229–244.

Parthasarathy, R. N. and Faeth, G. M. (1990). Turbulent dispersion of particles in self-generated homogeneous turbulence. *J. Fluid Mech.* **220**, 515–537.

Pismen, L. M. and Nir, A. (1978). On the motion of suspended particles in stationary homogeneous turbulence. *J. Fluid Mech.* **84**, 193–206.

Ranz, W. E. and Marshall, W. R. (1952). Evaporation from drops. *Chem. Engng Prog.* **48**, 141–173.

Shearer, A. J., Tamura, H., and Faeth, G. M. (1979). Evaluation of locally homogeneous flow model of spray evaporation. *J. Energy* **3**, 271–278.

Shuen, J-S., Solomon, A. S. P., Zhang, Q-F., and Faeth, G. M. (1983). A theoretical and experimental study of turbulent particle-laden jets. NASA CR 168293.

Shuen, J-S., Solomon, A. S. P., Zhang, Q-F., and Faeth, G. M. (1985). Structure of particle-laden jets: Measurements and predictions. *AIAA J.* **23**, 396–404.

Snyder, W. H. and Lumley, J. L. (1971). Some measurements of particle velocity auto-correlation functions in a turbulent flow. *J. Fluid Mech.* **48**, 41–47.

Solomon, A. S. P., Shuen, J-S., Zhang, Q-F., and Faeth, G. M. (1984). A theoretical and experimental study of turbulent evaporating sprays. NASA CR 174760.

Spalding, D. B. (1953). The combustion of liquid fuels. In *Proceedings of 4th Symp. (Int.) on Combustion*, pages 847–864. The Combustion Institute, Baltimore, MD.

Strehlow, R. A. (1985). *Combustion Fundamentals*. McGraw-Hill. New York, NY.

Wang, L-P. and Maxey, M. R. (1993). Settling velocity and concentration distribution of heavy particles in isotropic turbulence. *J. Fluid Mech.* **256**, 27–68.

Wells, M. R. and Stock, D. E. (1983). The effects of crossing trajectories on the dispersion of particles in a turbulent flow. *J. Fluid Mech.* **136**, 31–62.

Zhou, Q. and Leschziner, M. A. (1991). A time-correlated stochastic model for particle dispersion in anisotropic turbulence. In *8th Turbulent Shear Flows Symp.* Munich.

Figure Captions

Figure 1. Temporal variations of the particle velocity autocorrelation coefficient from the stochastic and direct numerical simulations. (a) In the absence of gravity, $R^p = \frac{1}{3}(R_{11}^p + R_{22}^p + R_{33}^p)$. (b) For $v_{dr} = 5v_k$, in the direction normal to the gravity direction.

Figure 2. Particle turbulence intensity from stochastic simulations and DNS, in the direction (a) normal and (b) parallel to the gravity direction.

Figure 3. Particle asymptotic diffusivity coefficient from stochastic simulations and DNS in the direction (a) normal and (b) parallel to the gravity direction.

Figure 4. Temporal variations of the mean particle Reynolds number for nonevaporating particles as calculated by stochastic and direct numerical simulations, in the absence of gravity.

Figure 5. Temporal variations of the minimum, the mean, and the maximum values of $(\tau_p/\tau_{p0})^{1/2}$ as calculated by stochastic and direct numerical simulations. $\tau_{p0} = 5\tau_k$, $\tau_{ec} = 5\tau_k$, and $Sc_p = 5$.

Figure 6. Temporal variations of the standard deviation of $\tau_p^{1/2}$ as calculated by stochastic and direct numerical simulations at different particle Schmidt numbers. $\tau_{p0} = 5\tau_k$ and $\tau_{ec} = 5\tau_k$.

Figure 7. Effects of the initial evaporation rate on the temporal variations of the skewness and kurtosis of $\tau_p^{1/2}$ as calculated by stochastic and direct numerical simulations. $\tau_{p0} = 5\tau_k$ and $Sc_p = 1$.

Figure 8. Temporal variation of the kurtosis of $\tau_p^{1/2}$ for different initial standard deviations as calculated by stochastic and direct numerical simulations. $\langle \tau_{p0} \rangle = 5\tau_k$ and $\tau_{ec} = 5\tau_k$.

Figure 9. Particle turbulence intensity from stochastic simulations and theory (Mei *et al.*, 1991) in the direction (a) normal and (b) parallel to the gravity direction.

Figure 10. Particle asymptotic diffusivity coefficient from stochastic simulations and theory (Mei *et al.*, 1991) in the direction (a) normal and (b) parallel to the gravity direction.

Figure 11. Comparison of the results of the Lagrangian stochastic model and theory (Mei *et al.*, 1991) for the particle asymptotic diffusivity coefficient.

Figure 12. Velocity autocorrelation coefficients of the heavy particle and its surrounding fluid particle. (a) Nonevaporating particles; effect of gravity. $\tau_p = 10\tau_k$. (b) Evaporating particles in zero gravity; effect of evaporation rate. $\tau_{p0} = 10\tau_k$ and $Sc_p = 0$.

Figure 13. Effects of the variations of the drift velocity on the depletion rate. $\tau_{p0} = 10\tau_k$ and $\tau_{ec} = 10\tau_k$.

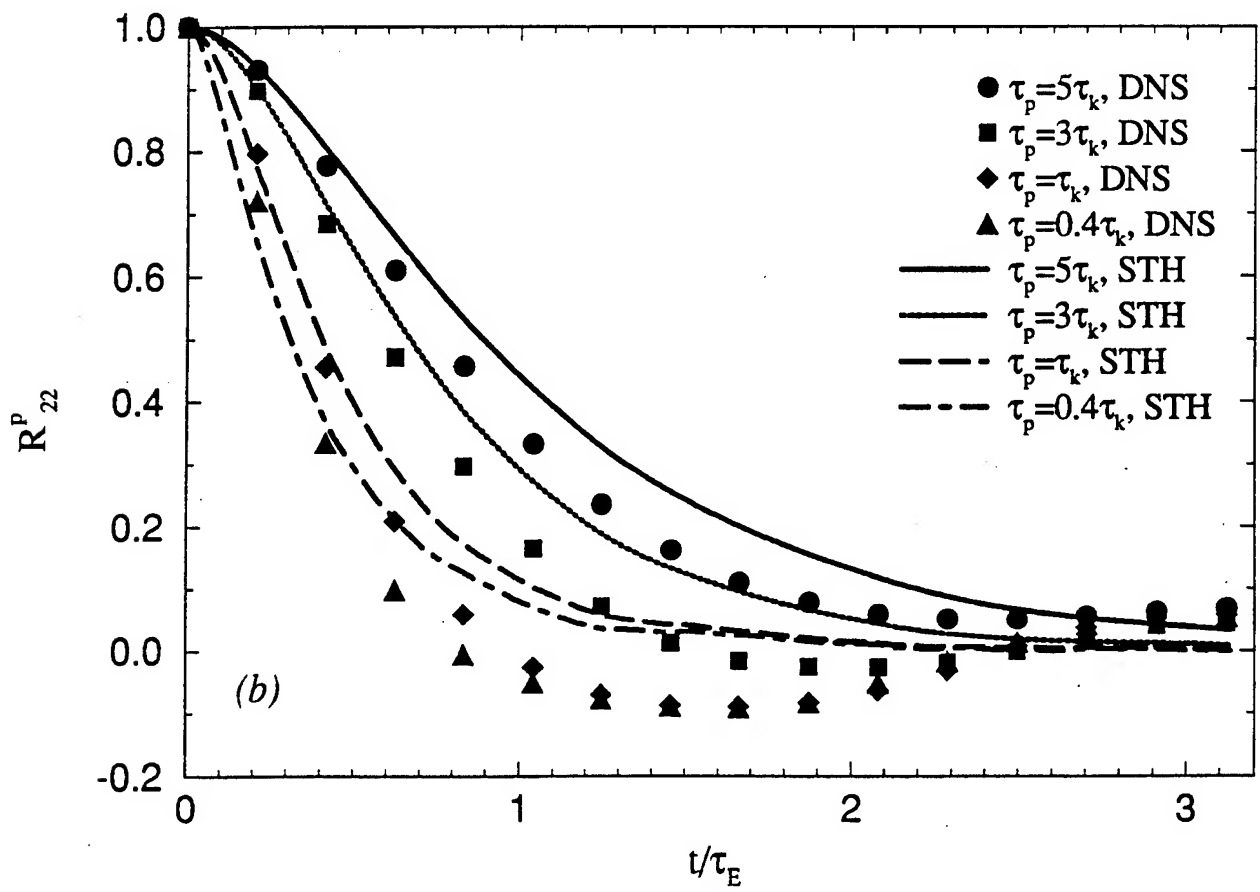
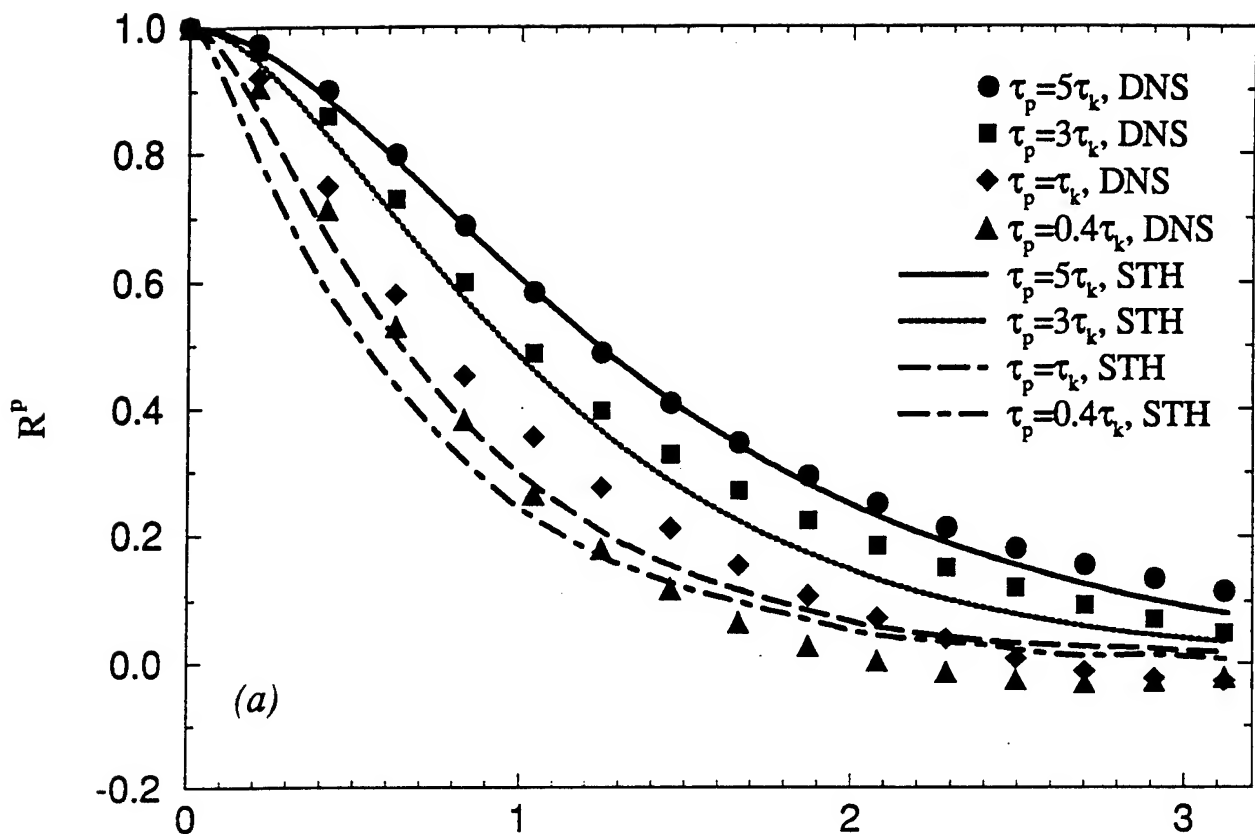
Figure 14. Effects of the variations of the drift velocity on the standard deviation and

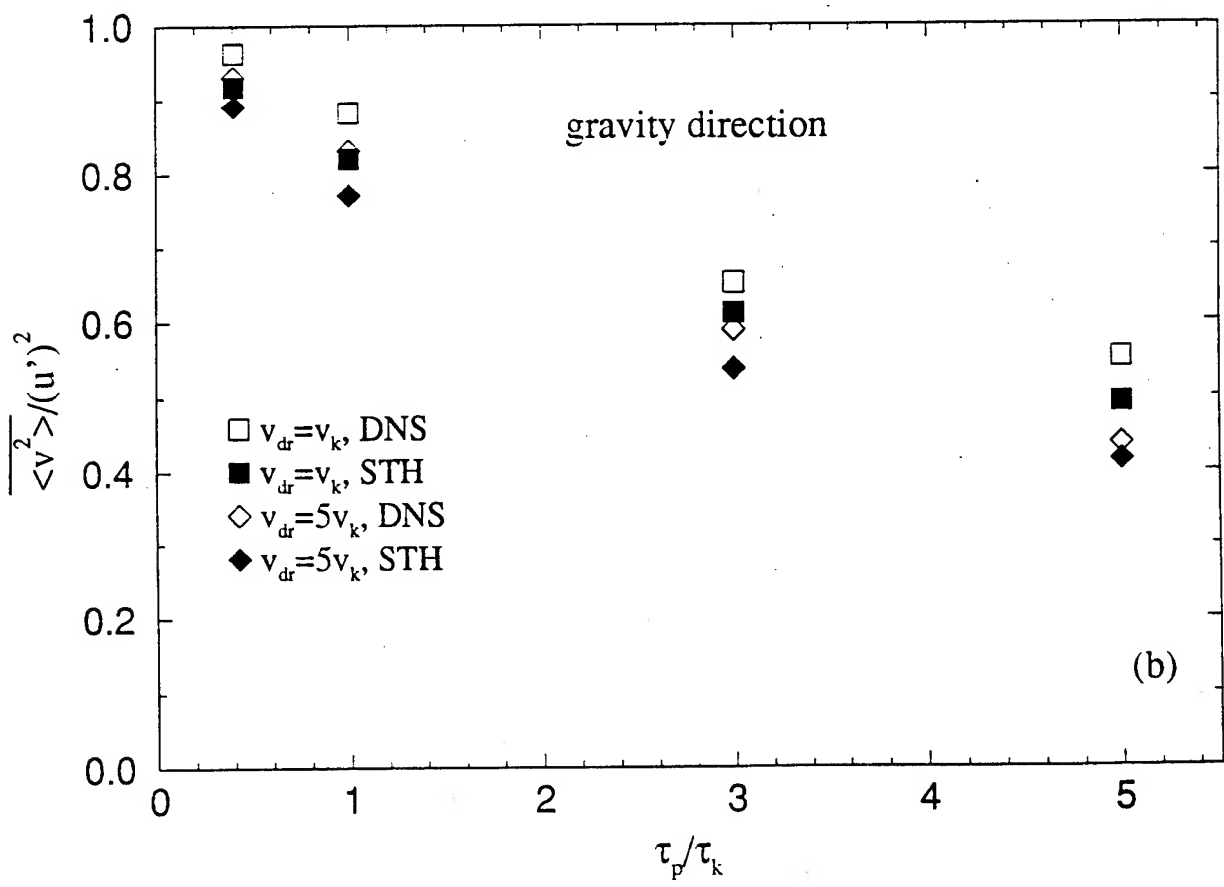
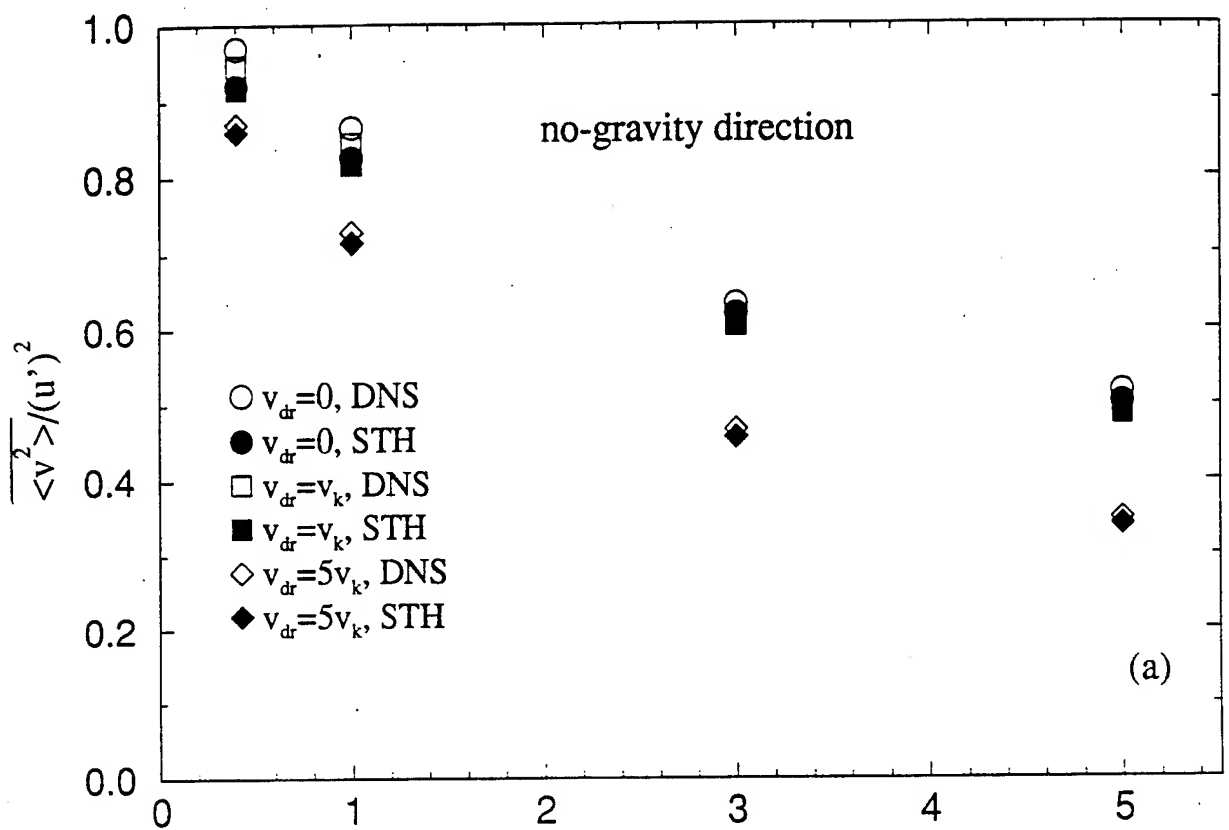
skewness of $\tau_p^{1/2}$. $\tau_{p0} = 10\tau_k$, $\tau_{ec} = 10\tau_k$, and $Sc_p = 1$.

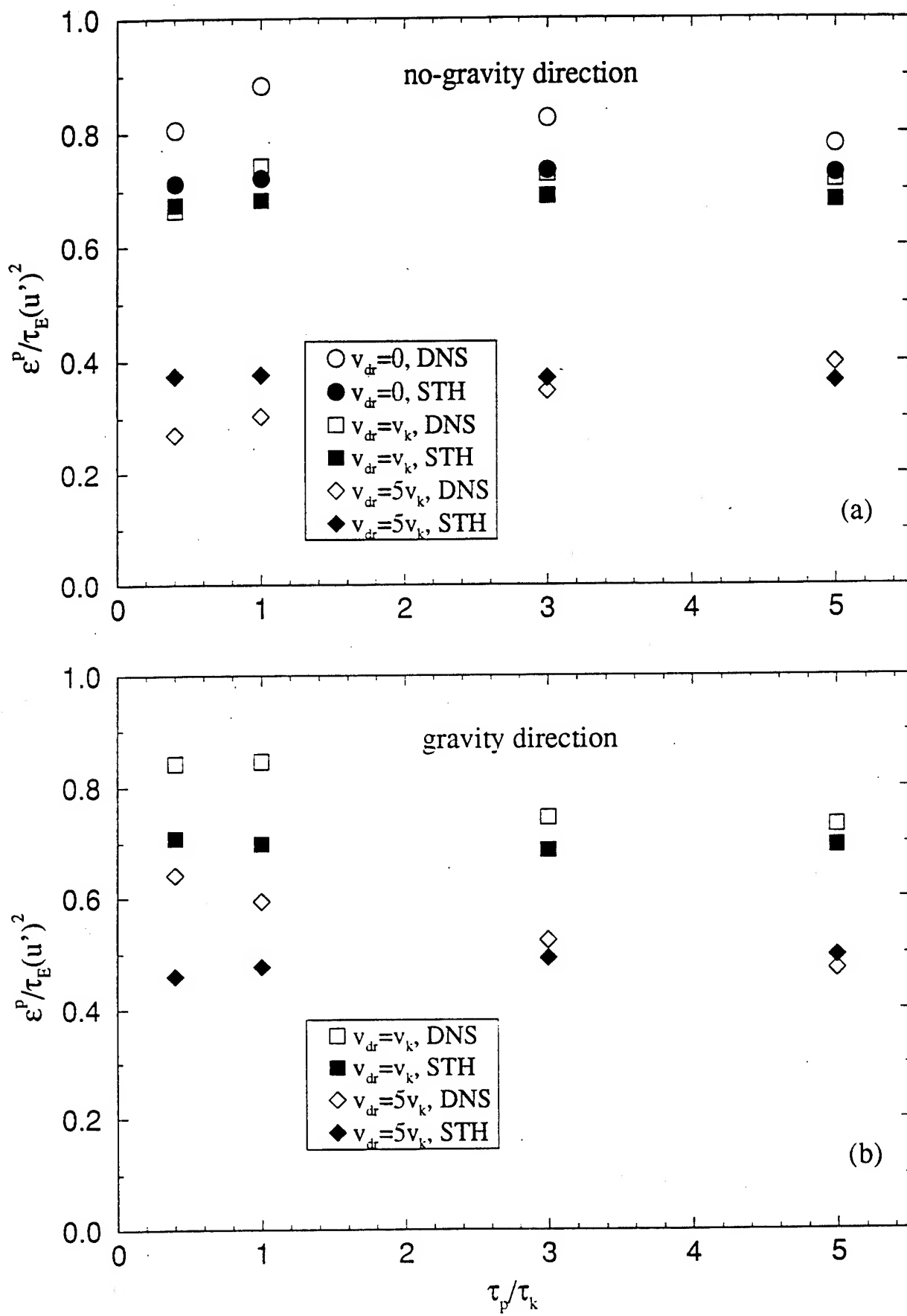
Figure 15. Effects of the variations of the drift velocity on the standard deviation and skewness of $\tau_p^{1/2}$. $\tau_{p0} = 10\tau_k$, $\tau_{ec} = \tau_k$, and $Sc_p = 1$.

Figure 16. Effects of the drift velocity on the dispersion of both nonevaporating and evaporating particles in the direction (a) normal and (b) parallel to the gravity direction. $\tau_{p0} = 10\tau_k$, $\tau_{ec} = 10\tau_k$, $Sc_p = 1$.

Figure 17. Effects of the drift velocity on the dispersion of both nonevaporating and evaporating particles in the direction (a) normal and (b) parallel to the gravity direction. $\tau_{p0} = 10\tau_k$, $\tau_{ec} = 10\tau_k$, $Sc_p = 5$.







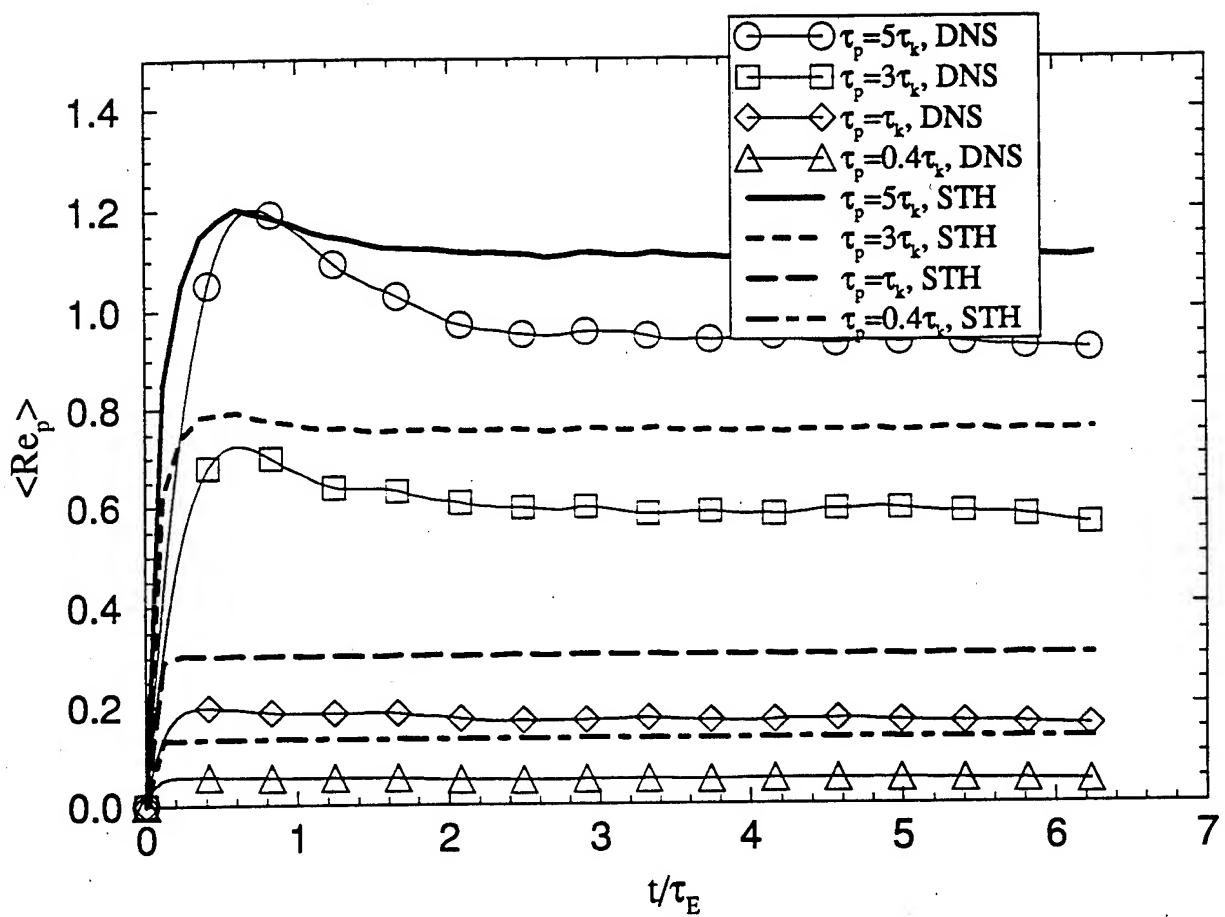


Fig. 4

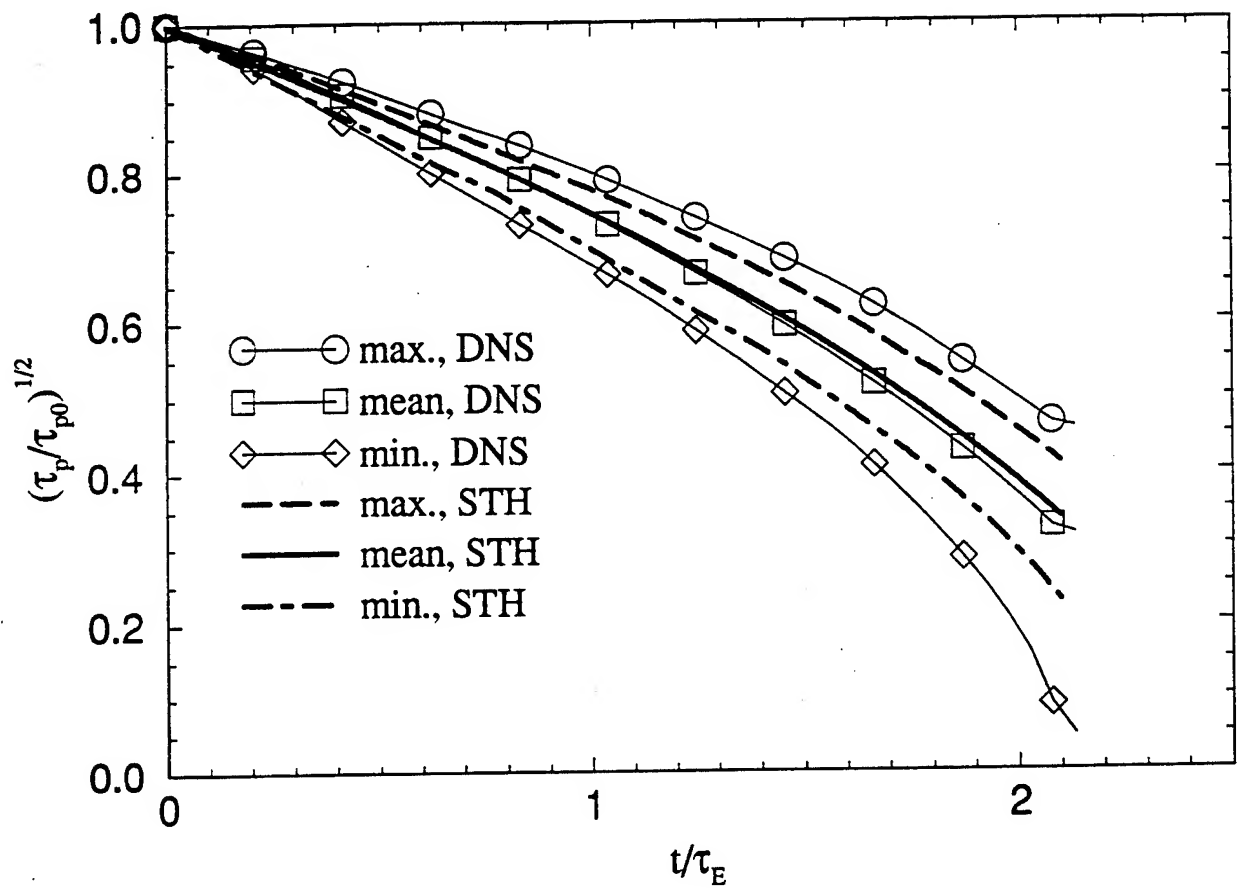


Fig. 5

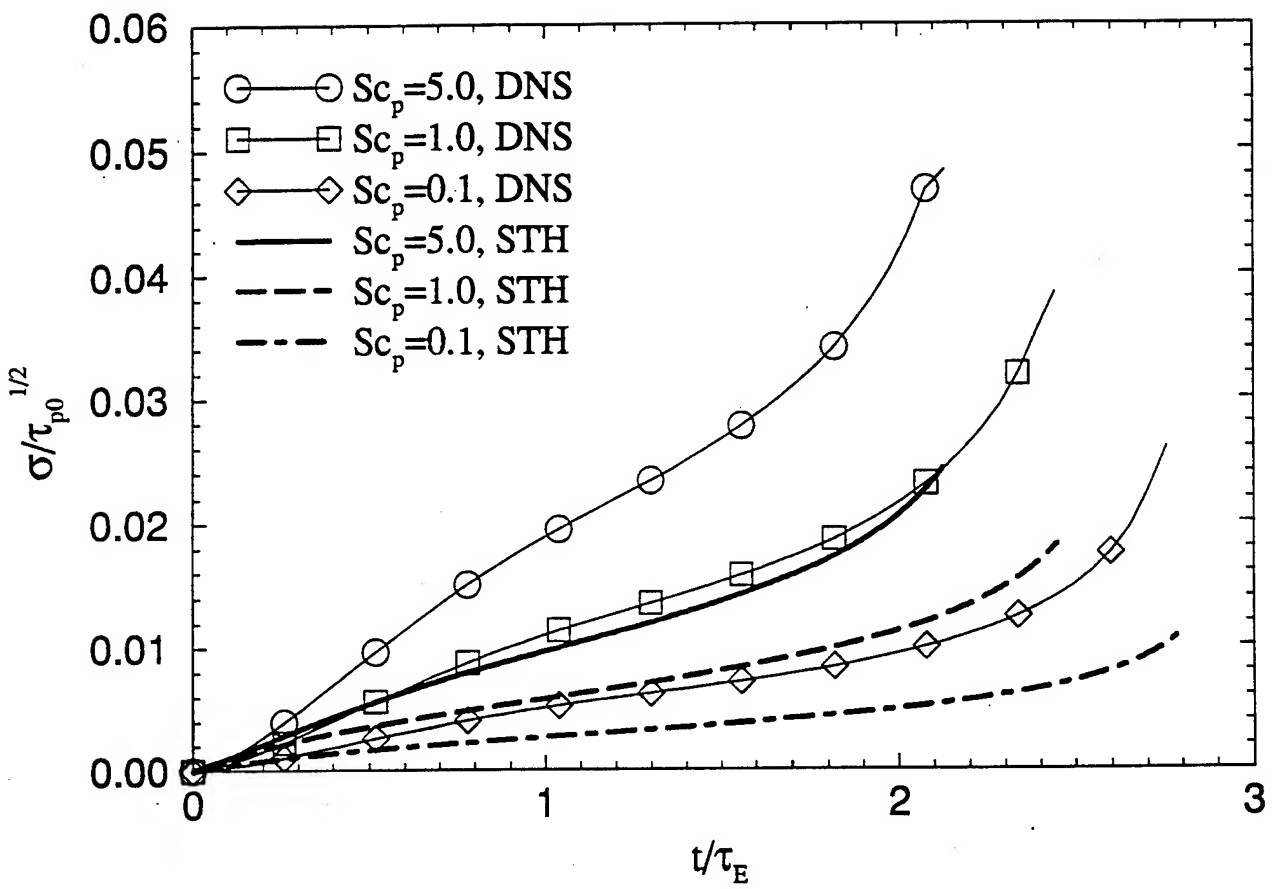


Fig. 6

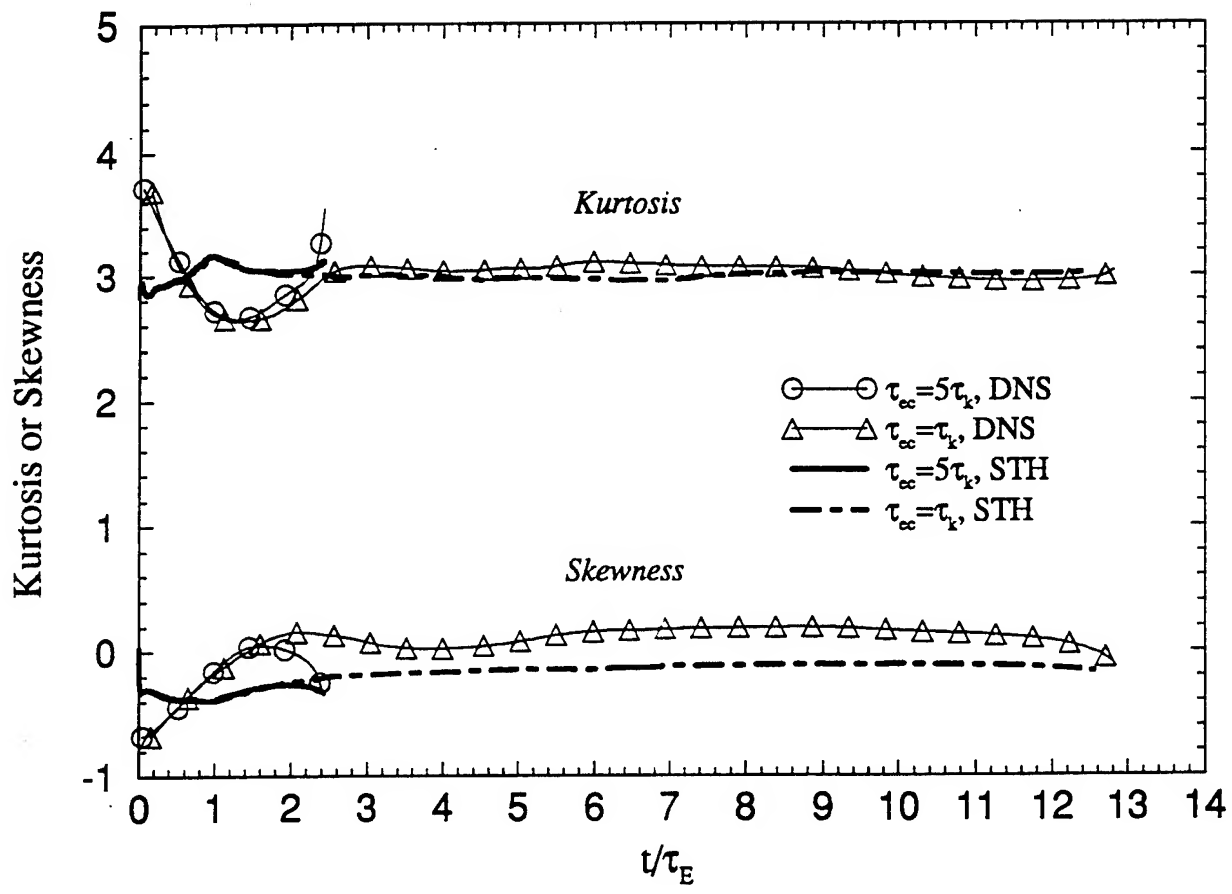


Fig. 7

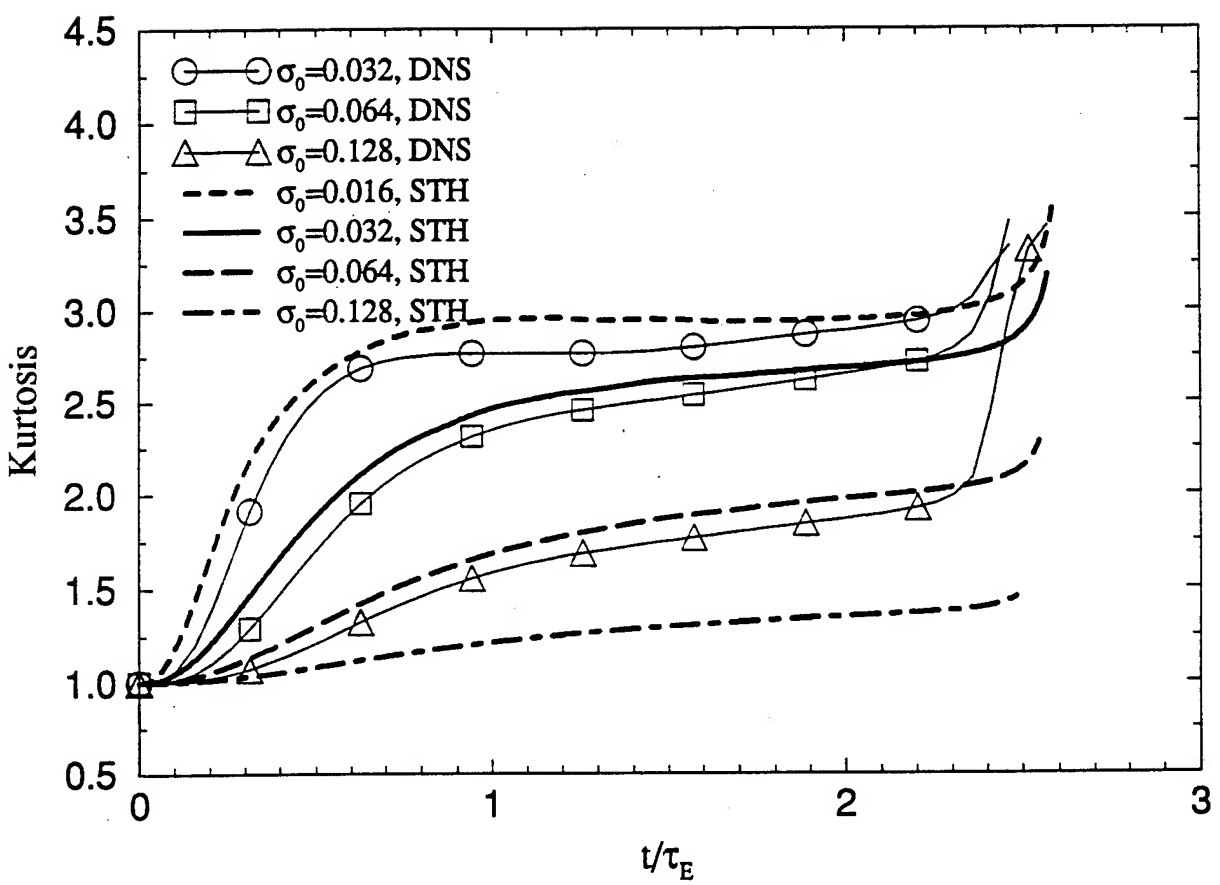
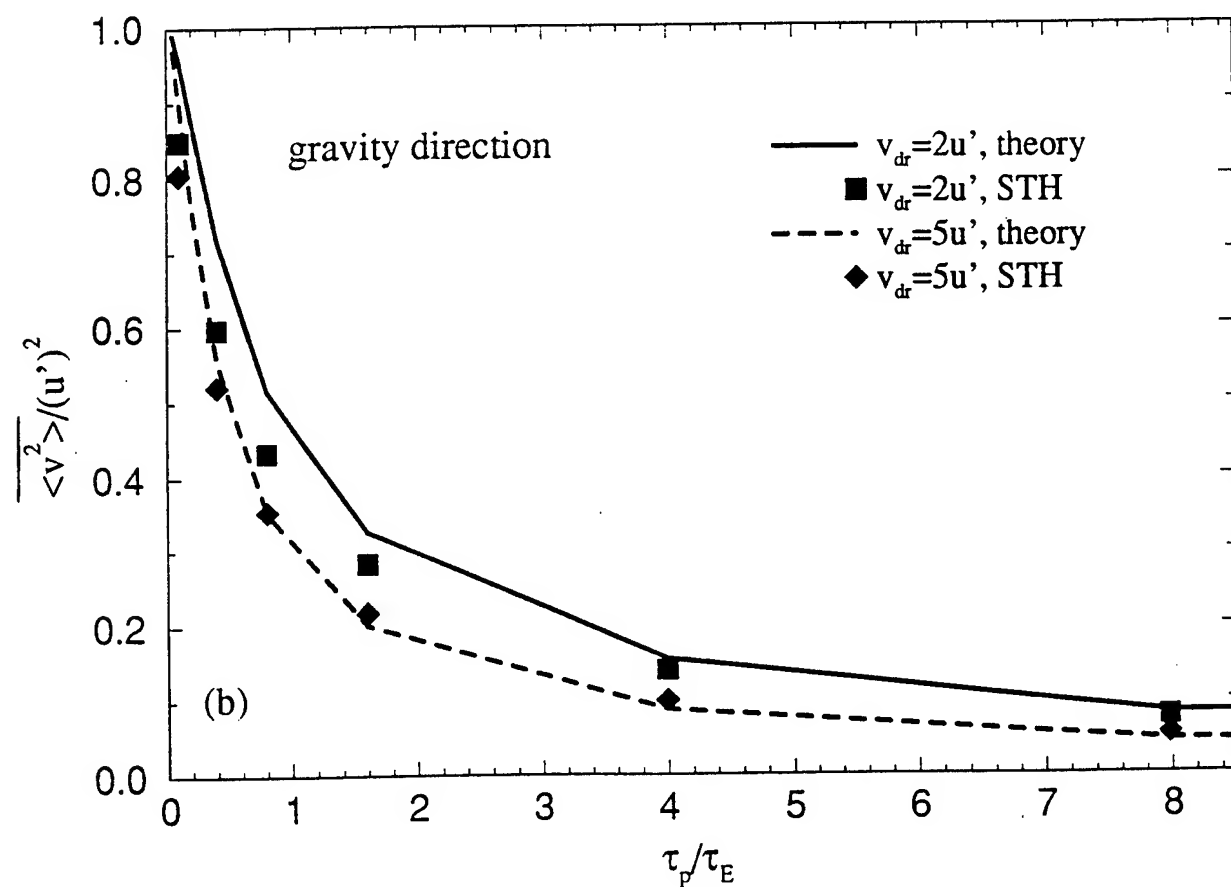
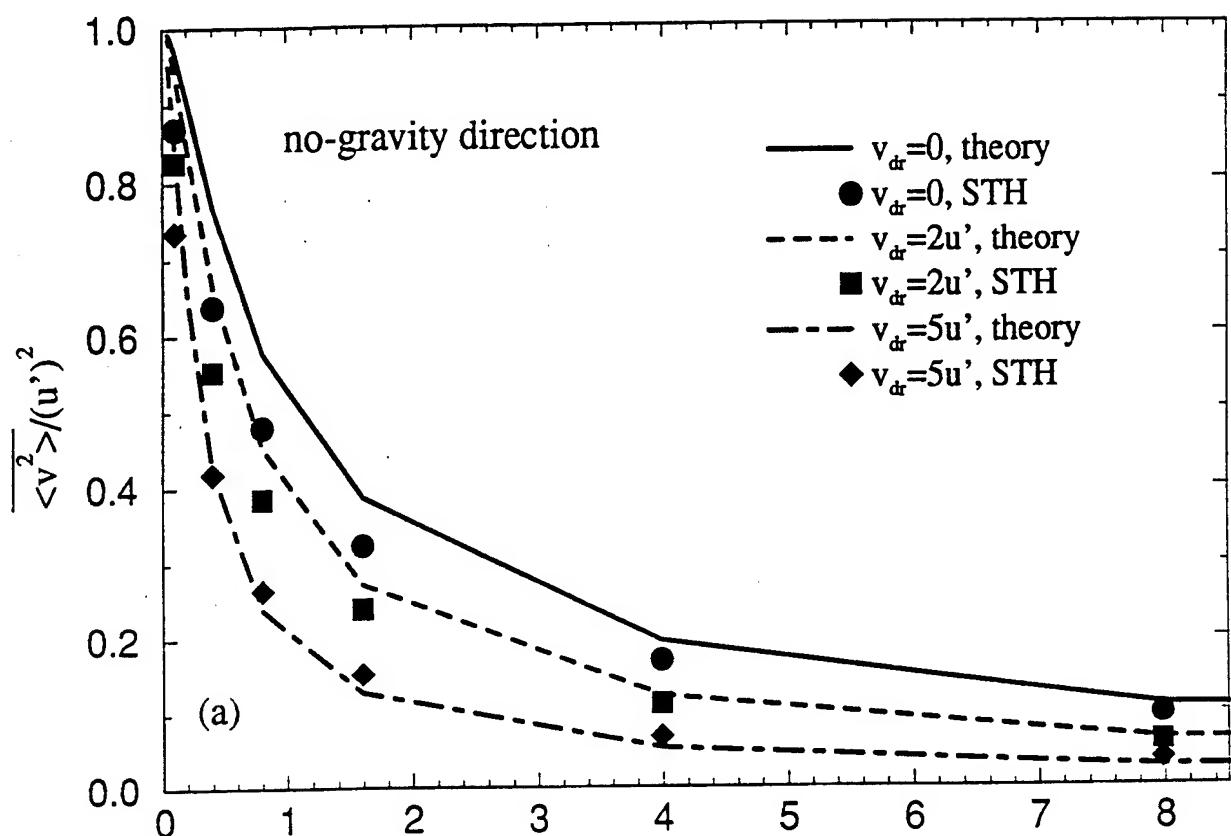
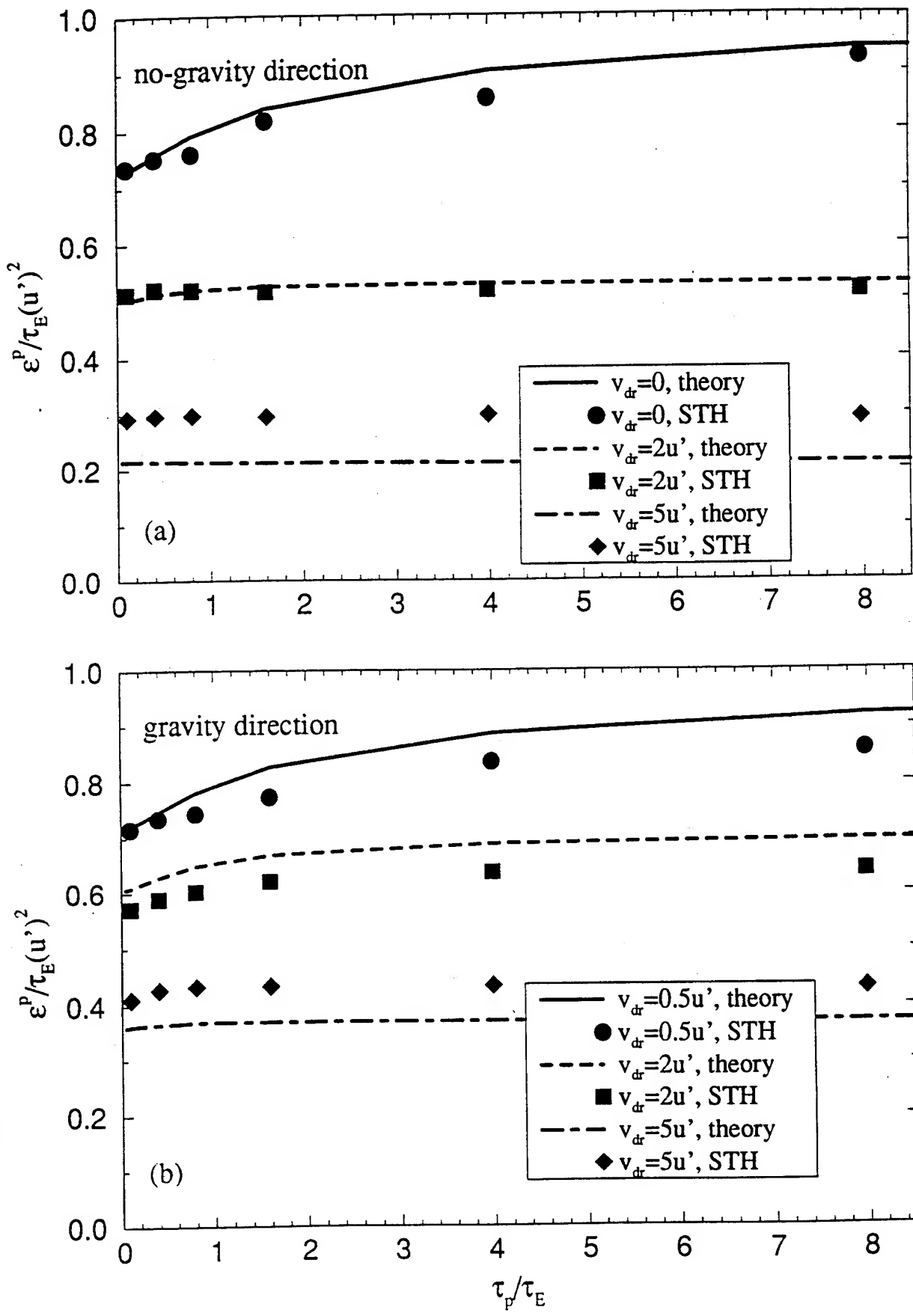


Fig. 8





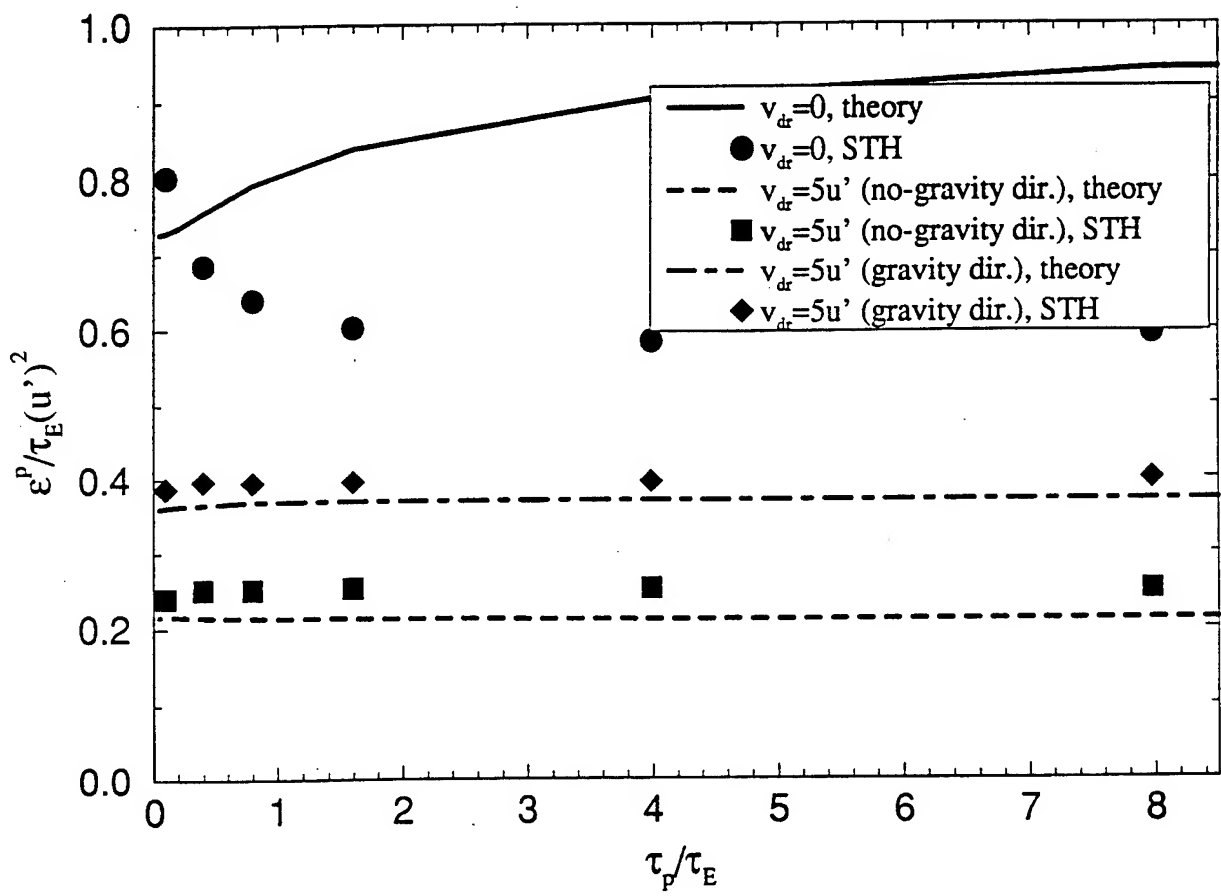
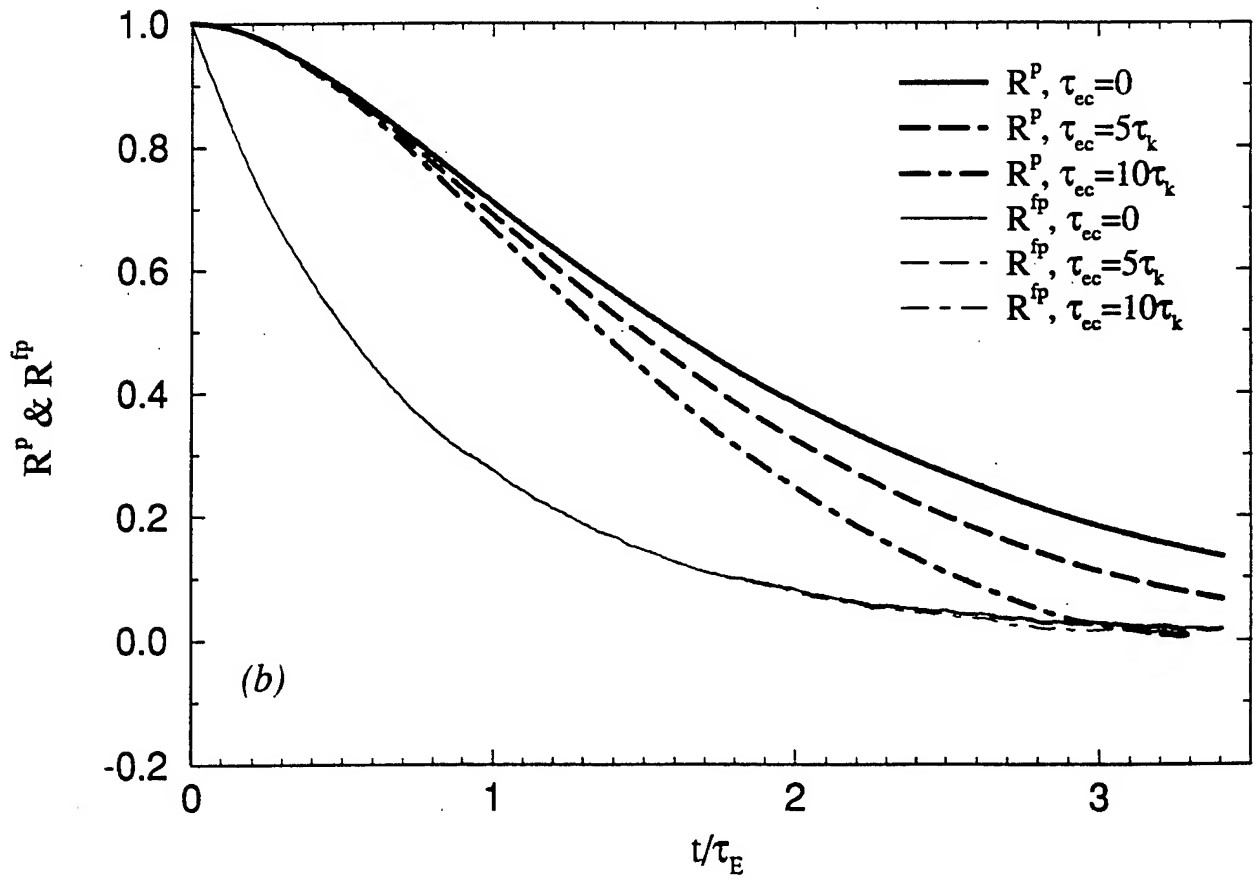
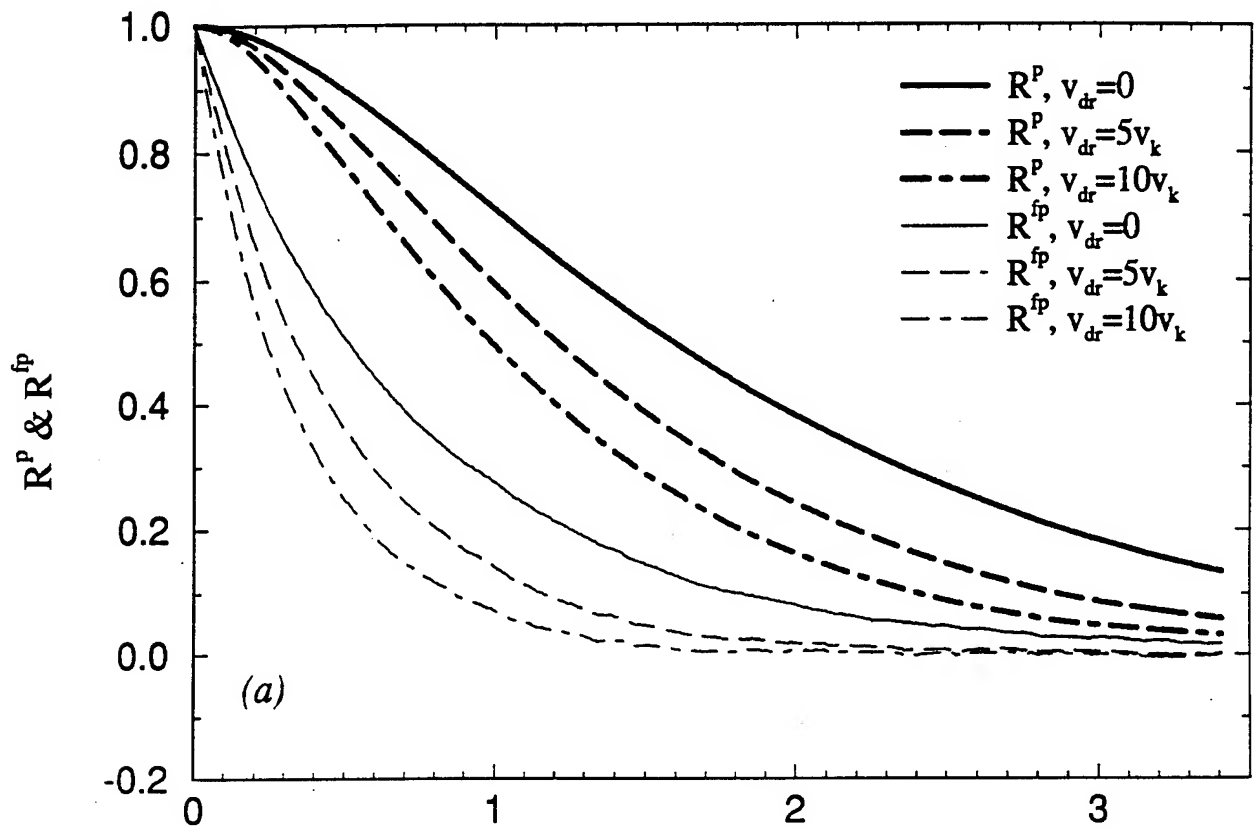


Fig. 11



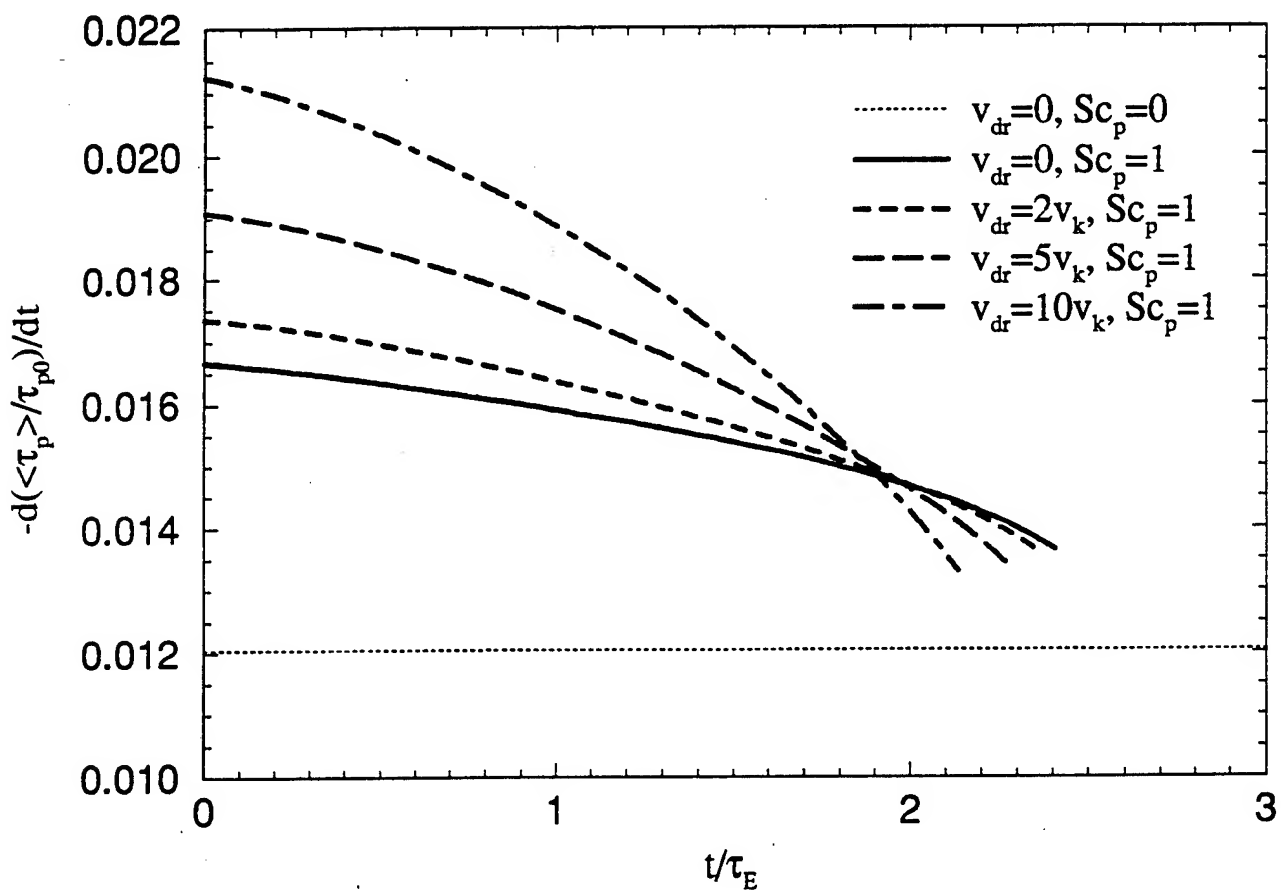
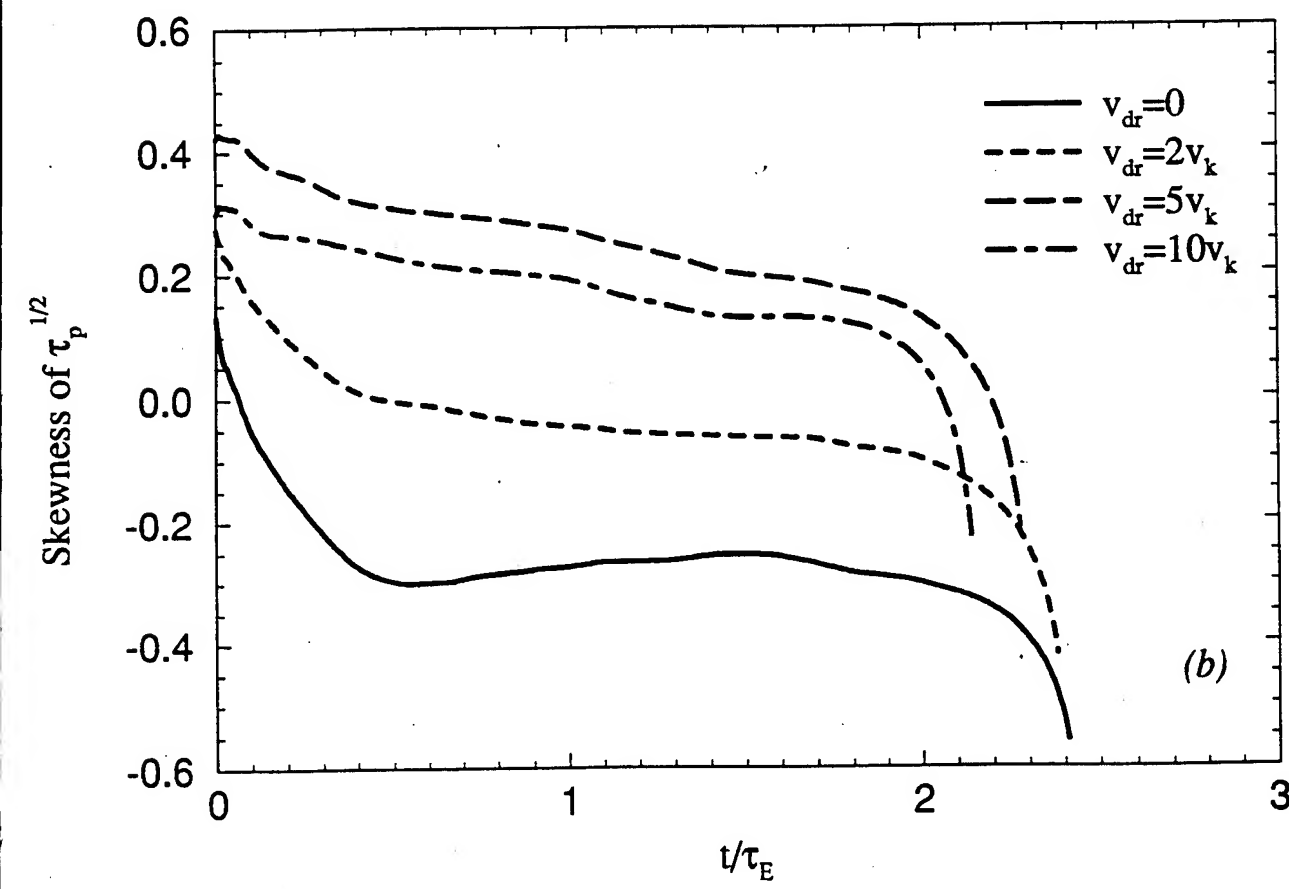
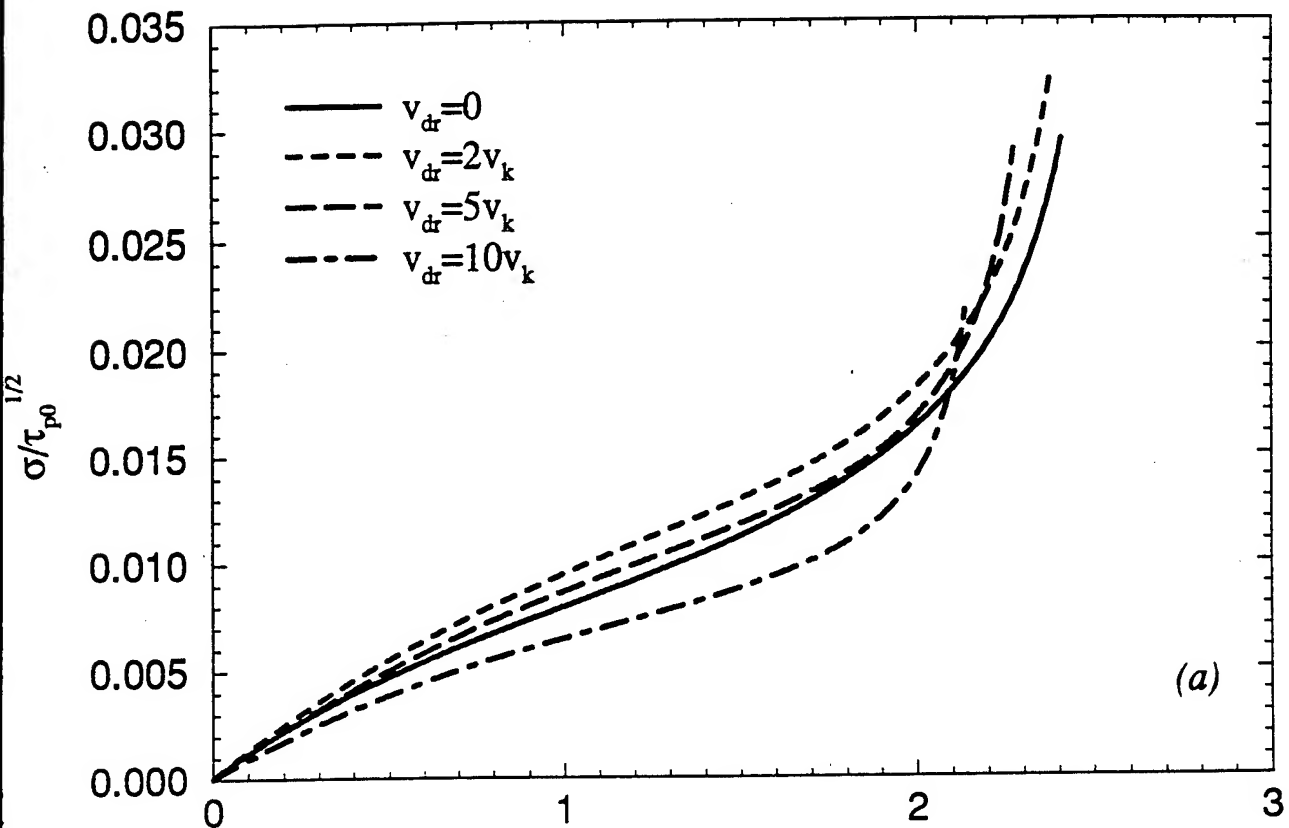
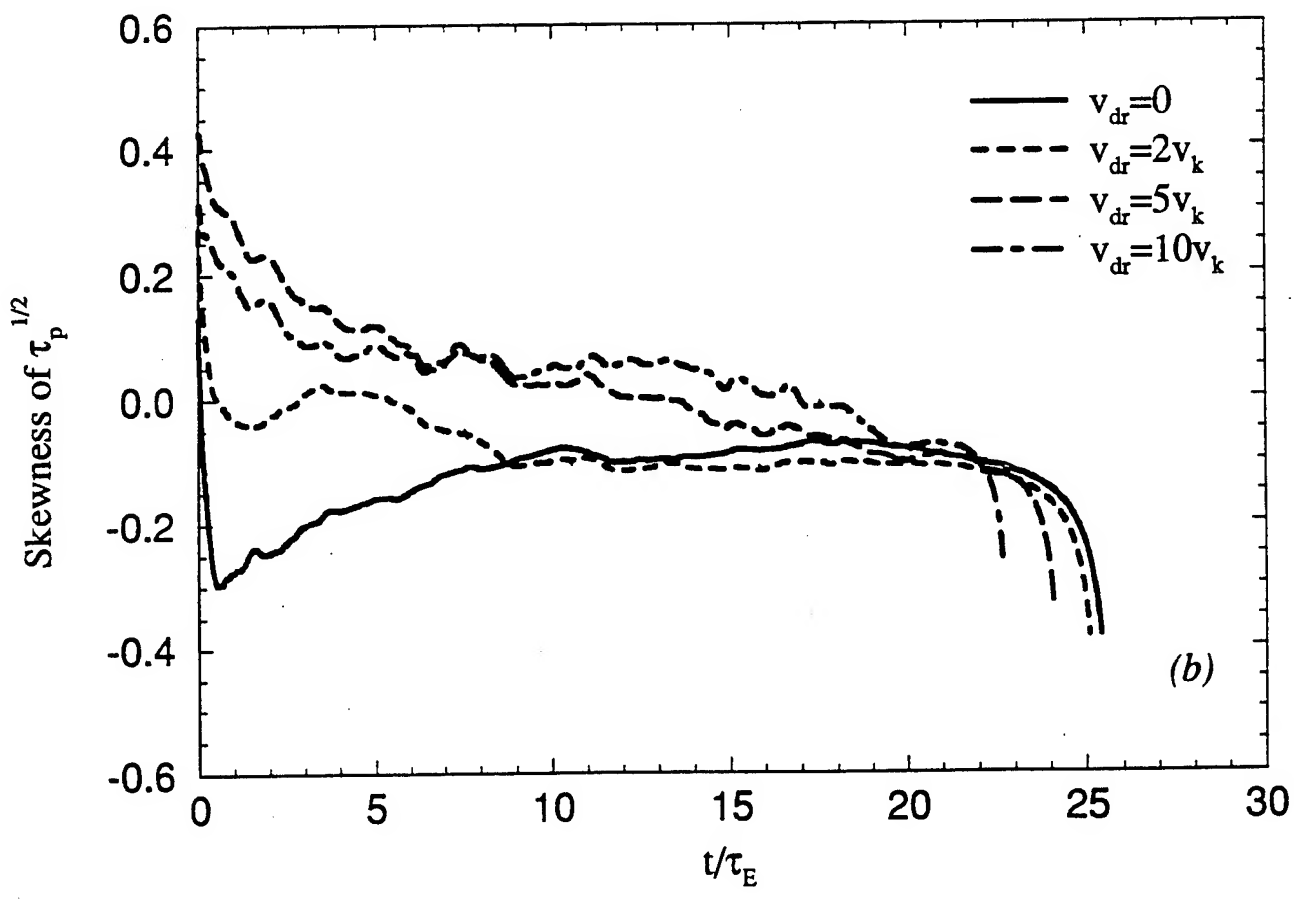
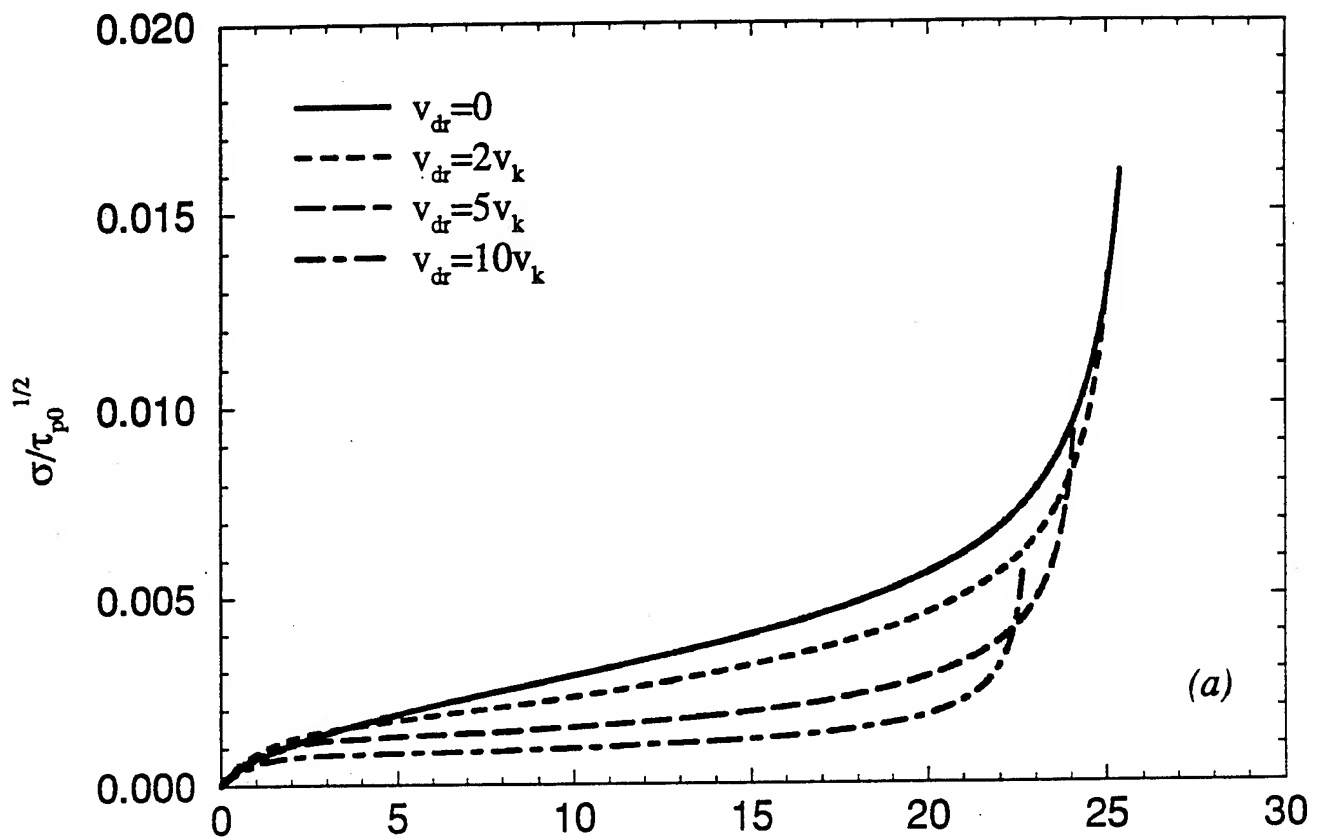
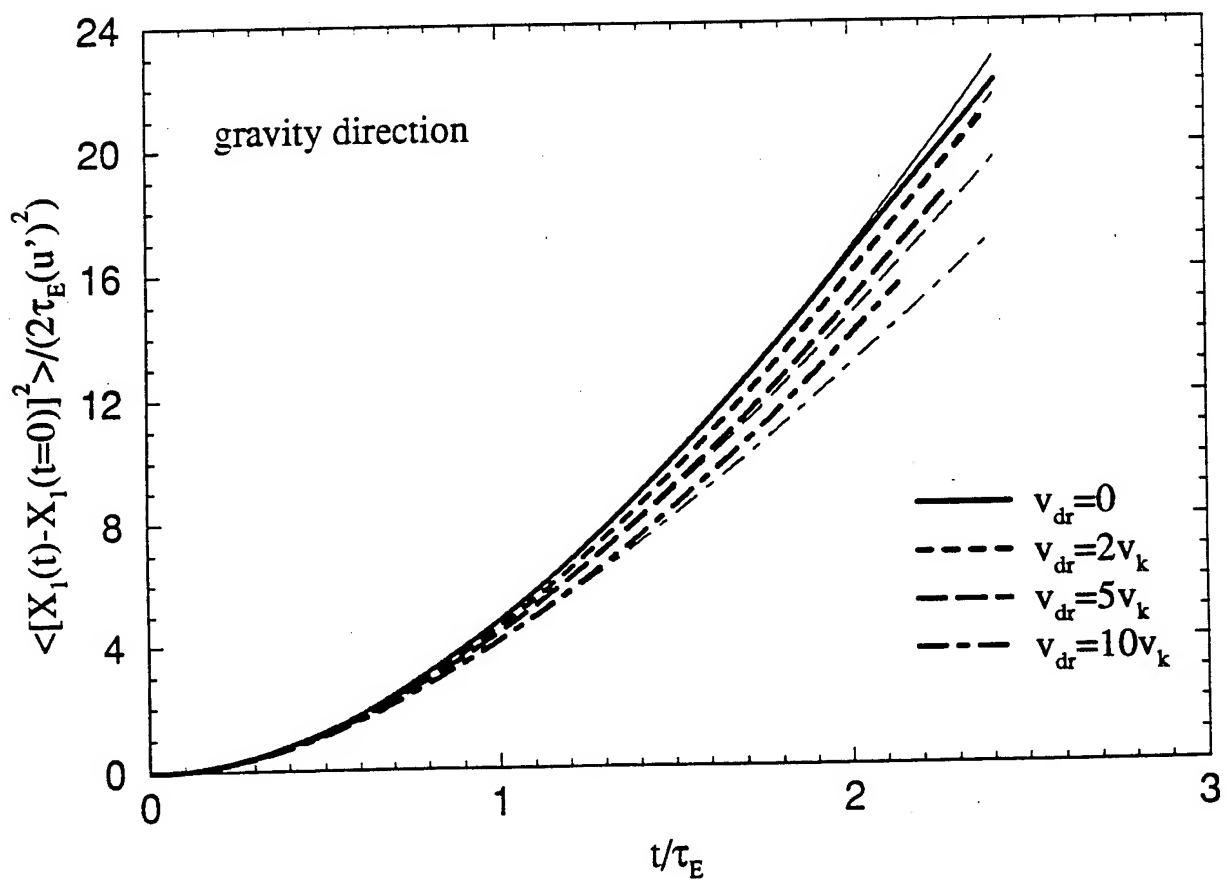
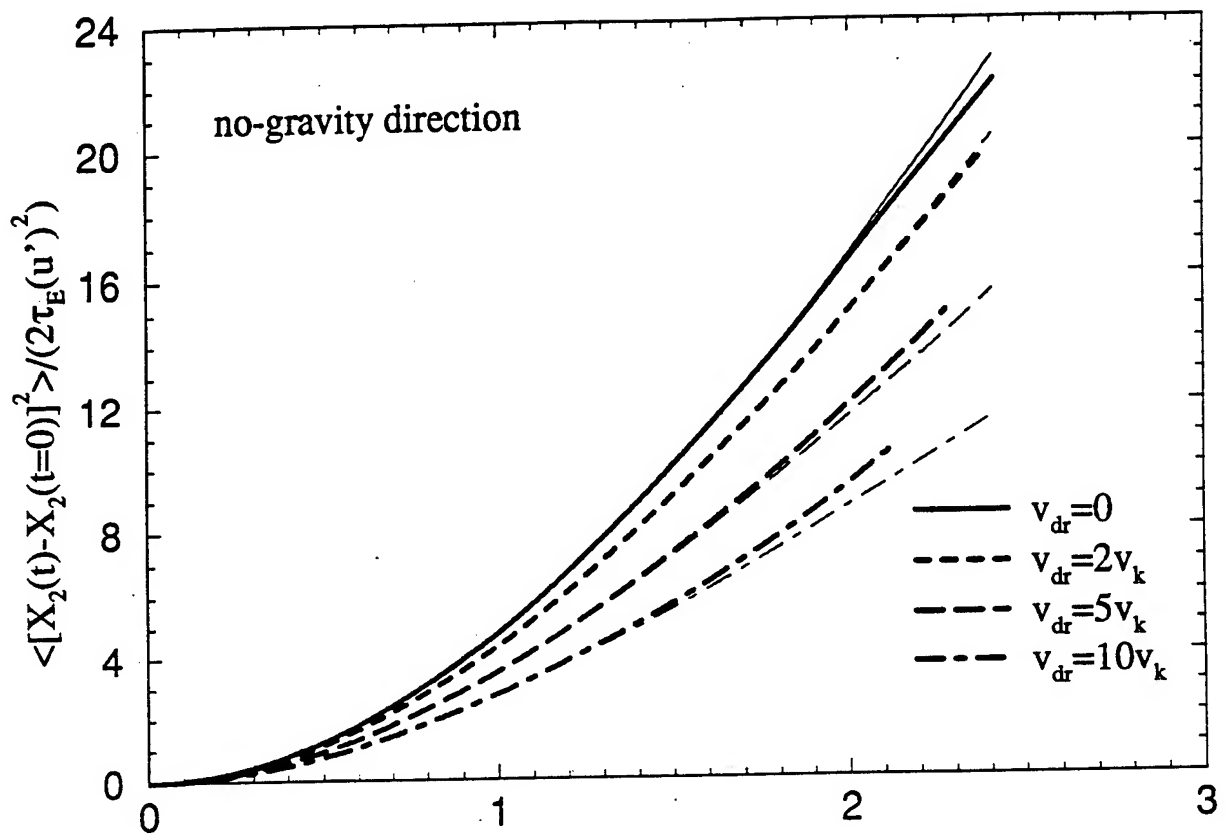


Fig. 13







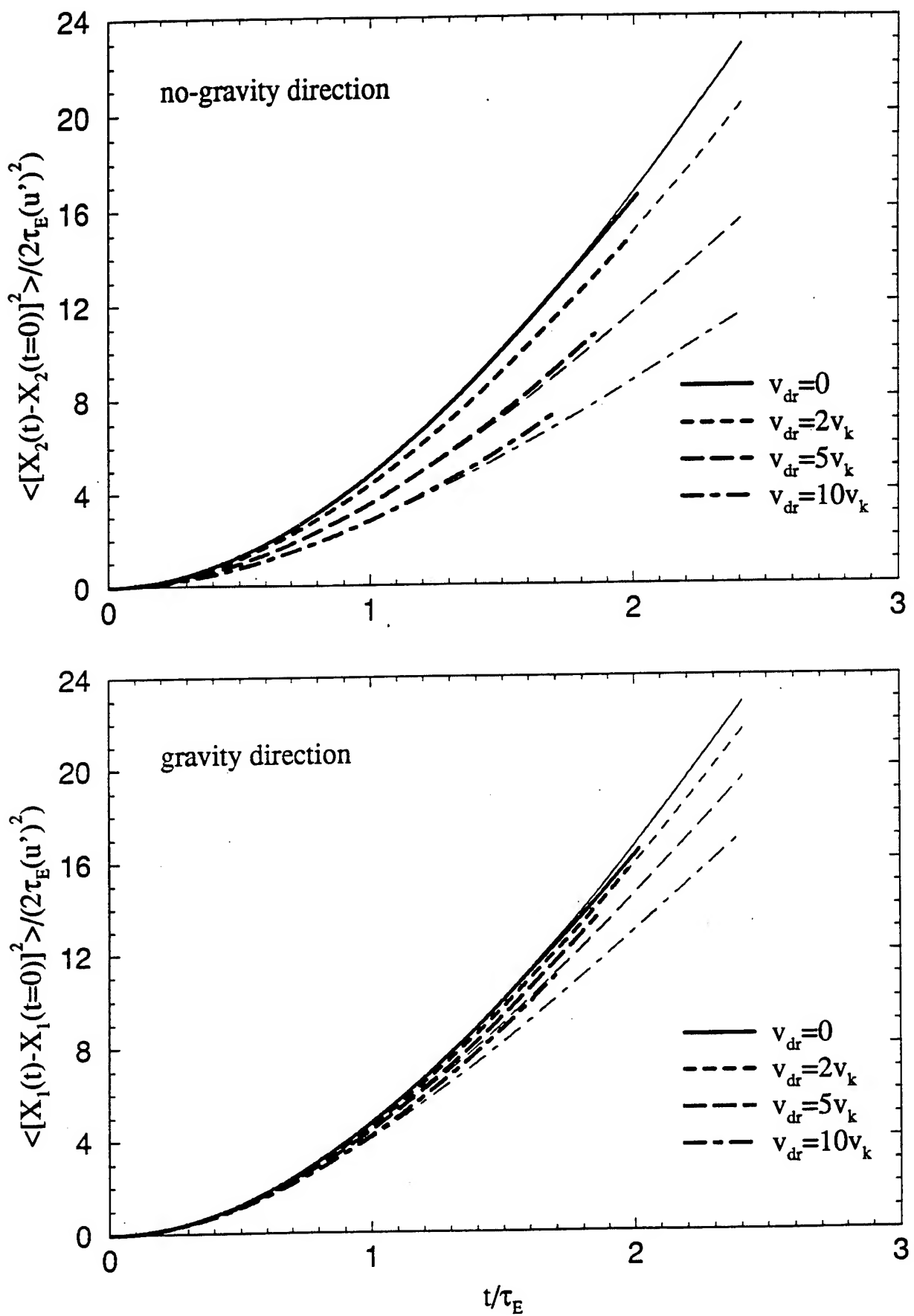


Fig. 17

APPENDIX III

Particle-Laden Turbulent Flows. Part I: Direct Simulations and Reynolds Stress Closures

Particle-Laden Turbulent Flows. Part I: Direct Simulations and Reynolds Stress Closures

F. Mashayek, D.B. Taulbee, and P. Givi

Department of Mechanical and Aerospace Engineering
State University of New York at Buffalo
Buffalo, NY 14260-4400

Abstract

This work deals with direct numerical simulation (DNS), and development of a new Reynolds stress model (RSM) for description of two-phase turbulent flows. DNS is conducted of a homogeneous turbulent shear flow laden with monosize particles. The dispersed phase is simulated in the Lagrangian frame and the carrier phase is considered in the Eulerian context. The coupling between the two phases is "two-way" which allows investigation of the effects of "the mass loading ratio" and "the particle time constant" on both phases. The RSM is based on a "two-fluid" methodology in which both the carrier phase and the dispersed phase are considered in the Eulerian frame. Closures are suggested for the unclosed terms (including the pressure-velocity gradient) which manifest the effects of two-way coupling. The DNS generated results are used to study some of the intricate physics of particle dispersion. These results are also used to determine the magnitudes of some of the empirical constants appearing in the RSM. The final model predictions for all the components of the fluid, the particle, and fluid-particle Reynolds stresses are assessed via detailed comparisons against DNS data.

1 Introduction

A variety of statistical models are available for prediction of multiphase turbulent flows (Faeth, 1987; Crowe *et al.*, 1996). A large number of "application oriented" investigations are based on the Eulerian description utilizing turbulence closures for both the dispersed and the carrier phases. The closure schemes for the carrier phase are mostly limited to

“Boussinesq” type approximations in conjunction with modified forms of the conventional $k-\epsilon$ model (Launder and Spalding, 1972). Examples are the contributions of Elghobashi and Abou-Arab (1983); Mostafa and Elghobashi (1985); Yokomine *et al.* (1994). The models for the dispersed phase are typically via the “Hinze-Tchen” algebraic relation (Chen and Wood, 1986; Zhou, 1993; Zhao, 1993) which relates the eddy viscosity of the dispersed phase to that of the carrier phase. While the simplicity of this model has promoted its use, its nonuniversality has been widely recognized (Chen and Wood, 1986; Mostafa and Elghobashi, 1986; Sargianos *et al.*, 1990; Zhou, 1993).

The literature of turbulence modeling in single-phase flows is very rich with predictive schemes based on Reynolds Averaged Navier Stokes (RANS) equations coupled with single-point statistical closures for higher order moments (Launder and Spalding, 1972; Launder and Spalding, 1974; Reynolds, 1976; Lumley, 1978; Taulbee, 1989; Launder, 1991; Wilcox, 1993). Referred to as Reynolds stress models, these schemes typically provide transport equations for various statistical moments up to the “second-order.” This methodology offers extensive advantages over the Boussinesq type approximations based on the “isotropic” eddy diffusivities (such as the $k-\epsilon$ model). However, the modeling is understandably more difficult as the number of unclosed terms in RANS is more than that in isotropic closures. The level of complexity is naturally escalated in two-phase flows. Due to enormous challenge in providing closures for statistical description of such flows, there is a need for experimental data. Because of the flow complexity, the extent of laboratory data is somewhat limited. However, direct numerical simulation (DNS) can provide a viable alternative. In the past, DNS has proven extremely effective in appraising the performance of turbulence closures in single phase flows (Givi, 1994), in addition to its value in elucidating many of the physical features of turbulence in such flows.

One of the first implementation of DNS in two-phase flows is due to Riley and Patterson (1974) who investigate particle dispersion in isotropic turbulence. McLaughlin (1989) simulates particle deposition in a channel, and Squires and Eaton (1990); Squires and Eaton (1991b); Squires and Eaton (1991a) have conducted extensive DNS of stationary and decaying turbulence fields with one- and two-way coupling. Squires and Eaton (1994) use DNS data to investigate some issues of relevance to turbulence modifications by particles. Elghobashi and Truesdell (1992); Elghobashi and Truesdell (1993); Truesdell and

Elghobashi (1994) report the results of related studies. The settling velocity of heavy particles in isotropic turbulence is studied by Wang and Maxey (1993), and Mashayek *et al.* (1997a) report results of a parametric study on dispersion and polydispersity of evaporating particles in stationary isotropic turbulence. While there are no reported DNS results on particle-laden homogeneous turbulent shear flows, several large eddy simulation (LES) results of such flows are available (Yeh and Lei, 1991; Simonin *et al.*, 1995). These studies are very useful for understanding the physics of particle-laden shear flows and for assessment of some of the recent theories pertaining to such flows (Reeks, 1993; Liljegren, 1993). However, the uncertainties associated with the subgrid scale closures as used in LES, does not allow for a complete assessment of turbulence closures. This assessment is better furnished via DNS.

The objective of this work is twofold: (1) conduct DNS of particle-laden turbulent shear flows, (2) provide a new second-order Reynolds stress model for statistical predictions of two-phase flows. While the DNS results are used to investigate some physical issues pertaining to the structure of such flows, their primary use is to aid the development of RSM. The model is associated with the Reynolds stresses in both phases and the cross-correlation between the velocities of the two phases. The extent of previous contributions in such modeling is somewhat limited (Shih and Lumley, 1986; Zhou, 1993; Zhou *et al.*, 1994; Simonin *et al.*, 1995). Therefore, DNS data are used rather extensively for both model parameterization (determination of some of the empirical constants appearing in the model), and model assessments. The RSM as proposed here is in the form of full second order transport equations. In the extension of this work in Part II (Mashayek *et al.*, 1997b), the corresponding “algebraic” form of the RSM is presented, and solutions are obtained for “explicit” representations of the Reynolds stresses and the fluxes of the void fractions. The results via this algebraic Reynolds stress model (ARSM) in Part II are also validated by the present DNS data.

It is stated here at the outset that the mathematical derivations leading to the final RSM here (and ARSM in Part II) are based on several assumptions and simplifications. Many of these assumptions are not related to “two-phase turbulent transport” and are required even if the flow is laminar and/or single phase. No attempt will be made to (re)justify these assumptions here. All the assumptions pertaining to two-phase transport will be elaborated

upon in detail. Section 2 deals with DNS in which the numerical methodology is described in §2.1 followed by presentation of results in §2.2. The development of the proposed RSM and its comparative assessment with DNS data are discussed in §3. The summary and concluding remarks are furnished in §4.

2 Simulations

Direct numerical simulation is conducted of particle dispersion in a three-dimensional homogeneous turbulent shear flow. This flow represents an ideal environment for the analysis of dispersion in that a natural forcing is present due to the mean shear, while the relative simplicity of full spatial homogeneity is maintained. In addition, the flow is inherently anisotropic, and thus offers a more desirable configuration (for model assessment) than that attainable by isotropic flows.

2.1 Problem formulation and computational methodology

The governing equations considered here are the continuity and Navier-Stokes equations for the continuous fluid phase, coupled with the Lagrangian equations for discrete particles. The particles are assumed to be spherical with diameter smaller than the smallest length scale of the turbulence and to obey an empirically corrected Stokesian drag relation. The particle density is much larger than the fluid density such that only the drag force and inertia are significant to the particle dynamics. In addition, the particle volume fraction is assumed to be relatively small and particle-particle interactions are neglected. The fluid velocity and pressure are denoted by \hat{U}_i and \hat{P} , and the particle position and velocity are denoted as X_i and \hat{V}_i , respectively, where the hat $\hat{\cdot}$ indicates the instantaneous quantity. With this nomenclature, the continuity and momentum equations for the fluid, and the Lagrangian equations of motion for a single particle are given by (Crowe *et al.*, 1977):

$$\frac{\partial \hat{U}_j}{\partial x_j} = 0, \quad (2.1)$$

$$\frac{\partial \hat{U}_i}{\partial t} + \frac{\partial}{\partial x_j} (\hat{U}_i \hat{U}_j) = -\frac{1}{\rho_f} \frac{\partial \hat{P}}{\partial x_i} + \nu \frac{\partial^2 \hat{U}_i}{\partial x_j \partial x_j} + S_i, \quad (2.2)$$

$$\frac{dX_i}{dt} = \hat{V}_i, \quad (2.3)$$

$$\frac{d\hat{V}_i}{dt} = \frac{f}{\tau_p} (\hat{U}_i^* - \hat{V}_i), \quad (2.4)$$

where x_i and t are the spatial and temporal coordinates, respectively, and ρ_f and ν are the fluid density and kinematic viscosity, respectively. The particle time constant for Stokesian drag of a spherical particle is $\tau_p = \frac{\rho_p d_p^2}{18\mu}$, where ρ_p and d_p are the particle density and diameter, respectively, and μ is the fluid viscosity. The function $f = 1 + 0.15 Re_p^{0.687}$ in (2.4) represents an empirical correction to Stokesian drag for large particle Reynolds numbers ($Re_p = \frac{\rho_p d_p |\hat{U}_i^* - \hat{V}_i|}{\mu}$) and is valid for $Re_p \leq 1000$ (Clift *et al.*, 1978). The superscript (*) indicates the values of the fluid variables at the particle location. In the simulations conducted here, the particle Reynolds number is of order unity and hence, the correction factor remains relatively small. The term S_i on the right-hand-side (RHS) of (2.2) represents the effects of the particle drag on the fluid. The procedure for calculating this Eulerian term from the discrete particle field is described below.

To configure a homogeneous shear flow, a linear mean velocity profile is applied to an initial zero mean random velocity field. Therefore, the carrier phase instantaneous velocity is expressed as $\hat{U}_i = Sx_2 \delta_{i1} + u_i$, where δ_{ij} is the Kroenecker delta function, and u_i is the carrier phase fluctuating velocity. The magnitude of the imposed shear is given by the amplitude of the mean velocity gradient, $S = dU_1/dx_2 = \text{const.}$, where U_i indicates the mean fluid velocity. The primary effect of the mean shear is to provide a natural (albeit idealistic) homogeneous forcing. In contrast to the isotropic case, no stationary state is achieved, and the Reynolds number grows until the turbulence structures outgrow the box size, at which time the simulation is stopped. To employ the Fourier spectral method, periodic boundary conditions must be imposed. This is accomplished by solving the Navier-Stokes equations for the fluctuating quantities on a grid which deforms with the mean flow. This transformation has been discussed in detail by Rogallo (1981) and is only summarized here. A computational coordinate system (x'_i) is related to the stationary system through

$x'_i = Q_{ij}x_j$ where the transformation tensor is defined as:

$$Q_{ij} = \begin{pmatrix} 1 & -St & 0 \\ 0 & 1 & 0 \\ 0 & 0 & 1 \end{pmatrix}, \quad (2.5)$$

for the present conditions. Performing the transformation on the Navier-Stokes equations and dropping the superscript $'$ on the coordinates, the governing equations in the transformed coordinates are described as:

$$Q_{ji}\frac{\partial u_i}{\partial x_j} = 0, \quad (2.6)$$

$$\frac{\partial u_i}{\partial t} + Q_{kj}\frac{\partial}{\partial x_k}(u_i u_j) = -\frac{Q_{ji}}{\rho_f}\frac{\partial p}{\partial x_j} - S u_2 \delta_{i1} + \frac{Q_{kj}Q_{lj}}{\nu}\frac{\partial^2 u_i}{\partial x_k \partial x_l} + S_i. \quad (2.7)$$

In the absence of gravity or other external body forces and by assuming that the particles start from the same initial velocities as those of their surrounding fluid elements, the particle instantaneous velocity is described as $\hat{V}_i = Sx_2\delta_{i1} + v_i$, with v_i denoting the particle fluctuating velocity. Therefore, the droplet position and momentum equations in the transformed coordinates are expressed as:

$$\frac{dX_i}{dt} = v_i - Stv_2\delta_{i1}, \quad (2.8)$$

$$\frac{dv_i}{dt} = \frac{f}{\tau_p}(u_i^* - v_i) - S v_2 \delta_{i1}. \quad (2.9)$$

Simulations are conducted within the domain $0 \leq x_i \leq L$, ($x_1 \equiv x, x_2 \equiv y, x_3 \equiv z$). A Fourier pseudospectral (Givi and Madnia, 1993) method with triply periodic boundary conditions is employed for the spatial representation of the fluid velocity and pressure. All calculations are performed in Fourier space with the exception of the non-linear terms. Aliasing errors are treated by truncating energies outside of a spherical wavenumber shell having radius $\sqrt{2}N/3$, (where N is the number of grid points in any direction) and time advancement is performed using an explicit second order accurate Adams-Bashforth method. Temporal advancement of the Lagrangian particle equations is also done by the Adams-Bashforth method. In order to evaluate fluid variables at the particle locations a fourth order accurate Lagrange polynomial interpolation scheme is employed. The particle drag source term appearing in the momentum equations (S_i) is numerically calculated in the Eulerian frame by volume averaging the

contributions from all of the individual particles residing within the cell volume ($\Delta V = \Delta x^3$, where Δx is the grid spacing) centered around each grid point:

$$S_i = -\frac{1}{\rho_f \Delta V} \sum_{p=1}^{n_p} \left\{ \frac{f m_p}{\tau_p} (u_i^* - v_i) \right\}, \quad (2.10)$$

where $m_p = \pi \rho_p d_p^3 / 6$ is the mass of a single particle and n_p is the number of particles within the cell volume.

The mean shear imposed by the grid transformation skews the grid in time. In order to allow the simulation to progress for a substantial time, it is necessary to remesh the grid at regular time intervals. The remeshing procedure is similar to that used by Rogallo (1981). The grid begins in an initial orthogonal state and proceeds to skew in the $x_1 - x_2$ plane. At a time of $St = 0.5$ the grid is then remeshed back to a hypothetical $St = -0.5$ grid. The fluid variables are then re-calculated onto the new mesh by use of the periodic boundary condition. The choice of time for the remesh process is optimal for the initially cubic domain in that no interpolation is required. After the remeshing, the variables are truncated in Fourier space outside of the spherical wavenumber shell of magnitude $\sqrt{2}N/3$. This results in a slight loss of kinetic energy; however, if the simulation is well resolved (i.e. only relatively small energies are present in the highest wavenumber bands) this truncation is considered to be negligible. The simulation is then allowed to proceed until the next remesh time is reached, or until the length scales of turbulence become too large to be accurately resolved, at which time the simulation is terminated.

The magnitude of the mean shear and all of the initial gas-phase conditions are held constant in all the simulations. We consider the initial hydrodynamic field with the highest possible Reynolds number without jeopardizing the small scale resolution. Detailed studies of the effects of initial conditions and the magnitude of the mean shear in single-phase flows are provided by Rogers *et al.* (1986). The velocity field is initialized as a random Gaussian, isotropic and solenoidal field in Fourier space. The initial energy spectrum is of the form $E(\kappa) \sim \kappa^4 \exp(-2(\kappa/\kappa_s)^2)$, where κ is the wave number and κ_s specifies the wave number location for the peak of the energy spectrum and is chosen to be $\kappa_s = 7$. The initial turbulence energy is $q^2 = \langle u_i u_i \rangle = 3 \text{ m}^2/\text{s}^2$ (where the single brackets $\langle \rangle$ indicate an ensemble average over the number of grid points). The value of the initial mean dissipation is

$\epsilon = \langle 2\nu s_{ij} s_{ij} \rangle = 29.15 \text{ m}^2/\text{s}^3$, where the symmetric rate of strain tensor is $s_{ij} = (u_{i,j} + u_{j,i})/2$ ($u_{i,j} \equiv \partial u_i / \partial x_j$). For all of the simulations $\nu = 1.59 \times 10^{-4} \text{ m}^2/\text{s}$, $\rho_f = 1 \text{ kg/m}^3$, $S = 62.8 \text{ s}^{-1}$ and $L = 0.2 \text{ m}$. The particle density is specified as $\rho_p = 721.8 \text{ kg/m}^3$, a value chosen to yield a reasonable number of particles for the ranges of parameters under consideration. All the simulations are performed on 96^3 grid points, with a constant time step of $\Delta t = 8 \times 10^{-5} \text{ s}$, and are terminated at a non-dimensional time of $St = 12$. The particles are initially distributed randomly throughout the domain, and are specified to have zero velocity difference with the local fluid (i.e. $v_i(t=0) = u_i^*(t=0)$).

The computational requirement for the Navier Stokes solver (on a Cray-YMP) is approximately 4.30 seconds per time-step for simulations with a resolution of 96^3 collocation points. Numerical integration of 6.67×10^5 particles with only one-way coupling ($S_i \equiv 0$) requires an additional 4.2 seconds per time-step, while the additional computational time for a full two-way coupling simulation is 8.7 seconds per iteration. Thus, greater than 50% of the particle simulation time is devoted to the calculation of the source term in the momentum equations. The reason for this high computational cost is that only a partial vectorization of these loops is possible. The time required for integrating the particles scales approximately linearly with the number of particles.

2.2 Results

There are two main parameters which influence the flow behavior: the particle time constant (τ_p) and the mass loading ratio (Φ_m). Table 1 provides a listing of the cases considered to study the effects of these parameters. In this table N_p indicates the total number of particles tracked in each simulation. The case with $\Phi_m = 0$ is performed to investigate the effects of the turbulence on the particle in one-way coupling ($S_i \equiv 0$). All the other cases are considered with two-way coupling.

In order to establish the accuracy of the single phase flow simulation, in table 2 comparisons are provided of some of the results obtained by one-way coupled DNS with previous numerical and experimental data in turbulent shear flows. The comparisons are made with DNS results of Rogers *et al.* (1986) (RMR), and the experiments of Tavoularis and

Corrsin (1981) (TC), Harris *et al.* (1977) (HGC), and Champagne *et al.* (1970) (CHC). The Reynolds number, Re_λ , is based on the Taylor microscale (λ_1) in the x_1 direction ($\lambda_1^2 = \langle u_1^2 \rangle / \langle (\partial u_1 / \partial x_1)^2 \rangle$) and the turbulence velocity scale (q); and the turbulence Reynolds number is $Re_T = q^4 / \langle \epsilon \rangle \nu$. Additional information is provided pertaining to the non-dimensional shear number ($Sq^2 / \langle \epsilon \rangle$), the relative energy ratios ($\langle u_i^2 \rangle / q^2$), and the non-zero off-diagonal Reynolds stress correlation coefficient.

The ensemble average value (denoted by $\langle\langle \rangle\rangle$) of particle Reynolds number provides a measure of the dynamic equilibrium between the particles and the flow. This is particularly of interest for model assessments as most turbulence closures are based on the assumption of dynamic equilibrium. In the present simulations, initially all of the particles have a zero velocity relative to their surrounding fluid. Furthermore, the initial flow field is isotropic, and before reaching equilibrium it evolves in a relatively fast rate. As a result, the particle velocity deviates from the local fluid velocity more rapidly and the mean particle Reynolds number increases to large values during a relatively short initial time. After peaking near $St \approx 1$ the particle Reynolds number decreases. Finally $\langle\langle Re_p \rangle\rangle$ increases due to the growth of turbulence. Based on the results in Fig. 1, the particle Reynolds number decreases with the increase of the mass loading ratio. This is mainly due to turbulence modification by the particles in two-way coupling. An increase in the particle time constant results in an increase of the particle Reynolds number due to increased particle inertia.

Figure 2 illustrates the temporal variations of the normalized energy components for both the fluid and the particles for the case with one-way coupling. Here, $q_p^2 = \langle\langle v_i v_i \rangle\rangle$, and no summation is assumed over the Greek indices. Due to initial isotropic conditions, all of the components have the same value at $St = 0$. In time, the production of the energy by the mean velocity gradient increases the energy component in the streamwise ($\alpha = 1$) direction. In the absence of a production mechanism, the other two components tend to decay. However, the fluid pressure redistributes the energy among the components, and after some initial time ($St < 6$) equilibrium values are reached in all three directions. A similar behavior is also observed for the particle energy components. However, it is clearly observed that the anisotropy of the particle energy components is substantially larger than that of the fluid. This is mainly due to lack of a mechanism similar to the pressure in the fluid phase by which energy may be exchanged among different components in the dispersed

phase. The extent of the particle energy anisotropy is, however, bounded at long times by the action of the drag force. An inspection of other cases (not shown), indicate the increase of the anisotropy in both the fluid and the particle phases with the increase of the particle time constant or the mass loading ratio.

The modification of turbulence by the particles is illustrated in Fig. 3 by considering the temporal variations of the fluid turbulent kinetic energy ($k = \frac{1}{2} \langle u_i u_i \rangle$) and its dissipation rate (ϵ). Both variables are normalized with their corresponding initial values denoted by subscript (0). For all of the cases, initially the fluid turbulent kinetic energy decays due to the absence of the off-diagonal (shear) Reynolds stress term. This term, along with the mean velocity gradient, are responsible for the production of energy in the streamwise direction. After the shear Reynolds stress component is produced by the action of the mean velocity gradient, the kinetic energy starts to increase ($St > 4$). The primary effect of the particles on the fluid is to decrease the turbulent kinetic energy with respect to its single phase value. This is also the case for the dissipation rate as shown in Fig. 3b. The decrease of the kinetic energy and its rate of dissipation in the presence of particles, suggests the existence of an extra dissipation which originates from the drag force.

The equation governing the particle turbulent kinetic energy ($k_p = \frac{1}{2} \langle\langle v_i v_i \rangle\rangle$) is obtained by multiplying (2.9) by v_i and then ensemble averaging over the number of particles,

$$\frac{Dk_p}{Dt} = -\langle\langle v_1 v_2 \rangle\rangle S + \frac{\langle\langle f \rangle\rangle}{\tau_p} (\langle\langle u_i^* v_i \rangle\rangle - 2k_p). \quad (2.11)$$

In deriving (2.11), the triple correlations between f and velocity components have been neglected after analyzing the DNS data. The first term on the RHS of (2.11) represents a production by the mean velocity gradient while the second term is due to drag. The temporal evolution of these terms in Fig. 4 indicates that for all of the cases the term due to drag always behaves as a dissipation and tends to balance the production. Obviously, during the initial times ($St < 4$), the dissipation overcomes the production and the particle turbulent kinetic energy experiences a rapid decay, similar to those for the fluid. This is in agreement with the results for the particle Reynolds number in Fig. 1. At longer times, Fig. 4 shows that the increase of the mass loading ratio results in the decrease of the magnitude of both the production and dissipation. However, the decrease of the production with the mass loading

ratio occurs with a faster rate than that of the dissipation. As a result, the growth rate of the particle turbulent kinetic energy is decreased with the increase of the mass loading ratio. A comparison of cases with different particle time constant values (at the same mass loading ratio) indicates that the initial evolutions of the production and the dissipation terms are more sensitive to the variations of the particle time constant, than are to the variations of the mass loading ratio. During the initial times, the increase of the particle time constant decreases the decay rate of the particle turbulence energy while at long times it results in the decrease of the growth rate of the kinetic energy.

The variations of the Reynolds stress of the fluid and particles are shown in Fig. 5. The Reynolds stress in x_3 direction exhibits a behavior similar to that in x_2 direction and is not shown. An interesting feature observed in Fig. 5 is the increase of the particle Reynolds stress in x_1 direction over that of the fluid. This is in agreement with the theoretical results of Reeks (1993), Liljegren (1993), LES results of Simonin *et al.* (1995), and is due to the lack of small scale dissipation in the dispersed phase as opposed to the fluid phase. In x_2 direction a crossing point is observed at $St \simeq 0.5$. The reason is that during the initial times the dispersed phase Reynolds stress decreases more slowly than that of the fluid due to the particle inertia. At longer times ($St > 0.5$) the fluid pressure transfers energy from the streamwise direction to other directions and causes the increase of the fluid Reynolds stress in x_2 direction over that of the particles. The initial larger values of $\langle\langle v_2 v_2 \rangle\rangle$ results in larger production of the shear component for the dispersed phase and increases the magnitude of this component to values larger than those of the fluid. The effect of mass loading ratio is realized by comparison of Figs. 5a and 5b. The trends are similar; however, the difference between the normal components of the Reynolds stress of the dispersed phase is smaller in the two-way coupling due to the indirect effects of the fluid pressure. Figure 5c indicates that the increase of the particle time constant has more sensible effects on the particle Reynolds stress components. A comparison of this case with the case having the same Φ_m but smaller τ_p (not shown) indicated that, in agreement with the results of Reeks (1993); Liljegren (1993) and Simonin *et al.* (1995), the increase of the particle time constant results in the increase of the particle Reynolds stress in the streamwise direction. This is in contrast to the decrease of the particle turbulence intensity with the increase of the particle time constant in isotropic flows.

Figure 6 shows the temporal variations of the particle velocity autocorrelation coefficient,

$$R_{\xi\xi}^p(t) = \frac{<< v_\xi(t_0)v_\xi(t_0 + t) >>}{\sqrt{<< v_\xi^2(t_0) >>} << v_\xi^2(t_0 + t) >>}, \quad \xi = 1, 2, 3. \quad (2.12)$$

The autocorrelations are calculated with the normalized time $St_0 = 2$. It is observed in the figure that the increase of the mass loading ratio results in the increase of the particle velocity autocorrelation in all directions and at all times. This is similar to the trend observed in decaying and stationary isotropic turbulence and is due to the modification of the velocity of the neighboring fluid elements by the particle. The variation of the autocorrelation with the increase of the particle time constant in x_3 direction is also in agreement with previous results for decaying and stationary turbulence – an increase of τ_p results in an increase of R_{33}^p at all times. However, an interesting feature is observed in the streamwise (x_1) and cross-stream (x_2) directions. A crossing is observed for the autocorrelation curves at different particle time constant values. The crossing occurs sooner in the x_2 direction but at long times the two curves overlap. In x_1 direction, the autocorrelation remains smaller for larger particle time constant for all times after the crossing.

Since the fluid turbulent kinetic energy decreases with the increase of the mass loading ratio, it may be expected that the flow Reynolds number shows a decreasing trend with the mass loading ratio. However, Fig. 7 indicates that this is not the case in x_1 direction and, except for a short initial time, the Taylor microscale Reynolds number increases with the increase of the mass loading ratio. This is due to the increase of the length scale as Φ_m is increased. An opposite behavior, i.e. the decrease of both Reynolds number and the flow length scale, was observed (not shown) in other flow directions. Also, an inspection of the temporal variations of $Re_{\lambda 1}$ for different τ_p values (not shown) indicated no specific trends.

The normalized fluid velocity energy spectra are shown in Fig. 8 for different cases at the nondimensional time $St = 10$. The anisotropic nature of homogeneous shear turbulence greatly increases the complexity of a complete study of the turbulence energy spectrum. In order to simplify the analysis the variation of spectra with the wavenumber magnitude only are considered. The primary effect of the increase of the mass loading ratio is to increase the energy at high wavenumbers while decreasing it at low wavenumbers. The energy spectra are observed to be rather insensitive to the variations of the particle time constant. The trends

observed here are in qualitative agreement with those in decaying turbulence (Elghobashi and Truesdell, 1993).

3 Reynolds stress closures

In this section a second-order moment Reynolds stress model is proposed for particle-laden flows that includes the effects of two-way coupling between the two phases. The final form of the model is presented in the context of homogeneous shear flows and its predictions are compared with the DNS generated data. The model is based on the two-fluid treatment of two-phase flows. Similarly to DNS, we consider the transport of an incompressible fluid (the carrier gas) laden with monosize particles (the dispersed phase). The Stokes drag relation is used for phase interactions and there is no mass transfer between the two phases. The particle-particle interactions are neglected and the dispersed phase viscosity and pressure do not appear in the particle momentum equation (Zaichik *et al.*, 1993; Zhou, 1993). The effect of the carrier phase pressure on the particles is assumed negligible as the pressure change across each particle is very small. The governing equations for both phases are expressed in the Eulerian frame by performing volume averaging which results in a continuum dispersed phase (Sha and Soo, 1978; Drew, 1983; Jackson and Davidson, 1983; Mostafa and Elghobashi, 1985). With the assumptions as stated, the equations indicating conservations of mass and momentum are:

$$\frac{\partial}{\partial t}[\rho_f(1 - \hat{\Phi})] + \frac{\partial}{\partial x_j}[\rho_f(1 - \hat{\Phi})\hat{U}_j] = 0, \quad (3.1)$$

$$\begin{aligned} \frac{\partial}{\partial t}[\rho_f(1 - \hat{\Phi})\hat{U}_i] + \frac{\partial}{\partial x_j}[\rho_f(1 - \hat{\Phi})\hat{U}_i\hat{U}_j] &= -\frac{\partial}{\partial x_i}[(1 - \hat{\Phi})\hat{P}] \\ &+ \mu \frac{\partial}{\partial x_j} \left[(1 - \hat{\Phi}) \left(\frac{\partial \hat{U}_i}{\partial x_j} + \frac{\partial \hat{U}_j}{\partial x_i} \right) \right] - \frac{\rho_p}{\tau_p} \hat{\Phi}(\hat{U}_i - \hat{V}_i), \end{aligned} \quad (3.2)$$

for the carrier phase, and

$$\frac{\partial}{\partial t}(\rho_p \hat{\Phi}) + \frac{\partial}{\partial x_j}(\rho_p \hat{\Phi} \hat{V}_j) = 0, \quad (3.3)$$

$$\frac{\partial}{\partial t}(\rho_p \hat{\Phi} \hat{V}_i) + \frac{\partial}{\partial x_j}(\rho_p \hat{\Phi} \hat{V}_j \hat{V}_i) = \frac{\rho_p}{\tau_p} \hat{\Phi}(\hat{U}_i - \hat{V}_i) + (\rho_p - \rho_f) \hat{\Phi} g e_i. \quad (3.4)$$

for the dispersed phase. In these equations, $\hat{\Phi}$ denotes the void (or volume) fraction, g is the gravity constant, and e_i is the unit vector in the gravity direction.

For a dilute dispersed phase, typically $\hat{\Phi} \sim \mathcal{O}(10^{-4})$. This simplifies the transport equations of the carrier phase significantly. For a constant ρ_f the continuity equation (3.1) and the viscous term in the momentum equation (3.2) simplify to the forms for an incompressible flow. Using the dispersed phase continuity equation, the void fraction is eliminated from the dispersed phase momentum equation and the instantaneous equations reduce to:

$$\frac{\partial \hat{U}_j}{\partial x_j} = 0, \quad (3.5)$$

$$\frac{\partial \hat{U}_i}{\partial t} + \frac{\partial(\hat{U}_j \hat{U}_i)}{\partial x_j} = -\frac{1}{\rho_f} \frac{\partial \hat{P}}{\partial x_i} + \nu \frac{\partial^2 \hat{U}_i}{\partial x_j \partial x_j} - \frac{\lambda \hat{\Phi}}{\tau_p} (\hat{U}_i - \hat{V}_i), \quad (3.6)$$

$$\frac{\partial \hat{\Phi}}{\partial t} + \frac{\partial(\hat{V}_j \hat{\Phi})}{\partial x_j} = 0, \quad (3.7)$$

$$\frac{\partial \hat{V}_i}{\partial t} + \hat{V}_j \frac{\partial \hat{V}_i}{\partial x_j} = \frac{1}{\tau_p} (\hat{U}_i - \hat{V}_i) + \left(1 - \frac{1}{\lambda}\right) g e_i, \quad (3.8)$$

where $\lambda = \frac{\rho_p}{\rho_f}$ is the density ratio. Following the standard Reynolds decomposition procedure, all the transport parameters are decomposed into the “ensemble-mean” and fluctuations about the mean:

$$\hat{U}_i = U_i + u_i, \quad \hat{V}_i = V_i + v_i, \quad \hat{\Phi} = \Phi + \phi, \quad \hat{P} = P + p.$$

The equations governing the transport of the mean variables are obtained by ensemble averaging (3.5)-(3.8):

$$\frac{\partial U_j}{\partial x_j} = 0, \quad (3.9)$$

$$\frac{\partial U_i}{\partial t} + \frac{\partial(U_j U_i)}{\partial x_j} = -\frac{1}{\rho_f} \frac{\partial P}{\partial x_i} + \nu \frac{\partial^2 U_i}{\partial x_j \partial x_j} - \frac{\partial \bar{u}_i u_j}{\partial x_j} - \frac{\lambda}{\tau_p} \Phi (U_i - V_i) - \frac{\lambda}{\tau_p} (\bar{u}_i \phi - \bar{v}_i \phi), \quad (3.10)$$

$$\frac{\partial \Phi}{\partial t} + \frac{\partial(V_j \Phi)}{\partial x_j} = -\frac{\partial \bar{v}_j \phi}{\partial x_j}, \quad (3.11)$$

$$\frac{\partial V_i}{\partial t} + V_j \frac{\partial V_i}{\partial x_j} = -\frac{\partial \bar{v}_i v_j}{\partial x_j} + \frac{1}{\tau_p} (U_i - V_i) + \overline{v_i \frac{\partial v_j}{\partial x_j}} + \left(1 - \frac{1}{\lambda}\right) g e_i, \quad (3.12)$$

where the overbar indicates the ensemble-averaged value.

The averaging procedure leading to the equations for the mean variables ((3.9)-(3.12)) involves two steps; a volume averaging followed by an ensemble averaging. As pointed out by Crowe *et al.* (1996), the volume averaging results in Reynolds stresses due to small deviations of the particle velocity from its volume averaged value. However, these volume averaged stresses are usually small in comparison to those resulting from the time averaging. The reason is that particles, due to their large inertia, interact with larger scales of the flow (Hinze, 1972) while the volume averaging is performed over volumes which are normally much smaller than the large scales of the flow in order to satisfy the conditions required in volume averaging. Nevertheless, it is noted that if the flow is very dilute such that a large volume (comparable to the particle-interacting scales of the flow) must be used to obtain homogeneous volume averaged quantities, then this assumption is not well justified.

There is also an extra (also referred to as secondary) viscosity for the carrier phase due to the presence of a suspension of particles in the flow. This viscosity is generated by the flow modification around the particles as well as local shearing effects on the particles. This issue has been extensively addressed in the literature (e.g. see Einstein (1906); Happel (1957); Frankel and Acrivos (1967)) where it has been shown that the extra viscosity varies as a function of the volume fraction. Based on these studies, the secondary viscosity is negligible for small volume fractions, especially when Reynolds stresses are present. In wall-bounded flows and in the region close to the wall this viscosity becomes important (Choi and Chung (1983); Chung *et al.* (1986)). Since we are not concerned with wall-bounded flows and are dealing with small volume fractions, the extra viscosity is not included.

The closure problem in (3.10)-(3.12) is exhibited by the Reynolds stress tensors pertaining to the two phases ($\overline{u_i u_j}$ and $\overline{v_i v_j}$), and the void fraction flux vectors ($\overline{u_i \phi}$ and $\overline{v_i \phi}$). In homogeneous flows the void fraction fluxes are zero ($\overline{u_i \phi} \equiv 0$ and $\overline{v_i \phi} \equiv 0$), therefore the modeling of these terms is not pursued here. The transport differential equations for other second-order moments (in homogeneous flows) are obtained by standard methods (Taulbee, 1989; Wilcox, 1993). These are expressed as:

$$\frac{D^u \overline{u_i u_j}}{Dt} = -\overline{u_i u_l} \frac{\partial U_j}{\partial x_l} - \overline{u_j u_l} \frac{\partial U_i}{\partial x_l} + \psi_{ij} - \epsilon_{ij} - \frac{\lambda \Phi}{\tau_p} [\overline{u_i(u_j - v_j)} + \overline{u_j(u_i - v_i)}] + \text{TOC}, \quad (3.13)$$

for the carrier phase Reynolds stress,

$$\frac{D^V \overline{v_i v_j}}{Dt} = -\overline{v_i v_l} \frac{\partial V_j}{\partial x_l} - \overline{v_j v_l} \frac{\partial V_i}{\partial x_l} - \frac{1}{\tau_p} (2\overline{v_i v_j} - \overline{u_i v_j} - \overline{u_j v_i}) + \overline{v_i v_j} \frac{\partial v_l}{\partial x_l}, \quad (3.14)$$

for the dispersed phase Reynolds stress, and

$$\begin{aligned} \frac{D^{vv} \overline{u_i v_j}}{Dt} = & -\overline{u_i v_l} \frac{\partial V_j}{\partial x_l} - \overline{u_l v_j} \frac{\partial U_i}{\partial x_l} + \chi_{ij} + \frac{1}{\tau_p} (\overline{u_i u_j} - \overline{u_i v_j}) - \frac{\lambda \Phi}{\tau_p} (\overline{u_i v_j} - \overline{v_i v_j}) \\ & + \nu \overline{v_j} \frac{\partial^2 u_i}{\partial x_l^2} + U_l \overline{u_i} \frac{\partial v_j}{\partial x_l} + V_l \overline{v_j} \frac{\partial u_i}{\partial x_l} + \overline{u_i} \frac{\partial u_l v_j}{\partial x_l} + \overline{v_j} \frac{\partial u_i v_l}{\partial x_l} + \text{TOC}, \end{aligned} \quad (3.15)$$

for fluid-particle velocity covariance. In these equations, $\frac{D^U}{Dt} = \frac{\partial}{\partial t} + U_l \frac{\partial}{\partial x_l}$, $\frac{D^V}{Dt} = \frac{\partial}{\partial t} + V_l \frac{\partial}{\partial x_l}$, and $\frac{D^{vv}}{Dt} = \frac{\partial}{\partial t} + (U_l + V_l) \frac{\partial}{\partial x_l}$ represent the total derivatives. In (3.13), $\psi_{ij} = \frac{p}{\rho_f} \left(\frac{\partial u_i}{\partial x_j} + \frac{\partial u_j}{\partial x_i} \right)$ is the pressure-strain correlation, and $\epsilon_{ij} = 2\nu \frac{\partial u_i}{\partial x_l} \frac{\partial u_j}{\partial x_l}$ indicates the dissipation rate. In (3.15), $\chi_{ij} = \frac{p}{\rho_f} \frac{\partial v_j}{\partial x_i}$ is the pressure-dispersed phase velocity gradient correlation. The terms denoted by TOC indicate the third order correlations involving both the velocity and the void fraction fluctuations. It is noted that the gravity appears only in the mean equations so there is no need for modeling of the terms involving gravity.

3.1 Modeling of the unclosed terms

The starting point in deriving a model for the fluid pressure-strain correlation is the “Poisson’s equation” (Rotta, 1951) which for the two-phase flow is obtained from the carrier phase momentum equation:

$$-\frac{1}{\rho_f} \frac{\partial^2 p}{\partial x_l^2} = \frac{\partial^2 (u_i u_l)}{\partial x_i \partial x_l} + 2 \frac{\partial U_k}{\partial x_l} \frac{\partial u_l}{\partial x_k} + \frac{\lambda}{\tau_p} \frac{\partial}{\partial x_l} [\phi(u_l - v_l) + \phi(U_l - V_l) + \Phi(u_l - v_l)]. \quad (3.16)$$

This equation shows that the proposed model for the correlations involving the pressure must exhibit the effects of the dispersed phase as manifested by the third term on the RHS in addition to the influence of carrier gas as portrayed by the first two terms on the RHS. The actual procedure involved in the development of the model is very lengthy and is outlined here very briefly. For details, we refer to Lumley (1978); Taulbee (1989); Wilcox (1993). The dissipation rate tensor (ϵ_{ij}) is expressed as the sum of an isotropic part

$(\frac{2}{3}\epsilon\delta_{ij})$ and a deviatoric part (ϵ_{ij}^D). The latter is combined with the pressure-strain correlation, and the resulting tensor ($\Pi_{ij} = \psi_{ij} - \epsilon_{ij}^D$) is modeled. In doing so, first the Poisson's equation (3.16) is transformed to an equation expressing the pressure-strain term explicitly in terms of various correlations of the velocity and void fraction fields. Assuming that the length scale of the mean flow gradients is larger than that of turbulence in homogeneous flows, it is straightforward to show (Taulbee, 1989; Wilcox, 1993):

$$\begin{aligned}
& \overline{\frac{p}{\rho_f} \left(\frac{\partial u_j}{\partial x_i} + \frac{\partial u_i}{\partial x_j} \right)} = \frac{j}{8\pi^3} \iint \frac{k_m k_n}{|k|^2} \left\{ k_i \overline{u_j(x) u_m(x+r) u_n(x+r)} \right. \\
& \quad \left. + k_j \overline{u_i(x) u_m(x+r) u_n(x+r)} \right\} e^{-jk \cdot r} dr dk \\
& + \frac{1}{4\pi^3} \frac{\partial U_m}{\partial x_n} \iint \frac{k_m}{|k|^2} \left\{ k_i \overline{u_j(x) u_n(x+r)} + k_j \overline{u_i(x) u_n(x+r)} \right\} e^{-jk \cdot r} dr dk \\
& + \frac{1}{8\pi^3} \frac{\lambda}{\tau_p} \iint \frac{k_l}{|k|^2} \left\{ k_i \overline{u_j(x) \phi(x+r) [u_l(x+r) - v_l(x+r)]} \right. \\
& \quad \left. + k_j \overline{u_i(x) \phi(x+r) [u_l(x+r) - v_l(x+r)]} \right\} e^{-jk \cdot r} dr dk \\
& + \frac{1}{8\pi^3} \frac{\lambda}{\tau_p} \iint \frac{k_l}{|k|^2} \left\{ k_i \left[(U_l - V_l) \overline{u_j(x) \phi(x+r)} + \Phi \overline{[u_j(x) u_l(x+r) - u_j(x) v_l(x+r)]} \right] \right. \\
& \quad \left. + k_j \left[(U_l - V_l) \overline{u_i(x) \phi(x+r)} + \Phi \overline{[u_i(x) u_l(x+r) - u_i(x) v_l(x+r)]} \right] \right\} e^{-jk \cdot r} dr dk, \quad (3.17)
\end{aligned}$$

where k denotes the Fourier wavenumber and $j = \sqrt{-1}$. The integrations on the RHS are performed over three-dimensional physical and wave number space. To model (3.17), values of the two-point correlations are assumed to be related to the single-point ($r = 0$) correlation values.

The first and the second integrals on the RHS of (3.17) include the interactions among the fluid quantities only. These are modeled here similarly to the widely utilized Launder-Reece-Rodi (LRR) (Launder *et al.*, 1975) closure. The third integral cannot be expressed in a form which contains only the fluctuating quantities and is consistent with the order of the tensor on the left hand side (LHS). It is possible to express this integral in the form of the product of the mean and fluctuating quantities. However, all the possible combinations also appear in the last integral. Therefore, the third integral is combined with the last one. The resulting integral carries different correlations as integrands which can be grouped in form of second, third, and fourth order tensor functions of the Reynolds stresses and void fraction fluxes.

These tensors are then expanded in terms of linear polynomials of the stresses and fluxes. The coefficients of these polynomials are found by applying the constraints of symmetry, incompressibility, and normalization (Lumley, 1978). The final result is expressed as:

$$\begin{aligned} \Pi_{ij} = & -C_{f1}\epsilon a_{ij}^f + \epsilon \left[\frac{4}{5}S_{ij}^f - 6C_{f2} \left(a_{ik}^f S_{kj}^f + a_{jk}^f S_{ki}^f - \frac{2}{3}a_{mn}^f S_{nm}^f \delta_{ij} \right) - \frac{4+14C_{f2}}{3} (a_{ik}^f \omega_{kj}^f + a_{jk}^f \omega_{ki}^f) \right] \\ & + C_{f3} \frac{\lambda \Phi}{\tau_p} [2ka_{ij}^f - \overline{u_m v_m} (b_{ij}^{fp} + b_{ji}^{fp})] + \frac{3}{10} \frac{\lambda}{\tau_p} [(U_i - V_i) \overline{u_j \phi} + (U_j - V_j) \overline{u_i \phi} - \frac{2}{3}(U_l - V_l) \overline{u_l \phi} \delta_{ij}], \end{aligned} \quad (3.18)$$

where C_{f1} , C_{f2} and C_{f3} are empirical constants to be determined,

$$a_{ij}^f = \frac{\overline{u_i u_j}}{k} - \frac{2}{3} \delta_{ij} \quad \text{and} \quad b_{ij}^{fp} = \frac{\overline{u_i v_j}}{\overline{u_m v_m}} - \frac{1}{3} \delta_{ij} \quad (3.19)$$

are the normalized form of the fluid-fluid and the fluid-particle Reynolds stresses, respectively; and

$$S_{ij}^f = \frac{1}{2} \frac{k}{\epsilon} \left(\frac{\partial U_i}{\partial x_j} + \frac{\partial U_j}{\partial x_i} \right) \quad \text{and} \quad \omega_{ij}^f = \frac{1}{2} \frac{k}{\epsilon} \left(\frac{\partial U_i}{\partial x_j} - \frac{\partial U_j}{\partial x_i} \right) \quad (3.20)$$

are the strain rate and the rotation tensors of the carrier phase, respectively.

Following a similar procedure, a model is derived for the pressure-dispersed phase velocity gradient correlation:

$$\chi_{ij} = -C_{fp1} \frac{\overline{u_i v_j}}{\tau} + C_{fp2} \overline{u_l v_j} \frac{\partial U_i}{\partial x_l} + C_{fp3} \frac{\lambda}{\tau_p} [(U_i - V_i) \overline{v_j \phi} + \Phi(\overline{u_i v_j} - \overline{v_i v_j})], \quad (3.21)$$

where $\tau = \frac{k}{\epsilon}$ is the carrier phase turbulent time scale, and C_{fp1} , C_{fp2} , and C_{fp3} are empirical constants. The procedure of determining the values of these constants is described later in this subsection. It is noted that for homogeneous flows the fluxes of void fraction are zero and (3.18) and (3.21) are simplified.

The term $\nu \overline{v_j \frac{\partial^2 u_i}{\partial x_i^2}}$ in (3.15) may be expressed in terms of an isotropic dissipation ($\nu \overline{\frac{\partial u_k}{\partial x_l} \frac{\partial v_k}{\partial x_l}}$); even though this term is not necessarily always positive. Determination of this dissipation requires the solution of a transport equation, which in turn contains additional unclosed terms. Due to excessive complexities and approximations involved in modeling of these unclosed terms, development of such a transport equation is not pursued. Note that this dissipation is due to the fluid-particle interaction the effects of which are also included in the drag. Therefore, the contribution of this term to the dissipation is considered indirectly

by adjusting the constants appearing in the model for the pressure-dispersed phase velocity gradient correlation in (3.21). Similar argument is applied to the TOC terms that involve both velocity and void fraction. These higher order terms are usually small and their effects may be absorbed in the pressure terms. The other correlations, $\overline{u_i \frac{\partial v_j}{\partial x_l}}$, $\overline{v_j \frac{\partial u_i}{\partial x_l}}$, $\overline{v_i v_j \frac{\partial v_l}{\partial x_l}}$, $\overline{u_i u_l v_j}$, and $\overline{v_j \frac{\partial u_i v_l}{\partial x_l}}$, are either zero or very small in homogeneous and thin shear layer flows which are considered for model validations in this work. Therefore, these terms are neglected. In more complex flows, these terms may be modeled by implementing the gradient-diffusion hypothesis.

Equations (3.18) and (3.21) indicate that the proposed closures involve six empirical constants which must be determined. The terms involving C_{f1} or C_{f2} in (3.18) are the equivalent of those in LRR. Thus, the magnitudes of these constants are set to be the same ($C_{f1} = 1.75$, $C_{f2} = -0.159$) to ensure that in the limit of one-way coupling (3.18) reduces to the equivalent LRR model for single phase flows. The magnitudes of the other four constants are determined by balancing the transport equations for all of the components of the fluid Reynolds stress tensor (equation 3.13) and the fluid-particle covariance tensor (equation 3.15). By considering all of the components of the stresses in all of the cases a large number of data points is provided to determine the optimized values of the remaining four model constants. Two sample cases are shown in Fig. 9 for the energy budgets of $\langle\langle u_1^2 \rangle\rangle$ and $\langle\langle u_1 v_1 \rangle\rangle$ for $\Phi_m = 0.25$ and $\tau_p = 0.032s$. In this figure, the production, the dissipation rate, and the contribution from drag are calculated from DNS. The values of the pressure-strain and the pressure-dispersed phase velocity gradient are based on the models as proposed. The term LHS indicates the derivative of the energy component and is obtained from DNS. This value is compared with $\sum \text{RHS}$ which is the sum of the production, dissipation rate, and drag contribution (from DNS), and the pressure term (from models). It is observed that the general agreement between the LHS and the RHS is good, especially for $St > 2$ when the DNS results are considered for model validation. Similar comparisons are performed for all the other components in all the cases. The final optimized values of the empirical constants are given in table 3.

3.2 The dissipation rate of the turbulent kinetic energy

The final form of the transport equations for all of the components of the Reynolds stress tensors (in the context of homogeneous shear flows) is given in Appendix A. It is noted that although the mean flow is two-dimensional, the turbulence is three-dimensional. Equations (A.1)-(A.4) and (A.9)-(A.17) constitute a set of Reynolds stress models for particle-laden homogeneous shear flows. To close, an equation must be provided for the dissipation rate of the fluid turbulent kinetic energy. This equation is derived similar to that in single-phase flows but also includes a term due to coupling with the dispersed phase. For high Reynolds numbers, the transport of the dissipation rate is governed by:

$$\begin{aligned}
 \frac{D\epsilon}{Dt} = & -2\nu \frac{\partial U_i}{\partial x_k} \left(\overline{\frac{\partial u_i}{\partial x_j} \frac{\partial u_k}{\partial x_j}} + \overline{\frac{\partial u_j}{\partial x_i} \frac{\partial u_j}{\partial x_k}} \right) - 2\nu \overline{\frac{\partial u_i}{\partial x_k} \frac{\partial u_i}{\partial x_j} \frac{\partial u_k}{\partial x_j}} \\
 & - 2 \left(\nu \overline{\frac{\partial^2 u_i}{\partial x_j \partial x_k}} \right)^2 - \frac{\partial}{\partial x_k} \left(\nu \overline{u_k \frac{\partial u_i}{\partial x_j} \frac{\partial u_i}{\partial x_j}} \right) - 2 \frac{\nu}{\rho} \frac{\partial}{\partial x_i} \left(\overline{\frac{\partial p}{\partial x_j} \frac{\partial u_i}{\partial x_j}} \right) \\
 & - \frac{\lambda \Phi}{\tau_p} 2\nu \overline{\frac{\partial u_i}{\partial x_j} \frac{\partial u_i}{\partial x_j}} + \frac{\lambda \Phi}{\tau_p} 2\nu \overline{\frac{\partial u_i}{\partial x_j} \frac{\partial v_i}{\partial x_j}} - \frac{\lambda}{\tau_p} (U_i - V_i) 2\nu \overline{\frac{\partial u_i}{\partial x_j} \frac{\partial \phi}{\partial x_j}} \\
 & - \frac{\lambda}{\tau_p} 2\nu \overline{\frac{\partial u_i}{\partial x_j} \frac{\partial (u_i \phi)}{\partial x_j}} + \frac{\lambda}{\tau_p} 2\nu \overline{\frac{\partial u_i}{\partial x_j} \frac{\partial (v_i \phi)}{\partial x_j}}. \tag{3.22}
 \end{aligned}$$

The first two lines of (3.22) are equivalent to the dissipation rate equation for single-phase flows and are modeled analogously (e.g. see Hanjalić and Launder (1972)). The last two lines in (3.22) are due to coupling with the particles. The correlation in the first term of the third line is the dissipation rate and needs no modeling. The correlations in the second and third terms of the third line are, respectively, modeled as $2\nu \overline{\frac{\partial u_i}{\partial x_j} \frac{\partial v_i}{\partial x_j}} \propto \frac{\overline{u_m v_m}}{\tau}$ and $2\nu \overline{\frac{\partial u_i}{\partial x_j} \frac{\partial \phi}{\partial x_j}} \propto \frac{\overline{u_i \phi}}{\tau}$. The third-order correlations appearing in the last line of (3.22) are usually small and can be neglected; the effects of these terms are, indirectly, considered in the evaluation of the empirical constants. The final form of the modeled transport equation for the dissipation rate is expressed as:

$$\frac{\partial \epsilon}{\partial t} + U_i \frac{\partial \epsilon}{\partial x_i} = - \frac{\partial}{\partial x_i} \left(\overline{u_i \epsilon'} \right) - C_{\epsilon 1} \frac{\epsilon}{k} \overline{u_i u_j} \frac{\partial U_j}{\partial x_i} - C_{\epsilon 2} \frac{\epsilon^2}{k}$$

$$-\frac{\epsilon}{k} \frac{\lambda}{\tau_p} \left\{ 2\Phi k - C_{\epsilon 3} [\Phi \bar{u_m v_m} - (U_i - V_i) \bar{u_i \phi}] \right\}, \quad (3.23)$$

where $\epsilon' = \nu \frac{\partial u_i}{\partial x_j} \frac{\partial u_i}{\partial x_j}$.

For homogeneous flows, (3.23) is simplified:

$$\frac{\partial \epsilon}{\partial t} = -C_{\epsilon 1} \frac{\epsilon}{k} \bar{u_1 u_2} \frac{\partial U_1}{\partial x_2} - C_{\epsilon 2} \frac{\epsilon^2}{k} - \frac{\epsilon}{k} \frac{\lambda \Phi}{\tau_p} (2k - C_{\epsilon 3} \bar{u_m v_m}), \quad (3.24)$$

where $C_{\epsilon 1}$, $C_{\epsilon 2}$, and $C_{\epsilon 3}$ are constants. The values for $C_{\epsilon 1}$ and $C_{\epsilon 2}$ are taken from their single-phase equivalents; $C_{\epsilon 1} = 1.45$ and $C_{\epsilon 2} = 1.85$. The value of constant $C_{\epsilon 3} = 0.8$ is found by comparison with DNS data as discussed below.

3.3 Model assessment via comparison with DNS

In this subsection, the data generated by DNS are used to assess the performance of RSM. In this assessment the stress and the dissipation rate values at $St = 2$ are taken from DNS as initial values. This time is chosen as the initial time in order to allow the flow and the particles to reach a dynamic equilibrium (see Fig. 1). All the cases are considered; however, the results of only three cases are presented and discussed here. These cases exhibit the effects of the mass loading ratio and the particle time constant. The numerical discretization procedure in RSM involves simultaneous integration of 14 coupled equations (13 for the Reynolds stresses and 1 for the dissipation rate). The time derivative term is discretized by a backward finite difference scheme. The decay term is evaluated by averaging between the two successive time levels to expedite convergence. Preliminary calculations indicated that the solution is not very sensitive to time increment; the results presented here are based on $\Delta t = 0.0032s$.

First we consider the case with one-way coupling ($\Phi_m = 0$) for $\tau_p = 0.016s$. The model predictions (lines) are compared with DNS results (symbols) in Fig. 10 for all of the components. The overall agreement is very good; however, the particle Reynolds stress components (Fig. 10b) show the best overall agreements. This is expected as the transport equations for the particle Reynolds stresses involve no modelings. Small deviations observed in Fig. 10b is due to $\bar{u_i v_j}$ terms. It is noted that the shear components which are of primary importance are predicted very closely to DNS. For this one-way coupling case, Fig. 10a essentially evaluates

the performance of the LRR model. Some deviations are observed in the streamwise ($\overline{u_1 u_1}$) component but other components are in reasonably good agreements.

The effects of two-way coupling at $\Phi_m = 0.25$ and $\tau_p = 0.016s$ are portrayed in Fig. 11. Again the agreement between the model predictions and DNS results is very promising. Similar to the case with one-way coupling, the largest deviations are observed in the streamwise direction, especially for the fluid. This is also observed in Fig. 12 for larger particle time constant ($\tau_p = 0.032s$). In this case, the streamwise component of the particle Reynolds stress is overpredicted while that of the fluid is underpredicted. However, interestingly, the fluid-particle Reynolds stress component in the streamwise direction is in a very good agreement with DNS results. Again, the model predictions for the shear components agree well with DNS results. Finally, Fig. 13 shows that the dissipation rate is also calculated very closely to DNS results for all of the cases.

4 Summary and concluding remarks

This work deals with direct numerical simulation of particle laden homogeneous shear flow, and proposes a new Reynolds stress model for statistical prediction of two-phase flows. The DNS generated data are used to address some issues of importance in regard to the structure of two-phase turbulent flows and to assess the performance of the RSM.

The DNS results indicate the decrease of both the fluid and the particle turbulent kinetic energies with the increase of the mass loading ratio. The dissipation rate of the fluid turbulent kinetic energy also decreases with the increase of the mass loading ratio. However, there is also a dissipation in the carrier phase due to drag which results in the increase of the total dissipation when the mass loading is increased. These parameters also show some sensitivity to the variations of the particle time constant. The increase of the particle time constant results in the increase of both the turbulent kinetic energy and its dissipation rate at early times when the turbulence is decaying. An opposite trend is observed in the stage of turbulence growth. The dispersed phase shows a higher degree of anisotropy in comparison to the carrier phase. This is mainly due to the lack of a mechanism similar to the pressure-strain correlation by which the energy could be exchanged among different directions in the

dispersed phase. The level of anisotropy of the dispersed phase is, however, bounded at long times by the action of the drag term which couples the two phases. The anisotropy of the dispersed phase decreases with the increase of the mass loading ratio due to the increase of the effects of the flow on the particles.

In agreement with some of the recent theories, it is observed that the particle rms velocity in the streamwise direction increases over that of the fluid. Also, this rms velocity component increases with the increase of the particle time constant which is opposite to the trend previously observed in isotropic turbulence. The magnitude of the shear component of the particle Reynolds stress tensor also exceeds the magnitude of its analogous term in the carrier phase. Similar to that in isotropic turbulence, the particle velocity autocorrelation increases with the increase of the mass loading ratio in all directions. The variation of this autocorrelation with the particle time constant is also similar to isotropic flows in the spanwise (x_3) direction – the autocorrelation increases with the increase of the particle time constant. However, in other directions (x_1 and x_2) a crossing is observed for the autocorrelation at different particle time constants. It is shown that the Reynolds number based on the Taylor microscale in the streamwise direction increases with the increase of the mass loading ratio. This happens in spite of the decrease of the rms fluid velocity, and is due to the increase of the Taylor microscale in this direction. Analysis of the normalized fluid velocity energy spectra indicates that the energy contents at high wavenumbers increases with the increase of the mass loading ratio. This is similar to that observed in decaying isotropic turbulence.

In development of RSM, we consider dilute, mono-dispersed particle-laden homogeneous turbulent flows. The “differential” transport equations for each of the two phases are developed in the Eulerian frame for the Reynolds stresses in both phases and the cross-correlation between the velocities of the two phases. There are several terms in these equations which are modeled in a fashion analogous to single-phase flows, but introduce empirical constants which need to be specified. In total, there are four empirical constants, in addition to those in single-phase flows (Launder *et al.*, 1975). The magnitudes of these constants are determined by considering the balance of the transport equations for the Reynolds stresses. The final predictions based on the model are then compared with DNS results for all of the components of the fluid, the particle, and the fluid-particle Reynolds stress tensors. Reasonable

agreements are observed, especially for the shear (off-diagonal) components which are of primary importance.

A very important feature of model as developed here is that the effects of the two-way coupling are captured in every aspect of the formulation. Contrary to most previous models which are based on *ad hoc* modifications of the single-phase turbulence closures, the models here clearly indicate how the Reynolds stresses of each phase are modified by the presence of the other phase. However, there is a drawback associated with RSM (in either single- or multi-phase flows) in that the solution of a relatively large number of coupled differential equations is required. This increased computational requirements could become prohibitive for practical applications. Also, it may cause numerical instability and stiffness problems. An obvious extension of this work would be the development of explicit algebraic models based on the Reynolds stress models proposed here. This is the subject of investigation in Part II of this work (Mashayek *et al.*, 1997b).

Acknowledgments

This work is sponsored by the Office of Naval Research under Grant N00014-94-10667.

Appendix A Transport equations for Reynolds stresses

The final form of the transport equations for Reynolds stresses are expressed as:

$$\frac{\partial}{\partial t}(\overline{u_1^2}) = -2\overline{u_1 u_2} \frac{\partial U_1}{\partial x_2} - \frac{2}{3}\epsilon - \frac{2\lambda\Phi}{\tau_p}(\overline{u_1^2} - \overline{u_1 v_1}) + \Pi_{11}, \quad (\text{A.1})$$

$$\frac{\partial}{\partial t}(\overline{u_2^2}) = -\frac{2}{3}\epsilon - \frac{2\lambda\Phi}{\tau_p}(\overline{u_2^2} - \overline{u_2 v_2}) + \Pi_{22}, \quad (\text{A.2})$$

$$\frac{\partial}{\partial t}(\overline{u_3^2}) = -\frac{2}{3}\epsilon - \frac{2\lambda\Phi}{\tau_p}(\overline{u_3^2} - \overline{u_3 v_3}) + \Pi_{33}, \quad (\text{A.3})$$

$$\frac{\partial}{\partial t}(\overline{u_1 u_2}) = -\overline{u_2^2} \frac{\partial U_1}{\partial x_2} - \frac{\lambda\Phi}{\tau_p}(2\overline{u_1 u_2} - \overline{u_1 v_2} - \overline{u_2 v_1}) + \Pi_{12}, \quad (\text{A.4})$$

$$\overline{u_1 u_3} = \overline{u_3 u_1} = \overline{u_2 u_3} = \overline{u_3 u_2} = 0,$$

where

$$\begin{aligned}\Pi_{11} &= \left(-\frac{C_{f1}}{\tau} + 2C_{f3}\frac{\lambda\Phi}{\tau_p} \right) (\bar{u}_1^2 - \frac{2}{3}k) + \frac{4+8C_{f2}}{3}\bar{u}_1\bar{u}_2\frac{\partial U_1}{\partial x_2} \\ &\quad - 2C_{f3}\frac{\lambda\Phi}{\tau_p}(\bar{u}_1\bar{v}_1 - \frac{1}{3}\bar{u}_m\bar{v}_m),\end{aligned}\tag{A.5}$$

$$\begin{aligned}\Pi_{22} &= \left(-\frac{C_{f1}}{\tau} + 2C_{f3}\frac{\lambda\Phi}{\tau_p} \right) (\bar{u}_2^2 - \frac{2}{3}k) - \frac{4+20C_{f2}}{3}\bar{u}_1\bar{u}_2\frac{\partial U_1}{\partial x_2} \\ &\quad - 2C_{f3}\frac{\lambda\Phi}{\tau_p}(\bar{u}_2\bar{v}_2 - \frac{1}{3}\bar{u}_m\bar{v}_m),\end{aligned}\tag{A.6}$$

$$\begin{aligned}\Pi_{33} &= \left(-\frac{C_{f1}}{\tau} + 2C_{f3}\frac{\lambda\Phi}{\tau_p} \right) (\bar{u}_3^2 - \frac{2}{3}k) + 4C_{f2}\bar{u}_1\bar{u}_2\frac{\partial U_1}{\partial x_2} \\ &\quad - 2C_{f3}\frac{\lambda\Phi}{\tau_p}(\bar{u}_3\bar{v}_3 - \frac{1}{3}\bar{u}_m\bar{v}_m),\end{aligned}\tag{A.7}$$

$$\begin{aligned}\Pi_{12} &= \left(-\frac{C_{f1}}{\tau} + 2C_{f3}\frac{\lambda\Phi}{\tau_p} \right) \bar{u}_1\bar{u}_2 + \frac{2}{5}k\frac{\partial U_1}{\partial x_2} - 3C_{f2}\left(\bar{u}_1^2 + \bar{u}_2^2 - \frac{4}{3}k\right)\frac{\partial U_1}{\partial x_2} \\ &\quad - \frac{4+14C_{f2}}{6}(\bar{u}_1^2 - \bar{u}_2^2)\frac{\partial U_1}{\partial x_2} - C_{f3}\frac{\lambda\Phi}{\tau_p}(\bar{u}_1\bar{v}_2 + \bar{u}_2\bar{v}_1),\end{aligned}\tag{A.8}$$

for the fluid,

$$\frac{\partial}{\partial t}(\bar{v}_1^2) = -2\bar{v}_1\bar{v}_2\frac{\partial V_1}{\partial x_2} - \frac{2}{\tau_p}(\bar{v}_1^2 - \bar{u}_1\bar{v}_1),\tag{A.9}$$

$$\frac{\partial}{\partial t}(\bar{v}_2^2) = -\frac{2}{\tau_p}(\bar{v}_2^2 - \bar{u}_2\bar{v}_2),\tag{A.10}$$

$$\frac{\partial}{\partial t}(\bar{v}_3^2) = -\frac{2}{\tau_p}(\bar{v}_3^2 - \bar{u}_3\bar{v}_3),\tag{A.11}$$

$$\frac{\partial}{\partial t}(\bar{v}_1\bar{v}_2) = -\bar{v}_2^2\frac{\partial V_1}{\partial x_2} - \frac{1}{\tau_p}(2\bar{v}_1\bar{v}_2 - \bar{u}_1\bar{v}_2 - \bar{u}_2\bar{v}_1),\tag{A.12}$$

$$\bar{v}_1\bar{v}_3 = \bar{v}_3\bar{v}_1 = \bar{v}_2\bar{v}_3 = \bar{v}_3\bar{v}_2 = 0,$$

for the dispersed phase, and

$$\frac{\partial}{\partial t}(\bar{u}_1\bar{v}_1) = -\bar{u}_1\bar{v}_2\frac{\partial V_1}{\partial x_2} - \bar{u}_2\bar{v}_1\frac{\partial U_1}{\partial x_2} + \frac{1}{\tau_p}(\bar{u}_1^2 - \bar{u}_1\bar{v}_1) - \frac{\lambda\Phi}{\tau_p}(\bar{u}_1\bar{v}_1 - \bar{v}_1^2) + \chi_{11},\tag{A.13}$$

$$\frac{\partial}{\partial t}(\bar{u}_2\bar{v}_2) = \frac{1}{\tau_p}(\bar{u}_2^2 - \bar{u}_2\bar{v}_2) - \frac{\lambda\Phi}{\tau_p}(\bar{u}_2\bar{v}_2 - \bar{v}_2^2) + \chi_{22},\tag{A.14}$$

$$\frac{\partial}{\partial t}(\bar{u}_3\bar{v}_3) = \frac{1}{\tau_p}(\bar{u}_3^2 - \bar{u}_3\bar{v}_3) - \frac{\lambda\Phi}{\tau_p}(\bar{u}_3\bar{v}_3 - \bar{v}_3^2) + \chi_{33},\tag{A.15}$$

$$\frac{\partial}{\partial t}(\overline{u_1v_2}) = -\overline{u_2v_2}\frac{\partial U_1}{\partial x_2} + \frac{1}{\tau_p}(\overline{u_1u_2} - \overline{u_1v_2}) - \frac{\lambda\Phi}{\tau_p}(\overline{u_1v_2} - \overline{v_1v_2}) + \chi_{12}, \quad (\text{A.16})$$

$$\frac{\partial}{\partial t}(\overline{u_2v_1}) = -\overline{u_2v_2}\frac{\partial V_1}{\partial x_2} + \frac{1}{\tau_p}(\overline{u_2u_1} - \overline{u_2v_1}) - \frac{\lambda\Phi}{\tau_p}(\overline{u_2v_1} - \overline{v_2v_1}) + \chi_{21}, \quad (\text{A.17})$$

$$\overline{u_1v_3} = \overline{u_3v_1} = \overline{u_2v_3} = \overline{u_3v_2} = 0,$$

where

$$\chi_{11} = -\frac{C_{fp1}}{\tau}\overline{u_1v_1} + C_{fp2}\overline{u_2v_1}\frac{\partial U_1}{\partial x_2} + C_{fp3}\frac{\lambda\Phi}{\tau_p}(\overline{u_1v_1} - \overline{v_1^2}), \quad (\text{A.18})$$

$$\chi_{22} = -\frac{C_{fp1}}{\tau}\overline{u_2v_2} + C_{fp3}\frac{\lambda\Phi}{\tau_p}(\overline{u_2v_2} - \overline{v_2^2}), \quad (\text{A.19})$$

$$\chi_{33} = -\frac{C_{fp1}}{\tau}\overline{u_3v_3} + C_{fp3}\frac{\lambda\Phi}{\tau_p}(\overline{u_3v_3} - \overline{v_3^2}), \quad (\text{A.20})$$

$$\chi_{12} = -\frac{C_{fp1}}{\tau}\overline{u_1v_2} + C_{fp2}\overline{u_2v_2}\frac{\partial U_1}{\partial x_2} + C_{fp3}\frac{\lambda\Phi}{\tau_p}(\overline{u_1v_2} - \overline{v_1v_2}), \quad (\text{A.21})$$

$$\chi_{21} = -\frac{C_{fp1}}{\tau}\overline{u_2v_1} + C_{fp3}\frac{\lambda\Phi}{\tau_p}(\overline{u_2v_1} - \overline{v_2v_1}), \quad (\text{A.22})$$

for the fluid-particle velocity covariance.

References

Champagne, F. H., Harris, V. G., and Corrsin, S. (1970). Experiments on nearly homogeneous shear flow. *J. Fluid Mech.* **41**, 81–139.

Chen, C. P. and Wood, P. E. (1986). Turbulence closure modeling of the dilute gas-particle axisymmetric jet. *AICHE J.* **32**, 163–166.

Choi, Y.D. and Chung, M.K. (1983). Analysis of turbulent gas-solid suspension flow in a pipe. *J. Fluids Eng.* **105**, 329–334.

Chung, M.K., Sung, H.J., and Lee, K.B. (1986). Computational study of turbulent gas-particle flow in a venturi. *J. Fluids Eng.* **108**, 248–253.

Clift, R., Grace, J. R., and Weber, M. E. (1978). *Bubbles, Drops, and Particles*. Academic Press, New York, NY.

Crowe, C. T., Sharma, M. P., and Stock, D. E. (1977). The Particle-Source in cell (PSI-Cell) model for Gas-Droplet flows. *J. Fluids Eng.* **6**, 325–332.

Crowe, C.T., Troutt, T.R., and Chung, J.N. (1996). Numerical models for two-phase turbulent flows. *Ann. Rev. Fluid Mech.* **28**, 11–43.

Drew, D. A. (1983). Mathematical modeling of two-phase flow. *Ann. Rev. Fluid Mech.* **15**, 261–291.

Einstein, A. (1906). *Ann. Physik* **19**, 289.

Elghobashi, S. E. and Abou-Arab, T. W. (1983). A two-equation turbulence model for two-phase flows. *Phys. Fluids* **26**, 931–938.

Elghobashi, S. and Truesdell, G. C. (1992). Direct simulation of particle dispersion in a decaying isotropic turbulence. *J. Fluid Mech.* **242**, 655–700.

Elghobashi, S. and Truesdell, G. C. (1993). On the two-way interaction between homogeneous turbulence and dispersed solid particles. I: Turbulence modification. *Phys. Fluids* **5**, 1790–1801.

Faeth, G. M. (1987). Mixing, transport and combustion in sprays. *Prog. Energy Combust. Sci.* **13**, 293–345.

Frankel, N.A. and Acrivos, A. (1967). On the viscosity of a concentrated suspension of solid spheres. *Chem. Eng. Sci.* **22**, 847–853.

Givi, P. and Madnia, C. K. (1993). Spectral methods in combustion. In Chung, T. J., editor, *Numerical Modeling in Combustion*, chapter 8, pages 409–452. Taylor & Francis, Washington, D.C.

Givi, P. (1994). Spectral and random vortex methods in turbulent reacting flows. In Libby, P. A. and Williams, F. A., editors, *Turbulent Reacting Flows*, chapter 8, pages 475–572. Academic Press, London, UK.

Hanjalić, K. and Launder, B. E. (1972). A Reynolds stress model of turbulence and its application to thin shear flows. *J. Fluid Mech.* **52**, 609–638.

Happel, J. (1957). Viscosity of suspensions of uniform spheres. *J. App. Phys.* **28**, 1288–1292.

Harris, V. G., Graham, A. H., and Corrsin, S. (1977). Further experiments in nearly homogeneous turbulent shear flow. *J. Fluid Mech.* **81**, 657–687.

Hinze, J.O. (1972). Turbulent fluid and particle interaction. In Hetsroni, G., editor, *Progress in Heat and Mass Transfer*, volume 6, pages 433–452. Pergamon Press, Oxford.

Jackson, R. and Davidson, B. J. (1983). An equation set for non-equilibrium two phase flow, and an analysis of some aspects of choking, acoustic propagation, and losses in low pressure wet steam. *Int. J. Multiphase Flow* **9**, 491–510.

Launder, B. E. and Spalding, D. B. (1972). *Lectures in Mathematical Modeling of Turbulence*. Academic Press, London, UK.

Launder, B. E. and Spalding, D. B. (1974). The numerical computation of turbulent flows. *Comput. Methods Appl. Mech. Engng* **3**, 269–289.

Launder, B. E., Reece, G. J., and Rodi, W. (1975). Progress in the development of a Reynolds-stress turbulence closure. *J. Fluid Mech.* **68**, 537–566.

Launder, B. E. (1991). Current capabilities for modelling turbulence in industrial flows. *Applied Scientific Research* **48**, 247–269.

Liljegren, L. M. (1993). The effect of a mean fluid velocity gradient on the streamwise velocity variance of a particle suspended in a turbulent flow. *Int. J. Multiphase Flow* **19**, 471–484.

Lumley, J. L. (1978). Computational modeling of turbulent flows. *Adv. Appl. Mech.* **18**, 123–176.

Mashayek, F., Jaber, F.A., Miller, R.S., and Givi, P. (1997a). Dispersion and polydispersity of droplets in stationary isotropic turbulence. *Int. J. Multiphase Flow* **23**, 337–355.

Mashayek, F., Taulbee, D. B., and Givi, P. (1997b). Particle-laden turbulent flows. Part II: Explicit algebraic closures. *J. Fluid Mech.* submitted.

McLaughlin, J. B. (1989). Aerosol particle deposition in numerically simulated channel flow. *Phys. Fluids* **1**, 1211–1224.

Mostafa, A. A. and Elghobashi, S. E. (1985). A two-equation turbulence model for jet flows laden with vaporizing droplets. *Int. J. Multiphase Flow* **11**, 515–533.

Mostafa, A. A. and Elghobashi, S. E. (1986). Effect of liquid droplets on turbulence in a round gaseous jet. NASA CR 175063.

Reeks, W.M. (1993). On the constitutive relations for dispersed particles in nonuniform flows. I: Dispersion in a simple shear flow. *Phys. Fluids* **5**, 750–761.

Reynolds, W. C. (1976). Computation of turbulent flows. *Annu. Rev. Fluid Mech.* **8**, 183–208.

Riley, J. J. and Patterson, G. S. (1974). Diffusion experiments with numerically integrated isotropic turbulence. *Phys. Fluids* **17**, 292–297.

Rogallo, R. S. (1981). Numerical experiments in homogeneous turbulence. NASA TM 81315.

Rogers, M. M., Moin, P., and Reynolds, W. C. (1986). The structure and modeling of the hydrodynamic and passive scalar fields in homogeneous turbulent shear flow. Department of Mechanical Engineering TF-25, Stanford University, Stanford, CA.

Rotta, J.C. (1951). Statistische theorie nichthomogener turbulenz. *Z. Phys.* **129**, 547. Translation in English available in NASA TM-14560 (1982).

Sargianos, N. P., Anagnostopoulos, J., and Bergeles, G. (1990). Turbulence modulation of particles, downstream of a two-phase, particle-laden, round jet. In Rodi, W. and Ganić, editors, *Engineering Turbulence Modeling and Experiments*, pages 897–906. Elsevier Science Publishers Co., Inc.

Sha, W. T. and Soo, S. L. (1978). Multidomain multiphase fluid mechanics. *Int. J. Heat Mass Transfer* **21**, 1581–1595.

Shih, T.-H. and Lumley, J. L. (1986). Second-order modelling of particle dispersion in a turbulent flow. *J. Fluid Mech.* **163**, 349–363.

Simonin, O., Deutsch, E., and Boivin, M. (1995). Large eddy simulation and second-moment closure model of particle fluctuating motion in two-phase turbulent shear flows. In Durst, F., Kasagi, N., Launder, B.E., Schmidt, F.W., and Whitelaw, J.H., editors, *Turbulent Shear Flows 9*, pages 85–115. Springer-Verlag.

Squires, K. D. and Eaton, J. K. (1990). Particle response and turbulence modification in isotropic turbulence. *Phys. Fluids* **2**, 1191–1203.

Squires, K. D. and Eaton, J. K. (1991a). Measurements of particle dispersion obtained from direct numerical simulations of isotropic turbulence. *J. Fluid Mech.* **226**, 1–35.

Squires, K. D. and Eaton, J. K. (1991b). Preferential concentration of particles by turbulence. *Phys. Fluids* **3**, 1169–1178.

Squires, K. D. and Eaton, J. K. (1994). Effect of selective modification of turbulence on two-equation models for particle-laden turbulent flows. *J. Fluids Eng.* **116**, 778–784.

Taulbee, D. B. (1989). Engineering turbulence models. In George, W. K. and Arndt, R., editors. *Advances in Turbulence*, pages 75–125. Hemisphere Publishing Co.. New York, NY.

Tavoularis, S. and Corrsin, S. (1981). Experiments in nearly homogenous turbulent shear flow with a uniform mean temperature gradient. Part 1. *J. Fluid Mech.* **104**, 311–347.

Truesdell, G. C. and Elghobashi, S. (1994). On the two-way interaction between homogeneous turbulence and dispersed solid particles. II: Particle dispersion. *Phys. Fluids* **6**, 1790–1801.

Wang, L-P. and Maxey, M. R. (1993). Settling velocity and concentration distribution of heavy particles in isotropic turbulence. *J. Fluid Mech.* **256**, 27–68.

Wilcox, David C. (1993). *Turbulence Modeling for CFD*. DCW Industries, Inc., La Cañada, CA.

Yeh, F. and Lei, U. (1991). On the motion of small particles in a homogeneous turbulent shear flow. *Phys. Fluids* **3**, 2758–2776.

Yokomine, T., Shimizu, A., Kawamura, H., and Hasegawa, S. (1994). Realistic modeling of turbulence modulations in $k-\epsilon$ equations for gas-solid flows. In Crowe, C. T., Johnson, R., Prosperetti, A., Sommerfeld, M., and Y., Tsuji, editors, *Numerical Methods in Multiphase Flows*, pages 301–306. ASME, FED-Vol. 185, New York, NY.

Zaichik, L. I., Kozelev, M. V., and Pershukov, V. A. (1993). Modeling of hydrodynamics in gas dispersed turbulent flows. In Rodi, W. and Martelli, F., editors, *Engineering Turbulence Modeling and Experiments 2*, pages 925–934. Elsevier Science Publishers B. V.

Zhao, Y. (1993), *Multiphase, Turbulent, Reacting Flow in a Liquid Metal Combustor*. Ph.D. Thesis, The University of Wisconsin, Wisconsin, Milwaukee.

Zhou, L. X., Liao, C. M., and Chen, T. (1994). A unified second-order-moment two-phase turbulent model for simulating gas-particle flows. In Crowe, C. T., Johnson, R., Prosperetti, A., Sommerfeld, M., and Y., Tsuji, editors, *Numerical Methods in Multiphase Flows*, pages 307–313. ASME, FED-Vol. 185, New York, NY.

Zhou, L.X. (1993). *Theory and Numerical Modeling of Turbulent Gas-Particle Flows and Combustion*. CRC Press, Boca Raton, FL.

Figure Captions

Figure 1: Temporal variations of the particle Reynolds number.

Figure 2: Temporal variations of normalized normal stresses of the fluid and particles for the case with one-way coupling at $\tau_p = 0.016s$.

Figure 3: Temporal variations of the fluid turbulent kinetic energy and its rate of dissipation. Both quantities are normalized with their initial values.

Figure 4: Temporal variations of the production and drag dissipation terms appearing in the particle turbulent kinetic energy equation.

Figure 5: Comparison of the Reynolds stress components for the fluid and the particles. (a) $\Phi_m = 0$, $\tau_p = 0.016s$, (b) $\Phi_m = 0.5$, $\tau_p = 0.016s$, and (c) $\Phi_m = 0.25$, $\tau_p = 0.032s$. $[w;w_j] = \langle u;u_j \rangle$ for the fluid and $[w;w_j] = \langle\langle v;v_j \rangle\rangle$ for the particles.

Figure 6: Particle velocity autocorrelations in (a) streamwise, (b) cross-stream, and (c) spanwise directions.

Figure 7: Effects of two-way coupling on the Taylor micro-scale Reynolds number of the fluid in streamwise direction.

Figure 8: Normalized fluid velocity energy spectra for different cases at the nondimensional time $St = 10$.

Figure 9: Energy budgets for $\langle\langle u_1^2 \rangle\rangle$ and $\langle\langle u_1 v_1 \rangle\rangle$ from the case with $\Phi_m = 0.25$ and $\tau_p = 0.032s$.

Figure 10: Comparisons of the Reynolds stress model predictions (symbols) with DNS data (lines) for components of the fluid, particle, and fluid-particle Reynolds stress tensors in the case with one-way coupling at $\tau_p = 0.016s$.

Figure 11: Comparisons of the Reynolds stress model predictions (symbols) with DNS data (lines) for components of the fluid, particle, and fluid-particle Reynolds stress tensors for $\Phi_m = 0.25$ and $\tau_p = 0.016s$.

Figure 12: Comparisons of the Reynolds stress model predictions (symbols) with DNS data (lines) for components of the fluid, particle, and fluid-particle Reynolds stress tensors for $\Phi_m = 0.25$ and $\tau_p = 0.032s$.

Figure 13: Comparisons of the Reynolds stress model predictions (symbols) with DNS data (lines) for the dissipation rate of the fluid turbulent kinetic energy. (a) $\Phi_m = 0$, $\tau_p = 0.016s$, (b) $\Phi_m = 0.25$, $\tau_p = 0.016s$, and (c) $\Phi_m = 0.25$, $\tau_p = 0.032s$.

Table 1: Parameter values considered in DNS.

Case	Φ_m	τ_p (s)	$N_p \times 10^{-5}$
1	0	0.016	1.0
2	0.075	0.016	1.0
3	0.25	0.016	3.33
4	0.5	0.016	6.67
5	0.25	0.032	1.19

Table 2: Comparison of the present single phase flow results with previous simulations of Rogers *et. al.* (1986) (RMR) and the experiments of Tavoularis and Corrsin (1981) (TC), Harris *et. al.* (1970) (HGC), and Champagne *et. al.* (1970) (CHC).

	Present results	RMR	RMR	TC	TC	HGC	CHC
St	8.0	2.0	8.0	8.6	12.7	11.9	3.3
Re_λ	96.9	14.2	72.6	284	364	300	180
Re_T	952	26.1	391	9900	15000	13000	3200
$Sq^2 / \langle \epsilon \rangle$	8.70	3.14	8.65	13	12	11	5.8
$\langle u_1^2 \rangle / q^2$	0.47	0.43	0.53	0.52	0.53	0.50	0.47
$\langle u_2^2 \rangle / q^2$	0.21	0.26	0.16	0.19	0.19	0.20	0.25
$\langle u_3^2 \rangle / q^2$	0.32	0.31	0.31	0.29	0.28	0.30	0.28
$\frac{\langle u_1 u_2 \rangle}{\sqrt{\langle u_1^2 \rangle \langle u_2^2 \rangle}}$	-0.53	-0.55	-0.57	-0.45	-0.45	-0.47	-0.50

Table 3: Empirical constants.

Constant	Magnitude	Basis for choice
C_{f1}	1.75	Launder <i>et al.</i> (1975)
C_{f2}	-0.159	Launder <i>et al.</i> (1975)
C_{f3}	0.5	Budget of $\overline{u_i u_j}$
C_{fp1}	2.5	Budget of $\overline{u_i v_j}$
C_{fp2}	0.5	Budget of $\overline{u_i v_j}$
C_{fp3}	0.2	Budget of $\overline{u_i v_j}$
C_{ϵ_1}	1.45	Standard $k-\epsilon$
C_{ϵ_2}	1.85	Standard $k-\epsilon$
C_{ϵ_3}	0.8	Overall performance of RSM

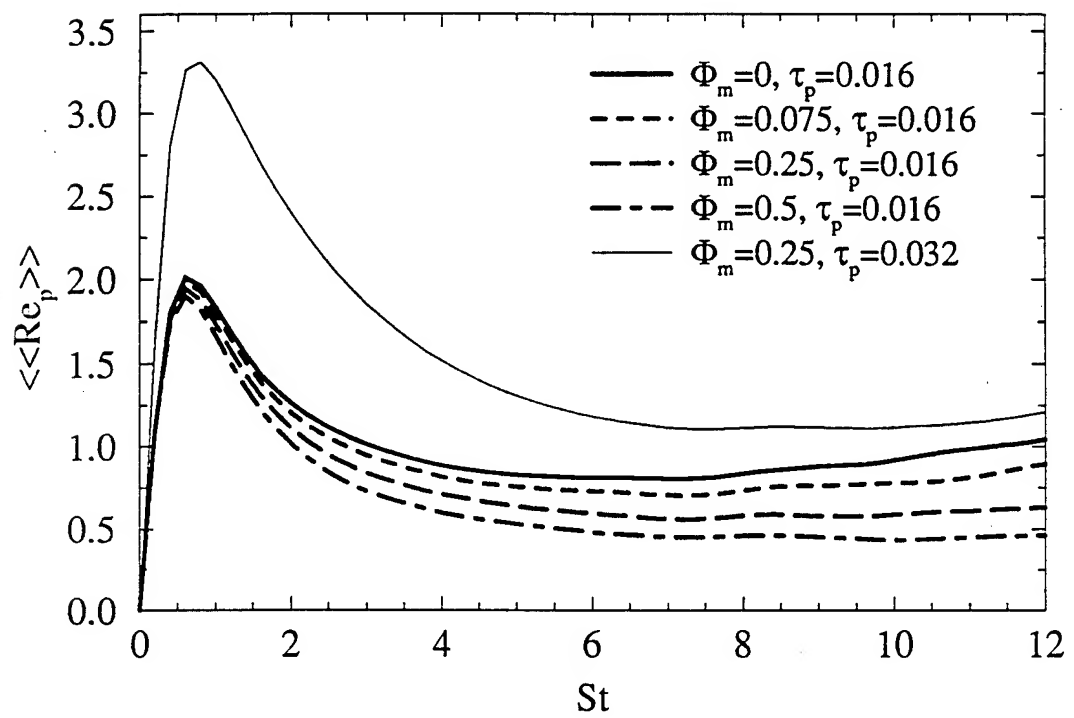


Fig. 1

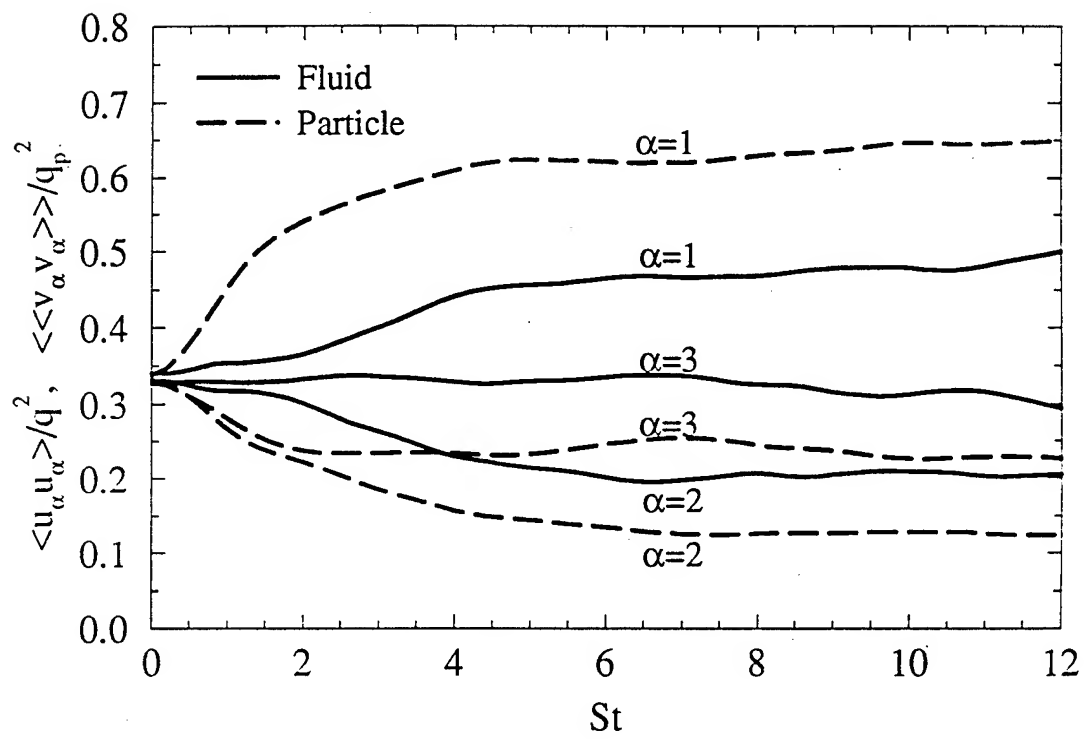


Fig. 2

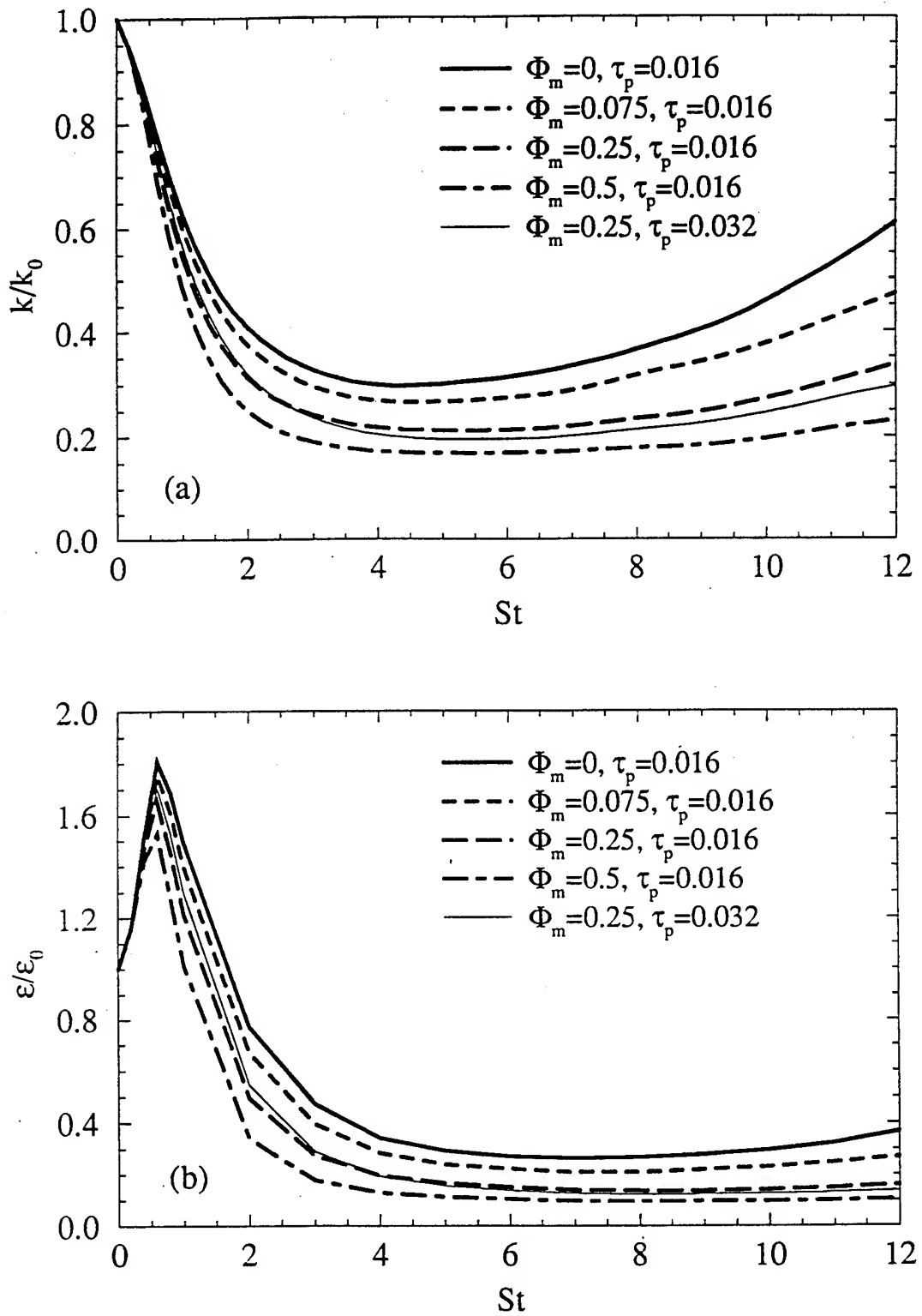


Fig. 3

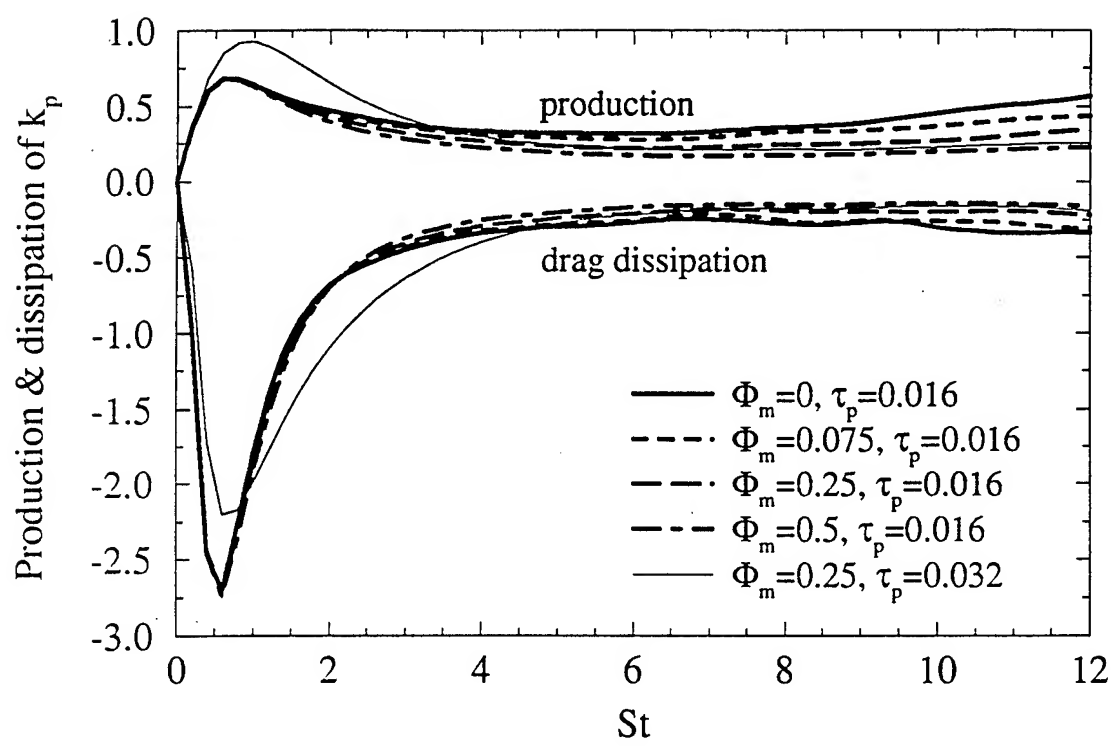


Fig. 4

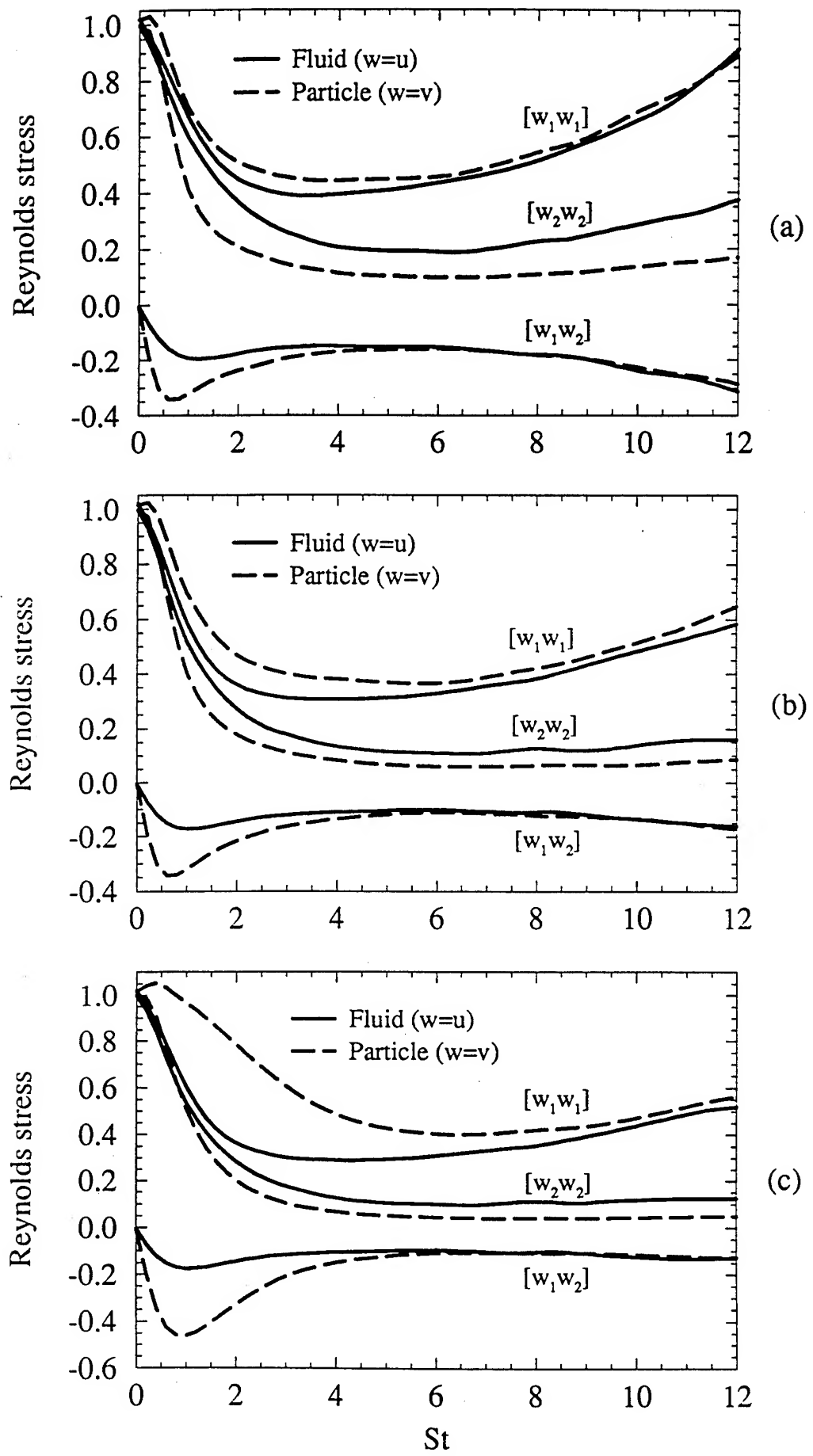


Fig. 5

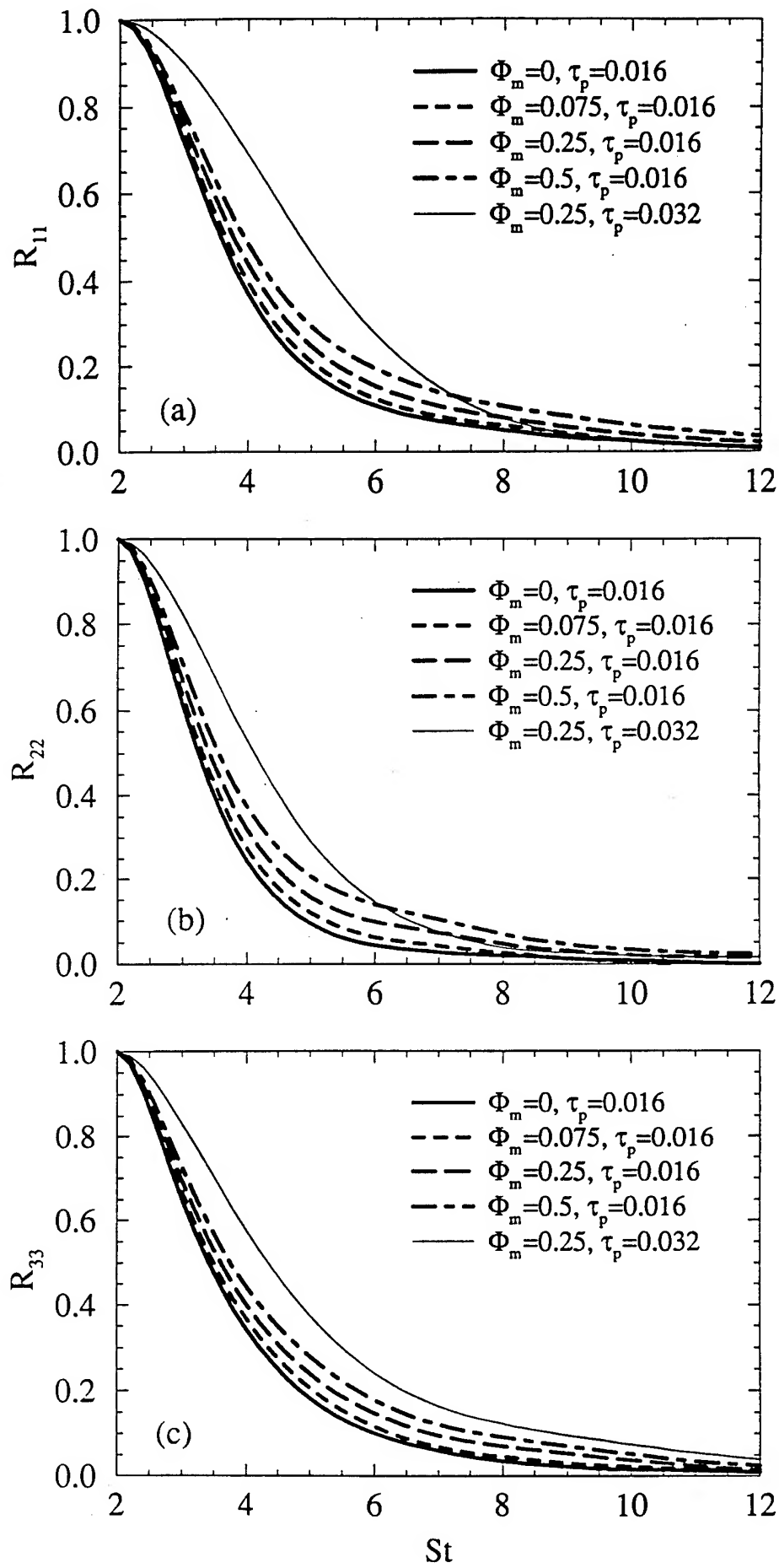


Fig. 6

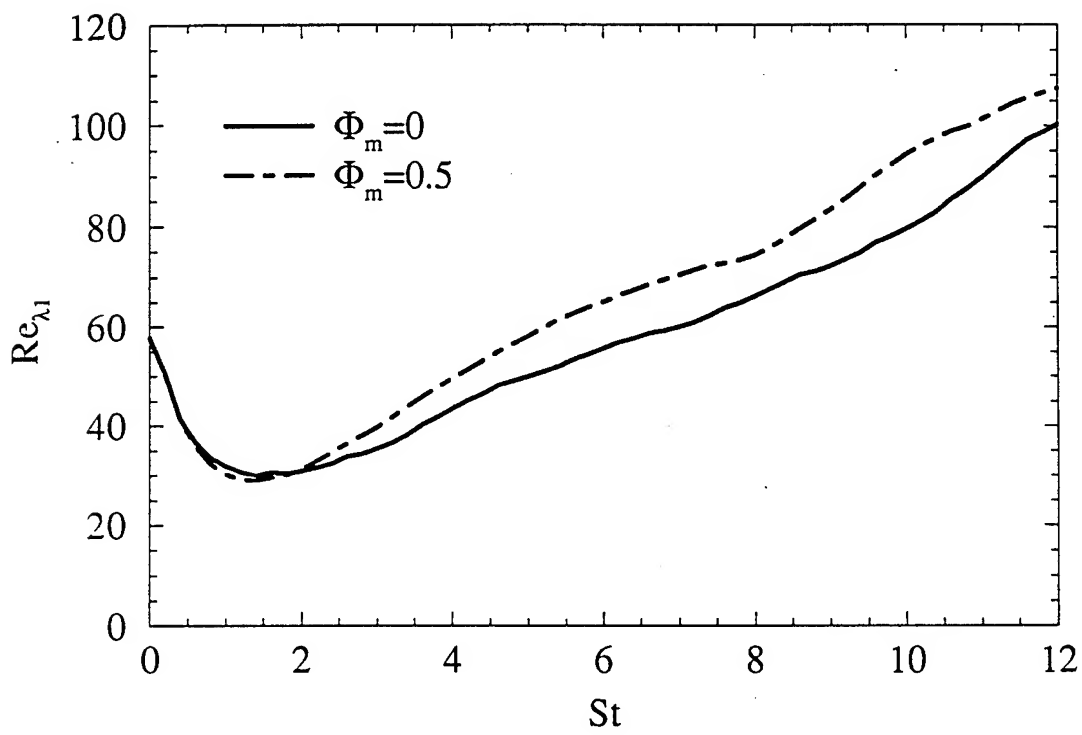


Fig. 7

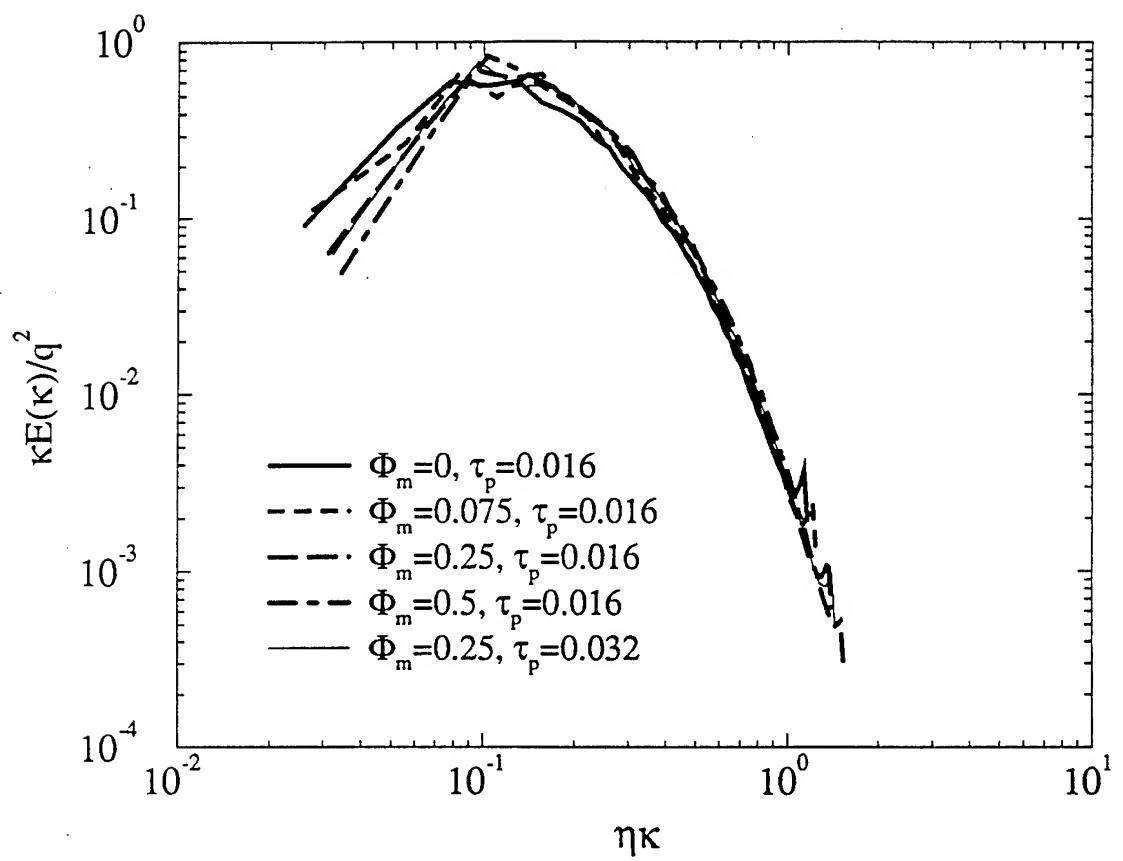


Fig. 8

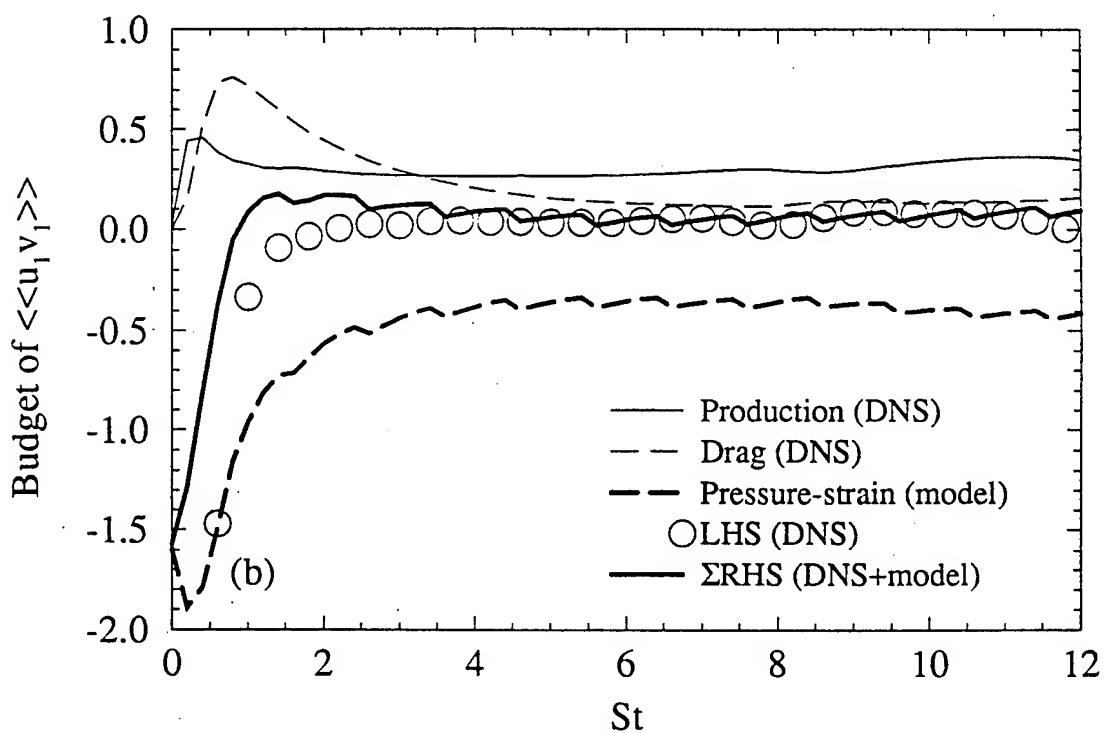
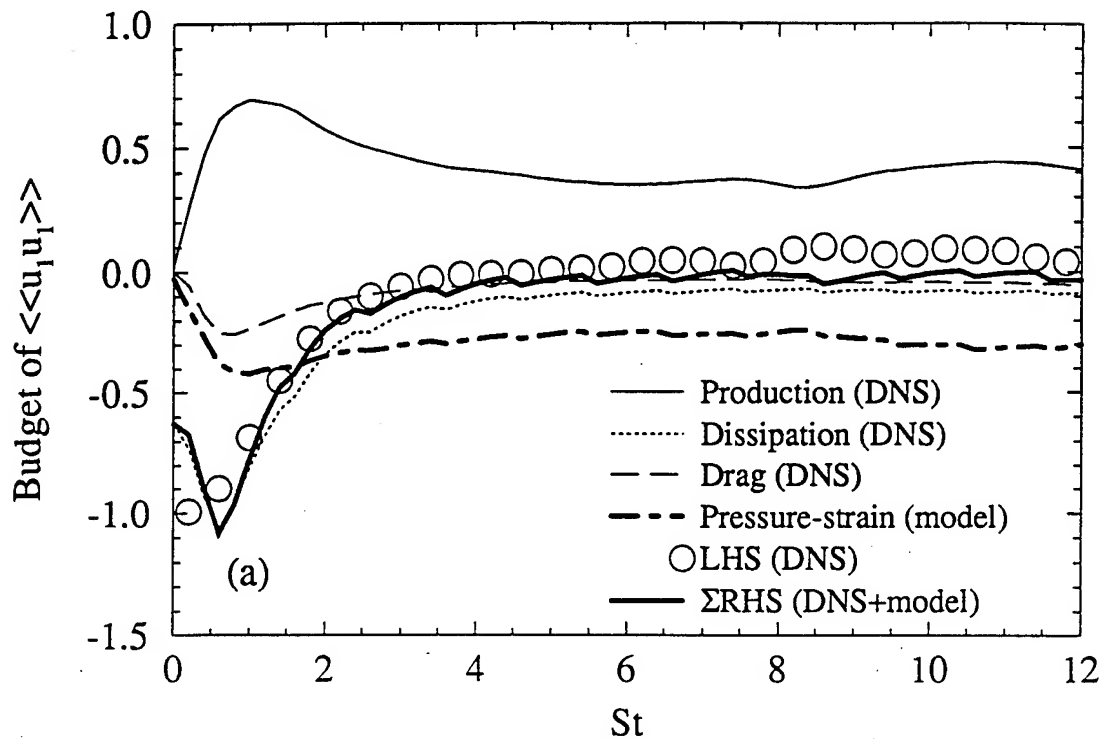


Fig. 9

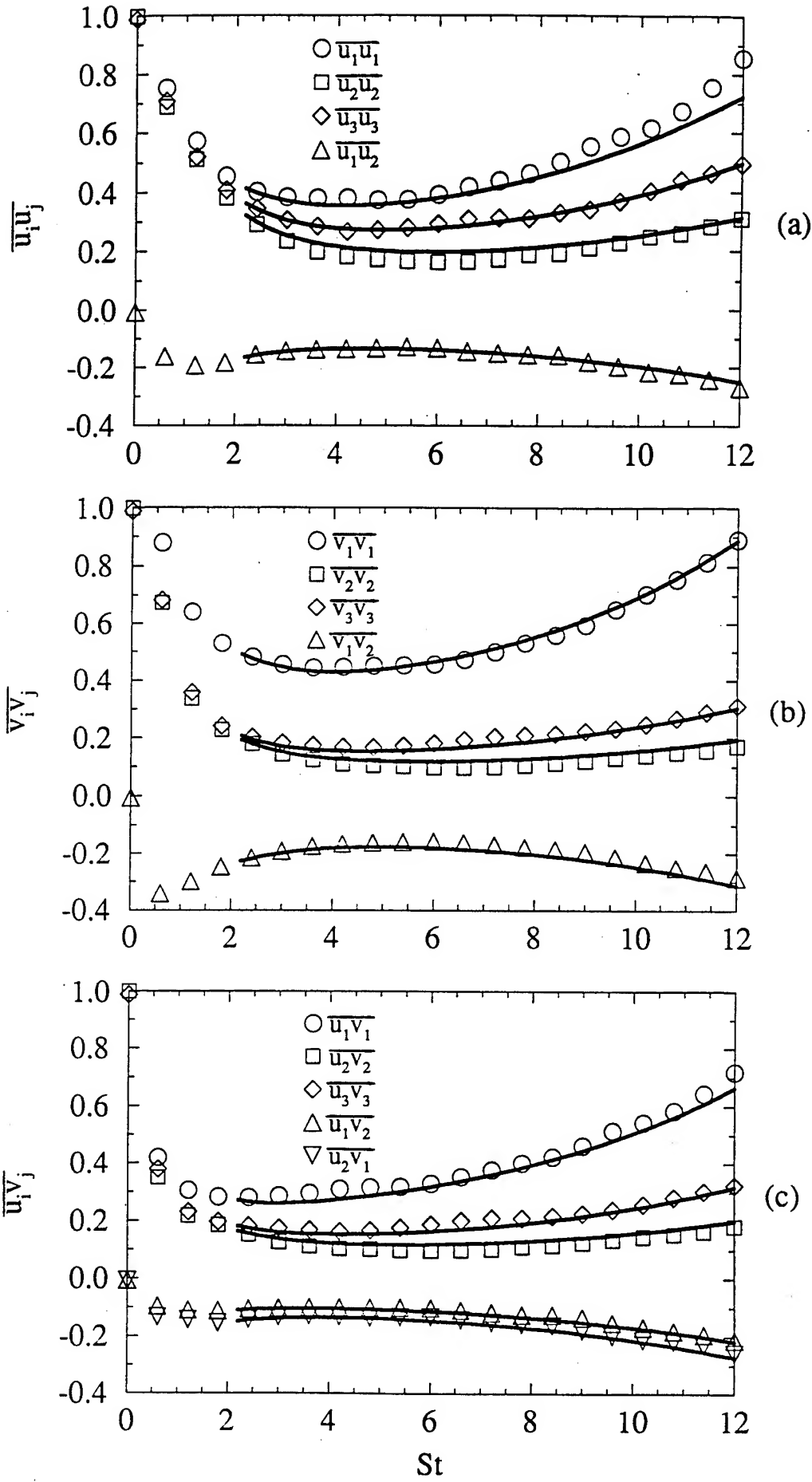


Fig. 10

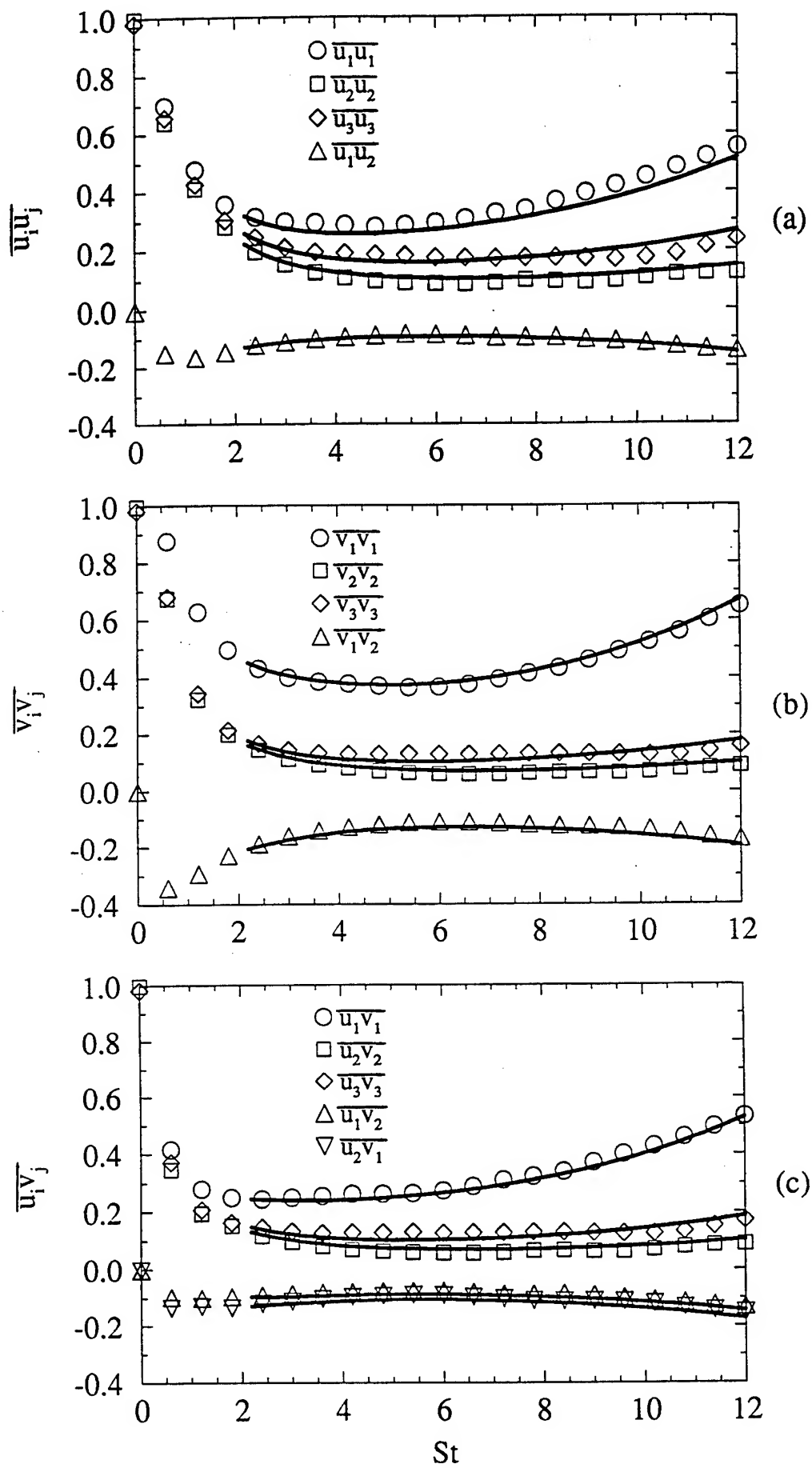


Fig. 11

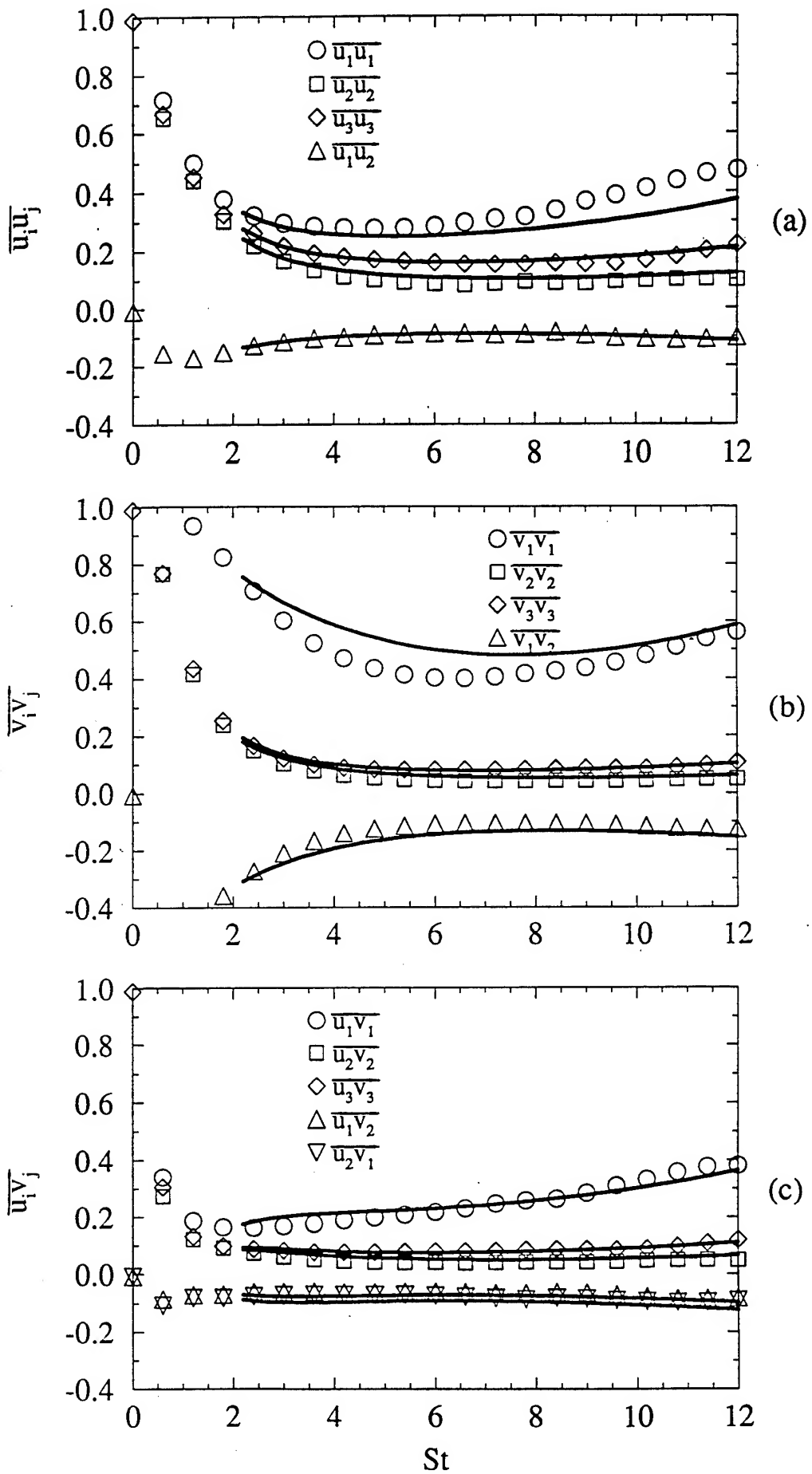


Fig. 12

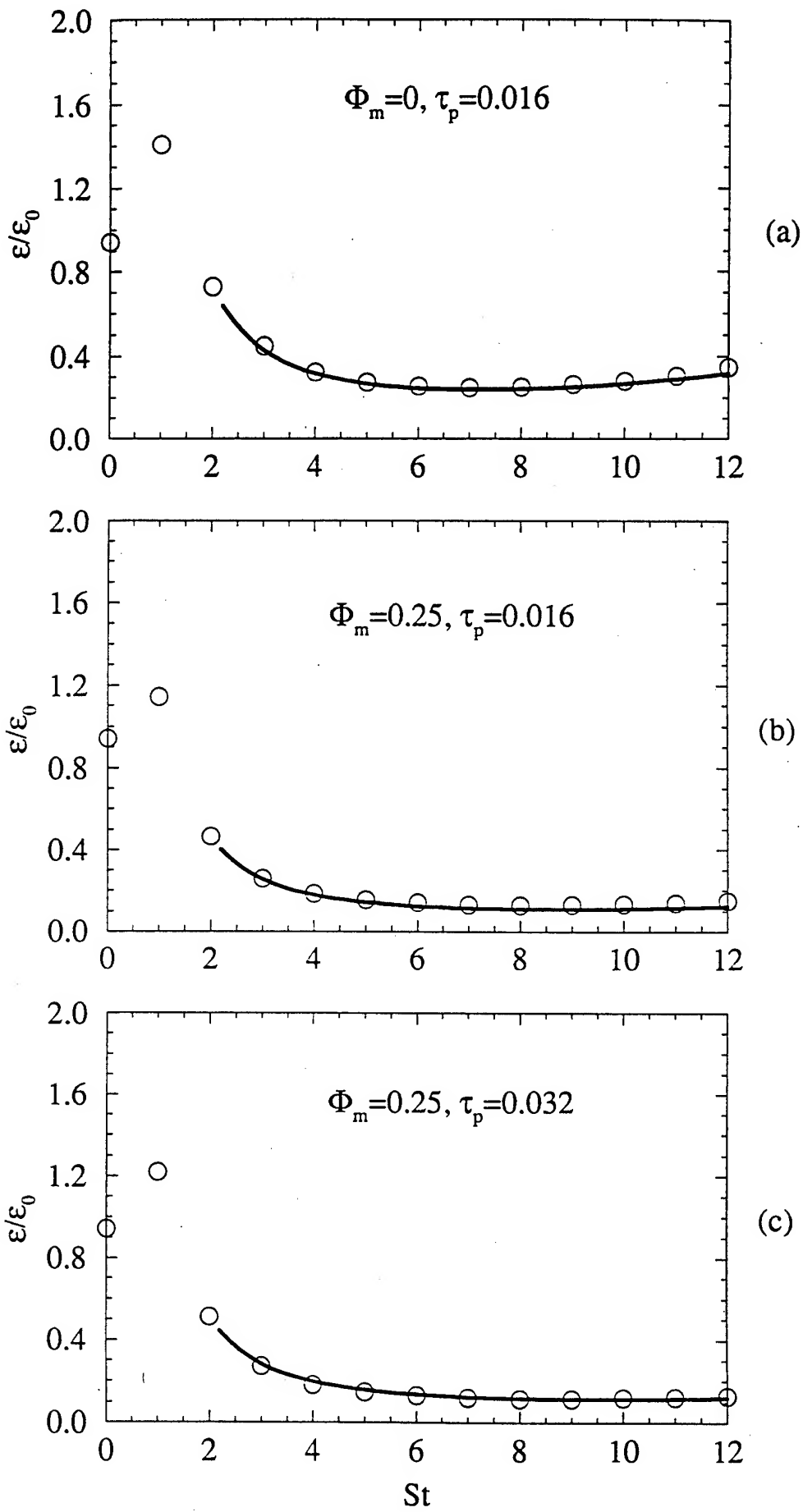


Fig. 13

APPENDIX IV

Particle-Laden Turbulent Flows. Part II: Explicit Algebraic Closures

Particle-Laden Turbulent Flows. Part II: Explicit Algebraic Closures

F. Mashayek, D.B. Taulbee, and P. Givi

Department of Mechanical and Aerospace Engineering
State University of New York at Buffalo
Buffalo, NY 14260-4400

Abstract

General “algebraic” closures are derived for the Reynolds stresses and the fluxes of the void fraction in the Reynolds averaged transport equations of two-phase turbulent flows. These closures are obtained from the hierarchy of second-order moment closures and are favored over conventional models based on the Boussinesq type (linear gradient diffusion) approximations. With a liberal use of the Cayley-Hamilton theorem, “explicit” solutions of the algebraic equations are obtained for the Reynolds stresses of both the carrier and the dispersed phases, and the turbulent fluxes of the void fraction. To close the system of equations for the algebraic models, a “four-equation” model is proposed based on the transport equations for the turbulent kinetic energy and its dissipation rate in the carrier phase, the turbulent kinetic energy in the dispersed phase, and the trace of the fluid-particle velocity covariance tensor. Explicit algebraic models are also derived for the triple order correlations in these equations. The predictions of the four-equation model for the Reynolds stresses are shown to compare well with direct numerical simulation (DNS) data of particle-laden homogeneous turbulent shear flows. By manipulating the explicit algebraic solutions, relations are provided for the “effective” turbulent diffusivities of the Reynolds stresses and the void fraction flux. These relations are utilized in parabolic (thin layer) formulation of two-phase turbulent shear flows. The predicted results for a particle-laden axisymmetric jet show good agreements with available laboratory data.

1 Introduction

In Part I of this work (Mashayek *et al.* (1997), hereinafter referred to as Part I), we propose a second-order Reynolds stress model (RSM) for statistical description of two-phase turbulent flows. The advantages of RSM over the Boussinesq type approximations with “isotropic”

eddy diffusivities are also demonstrated in Part I. Similar to single-phase flows, the primary advantage is that with accurate representation of all the Reynolds stresses, the overall predictive capabilities are improved. Despite this advantage, the need for solving additional moment "transport equations" makes RSM potentially less attractive for practical applications. For example, as recently demonstrated by Höfler (1993) the computational requirements associated with RSM for predictions of three-dimensional incompressible single-phase flows is significantly higher than those required to implement the $k-\epsilon$ model. The increase is naturally expected to be higher in multi-phase flows.

A remedy to overcome the high computational cost associated with RSM is to utilize "algebraic" closures (Pope, 1975; Rodi, 1976; Launder, 1975; Speziale, 1991; Taulbee, 1992; Gatski and Speziale, 1993; Taulbee *et al.*, 1993). Such closures are either derived directly from the RSM transport equations, or other types of representations (Yakhot and Orszag, 1986; Horiuti, 1969; Yoshizawa, 1984; Yoshizawa, 1988) which lead to anisotropic eddy diffusivities. One of the original contributions in the development of algebraic Reynolds stress models (ARSM) is due to Rodi (1976). In this work, all the stresses are determined from a set of "implicit" equations which must be solved in an iterative manner. Pope (1975) offers an improvement of the procedure by providing an "explicit" solution for the Reynolds stresses. This solution is generated with the use of the *Cayley-Hamilton* theorem (CHT), but is only applicable for predictions of two-dimensional (mean) flows. The extension of Pope's formulation to three-dimensional flows has been done by Taulbee (1992), Taulbee *et al.* (1993) and Gatski and Speziale (1993). In these efforts, CHT is used to generate explicit algebraic Reynolds stress models which are valid in both two- and three-dimensional flows. Adumitroaie (1997); Adumitroaie *et al.* (1997) have extended this methodology for treatment of chemically reacting, single-phase flows under both incompressible and highly compressible (high-speed) conditions.

The objective of this work is to develop explicit algebraic relations for statistical description of two-phase turbulent flows. These relations are provided for the Reynolds stresses (in both phases), the cross-correlation between the velocities of the two phases, and the turbulent fluxes of the void fraction which are appeared as unclosed terms in the transport equations

for the mean variables (Mashayek *et al.*, 1997):

$$\frac{\partial U_j}{\partial x_j} = 0, \quad (1.1)$$

$$\frac{\partial U_i}{\partial t} + \frac{\partial(U_j U_i)}{\partial x_j} = -\frac{1}{\rho_f} \frac{\partial P}{\partial x_i} + \nu \frac{\partial^2 U_i}{\partial x_j \partial x_j} - \frac{\partial \bar{u}_i u_j}{\partial x_j} - \frac{\lambda}{\tau_p} \Phi (U_i - V_i) - \frac{\lambda}{\tau_p} (\bar{u}_i \phi - \bar{v}_i \phi), \quad (1.2)$$

$$\frac{\partial \Phi}{\partial t} + \frac{\partial(V_j \Phi)}{\partial x_j} = -\frac{\partial \bar{v}_j \phi}{\partial x_j}, \quad (1.3)$$

$$\frac{\partial V_i}{\partial t} + V_j \frac{\partial V_i}{\partial x_j} = -\frac{\partial \bar{v}_i v_j}{\partial x_j} + \frac{1}{\tau_p} (U_i - V_i) + \bar{v}_i \frac{\partial v_j}{\partial x_j} + \left(1 - \frac{1}{\lambda}\right) g e_i, \quad (1.4)$$

where the overbar indicates the ensemble-averaged value. These equations are based on the two-fluid description of the transport of an incompressible fluid (the carrier phase) laden with monosize particles (the dispersed phase). The assumptions involved in the derivation of these equations are explained in Part I, thus will not be repeated here. In (1.1)-(1.4), U_i , P , V_i , and Φ indicate the mean variables for the carrier phase velocity, the carrier phase pressure, the dispersed phase velocity, and the void (or volume) fraction, respectively. The respective fluctuating variables are denoted by u_i , p , v_i , and ϕ ; and ν indicates the fluid kinematic viscosity. The parameter λ is the ratio of the particle material density (ρ_p) to that of the fluid (ρ_f), g is the gravity constant, and e_i is the unit vector in the gravity direction. The particle time constant is defined as $\tau_p = \frac{\rho_p d_p^2}{18\mu}$, where d_p is the particle diameter and μ is the fluid dynamic viscosity.

The starting point in this (part II) investigation is the transport equations for the second order moments. The primary contribution here is to simplify these equations into algebraic forms and to provide explicit solutions of the resulting algebraic equations. The feasibility of the final ARSM is demonstrated by construction of “effective” eddy diffusivities. The determination of the second order moments from the explicit relations, requires the knowledge of the turbulent kinetic energy and its dissipation rate in the carrier phase, the turbulent kinetic energy in the dispersed phase, and the trace of the fluid-particle velocity covariance tensor. We evaluate these variables by considering their transport equations, thus proposing a four-equation model. The triple order correlations in these transport equations are also expressed in terms of convenient gradient type models which can be directly implemented as diffusion terms. The final form of the closure is assessed via direct numerical simulation

(DNS) results as generated in Part I and with available laboratory data. The relative superiority of the model over currently available models is also demonstrated by this comparative assessment. With the explicit and relatively simple forms of the closures, it is hoped that they can be used in routine predictions of two-phase turbulent flows. However, as indicated in Part I, the mathematical derivations leading to the final model are somewhat complex and are based on several assumptions and simplifications. Again, many of these assumptions are not related to “two-phase turbulent transport” and are required even if the flow is laminar and/or single phase. No attempt will be made to (re)justify these assumptions here. All the assumptions pertaining to two-phase turbulent transport will be elaborated upon in detail.

In the next section all the steps involved in derivations of algebraic models for second-order moments are explained and the final form of the explicit solution is presented. To avoid lengthy sections and/or the possibility of losing the content in “a mist” of equations, only samples of derivations are given in the main text and other complementary equations are provided in Appendix A and Appendix B. In §3, a four-equation model is proposed and the procedure leading to algebraic models for third-order velocity correlations is described. In §4, the model is applied to a particle-laden homogeneous shear flow and the results are assessed via comparison with DNS data as obtained in Part I. Further model assessment is made in §5 where the model is presented in a form appropriate for conventional parabolic flow solvers. The predicted results based on this solver for a particle-laden axisymmetric jet are appraised by comparison against laboratory data. The paper ends in §6 with concluding remarks including reiteration on some of the main assumptions made for model developments and some suggestion for possible future work.

2 Explicit algebraic models for second-order moments

The operational procedure for the model development involves the followings: (1) construction of “differential” transport equations for the second-order moments, (2) modeling of various terms in the transport equations, specially the pressure-strain and the pressure-void fraction gradient correlations, (3) simplification of the transport differential equations to implicit “algebraic equations,” and (4) the solution of the algebraic equations to generate

“explicit” algebraic models. These steps are described below in order.

2.1 Transport equations for the second-order moments

The transport differential equations for the second-order moments are obtained by standard methods (Taulbee, 1989; Wilcox, 1993). These are expressed as:

$$\frac{D^V \overline{u_i u_j}}{Dt} = -\frac{\partial}{\partial x_l} \left[-\nu \frac{\partial \overline{u_i u_j}}{\partial x_l} + T_{ijl} \right] + \mathcal{P}_{ij}^f + \psi_{ij} - \epsilon_{ij} - \mathcal{D}_{ij}^f + \text{TOC}, \quad (2.1)$$

for the carrier phase Reynolds stress,

$$\frac{D^V \overline{v_i v_j}}{Dt} = -\frac{\partial}{\partial x_l} (\overline{v_l v_i v_j}) + \overline{v_i v_j \frac{\partial v_l}{\partial x_l}} + \mathcal{P}_{ij}^p - \mathcal{D}_{ij}^p, \quad (2.2)$$

for the dispersed phase Reynolds stress,

$$\begin{aligned} \frac{D^V \overline{u_i \phi}}{Dt} &= -\frac{\partial}{\partial x_l} (\overline{u_l u_i \phi} + \frac{1}{\rho_f} \overline{p \phi} \delta_{il}) - \overline{u_l \phi} \frac{\partial U_i}{\partial x_l} - \overline{u_i \phi} \frac{\partial V_l}{\partial x_l} - \overline{u_i v_l} \frac{\partial \Phi}{\partial x_l} + \overline{\frac{p}{\rho_f} \frac{\partial \phi}{\partial x_i}} \\ &- \frac{\lambda}{\tau_p} [\Phi(\overline{u_i \phi} - \overline{v_i \phi}) + \overline{\phi^2} (U_i - V_i)] + \nu \overline{\phi \frac{\partial^2 u_i}{\partial x_l^2}} - \overline{\Phi u_i \frac{\partial v_l}{\partial x_l}} + (U_l - V_l) \overline{u_i \frac{\partial \phi}{\partial x_l}} + \text{TOC}, \end{aligned} \quad (2.3)$$

for the carrier phase void fraction flux, and

$$\frac{D^V \overline{v_i \phi}}{Dt} = -\frac{\partial}{\partial x_l} (\overline{v_l v_i \phi}) - \overline{v_i \phi} \frac{\partial V_l}{\partial x_l} - \overline{v_l \phi} \frac{\partial V_i}{\partial x_l} - \overline{v_i v_l} \frac{\partial \Phi}{\partial x_l} + \frac{1}{\tau_p} (\overline{u_i \phi} - \overline{v_i \phi}) - \overline{\Phi v_i \frac{\partial v_l}{\partial x_l}} \quad (2.4)$$

for the dispersed phase void fraction flux. In these equations, $\frac{D^U}{Dt} = \frac{\partial}{\partial t} + U_l \frac{\partial}{\partial x_l}$, $\frac{D^V}{Dt} = \frac{\partial}{\partial t} + V_l \frac{\partial}{\partial x_l}$ represent the total derivatives. In the carrier phase, $T_{ijl} = \overline{u_l u_i u_j} + \frac{1}{\rho_f} \overline{p u_i} \delta_{jl} + \frac{1}{\rho_f} \overline{p u_j} \delta_{il}$ is the turbulent transport, $\mathcal{P}_{ij}^f = -\overline{u_i u_l} \frac{\partial U_j}{\partial x_l} - \overline{u_j u_l} \frac{\partial U_i}{\partial x_l}$ is the rate of production, $\psi_{ij} = \frac{p}{\rho_f} \left(\frac{\partial u_i}{\partial x_j} + \frac{\partial u_j}{\partial x_i} \right)$ is the pressure-strain correlation, $\epsilon_{ij} = 2\nu \frac{\partial u_i}{\partial x_l} \frac{\partial u_j}{\partial x_l}$ indicates the dissipation rate, and $\mathcal{D}_{ij}^f = \frac{\lambda}{\tau_p} [(U_i - V_i) \overline{u_j \phi} + (U_j - V_j) \overline{u_i \phi} + \Phi \overline{u_i (u_j - v_j)} + \Phi \overline{u_j (u_i - v_i)}]$ is the contribution from the particle drag. Similarly, in the dispersed phase, $\mathcal{P}_{ij}^p = -\overline{v_i v_l} \frac{\partial V_j}{\partial x_l} - \overline{v_j v_l} \frac{\partial V_i}{\partial x_l}$ is the rate of production and $\mathcal{D}_{ij}^p = \frac{1}{\tau_p} (2\overline{v_i v_j} - \overline{u_i v_j} - \overline{u_j v_i})$. The terms denoted by TOC indicate the third-order correlations involving both the velocity and the void fraction fluctuations. It is noted that the gravity appears only in the mean equations so there is no need for modeling

of the terms involving gravity.

Inspection of (2.1)-(2.4) reveals the additional correlations $\overline{u_i v_j}$ and $\overline{\phi^2}$. These correlations are governed by:

$$\begin{aligned} \frac{D^{uv}}{Dt} \overline{u_i v_j} = & -\frac{\partial}{\partial x_l} (\overline{u_l u_i v_j} + \overline{v_l u_i v_j} + \frac{1}{\rho_f} \overline{p v_j} \delta_{il}) - \overline{u_i v_l} \frac{\partial V_j}{\partial x_l} - \overline{u_l v_j} \frac{\partial U_i}{\partial x_l} + \frac{\overline{p}}{\rho_f} \frac{\partial v_j}{\partial x_i} \\ & + \frac{1}{\tau_p} (\overline{u_i u_j} - \overline{u_i v_j}) - \frac{\lambda}{\tau_p} [\Phi (\overline{u_i v_j} - \overline{v_i v_j}) + \overline{v_j \phi} (U_i - V_i)] \\ & + \nu v_j \frac{\partial^2 u_i}{\partial x_l^2} + U_l u_i \frac{\partial v_j}{\partial x_l} + V_l v_j \frac{\partial u_i}{\partial x_l} + u_i \frac{\partial u_l v_j}{\partial x_l} + v_j \frac{\partial u_i v_l}{\partial x_l} + \text{TOC}, \end{aligned} \quad (2.5)$$

$$\frac{D^\nu}{Dt} (\overline{\phi^2}/2) = \mathcal{P}^\phi - \mathcal{D}^\phi, \quad (2.6)$$

where $\frac{D^{uv}}{Dt} = \frac{\partial}{\partial t} + (U_l + V_l) \frac{\partial}{\partial x_l}$, $\mathcal{P}^\phi = -\overline{v_l \phi} \frac{\partial \Phi}{\partial x_l} - \overline{\phi^2} \frac{\partial V_l}{\partial x_l}$, and $\mathcal{D}^\phi = \Phi \overline{\phi \frac{\partial v_l}{\partial x_l}} - \overline{v_l \phi \frac{\partial \phi}{\partial x_l}}$.

The procedure of deriving a model for the pressure-strain correlation in the carrier phase is described in Part I. The final result is expressed as:

$$\begin{aligned} \Pi_{ij} = & -C_{f1} \epsilon a_{ij}^f + \epsilon \left[\frac{4}{5} S_{ij}^f - 6 C_{f2} \left(a_{ik}^f S_{kj}^f + a_{jk}^f S_{ki}^f - \frac{2}{3} a_{mn}^f S_{nm}^f \delta_{ij} \right) - \frac{4 + 14 C_{f2}}{3} (a_{ik}^f \omega_{kj}^f + a_{jk}^f \omega_{ki}^f) \right] \\ & + C_{f3} \frac{\lambda \Phi}{\tau_p} [2 k a_{ij}^f - k_{fp} (a_{ij}^{fp} + a_{ji}^{fp})] + \frac{3}{10} \frac{\lambda}{\tau_p} \left[(U_i - V_i) \overline{u_j \phi} + (U_j - V_j) \overline{u_i \phi} - \frac{2}{3} (U_l - V_l) \overline{u_l \phi} \delta_{ij} \right], \end{aligned} \quad (2.7)$$

where C_{f1} , C_{f2} , and C_{f3} are empirical constants to be determined,

$$a_{ij}^f = \frac{\overline{u_i u_j}}{k} - \frac{2}{3} \delta_{ij} \quad \text{and} \quad a_{ij}^{fp} = \frac{\overline{u_i v_j}}{k_{fp}} - \frac{2}{3} \delta_{ij} \quad (2.8)$$

are the anisotropic parts of the fluid-fluid and the fluid-particle Reynolds stresses, respectively; and

$$S_{ij}^f = \frac{1}{2} \frac{k}{\epsilon} \left(\frac{\partial U_i}{\partial x_j} + \frac{\partial U_j}{\partial x_i} \right) \quad \text{and} \quad \omega_{ij}^f = \frac{1}{2} \frac{k}{\epsilon} \left(\frac{\partial U_i}{\partial x_j} - \frac{\partial U_j}{\partial x_i} \right) \quad (2.9)$$

are the strain rate and the rotation tensors of the carrier phase, respectively. In these equations $k = \frac{1}{2} \overline{u_i u_i}$ and $\epsilon = \frac{1}{2} \epsilon_{ii}$ are the carrier phase turbulent kinetic energy and its rate of dissipation, respectively, and $k_{fp} = \frac{1}{2} \overline{u_i v_i}$ is referred to (by analogy) as the fluid-particle turbulent kinetic energy.

Following a similar procedure, models are derived for the fluid pressure-void fraction gradient correlation:

$$\overline{\frac{p}{\rho_f} \frac{\partial \phi}{\partial x_i}} = -C_{\phi 1} \frac{\overline{u_i \phi}}{\tau} + \frac{4}{5} \overline{u_l \phi} \frac{\partial U_i}{\partial x_l} - \frac{1}{5} \overline{u_l \phi} \frac{\partial U_l}{\partial x_i} + C_{\phi 2} \frac{\lambda}{\tau_p} (U_i - V_i) \overline{\phi^2} + C_{\phi 3} \frac{\lambda}{\tau_p} \Phi (\overline{u_i \phi} - \overline{v_i \phi}), \quad (2.10)$$

and the pressure-dispersed phase velocity gradient correlation:

$$\overline{\frac{p}{\rho_f} \frac{\partial v_j}{\partial x_i}} = -C_{f p 1} \frac{\overline{u_i v_j}}{\tau} + C_{f p 2} \overline{u_l v_j} \frac{\partial U_i}{\partial x_l} + C_{f p 3} \frac{\lambda}{\tau_p} [(U_i - V_i) \overline{v_j \phi} + \Phi (\overline{u_i v_j} - \overline{v_i v_j})], \quad (2.11)$$

where $\tau = \frac{k}{\epsilon}$ is the carrier phase turbulence time scale. Equations (2.7), (2.10), and (2.11) indicate that the proposed closures involve nine empirical constants which must be determined. The terms involving $C_{f 1}$ or $C_{f 2}$ in (2.7) are the equivalent of those in the widely utilized Launder *et al.* (1975) (LRR) model in single phase flows. Thus, the magnitudes of these constants are set to be the same ($C_{f 1} = 1.75$, $C_{f 2} = -0.159$) to ensure that in the limit of one-way coupling (2.7) reduces to the equivalent LRR model. The other seven parameters are discussed in §§4.1 and 5.2.

The term $\nu v_j \overline{\frac{\partial^2 u_i}{\partial x_l^2}}$ in (2.5) may be expressed in terms of an isotropic dissipation ($\nu \overline{\frac{\partial u_k}{\partial x_l} \frac{\partial v_k}{\partial x_l}}$); even though this term is not necessarily always positive. Determination of this dissipation requires the solution of a transport equation which in turn contains additional unclosed terms. Due to excessive complexities and approximations involved in modeling of these unclosed terms, development of such a transport equation is not pursued. Note that this dissipation is due to the fluid-particle interaction the effects of which are also included in the drag. Therefore, the contribution of this term to the dissipation is, indirectly, considered by adjusting the constants appearing in the model for the pressure-dispersed phase velocity gradient correlation in (2.11). Similar argument is applied to the term $\nu \overline{\phi \frac{\partial^2 u_i}{\partial x_l^2}}$ in (2.3). The TOC terms that involve both velocity and void fraction are also treated similarly. These higher order terms are usually small and their effects may be absorbed in the pressure terms. The other correlations, $\overline{u_i \frac{\partial \phi}{\partial x_l}}$, $\overline{u_i \frac{\partial v_j}{\partial x_l}}$, $\overline{v_j \frac{\partial u_i}{\partial x_l}}$, $\overline{u_i \frac{\partial v_l}{\partial x_l}}$, $\overline{v_i \frac{\partial v_l}{\partial x_l}}$, $\overline{v_i v_j \frac{\partial v_l}{\partial x_l}}$, $\overline{u_i \frac{\partial u_i v_j}{\partial x_l}}$, and $\overline{v_j \frac{\partial u_i v_l}{\partial x_l}}$, are either zero or very small in homogeneous and thin shear layer flows which are considered for model validations in this work. Therefore, these terms are neglected. In more complex flows, these terms may be modeled by implementing the gradient-diffusion hypothesis.

2.2 Implicit algebraic equations

The procedure for driving algebraic equations from the differential equations presented above is similar to that in single-phase flows (Taulbee, 1992; Gatski and Speziale, 1993). This procedure involves two fundamental assumptions: (I) The flow is in the “equilibrium state.” This assumption is mathematically expressed as:

$$\frac{D^u a_{ij}^f}{Dt} = 0, \quad \frac{D^v a_{ij}^p}{Dt} = 0, \quad \frac{D^u q_i^u}{Dt} = 0, \quad \frac{D^v q_i^v}{Dt} = 0, \quad \frac{D^{uv} a_{ij}^{fp}}{Dt} = 0, \quad (2.12)$$

with

$$a_{ij}^p = \frac{\bar{v}_i \bar{v}_j}{k_p} - \frac{2}{3} \delta_{ij}, \quad q_i^u = \frac{\bar{u}_i \bar{\phi}}{(2k)^{1/2} \bar{\phi}^{1/2}}, \quad q_i^v = \frac{\bar{v}_i \bar{\phi}}{(2k_p)^{1/2} \bar{\phi}^{1/2}}, \quad (2.13)$$

and $k_p = \frac{1}{2} \bar{v}_i \bar{v}_i$ denoting the dispersed phase kinetic energy. (II) The difference in the transport terms is negligible. To demonstrate the operational procedure in implementing these two assumptions, consider the Reynolds stress equation (2.1) for the carrier phase. First, the Reynolds stress equation is described in terms of the anisotropic stress tensor (Taulbee, 1992): $k \frac{D a_{ij}^f}{Dt} = \frac{\partial T_{ijl}}{\partial x_l} - \frac{\bar{u}_i \bar{u}_l}{k} \frac{\partial T_l}{\partial x_i} - \frac{\bar{u}_i \bar{u}_j}{k} (\mathcal{P}^f - \epsilon - \mathcal{D}^f) + \mathcal{P}_{ij}^f + \psi_{ij} - \epsilon_{ij} - \mathcal{D}_{ij}^f$, where $T_l = \frac{1}{2} T_{iil}$, $\mathcal{P}^f = \frac{1}{2} \mathcal{P}_{ii}^f$, and $\mathcal{D}^f = \frac{1}{2} \mathcal{D}_{ii}^f$. Then, implementing assumptions I and II yields:

$$\begin{aligned} & \left[C_{f1} + \frac{\mathcal{P}^f}{\epsilon} - 1 - \frac{\mathcal{D}^f}{\epsilon} + 2(1 - C_{f3}) \frac{\lambda \Phi \tau}{\tau_p} \right] \frac{a_{ij}^f}{\tau} = -\frac{8}{15} \frac{\epsilon}{k} S_{ij}^f \\ & -(1 + 6C_{f2}) \frac{\epsilon}{k} \left(S_{iil}^f a_{lj}^f + S_{jl}^f a_{li}^f - \frac{2}{3} S_{kl}^f a_{lk}^f \delta_{ij} \right) + \frac{1 + 14C_{f2}}{3} \frac{\epsilon}{k} (\omega_{il}^f a_{lj}^f + \omega_{jl}^f a_{li}^f) \\ & + (1 - C_{f3}) \frac{\lambda \Phi}{\tau_p} \frac{k_{fp}}{k} (a_{ij}^{fp} + a_{ji}^{fp}) - \frac{7}{10} \frac{\lambda}{k \tau_p} \left[(U_i - V_i) \bar{u}_j \bar{\phi} + (U_j - V_j) \bar{u}_i \bar{\phi} - \frac{2}{3} (U_l - V_l) \bar{u}_l \bar{\phi} \delta_{ij} \right]. \end{aligned} \quad (2.14)$$

The procedure for providing algebraic equations for the other correlations is similar and is not repeated here. Appendix A provides the final forms of the algebraic equations for the dispersed phase Reynolds stress, the void fraction fluxes, and the fluid-particle velocity covariance.

2.3 Explicit algebraic models

In the form presented above (and in Appendix A), the algebraic moment equations can be used for modeling. However, the “implicit” form of these equations makes them very inconvenient for actual computational use. This has been the primary factor in motivating the development of algebraic closures in single phase flows (Rodi, 1976; Pope, 1975); here the explicit forms of the moments are provided as determined by the exact solution to the algebraic equation set.

To generate explicit algebraic models, (2.14) and (A.1)-(A.3) are presented in tensor forms:

$$\underline{\underline{a}}^f - C_1^f \underline{\underline{q}}^f - C_2^f \left(\underline{\underline{a}}^f \underline{\underline{S}}^f + \underline{\underline{S}}^f \underline{\underline{a}}^f - \frac{2}{3} \{ \underline{\underline{S}}^f \underline{\underline{a}}^f \} \underline{\underline{I}}_3 \right) - C_3^f (\underline{\underline{a}}^f \underline{\underline{\omega}}^f - \underline{\underline{\omega}}^f \underline{\underline{a}}^f) = 0, \quad (2.15)$$

$$\underline{\underline{a}}^p - C_1^p \underline{\underline{q}}^p - C_2^p \left(\underline{\underline{a}}^p \underline{\underline{S}}^p + \underline{\underline{S}}^p \underline{\underline{a}}^p - \frac{2}{3} \{ \underline{\underline{S}}^p \underline{\underline{a}}^p \} \underline{\underline{I}}_3 \right) - C_3^p (\underline{\underline{a}}^p \underline{\underline{\omega}}^p - \underline{\underline{\omega}}^p \underline{\underline{a}}^p) = 0, \quad (2.16)$$

$$\underline{\varphi}^f + D^f \underline{\underline{A}}^f \underline{\varphi}^f + B^f \underline{\varphi}^p + \underline{\underline{C}}^f = 0, \quad (2.17)$$

$$\underline{\varphi}^p + D^p \underline{\underline{A}}^p \underline{\varphi}^p + B^p \underline{\varphi}^f + \underline{\underline{C}}^p = 0, \quad (2.18)$$

where a single underline indicates a vector, a double underline denotes a second order tensor, $\underline{\underline{I}}_3$ is the three-dimensional identity tensor, $\underline{\underline{a}}^f = a_{ij}^f$, $\underline{\underline{a}}^p = a_{ij}^p$, $\underline{\varphi}^f = \overline{u_i \phi}$, and $\underline{\varphi}^p = \overline{v_i \phi}$. The relations for the newly introduced coefficients and tensors are obtained by the comparison of (2.15)-(2.18) with (2.14) and (A.1)-(A.3). These relations are given in Appendix B.

At this stage, the fluid-particle velocity covariance ($\overline{u_i v_j}$) is assumed known (the solution of (A.4) for a_{ij}^{fp} is discussed later; the updated values of a_{ij}^{fp} are implemented in the solution of (2.15)-(2.18) in a trial-and-error manner.) With the knowledge of a_{ij}^{fp} , the system of equations (2.15)-(2.18) are solved by the following procedure: First, (2.16) is solved for the dispersed phase Reynolds stress. Then, (2.17) and (2.18) are solved simultaneously to determine the void fraction fluxes. Finally, (2.15) is solved for the fluid Reynolds stress. The solution for (2.15)-(2.18) with a three-dimensional mean flow is possible. However, the solution will be too complicated to be of practical use. In the following, the solution is presented for two-dimensional mean flow with three-dimensional turbulence.

The solution for the coupled equations (2.17) and (2.18) is obtained via direct utilization

of the CHT (Eringen, 1971). Details of the mathematical procedure at this stage are not necessary (Adumitroaie (1997) provides a tutorial description of this procedure). Here, we present the final results:

$$\underline{\varphi}^f = \underline{\underline{M}}^{-1} [E^p(D^f \underline{\underline{A}}^f - \underline{\underline{I}}_2) \underline{\underline{C}}^f + (D^f \underline{\underline{A}}^f - \underline{\underline{I}}_2)(D^p \underline{\underline{A}}^p - D^p \{\underline{\underline{S}}^p\} \underline{\underline{I}}_2 - \underline{\underline{I}}_2) B^f \underline{\underline{C}}^p], \quad (2.19)$$

$$\underline{\varphi}^P = \underline{\underline{M}}^{-1} [(D^p \underline{\underline{A}}^p - D^p \{\underline{\underline{S}}^p\} \underline{\underline{I}}_2 - \underline{\underline{I}}_2)(D^f \underline{\underline{A}}^f - \underline{\underline{I}}_2) B^p \underline{\underline{C}}^f + E^f (D^p \underline{\underline{A}}^p - D^p \{\underline{\underline{S}}^p\} \underline{\underline{I}}_2 - \underline{\underline{I}}_2) \underline{\underline{C}}^p], \quad (2.20)$$

where

$$\underline{\underline{M}} = E^f E^p \underline{\underline{I}}_2 - (D^f \underline{\underline{A}}^f - \underline{\underline{I}}_2)(D^p \underline{\underline{A}}^p - D^p \{\underline{\underline{S}}^p\} \underline{\underline{I}}_2 - \underline{\underline{I}}_2) B^f B^p, \quad (2.21)$$

and $E^f = -\frac{1}{2} D^{f^2} \{\underline{\underline{A}}^{f^2}\} + \frac{1}{2} \{\underline{\underline{I}}_2\}$, $E^p = D^p \{\underline{\underline{S}}^p\} + \frac{1}{2} D^{p^2} (\{\underline{\underline{S}}^p\}^2 - \{\underline{\underline{A}}^{p^2}\}) + \frac{1}{2} \{\underline{\underline{I}}_2\}$, $\underline{\underline{I}}_2$ is the two-dimensional identity vector, and the notation $\{\}$ indicates the trace of a tensor.

The solution procedures for $\underline{\underline{a}}^f$ and $\underline{\underline{a}}^p$ are identical. Therefore, we consider the general form of the tensor $\underline{\underline{a}}$ governed by:

$$\underline{\underline{a}} = C_1 \underline{\underline{q}} + C_2 \left(\underline{\underline{a}} \underline{\underline{S}} + \underline{\underline{S}} \underline{\underline{a}} - \frac{2}{3} \{\underline{\underline{S}} \underline{\underline{a}}\} \underline{\underline{I}}_3 \right) + C_3 (\underline{\underline{a}} \underline{\underline{\omega}} - \underline{\underline{\omega}} \underline{\underline{a}}). \quad (2.22)$$

The solution for $\underline{\underline{a}}$ is also obtained via CHT, but is a bit more complex. The procedure is analogous to (but much more involved than) those in single-phase turbulent flows (Pope, 1975; Taulbee, 1992; Gatski and Speziale, 1993; Taulbee *et al.*, 1993; Adumitroaie, 1997). The complexity is due to the fact that the tensor $\underline{\underline{a}}$ here is a function of “three tensors” ($\underline{\underline{S}}$, $\underline{\underline{\omega}}$, and $\underline{\underline{q}}$) in contrast to the case of a single-phase flow where $\underline{\underline{a}}$ is a function of only two tensors ($\underline{\underline{S}}$ and $\underline{\underline{\omega}}$). As a result, new integrity basis and irreducible matrix polynomials must be specified. The integrity basis and the corresponding matrix polynomials for a two-dimensional mean flow with three-dimensional turbulence have been identified by making use of various theorems originated from CHT. For that, several important theorems proposed (in a somewhat different form) by Rivlin (1955), and more recently reviewed by Spencer (1971) are utilized. By making a liberal use of many of these theorems, we are able to express $\underline{\underline{a}}$ via a “finite” set of polynomials:

$$\underline{\underline{a}} = \sum_{\lambda} G^{\lambda} \underline{\underline{T}}^{\lambda}, \quad (2.23)$$

where only the finite values $\lambda = 1, 2, 3, 4, 5$ need to be considered, and $\underline{\underline{T}}^{\lambda}$ s are the matrix

polynomial functions of $\underline{\underline{S}}$, $\underline{\underline{\omega}}$, \underline{q} , $\underline{\underline{I}}_2$, and $\underline{\underline{I}}_3$:

$$\underline{\underline{T}}^1 = \frac{1}{3}\underline{\underline{I}}_3 - \frac{1}{2}\underline{\underline{I}}_2, \quad \underline{\underline{T}}^2 = \underline{\underline{S}}, \quad \underline{\underline{T}}^3 = \underline{\underline{S}}\underline{\underline{\omega}} - \underline{\underline{\omega}}\underline{\underline{S}}, \quad \underline{\underline{T}}^4 = \underline{q}, \quad \underline{\underline{T}}^5 = \underline{q}\underline{\underline{\omega}} - \underline{\underline{\omega}}\underline{q}. \quad (2.24)$$

The coefficients G^λ of the matrix polynomials are functions of the “invariants” which may be obtained either from a “known” integrity basis, or directly via CHT (Eringen, 1971). The latter procedure is implemented here and yields the following (finite) set of invariants:

$$\eta_1 = \{\underline{\underline{S}}^2\}, \quad \eta_2 = \{\underline{\underline{\omega}}^2\}, \quad \eta_3 = \{\underline{\underline{S}}\underline{q}\}, \quad \eta_4 = \{\underline{\underline{S}}\underline{\underline{\omega}}\underline{q}\} + \{\underline{\underline{\omega}}\underline{q}\underline{\underline{S}}\}. \quad (2.25)$$

The final step is to determine the coefficients G^λ in terms of the invariants η_ℓ , $\ell = 1, 2, 3, 4$. Substitution of (2.23) into (2.22) yields:

$$\sum_\lambda G^\lambda \underline{\underline{T}}^\lambda = C_1 \sum_\lambda \delta_{4\lambda} \underline{\underline{T}}^\lambda + C_2 \sum_\lambda G^\lambda [\underline{\underline{T}}^\lambda \underline{\underline{S}} + \underline{\underline{S}} \underline{\underline{T}}^\lambda] - \frac{2}{3} \{\underline{\underline{S}} \underline{\underline{T}}^\lambda\} \underline{\underline{I}}_3 + C_3 \sum_\lambda G^\lambda (\underline{\underline{T}}^\lambda \underline{\underline{\omega}} - \underline{\underline{\omega}} \underline{\underline{T}}^\lambda). \quad (2.26)$$

Tensors $\underline{\underline{T}}^\lambda$ are linearly independent functions of $\underline{\underline{S}}$ and $\underline{\underline{\omega}}$, therefore tensors H_γ^λ and J_γ^λ can be defined as (Spencer, 1971; Pope, 1975):

$$\underline{\underline{T}}^\lambda \underline{\underline{S}} + \underline{\underline{S}} \underline{\underline{T}}^\lambda - \frac{2}{3} \{\underline{\underline{S}} \underline{\underline{T}}^\lambda\} \underline{\underline{I}}_3 = \sum_\gamma H_\gamma^\lambda \underline{\underline{T}}^\gamma, \quad (2.27)$$

$$\underline{\underline{T}}^\lambda \underline{\underline{\omega}} + \underline{\underline{\omega}} \underline{\underline{T}}^\lambda = \sum_\gamma J_\gamma^\lambda \underline{\underline{T}}^\gamma. \quad (2.28)$$

Substitution of (2.27) and (2.28) in (2.26) yields:

$$G^\lambda = C_1 \delta_{4\lambda} + C_2 \sum_\gamma G^\gamma H_\gamma^\lambda + C_3 \sum_\gamma G^\gamma J_\gamma^\lambda. \quad (2.29)$$

Once H_γ^λ and J_γ^λ are determined from (2.27)-(2.28), (2.29) provides a 5×5 linear system for the coefficients G^λ . After extensive algebraic manipulations, these coefficients are expressed as:

$$G^1 = \frac{-6C_1C_2C_3\eta_4 + 6C_1C_2\eta_3}{2C_2^2\eta_1 + 6C_3^2\eta_2 - 3}, \quad G^2 = \frac{2C_1C_2^2C_3\eta_4 - 2C_1C_2^2\eta_3}{(1 - 2C_3^2\eta_2)(2C_2^2\eta_1 + 6C_3^2\eta_2 - 3)}, \\ G^3 = \frac{2C_1C_2^2C_3^2\eta_4 - 2C_1C_2^2C_3\eta_3}{(1 - 2C_3^2\eta_2)(2C_2^2\eta_1 + 6C_3^2\eta_2 - 3)}, \quad G^4 = \frac{C_1}{1 - 2C_3^2\eta_2}, \quad G^5 = \frac{C_1C_3}{1 - 2C_3^2\eta_2}. \quad (2.30)$$

By this procedure it is not possible to obtain a practical explicit solution for a_{ij}^{fp} as this

tensor is a non-symmetric function of four symmetric tensors ($\underline{\underline{S}}^f$, $\underline{\underline{\omega}}^f$, $\underline{\underline{S}}^p$, and $\underline{\underline{\omega}}^p$) and one non-symmetric tensor which includes the coupling between the phases defined similarly to $\underline{\underline{q}}^f$ or $\underline{\underline{q}}^p$. The number of matrix polynomials needed to express a_{ij}^{fp} increases significantly and complicates the explicit solution to a level not suitable for practical use. It must be mentioned that it is possible to express the implicit equation for a_{ij}^{fp} in terms of three non-symmetric tensors. However, the loss of symmetry condition again results in a large increase in the number of matrix polynomials. Therefore, the solution for a_{ij}^{fp} is limited to the implicit level. Note that only the terms $\overline{u_i u_j}$, $\overline{v_i v_j}$, and $\overline{v_i \phi}$ must be explicit to provide diffusion terms in (1.2)-(1.4) for stable computations. Treating a_{ij}^{fp} in an implicit manner does not affect the stability of the overall computations.

3 A four-equation model

An inspection of algebraic models in §2, reveals that the evaluation of the Reynolds stresses requires the knowledge of k , ϵ , k_p , and k_{fp} . Analogous to the two-equation ($k-\epsilon$) treatment of single phase flows, here we consider equations for k , ϵ , k_p , and k_{fp} . The transport equations for k , k_p , and k_{fp} are derived by contracting (2.1), (2.2), and (2.5), respectively. The transport equation for the dissipation rate of the fluid turbulent kinetic energy is derived similarly to the ϵ -equation of the single-phase flow as described in Part I. The final form of the transport equations for k , ϵ , k_p , and k_{fp} are expressed as:

$$\begin{aligned} \frac{\partial k}{\partial t} + U_i \frac{\partial k}{\partial x_i} &= - \frac{\partial}{\partial x_i} (\overline{u_i k'}) - \overline{u_i u_j} \frac{\partial U_j}{\partial x_i} - \epsilon \\ &- \frac{\lambda}{\tau_p} [2\Phi(k - k_{fp}) + (U_i - V_i)\overline{u_i \phi}], \end{aligned} \quad (3.1)$$

$$\begin{aligned} \frac{\partial \epsilon}{\partial t} + U_i \frac{\partial \epsilon}{\partial x_i} &= - \frac{\partial}{\partial x_i} (\overline{u_i \epsilon'}) - C_{\epsilon 1} \frac{\epsilon}{k} \overline{u_i u_j} \frac{\partial U_j}{\partial x_i} - C_{\epsilon 2} \frac{\epsilon^2}{k} \\ &- \frac{\epsilon \lambda}{k \tau_p} \{2\Phi k - C_{\epsilon 3} [2\Phi k_{fp} - (U_i - V_i)\overline{u_i \phi}]\}, \end{aligned} \quad (3.2)$$

$$\frac{\partial k_p}{\partial t} + V_i \frac{\partial k_p}{\partial x_i} = - \frac{\partial}{\partial x_i} (\overline{v_i k'_p}) - \overline{v_i v_j} \frac{\partial V_j}{\partial x_i} - \frac{2}{\tau_p} (k_p - k_{fp}), \quad (3.3)$$

$$\frac{\partial k_{fp}}{\partial t} + (U_i + V_i) \frac{\partial k_{fp}}{\partial x_i} = - \frac{\partial}{\partial x_i} (\overline{u_i k'_{fp}} + \overline{v_i k'_{fp}}) - (1 - C_{fp 2}) \frac{1}{2} \overline{u_i v_j} \frac{\partial U_j}{\partial x_i} - \frac{1}{2} \overline{u_j v_i} \frac{\partial V_j}{\partial x_i}$$

$$\begin{aligned}
& - C_{fp1} \frac{k_{fp}}{\tau_p} + \frac{1}{\tau_p} (k - k_{fp}) + (1 - C_{fp3}) \frac{\lambda \Phi}{\tau_p} (k_p - k_{fp}) \\
& - (1 - C_{fp3}) \frac{\lambda}{\tau_p} (U_j - V_j) \overline{v_j \phi},
\end{aligned} \tag{3.4}$$

where $k' = \frac{1}{2} u_i u_i$, $\epsilon' = \nu \frac{\partial u_i}{\partial x_j} \frac{\partial u_i}{\partial x_j}$, $k'_p = \frac{1}{2} v_i v_i$, and $k'_{fp} = \frac{1}{2} u_i v_i$. In (3.2), $C_{\epsilon 1}$, $C_{\epsilon 2}$, and $C_{\epsilon 3}$ are empirical constants. The values for $C_{\epsilon 1}$ and $C_{\epsilon 2}$ are taken from their single-phase equivalents; $C_{\epsilon 1} = 1.45$ and $C_{\epsilon 2} = 1.85$. The value of the constant $C_{\epsilon 3} = 0.8$ is found by comparing the values of ϵ from DNS with those obtained from the overall solution of the Reynolds stress model (Mashayek *et al.*, 1997).

3.1 Algebraic models for third-order velocity correlations

In order to close the four-equation model, the third-order correlations: $\overline{u_i k'}$, $\overline{u_i \epsilon'}$, $\overline{v_i k'_p}$, $\overline{u_i k'_{fp}}$, and $\overline{v_i k'_{fp}}$ must be modeled. Here we consider modeling of the correlations involving velocity fluctuations only; modeling of $\overline{u_i \epsilon'}$ will be discussed in §5.1.

The procedure of closing the third-order correlations is analogous to (but more involved than) that in single phase flows (Hanjalić and Launder, 1972). Here, we detail the procedure leading to an implicit model for $\overline{u_i k'}$ (in high Reynolds number flows) in order to indicate the underlying assumptions. Similar to modeling of the second-order correlations, the starting point is the transport equation for $\overline{u_i k'}$. This equation is obtained by manipulating the transport equation for the fluctuating velocity of the carrier phase:

$$\begin{aligned}
& \frac{\partial u_i}{\partial t} + U_\ell \frac{\partial u_i}{\partial x_\ell} + u_\ell \frac{\partial U_i}{\partial x_\ell} + u_\ell \frac{\partial u_i}{\partial x_\ell} - \overline{u_\ell \frac{\partial u_i}{\partial x_\ell}} = - \frac{1}{\rho_f} \frac{\partial p}{\partial x_i} \\
& - \frac{\lambda \Phi}{\tau_p} (u_i - v_i) - \frac{\lambda}{\tau_p} [(U_i - V_i) \phi + (u_i \phi - v_i \phi) - (\overline{u_i \phi} - \overline{v_i \phi})].
\end{aligned} \tag{3.5}$$

Before we proceed, this equation is simplified using the following two assumptions: (I) The term $u_\ell \frac{\partial U_i}{\partial x_\ell}$ is neglected. In the final form of the transport equation for $\overline{u_i k'}$, this term generates third-order correlations multiplied by a mean velocity gradient. The resulting terms are usually negligible in comparison to other terms in the transport equation of $\overline{u_i k'}$ (Hanjalić and Launder, 1972). (II) The terms inside the brackets in (3.5), result in third-

and fourth-order correlations involving both velocity and void fraction fluctuations. These higher order terms are also small and are neglected. For the following discussion, it is more convenient to describe the final form of the equation in terms of $\overline{u_i u_j u_\ell}$ ($= 2\overline{u_i u_\ell}$):

$$\begin{aligned} \frac{D\overline{u_i u_j u_\ell}}{Dt} &= \left(\overline{u_i u_j} \frac{\partial \overline{u_i u_\ell}}{\partial x_\ell} + 2\overline{u_i u_\ell} \frac{\partial \overline{u_j u_\ell}}{\partial x_\ell} \right) - \frac{\partial}{\partial x_\ell} (\overline{u_i u_j u_\ell u_\ell}) \\ &- \left(\frac{1}{\rho_f} \overline{u_j u_j} \frac{\partial p}{\partial x_i} + \frac{2}{\rho_f} \overline{u_i u_j} \frac{\partial p}{\partial x_j} \right) - \frac{\lambda \Phi}{\tau_p} (3\overline{u_i u_j u_\ell} - \overline{v_i u_j u_\ell} - 2\overline{u_i u_j v_\ell}). \end{aligned} \quad (3.6)$$

Following Hanjalić and Launder (1972), by assuming the quasi-Gaussian distribution for triple correlations, the fourth-order correlation in (3.6) is expressed in terms of second-order correlations:

$$\overline{u_i u_j u_\ell u_\ell} = 2\overline{u_i u_j} \cdot \overline{u_j u_\ell} + \overline{u_i u_\ell} \cdot \overline{u_j u_j},$$

and the pressure terms are modeled as a decay term:

$$\left(\frac{1}{\rho_f} \overline{u_j u_j} \frac{\partial p}{\partial x_i} + \frac{2}{\rho_f} \overline{u_i u_j} \frac{\partial p}{\partial x_j} \right) = \frac{1}{C_{s1}} \frac{\overline{u_i u_j u_j}}{\tau}, \quad (3.7)$$

Where C_{s1} is an empirical constant. Finally, upon neglecting the convective transport, the implicit model for $\overline{u_i u_j u_\ell}$ reads:

$$\overline{u_i u_j u_\ell} = -\frac{1}{\frac{1}{C_{s1}\tau} + \frac{3\lambda\Phi}{\tau_p}} \left(\overline{u_i u_\ell} \frac{\partial \overline{u_j u_j}}{\partial x_\ell} + 2\overline{u_j u_\ell} \frac{\partial \overline{u_i u_j}}{\partial x_\ell} \right) + \frac{\frac{\lambda\Phi}{\tau_p}}{\frac{1}{C_{s1}\tau} + \frac{3\lambda\Phi}{\tau_p}} (\overline{v_i u_j u_\ell} + 2\overline{u_i u_j v_\ell}). \quad (3.8)$$

Implicit models for other third-order correlations are derived similarly. In the process of deriving the transport equations, $\overline{v_i u_j u_\ell}$ and $\overline{u_i v_j v_\ell}$ emerge as two new third-order correlations. The implicit models for these correlations are also derived analogously, leading to a system of six equations for six third-order correlations. The coupling between the two phases in these equations is explicitly exhibited by employing the nondimensional variables:

$$u_i^* = \frac{u_i}{U_0}, \quad v_i^* = \frac{v_i}{U_0}, \quad \theta = \frac{\tau_p}{\tau}, \quad x_i^* = \frac{x_i}{U_0\tau}, \quad (3.9)$$

where U_0 is a reference velocity. The final normalized form of the models is expressed as:

$$\overline{u_i^* u_j^* u_j^*} - \frac{\frac{\Phi_m}{\theta}}{\frac{1}{C_{s1}} + \frac{3\Phi_m}{\theta}} (\overline{v_i^* u_j^* u_j^*} + 2\overline{u_i^* u_j^* v_j^*}) = F_{uuu}^*, \quad (3.10)$$

$$\overline{v_i^* v_j^* v_j^*} - \frac{1}{3} (\overline{u_i^* v_j^* v_j^*} + 2\overline{v_i^* u_j^* v_j^*}) = F_{vvv}^*, \quad (3.11)$$

$$\overline{v_i^* u_j^* u_j^*} - \frac{\frac{1}{\theta}}{\frac{1}{C_{s2}} + \frac{1+2\Phi_m}{\theta}} (\overline{u_i^* u_j^* u_j^*} + 2\Phi_m \overline{v_i^* u_j^* v_j^*}) = F_{vuu}^*, \quad (3.12)$$

$$\overline{u_i^* v_j^* v_j^*} - \frac{\frac{1}{\theta}}{\frac{1}{C_{s3}} + \frac{2+\Phi_m}{\theta}} (2\overline{u_i^* u_j^* v_j^*} + \Phi_m \overline{v_i^* v_j^* v_j^*}) = F_{uvv}^*, \quad (3.13)$$

$$\overline{u_i^* u_j^* v_j^*} - \frac{\frac{1}{\theta}}{\frac{1}{C_{s4}} + \frac{1+2\Phi_m}{\theta}} (\overline{u_i^* u_j^* u_j^*} + \Phi_m \overline{v_i^* u_j^* v_j^*} + \Phi_m \overline{u_i^* v_j^* v_j^*}) = F_{uuv}^*, \quad (3.14)$$

$$\overline{v_i^* u_j^* v_j^*} - \frac{\frac{1}{\theta}}{\frac{1}{C_{s5}} + \frac{2+\Phi_m}{\theta}} (\overline{v_i^* u_j^* u_j^*} + \overline{u_i^* u_j^* v_j^*} + \Phi_m \overline{v_i^* v_j^* v_j^*}) = F_{vuv}^*, \quad (3.15)$$

where $\Phi_m = \lambda\Phi$, and

$$F_{uuu}^* = -\frac{1}{\frac{1}{C_{s1}} + \frac{3\Phi_m}{\theta}} \left(\overline{u_i^* u_\ell^*} \frac{\partial \overline{u_j^* u_j^*}}{\partial x_\ell^*} + 2\overline{u_j^* u_\ell^*} \frac{\partial \overline{u_i^* u_j^*}}{\partial x_\ell^*} \right), \quad (3.16)$$

$$F_{vvv}^* = -\frac{\theta}{3} \left(\overline{v_i^* v_\ell^*} \frac{\partial \overline{v_j^* v_j^*}}{\partial x_\ell^*} + 2\overline{v_j^* v_\ell^*} \frac{\partial \overline{v_i^* v_j^*}}{\partial x_\ell^*} \right), \quad (3.17)$$

$$F_{vuu}^* = -\frac{1}{\frac{1}{C_{s2}} + \frac{1+2\Phi_m}{\theta}} \left(\overline{v_i^* v_\ell^*} \frac{\partial \overline{u_j^* u_j^*}}{\partial x_\ell^*} + 2\overline{u_j^* u_\ell^*} \frac{\partial \overline{u_i^* v_j^*}}{\partial x_\ell^*} \right), \quad (3.18)$$

$$F_{uvv}^* = -\frac{1}{\frac{1}{C_{s3}} + \frac{2+\Phi_m}{\theta}} \left(\overline{u_i^* u_\ell^*} \frac{\partial \overline{v_j^* v_j^*}}{\partial x_\ell^*} + 2\overline{v_j^* v_\ell^*} \frac{\partial \overline{u_i^* v_j^*}}{\partial x_\ell^*} \right), \quad (3.19)$$

$$F_{uuv}^* = -\frac{1}{\frac{1}{C_{s4}} + \frac{1+2\Phi_m}{\theta}} \left(\overline{u_i^* u_\ell^*} \frac{\partial \overline{u_j^* v_j^*}}{\partial x_\ell^*} + \overline{u_j^* u_\ell^*} \frac{\partial \overline{u_i^* v_j^*}}{\partial x_\ell^*} + \overline{v_j^* v_\ell^*} \frac{\partial \overline{u_i^* u_j^*}}{\partial x_\ell^*} \right), \quad (3.20)$$

$$F_{vuv}^* = -\frac{1}{\frac{1}{C_{s5}} + \frac{2+\Phi_m}{\theta}} \left(\overline{v_i^* v_\ell^*} \frac{\partial \overline{u_j^* v_j^*}}{\partial x_\ell^*} + \overline{u_j^* u_\ell^*} \frac{\partial \overline{v_i^* v_j^*}}{\partial x_\ell^*} + \overline{v_j^* v_\ell^*} \frac{\partial \overline{v_i^* u_j^*}}{\partial x_\ell^*} \right). \quad (3.21)$$

While (3.10)-(3.15) can be solved in their general form to generate explicit models for the third-order correlations, the final form of the models are too lengthy for practical use. For the limit of small mass loading ratio ($\Phi_m \simeq 0$), however, (3.10)-(3.15) can be significantly simplified. In this limit, the explicit forms of the models are expressed as:

$$\overline{u_i^* u_j^* u_j^*} = F_{uuu0}^*, \quad (3.22)$$

$$\overline{v_i^* v_j^* v_k^*} = F_{vvv0}^* + \frac{2}{3} \frac{C_{s5}}{2C_{s5} + \theta} F_{vuu0}^* + \frac{1}{3} F_{uvv0}^* + \frac{2}{3} \left[\frac{C_{s3}}{2C_{s3} + \theta} + \frac{C_{s5}}{2C_{s5} + \theta} \right] F_{uuv0}^* + \frac{2}{3} F_{vuv0}^* \\ + \frac{2}{3} \left[\frac{C_{s2} C_{s5}}{(C_{s2} + \theta)(2C_{s5} + \theta)} + \frac{C_{s3} C_{s4}}{(2C_{s3} + \theta)(C_{s4} + \theta)} + \frac{C_{s4} C_{s5}}{(C_{s4} + \theta)(2C_{s5} + \theta)} \right] F_{uuu0}^*, \quad (3.23)$$

$$\overline{v_i^* u_j^* u_k^*} = F_{vuu0}^* + \frac{C_{s2}}{C_{s2} + \theta} F_{uuu0}^*, \quad (3.24)$$

$$\overline{u_i^* v_j^* v_k^*} = F_{uvv0}^* + \frac{2C_{s3} C_{s4}}{(2C_{s3} + \theta)(C_{s4} + \theta)} F_{uuu0}^* + \frac{2C_{s3}}{2C_{s3} + \theta} F_{uvv0}^*, \quad (3.25)$$

$$\overline{u_i^* u_j^* v_k^*} = F_{uuv0}^* + \frac{C_{s4}}{C_{s4} + \theta} F_{uuu0}^*, \quad (3.26)$$

$$\overline{v_i^* u_j^* v_k^*} = F_{vuv0}^* + \frac{C_{s5}}{2C_{s5} + \theta} \left[\left(\frac{C_{s2}}{C_{s2} + \theta} + \frac{C_{s4}}{C_{s4} + \theta} \right) F_{uuu0}^* + F_{vuu0}^* + F_{uvv0}^* \right], \quad (3.27)$$

where the subscript 0 indicates values of F^* 's for $\Phi_m = 0$. It is noted that the model given by (3.22) (for the carrier phase) is the same as that given in Hanjalić and Launder (1972) for single-phase flows.

4 Model implementation in homogeneous shear flow

In this section, the four-equation model is applied for description of a homogeneous turbulent shear flow. The simplicity of this flow configuration provides a suitable framework for model implementation. Furthermore, some recent data obtained by DNS are available and can be used for model parameterization and validations. In the homogeneous shear flow, the mean velocity gradient tensor is given by:

$$\frac{\partial W_i}{\partial x_j} = \begin{pmatrix} 0 & \frac{\partial W_1}{\partial x_2} \\ 0 & 0 \end{pmatrix}, \quad (4.1)$$

where, $W \equiv U$ for the carrier and $W \equiv V$ for the dispersed phase. It is emphasized again that although the mean flow is two-dimensional, the Reynolds stress tensors are three-dimensional. Based on our model results in §2.3, the explicit solutions for the Reynolds stresses of the two phases are expressed as:

$$\frac{\overline{w_1^2}}{k_\alpha} = -\frac{1}{6} G_1^\alpha - \frac{1}{2} G_3^\alpha \left(\frac{\partial W_1}{\partial x_2} \right)^2 + G_4^\alpha q_{11}^\alpha - \frac{1}{2} G_5^\alpha (q_{12}^\alpha + q_{21}^\alpha) \frac{\partial W_1}{\partial x_2} + \frac{2}{3}, \quad (4.2)$$

$$\frac{\overline{w_2^2}}{k_\alpha} = -\frac{1}{6}G_1^\alpha + \frac{1}{2}G_3^\alpha \left(\frac{\partial W_1}{\partial x_2} \right)^2 + G_4^\alpha q_{22}^\alpha + \frac{1}{2}G_5^\alpha (q_{12}^\alpha + q_{21}^\alpha) \frac{\partial W_1}{\partial x_2} + \frac{2}{3}, \quad (4.3)$$

$$\frac{\overline{w_3^2}}{k_\alpha} = \frac{1}{3}G_1^\alpha + G_4^\alpha q_{33}^\alpha + \frac{2}{3}, \quad (4.4)$$

$$\frac{\overline{w_1 w_2}}{k_\alpha} = \frac{\overline{w_2 w_1}}{k_\alpha} = \frac{1}{2}G_2^\alpha \frac{\partial W_1}{\partial x_2} + G_4^\alpha q_{12}^\alpha + \frac{1}{2}G_5^\alpha (q_{11}^\alpha - q_{22}^\alpha) \frac{\partial W_1}{\partial x_2}, \quad (4.5)$$

$$\overline{w_1 w_3} = \overline{w_2 w_3} = \overline{w_3 w_1} = \overline{w_3 w_2} = 0. \quad (4.6)$$

Equations (4.2)-(4.6) yield the carrier phase Reynolds stresses with $w \equiv u$, $\alpha \equiv f$, and the dispersed phase Reynolds stresses with $w \equiv v$, $\alpha \equiv p$. The implicit algebraic model for the fluid-particle velocity covariance is of the form:

$$\begin{aligned} \frac{\overline{u_1 v_1}}{k_{fp}} &= \frac{2}{\Delta_{fp}} \left\{ -\frac{2}{3} \left[\overline{u_1 v_2} \frac{\partial V_1}{\partial x_2} + (1 - C_{fp2}) \overline{u_2 v_1} \frac{\partial U_1}{\partial x_2} \right] + (1 - C_{fp3}) \frac{\lambda \Phi}{\tau_p} \left(\overline{v_1^2} - \frac{2}{3} k_p \right) \right. \\ &\quad \left. + \frac{1}{\tau_p} \left(\overline{u_1^2} - \frac{2}{3} k \right) - (1 - C_{fp3}) \frac{\lambda}{3\tau_p} [2(U_1 - V_1) \overline{v_1 \phi} - (U_2 - V_2) \overline{v_2 \phi}] \right\} + \frac{2}{3}, \end{aligned} \quad (4.7)$$

$$\begin{aligned} \frac{\overline{u_2 v_2}}{k_{fp}} &= \frac{2}{\Delta_{fp}} \left\{ \frac{1}{3} \left[\overline{u_1 v_2} \frac{\partial V_1}{\partial x_2} + (1 - C_{fp2}) \overline{u_2 v_1} \frac{\partial U_1}{\partial x_2} \right] + (1 - C_{fp3}) \frac{\lambda \Phi}{\tau_p} \left(\overline{v_2^2} - \frac{2}{3} k_p \right) \right. \\ &\quad \left. + \frac{1}{\tau_p} \left(\overline{u_2^2} - \frac{2}{3} k \right) - (1 - C_{fp3}) \frac{\lambda}{3\tau_p} [-(U_1 - V_1) \overline{v_1 \phi} + 2(U_2 - V_2) \overline{v_2 \phi}] \right\} + \frac{2}{3}, \end{aligned} \quad (4.8)$$

$$\begin{aligned} \frac{\overline{u_3 v_3}}{k_{fp}} &= \frac{2}{\Delta_{fp}} \left\{ \frac{1}{3} \left[\overline{u_1 v_2} \frac{\partial V_1}{\partial x_2} + (1 - C_{fp2}) \overline{u_2 v_1} \frac{\partial U_1}{\partial x_2} \right] + (1 - C_{fp3}) \frac{\lambda \Phi}{\tau_p} \left(\overline{v_3^2} - \frac{2}{3} k_p \right) \right. \\ &\quad \left. + \frac{1}{\tau_p} \left(\overline{u_3^2} - \frac{2}{3} k \right) - (1 - C_{fp3}) \frac{\lambda}{3\tau_p} [-(U_1 - V_1) \overline{v_1 \phi} - (U_2 - V_2) \overline{v_2 \phi}] \right\} + \frac{2}{3}, \end{aligned} \quad (4.9)$$

$$\begin{aligned} \frac{\overline{u_1 v_2}}{k_{fp}} &= \frac{2}{\Delta_{fp}} \left\{ -(1 - C_{fp2}) \overline{u_2 v_2} \frac{\partial U_1}{\partial x_2} + (1 - C_{fp3}) \frac{\lambda \Phi}{\tau_p} \overline{v_1 v_2} + \frac{1}{\tau_p} \overline{u_1 u_2} \right. \\ &\quad \left. - (1 - C_{fp3}) \frac{\lambda}{\tau_p} (U_1 - V_1) \overline{v_2 \phi} \right\}, \end{aligned} \quad (4.10)$$

$$\begin{aligned} \frac{\overline{u_2 v_1}}{k_{fp}} &= \frac{2}{\Delta_{fp}} \left\{ -\overline{u_2 v_2} \frac{\partial V_1}{\partial x_2} + (1 - C_{fp3}) \frac{\lambda \Phi}{\tau_p} \overline{v_1 v_2} + \frac{1}{\tau_p} \overline{u_1 u_2} \right. \\ &\quad \left. - (1 - C_{fp3}) \frac{\lambda}{\tau_p} (U_2 - V_2) \overline{v_1 \phi} \right\}, \end{aligned} \quad (4.11)$$

where

$$\Delta_{fp} = -\overline{u_m v_l} \frac{\partial V_m}{\partial x_l} - (1 - C_{fp2}) \overline{u_l v_m} \frac{\partial U_m}{\partial x_l} + \frac{2}{\tau_p} k + (1 - C_{fp3}) \frac{2\lambda \Phi}{\tau_p} k_p + (C_{fp3} - 1) \frac{\lambda}{\tau_p} (U_m - V_m) \overline{v_m \phi}. \quad (4.12)$$

It is noted that in homogeneous flows the turbulent transport terms are zero, therefore, there is no need to consider the models for the third-order correlations here. It is also straightforward to describe the transport equations for k , ϵ , k_p , and k_{fp} in the homogeneous flow configuration. These equations are not repeated here for brevity.

4.1 Comparison with DNS

The final four-equation model is appraised by comparative assessment via DNS results of Part I. A variety of cases have been considered for model validation. Here, we present comparisons between the model predictions and DNS results for three cases: C1 ($\tau_p = 0.016\text{s}$, $\Phi_m = 0$; one-way coupling), C3 ($\tau_p = 0.016\text{s}$, $\Phi_m = 0.25$), and C5 ($\tau_p = 0.032\text{s}$, $\Phi_m = 0.25$). For all of the cases $\lambda = 721.8$ and $S = \frac{\partial U_1}{\partial x_2} = \frac{\partial V_1}{\partial x_2} = 62.8\text{s}^{-1}$. The Reynolds stress tensors for both the carrier and the dispersed phases, as well as the fluid-particle velocity covariance tensor are generated from the DNS results and are used to appraise the model's performance. The evaluation of the void fraction fluxes, however, is not possible within the framework of homogeneous shear flow; this is done in §5.2 with the help of laboratory data. In the assessment of the model, the values of k , ϵ , k_p , and k_{fp} at $St = 3$ are taken from DNS as initial values. This time is chosen as the initial time for model assessment in order to allow the flow and the particles to reach a dynamic equilibrium, while the turbulence becomes well-developed and falls in the growth region. The magnitudes of the empirical constants C_{f3} , C_{fp1} , C_{fp2} , and C_{fp3} are determined by analyzing the DNS data. Details of procedure for determination of these constants are given in Part I; the final optimized values are listed in table 1.

First, we consider the case with one-way coupling ($\Phi_m = 0$) for $\tau_p = 0.016\text{s}$. The model predictions (lines) are compared with DNS results (symbols) in Fig. 1 for all of the Reynolds stress components. Some deviations are observed in the streamwise component but other components are in reasonably good agreement. The solution of the Reynolds stress equations (Mashayek *et al.*, 1997) has indicated that the deviations in the streamwise component originate from the model used for the fluid pressure strain correlation in single-phase flow – for single-phase flows, this model is the same as the LRR model. The effects of two-way coupling at $\Phi_m = 0.25$ are portrayed in Figs. 2 and 3 for $\tau_p = 0.016\text{s}$ and $\tau_p = 0.032\text{s}$, respectively.

Again the agreement between the model predictions and DNS results is promising. It is worth noting that the shear components which are of primary importance (in calculating the mean variables) are predicted very closely to DNS data. It is also important to note that the model is capable of predicting the antisymmetry of the shear components of the fluid-particle velocity covariance tensor. The model predictions for the dissipation rate of the fluid turbulent kinetic energy are compared with DNS results in Fig. 4 for all of the cases. The figure shows that the model predictions are in fair agreement with DNS results and that the model is capable of capturing the trends of variations of the dissipation rate with the particle time constant and the mass loading ratio.

5 Model implementation for thin shear flows

With the manipulation of the algebraic models presented in §§2 and 3, the four-equation model is simplified for thin shear flows. The model is then assessed via comparison with laboratory data of an axisymmetric two-phase turbulent jet. Due to large variations of time scales in these flows, a modification of the algebraic models is necessary (Taulbee, 1992). Equation (2.14), for the fluid Reynolds stress, is valid in the asymptotic limit given by (2.12) which requires that the time scales ratio, defined as the turbulent time scale τ divided by the mean flow time scale $(S_{kl}S_{kl})^{-1/2}$ is large. However, there are situations in the flow field, mostly due to boundary conditions, when this condition is not met. To rectify this situation, Taulbee (1992) modified the formulation so that the result is valid for very small as well as relatively large values of the time scale parameter. This requires that the term $\dot{\tau} = \frac{d(k/\epsilon)}{dt} = \frac{\tau}{k} \frac{dk}{dt} - \frac{\tau}{\epsilon} \frac{d\epsilon}{dt}$ to be added to the coefficient on the LHS of (2.14). The implementation of this modification is straightforward in single phase flows. However, in particle-laden flows it is not clear how to modify the other transport equations since only the carrier fluid dissipation is considered. Therefore, this correction is applied to each equation; by assuming that the small time scale behavior of that quantity is similar to that of the fluid. For the particle Reynolds stress and the fluid-particle covariance, we simply add $\dot{\tau}$ to the coefficient on the LHS. For the void fraction fluxes, $C_{\phi p}\dot{\tau}$ is added where $C_{\phi p}$ is a constant.

In parabolic flows, the streamwise (axial) gradients of the transport parameters are assumed

negligible in comparison to their gradients in the cross stream (radial) direction. In the computations, the algebraic models in the form given in §2 can be used directly. However, it is more convenient to express the final closures via equivalent eddy diffusivities. These diffusivities have the additional advantage of exhibiting the coupling between the phases in an explicit manner.

The diffusivity pertaining to the fluid shear stress is determined by recognizing that from (4.5):

$$\overline{u_1 u_2} = k G_4^f q_{12}^f + \frac{k}{2} [G_2^f + G_5^f (q_{11}^f - q_{22}^f)] \frac{\partial U_1}{\partial x_2}. \quad (5.1)$$

From (2.30) and (B.2), it is recognized that:

$$G_4^f = \frac{1}{\Delta_f} \left[1 + \frac{1}{\Delta_f^2} \left(\frac{1+14C_{f2}}{3} \right)^2 \left(\frac{\partial U_1}{\partial x_2} \right)^2 \right]^{-1},$$

$$q_{12}^f = -\frac{4}{15} \frac{\partial U_1}{\partial x_2} + (1 - C_{f3}) \frac{\lambda \Phi}{k \tau_p} (\overline{u_1 v_2} + \overline{u_2 v_1}) - \frac{7}{10} \frac{\lambda}{k \tau_p} [(U_1 - V_1) \overline{u_2 \phi} + (U_2 - V_2) \overline{u_1 \phi}]. \quad (5.2)$$

Substituting these relations into (4.5) provides:

$$\begin{aligned} \overline{u_1 u_2} &= -C_\mu \tau k \frac{\partial U_1}{\partial x_2} + k G_4^f \left\{ (1 - C_{f3}) \frac{\lambda \Phi}{k \tau_p} (\overline{u_1 v_2} + \overline{u_2 v_1}) \right. \\ &\quad \left. - \frac{7}{10} \frac{\lambda}{k \tau_p} [(U_1 - V_1) \overline{u_2 \phi} + (U_2 - V_2) \overline{u_1 \phi}] \right\}, \end{aligned} \quad (5.3)$$

where

$$C_\mu = \frac{\frac{4}{15}}{\tau \Delta_{f1} + \tau \Delta_{f2} + \frac{\tau}{\Delta_{f1} + \Delta_{f2}} \left(\frac{1+14C_{f2}}{3} \right)^2 \left(\frac{\partial U_1}{\partial x_2} \right)^2} - \frac{1}{2\tau} [G_2^f + G_5^f (q_{11}^f - q_{22}^f)]. \quad (5.4)$$

In this relation, $\Delta_{f1} = \frac{1}{\tau} \left(C_{f1} + \frac{p_f}{\epsilon} - 1 + \dot{\tau} \right)$ and $\Delta_{f2} = \frac{1}{\tau} \left[-\frac{D_f}{\epsilon} + 2(1 - C_{f3}) \frac{\lambda \Phi \tau}{\tau_p} \right]$ portray the contributions from the carrier fluid and the particles, respectively. Equation (5.3) shows the coupling effects between the phases and reduces to the algebraic model for a single-phase flow when $\lambda = 0$. Some of previous models, e.g. by Elghobashi and Abou-Arab (1983); Chen and Wood (1986); Zhao (1993) consider only the first term in (5.3) with C_μ the same as in the single-phase $k-\epsilon$ model. This implies that the modifications of the carrier phase shear stress is modeled only through the changes in k and ϵ . However, our model presented

by (5.3) indicates that in addition to “direct” modifications through C_μ , the carrier phase shear stress includes other terms which are due to the presence of particles.

Following a similar procedure, the dispersed phase shear stress is expressed by:

$$\overline{v_1 v_2} = -C_\mu^p \tau k_p \frac{\partial V_1}{\partial x_2} + \frac{G_4^p}{\tau_p} (\overline{u_1 v_2} + \overline{u_2 v_1}), \quad (5.5)$$

where,

$$C_\mu^p = \frac{\frac{2}{3}}{\tau \Delta_p + \frac{\tau}{\Delta_p} \left(\frac{\partial V_1}{\partial x_2} \right)^2} - \frac{1}{2\tau} [G_2^p + G_5^p (q_{11}^p - q_{22}^p)], \quad (5.6)$$

with $\Delta_p = \frac{p p}{k_p} + \frac{2k_f p}{\tau_p k_p} + \frac{\dot{\tau}}{\tau}$. The relative importance of the terms in (5.5) depends on the magnitude of the gradient of the mean velocity. For instance, in the experiments of Shuen *et al.* (1985), the dispersed phase shows a very steep mean velocity profile (especially near the jet centerline); and the term $\frac{1}{2} k_p G_2^p \frac{\partial V_1}{\partial x_2}$ becomes of the same order of magnitude as $-C_\mu^p \tau k_p \frac{\partial V_1}{\partial x_2}$. In the model implementation, the first term on the RHS of (5.3) and the first term on the RHS of (5.5) are used for eddy viscosities, and the remaining terms are treated as source terms in the axial momentum equations.

Of significant importance in the solution of the dispersed phase variables are the fluxes of the void fraction. In most cases, these fluxes are modeled in a format analogous to modeling of scalar fluxes (e.g. Elghobashi and Abou-Arab (1983)). Considering the differences between the basic transport equations governing the void fraction and a scalar, it is not expected for this analogy to yield accurate predictions. With the explicit models for the void fraction fluxes ((2.19)-(2.20)), it is possible to provide relations for the corresponding eddy diffusivities. For example, consider the radial flux of the void fraction ($\overline{v_2 \phi}$). With the thin shear layer assumption, the algebraic model for this flux is approximated as:

$$\overline{v_2 \phi} \simeq \frac{-1}{1 - B^f B^p} \left[\frac{\overline{v_2^2}}{\Delta_{\phi p} \partial x_2} \frac{\partial \Phi}{\partial x_2} + \frac{\overline{u_2 v_2}}{\tau_p \Delta_{\phi f} \Delta_{\phi p}} \frac{\partial \Phi}{\partial x_2} + \frac{(1 - C_{\phi 2}) \lambda}{\tau_p^2 \Delta_{\phi f} \Delta_{\phi p}} (U_2 - V_2) \overline{\phi^2} \right]. \quad (5.7)$$

where $\Delta_{\phi f} = \frac{1}{2k} (\mathcal{P}^f - \epsilon - \mathcal{D}^f) + \frac{1}{\phi^2} (\mathcal{P}^\phi - \epsilon^\phi) + \frac{C_{\phi 1}}{\tau} + C_{\phi p} \frac{\dot{\tau}}{\tau} + (1 - C_{\phi 3}) \frac{\lambda \Phi}{\tau_p} + \frac{\epsilon}{k_p} S_{ll}^p$, $\Delta_{\phi p} = \frac{1}{2k_p} (\mathcal{P}^p - \mathcal{D}^p) + \frac{1}{\phi^2} (\mathcal{P}^\phi - \epsilon^\phi) + \frac{1}{\tau_p} + C_{\phi p} \frac{\dot{\tau}}{\tau} + \frac{\epsilon}{k_p} S_{ll}^p$, and expressions for B^f and B^p are provided in Appendix B. Since $\Delta_{\phi f}$ can take large values, the second and the third terms on the RHS

of (5.7) are small compared to the first term. Thus:

$$\overline{v_2\phi} \simeq -\nu_t^\phi \frac{\partial \Phi}{\partial x_2}, \quad \nu_t^\phi = \frac{\frac{\overline{v_2^2}}{\Delta_{\phi p}}}{1 - (C_{\phi f 3} + 1) \frac{\lambda \Phi}{\tau_p^2 \Delta_{\phi f} \Delta_{\phi p}}}. \quad (5.8)$$

The results of primary calculations of the axisymmetric jet flow (discussed below) indicates that the denominator of the second of (5.8) is very close to unity; thus: $\nu_t^\phi = \frac{\overline{v_2^2}}{\Delta_{\phi p}}$. This should be compared with conventional gradient diffusion closures $\nu_t^\phi = \frac{\nu_t^p}{\sigma_\phi}$ ($\sigma_\phi = 1.3$).

The complete set of equations describing the four-equation (k - ϵ - k_p - k_{fp}) model is presented in Appendix C for axisymmetric thin shear flows. To close this set, additional relations are needed for $\overline{\phi^2}$, \mathcal{P}^ϕ and \mathcal{D}^ϕ . It is possible to solve a modeled transport equation for $\overline{\phi^2}$. But none of the available experiments (including the one considered here as will be discussed below) report the measurements of $\overline{\phi^2}$, and there is no rational way of estimating the initial conditions of this variance for subsequent calculations. Due to these uncertainties, and also noting that the contribution of this quantity to $\overline{v_2\phi}$ is negligible (based on an order of magnitude estimation), the transport equation for $\overline{\phi^2}$ is not considered. Furthermore, it is noted that $\overline{\phi^2}$ is always accompanied by the coefficient $1 - C_{\phi 2}$; therefore if $C_{\phi 2} \approx 1$ the term $\overline{\phi^2}$ is effectively eliminated. A more detailed investigation on the significance of this term requires reliable experimental data.

The term $\frac{1}{\sigma^2}(\mathcal{P}^\phi - \mathcal{D}^\phi)$, in (B.11)-(B.12) is modeled by assuming that the time scale of the void fraction is proportional to that of the dispersed phase:

$$C_{\phi\phi} = \frac{k_p/\mathcal{D}^p}{\overline{\phi^2}/\mathcal{D}^\phi}, \quad (5.9)$$

where $C_{\phi\phi}$ is another empirical constant. It is also assumed that $\frac{\mathcal{P}^\phi}{\mathcal{D}^\phi} = \frac{\mathcal{P}^p}{\mathcal{D}^p}$ which together with (5.9) yields:

$$\frac{1}{\overline{\phi^2}}(\mathcal{P}^\phi - \mathcal{D}^\phi) = \frac{C_{\phi\phi}}{k_p}(\mathcal{P}^p - \mathcal{D}^p). \quad (5.10)$$

5.1 Explicit forms of the third-order correlations

The implicit models for the third-order velocity correlations as derived in §3.1 are manipulated here to extract convenient gradient type models for parabolic flows. The functions F^* 's in (3.16)-(3.21) are significantly simplified for parabolic flows since only one shear stress component and one normal stress component remain in the formulations. Furthermore, the contribution from the shear stress component to F^* 's always involve the product of this stress by its derivative. Due to particular profile of the shear stress in the radial direction, these products are small; therefore, the contributions from the shear stresses can be neglected.

The simplifications in F^* 's for parabolic flows, however, do not reduce the level of complexity of the explicit solution in its general form. To make the models "practical", a parametric study is considered. For that, we use the isotropic relations: $\overline{u_2^* u_2^*} = \frac{2}{3} k^*$, $\overline{v_2^* v_2^*} = \frac{2}{3} k_p^*$, and $\overline{u_2^* v_2^*} = \frac{2}{3} k_{fp}^*$ to reduce the number of parameters. Therefore,

$$F_{uuu}^* = -\frac{1}{\frac{1}{C_{s1}} + \frac{3\Phi_m}{\theta}} \frac{20}{9} k^* \frac{\partial k^*}{\partial x_2^*}, \quad (5.11)$$

$$F_{vvv}^* = -\frac{20}{27} \theta k_p^* \frac{\partial k_p^*}{\partial x_2^*}, \quad (5.12)$$

$$F_{vuu}^* = -\frac{1}{\frac{1}{C_{s2}} + \frac{1+2\Phi_m}{\theta}} \left(\frac{4}{3} k_p^* \frac{\partial k^*}{\partial x_2^*} + \frac{8}{9} k^* \frac{\partial k_{fp}^*}{\partial x_2^*} \right), \quad (5.13)$$

$$F_{uvv}^* = -\frac{1}{\frac{1}{C_{s3}} + \frac{2+\Phi_m}{\theta}} \left(\frac{4}{3} k^* \frac{\partial k_p^*}{\partial x_2^*} + \frac{8}{9} k_p^* \frac{\partial k_{fp}^*}{\partial x_2^*} \right), \quad (5.14)$$

$$F_{uuv}^* = -\frac{1}{\frac{1}{C_{s4}} + \frac{1+2\Phi_m}{\theta}} \left(\frac{16}{9} k^* \frac{\partial k_{fp}^*}{\partial x_2^*} + \frac{4}{9} k_p^* \frac{\partial k^*}{\partial x_2^*} \right), \quad (5.15)$$

$$F_{vvu}^* = -\frac{1}{\frac{1}{C_{s5}} + \frac{2+\Phi_m}{\theta}} \left(\frac{16}{9} k_p^* \frac{\partial k_{fp}^*}{\partial x_2^*} + \frac{4}{9} k^* \frac{\partial k_p^*}{\partial x_2^*} \right). \quad (5.16)$$

Furthermore, we express k_p^* and k_{fp}^* in terms of k^* : $k_p^* = \kappa k^*$ and $k_{fp}^* = C_{fp4} \sqrt{k^* k_p^*}$, where κ is a new parameter and $C_{fp4} = 0.8$ is taken from DNS results. We also use $C_{s1} = C_{s2} = \dots = C_{s5} = C_s = 0.08$ (Hanjalić and Launder, 1972). It must be emphasized that since we are only comparing the relative magnitudes of the third-order correlations, the specific values used for C_{fp4} and C_s are not very important. The final set of significant parameters includes: the mass loading ratio (Φ_m), the time scale ratio (θ), and the kinetic energy ratio (κ).

Figures 5 and 6 show the variations of all of the third-order velocity correlations with Φ_m for different values of θ at $\kappa = 1$ and $\kappa = 0.1$, respectively. It is observed that $\overline{v_2^* v_j^* v_j^*}$ is the most sensitive to the variations of the kinetic energy ratio. On the contrary, this correlation appears rather independent of the mass loading ratio. This suggests that the dispersed phase third-order velocity correlation can be reasonably described by (3.23). The other correlations depend on the mass loading ratio, specially for small values of the time scale ratio. However, as the ratio of the kinetic energies is increased, these correlations become more independent of the mass loading ratio. Therefore, for large values of the particle turbulent kinetic energy (as compared to the fluid turbulent kinetic energy) the third-order correlations comply with the explicit forms given in (3.22)-(3.27) for $\Phi_m \simeq 0$.

As mentioned earlier, in model implementation, it is very desirable to express the third-order velocity correlations in simple gradient forms. A simple way to produce such gradient type models for each third-order correlation, is to neglect the contribution from other correlations, that is, to express each correlation in terms of its own F^* only, i.e.

$$\begin{aligned} \overline{u_2^* u_j^* u_j^*} &\simeq F_{uuu}^*, & \overline{v_2^* v_j^* v_j^*} &\simeq F_{vvv}^*, & \overline{v_2^* u_j^* u_j^*} &\simeq F_{vuu}^*, \\ \overline{u_2^* v_j^* v_j^*} &\simeq F_{uvv}^*, & \overline{u_2^* u_j^* v_j^*} &\simeq F_{uuv}^*, & \overline{v_2^* u_j^* v_j^*} &\simeq F_{vuv}^*. \end{aligned} \quad (5.17)$$

In order to find the range of variations of Φ_m , θ , and κ within which the above assumption results in reasonable approximations for the third order correlations, we consider the relative error parameter χ . This parameter is defined based on the values of the third-order velocity correlations calculated using (5.17) and those calculated from the full solution of (3.10)-(3.21):

$$\chi = \frac{\text{correlation value by full solution} - \text{correlation value by (5.17)}}{\text{correlation value by full solution}} \times 100.$$

The variations of the parameter χ for wide ranges of Φ_m and θ values are shown in Figs. 7 and 8 for $\kappa = 1$ and $\kappa = 0.1$, respectively. It is concluded from these figures that for $\Phi_m < 0.4$, $\theta > 1$, and $\kappa > 1$ the relative error is less than 20 percent. Therefore, for $\Phi_m < 0.4$, $\tau_p > \tau$,

and $k_p > k$, the third-order correlations may be approximated as:

$$\overline{u_2 k'} = -\frac{1}{\frac{1}{C_{s1}\tau} + \frac{3\Phi_m}{\tau_p}} \left(\overline{u_2 u_2} \frac{\partial k}{\partial x_2} + \overline{u_2 u_2} \frac{\partial \overline{u_2 u_2}}{\partial x_2} \right), \quad (5.18)$$

$$\overline{v_2 k'_p} = -\frac{\tau_p}{3} \left(\overline{v_2 v_2} \frac{\partial k_p}{\partial x_2} + \overline{v_2 v_2} \frac{\partial \overline{v_2 v_2}}{\partial x_2} \right), \quad (5.19)$$

$$\begin{aligned} \overline{u_2 k'_{fp}} + \overline{v_2 k'_{fp}} &= -\frac{1}{\frac{1}{C_{s4}\tau} + \frac{1+2\Phi_m}{\tau_p}} \left(\overline{u_2 u_2} \frac{\partial k_{fp}}{\partial x_2} + \frac{1}{2} \overline{u_2 u_2} \frac{\partial \overline{u_2 v_2}}{\partial x_2} + \frac{1}{2} \overline{v_2 v_2} \frac{\partial \overline{u_2 u_2}}{\partial x_2} \right) \\ &\quad - \frac{1}{\frac{1}{C_{s5}\tau} + \frac{2+\Phi_m}{\tau_p}} \left(\overline{v_2 v_2} \frac{\partial k_{fp}}{\partial x_2} + \frac{1}{2} \overline{u_2 u_2} \frac{\partial \overline{v_2 v_2}}{\partial x_2} + \frac{1}{2} \overline{v_2 v_2} \frac{\partial \overline{u_2 v_2}}{\partial x_2} \right). \end{aligned} \quad (5.20)$$

For dilute particle-laden flows, the ratio $\frac{\Phi_m}{\theta}$ is usually small. This is particularly true if the particles are large or the density ratio is high. In this case (by using the isotropic relations), the third-order velocity correlations may be further simplified to:

$$\overline{u_2 k'} = -\frac{10}{9} C_s \tau k \frac{\partial k}{\partial x_2}, \quad (5.21)$$

$$\overline{u_2 \epsilon'} = -0.5 C_\epsilon \tau k \frac{\partial \epsilon}{\partial x_2}, \quad (5.22)$$

$$\overline{v_2 k'_p} = -\frac{10}{27} \tau_p k_p \frac{\partial k_p}{\partial x_2}, \quad (5.23)$$

$$\overline{u_2 k'_{fp}} + \overline{v_2 k'_{fp}} = -\frac{8}{9} C_s \tau (k + k_p) \frac{\partial k_{fp}}{\partial x_2} - \frac{2}{9} C_s \tau \left(k_p \frac{\partial k}{\partial x_2} + k \frac{\partial k_p}{\partial x_2} \right), \quad (5.24)$$

where C_s and C_ϵ are empirical constants with the values given in table 1. Equation (5.22) provides a model for the correlation $\overline{u_i \epsilon'}$ appearing in the transport equation for the rate of dissipation of the carrier phase turbulent kinetic energy. This model is the same as that used in single-phase flows (Hanjalić and Launder, 1972). The use of this model for two-phase flows (within the parameter range described above) is expected to provide reasonable accuracy as the model (5.21) proposed for the fluid turbulent kinetic energy is also reduced to that in single-phase flows.

5.2 Comparison with laboratory data

The proposed four-equation model is now applied for the prediction of the flow configuration considered in the experiment of Shuen *et al.* (1985). In this experiment, comprehensive data are available of an axisymmetric turbulent jet flow laden with monosize particles. The jet is directed vertically downward with an inside diameter of $d = 10.9\text{mm}$. Air is used as the carrier fluid and the velocity at the nozzle exit is 26.1m/s . Sand particles with a Sauter mean diameter 79μ and a density of 2620kg/m^3 are fed into the jet with a mass loading ratio of 0.2 at the nozzle exit. Uncertainties up to 10% for the carrier gas, and 15% for particles are reported in the measured profiles of the mean and fluctuating velocities. The measured results for cross-stream variations of statistical quantities are reported at streamwise stations $x_1/d = 20$ and $x_1/d = 40$. In the calculations, the data at $x_1/d = 20$ are used as "initial conditions" and the predicted results are compared with the experimental data at $x_1/d = 40$. The initial dissipation rate of the carrier phase kinetic energy is determined from the measured mean axial velocity and shear stress using the shear stress model. The mean void fraction is calculated from the dispersed phase mass flux, and the mean velocity distribution. The initial values for k_{fp} is obtained from the turbulent kinetic energies of the two phases using $k_{fp} = C_{fp4}\sqrt{kk_p}$ with $C_{fp4} = 0.55$.

The numerical algorithm used in the solution of the model equations is based on a first order upwind differencing for the convection terms and a second order accurate central differencing scheme for all the other terms. Table 1 provides the values of the empirical constants as used in the $k-\epsilon-k_p-k_{fp}$ model. The values of $C_{\epsilon 1}$, $C_{\epsilon 2}$, and $C_{\epsilon 4}$ are the same as those used in single phase flow predictions. The values of $C_{\phi 1}$, $C_{\phi 2}$, $C_{\phi 3}$, $C_{\phi p}$, and $C_{\phi \phi}$ are obtained through comparisons with the results in this experiment. The other constants are the same as those determined in Part I.

The final model predicted results are compared with data from the experiment of Shuen *et al.* (1985). The profiles of the mean axial velocities and the mean void fraction are presented in Fig. 9. While the agreement for the mean velocity of the carrier gas and the mean void fraction is reasonable, the dispersed phase axial velocity shows some deviations from the experimental results near the jet centerline. However, the streamwise variations of the predicted results for the centerline values of the mean axial velocities in both phases

and the mean void fraction are in good agreement with data (Fig. 10). Notice that, due to gravity, the mean particle axial velocity has nonzero values for large x_2 . The profiles of the kinetic energies (Fig. 11) and the shear stress of the carrier gas (Fig. 12) are in accord with laboratory data. However, similar to the behavior portrayed in Fig. 11(a), the predicted normal stresses (Fig. 13) deviate from the laboratory results near the centerline. This deviation is partly attributed to the neglect of the diagonal terms in the strain rate tensor. With this assumption, the model predicts an isotropic Reynolds stress tensor at the centerline where $\frac{\partial U_1}{\partial x_2} = 0$.

A comment is in order here in regard to the so-called Hinze-Tchen relation (Chen and Wood, 1986; Zhou, 1993; Zhao, 1993) used for modeling of the dispersed phase turbulent viscosity:

$$\frac{\nu_t^p}{\nu_t} = \left(\frac{k_p}{k} \right)^{0.5} = \frac{1}{1 + \frac{\tau_p}{\tau_e}}. \quad (5.25)$$

Here τ_e is a turbulence time scale which is typically modeled as $\tau_e = C_T \frac{k}{\epsilon}$, with different suggested values for the empirical constant C_T (Chen and Wood, 1986; Mostafa and Elghobashi, 1986; Sargianos *et al.*, 1990; Zhou, 1993). Here, we consider $C_T = 0.2$. In tables 2 and 3, we compare the predictions of the Hinze-Tchen relation (5.25) for the ratio of the kinetic energies with those measured in DNS and experiment, respectively. According to tables 2 and 3, large deviations are observed between the model predictions and the data; the extent of deviation from the laboratory data is much more significant. This deviation is due to the fundamental model assumption in that the solid particle does not change its neighboring fluid element throughout its course of motion. This assumption would be valid only if the particle time constant is small compared to the fluid time scale (i.e. small Stokes numbers) so that the particle responds to the flow fluctuations promptly. The ratio $\frac{\tau_p}{\tau_e}$ is in the range 0.5 to 1.5 in DNS, and in the range 20 to 30 in the experiment (at $x_1/d = 20$). Obviously, particles with such large Stokes numbers are not capable of adjusting to rapid changes in shear flows, thus the basic assumptions made in the derivation of the model cannot be justified. Based on these comparative assessments, it is obvious that the use of Hinze-Tchen relation, as typically used for modeling of the particle turbulent kinetic energy and/or the eddy diffusivity, can lead to significant errors. The explicit algebraic model developed here alleviates many of the drawbacks of previous closures including the Hinze-Tchen relation.

Finally, the use of the Stokesian drag can, understandably, raise some doubts when the algebraic models are used in high Reynolds number two-phase flows. In general, for high particle Reynolds numbers (Re_p , defined based on the particle diameter, the fluid viscosity, and the particle-fluid relative velocity) an empirical correction factor is multiplied by the Stokes' drag relation. The correction factor is described as a function of the particle Reynolds number ($f(Re_p)$) (Clift *et al.*, 1978) and in statistical models it is evaluated using a particle Reynolds number based on the relative "mean" velocity. This approach results (in essence) in a modified particle time constant which is described as $\tau_p^* = \frac{\tau_p}{f(Re_p)}$. The implementation of the modified particle time constant in the present model is straightforward. A typical calculation with τ_p^* based on $f(Re_p) = 1 + 0.15Re_p^{0.687}$ in the axisymmetric jet indicated small, although noticeable, changes in the results.

6 Summary and concluding remarks

The primary objective of this work is to expand upon the capabilities of algebraic turbulence models, as previously developed in single-phase flows, for predictive analysis of two-phase turbulent transport. More specifically, the essential goal is to provide models which are "simple" to use and yet are more "effective" than currently available closures. To achieve this goal, several simplifying assumptions are made in regard to both the structure of the flow and the equations governing its transport. In this section, a summary is provided of the procedures leading to the final results with a critical assessment of the assumptions invoked. Some directions for future related work are also suggested.

We consider dilute, mono-dispersed particle-laden turbulent flows. The "differential" transport equations for each of the two phases, as developed in Part I (Mashayek *et al.*, 1997), are considered in the Eulerian frame for the ensemble-means and several of the pertinent second-order moments of the transport parameters. There are several terms in these equations which are modeled in a fashion analogous to single-phase flows, but introduce empirical constants which need to be determined. The final differential equations are reduced to "implicit algebraic" equations by making two assumptions, again analogous to those in single-phase flows. In the context considered, the implicit coupled algebraic relations govern the fol-

lowing second-order moments: the Reynolds stresses in both the carrier and the dispersed phases, the fluxes of the void fraction due to both the carrier and dispersed phase velocities, and the fluid-particle velocity covariance. For flows with two-dimensional mean transport (but three-dimensional turbulent motion), the implicit relations are manipulated further via a liberal use of the *Cayley-Hamilton* theorem. This leads to “explicit” algebraic solution for all of the above moments except the fluid-particle velocity covariance, the relation for which is left in an implicit manner. The final algebraic relations provide useful constitutive relations for the Reynolds stresses and the void fraction fluxes which manifest the effects of the two-way coupling between the two phases in an explicit manner. These relations are presented in the form of eddy diffusivities which are very convenient for application in standard computational methodologies. In this form the model is applied to a particle-laden homogeneous shear flow for which recent DNS data are available. These data are used for both determining the magnitudes of some of the empirical constants appearing in the closures, and for appraising the performance of the model. The algebraic models are further manipulated and a four-equation model ($k-\epsilon-k_p-k_{fp}$) is proposed for prediction of parabolic two-phase turbulent shear flows. This model augmented by algebraic relations for the trace of the fluid-particle velocity covariance tensor and the variance of the void fraction is applied to an axisymmetric particle laden turbulent jet. The predicted results are compared with available laboratory data. While these data are used to determine the magnitudes of some of the empirical constants, the overall agreement between the predictions and data is encouraging.

As was the case in Part I, a very important feature of model is that the effects of the two-way coupling are captured. Contrary to most previous models which are based on *ad hoc* modifications of the single-phase turbulence closures, the models here clearly indicate how the Reynolds stresses and the void fraction fluxes of each phase are modified by the presence of the other phase. Therefore, it is not surprising that the overall behavior of the model is significantly better than most of the currently available algebraic models, such as the Hinze-Tchen relation.

Similar to all modeling strategies, assumptions are necessary and are made at different stages in the process of developing algebraic models and in their applications. Some of these assumptions are “essential” without which it would be impossible to develop algebraic

closures. An example is the equilibrium assumption as represented by (4.2). Some of the other assumptions made here, however, can be relaxed. These are discussed below.

The derivation leading to explicit algebraic relations as outlined in §2.4 is possible by treating the fluid-particle covariance in an implicit manner. Inclusion of this covariance in the explicit formulation is possible. But the form of the solution, even if it can be generated (via CHT or other means), is expected to be complicated. The same goes for extending the methodology for treating three-dimensional mean flows. Due to the nature of three-dimensional flows, a much larger number of matrix polynomials (and a wider integrity basis) is required. For instance, in single-phase flows the three-dimensional solution is achieved with 10 matrix polynomials as compared to 3 matrix polynomials in the two-dimensional solution (Pope, 1975). Based on our previous experience, we suggest to extend in the line of Taulbee's (1992) approach. In this approach, the implicit algebraic equations are first simplified using an order of magnitude analysis. This analysis is based on the values of the empirical constants which are rather well-established in single-phase flows. Therefore, before any step is taken toward the extension of such analysis to two-phase flows, it would be necessary to build a reliable data base for particle-laden flows. This data base must include a variety of flow configurations in order to help in evaluating the empirical constants.

In the implementation of the four-equation model, the variance of the void fraction fluctuations ($\overline{\phi^2}$) is modeled here in a somewhat "naive" manner. It is straightforward to evaluate this parameter from its own transport equation; thus suggesting a "five-equation" model. This was not followed here because of the lack of proper laboratory data. Such "sophistication" is justified in future when proper laboratory data become available. The same is true of the TOC terms in (2.1), (2.3), and (2.5). Development of turbulence models for these correlation and their laboratory measurements are recommended. With a reliable model, the inclusion of these correlations in the algebraic formulation is not expected to be difficult.

Finally, it is re-emphasized that all the turbulence models presented here are based on basic Eulerian transport equations of multi-phase flow augmented with empirical relations for the phase interactions. No attempt is made here to consider different scenarios with inclusions of a wide variety of interphase transport models. It is expected that the operational means of model development as outlined here would remain the same with such considerations.

Acknowledgments

This work is sponsored by the Office of Naval Research under Grant N00014-94-10667.

Appendix A

Implicit algebraic equations for the dispersed phase Reynolds stress, the void fraction fluxes, and the fluid-particle covariance are derived in a manner similar to those for the fluid Reynolds stress. The final form of these equations are expressed as:

Dispersed phase Reynolds stress:

$$\begin{aligned} \left(\frac{\mathcal{P}^p}{k_p} + \frac{2}{\tau_p} \frac{k_{fp}}{k_p} \right) a_{ij}^p &= -\frac{4}{3} \frac{\epsilon}{k_p} \left(S_{ij}^p - \frac{1}{3} S_{ll}^p \delta_{ij} \right) - \frac{\epsilon}{k_p} \left(S_{il}^p a_{lj}^p + S_{jl}^p a_{li}^p - \frac{2}{3} S_{kl}^p a_{lk}^p \delta_{ij} \right) \\ &\quad - \frac{\epsilon}{k_p} (\omega_{il}^p a_{lj}^p + \omega_{jl}^p a_{li}^p) + \frac{1}{\tau_p} \frac{k_{fp}}{k_p} (a_{ij}^{fp} + a_{ji}^{fp}), \end{aligned} \quad (\text{A.1})$$

Carrier phase void fraction flux:

$$\begin{aligned} \left[\frac{1}{2k} (\mathcal{P}^f - \epsilon - \mathcal{D}^f) + \frac{1}{\bar{\phi}^2} (\mathcal{P}^\phi - \epsilon^\phi) + \frac{C_{\phi 1}}{\tau} + (1 - C_{\phi 3}) \frac{\lambda \Phi}{\tau_p} + \frac{\epsilon}{k_p} S_{ll}^p \right] \varphi_i^f &= \\ - \frac{1}{5} \frac{\epsilon}{k} S_{il}^f \varphi_l^f + (1 - C_{\phi 3}) \frac{\lambda \Phi}{\tau_p} \varphi_i^p &- \bar{u}_i \bar{v}_l \frac{\partial \Phi}{\partial x_l} + (C_{\phi 2} - 1) \frac{\lambda}{\tau_p} (U_i - V_i) \bar{\phi}^2, \end{aligned} \quad (\text{A.2})$$

Dispersed phase void fraction flux:

$$\begin{aligned} \left[\frac{1}{2k_p} (\mathcal{P}^p - \mathcal{D}^p) + \frac{1}{\bar{\phi}^2} (\mathcal{P}^\phi - \epsilon^\phi) + \frac{1}{\tau_p} + \frac{\epsilon}{k_p} S_{ll}^p \right] \varphi_i^p &= \\ - \frac{\epsilon}{k_p} (S_{il}^p + \omega_{il}^p) \varphi_l^p + \frac{1}{\tau_p} \varphi_i^f - k_p \left(a_{il}^p + \frac{2}{3} \delta_{il} \right) \frac{\partial \Phi}{\partial x_l}, & \end{aligned} \quad (\text{A.3})$$

Fluid-particle co-variance:

$$\left[\frac{D^v k_{fp}}{Dt} + \left(\frac{C_{fp1}}{\tau} + \frac{1}{\tau_p} + (1 - C_{fp3}) \frac{\lambda \Phi}{\tau_p} \right) k_{fp} \right] a_{ij}^{fp} = -\frac{\epsilon}{k_p} k_{fp} \left(a_{il}^{fp} S_{lj}^p - \frac{1}{3} a_{lk}^{fp} S_{kl}^p \delta_{ij} \right)$$

$$\begin{aligned}
& + \frac{\epsilon}{k_p} k_{fp} \left(a_{il}^{fp} \omega_{lj}^p - \frac{1}{3} a_{lk}^{fp} \omega_{kl}^p \delta_{ij} \right) - \frac{2}{3} \frac{\epsilon}{k_p} k_{fp} \left(S_{ij}^p - \frac{1}{3} S_{ll}^p \delta_{ij} \right) + \frac{2}{3} \frac{\epsilon}{k_p} k_{fp} \omega_{ij}^p \\
& - (1 - C_{fp2}) \frac{\epsilon}{k} k_{fp} \left(a_{lj}^{fp} S_{li}^f - \frac{1}{3} a_{lk}^{fp} S_{lk}^f \delta_{ij} \right) + (1 - C_{fp2}) \frac{\epsilon}{k} k_{fp} \left(a_{lj}^{fp} \omega_{li}^f - \frac{1}{3} a_{lk}^{fp} \omega_{lk}^f \delta_{ij} \right) \\
& - (1 - C_{fp2}) \frac{2}{3} \frac{\epsilon}{k} k_{fp} \left(S_{ij}^f + \omega_{ij}^f \right) + \frac{k}{\tau_p} a_{ij}^f + (1 - C_{fp3}) \frac{\lambda \Phi k_p}{\tau_p} a_{ij}^p \\
& - (1 - C_{fp3}) \frac{\lambda}{\tau_p} \left[(U_i - V_i) \overline{v_j \phi} - \frac{1}{3} (U_l - V_l) \overline{v_l \phi} \delta_{ij} \right], \tag{A.4}
\end{aligned}$$

where $\mathcal{P}^p = \frac{1}{2} \mathcal{P}_{ii}^p$, $\mathcal{D}^p = \frac{1}{2} \mathcal{D}_{ii}^p$, $\varphi_i^f = \overline{u_i \phi}$, and $\varphi_i^p = \overline{v_i \phi}$. The rate of strain (S_{ij}^p) and the rotation (ω_{ij}^p) tensors for the dispersed phase are defined similarly to those of the carrier phase (2.9) by replacing U with V and k with k_p .

Appendix B

Relations for the coefficients and tensors appearing in (2.15)-(2.18) are obtained by the comparison of these equations with (2.14) and (A.1)-(A.3):

Carrier phase Reynolds stress (2.15):

$$C_1^f = \frac{1}{\Delta_f}, \quad C_2^f = -\frac{1+6C_{f2}}{\Delta_f} \frac{\epsilon}{k}, \quad C_3^f = -\frac{1+14C_{f2}}{3\Delta_f} \frac{\epsilon}{k}, \tag{B.1}$$

$$\begin{aligned}
q_{ij}^f &= -\frac{8}{15} \frac{\epsilon}{k} S_{ij}^f + (1 - C_{f3}) \frac{\lambda \Phi}{\tau_p} \frac{k_{fp}}{k} (a_{ij}^{fp} + a_{ji}^{fp}) \\
& - \frac{7}{10} \frac{\lambda}{k \tau_p} \left[(U_i - V_i) \overline{u_j \phi} + (U_j - V_j) \overline{u_i \phi} - \frac{2}{3} (U_l - V_l) \overline{u_l \phi} \delta_{ij} \right], \tag{B.2}
\end{aligned}$$

Dispersed phase Reynolds stress (2.16):

$$C_1^p = \frac{1}{\Delta_p}, \quad C_2^p = -\frac{1}{\Delta_p} \frac{\epsilon}{k_p}, \quad C_3^p = \frac{1}{\Delta_p} \frac{\epsilon}{k_p}, \tag{B.3}$$

$$q_{ij}^p = -\frac{4}{3} \frac{\epsilon}{k_p} \left(S_{ij}^p - \frac{1}{3} S_{ll}^p \delta_{ij} \right) + \frac{1}{\tau_p} \frac{k_{fp}}{k_p} (a_{ij}^{fp} + a_{ji}^{fp}), \tag{B.4}$$

Carrier phase void fraction flux (2.17):

$$A_{il}^f = S_{il}^f, \quad B^f = \frac{C_{\phi 3} - 1}{\Delta_{\phi f}} \frac{\lambda \Phi}{\tau_p}, \quad D^f = \frac{1}{5\Delta_{\phi f}} \frac{\epsilon}{k}, \quad (\text{B.5})$$

$$C_i^f = \frac{1}{\Delta_{\phi f}} \left[\overline{u_i v_l} \frac{\partial \Phi}{\partial x_l} + (1 - C_{\phi 2}) \frac{\lambda}{\tau_p} (U_i - V_i) \overline{\phi^2} \right], \quad (\text{B.6})$$

Dispersed phase void fraction flux (2.18):

$$A_{il}^p = (S_{il}^p + \omega_{il}^p), \quad B^p = -\frac{1}{\Delta_{\phi p} \tau_p}, \quad (\text{B.7})$$

$$C_i^p = \frac{1}{\Delta_{\phi p}} k_p (a_{il}^p + \frac{2}{3} \delta_{il}) \frac{\partial \Phi}{\partial x_l}, \quad D^p = \frac{1}{\Delta_{\phi p}} \frac{\epsilon}{k_p}, \quad (\text{B.8})$$

where,

$$\Delta_f = \frac{1}{\tau} \left[C_{f1} + \frac{\mathcal{P}^f}{\epsilon} - 1 - \frac{\mathcal{D}^f}{\epsilon} + 2(1 - C_{f3}) \frac{\lambda \Phi \tau}{\tau_p} \right], \quad (\text{B.9})$$

$$\Delta_p = \frac{\mathcal{P}^p}{k_p} + \frac{2}{\tau_p} \frac{k_{fp}}{k_p}, \quad (\text{B.10})$$

$$\Delta_{\phi f} = \frac{1}{2k} (\mathcal{P}^f - \epsilon - \mathcal{D}^f) + \frac{1}{\overline{\phi^2}} (\mathcal{P}^\phi - \epsilon^\phi) + \frac{C_{\phi 1}}{\tau} + (1 - C_{\phi 3}) \frac{\lambda \Phi}{\tau_p} + \frac{\epsilon}{k_p} S_{ll}^p, \quad (\text{B.11})$$

$$\Delta_{\phi p} = \frac{1}{2k_p} (\mathcal{P}^p - \mathcal{D}^p) + \frac{1}{\overline{\phi^2}} (\mathcal{P}^\phi - \epsilon^\phi) + \frac{1}{\tau_p} + \frac{\epsilon}{k_p} S_{ll}^p. \quad (\text{B.12})$$

Appendix C

This appendix presents the transport equations for the mean of the transport parameters as well as the three-equation model of §5 in a form appropriate for predictions of axisymmetric particle-laden jets. The equations are expressed in the parabolic form by assuming that the gradients of the mean quantities in the axial direction are negligible in comparison to the mean gradients in the radial directions. The gravity acts in x_1 -direction.

The carrier phase continuity:

$$\frac{\partial U_1}{\partial x_1} + \frac{1}{x_2} \frac{\partial (x_2 U_2)}{\partial x_2} = 0, \quad (\text{C.1})$$

The carrier phase momentum in x_1 -direction:

$$\begin{aligned} \frac{\partial(U_1 U_1)}{\partial x_1} + \frac{1}{x_2} \frac{\partial(x_2 U_1 U_2)}{\partial x_2} &= -\frac{1}{\rho_f} \frac{\partial P}{\partial x_1} + \frac{1}{x_2} \frac{\partial}{\partial x_2} \left(x_2 \nu \frac{\partial U_1}{\partial x_2} \right) - \frac{1}{x_2} \frac{\partial}{\partial x_2} (x_2 \bar{u}_1 \bar{u}_2) \\ &\quad - \frac{\lambda \Phi}{\tau_p} (U_1 - V_1) - \frac{\lambda}{\tau_p} (\bar{u}_1 \bar{\phi} - \bar{v}_1 \bar{\phi}), \end{aligned} \quad (\text{C.2})$$

The dispersed phase continuity:

$$\frac{\partial(\Phi V_1)}{\partial x_1} + \frac{1}{x_2} \frac{\partial(x_2 \Phi V_2)}{\partial x_2} = -\frac{1}{x_2} \frac{\partial}{\partial x_2} (x_2 \bar{v}_2 \bar{\phi}), \quad (\text{C.3})$$

The dispersed phase momentum in x_1 -direction:

$$\frac{\partial(V_1 V_1)}{\partial x_1} + \frac{1}{x_2} \frac{\partial(x_2 V_1 V_2)}{\partial x_2} = -\frac{1}{x_2} \frac{\partial}{\partial x_2} (x_2 \bar{v}_1 \bar{v}_2) + \frac{1}{\tau_p} (U_1 - V_1) + \left(1 - \frac{1}{\lambda}\right) g, \quad (\text{C.4})$$

The dispersed phase momentum in x_2 -direction:

$$\frac{\partial(V_1 V_2)}{\partial x_1} + \frac{1}{x_2} \frac{\partial(x_2 V_2 V_2)}{\partial x_2} = \frac{1}{x_2} \frac{\partial}{\partial x_2} \left(x_2 \nu_t^p \frac{\partial V_2}{\partial x_2} \right) + \frac{1}{\tau_p} (U_2 - V_2), \quad (\text{C.5})$$

The carrier phase turbulent kinetic energy:

$$\begin{aligned} \frac{\partial(U_1 k)}{\partial x_1} + \frac{1}{x_2} \frac{\partial(x_2 U_2 k)}{\partial x_2} &= -\bar{u}_1 \bar{u}_2 \frac{\partial U_1}{x_2} - \epsilon - \frac{1}{x_2} \frac{\partial}{\partial x_2} (x_2 \bar{u}_2 \bar{k}') \\ &\quad - \frac{\lambda}{\tau_p} [(U_1 - V_1) \bar{u}_1 \bar{\phi} + (U_2 - V_2) \bar{u}_2 \bar{\phi} + 2\Phi(k - k_{fp})], \end{aligned} \quad (\text{C.6})$$

The carrier phase dissipation rate of the turbulent kinetic energy:

$$\begin{aligned} \frac{\partial(U_1 \epsilon)}{\partial x_1} + \frac{1}{x_2} \frac{\partial(x_2 U_2 \epsilon)}{\partial x_2} &= -C_{\epsilon_1} \frac{\epsilon}{k} \bar{u}_1 \bar{u}_2 \frac{\partial U_1}{x_2} - C_{\epsilon_2} \frac{\epsilon^2}{k} - \frac{1}{x_2} \frac{\partial}{\partial x_2} (x_2 \bar{u}_2 \bar{\epsilon}') \\ &\quad - \frac{\epsilon}{k} \frac{\lambda}{\tau_p} \left\{ 2\Phi k - C_{\epsilon_3} [2\Phi k_{fp} - (U_1 - V_1) \bar{u}_1 \bar{\phi} - (U_2 - V_2) \bar{u}_2 \bar{\phi}] \right\} + \frac{1}{4} C_{\epsilon_4} \left(\frac{k}{\epsilon} \right)^2 \epsilon \left(\frac{\partial U_1}{\partial x_2} \right)^2 \frac{U_2}{x_2}, \end{aligned} \quad (\text{C.7})$$

The dispersed phase turbulent kinetic energy:

$$\frac{\partial(V_1 k_p)}{\partial x_1} + \frac{1}{x_2} \frac{\partial(x_2 V_2 k_p)}{\partial x_2} = -\bar{v}_1 \bar{v}_2 \frac{\partial V_1}{x_2} - \frac{1}{x_2} \frac{\partial}{\partial x_2}(x_2 \bar{v}_2 \bar{k}'_p) - \frac{2}{\tau_p} (k_p - k_{fp}), \quad (\text{C.8})$$

The fluid-particle turbulent kinetic energy:

$$\begin{aligned} \frac{\partial}{\partial x_1} [(U_1 + V_1) k_{fp}] + \frac{1}{x_2} \frac{\partial}{\partial x_2} [x_2 (U_2 + V_2) k_{fp}] &= -\frac{1}{2} \bar{u}_1 \bar{v}_2 \frac{\partial V_1}{x_2} - (1 - C_{fp2}) \frac{1}{2} \bar{u}_2 \bar{v}_1 \frac{\partial U_1}{x_2} \\ &\quad - \frac{1}{x_2} \frac{\partial}{\partial x_2} (\bar{u}_2 \bar{k}'_{fp} + \bar{v}_2 \bar{k}'_{fp}) - C_{fp1} \frac{k_{fp}}{\tau} + \frac{2}{\tau_p} (k - k_{fp}) \\ &\quad + (1 - C_{fp3}) \frac{2\lambda\Phi}{\tau_p} (k_p - k_{fp}) + (C_{fp3} - 1) \frac{\lambda}{\tau_p} [(U_1 - V_1) \bar{v}_1 \bar{\phi} + (U_2 - V_2) \bar{v}_2 \bar{\phi}]. \end{aligned} \quad (\text{C.9})$$

References

Adumitroaie, V., Taulbee, D. B., and Givi, P. (1997). Algebraic scalar flux models for turbulent reacting flows. *AICHE Journal*. in press.

Adumitroaie, V. (1997). Ph.D. Thesis, Department of Mechanical and Aerospace Engineering, State University of New York at Buffalo, Buffalo, NY. In preparation.

Chen, C. P. and Wood, P. E. (1986). Turbulence closure modeling of the dilute gas-particle axisymmetric jet. *AICHE J.* **32**, 163–166.

Clift, R., Grace, J. R., and Weber, M. E. (1978). *Bubbles, Drops, and Particles*. Academic Press, New York, NY.

Elghobashi, S. E. and Abou-Arab, T. W. (1983). A two-equation turbulence model for two-phase flows. *Phys. Fluids* **26**, 931–938.

Eringen, A. C., editor. (1971). *Continuum Physics*, volume 1. Academic.

Gatski, T. B. and Speziale, C. G. (1993). On explicit algebraic stress models for complex turbulent flows. *J. Fluid Mech.* **254**, 59–78.

Hanjalić, K. and Launder, B. E. (1972). A Reynolds stress model of turbulence and its application to thin shear flows. *J. Fluid Mech.* **52**, 609–638.

Höfler, T. (1993). Reynolds stress model (RSM) in FIRE. *FIRE Newsletter* **5**, 1. Fluid Dynamics Research Newsletter of AVL Inc., Graz, Austria.

Horiuti, K. (1969). Higher order terms in the anisotropic representation of Reynolds stresses. *Phys. Fluids* **2**, 1708–1711.

Launder, B. E., Reece, G. J., and Rodi, W. (1975). Progress in the development of a Reynolds-stress turbulence closure. *J. Fluid Mech.* **68**, 537–566.

Launder, B. E. (1975). On the effects of a gravitational field on the turbulent transport of heat and momentum. *J. Fluid Mech.* **67**, 569–581.

Mashayek, F., Taulbee, D. B., and Givi, P. (1997). Particle-laden turbulent flows. Part I: Direct simulations and Reynolds stress closures. *J. Fluid Mech.* submitted.

Mostafa, A. A. and Elghobashi, S. E. (1986). Effect of liquid droplets on turbulence in a round gaseous jet. NASA CR 175063.

Pope, S. B. (1975). A more general effective-viscosity hypothesis. *J. Fluid Mech.* **72**, 331–340.

Pope, S. B. (1978). An explanation of the turbulent round-jet/plane-jet anomaly. *AIAA J.* **16**, 279–281.

Rivlin, R. S. (1955). Further remarks on the stress-deformation relations for isotropic materials. *J. Rat. Mech. Anal.* **4**, 681–702.

Rodi, W. (1976). A new algebraic relation for calculating the Reynolds stresses. *ZAMM* **56**, T219–T221.

Sargianos, N. P., Anagnostopoulos, J., and Bergeles, G. (1990). Turbulence modulation of particles, downstream of a two-phase, particle-laden, round jet. In Rodi, W. and Ganić, editors, *Engineering Turbulence Modeling and Experiments*, pages 897–906. Elsevier Science Publishers Co., Inc.

Shuen, J-S., Solomon, A. S. P., Zhang, Q-F., and Faeth, G. M. (1985). Structure of particle-laden jets: Measurements and predictions. *AIAA J.* **23**, 396–404.

Spencer, A. J. M. (1971). Theory of invariants. In Eringen (1971), pages 240–352.

Speziale, C. G. (1991). Analytical methods for the development of Reynolds stress closures in turbulence. *Ann. Rev. Fluid Mech.* **23**, 107–157.

Taulbee, D. B., Sonnenmeier, J. R., and Wall, K. W. (1993). Stress relation for three-dimensional turbulent flows. *Phys. Fluids* **6**, 1399–1401.

Taulbee, D. B. (1989). Engineering turbulence models. In George, W. K. and Arndt, R., editors, *Advances in Turbulence*, pages 75–125. Hemisphere Publishing Co., New York, NY.

Taulbee, D. B. (1992). An improved algebraic Reynolds stress model and corresponding nonlinear stress model. *Phys. Fluids A* **4**, 2555–2561.

Wilcox, David C. (1993). *Turbulence Modeling for CFD*. DCW Industries, Inc., La Cañada, CA.

Yakhot, V. and Orszag, S. A. (1986). Renormalization group analysis of turbulence. I. Basic theory. *J. Sci. Comput.* **1**, 3–52.

Yoshizawa, A. (1984). Statistical analysis of the deviation of the Reynolds stress from its eddy-viscosity representation. *Phys. Fluids* **27**, 1377–1387.

Yoshizawa, A. (1988). Statistical modelling of passive-scalar diffusion in turbulent shear flows. *J. Fluid Mech.* **195**, 541–555.

Zhao, Y. (1993), *Multiphase, Turbulent, Reacting Flow in a Liquid Metal Combustor*. Ph.D. Thesis, The University of Wisconsin, Wisconsin, Milwaukee.

Zhou, L.X. (1993). *Theory and Numerical Modeling of Turbulent Gas-Particle Flows and Combustion*. CRC Press, Boca Raton, FL.

Figure Captions

Figure 1. Comparisons of the four-equation model predictions (lines) with DNS data (symbols) for components of the fluid, particle, and fluid-particle Reynolds stress tensors in the case with one-way coupling at $\tau_p = 0.016s$.

Figure 2. Comparisons of the four-equation model predictions (lines) with DNS data (symbols) for components of the fluid, particle, and fluid-particle Reynolds stress tensors for $\Phi_m = 0.25$ and $\tau_p = 0.016s$.

Figure 3. Comparisons of the four-equation model predictions (lines) with DNS data (symbols) for components of the fluid, particle, and fluid-particle Reynolds stress tensors for $\Phi_m = 0.25$ and $\tau_p = 0.032s$.

Figure 4. Comparisons of the four-equation model predictions (lines) with DNS data (symbols) for the rate of dissipation of the carrier phase turbulent kinetic energy for all of the DNS cases. The dissipation rate is normalized with its initial value ϵ_0 .

Figure 5. Variations of the third-order velocity correlations with the mass loading ratio and the time scale ratio at $\kappa = 1$.

Figure 6. Variations of the third-order velocity correlations with the mass loading ratio and the time scale ratio at $\kappa = 0.1$.

Figure 7. Variations of the relative error χ with the mass loading ratio and the time scale ratio at $\kappa = 1$.

Figure 8. Variations of the relative error χ with the mass loading ratio and the time scale ratio at $\kappa = 0.1$.

Figure 9. Comparison of the mean variables with the experimental data of Shuen *et al.* (1985) at $x_1/d = 40$. (a) Mean fluid axial velocity, (b) mean particle axial velocity, and (c) mean axial void fraction.

Figure 10. Comparisons of the model predictions (solid lines) of the centerline mean variables with those of the experiment (symbols) of Shuen *et al.* (1985).

Figure 11. Comparison of (a) the fluid and (b) the particle turbulent kinetic energy with the experimental data of Shuen *et al.* (1985) at $x_1/d = 40$.

Figure 12. Comparison of the fluid shear stress with the experimental data of Shuen *et al.* (1985) at $x_1/d = 40$.

Figure 13. Comparison of the fluid normal stress in (a) the axial and (b) the radial direction with the experimental data of Shuen *et al.* (1985) at $x_1/d = 40$.

Table 1: Suggested values of the empirical constants for the four-equation (k - ϵ - k_p - k_{fp}) model.

Constant	Magnitude	Basis for choice
C_{f1}	1.75	Launder <i>et al.</i> (1975)
C_{f2}	-0.159	Launder <i>et al.</i> (1975)
C_{f3}	0.5	Part I
C_{fp1}	2.5	Part I
C_{fp2}	0.5	Part I
C_{fp3}	0.2	Part I
$C_{\phi 1}$	1.5	Axisymmetric jet (experiment)
$C_{\phi 2}$	0.5	Axisymmetric jet (experiment)
$C_{\phi 3}$	0.5	Axisymmetric jet (experiment)
$C_{\phi p}$	3.0	Axisymmetric jet (experiment)
$C_{\phi \phi}$	3.0	Axisymmetric jet (experiment)
$C_{\epsilon 1}$	1.45	Standard k - ϵ
$C_{\epsilon 2}$	1.9†	Standard k - ϵ
$C_{\epsilon 3}$	0.8	Part I
$C_{\epsilon 4}$	0.79	Pope (1978)
C_s	0.08	Hanjalić and Launder (1972)
C_ϵ	0.13	Hanjalić and Launder (1972)

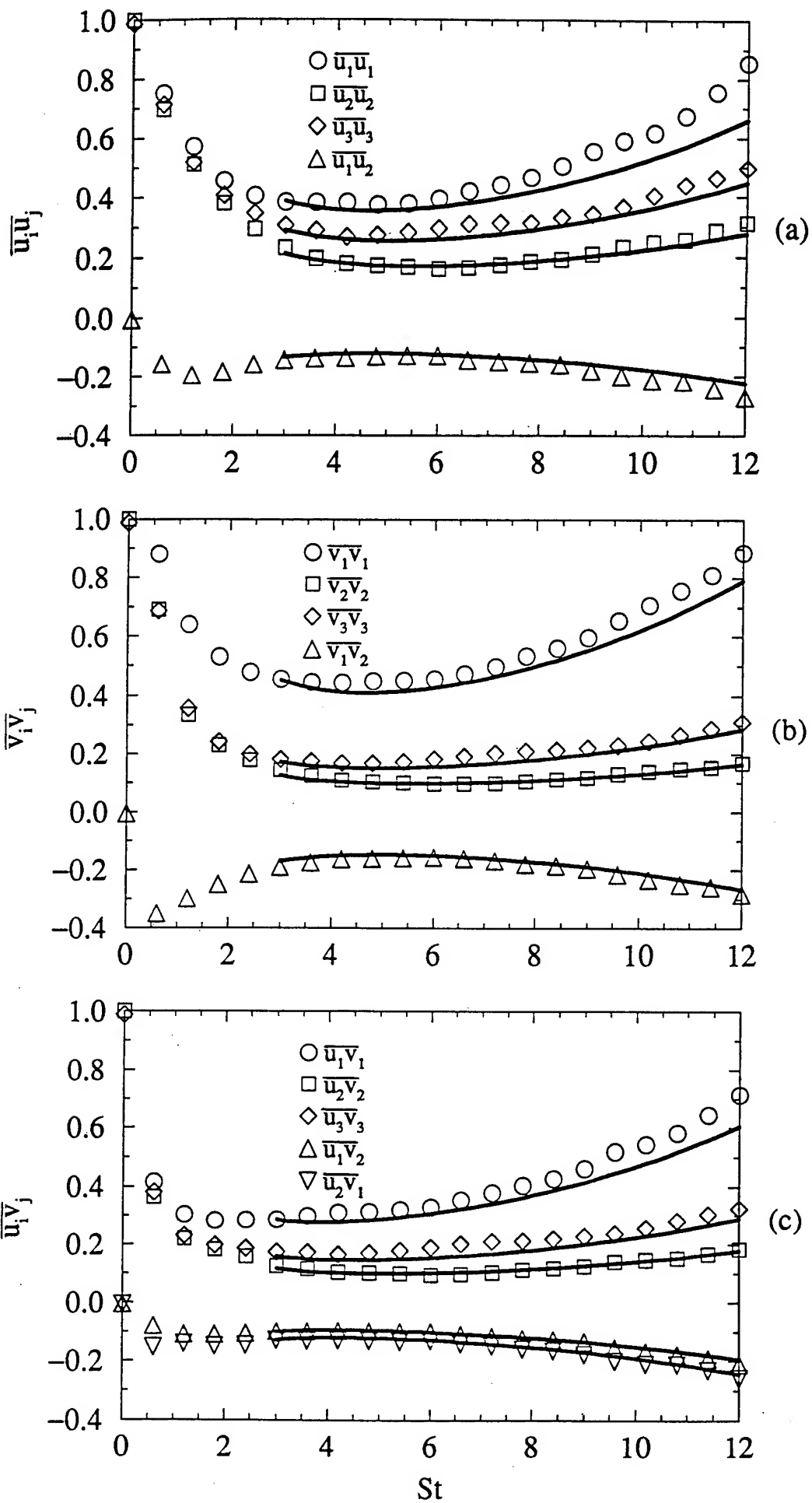
† 1.85 is used in comparison with DNS.

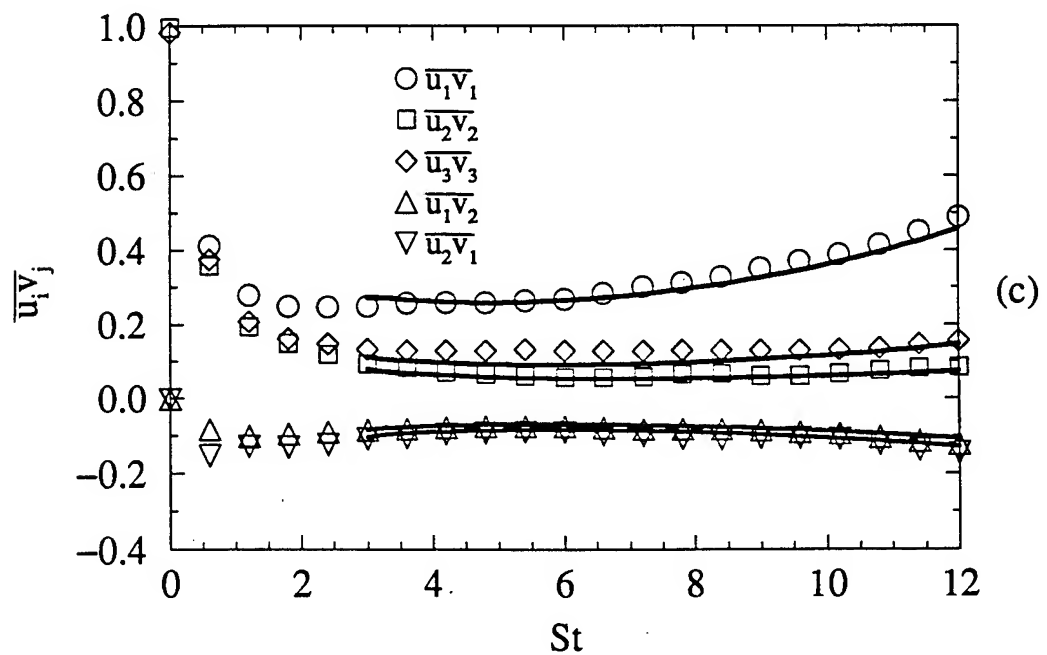
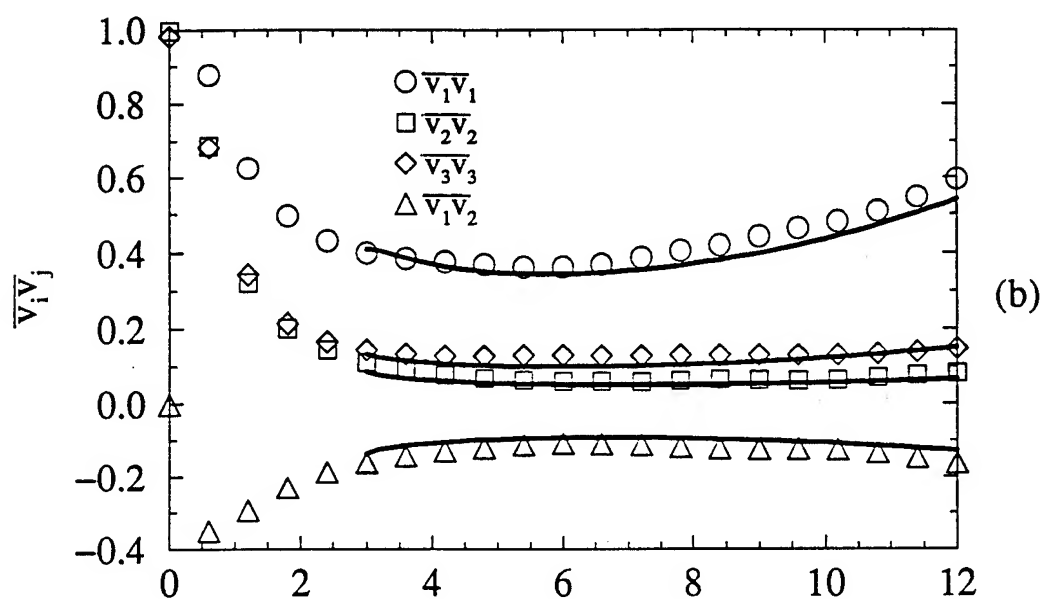
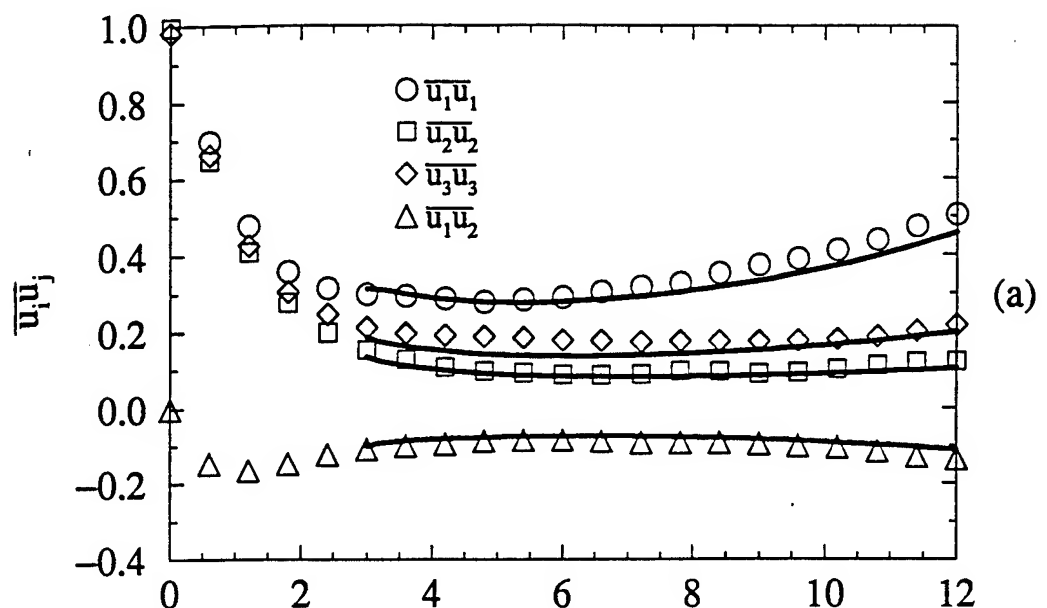
Table 2: Comparison of the values of k/k_p calculated from DNS (at $St = 12$) with those predicted by the Hinze-Tchen algebraic relation.

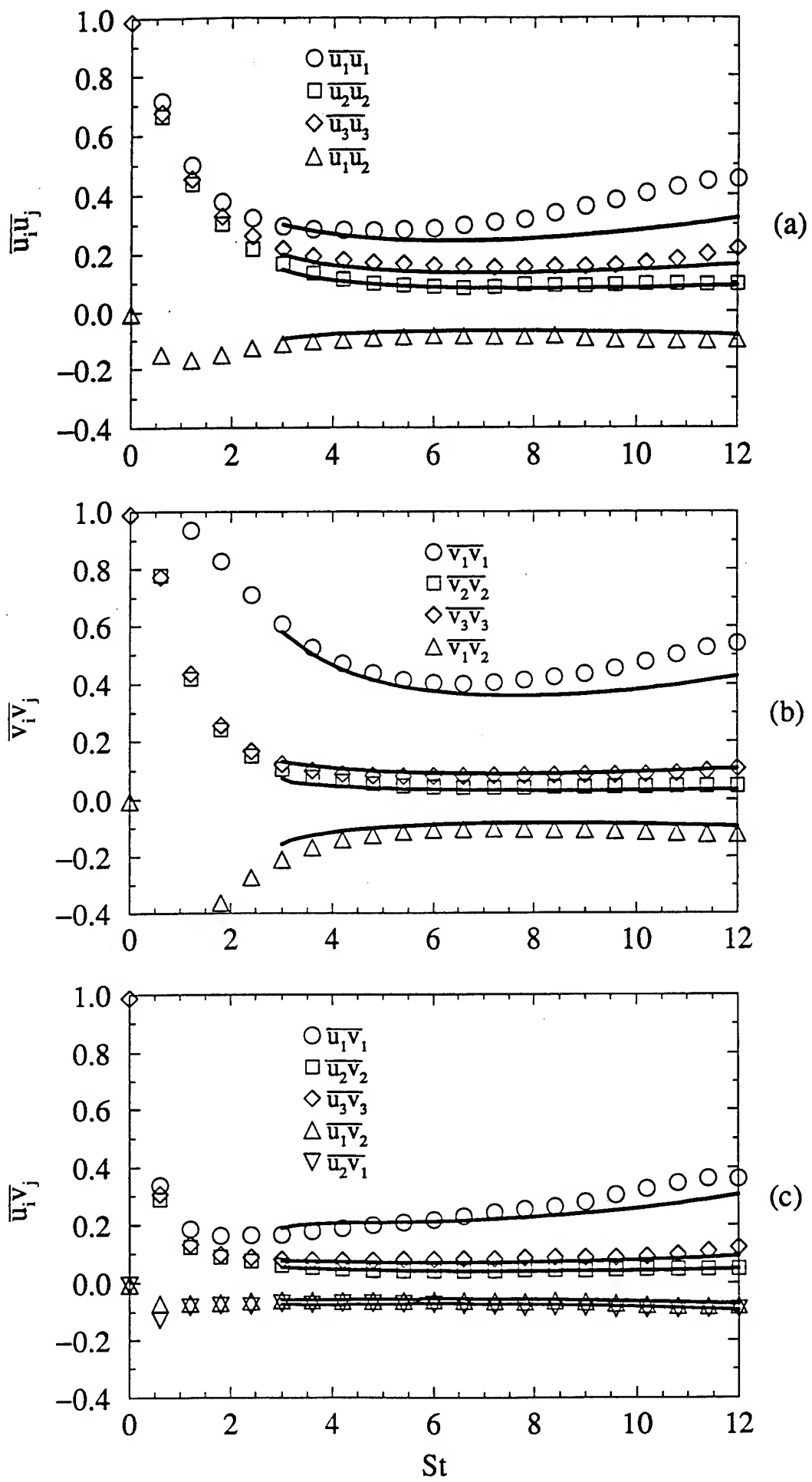
Case	C1	C3	C5
k/k_p (DNS)	1.21	1.02	1.10
k/k_p (Eq. 5.25)	3.61	3.04	5.71

Table 3: Comparison of the values of k/k_p from experiment (at $x_1/d = 20$) with those predicted by the Hinze-Tchen algebraic relation.

x_2/d	0	0.013	0.031	0.051	0.071	0.092	0.11
k/k_p (Exp.)	0.91	0.78	1.03	1.11	1.27	1.22	1.30
k/k_p (Eq. 5.25)	930	910	1150	800	580	610	400







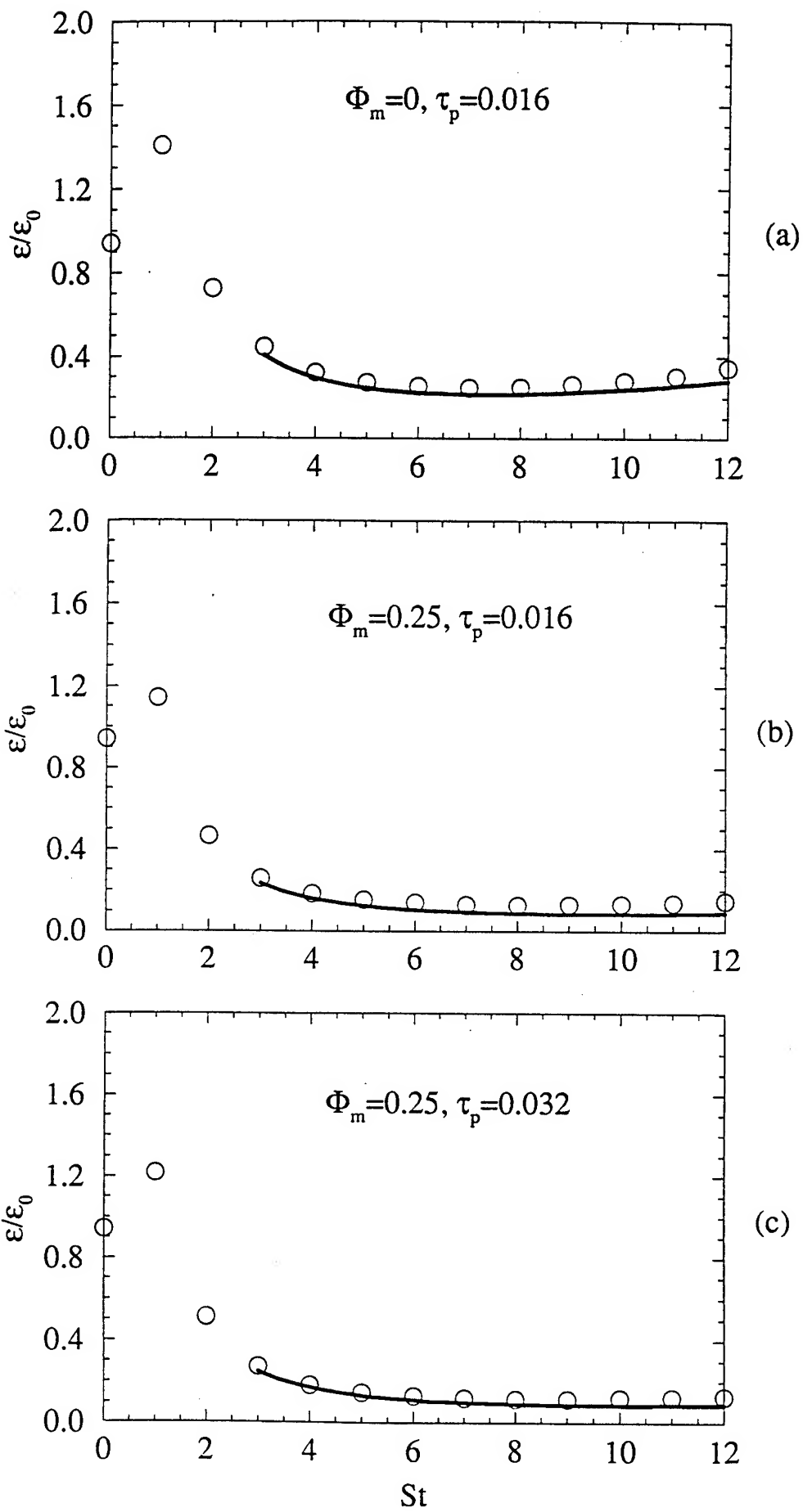


Fig. 4

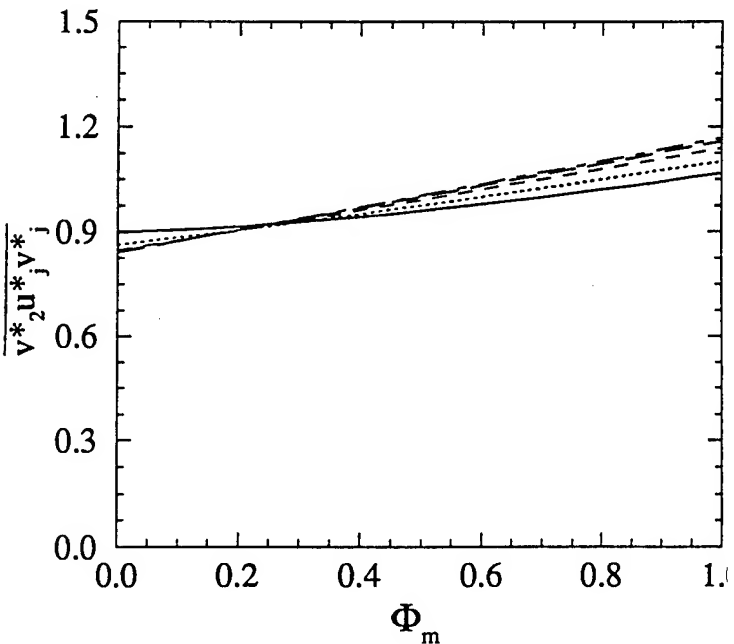
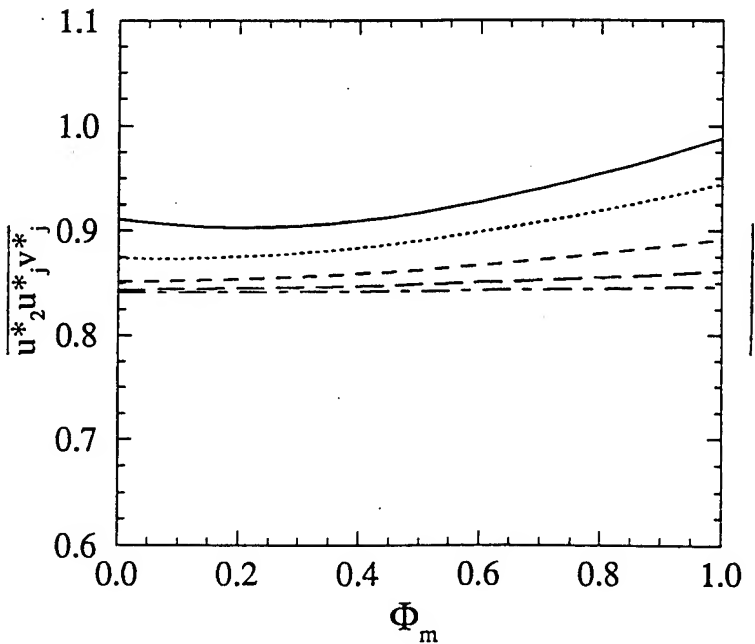
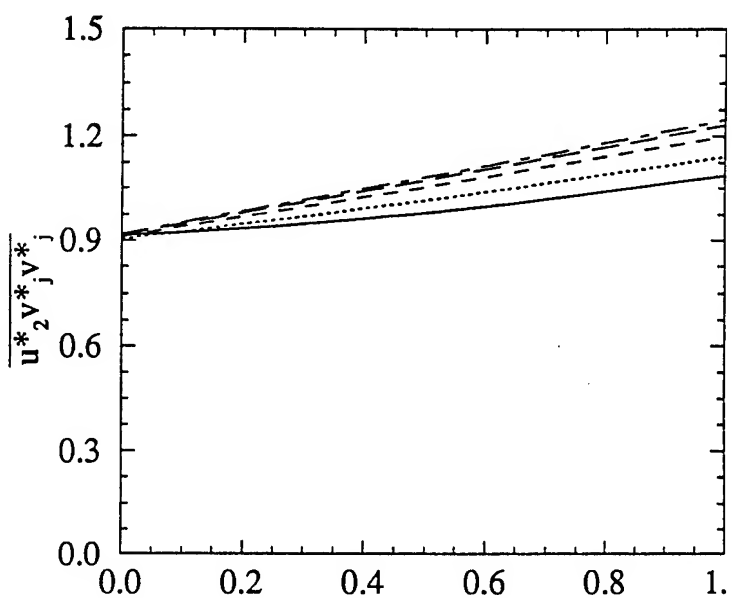
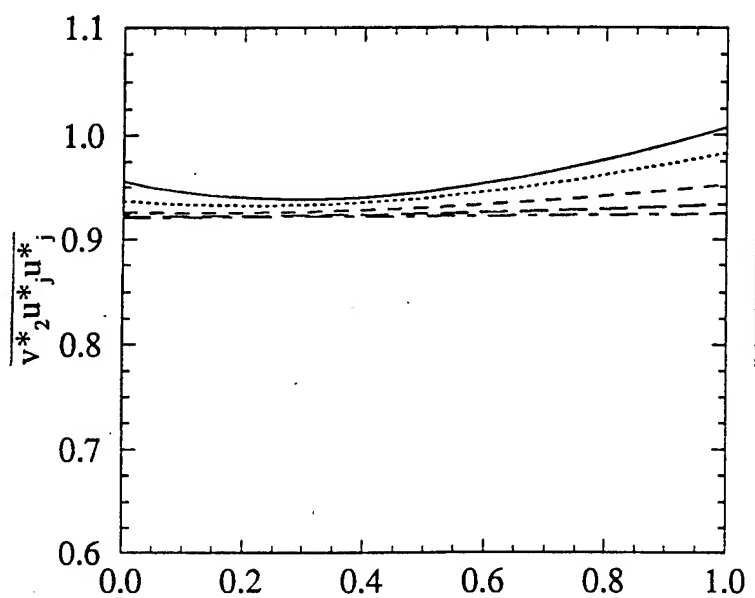
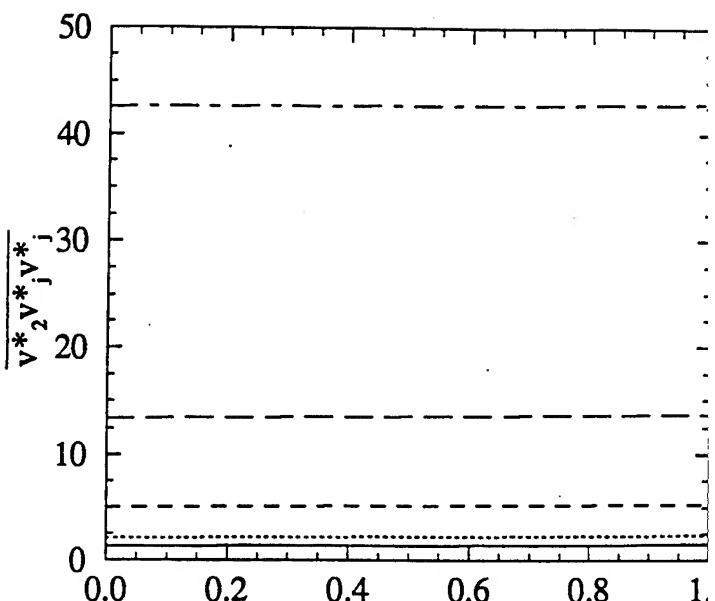
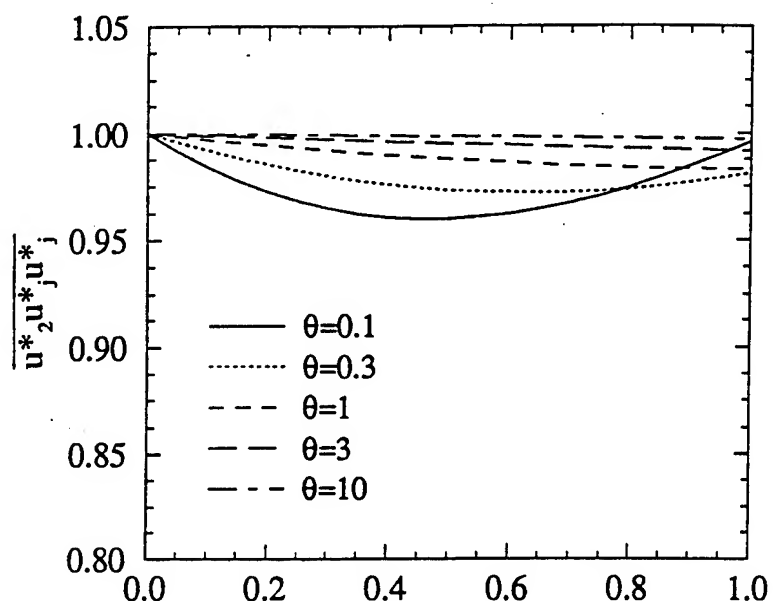
$\kappa=1$ 

Fig. 5

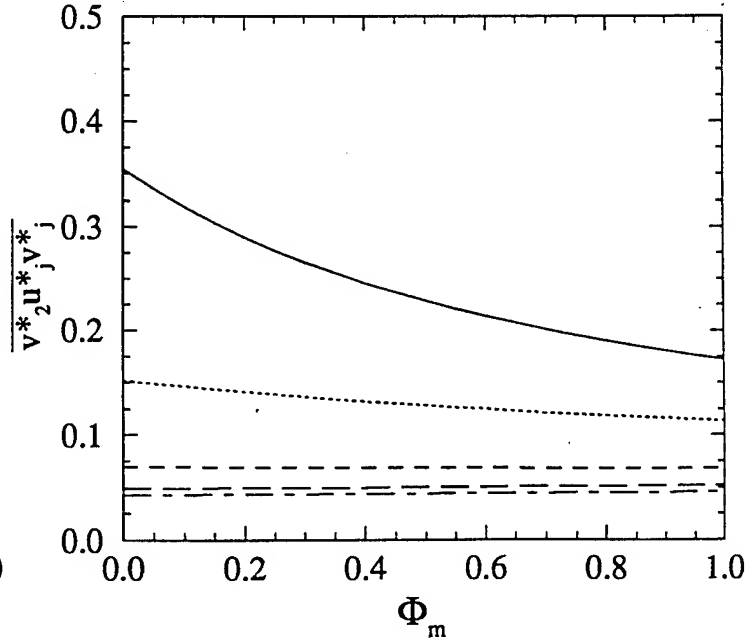
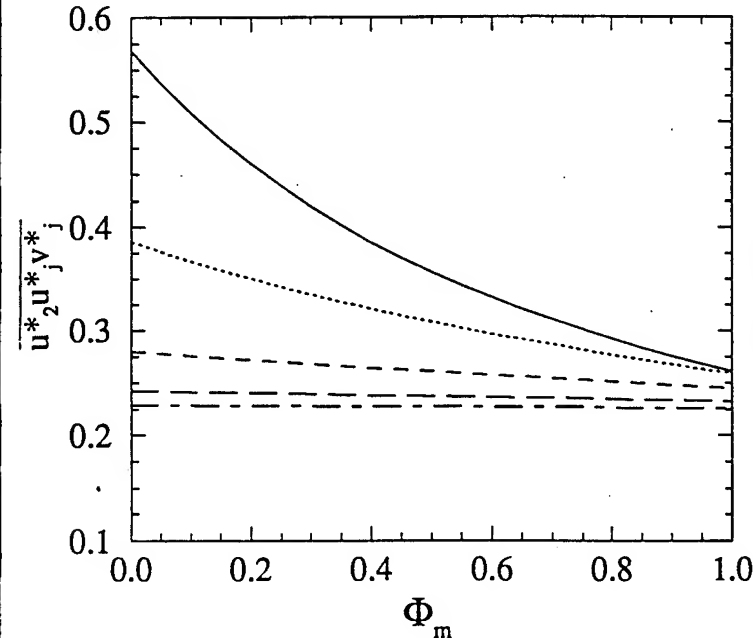
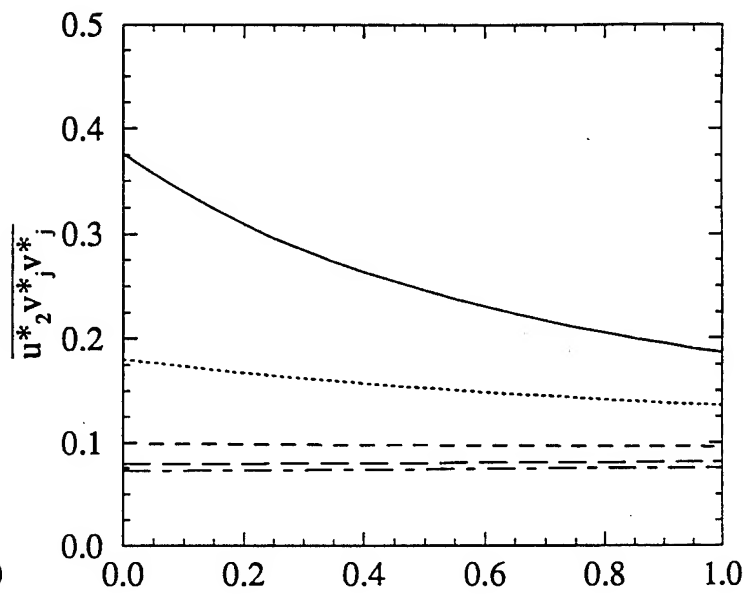
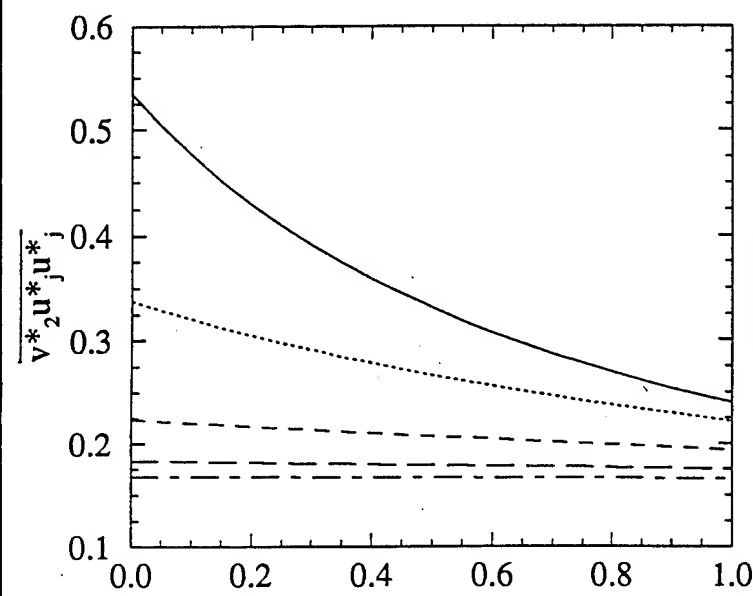
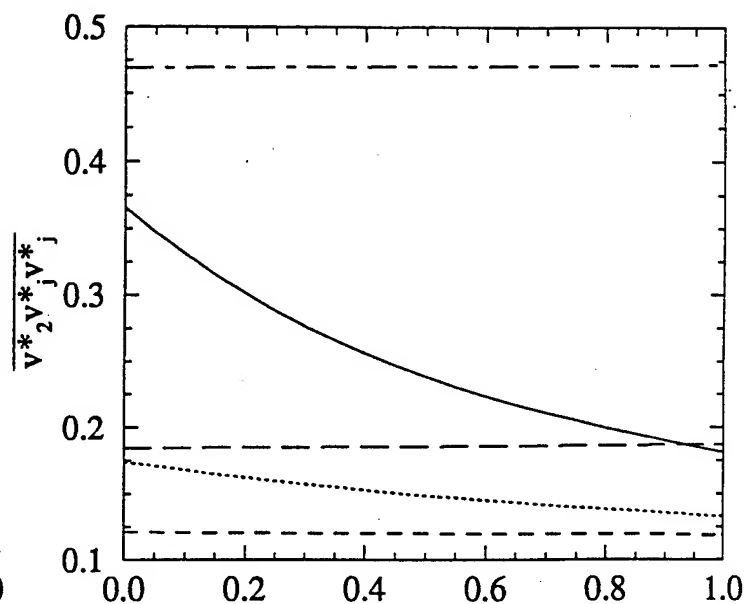
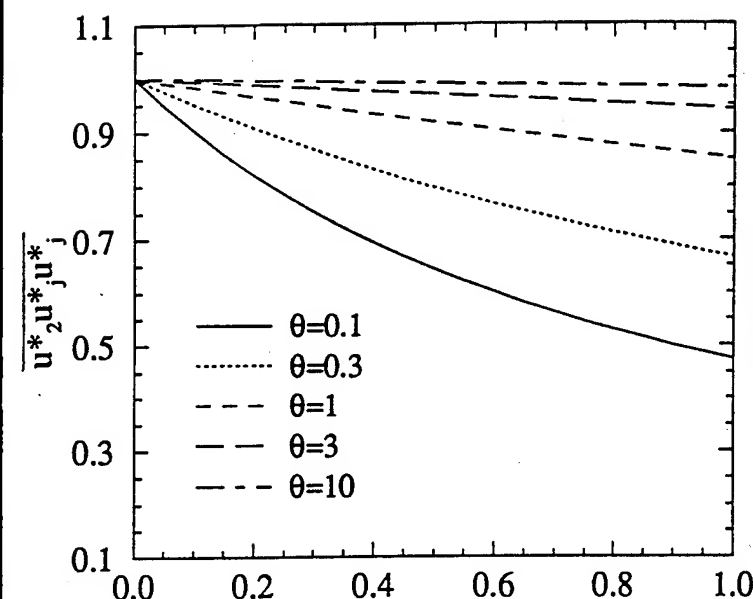
$\kappa=0.1$ 

Fig. 6

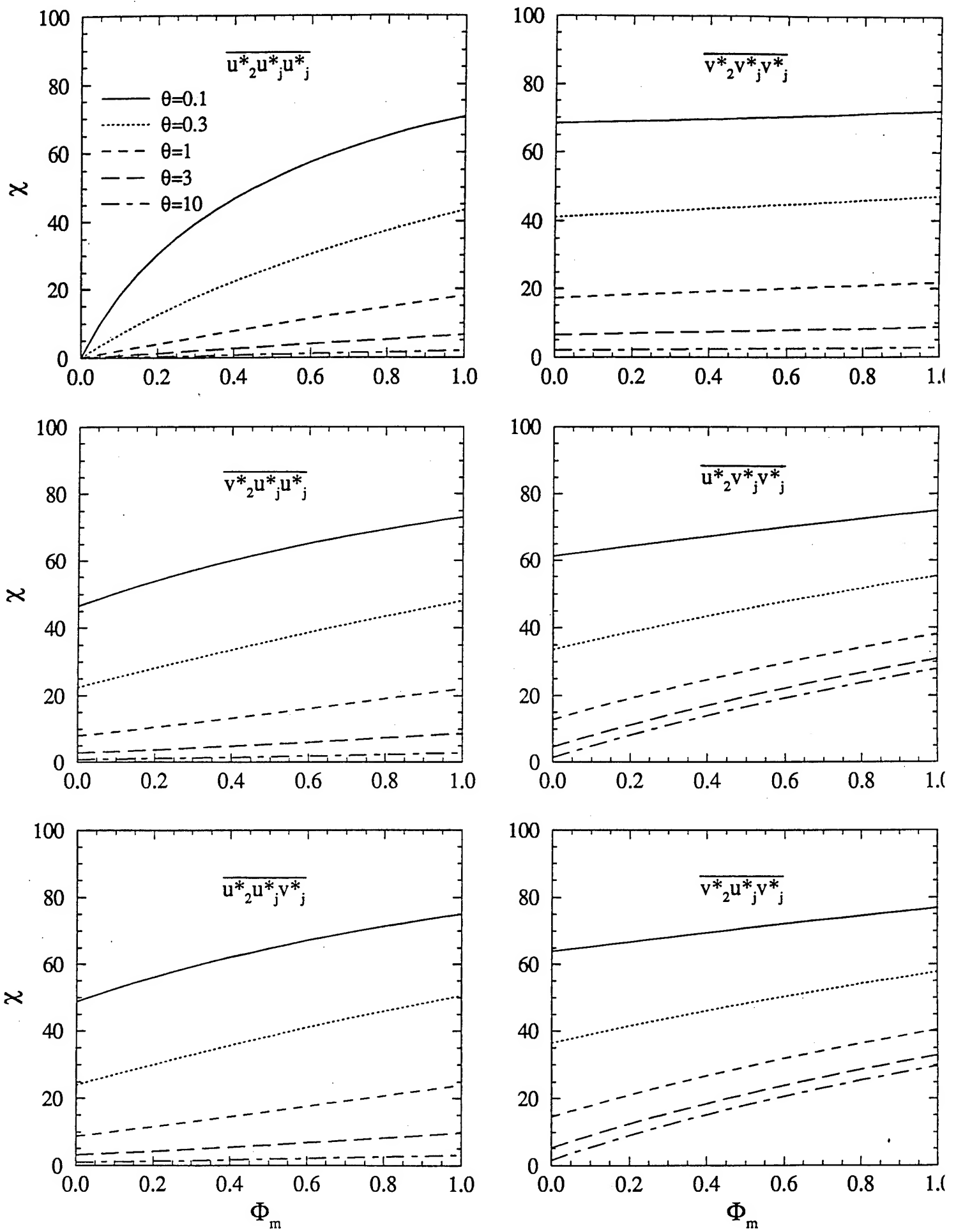
$\kappa=1$ 

Fig. 7

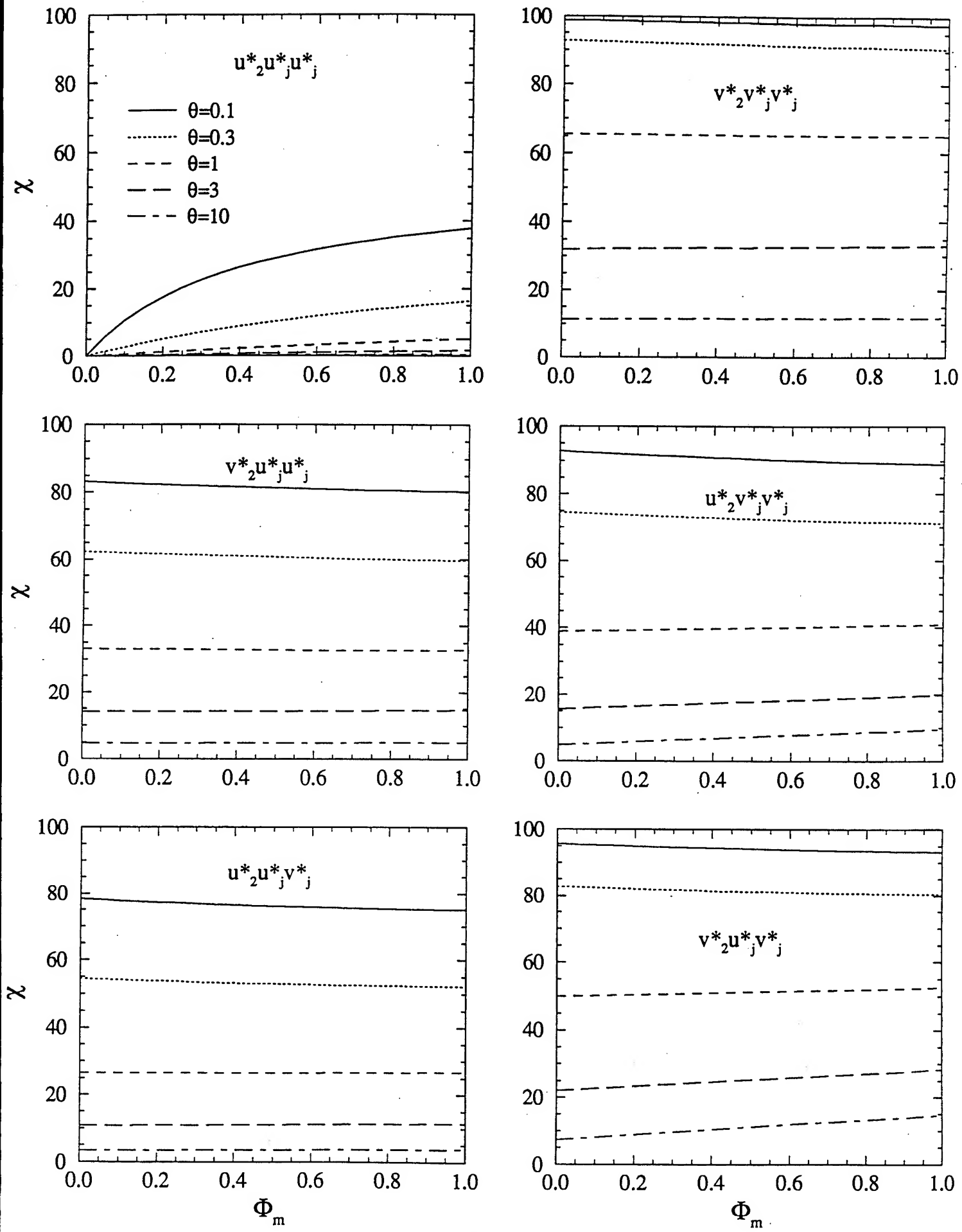
$\kappa=0.1$ 

Fig. 8

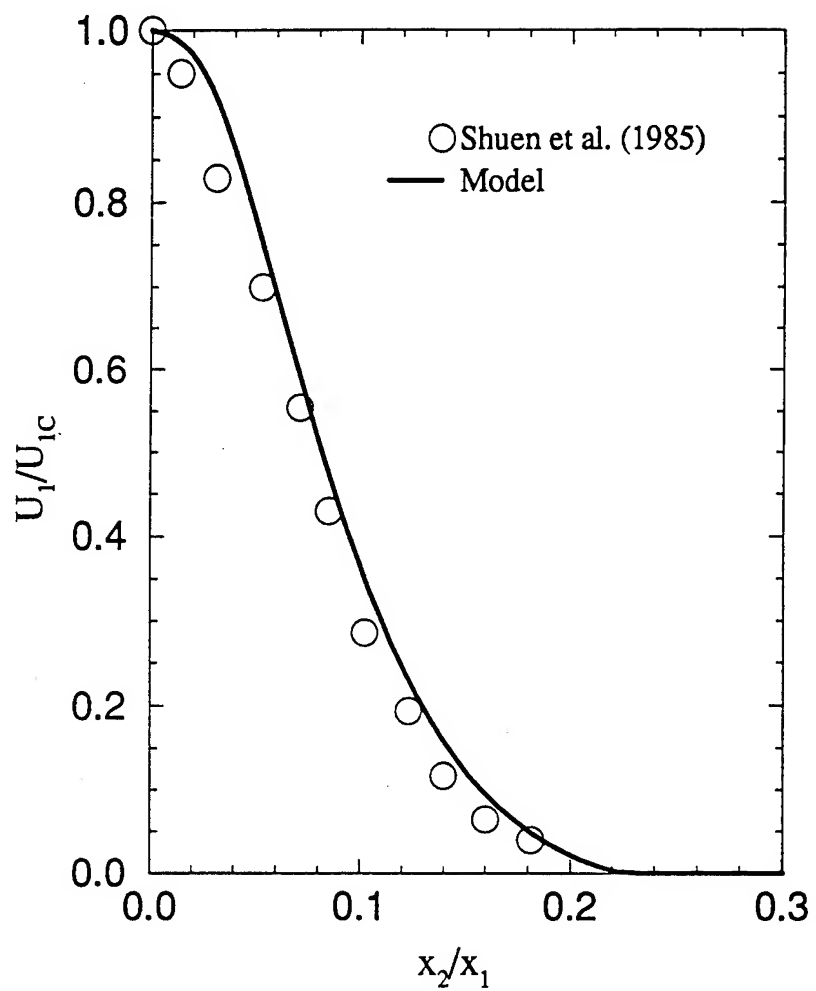


Fig. 9a

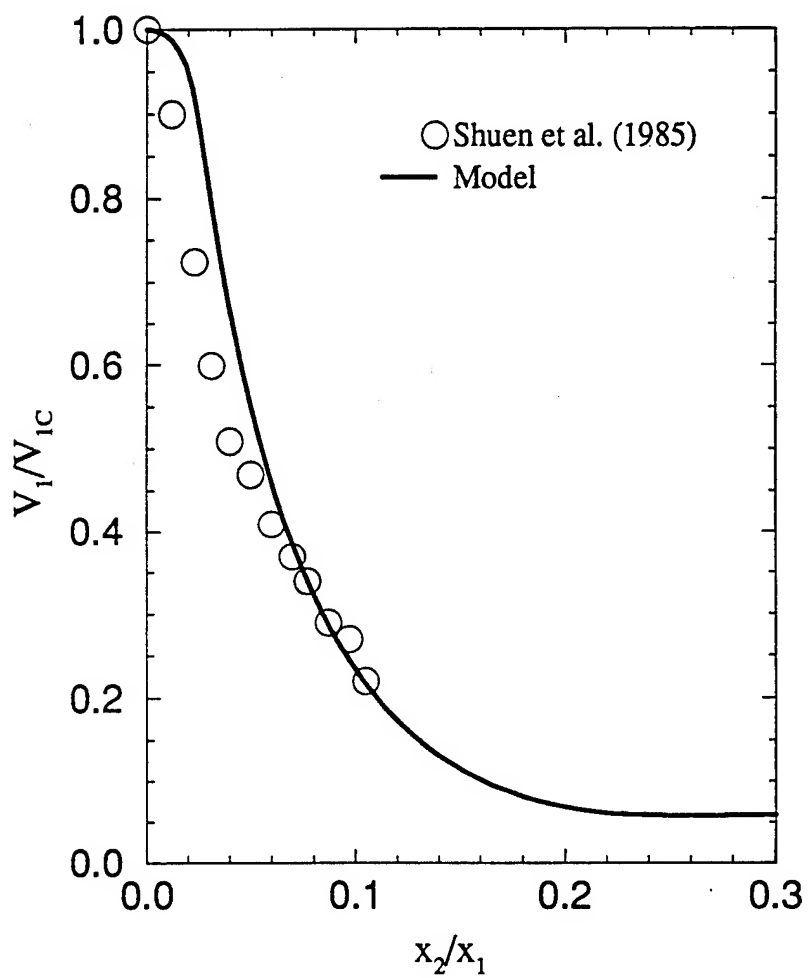


Fig. 9b

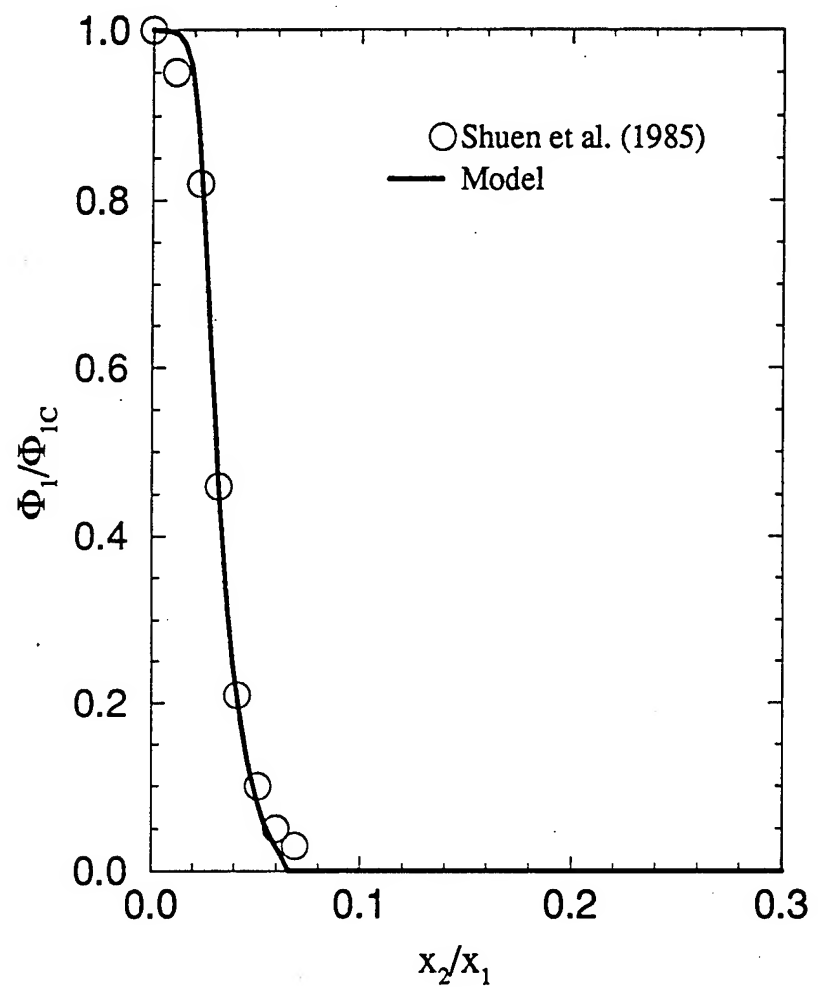


Fig. 9C

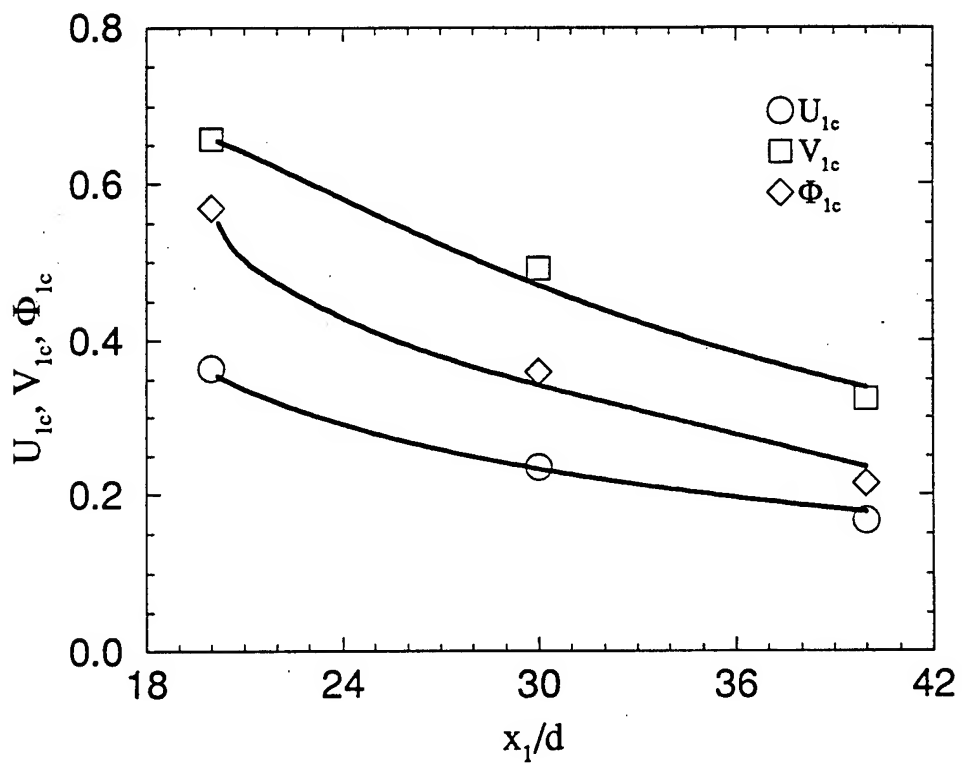


Fig. 10

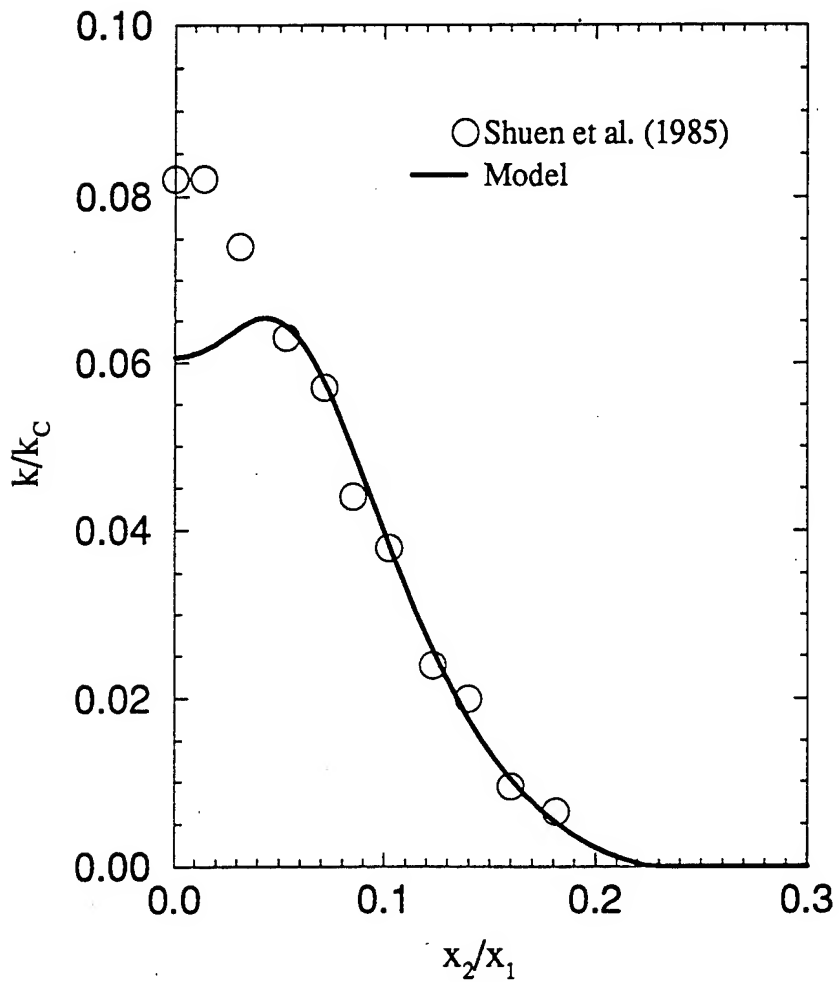


Fig. 11a

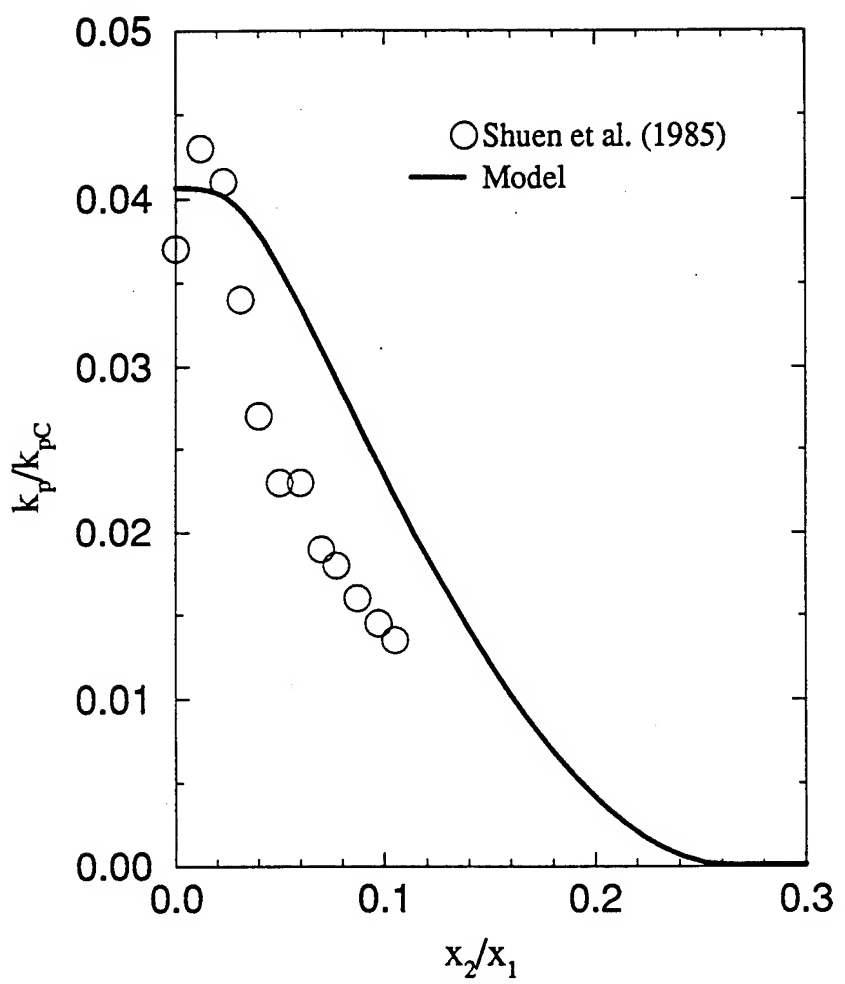


Fig. 11b

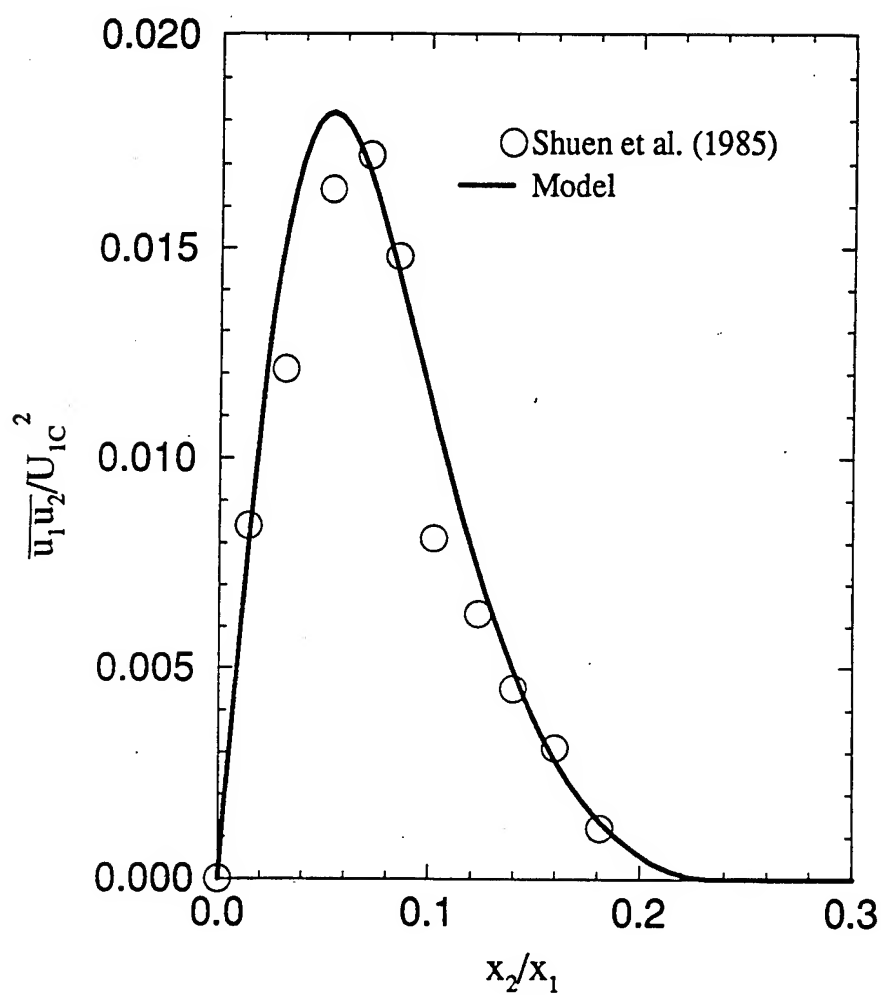


Fig. 12

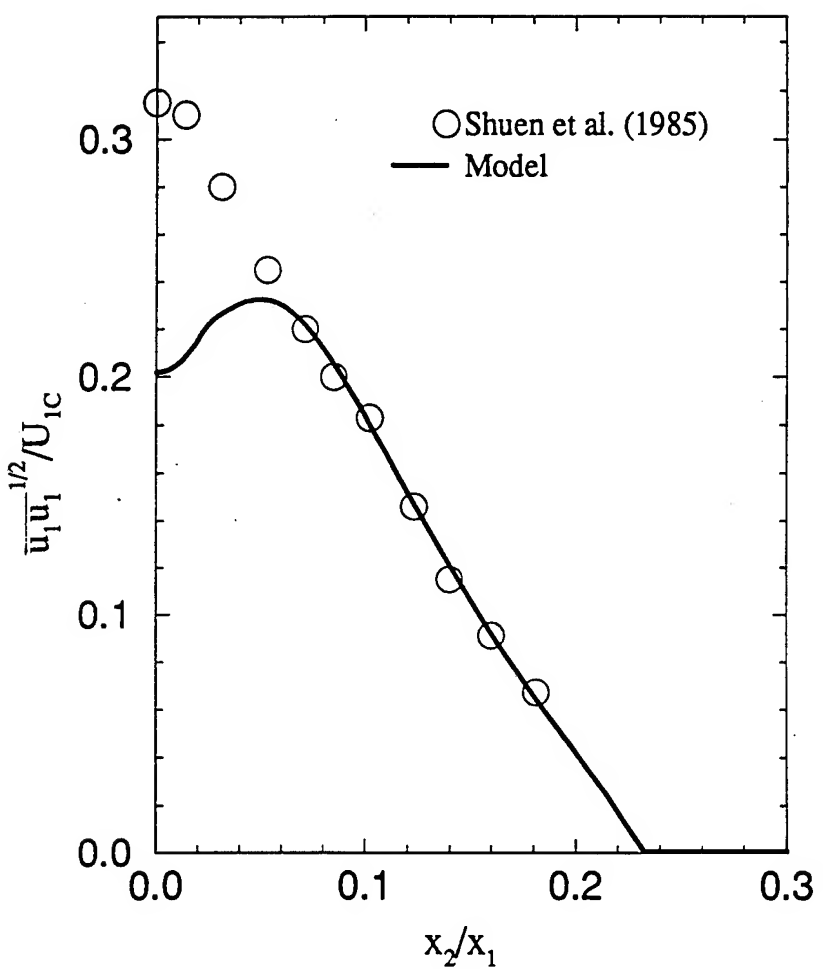


Fig. 13a

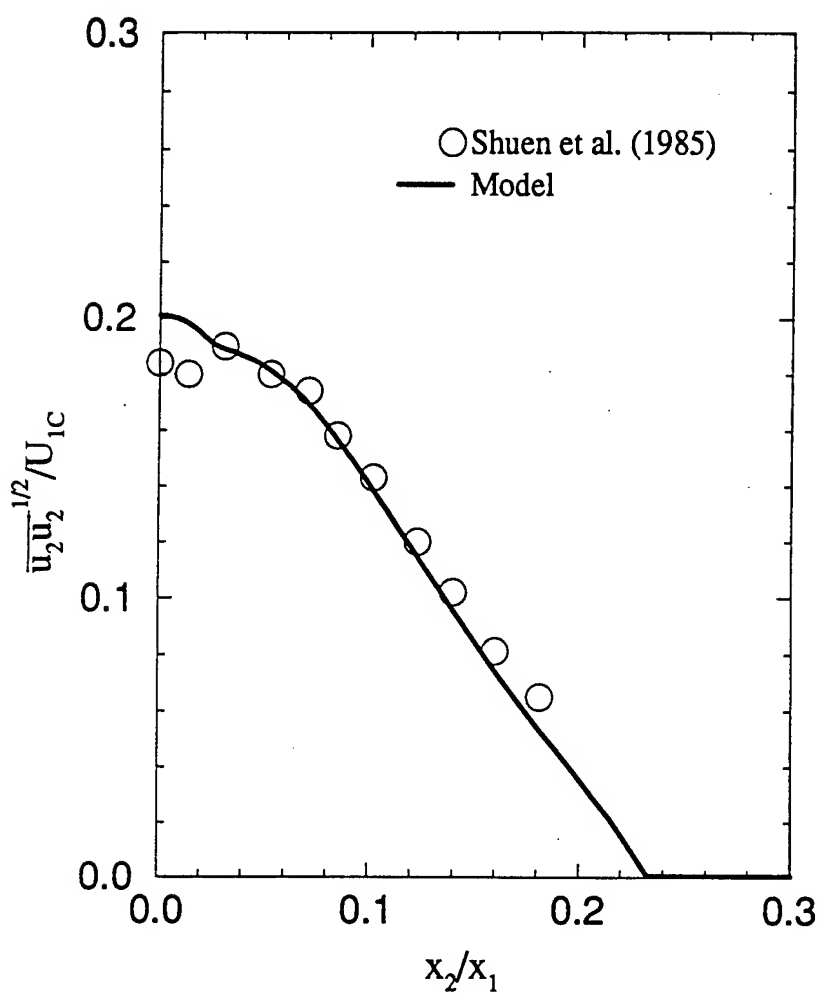


Fig. 13b

APPENDIX V

Large and Direct Numerical Simulations of a Methane Jet Flame

Large and Direct Numerical Simulations of a Methane Jet Flame

S. James, F.A. Jaber and P. Givi

Department of Mechanical and Aerospace Engineering
State University of New York at Buffalo
Buffalo, NY 14260-4400

Abstract

We make use of the “filtered mass density function” (FMDF) for large eddy simulation (LES) of a jet flame involving methane. The FMDF represents the single point joint probability density function of the subgrid scale (SGS) scalar quantities and is obtained by solution of its modeled transport equation. In this equation, the chemical reactions appear in closed form but the influences of scalar mixing and convection within the subgrid are modeled. The stochastic differential equations (SDEs) which yield statistically equivalent results to that of the FMDF transport equation are derived and are solved via a Lagrangian Monte Carlo scheme. The consistency, convergence, and accuracy of FMDF and the Monte Carlo solution of its equivalent SDEs are assessed via comparison with data generated by direct numerical simulation (DNS) and with experimental data.

1 Introduction

We have previously developed a methodology termed the “filtered density function” (FDF) for LES of chemically reacting flows. This methodology is based on the idea originally proposed by Pope (1991). The fundamental property of the FDF is to account for the effects of subgrid scale (SGS) scalar fluctuations in a probabilistic manner. Colucci *et al.* (1998) developed a transport equation for the FDF in which the effects of unresolved convection and subgrid were modeled similarly to those in conventional LES and Reynolds averaging (RA) procedures. This transport equation was solved numerically by a Lagrangian Monte Carlo procedure and the results were compared with those obtained by direct numerical simulations (DNS) and by the conventional LES in different free shear flows. It was shown that in non-reacting flows, the first moment of the FDF as obtained by the Monte Carlo solution is the

same as that obtained by the finite difference solution of the transport equation governing the mean scalar value (LES-FD). The advantage of the FDF was demonstrated in reacting flows in which its results were shown to deviate significantly from those based on LES-FD. Detailed comparison with DNS data indicated clear advantage of FDF over LES-FD.

The encouraging results generated by FDF warrants its extensions and applications to more complex flows. Further assessment of its predictive capability are also in order. The objective in this work is to extend the methodology for treatment of reactive flows with variable density flows so that exothermic chemical reactions can be simulated. For that, we have introduced the “filtered mass density function” (FMDF)(Jaberi *et al.*, 1997) which essentially is the density weighted PDF of SGS scalar variables. With the definition of the FMDF, the mathematical framework for its implementation in LES of reacting flows is established.

2 Fundamental Assumptions

We consider the unsteady evolution of a nonpremixed methane-air jet flame. LES/FMDF is conducted of this flow and all the results are validated by comparison with data obtained by DNS of the flame with the same parameter values. Here, all our basic assumptions are explicitly stated.

- The primary emphasis in this work is on LES of “reacting flows.” Thus, the FMDF is employed only for LES of the scalar field. The LES of the hydrodynamic field is conducted via the “conventional” LES-FD. The SGS closures in LES-FD are the same as those typically used in fluid mechanics.
- The chemistry of methane-air oxidation is simulated via the “reduced scheme” of Seshadri and Peters (1988) and a 25-step skeletal mechanism (Smooke and Giovangigli, 1991). These provide a realistic means of simulating combustion in a computationally affordable manner. The difference between this (and other) reduced scheme(s) and more sophisticated (detailed and/or skeletal) mechanisms is recognized.
- The problem formulation considers variable density flow in which the exothermicity effects are taken into account. However, the flow Mach number is small and the compressibility effects as observed in very high speed flows are not included. With this formulation and considering assumption (1), the Monte Carlo procedure is employed for the FMDF of the scalar field, and the hydrodynamic field is simulated by a finite difference scheme (LES-FD). The two simulations are, of course, coupled.

- Both LES and DNS are conducted of two-dimensional (2D) flows. The obvious issue regarding the 3D nature of turbulence, and all the concerns associated with 2D analysis of turbulence are well recognized. It is also recognized that for (future) comparisons with experimental data 3D simulations are essential. However, based on our previous work (Colucci *et al.*, 1998; Jaber *et al.*, 1997), in the context considered, *all the conclusions drawn from this work remain the same in 3D*. Due to space limitation, no further justifications in this regard are provided.
- While the effects of chemical reaction are taken into account in a closed form in the FMDF formulation, the problem with turbulence closure is not fully eliminated. For other closures, we make use of currently available methodologies. The magnitudes of some of the empirical constants appearing in these closures are obtained via *a priori* analysis of non-reacting flows. These values are subsequently employed, without further optimizations, for LES of the methane flame.
- The Newton's law of viscosity, the Fourier law of heat conduction and the Fick's law of mass diffusion are employed in the problem formulation. The caveats in the use of these laws in reacting flows are recognized, but no further justifications are made here.

These assumptions, and all other (secondary) approximations are also made clear in the presentation below.

3 Governing Equations and Closure Models

Large eddy simulation involves the spatial filtering operation (Aldama, 1990),

$$\langle f(\mathbf{x}, t) \rangle_\ell = \int_{-\infty}^{+\infty} f(\mathbf{x}', t) \mathcal{G}(\mathbf{x}', \mathbf{x}) d\mathbf{x}' \quad (1)$$

where \mathcal{G} denotes the filter function, $\langle f(\mathbf{x}, t) \rangle_\ell$ represents the filtered value of the transport variable $f(\mathbf{x}, t)$. In variable density flows it is more convenient to consider the Favre filtered quantity, $\langle f(\mathbf{x}, t) \rangle_L = \langle \rho f \rangle_\ell / \langle \rho \rangle_\ell$. We consider spatially & temporally invariant and localized filter functions, thus $\mathcal{G}(\mathbf{x}', \mathbf{x}) \equiv G(\mathbf{x}' - \mathbf{x})$ with the properties (Aldama, 1990), $G(\mathbf{x}) = G(-\mathbf{x})$, and $\int_{-\infty}^{\infty} G(\mathbf{x}) d\mathbf{x} = 1$. Moreover, we only consider "positive" filter functions as defined by Vreman *et al.* (1994) for which all the moments $\int_{-\infty}^{\infty} x^m G(x) dx$ exist for $m \geq 0$. The application of the filtering operation to the fundamental transport equations of reacting flows (Williams, 1985) yields:

$$\frac{\partial \langle \rho \rangle_\ell}{\partial t} + \frac{\partial \langle \rho \rangle_\ell \langle u_i \rangle_L}{\partial x_i} = 0 \quad (2)$$

$$\frac{\partial \langle \rho \rangle_\ell \langle u_j \rangle_L}{\partial t} + \frac{\partial \langle \rho \rangle_\ell \langle u_i \rangle_L \langle u_j \rangle_L}{\partial x_i} = - \frac{\partial \langle p \rangle_\ell}{\partial x_j} + \frac{\partial \langle \tau_{ij} \rangle_\ell}{\partial x_i} - \frac{\partial T_{ij}}{\partial x_i} \quad (3)$$

$$\frac{\partial \langle \rho \rangle_\ell \langle \phi_\alpha \rangle_L}{\partial t} + \frac{\partial \langle \rho \rangle_\ell \langle u_i \rangle_L \langle \phi_\alpha \rangle_L}{\partial x_i} = - \frac{\partial \langle J_i^\alpha \rangle_\ell}{\partial x_i} - \frac{\partial M_i^\alpha}{\partial x_i} + \langle \rho S_\alpha \rangle_\ell, \quad \alpha = 1, 2, \dots, N_s \quad (4)$$

where, t is the time, x_i is the i th component of the position vector. ρ is the density, u_i is the i th component of the velocity, p is the pressure and S_α is the production rate of species α . The scalar field is denoted by $\phi_\alpha \equiv Y_\alpha$, $\alpha = 1, 2, \dots, N_s$, $\phi_\sigma \equiv h = \sum_{\alpha=1}^{N_s} h_\alpha \phi_\alpha$, in which $h_\alpha = h_\alpha^0 + \int_{T_0}^T c_{p\alpha}(T') dT'$, where, h is the static enthalpy, h_α is the heat of formation of species α , h_α^0 is the heat of formation for species α at temperature T_0 and $c_{p\alpha}$ is the specific heat at constant pressure for species α at temperature T_0 . These equations are closed by the constitutive relations (Smooke and Giovangigli, 1991; Kee *et al.*, 1994)

$$\langle p \rangle_l \approx \langle \rho \rangle_\ell R^0 \langle T \rangle_L \sum_1^{N_s} \frac{\langle \phi_\alpha \rangle_L}{W_\alpha} \quad (5)$$

where, R^0 is the universal gas constant, W_α is the molecular weight of species α and T is the temperature.

$$\langle \tau_{ij} \rangle_l \approx \langle \mu \rangle_l \left(\frac{\partial \langle u_i \rangle_L}{\partial x_j} + \frac{\partial \langle u_j \rangle_L}{\partial x_i} - \frac{2}{3} \delta_{ij} \frac{\partial \langle u_k \rangle_L}{\partial x_k} \right), \quad \langle \mu \rangle_l = Pr \langle k/c_p \rangle_l \quad (6)$$

where, μ is the coefficient of viscosity, δ_{ij} is the Kronecker-Delta, Pr is the Prandtl number, k is the thermal conductivity and c_p is the mixture averaged specific heat at constant pressure.

$$\langle J_i^\alpha \rangle_l \approx - \langle \rho \rangle_\ell \langle D \rangle_L \frac{\partial \langle \phi_\alpha \rangle_L}{\partial x_i}, \quad \langle D \rangle_L = \frac{1}{\langle \rho \rangle_\ell Le} \langle \frac{k}{c_p} \rangle_l, \quad \langle \frac{k}{c_p} \rangle_l \approx 2.58 \times 10^{-5} \left(\frac{\langle T \rangle_L}{298} \right)^{0.7} \quad (7)$$

where, D is the molecular diffusion coefficient and Le is the Lewis number.

3.1 SGS Closure

In LES of non-reacting flows the hydrodynamic SGS closure problem is associated with (Rogallo and Moin, 1984) $T_{ij} = \langle \rho \rangle_\ell (\langle u_i u_j \rangle_L - \langle u_i \rangle_L \langle u_j \rangle_L)$ and $M_i^\alpha = \langle \rho \rangle_\ell (\langle u_i \phi_\alpha \rangle_L - \langle u_i \rangle_L \langle \phi_\alpha \rangle_L)$ denoting the SGS stresses and the SGS scalar fluxes, respectively. In reacting flows, an additional model is required for $\langle \rho S_\alpha \rangle_\ell = \langle \rho \rangle_\ell \langle S_\alpha \rangle_L$ ($\alpha = 1, 2, \dots, N_s$) denoting the filtered reaction rates for the mass fractions (with the assumption of low Mach number, $\langle \rho S_h \rangle_\ell = 0$). Modeling of the reaction rates is the subject of main focus in the FMDF formulation as described below. The hydrodynamic SGS closure is based on models which are well-established

in non-reacting flows (Rogallo and Moin, 1984). The term T_{ij} is modeled via,

$$T_{ij} = -2C_{R2}\langle\rho\rangle_\ell\Delta_G E^{1/2} \left(\langle S_{ij} \rangle_L - \frac{1}{3}\langle S_{kk} \rangle_L \delta_{ij} \right) + \frac{2}{3}C_{I2}\langle\rho\rangle_\ell E \delta_{ij} \quad (8)$$

where $E = |\langle u_i^* \rangle_L \langle u_i^* \rangle_L - \langle \langle u_i^* \rangle_L \rangle_{\ell'} \langle \langle u_i^* \rangle_L \rangle_{\ell'}|$, $u_i^* = u_i - \mathcal{U}_i$ and \mathcal{U}_i is a reference velocity in the x_i direction. The subscript ℓ' denotes the filter at the secondary level which has a characteristic size (denoted by $\Delta_{G'}$) larger than that of grid level filter. This model is essentially a modified version of that proposed by Bardina *et al.* (1983), where the grid and secondary filters are of equal sizes. We refer to this as the modified kinetic energy viscosity (MKEV) closure. The subgrid viscosity in Eq. (8) is $\nu_t = C_{R2}\Delta_G \sqrt{|\langle u_i^* \rangle_L \langle u_i^* \rangle_L - \langle \langle u_i^* \rangle_L \rangle_{\ell'} \langle \langle u_i^* \rangle_L \rangle_{\ell'}|}$. A similar diffusivity model is used for the closure of the SGS mass fluxes (Eidson, 1985):

$$M_i^\alpha = -\langle\rho\rangle_\ell D_t \frac{\partial \langle\phi_\alpha\rangle_L}{\partial x_i}, \quad \alpha = 1, 2, \dots, \sigma, \quad D_t = \nu_t / Sc_t \quad (9)$$

3.2 Filtered Mass Density Function (FMDF)

Let $\phi(\mathbf{x}, t)$ denote the scalar array. We define the “filtered mass density function” (FMDF), denoted by F_L , as:

$$F_L(\psi, \mathbf{x}; t) \equiv \int_{-\infty}^{+\infty} \rho(\mathbf{x}', t) \zeta[\psi, \phi(\mathbf{x}', t)] G(\mathbf{x}' - \mathbf{x}) d\mathbf{x}' \quad (10)$$

$$\zeta[\psi, \phi(\mathbf{x}, t)] = \delta[\psi - \phi(\mathbf{x}, t)] \equiv \prod_{\alpha=1}^{\sigma} \delta[\psi_\alpha - \phi_\alpha(\mathbf{x}, t)] \quad (11)$$

where δ denotes the delta function and ψ denotes the composition domain of the scalar array. The term $\zeta[\phi, \psi(\mathbf{x}, t)]$ is the “fine-grained” density (O’Brien, 1980; Pope, 1985), and Eq. (10) implies that the FMDF is the *mass weighted spatially filtered* value of the fine-grained density. The integral property of the FMDF is such that

$$\int_{-\infty}^{+\infty} F_L(\psi, \mathbf{x}; t) d\psi = \int_{-\infty}^{+\infty} \rho(\mathbf{x}', t) G(\mathbf{x}' - \mathbf{x}) d\mathbf{x}' = \langle \rho(\mathbf{x}, t) \rangle_\ell. \quad (12)$$

The FMDF is related to the FDF ($f_L(\psi; \mathbf{x}, t)$) (Colucci *et al.*, 1998)) by $\hat{\rho}(\psi) f_L(\psi; \mathbf{x}, t) = F_L(\psi, \mathbf{x}; t)$. Additionally, it is useful to define the Favre-weighted FDF $\mathcal{F}_L(\psi; \mathbf{x}, t)$ such that $\langle \rho \rangle_\ell \mathcal{F}_L(\psi; \mathbf{x}, t) = \hat{\rho}(\psi) f_L(\psi; \mathbf{x}, t) = F_L(\psi, \mathbf{x}; t)$. For further developments, it is useful to define the mass weighted conditional filtered mean of the variable $Q(\mathbf{x}, t)$ as:

$$\langle Q(\mathbf{x}, t) | \psi \rangle_\ell \equiv \frac{\int_{-\infty}^{+\infty} \rho(\mathbf{x}', t) Q(\mathbf{x}', t) \zeta[\psi, \phi(\mathbf{x}', t)] G(\mathbf{x}' - \mathbf{x}) d\mathbf{x}'}{F_L(\psi, \mathbf{x}; t)}. \quad (13)$$

Equation (13) implies the following properties:

$$(i) \quad \text{For } Q(\mathbf{x}, t) = c, \quad \langle Q(\mathbf{x}, t) | \psi \rangle_\ell = c \quad (14)$$

$$(ii) \quad \text{For } Q(\mathbf{x}, t) \equiv \hat{Q}(\phi(\mathbf{x}, t)), \quad \langle Q(\mathbf{x}, t) | \psi \rangle_\ell = \hat{Q}(\psi) \quad (15)$$

$$(iii) \quad \text{Integral property :} \quad \int_{-\infty}^{+\infty} \langle Q(\mathbf{x}, t) | \psi \rangle_\ell F_L(\psi, \mathbf{x}; t) d\psi \\ = \langle \rho(\mathbf{x}, t) \rangle_\ell \langle Q(\mathbf{x}, t) \rangle_L \quad (16)$$

where c is a constant, and $\hat{Q}(\phi(\mathbf{x}, t)) \equiv Q(\mathbf{x}, t)$ denotes the case where the variable Q can be completely described by the compositional variable $\phi(\mathbf{x}, t) \equiv [\phi_1, \phi_2, \dots, \phi_\sigma]$. From these properties, it follows that the filtered value of any function of the scalar variables (such as $\rho \equiv \hat{\rho}[\phi(\mathbf{x}, t)]$ and $S_\alpha \equiv \hat{S}_\alpha[\phi(\mathbf{x}, t)]$) is obtained by integration over the composition space. It is noted that the mass weighted conditional filtered mean reduces to the conditional filtered mean (Colucci *et al.*, 1998) when the density can be completely expressed in terms of the compositional variables.

By applying the method developed by Lundgren (1969) and others (Pope, 1976; O'Brien, 1980) to Eq. (3) it can be shown that the fine-grained density evolves according to:

$$\frac{\partial \hat{\rho}(\psi) \zeta(\phi, \psi)}{\partial t} + \frac{\partial \hat{\rho}(\phi) u_i(\mathbf{x}, t) \zeta(\phi, \psi)}{\partial x_i} = \frac{\partial \zeta(\phi, \psi)}{\partial \psi_\alpha} \frac{\partial J_i^\alpha}{\partial x_i} - \hat{\rho}(\phi) \frac{\partial}{\partial \psi_\alpha} [\hat{S}_\alpha(\psi) \zeta(\phi, \psi)]. \quad (17)$$

The transport equation for $F_L(\psi, \mathbf{x}; t)$ is obtained by multiplying Eq. (17) by the filter function $G(\mathbf{x}' - \mathbf{x})$ and integrating over \mathbf{x}' space. The final result after some algebraic manipulation is

$$\frac{\partial F_L(\psi, \mathbf{x}; t)}{\partial t} + \frac{\partial [\langle u_i(\mathbf{x}, t) | \psi \rangle_\ell F_L(\psi, \mathbf{x}; t)]}{\partial x_i} = \frac{\partial}{\partial \psi_\alpha} \left[\left\langle \frac{1}{\hat{\rho}(\phi)} \frac{\partial J_i^\alpha}{\partial x_i} | \psi \right\rangle_\ell F_L(\psi, \mathbf{x}; t) \right] \\ - \frac{\partial [\hat{S}_\alpha(\psi) F_L(\psi, \mathbf{x}; t)]}{\partial \psi_\alpha}. \quad (18)$$

The unclosed nature of SGS convection and mixing is indicated by the conditional filtered values in Eq. (18). The convection term is decomposed via

$$\langle u_i | \psi \rangle_\ell F_L = \langle u_i \rangle_L F_L + [\langle u_i | \psi \rangle_\ell - \langle u_i \rangle_L] F_L. \quad (19)$$

The first term on the r.h.s. of Eq. (18) is decomposed as

$$\frac{\partial}{\partial \psi_\alpha} \left[\left\langle -\frac{1}{\hat{\rho}} \frac{\partial}{\partial x_i} \left(\rho D \frac{\partial \phi_\alpha}{\partial x_i} \right) | \psi \right\rangle_\ell F_L \right] = \frac{\partial}{\partial x_i} \left\langle \rho D \frac{\partial \zeta}{\partial x_i} \right\rangle_\ell - \frac{\partial^2}{\partial \psi_\alpha \partial \psi_\beta} \left[\left\langle \rho D \frac{\partial \phi_\alpha}{\partial x_i} \frac{\partial \phi_\beta}{\partial x_i} | \psi \right\rangle_\ell F_L / \hat{\rho} \right]. \quad (20)$$

Substitutions of Eqs. (19) and (20) in Eq. (18) yield:

$$\begin{aligned} \frac{\partial F_L}{\partial t} + \frac{\partial \langle u_i \rangle_L F_L}{\partial x_i} &= \frac{\partial}{\partial x_i} \left\langle \rho D \frac{\partial \zeta}{\partial x_i} \right\rangle_\ell - \frac{\partial^2}{\partial \psi_\alpha \partial \psi_\beta} \left[\left\langle \rho D \frac{\partial \phi_\alpha}{\partial x_i} \frac{\partial \phi_\beta}{\partial x_i} |\psi \right\rangle_\ell F_L / \hat{\rho} \right] \\ &\quad - \frac{\partial [\langle u_i | \psi \rangle_\ell - \langle u_i \rangle_L] F_L}{\partial x_i} - \frac{\partial [\hat{S}_\alpha(\psi) F_L]}{\partial \psi_\alpha}. \end{aligned} \quad (21)$$

This is an exact transport equation for the FMDF. The last term on the right hand-side of this equation is due to chemical reaction and is in closed form. The first term on the right-hand side represents the effects of molecular diffusion of the FMDF in physical space and is approximated as:

$$\frac{\partial}{\partial x_i} \left\langle \rho D \frac{\partial \zeta}{\partial x_i} \right\rangle_\ell \approx \frac{\partial}{\partial x_i} \left[\langle \rho \rangle_\ell \langle D \rangle_L \frac{\partial (F_L / \langle \rho \rangle_\ell)}{\partial x_i} \right] = \frac{\partial}{\partial x_i} \left[\langle \rho \rangle_\ell \langle D \rangle_L \frac{\partial \mathcal{F}_L}{\partial x_i} \right] \quad (22)$$

where $\langle D \rangle_L = D(\langle \phi \rangle_L)$. In this approximation, the correlation between the diffusion coefficients and the scalars is neglected and only the Favre filtered quantities are considered. This is made clear through examination of the first moment:

$$\left\langle \rho D \frac{\partial \phi_\alpha}{\partial x_i} \right\rangle_\ell \approx \frac{\partial}{\partial x_i} \left[\langle \rho \rangle_\ell \langle D \rangle_L \frac{\partial \langle \phi_\alpha \rangle_L}{\partial x_i} \right]$$

as typically used.

The second term on the left-hand side represents convection of the FMDF in physical space and is closed if $\langle u_i \rangle_L$ is known. The second and the third terms on the right-hand side representing the effects of SGS mixing and convection, respectively. These terms are modeled in a manner consistent with conventional LES in non-reacting flows. The SGS convective flux is modeled via:

$$[\langle u_i | \psi \rangle_\ell - \langle u_i \rangle_L] F_L = -\langle \rho \rangle_\ell D_t \frac{\partial (F_L / \langle \rho \rangle_\ell)}{\partial x_i} \quad (23)$$

The advantage of the decomposition (Eq. (19)) and the subsequent model (Eq. (23)) is that they yield results similar to that in conventional LES (Germano, 1992; Salvetti and Banerjee, 1995). The first two Favre moments corresponding to Eqs. (19) and (23) are:

$$\langle u_i \phi_\alpha \rangle_L = \langle u_i \rangle_L \langle \phi_\alpha \rangle_L + [\langle u_i \phi_\alpha \rangle_L - \langle u_i \rangle_L \langle \phi_\alpha \rangle_L], \quad (24)$$

$$\langle \rho \rangle_\ell [\langle u_i \phi_\alpha \rangle_L - \langle u_i \rangle_L \langle \phi_\alpha \rangle_L] = -\langle \rho \rangle_\ell D_t \frac{\partial \langle \phi_\alpha \rangle_L}{\partial x_i} \quad (25)$$

The term within brackets in Eq. (24) is the generalized scalar flux. This makes Eq. (25) identical to Eq. (9).

The closure adopted for the SGS mixing is based on the linear mean square estimation (LMSE) model (O'Brien, 1980; Dopazo and O'Brien, 1976), also known as the IEM (interaction by exchange with the mean): (Borghi, 1988):

$$\frac{\partial^2}{\partial \psi_\alpha \partial \psi_\beta} \left[\left\langle \rho D \frac{\partial \phi_\alpha}{\partial x_i} \frac{\partial \phi_\beta}{\partial x_i} | \psi \right\rangle_\ell F_L / \hat{\rho} \right] = - \frac{\partial}{\partial \psi_\alpha} [\Omega_m (\psi_\alpha - \langle \phi_\alpha \rangle_L) F_L], \quad (26)$$

where $\Omega_m(\mathbf{x}, t)$ is the “frequency of mixing within the subgrid” which is not known *a priori*. This frequency is modeled as $\Omega_m = C_\Omega (\langle D \rangle_L + D_t) / (\Delta_G^2)$. The second moment of Eq. (26) provides an expression for the SGS scalar dissipation of species α :

$$\epsilon_\alpha = 2 \left\langle \rho D \frac{\partial \phi_{(\alpha)}}{\partial x_i} \frac{\partial \phi_{(\alpha)}}{\partial x_i} \right\rangle_\ell = 2 \Omega_m \langle \rho \rangle_\ell (\langle \phi_\alpha^2 \rangle_L - \langle \phi_\alpha \rangle_L^2) \quad (27)$$

where the subscripts in parenthesis are excluded from the summation convention.

With the closures given by Eqs. (23) and (26) and the approximation in Eq. (22), the modeled FMDF transport equation is:

$$\frac{\partial F_L}{\partial t} + \frac{\partial [\langle u_i \rangle_L F_L]}{\partial x_i} = \frac{\partial}{\partial x_i} \left[\langle \rho \rangle_\ell (\langle D \rangle_L + D_t) \frac{\partial (F_L / \langle \rho \rangle_\ell)}{\partial x_i} \right] + \frac{\partial}{\partial \psi_\alpha} [\Omega_m (\psi_\alpha - \langle \phi_\alpha \rangle_L) F_L] - \frac{\partial [\hat{S}_\alpha F_L]}{\partial \psi_\alpha}. \quad (28)$$

This equation may be integrated to obtain transport equations for the SGS moments. The equation for the first subgrid Favre moment, $\langle \phi_\alpha \rangle_L$, and the generalized subgrid variance, $\sigma_\alpha^2 = \langle \phi_\alpha^2 \rangle_L - \langle \phi_\alpha \rangle_L^2$ are:

$$\frac{\partial (\langle \rho \rangle_\ell \langle \phi_\alpha \rangle_L)}{\partial t} + \frac{\partial (\langle \rho \rangle_\ell \langle u_i \rangle_L \langle \phi_\alpha \rangle_L)}{\partial x_i} = \frac{\partial}{\partial x_i} \left[\langle \rho \rangle_\ell (\langle D \rangle_L + D_t) \frac{\partial \langle \phi_\alpha \rangle_L}{\partial x_i} \right] + \langle \rho \rangle_\ell \langle S_\alpha \rangle_L \quad (29)$$

$$\begin{aligned} \frac{\partial (\langle \rho \rangle_\ell \sigma_\alpha^2)}{\partial t} + \frac{\partial (\langle \rho \rangle_\ell \langle u_i \rangle_L \sigma_\alpha^2)}{\partial x_i} &= \frac{\partial}{\partial x_i} \left[\langle \rho \rangle_\ell (\langle D \rangle_L + D_t) \frac{\partial \sigma_\alpha^2}{\partial x_i} \right] \\ &+ 2 \langle \rho \rangle_\ell (\langle D \rangle_L + D_t) \left[\frac{\partial \langle \phi_{(\alpha)} \rangle_L}{\partial x_i} \frac{\partial \langle \phi_{(\alpha)} \rangle_L}{\partial x_i} \right] - 2 \Omega_m \langle \rho \rangle_\ell \sigma_\alpha^2 \\ &+ 2 \langle \rho \rangle_\ell \left(\langle \phi_{(\alpha)} S_{(\alpha)} \rangle_L - \langle \phi_{(\alpha)} \rangle_L \langle S_{(\alpha)} \rangle_L \right). \end{aligned} \quad (30)$$

These equations are identical to those which can be derived by filtering Eq. (3) directly, and adopting Eqs. (25) and (27) for the subgrid flux and the dissipation. In such direct moment closure formulation, however, the terms involving $\langle S_\alpha \rangle_L$ remain unclosed.

Table 1: 25-Step Skeletal Mechanism

	<i>REACTION</i>
1f	$H + O_2 \rightarrow OH + O$
1b	$OH + O \rightarrow H + O_2$
2f	$O + H_2 \rightarrow OH + H$
2b	$OH + H \rightarrow O + H_2$
3f	$H_2 + OH \rightarrow H_2O + H$
3b	$H_2O + H \rightarrow H_2 + OH$
4f	$OH + OH \rightarrow O + H_2O$
4b	$O + H_2O \rightarrow OH + OH$
5	$H + O_2 + M^a \rightarrow HO_2 + M^a$
6	$H + HO_2 \rightarrow OH + OH$
7	$H + HO_2 \rightarrow H_2 + O_2$
8	$OH + HO_2 \rightarrow H_2O + O_2$
9f	$CO + OH \rightarrow CO_2 + H$
9b	$CO_2 + H \rightarrow CO + OH$
10f	$CH_4(+M)^b \rightarrow CH_3 + H(+M)^b$
10b	$CH_3 + H(+M)^b \rightarrow CH_4(+M)^b$
11f	$CH_4 + H \rightarrow CH_3 + H_2$
11b	$CH_3 + H_2 \rightarrow CH_4 + H$
12f	$CH_4 + OH \rightarrow CH_3 + H_2O$
12b	$CH_3 + H_2O \rightarrow CH_4 + OH$
13	$CH_3 + O \rightarrow CH_2O + H$
14	$CH_2O + H \rightarrow HCO + H_2$
15	$CH_2O + OH \rightarrow HCO + H_2O$
16	$HCO + H \rightarrow CO + H_2$
17	$HCO + M \rightarrow CO + H + M$
18	$CH_3 + O_2 \rightarrow CH_3O + O$
19	$CH_3O + H \rightarrow CH_2O + H_2$
20	$CH_3O + M \rightarrow CH_2O + H + M$
21	$HO_2 + HO_2 \rightarrow H_2O_2 + O_2$
22f	$H_2O_2 + M \rightarrow OH + OH + M$
22b	$OH + OH + M \rightarrow H_2O_2 + M$
23f	$H_2O_2 + OH \rightarrow H_2O + HO_2$
23b	$H_2O + HO_2 \rightarrow H_2O_2 + OH$
24	$OH + H + M^a \rightarrow H_2O + M^a$
25	$H + H + M^a \rightarrow H_2 + M^a$

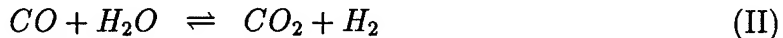
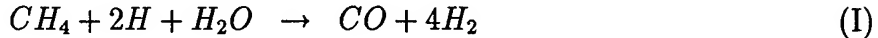
^a Third body efficiencies: $CH_4 = 6.5$, $H_2O = 6.5$, $CO_2 = 1.5$, $H_2 = 1.0$, $CO = 0.75$, $O_2 = 0.4$, $N_2 = 0.4$. All other species=1.0.

^b Lindemann form, $k = k_\infty / (1 + k_{fall}/[M])$ where $k_{fall} = 0.0063 \exp(-18000/RT)$.

3.3 Reaction Mechanisms

The model for the methane oxidation is based on the 25-step skeletal mechanism of Smooke and Giovangigli (1991) (Table 1). This mechanism is described by 10 reversible and 15 irreversible reactions. For lean to stoichiometric methane flames, this mechanism is a sufficiently good representation of the elementary kinetics. Due to the absence of the C_2 -chain, it may be inadequate for the accurate prediction of rich methane flames. Nevertheless, the primary reason for its use here is the relatively few number of species (16) involved in comparison to other more complex mechanisms.

An alternate chemistry model based on the 4-step mechanism of Seshadri and Peters (1988) is also considered. This mechanism is reduced from a set of 22 elementary reactions via the steady state assumption for O , OH , HO_2 , CH_3 , CH_2O and CHO and is given by



where the reaction rates are given by

$$\begin{aligned} \omega_I &= k_{11}[CH_4][H] \\ \omega_{II} &= \frac{k_{10}}{K_3[H_2]} \left([CO][H_2O] - \frac{[CO_2][H_2]}{K_{II}} \right) \\ \omega_{III} &= k_5[O_2][H][M] \\ \omega_{IV} &= k_1[H] \left([O_2] - \frac{[H]^2[H_2O]^2}{[H_2]^3 K_{IV}} \right) \end{aligned} \quad (31)$$

$[M]$ denote the concentration of species M and the subscripts for k refer to the reactions given in Table 1 of Seshadri and Peters (1988). The equilibrium constants are

$$\begin{aligned} K_3 &= 0.2657T^{-0.0247} \exp\left(\frac{15083}{RT}\right) \\ K_{II} &= 3.828 \times 10^{-5} T^{0.8139} \exp\left(\frac{9839}{RT}\right) \\ K_{IV} &= 11.283T^{-0.2484} \exp\left(\frac{11400}{RT}\right). \end{aligned} \quad (32)$$

The selection of the above 4-step mechanism is based on its ease of implementation and reduced number of computational operations. More sophisticated 4-step mechanisms can

also be considered, but the results are not expected to be significantly different.

4 Numerical Simulation Procedure

The complete numerical solution of the equations governing the resolved field is based on a hybrid procedure in which the hydrodynamic Favre-filtered equations (Eqs. (2)-(4)) are discretized by a finite difference method and the modeled FMDF transport equation (34) is simulated via a Lagrangian Monte Carlo procedure. The finite difference discretization procedure is based on the “compact parameter” scheme (Carpenter, 1990) and is not described here. All the finite difference operations are performed on fixed and equally sized grid points. Thus, the filtered values of the hydrodynamic variables are determined on these points. The Monte Carlo procedure is by consideration of “notional particles” whose evolution can be computed from the known filtered field to yield a PDF transport equation which is identical to that of FMDF transport. This is the basis for the concept of *equivalent systems* (Pope, 1985; Pope, 1994). In this context, the notional particles evolve via a “stochastic process” to simulate motion in physical space by convection and diffusion. The compositional values on each particles are changed due to mixing and reaction. These are represented by the stochastic differential equations (SDE) (Risken, 1989; Gardiner, 1990):

$$dX_i(t) = D_i(\mathbf{X}(t), t)dt + E(\mathbf{X}(t), t)dW_i(t), \quad d\phi_\alpha^*(t) = D_\alpha(\phi^*, t)dt. \quad (33)$$

where X_i is the Lagrangian position of the particles, D and E are known as the “drift” and “diffusion” coefficients, and W_i denotes the Wiener-Levy process (Karlin and Taylor, 1981). ϕ_α^* denotes the scalar value of the particle with the Lagrangian position vector X_i . A comparison of the PDF (Fokker Planck) equation corresponding to SDEs (33) with Eq. (28) yields

$$E \equiv \sqrt{2(\langle D \rangle_L + D_t)}, \quad D_i \equiv \langle u_i \rangle_L + \frac{1}{\langle \rho \rangle_\ell} \frac{\partial[\langle \rho \rangle_\ell (\langle D \rangle_L + D_t)]}{\partial x_i}, \quad D_\alpha \equiv -\Omega_m(\phi_\alpha^* - \langle \phi_\alpha \rangle_L) + \hat{S}_\alpha(\phi^*). \quad (34)$$

With this analogy, the FMDF is represented by an ensemble of Monte Carlo particles, each with a set of scalars $\phi_\alpha^{(n)}(t) = \phi_\alpha(\mathbf{X}^{(n)}(t), t)$ and Lagrangian position vector $\mathbf{X}^{(n)}$. A splitting operation is employed in which the transports in physical and compositional domains are treated separately. The simplest means of simulating the spatial transport in Eq. (33) is via the Euler-Maruyama approximation (Kloeden and Platen, 1995):

$$X_i^{(n)}(t_{k+1}) = X_i^{(n)}(t_k) + D_i^{(n)}(t_k)\Delta t + E^{(n)}(t_k)(\Delta t)^{1/2}\xi_i^{(n)}(t_k) \quad (35)$$

where $D_i^{(n)}(t_k) = D_i(\mathbf{X}^{(n)}(t_k))$, $E^{(n)}(t_k) = E(\mathbf{X}^{(n)}(t_k))$ and $\xi_i^{(n)}$ is a Gaussian random variable with zero mean and unit variance. The compositional values are subject to change due to SGS mixing and chemical reaction and are implemented in a split form. This provides an analytical expression for the subgrid mixing. Subsequently, the influence of chemical reaction is determined by evaluating the fine grain reaction rates $S_\alpha^{(n)}$ and modifying the composition of the elements.

The transfer of information from the fixed finite difference point to the location of the Monte Carlo particles is conducted via interpolation. The Favre-filtered statistics are estimated by sampling over particles within a volume centered at the point of interest. Effectively, this finite volume constitutes an “ensemble domain” characterized by the length scale Δ_E (not to be confused with Δ_G) in which the FMDF is discretely represented. The Monte Carlo particles are of non-equal weights to allow a small (or high) number of particles to be imposed in regions where a low (or high) degree of variability is expected.

5 Results and Discussions

The flow configuration consists of a stream of 20 % CH_4 and 80 % N_2 discharging from a planar jet of width d into a coflowing stream of 50 % O_2 and 50 % N_2 . The temperatures of the fuel and oxidizer streams are maintained at 500 K and the Reynolds number based on the inner jet width and velocity is 7,000. The ratio of the jet velocity to that of the coflowing streams is 2. A double hyperbolic tangent function for the u -velocity and the mixture fraction (Z) is assigned at the inlet plane. Based on this Z distribution and the reacting field calculated from a laminar counterflow diffusion flame at a strain rate of 100/s, all the other scalar values are initialized at the inlet. The flow is forced by a low amplitude perturbation at the inlet to promote the formation of large scale structures. The characteristic boundary conditions of Poinsot and Lele (1992) are imposed at the inlet, free-slip boundary conditions are imposed at the cross stream boundaries, and the pressure boundary condition of Rudy and Strikwerda (1980) is imposed at the outflow.

The computational domain covers the region $0 \leq x \leq 10d$ and $-2.5d \leq y \leq 2.5d$. All the simulations are conducted with equal-spaced square grids, *i.e.*, $\delta x = \delta y = \Delta$. LES is conducted with a resolution of 201×101 grid points and DNS is conducted on 801×401 points. In LES, the top-hat filter function (Aldama, 1990) of the form

$$G(\mathbf{x}' - \mathbf{x}) = \prod_{i=1}^2 \hat{G}(x'_i - x_i)$$

$$\hat{G}(x'_i - x_i) = \begin{cases} \frac{1}{\Delta_G} & |x'_i - x_i| \leq \frac{\Delta_G}{2} \\ 0 & |x'_i - x_i| > \frac{\Delta_G}{2} \end{cases} \quad (36)$$

is used in which $\Delta_G = 2\Delta$. The size of the ensemble domain for evaluation of the Favre-filtered quantities is $\Delta_E = 2\Delta$. The total number of Monte Carlo particles in LES is 226125. The Monte-Carlo particles are initially distributed within $-1.25d < y < 1.25d$. Based on the spatial location of the particles, the magnitudes of the scalars are interpolated from the laminar counterflow diffusion flame solution. With the prescription of the filtered fluid density, the particles weights are assigned to yield the proper mass flux across the boundary. The particles are introduced at the inlet at a rate corresponding to the local particle number density and the fluid velocity (with satisfaction of the continuity equation). The reference velocity U_0 in the MKEV model is set to zero in the cross stream direction and to the average of the high and low speed streams in the streamwise direction. The ratio of the filter size at the secondary level to that at the grid level is $\Delta_{G'}/\Delta_G = 3$.

The magnitudes of the molecular parameters are the same as those in typically suggested for methane-air flame with $Pr = 0.75$, $Le = 1$ and c_{p_α} is specified through polynomial fits as functions of the temperature as suggested by the Chemkin thermodynamic database(Kee *et al.*, 1994). The model parameters in LES are $C_I = 0.01$, $C_R = 0.021$, $Sc_t = 0.7$ and $C_\Omega = 10$. No attempt is made to evaluate these constant in a “dynamic manner.” All the LES results are compared with those of DNS. For a consistent comparison, the DNS data are filtered and then downsampled to the same resolution as that used in the LES. Typical DNS requires about 70 hours and typical LES requires about 17 hours on a CRAY-C90 for the 4-step reduced chemistry mechanism. The comparison are made between both the instantaneous and time (Reynolds) averaged data. For constructing of the timed averaged statistics a total of 20000 sample data are considered. These statistics are identified by an overbar in the results presented below.

First for the purposes of flow visualization and a qualitative comparison between the LES and DNS results, the contour plots of the temperature and reacting species field are considered. Figure 1 shows the instantaneous contours of $\langle T \rangle_L$ in the 4-step mechanism and Fig. 2 shows the contours of $\langle Y_H \rangle_L$ in the 25-step mechanism. The results indicate that the instantaneous snapshot from LES are similar to that from the DNS for both chemistry mechanisms. A point to be emphasized here is that when the contribution of the SGS scalar fluctuations are neglected, the calculations become unstable. The qualitative comparisons for all the other species mass fractions and the temperature is the same as that presented in Figs. 1 and 2.

A more quantitative comparison is made in Figs. 3-6 in which the cross stream variations of the Reynolds averaged values of the Favre filtered temperature and mass fractions of H_2O , CO and H are shown at two streamwise locations for the 4-step and the 25-step mech-

anisms. These results (and all the other results not shown) indicate a very good agreement between LES and DNS for the temperature, and the mass fractions of the major and the minor species.

For further comparisons, the instantaneous “scatter” plots as obtained by LES and DNS are presented in Figs. 7-10. In LES, the data points correspond to the stochastic Monte Carlo particles and in DNS they correspond to the values at the fine grid points. Also shown in the figure are the laminar counterflow results at low and high values of the strain rate. The finite-rate chemistry effects as portrayed by the range of the scatter are captured equivalently by DNS and LES. For the most part, the DNS and LES results for the *CO* and the temperature are bounded by the corresponding laminar flame values at high and low strain rates. For the *H* and *OH* radicals, both DNS and LES values are significantly higher than those of the laminar flames for both chemistry mechanisms. Such a “superflamelet” behavior is observed in the measurements of radical species in turbulent *CH₄*, *H₂/CO₂* and *CH₃OH* flames (Masri *et al.*, 1992; Masri *et al.*, 1996). The experimental results also show superflamelet for *CO*. PDF calculations in the context of RANS (Chen *et al.*, 1989; Sion and Chen, 1992) indicate superflamelet behavior for *OH* but not for *CO*. The reasons cited for the discrepancy in *CO* are the possible uncertainties in the measurement of *CO* and also the differential diffusion effects in the turbulent flames (Sion and Chen, 1992). In the present computations, it is noted that *CO* does not exhibit a superflamelet behavior; however, both *H* and *OH* overshoot the flamelet results and the degree of overshoot is significantly higher for *H*. It should be noted that the laminar flamelet calculations include differential diffusion, but the DNS and LES do not. In the flamelet calculations, the Lewis number for *H*, *OH* and *CO* are 0.3, 0.73 and 1.1 respectively. Therefore the assumption of unity Lewis number in the DNS and LES should result in the highest deviation from the flamelet results for *H* and the least deviation for *CO*. This is consistent with the results of present calculations.

Another feature of Figs. 7-10 is the widely different scatter in the results via the 4-step and 25-step mechanisms. The reduced mechanism is derived and validated for fuel and oxidizer stream temperatures of 300 K. The extent of accuracy of this mechanism at higher temperatures is not determined; therefore, a comparison between the 4-step and the 25-step mechanisms should be dealt with caution.

6 Summary and Conclusions

It is demonstrated that the filtered mass density function (FMDF) provides a reliable means of conducting LES of turbulent reacting flows. The primary point of this work is to show that LES of methane combustion is possible and the results are very close to those of DNS but at a fraction of the computational cost. Despite this demonstrated capability of the LES/FMDF, there are several issues which require future investigations. These are summarized here:

- Further assessment of LES is required by comparison with laboratory data. For such comparisons the simulations must be 3D and may require the use of more sophisticated chemistry models. However, DNS of most laboratory flames are not currently possible.
- Similar to PDF methods, the closure problems associated with the FDF are the correlations involving the velocity field (such as SGS stresses and mass fluxes). This may be overcome by considering the joint velocity-scalar FDF.
- The computational requirement for LES/FDF is less than that for DNS. While LES is not claimed to replace DNS, it provides a very attractive alternative for cases in which DNS is not possible. In this regard the computational overhead associated with LES/FDF in comparison to those of “conventional” LES can be tolerated. However, it is important to find ways of reducing the computational costs to make the scheme attractive for practical simulations. This is particularly important for 3D simulations.
- The submodels considered here for the closure of the FDF transport equations are the same as those used in LES of non-reacting flow and/or the PDF methods. Thus the non-universality of the empirical constant appearing in the closure are understandable (and were expected). In this regard, the methodology will benefit from ongoing and future improvements in PDF schemes from both modeling and computational standpoints (Pope, 1994).
- The “superflamelet” behavior for the radical species may be attributed to the unity Lewis number assumption in the calculations.
- Some of the differences between the results obtained by the 4-step and the 25-step mechanisms may be attributed to the high values of the temperature at the fuel and oxidizer streams.

References

Aldama, A. A. (1990). Filtering techniques for turbulent flow simulations. volume 49 of *Lecture Notes in Engineering*. Springer-Verlag, New York, NY.

Bardina, J., Ferziger, J. H., and Reynolds, W. C. (1983). Improved turbulence models based on large eddy simulations of homogeneous, incompressible, turbulent flows. Department of Mechanical Engineering Report TF-19, Stanford University, Stanford, CA.

Borghi, R. (1988). Turbulent combustion modeling. *Prog. Energy Combust. Sci.* **14**, 245–292.

Carpenter, M. H. (1990). A high-order compact numerical algorithm for supersonic flows. In Morton, K. W., editor, *Twelfth International Conference on Numerical Methods in Fluid Dynamics*, volume 371 of *Lecture Notes in Physics*, pages 254–258. Springer-Verlag, New York, NY.

Chen, J.-Y., Kollmann, W., and Dibble, R. W. (1989). PDF modeling of turbulent non-premixed methane jet flames. Technical Report SAND89-8403, Sandia National Laboratories, Albuquerque, NM.

Colucci, P. J., Jaber, F. A., Givi, P., and Pope, S. B. (1998). Filtered density function for large eddy simulation of turbulent reacting flows. *Phys. Fluids* **10**, 499–515.

Dopazo, C. and O'Brien, E. E. (1976). Statistical treatment of non-isothermal chemical reactions in turbulence. *Combust. Sci. and Tech.* **13**, 99–112.

Eidson, T. M. (1985). Numerical simulation of the turbulent rayleigh-benard problem using subgrid modelling. *J. Fluid Mech.* **158**, 245–268.

Gardiner, C. W. (1990). *Handbook of Stochastic Methods*. Springer-Verlag, New York, NY.

Germano, M. (1992). Turbulence: The filtering approach. *J. Fluid Mech.* **238**, 325–336.

Jaber, F. A., Colucci, P. J., James, S., Givi, P., and Pope, S. B. (1997). Filtered mass density function for large eddy simulation of turbulent reacting flows. *J. Fluid Mech.* . submitted.

Karlin, S. and Taylor, H. M. (1981). *A Second Course in Stochastic Processes*. Academic Press, New York, NY.

Kee, R. J., Rupley, F. M., and Miller, J. A. (1994). The Chemkin Thermodynamic Database. Technical Report SAND87-8215B, Sandia National Laboratory, Livermore, CA.

Kloeden, P. E. and Platen, E. (1995). *Numerical Solution of Stochastic Differential Equations*, volume 23 of *Applications of Mathematics, Stochastic Modelling and Applied Probability*. Springer-Verlag, New York, NY.

Lundgren, T. S. (1969). Model equation for nonhomogeneous turbulence. *Phys. Fluids* **12**, 485–497.

Masri, A. R., Dibble, R. W., and Barlow, R. S. (1992). The structure of turbulent non-premixed flames of methanol over a range of mixing rates. *Combust. Flame* **89**, 167–185.

Masri, A. R., Dibble, R. W., and Barlow, R. S. (1996). The structure of turbulent non-premixed flames revealed by Raman-Rayleigh-LIF measurements. *Prog. Energy Combust. Sci.* **22**, 307–362.

O'Brien, E. E. (1980). The probability density function (PDF) approach to reacting turbulent flows. In Libby, P. A. and Williams, F. A., editors, *Turbulent Reacting Flows*, chapter 5, pages 185–218. Springer-Verlag, Heidelberg.

Poinsot, T. J. and Lele, S. K. (1992). Boundary conditions for direct simulations of compressible viscous flows. *J. Comp. Phys.* **101**, 104–129.

Pope, S. B. (1976). The probability approach to modeling of turbulent reacting flows. *Combust. Flame* **27**, 299–312.

Pope, S. B. (1985). PDF methods for turbulent reactive flows. *Prog. Energy Combust. Sci.* **11**, 119–192.

Pope, S. B. (1991). Mapping closures for turbulent mixing and reaction. *Theoret. Comput. Fluid Dynamics* **2**, 255–270.

Pope, S. B. (1994). Lagrangian pdf methods for turbulent flows. *Ann. Rev. Fluid Mech.* **26**, 23–63.

Risken, H. (1989). *The Fokker-Planck Equation, Methods of Solution and Applications*. Springer-Verlag, New York, NY.

Rogallo, R. S. and Moin, P. (1984). Numerical simulation of turbulent flow. *Ann. Rev. Fluid Mech.* **16**, 99–137.

Rudy, D. H. and Strikwerda, J. C. (1980). Boundary conditions for subsonic compressible navier-stokes calculations. *J. Comp. Phys.* **36**, 327–338.

Salvetti, M. V. and Banerjee, S. (1995). A priori tests of a new dynamic subgrid-scale model for finite-difference large-eddy simulations. *Phys. Fluids* **7**, 2831–2847.

Seshadri, K. and Peters, N. (1988). Asymptotic structure and extinction of methane-air diffusion flames. *Combust. Flame* **73**, 23.

Sion, M. and Chen, J. Y. (1992). Scalar pdf modelling of turbulent nonpremixed methanol-air flame. *Combust. Sci. and Tech.* **88**, 89–114.

Smooke, M. D. and Giovangigli, V. (1991). Formulation of the premixed and nonpremixed test problems. In Smooke, M. D., editor, *Reduced Kinetic Mechanisms and Asymptotic Approximations for Methane-Air Flames*, page 1. Springer-Verlag.

Vreman, B., Geurts, B., and Kuerten, H. (1994). Realizability conditions for the turbulent stress tensor in large-eddy simulation. *J. Fluid Mech.* **278**, 351–362.

Williams, F. A. (1985). *Combustion Theory*. The Benjamin/Cummings Publishing Company, Menlo Park, CA, 2nd edition.

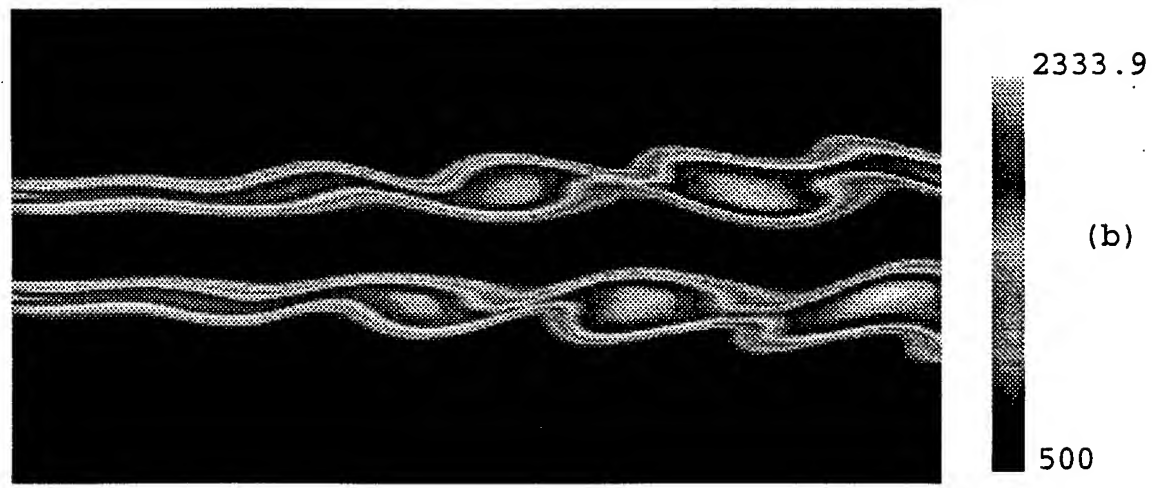
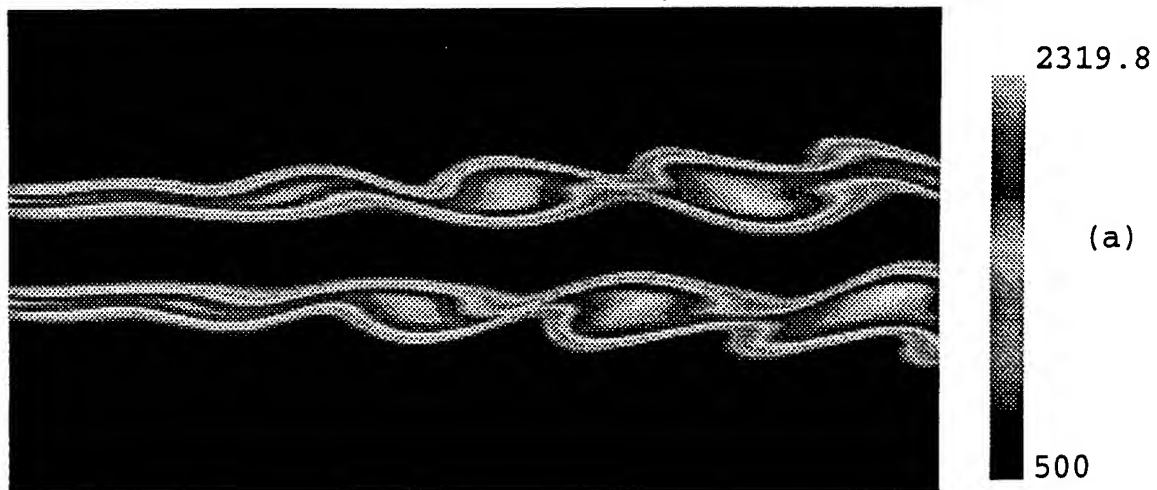


Figure 1: Snapshot of $\langle T \rangle_L$ in the 4-step mechanism (a) DNS (b) LES.

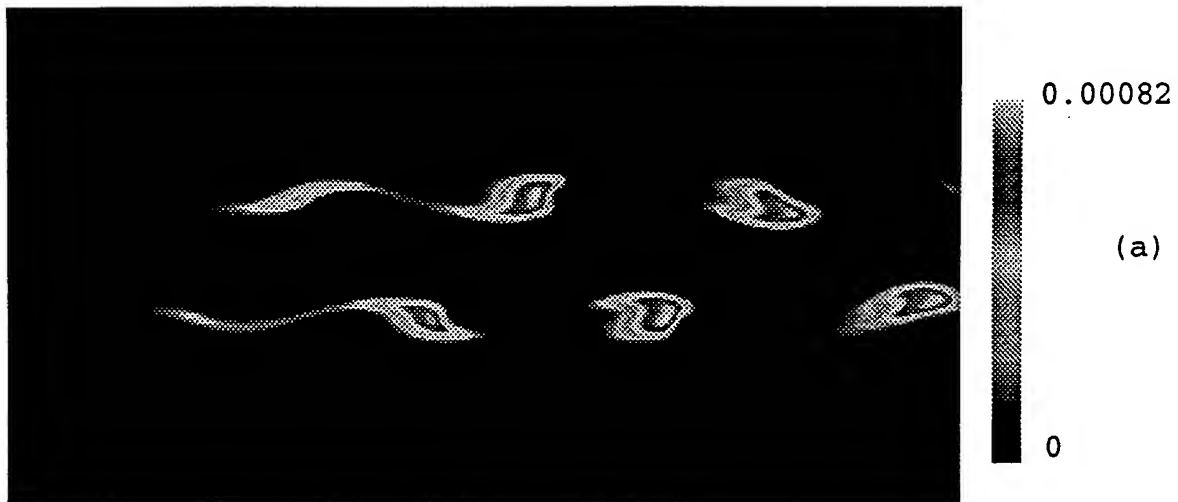


Figure 2: Snapshot of $\langle Y_H \rangle_L$ in the 25-step mechanism (a) DNS (b) LES.

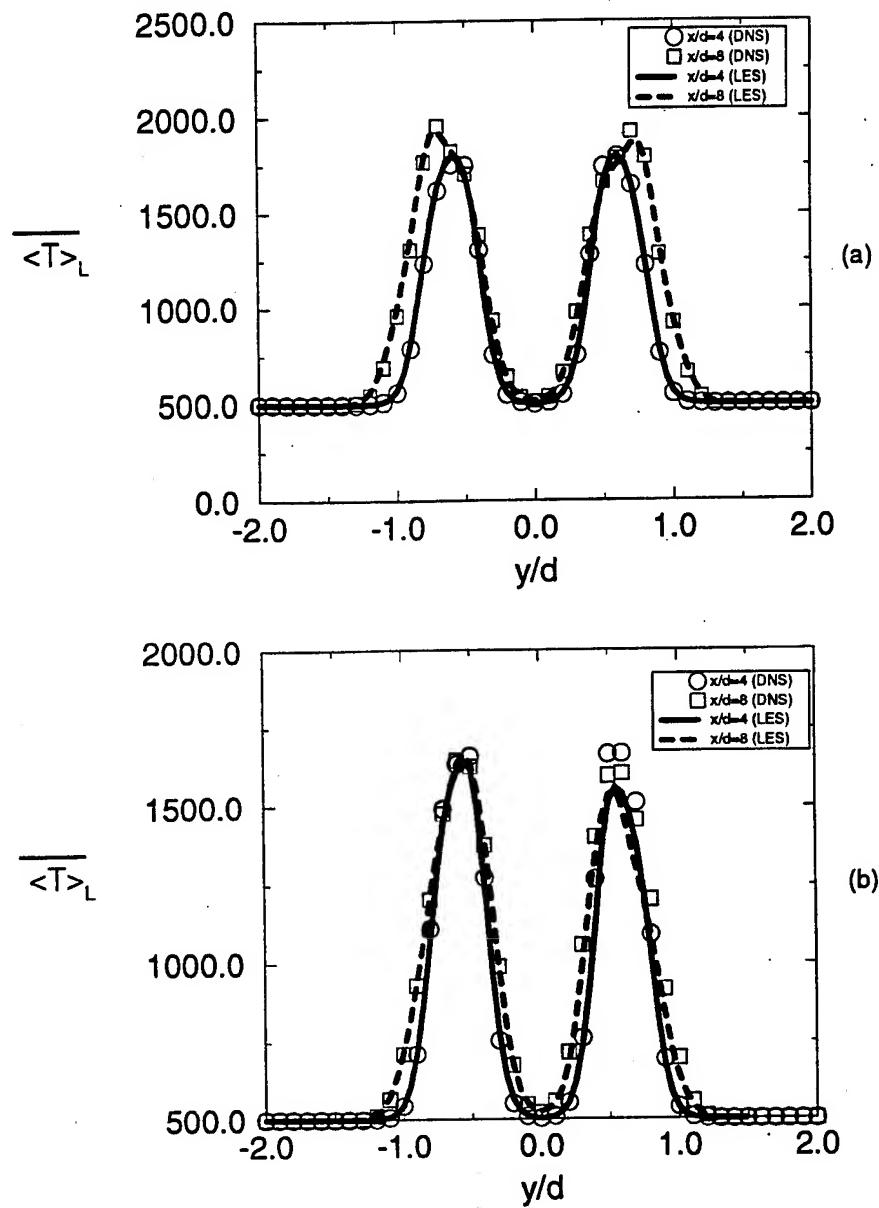


Figure 3: Cross stream variation of the Reynolds averaged $\langle T \rangle_L$ at $x/d = 4, 8$ (a) 4-step mechanism (b) 25-step mechanism.

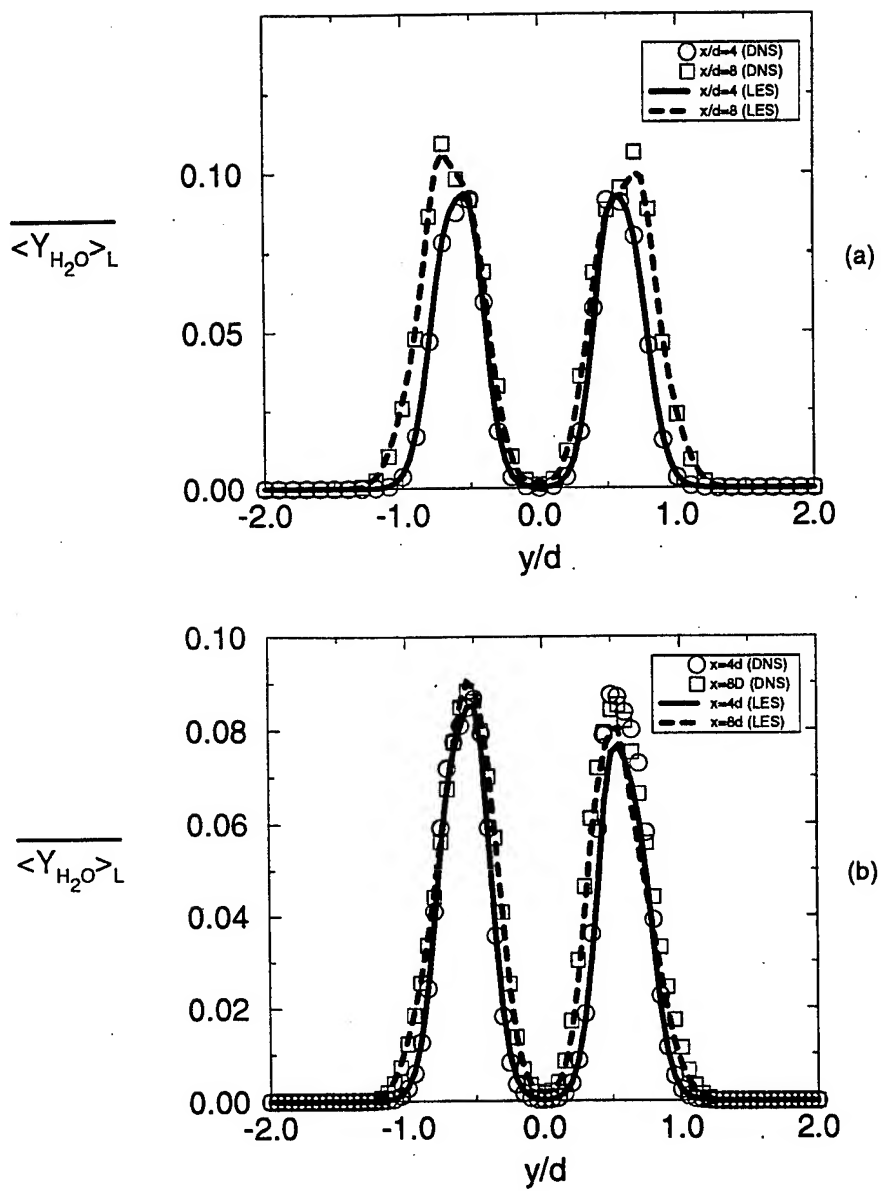


Figure 4: Cross stream variation of the Reynolds averaged $\langle Y_{H_2O} \rangle_L$ at $x/d = 4, 8$ (a) 4-step mechanism (b) 25-step mechanism.

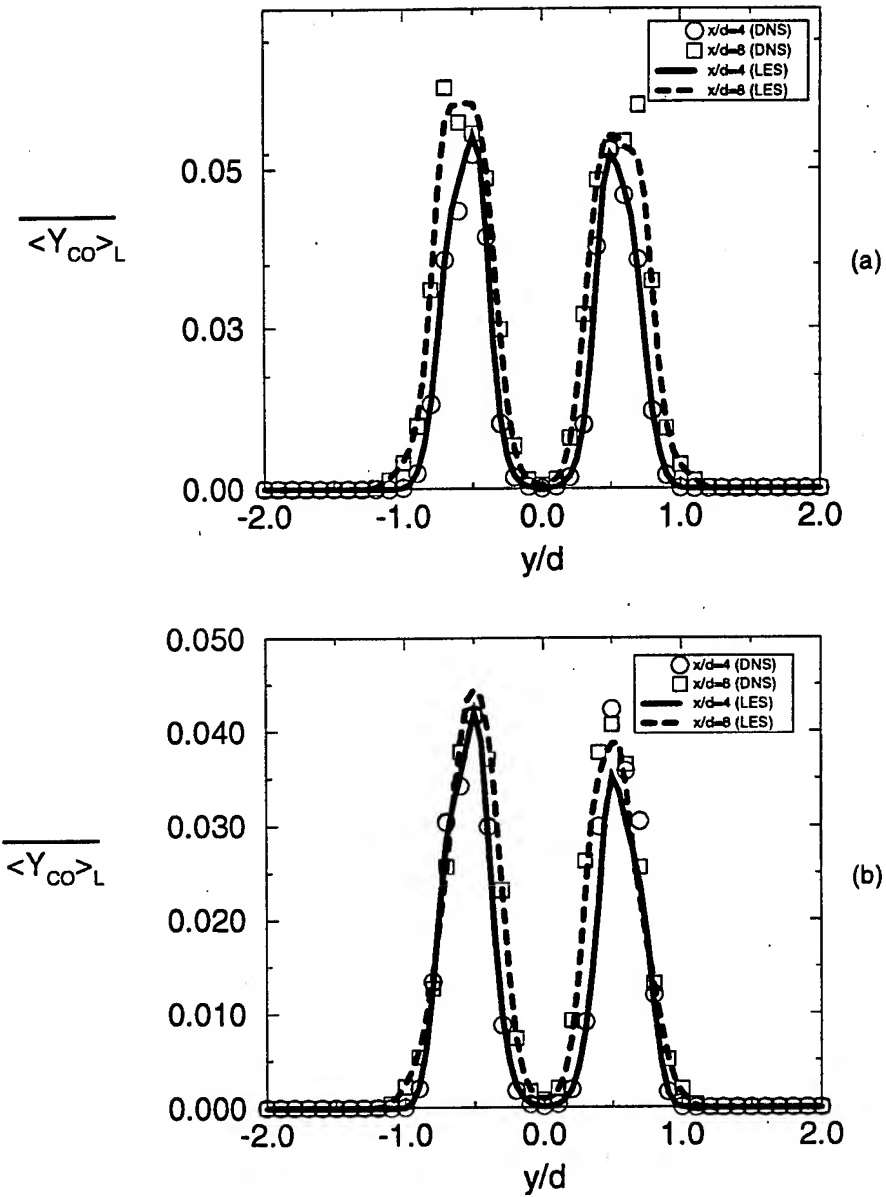


Figure 5: Cross stream variation of the Reynolds averaged $\langle Y_{CO} \rangle_L$ at $x/d = 4, 8$ (a) 4-step mechanism (b) 25-step mechanism.

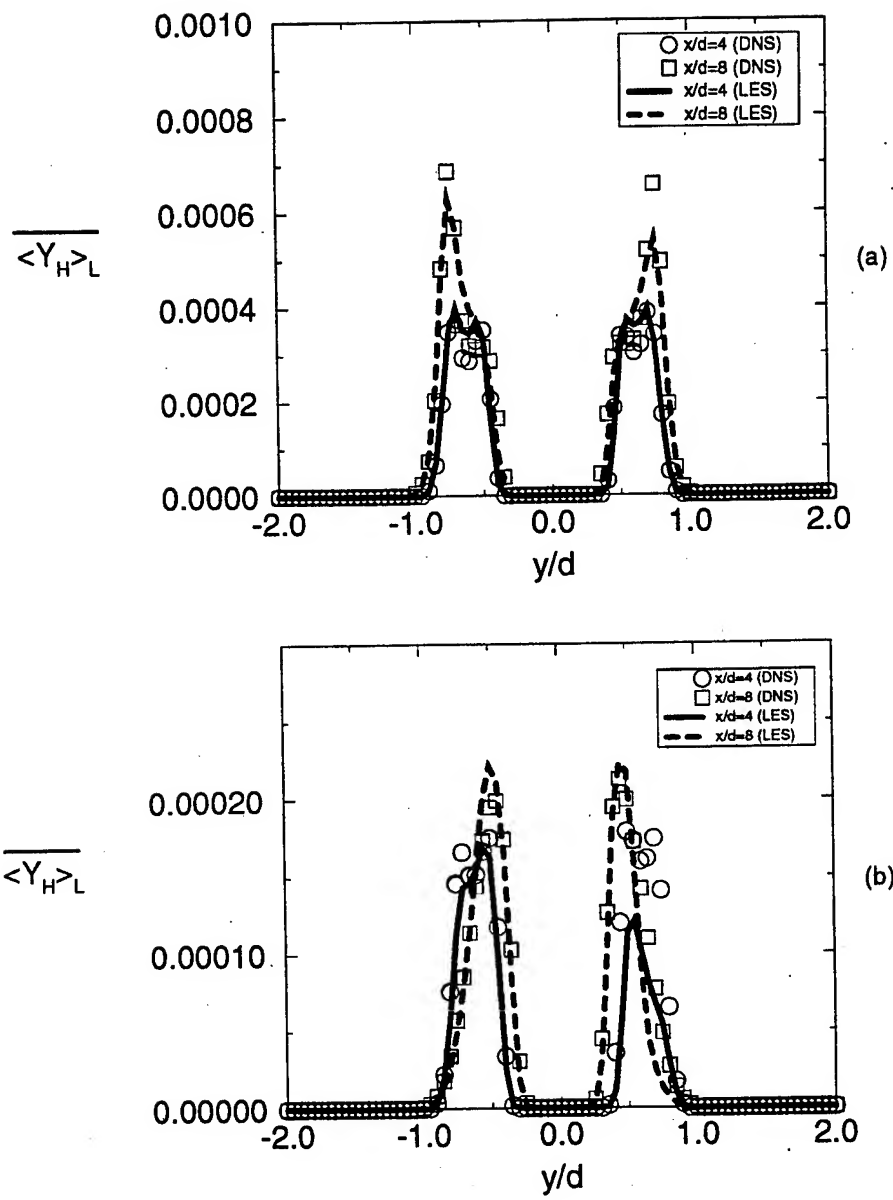


Figure 6: Cross stream variation of the Reynolds averaged $\langle Y_H \rangle_L$ at $x/d = 4, 8$ (a) 4-step mechanism (b) 25-step mechanism.

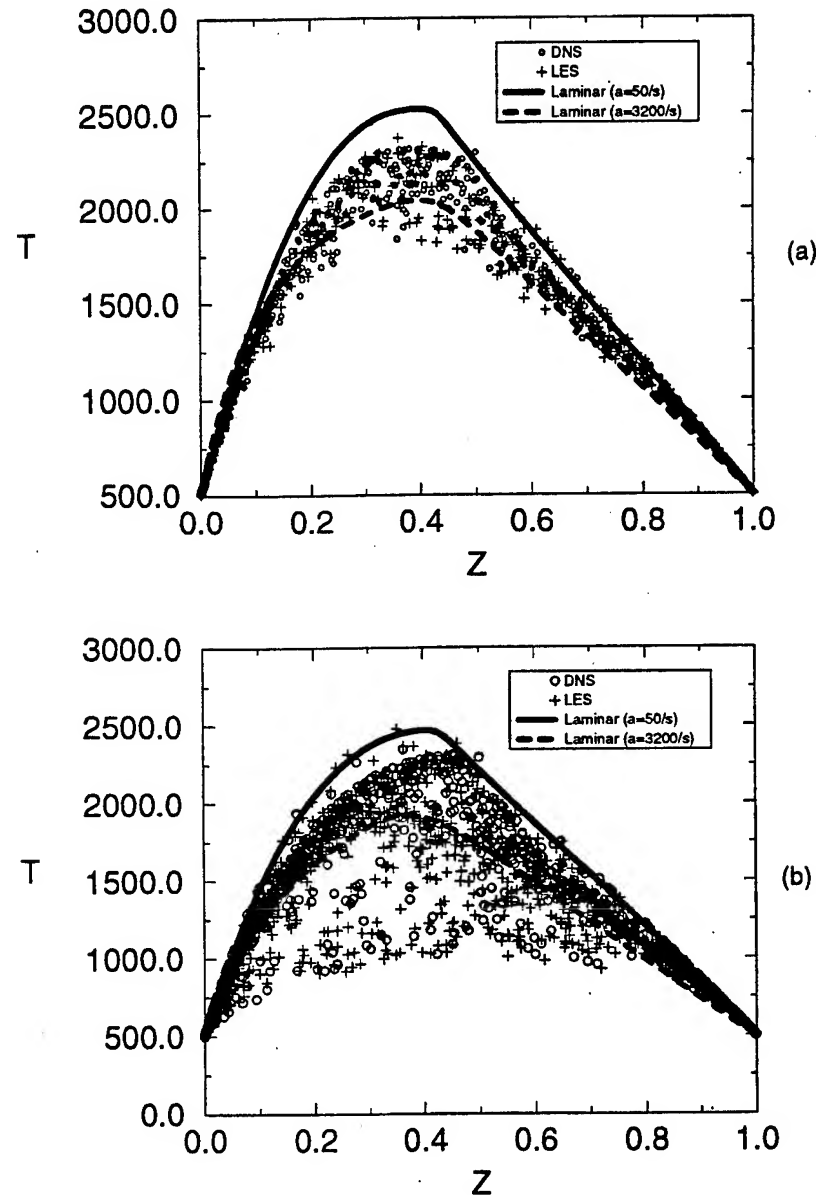


Figure 7: Scatter plot of T (a) 4-step mechanism (b) 25-step mechanism.

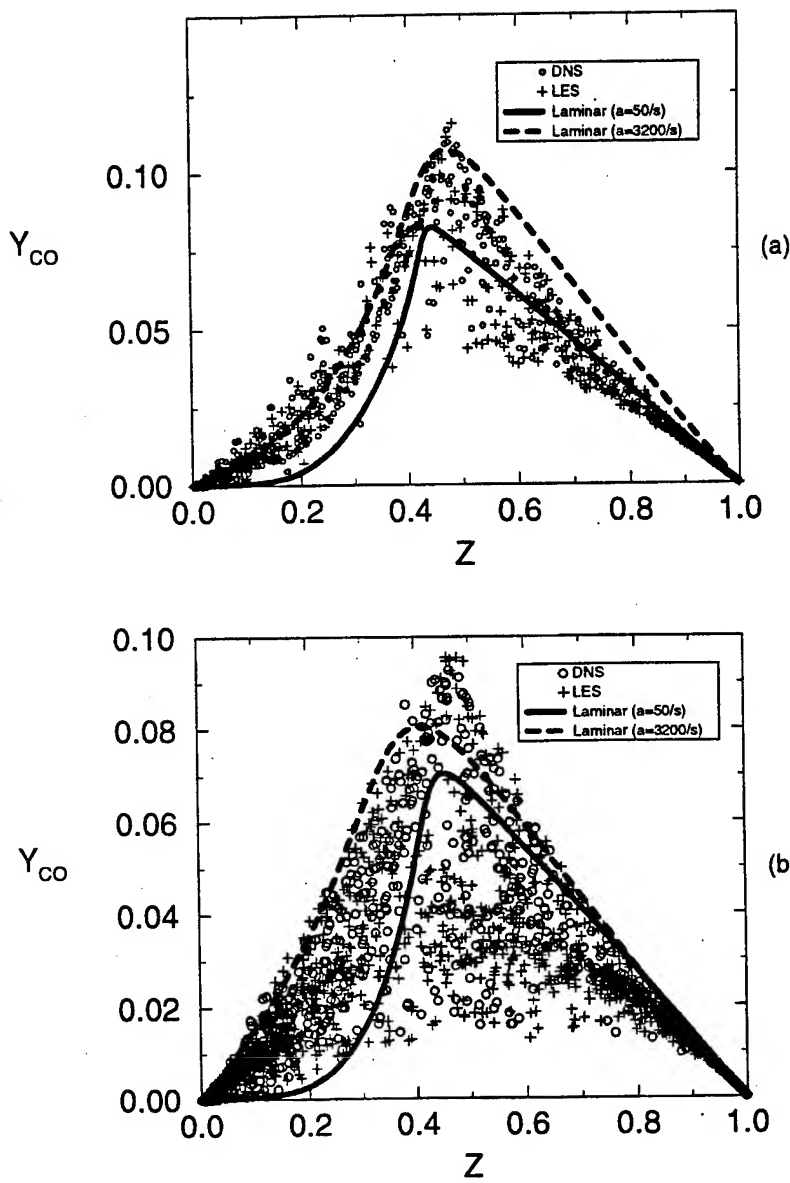


Figure 8: Scatter plot of Y_{CO} (a) 4-step mechanism (b) 25-step mechanism.

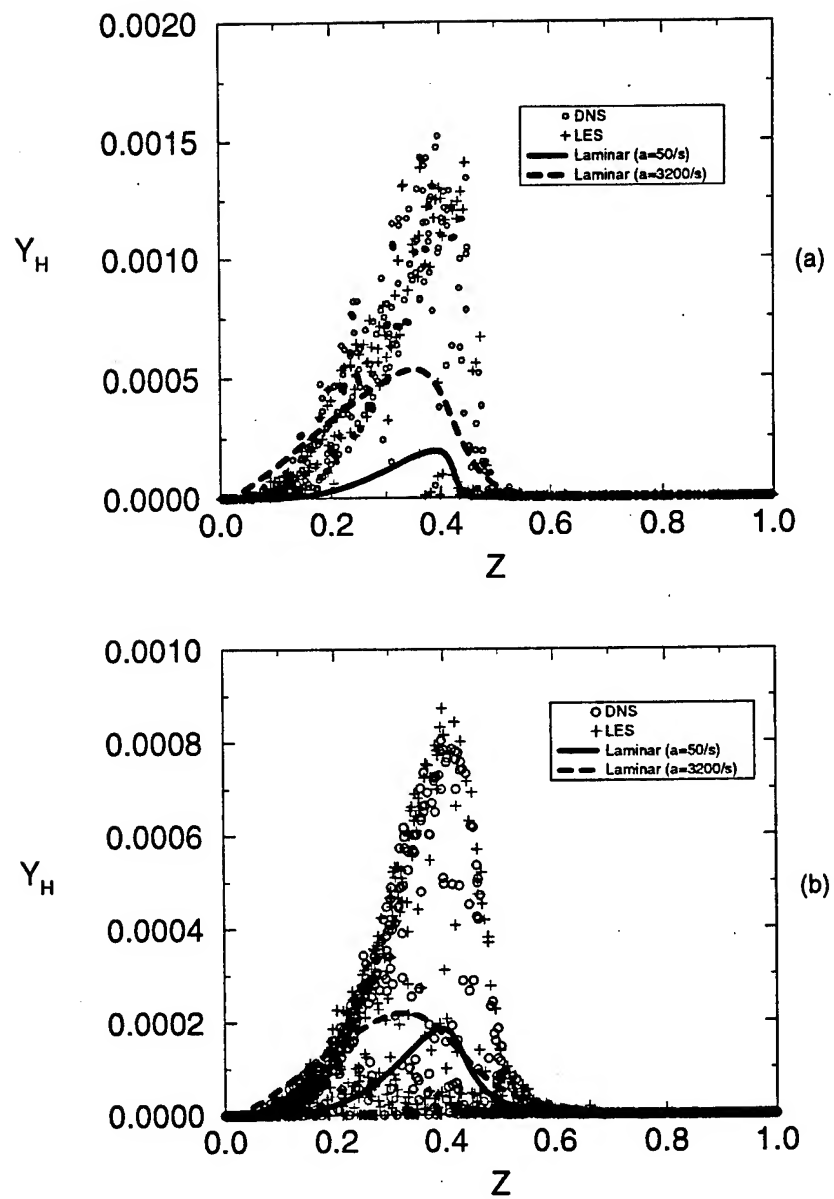


Figure 9: Scatter plot of Y_H (a) 4-step mechanism (b) 25-step mechanism.

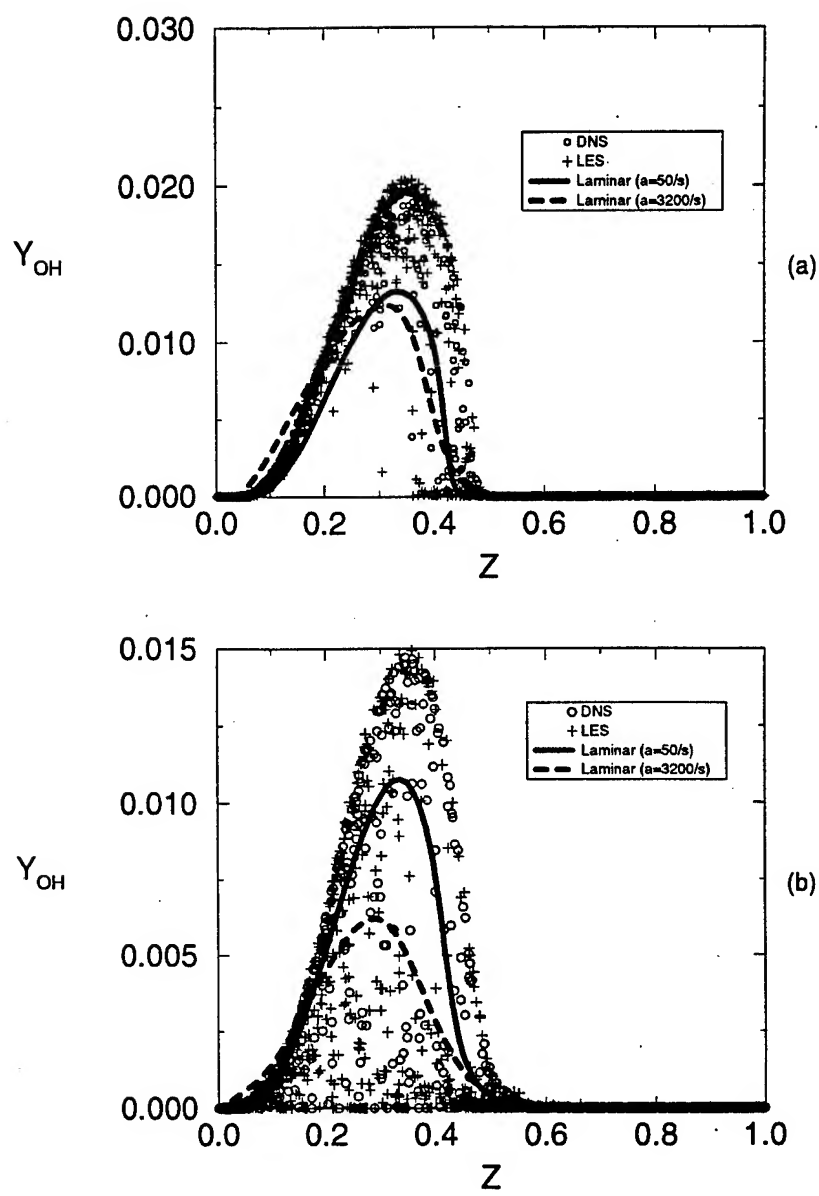


Figure 10: Scatter plot of Y_{OH} (a) 4-step mechanism (b) 25-step mechanism.

APPENDIX VI

Structure of Homogeneous Non-Helical Magnetohydrodynamic Turbulence

Structure of homogeneous nonhelical magnetohydrodynamic turbulence

R. S. Miller,^{a)} F. Mashayek, V. Adumitroaie, and P. Givi

Department of Mechanical and Aerospace Engineering, State University of New York at Buffalo, Buffalo, New York 14260-4400

(Received 10 July 1995; accepted 24 May 1996)

Results are presented for three-dimensional direct numerical simulations of nonhelical magnetohydrodynamic (MHD) turbulence for both stationary isotropic and homogeneous shear flow configurations with zero mean induction and unity magnetic Prandtl number. Small scale dynamo action is observed in both flows, and stationary values for the ratio of magnetic to kinetic energy are shown to scale nearly linearly with the Taylor microscale Reynolds numbers above a critical value of $Re_\lambda \approx 30$. The presence of the magnetic field has the effect of decreasing the kinetic energy of the flow, while simultaneously increasing the Taylor microscale Reynolds number due to enlargement of the hydrodynamic length scales. For shear flows, both the velocity and the magnetic fields become increasingly anisotropic with increasing initial magnetic field strength. The kinetic energy spectra show a relative increase in high wave-number energy in the presence of a magnetic field. The magnetic field is found to portray an intermittent behavior, with peak values of the flatness near the critical Reynolds number. The magnetic field of both flows is organized in the form of "flux tubes" and magnetic "sheets." These regions of large magnetic field strength show a small correlation with moderate vorticity regions, while the electric current structures are correlated with large amplitude strain regions of the turbulence. Some of the characteristics of small scale MHD turbulence are explained via the "structural" description of turbulence. © 1996 American Institute of Physics. [S1070-664X(96)01009-9]

I. INTRODUCTION

Fifty years of widespread scientific investigation have passed since Kolmogorov's original theory of incompressible hydrodynamic (HD) turbulence.¹ Yet, due to its chaotic nature HD turbulence remains among the most complex unsolved problems in classical physics. Even more challenging is the problem of turbulence in electrically conducting fluids obeying the magnetohydrodynamic (MHD) equations.² Nonlinear coupling between the velocity and the magnetic induction fields produces many additional phenomena. In particular, production due to stretching and folding of field lines can lead to growth or sustainment of the magnetic field (the "MHD dynamo" effect^{3,4}). The production effect is a direct result of Maxwell's equations, i.e., an electromotive force is produced through Ohm's law when a conductor moves across magnetic field lines. Unbounded magnetic growth is prevented by the action of the Lorentz force on the velocity field resulting in a so-called saturated field condition.

Some of the earliest theoretical considerations of the dynamo problem suggest that the magnetic Reynolds number is one of the primary parameters in determining the strength (or lack) of field amplification and sustainment.³ Analytic studies of this phenomenon are performed by modeling the nonlinear terms,^{5,6} and by multiple scale analyses.⁷⁻⁹ These studies emphasize the importance of the magnetic helicity in amplifying the dynamo phenomenon. Other early studies enlist second order closure techniques to quantify this effect, and find that a magnetic steady state is achieved above a critical magnetic Reynolds number of order 30.¹⁰ The dy-

namo effect is difficult to observe in the laboratory due to the small values of the magnetic Prandtl number of available conducting fluids; see, e.g., Roberts and Hensen.¹¹ However, direct numerical simulation (DNS) offers a viable alternative to conventional laboratory experiments. Although current supercomputer technology limits DNS to moderate values of flow parameters (e.g., the Reynolds number) many important features of turbulence may be captured by such simulations.^{12,13}

One of the first three-dimensional (3-D) DNS of MHD turbulence is conducted by Pouquet and Patterson.¹⁴ They propose that large scale kinetic energy is transferred to high wave numbers through the traditional cascade process, where it is distributed between the velocity and the magnetic fields by Alfvén waves. In the presence of magnetic helicity the energy then follows an inverse cascade process from the small scales of the magnetic field to the large scales. Due to the turbulence decay, no validation of field sustainment is given; however, rapid field growth during early times of the simulation is observed. One of the first genuine nonlinear simulated dynamo effects is a convection driven dynamo in a spherical shell.¹⁵ This configuration is chosen to study some issues of importance to the solar dynamo. Meneguzzi, Frisch, and Pouquet¹⁶ study stationary isotropic turbulence and observe a small scale dynamo effect in the absence of helicity above a critical magnetic Reynolds number (of order 40). Several numerical simulations of 3-D MHD turbulence confirm that the magnetic Reynolds number is the primary parameter influencing the dynamo effect.^{10,15-17}

The scope of research pertaining to turbulence modification, intermittency, and coherent structures in MHD turbulence is somewhat limited. Most previous numerical simulations are confined to two-dimensional (2-D) flows. Biskamp,

^{a)}Present address: Jet Propulsion Laboratory, California Institute of Technology, Pasadena, California 91109-8099.

Welter, and Walter¹⁸ employ high resolution simulations of 2-D isotropic turbulence to address issues related to intermittency. By adapting the β model¹⁹ they conclude that while second order correlation functions are relatively unaffected by intermittency, the corrections necessary for fourth- and higher-order coefficients become significant. In addition, they observe departures from lognormality for small values of the local energy dissipation, a result in agreement with HD studies (e.g., Miller²⁰). Pouquet, Sulem, and Meneguzzi,²¹ incorporating both 2-D and 3-D simulations, illustrate how the correlations between the velocity and the magnetic fields can damp the energy exchange and reduce the amplitude and the intermittency of the derivative fields. Orszag and Tang²² find that the magnetic field is more intermittent than the velocity field in 2-D MHD turbulence. This observation is verified in 3-D flows for the thermal convection problem,¹⁷ and also in isotropic turbulence.¹⁶ Intermittent magnetic field regions organize into magnetic "flux tube" structures similar to the vorticity tubes of hydrodynamic turbulence. These magnetic structures are observed in 3-D MHD simulations of isotropic turbulence,¹⁶ high symmetry turbulence employing hyperviscosity and hypermagnetic diffusivity,²³ and in compressible stratified convection above a stable overshoot layer.^{24,25}

Although a zero mean magnetic field can be sustained through dynamo action, most MHD flows in nature occur with a mean field. The mean field is typically "slowly" varying with respect to the dynamic fluctuations. Thus, in some cases, it is possible to consider the mean field to be locally steady and uniform. The most obvious effect of a mean magnetic field is to create an anisotropic turbulence state for both the velocity and the magnetic fields. The Lorentz force has zero component parallel to the induction field, and anisotropic states occur due to less restriction of fluid motions parallel to the mean. Shebalin, Matthaeus, and Montgomery²⁶ and Oughton, Priest, and Matthaeus²⁷ investigate the influence of a mean magnetic field in both 2-D and 3-D homogeneous flow simulations. Their results indicate that an externally applied dc field preferentially transfers energy to modes with wave vectors perpendicular to the mean field and also inhibits the development of turbulence. These observations indicate that traditional "return to isotropy" theories may not be applicable to the small scales of naturally occurring MHD turbulence, and that increased understanding of anisotropic MHD turbulence is warranted.

In this article, results are presented of DNS of 3-D homogeneous magnetohydrodynamic turbulence for both stationary isotropic and homogeneous shear flow configurations. For simplicity, only incompressible nonhelical velocity fields and zero mean magnetic fields with magnetic Prandtl number equal to unity are considered. However, many important features of MHD turbulence are captured, including small scale dynamo action, equipartition of energies in the small scales, and effects of the Lorentz force on the velocity field. All MHD simulations are repeated for the case of HD turbulence. The homogeneous shear flow is a relatively simple configuration, and is convenient for the study of anisotropic MHD turbulence in the absence of a mean magnetic field. The specific objectives of the study are to (1) assess

modifications to the turbulence due to the magnetic field, (2) quantify the dynamo effect in both isotropic and homogeneous shear flows, and (3) investigate some issues of importance in relation to coherency and intermittency in MHD turbulence.

II. FORMULATION AND PARAMETRIZATION

The incompressible form of the MHD equations are employed to describe the turbulent transport in both isotropic and homogeneous shear "box" flows. The nondimensional MHD equations for the fluctuation fields (zero mean) are considered in conservative form:

$$\frac{\partial u_j}{\partial x_j} = 0, \quad \frac{\partial b_j}{\partial x_j} = 0, \quad (1)$$

$$\frac{\partial u_i}{\partial t} + \frac{\partial}{\partial x_j} (u_i u_j) = - \frac{\partial p^t}{\partial x_i} + \frac{\partial}{\partial x_j} (b_i b_j) + \frac{1}{Re_0} \frac{\partial^2 u_i}{\partial x_j \partial x_j} + f_i, \quad (2)$$

$$\frac{\partial b_i}{\partial t} + \frac{\partial}{\partial x_j} (b_i u_j) = \frac{\partial}{\partial x_j} (u_i b_j) + \frac{1}{Re_{0m}} \frac{\partial^2 b_i}{\partial x_j \partial x_j}. \quad (3)$$

Here u_i ($i=1,2,3$) denotes the components of the velocity vector \mathbf{u} (boldface indicates a vector), b_i represents the components of the magnetic induction vector \mathbf{b} , and p^t denotes the total pressure. The transport variables are normalized with respect to the reference length (L_0), velocity (U_0), induction (B_0), and density (ρ_0) scales. The nondimensional diffusivity is the inverse of the "box Reynolds number," $Re_0 = U_0 L_0 / \nu$, where ν is the kinematic viscosity. The box magnetic Reynolds number is defined as $Re_{0m} = U_0 L_0 / \nu_m = Pr_m Re_0$, where the ratio of kinetic to magnetic diffusivities is denoted by the magnetic Prandtl number, $Pr_m = \nu / \nu_m$. In Eq. (2), f_i is a forcing term to be discussed below.

Simulations are conducted of both stationary isotropic and homogeneous shear turbulence within the domain $0 \leq x_i \leq L = 2\pi$ ($x_1 \equiv x$, $x_2 \equiv y$, $x_3 \equiv z$). A Fourier pseudospectral method with triply periodic boundary conditions is employed for the spatial discretization of all transport variables. All calculations are performed in Fourier space with the exception of the nonlinear terms, and time advancement is performed using an explicit second order accurate Adams-Basforth technique. The computational routine is capable of simulating both stationary or decaying isotropic, and homogeneous shear flows for either the HD ($\mathbf{b}=0$) or the MHD equations. The computational requirement for the solution of the Navier-Stokes equations (on a Cray-C90 supercomputer) is approximately 0.18, 0.60, 1.25, and 4.80 s per iteration for 32^3 , 48^3 , 64^3 , and 96^3 collocation points, respectively. For the full MHD equations, 0.40, 1.35, 3.2, and 10.8 s per iteration are required for the same respective resolution.

To emulate the stationary isotropic turbulence field, a low wave-number forcing scheme is imposed. This is implemented by adding energy to the large scales of the turbulence at a statistically constant rate, whereby an energy cascade is developed for sufficiently large Reynolds numbers. The energy is then dissipated at high wave numbers at the same rate and a statistically stationary state is achieved. Provided that

there is sufficient separation between the low and high wave numbers, the small scale turbulence is considered to be unaffected by the artificial forcing. The forcing algorithm employed is based on a scheme developed by Eswaran and Pope²⁸ and is described in detail by Miller.²⁰

In homogeneous shear turbulence simulation, a linear mean velocity profile is added to the fluctuating velocity. The primary effect of the mean shear is to provide a natural (albeit idealistic) homogeneous forcing. In contrast to the isotropic case, no stationary state is achieved and the Reynolds number grows until the turbulence structures outgrow the box size. The magnitude of the imposed shear is given with the amplitude of the mean gradient, in this case $Y=dU_1/dx_2=\text{const}$ (where U_1 denotes the mean component of the velocity in the $i=1$ direction). In order to use the Fourier spectral method, the governing equations are solved for their fluctuating quantities on a grid which deforms with the mean flow. The transformation is an extension of the procedure employed by Rogallo²⁹ for HD turbulence and details of its implementation of MHD flows are provided by Miller.²⁰ The mean shear imposed by the grid transformations skews the grid in time. In order to allow the simulation to progress for a substantial time, it is necessary to remesh the grid at regular intervals. Aliasing errors introduced by the remesh process are removed via a truncation of the variables in Fourier space outside of the spherical wave-number shell of magnitude $\sqrt{2}N/3$, where N is the number of collocation points in any direction. This results in a slight loss of kinetic and magnetic energy; however, if the simulation is well resolved this truncation is considered to be negligible. The simulations are performed until the length scales of the turbulence become too large to be accurately resolved, at which time the simulation is terminated.

Both the velocity and magnetic fields are initialized as random Gaussian, isotropic, and solenoidal fields. Non-mirror-symmetric \mathbf{b} fields with arbitrary magnetic helicities are generated by the method described in Pouquet and Patterson.¹⁴ The relative magnitude of the helicity is specified through the correlation coefficient of the \mathbf{b} field and its vector potential \mathbf{a} ($\mathbf{b}=\nabla\times\mathbf{a}$): This coefficient is defined as $C(\mathbf{a},\mathbf{b})=\langle a_i b_i \rangle / \sqrt{\langle a_j a_j \rangle \langle b_k b_k \rangle}$, where the angular brackets ($\langle \rangle$) indicate an ensemble average over all grid points. The initial energy for the velocity is $E_v=\langle u_i u_i \rangle = 3$ in all cases. The forcing amplitude ($A_F=1.25$), forcing radius ($K_F=2\sqrt{2}$), and the magnitude of the mean velocity gradient ($Y=2$) are kept fixed for the respective flows. In the isotropic simulations, an initial kinetic energy spectrum having $E'_v(k) \sim k^{-5/3}$ (the prime indicates the energy spectra as a function of the wave-number magnitude) is imposed. This choice is somewhat arbitrary since the asymptotic statistical state of the turbulence is independent of the initial conditions, and is primarily dependent on the forcing parameters and the box Reynolds number. For the shear (SHR) flow simulation cases, the velocity field and all of the magnetic fields are specified with a spectrum $\sim k^4 \exp[-2(k/k_s)^2]$, where the parameter k_s specifies the wave-number location for the maximum amplitude of the energy spectrum. The value $k_s=7$ is chosen for the initial velocity spectrum in all shear simulations, whereas k_s is varied for the magnetic fields in

TABLE I. Conditions for the ISO simulations. All simulations are repeated with $E_m=0$.

	Re_0	E_M/E_V	k_s	$C(\mathbf{a},\mathbf{b})$	N	$\Delta t (\times 10^{-3})$	t_{final}	τ_e	ηk_{\max}
IRun0	200	0.01	7	0	96	2.5	45	1.80	1.65
IRun1	150	0.01	7	0	64	3.75	56	1.51	1.28
IRun2	150	1.00	7	0	64	3.75	56	1.50	1.24
IRun3	150	0.01	2	0	64	3.75	56	1.51	1.29
IRun4	150	0.01	7	1	64	3.75	56	1.49	1.22
IRun5	110	0.01	7	0	64	3.75	70	1.41	1.48
IRun6	60	0.01	7	0	48	5.0	70	1.33	1.43
IRun7	40	0.01	7	0	48	5.0	120	1.47	1.84
IRun8	20	0.1	7	0	32	7.5	150	1.52	1.98
IRun9	10	0.1	7	0	32	7.5	150	2.07	3.33

order to study its influence. Detailed studies of the effects of both the initial conditions and the rate of shear have been conducted by Rogallo²⁹ for HD flows.

A listing of all the simulation parameters are provided in Table I for the isotropic (ISO) flow simulations and in Table II for the SHR flow simulations. The labels in the first column of each table are preceded by "I" and "S" for the ISO and the SHR flow simulations, respectively. The information listed for each simulation includes the box Reynolds number (Re_0), the ratio of initial magnetic and kinetic energies (E_m/E_V , where $E_m=\langle b_i b_i \rangle$), the wave number of maximal initial magnetic energy (k_s), the magnetic helicity, the grid resolution, the time step, the duration of simulation, the eddy turnover time (τ_e), and the resolution parameter (ηk_{\max}). The eddy turnover time is defined as the ratio of the integral length scale to a characteristic velocity:

$$\tau_e = \frac{\Lambda}{u_{\text{rms}}}, \quad \Lambda = \frac{3\pi}{2E_v} \int_0^{k_{\max}} \frac{E'_v(k)}{k} dk. \quad (4)$$

where the subscript rms denotes the root mean square (u_{rms} is calculated as the average of the rms of all three velocity components) and Λ is the integral length scale. The resolution parameter is the product of the Kolmogorov length scale [$\eta=(\nu^3/\epsilon)^{1/4}$, $\epsilon=2\nu s_{ij} s_{ij}$, where the symmetric rate of strain tensor is $s_{ij}=(u_{i,j}+u_{j,i})/2$ and the derivative notation is $u_{i,j}=\partial u_i / \partial x_j$] and the maximum resolved wave number (k_{\max}). The box Reynolds number, the grid resolution, and the time step are held constant for the SHR flow simulations and take the values $Re_0=200$, $N=96$, and $\Delta t=2.5 \times 10^{-3}$. For all cases the magnetic Prandtl number is $Pr_m=1$, in which case η represents the smallest length scale of both the turbulence and the magnetic field. The values given for both τ_e and ηk_{\max} correspond to time averaged values for the

TABLE II. Conditions for the SHR simulations. $Re_0=200$, $N=96$, $\Delta t=2.5 \times 10^{-3}$.

	E_M/E_V	k_s	$C(\mathbf{a},\mathbf{b})$	t_{final}	τ_e	ηk_{\max}
SRun0	5	1.05	1.16
SRun1	0.01	7	0	6	1.18	1.26
SRun2	0.1	7	0	6	1.48	1.45
SRun3	1.00	7	0	6	2.06	1.74
SRun4	0.01	2	0	6	1.39	1.34
SRun5	0.01	7	1	6	1.17	1.25

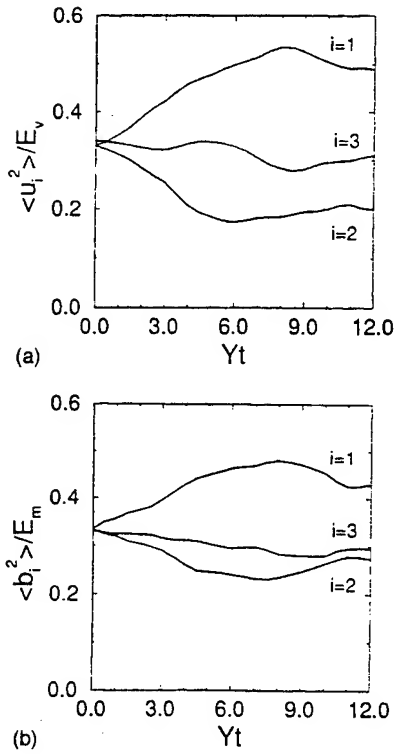


FIG. 1. Temporal evolution of the relative component energies for the homogeneous shear simulation SRun1: (a) kinetic energy, (b) magnetic energy.

stationary ISO runs in the presence of the magnetic field. For the SHR simulations, these parameters are given at the time when the relative energy of the u_1 velocity component reaches its maximal value (discussed below). All of the ISO MHD cases corresponding to different Re_0 values are repeated with purely HD flow, and SRun0 represents a purely HD case having the same parameters as cases SRun1–SRun5.

III. RESULTS

In each of the ISO simulations, the equations governing the hydrodynamics are first integrated forward in time for a minimum of five eddy turnover times to reach a stationary state. At this time, the magnetic field is added to begin the simulation or, in the HD cases, the integration is continued for more than 10 eddy turnover times to calculate time averaged statistics. The MHD simulations are conducted for a sufficient duration to determine the existence of stationary magnetic states. Those simulations which attain stationary states are continued for more than 10 additional eddy turnover times so that time averaging can be performed on the data. Time is normalized by the HD eddy turnover time (t/τ_e) for the ISO flow simulations.

For the SHR flow cases, the mean shear is directly applied to the initial isotropic fields. No stationary states exist in this flow; however, energy component ratios (relative energies) are known to attain approximate “asymptotic” values as indicated in previous HD simulations (e.g., Rogers and Moin³⁰). This is observed to be the case in the MHD flow also. Figure 1 portrays an example of this effect for case

SRun1 (time is normalized via the mean shear magnitude for the SHR flow simulations). The relative energy of a vector component is defined as the ratio of the variance of that particular component relative to the total vector energy, i.e., $\langle u_i^2 \rangle / E_v$ and $\langle b_i^2 \rangle / E_m$. The time at which the ratio $\langle u_i^2 \rangle / E_v$ reaches a maximum value is denoted as the “peak time.” Note that the relative energies of all components of both the \mathbf{u} and \mathbf{b} fields are initially about $\frac{1}{3}$, due to the initial isotropic conditions.

Comprehensive resolution studies have been conducted to assess the effects of grid resolution on both the time averaged ISO simulation statistics and on the temporal evolution for the SHR flows. Two of the low Reynolds number cases, IRun6 and IRun8, were repeated with 16^3 , 24^3 , 32^3 , 48^3 , and 64^3 grid points and case IRun1 was repeated with 32^3 , 48^3 , and 96^3 grid points. In addition, the SHR flow resolution was investigated by repeating case SRun1 with 48^3 , 64^3 , and 128^3 grid points. In all cases, the magnetic field moments are more sensitive to resolution than the equivalent statistics of either the velocity field or its gradients. An evaluation of statistical moments as large as fourth order reveals that the parameter ηk_{\max} is the primary parameter for the resolution consideration. Results from the larger Reynolds number ISO and SHR cases indicate that adequate resolution is obtained for $\eta k_{\max} \approx 1.2$ and larger. This is in agreement with previous findings in the case of HD stationary turbulence.²⁸ However, for smaller ISO grid sizes (IRun6 and IRun8) a larger resolution is necessary to yield accurate statistics for the magnetic field; $\eta k_{\max} \approx 1.4$ and larger. This is a result of the relatively small separation between the smallest scales of the turbulence and the forcing scales. All of the results indicate that the simulations listed in the tables are sufficiently resolved, and the results presented hereinafter are independent of the grid size.

A. Effects of initial conditions

For both the ISO and SHR simulations, a variety of initial conditions are considered to study the effects of the initial ratio of the magnetic and hydrodynamic energies, the initial length scale of the magnetic field, and the initial magnetic helicity on flow evolutions. This is particularly important in the ISO simulations, as it is important to establish that stationary states are independent of initial conditions before making quantitative comparisons. The SHR flow does not relax to a steady state condition; therefore, it is expected that the effects of initial conditions will prevail throughout the simulated times considered here.

Simulations IRun1 through IRun4 are considered to establish the independence of ISO steady state results to initial conditions. Figure 2 presents the time evolution of both the energy ratio (E_m/E_v) and the magnetic enstrophy ($H_m = \langle j_i j_i \rangle$, where $\mathbf{j} = \nabla \times \mathbf{b}$ is the electric current density) for a duration of approximately 37 eddy turnover times. It appears that both quantities asymptotically approach the steady state condition. Analysis of other quantities (not shown here) confirms that this is the case. However, the early temporal evolutions are highly dependent on the initial \mathbf{b} fields. Figure 2 is also useful in assessing the effects of the initial conditions at early times. Simulations IRun1 and

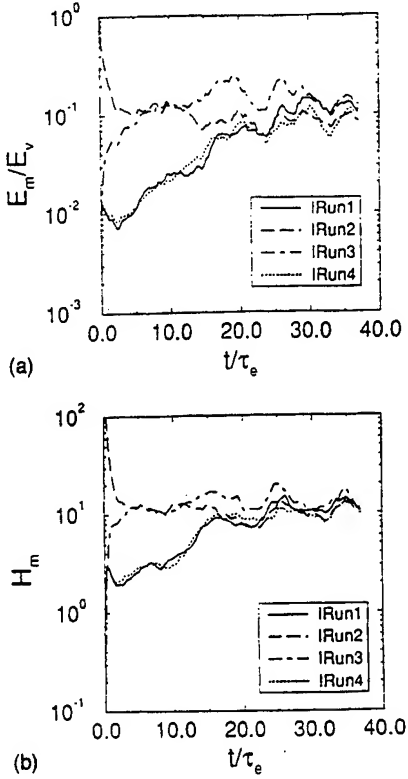


FIG. 2. Effect of initial conditions on the stationary isotropic simulations as shown by the temporal evolutions of (a) the energy ratio and (b) the magnetic enstrophy.

IRun3 contain initially relatively small scale ($k_s=7$) and large scale ($k_s=2$) magnetic fields, respectively, and otherwise have identical parameters [$E_m/E_v=0.01$ and $C(a,b)=0$]. The early time behavior of both the energy ratio and the magnetic enstrophy exhibits substantially larger initial growth rates for the large scale \mathbf{b} field (IRun3). The expected value of the magnetic dissipation is the primary parameter affecting the early time evolutions of these fields. The relatively large energy at high wave numbers in simulation IRun1 results in a mean dissipation which is more than an order of magnitude larger than that of IRun3 with an initially large scale field (the respective values are $\langle \epsilon_m \rangle = v_m \langle b_{i,j} b_{i,j} \rangle = 6.81 \times 10^{-3}$ and 6.38×10^{-4}).

The early time effects of initial magnetic helicity are also illustrated in Fig. 2 by the data of simulations IRun1 and IRun4. The temporal evolutions of both the energy ratio and the magnetic helicity are nearly independent of the initial magnetic helicity. This is due to the absence of any mechanism by which the magnetic helicity can be supported. The correlation between the \mathbf{b} field and its potential in simulation IRun4 decreases to less than 10% of its initial value in less than two eddy turnover times. Note that case IRun2 with an initial unity energy ratio is observed to decay rapidly towards the same approximate stationary state as cases IRun1, IRun3, and IRun4. The long time fields are thus considered to be independent of initial conditions and, of these runs, only the time averaged data of simulation IRun1 are considered in the remainder of the article.

The above discussion of the early time effects of the

magnetic field initial conditions is also applicable to the SHR configuration. However, in these flows the hydrodynamic field also experiences rapid modifications at early times due to the action of the applied mean velocity gradient, and no stationary state exists. Due to the action of the Lorentz force, additional initial condition effects with regard to turbulence modification are expected. As such, the effects of initial conditions are felt throughout the simulations.

B. Integral flow statistics

For the ISO cases, the statistical analyses of the data are most often conducted in terms of both spatial and temporal averaging (when stationary states exist). Statistics gathered from several simulations can be used to study the effects of the flow parameters. There are a number of choices by which to parametrize the problem, including the box size, the integral length scale, and the Taylor microscale Reynolds numbers (Re_λ), etc. Analysis of the data indicates that Re_λ yields the most insight into the problem. For SHR flows Re_λ is based on the Taylor microscale (λ_1) in the x_1 direction ($\lambda_\alpha^2 = \langle u_\alpha^2 \rangle / ((\partial u_\alpha / \partial x_\alpha)^2)$) (no summation over repeated Greek indices hereinafter) and the turbulent velocity scale ($\sqrt{E_v}$). For ISO flows the Reynolds number is defined as the average over all three directions x_ξ with corresponding length and velocity scales λ_ξ and $\sqrt{\langle u_\xi^2 \rangle}$, respectively. Results for the SHR runs are presented as both temporal evolutions and occasionally in the form of tabular data at the peak times of the simulations.

Leorat, Pouquet, and Frisch¹⁰ find a bifurcation to a magnetic state in their eddy damped quasinormal Markovian (EDQNM) approximation study of nonhelical MHD turbulence above a critical magnetic Reynolds number of a few tens. Figure 3 presents both the Reynolds number (in ISO) and temporal (in SHR) dependence of the kinetic, the magnetic and the total ($E_t = E_v + E_m$) energies. The data in both figures are normalized by the kinetic energy of the purely HD flow (SRun0 for the SHR flow). The ISO results are in good qualitative agreement with the EDQNM predictions¹⁰ and show a transition to "magnetic states" occurring at a critical Reynolds number of $Re_{\lambda,c} \approx 30$. Above this critical value, sustained \mathbf{b} fields are observed, and both the kinetic and total energies decrease with the Reynolds number. The transition is more gradual in the present results than that predicted by the EDQNM approximation. The SHR data correspond to case SRun4 having a large scale initial \mathbf{b} field with 1% energy ratio. In this simulation, the initial seed magnetic field is rapidly amplified in the early stages of development and then gradually decreases. Note that no conclusions can be made from this figure in regard to a sustained dynamo effect for the SHR simulation. This is because the energies are normalized by the kinetic energy of the HD simulation. However, these results do illustrate several effects of the \mathbf{b} field. In both the ISO and the SHR cases the presence of the magnetic field acts to damp the turbulence energy (also observed in all the other SHR simulations). In addition, the normalized kinetic energy for the SHR simulation reaches a nearly constant value after $Yt \approx 2$.

Time averaged values of the steady state ISO energy

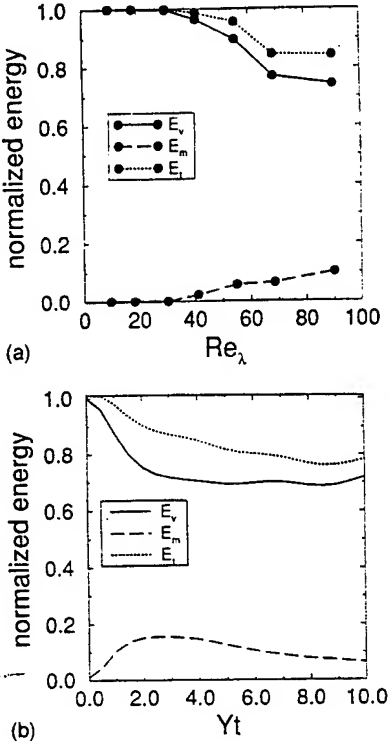


FIG. 3. Development of the kinetic, magnetic, and total energies as normalized by the purely hydrodynamic kinetic energy E_v (HD). (a) ISO simulation time averaged results as a function of the Reynolds number for cases IRun0, 1, 5, 6, 7, 8, and 9 (right to left) and (b) temporal evolution of SHR simulation, case SRUn4.

ratios in MHD turbulence are listed in Table III as a function of various Reynolds numbers (the normalization is with the MHD E_v). The ratios for the higher Reynolds number cases ($E_m/E_v \sim 0.1$ for $Re_\lambda \approx 100$) are in accord with the results of Meneguzzi, Frisch, and Pouquet.¹⁶ When presented graphically (not shown), the energy ratios portray a nearly linear dependence on the Taylor microscale Reynolds number for the range of parameters considered. A very weak magnetic field is sustained for case IRun7 with $Re_\lambda = 30.3$ (for more than 100 HD eddy turnover times), while the two simulations with lower Reynolds numbers do not support a magnetic field. The magnetic energy in simulation IRun8 was allowed to decay to a value of $E_m/E_v \sim 10^{-25}$ and no evidence of a magnetic steady state was observed. Based on these observations, the critical value of the Reynolds number for small scale dynamo action is concluded to be $Re_{\lambda,c} \approx 30$ (or $Re_{\lambda,c} \approx 55$).

TABLE III. Time averaged values for the ratio of magnetic to kinetic energy for the ISO flow simulations.

	Re_0	Re_λ	Re_λ	E_m/E_v
IRun9	10	9.66	13.8	...
IRun8	20	18.4	31.2	...
IRun7	40	30.3	55.6	2.0×10^{-4}
IRun6	60	41.2	79.9	2.3×10^{-2}
IRun5	110	55.0	118	6.5×10^{-2}
IRun1	150	68.5	150	1.2×10^{-1}
IRun0	200	90.0	205	1.6×10^{-1}

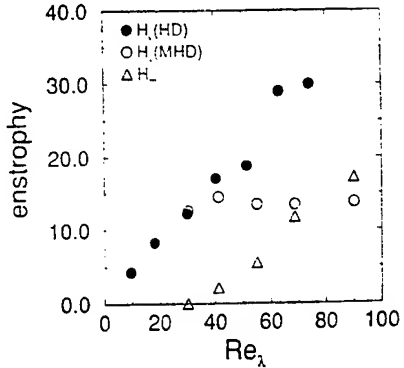


FIG. 4. Reynolds number dependence of the kinetic and the magnetic enstrophy for the ISO simulations IRun0, 1, 5, 6, 7, 8, and 9 (right to left).

The transition to magnetic states is characterized by several changes in both the hydrodynamic and the electromagnetic structure of the flow field. In particular, the kinetic and magnetic enstrophies provide a measure of the respective rotational and electric current density energies of the velocity and the magnetic fields (the kinetic enstrophy is defined as $H_v = \langle \omega_i \omega_i \rangle$, ω is the vorticity vector). Figure 4 depicts these quantities as a function of Re_λ for the steady state values of the ISO simulations. This figure indicates a significant drop in H_v in the presence of a sustained dynamo effect. The HD data show a near linear rise in H_v over the range of Reynolds numbers simulated. However, the MHD flow shows an apparent plateau value of the kinetic enstrophy for Reynolds numbers above the critical value. As the ratio of the magnetic to kinetic energy grows, the Lorentz force becomes increasingly significant to small scale flow dynamics. As will be shown later, this force tends to align perpendicular to the vorticity vector and acts to disperse high vorticity regions of the turbulence, hence decreasing the kinetic enstrophy. Figure 4 also shows that the magnetic enstrophy increases steadily for $Re_\lambda > Re_{\lambda,c}$ and eventually becomes larger than H_v . This trend is observed in spite of the fact that the largest energy ratio observed in the ISO simulations is "only" about 15% (see Table III). The larger magnetic enstrophy in comparison to the kinetic enstrophy is due to a more intermittent behavior of the magnetic field in comparison to the velocity field.

Significant insight into MHD small scale dynamics and intermittency is gained by the examination of the higher order statistics of the field variables and their derivatives. These statistics are important in characterizing the transition to magnetic states. The skewness and flatness of a zero mean random variable v_ξ are defined as $\mu_3(v_\xi) = \langle v_\xi^3 \rangle / \langle v_\xi^2 \rangle^{3/2}$ and $\mu_4(v_\xi) = \langle v_\xi^4 \rangle / \langle v_\xi^2 \rangle^2$, respectively. In agreement with previous HD and MHD studies,^{31,32} the velocity field is found to be nearly Gaussian for all flow fields considered, while the statistics of both the velocity and magnetic fields and their longitudinal derivatives are observed to be symmetrically distributed about the mean (i.e., zero skewness). The time averaged flatness values of the magnetic field are presented in Fig. 5 for the ISO simulations (presented as the average of the three coordinate components). Below the critical Reynolds number ($Re_{\lambda,c} \approx 30$) the dynamo effect is not present,

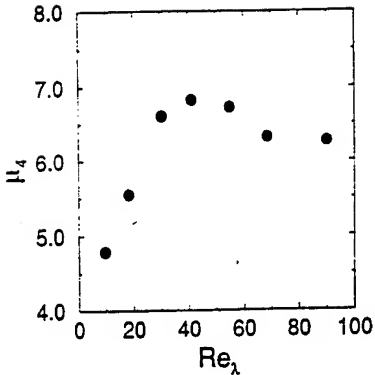


FIG. 5. Reynolds number dependence of the flatness factor for the magnetic field for the ISO simulations IRun0, 1, 5, 6, 7, 8, and 9 (right to left).

but the magnetic field maintains an approximate “self-similar” decay and time averaged flatness values are calculated. In these low Reynolds number cases, the flatness factors for the \mathbf{b} field are observed to be considerably larger than that of Gaussian. The flatness for the \mathbf{b} field exhibits a maximum value at $Re_\lambda \approx 40$ and then decreases. It is suggested that this can be explained in terms of the energy ratio. In the next section it is shown that the crossing point (equipartition) of the kinetic and the magnetic energy spectra moves towards lower wave numbers as the Reynolds number and the energy ratios are increased. The magnetic stretching term in the transport equation for the \mathbf{b} field is the inner product of a large scale field (\mathbf{b}) with a hydrodynamic dissipation scale gradient term. Therefore, as the relative strength of the \mathbf{b} field is increased and the corresponding equipartition wave number migrates away from the dissipation scales, the magnetic field stretching term in Eq. (3) appears more “space filling” (less intermittent). For Reynolds numbers below the critical value, the primary scales for interactions between the magnetic field and the velocity field are the dissipation scales. In this case, the magnetic field intermittency therefore increases with the magnetic field strength. Additional larger Reynolds number simulations are needed to investigate the fate of the magnetic flatness at large Reynolds numbers.

Some insight into the existence of a dynamo effect for SHR simulations is gained by examining the evolutions of the energy ratio and the magnetic energy (normalized by its initial value), as shown in Fig. 6. All \mathbf{b} fields except the unity energy ratio case (SRun3) experience an initial rise in energy due to the abrupt application of the mean velocity gradient at time $Yt=0$. This causes strong stretching and bending effects on the initial random magnetic fields, and hence amplification of the magnetic energy. Simulation SRun3 has a sufficiently large energy to resist these effects and actually damps the \mathbf{u} field to a large enough extent to display no initial magnetic energy growth [Fig. 6(b)]. The sharpest relative increase in magnetic energy occurs for the large scale initial field of SRun4 with nearly an order of magnitude increase within the first large scale turnover time. The positive growth rates of the magnetic energies observed in the latest stages of the simulations (except SRun3) in Fig. 6(b) suggest the presence of a dynamo effect. The rates of growth of the magnetic

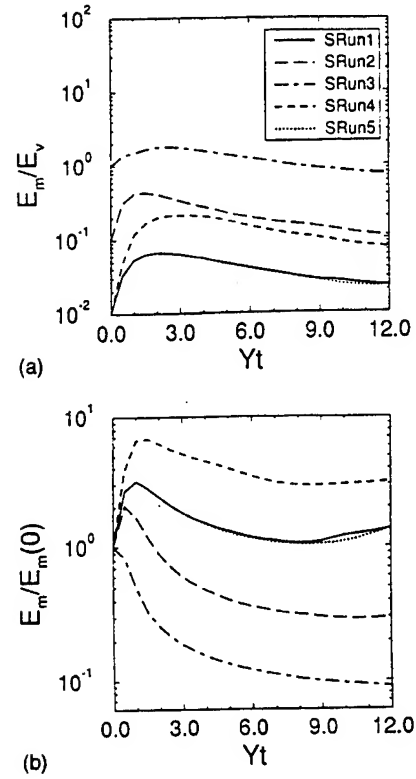


FIG. 6. Temporal development of the energies for the SHR simulations: (a) the energy ratio, and (b) the magnetic energy normalized by the initial value. The legends are the same for both figures.

fields are slower than those of the velocity field, as evidenced by the monotonically decreasing energy ratios at later times in Fig. 6(a).

Some results portraying the anisotropy of the SHR flow are presented in Table IV. This table lists various statistics of both the HD and MHD flows. Previous DNS data of Rogers and Moin³⁰ (RM) are also included for comparison. The correlation coefficient in the table is defined as $C(v_\alpha, v_\beta) = \langle v_\alpha v_\beta \rangle / \sqrt{\langle v_\alpha^2 \rangle \langle v_\beta^2 \rangle}$ for the vector v . The addition of a magnetic field delays the turbulence development and results in the increased peak times used for comparisons. The table suggests that an important parameter influencing the anisotropy and the Reynolds stress development is the instantaneous energy ratio at the peak times. Notwithstanding SRun4, as the instantaneous energy ratio is increased, the primary effects on the turbulence are to increase the anisotropy of both the velocity and the magnetic fields and also to decrease the magnitude of the Reynolds number. The case SRun4 is initialized with a relatively large scale (“force-free”) magnetic field and is able to develop the largest value of the Reynolds number despite having a moderate energy ratio. The reason for the increase in anisotropy with the energy ratio is that the Lorentz force exhibits preferred orientations in the x_2-x_3 plane. Therefore, this force causes the relatively largest resistance to fluid motions in directions perpendicular to the streamwise direction, thus increasing the fluid anisotropy. This preferential orientation of the Lorentz force is discussed in Sec. III D. Table IV also illustrates that the correlation $C(u_1, u_2)$ decreases as the energy ratio is

TABLE IV. Comparisons of instantaneous parameters for the SHR simulations at the peak times.

	RM	SRun0	SRun1	SRun2	SRun3	SRun4	SRun5
Yt_{peak}	8.0	8.0	8.0	10.0	12.0	10.0	8.0
Re_λ	72.6	101	112	107	88.0	132	110
$\langle u_1^2 \rangle / E_v$	0.53	0.50	0.53	0.59	0.65	0.58	0.54
$\langle u_2^2 \rangle / E_v$	0.16	0.20	0.18	0.16	0.11	0.17	0.18
$\langle u_3^2 \rangle / E_v$	0.31	0.30	0.29	0.25	0.24	0.25	0.28
$C(u_1, u_2)$	-0.57	-0.54	-0.56	-0.51	-0.36	-0.55	-0.55
E_m / E_v	0.031	0.128	0.747	0.089	0.030
$\langle b_1^2 \rangle / E_m$	0.48	0.65	0.84	0.58	0.47
$\langle b_2^2 \rangle / E_m$	0.23	0.15	0.06	0.23	0.23
$\langle b_3^2 \rangle / E_m$	0.29	0.20	0.10	0.19	0.30
$C(b_1, b_2)$	0.21	0.39	0.47	0.30	0.22

increased, while the correlation $C(b_1, b_2)$ displays the opposite behavior. The production terms in the mean kinetic and magnetic energy equations are related to these correlations and are proportional to $\langle u_1 u_2 \rangle$ and $\langle b_1 b_2 \rangle$, respectively. Hence, as the correlation $C(u_1, u_2)$ is decreased, the relative production of kinetic energy is also decreased and the turbulence grows at a slower rate. On the other hand, the relative increase of the magnetic Reynolds (Maxwell) stress component $\langle b_1 b_2 \rangle$ results in an increased relative production of magnetic energy. Note also that the correlations $C(u_1, u_2)$ and $C(b_1, b_2)$ have opposite signs. This is a result of the opposite sign of the source terms due to the mean velocity gradient in the transport equations of the fluctuating \mathbf{u} and \mathbf{b} fields.

Based on the previous discussions, it may be expected that the magnetic field, by damping the turbulence energy, should yield a lower Reynolds number. This, however, is not necessarily the case. Figure 7 illustrates this effect for both the ISO and the SHR cases. The ISO data show a transition at the critical box Reynolds number into distinct HD and MHD states. Above the critical value, a larger Re_λ is observed for the magnetic turbulence. The difference between these states increases as Re_0 increases. A similar trend is observed in the SHR flows. The Reynolds number is increased over its HD values (at the same Yt values) for all of the three simulations which are initialized with a 1% energy ratio (SRun1, SRun4, and SRun5). The obvious explanation for these trends is that the magnetic field, while decreasing the kinetic energy, also causes an increase in the length scales of the turbulence. However, if the initial magnetic field strength is large (SRun2 and SRun3), the kinetic energy can be damped sufficiently to result in a net decrease of the Reynolds number. The results for cases SRun5 and SRun1 again show similar trends; in the discussions below, case SRun5 is no longer considered.

The variation of the Taylor length scale is presented in Fig. 8 for both the ISO and the SHR flows. The Taylor scale is presented as the average over its value along all three directions. This average value is used in the SHR results as a representative length scale. In both flows, the length scale is observed to increase in the presence of a magnetic field. A similar behavior is observed for both the Kolmogorov and the integral length scales (not shown). In nonhelical MHD turbulence, a steepening of the kinetic energy spectrum in

the inertial range has been observed in EDQNM predictions.¹⁰ The integral length scales would be increased by this steepening. However, the enlargement of the Taylor scale is best explained in a structural sense as discussed below. The Taylor length scale in the MHD flows remain consistently larger than the HD case for the SHR flows except for the case with a 100% initial energy ratio (SRun3). In this case, the magnitude of the Lorentz force is of the same order as the pressure gradient. The initial magnetic field is uncorrelated with the velocity field, so that the Lorentz force acts as though it is a random forcing term applied as a step function at time $Yt=0$. This random force has the effect of initially increasing the relative amount of high wave-number energy, thus decreasing the length scales at early times.

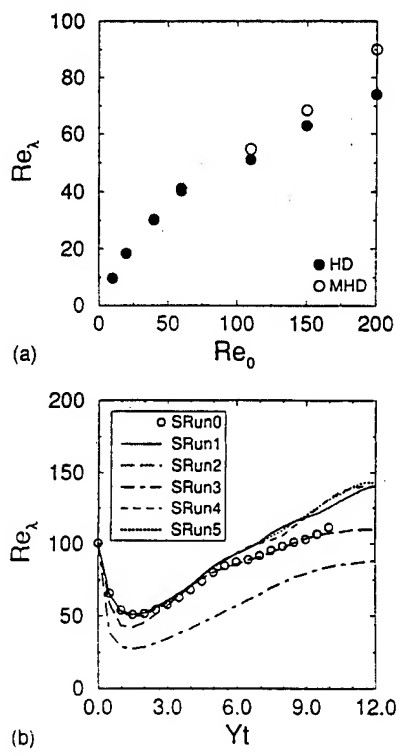


FIG. 7. Development of the Reynolds number based on the Taylor microscale (a) vs the box Reynolds number for the ISO simulations IRun0, 1, 5, 6, 7, 8, and 9 (right to left), (b) vs time for the SHR simulations.

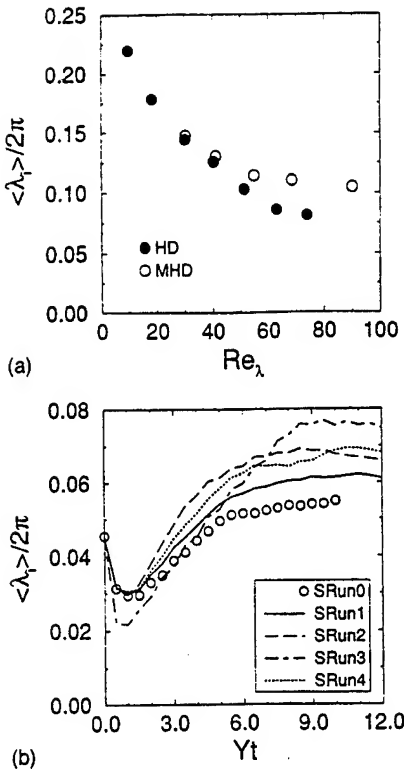


FIG. 8. Development of the Taylor length scale (a) for the ISO simulations IRun0, 1, 5, 6, 7, 8, and 9 (right to left) and (b) for the SHR simulations.

C. Energy spectra

Of primary concern in this section are the modifications of the HD spectra as caused by the magnetic field, and the relationship of the kinetic and magnetic spectra including equipartition. Equipartition refers to the tendency of MHD turbulence to develop nearly equal values for both the kinetic and magnetic energy at high wave numbers. This occurs due to the small scale exchange of energy between the two fields through the action of Alfvén waves. Figure 9 presents the normalized kinetic energy spectra for both the ISO and the SHR flows. The time averaged ISO spectra are taken from the high Reynolds number case IRun0. The SHR spectra are presented for cases SRun0–SRun3. These spectra are actually functions of the wave-number vector component for the anisotropic flow fields. However, in order to simplify the analysis, they are presented versus the wave-number magnitude. The SHR energy spectra are given for instantaneous flow conditions corresponding to the peak times. The primary effects of the magnetic field on the energy spectrum for the ISO data are to steepen the slope in the moderate wave-number region and to increase the relative energy in the high wave numbers [Fig. 9(a)]. There is no distinct inertial range at these Reynolds numbers. However, the steepening is in agreement with the EDQNM predictions.¹⁰ The Lorentz force creates a relative increase in the small scale energy of the turbulence. Of course, this is only a relative effect as the total energy is decreased. The SHR flows display this increase most significantly for case SRun3 which displays the largest instantaneous energy ratio [Fig. 9(b)]. The dissipation spectra (not shown) for both flows display a mild flattening

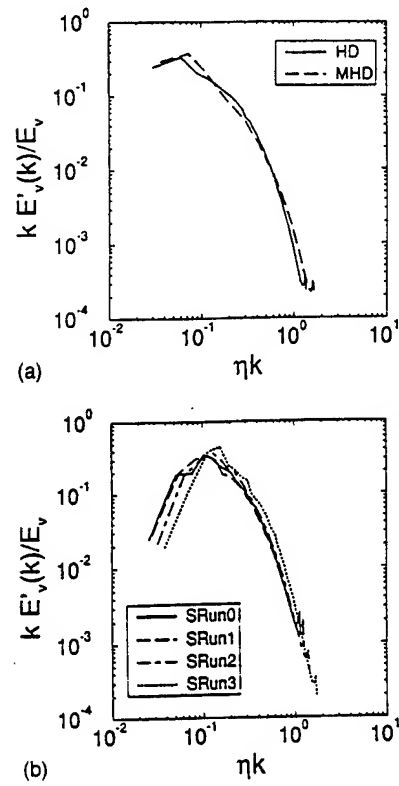


FIG. 9. Normalized energy spectra: (a) kinetic energy spectra for IRun0, (b) kinetic energy spectra for SHR flows. The ISO results are time averaged and the SHR results are for the peak times.

in the moderate wave-number regions. The wave-number location of the maximum dissipation does not appear to change. The broadening effect implies that the transfer of the kinetic energy to the magnetic energy occurs over a relatively large range of scales and is centered around the scale corresponding to maximal viscous dissipation. The maximal magnetic and kinetic dissipation scales are approximately the same due to the unit magnetic Prandtl number considered here.

Examination of the equipartition effect is facilitated by the normalized kinetic and magnetic spectra in Fig. 10. Both energies are normalized by the kinetic energy to retain the relative crossing points. These results represent both relatively large and small E_m/E_v ratios for both flows. Parts (a) and (b) of Fig. 10 depict results of IRun0 and IRun6 with time averaged energy ratios of 0.16 and 0.023, respectively. The SHR spectra are shown in Figs. 10(c) and 10(d) for the instantaneous peak time data of simulations SRun2 and SRun1 with respective energy ratios of 0.128 and 0.031. The forms of both the kinetic and magnetic spectra remain approximately self-similar. However, the equipartition wave number is observed to migrate towards smaller wave numbers for larger energy ratios (i.e., from case IRun6 to IRun0 and from case SRun1 to SRun2). This migration also results in a magnetic field with a larger length scale. This was briefly discussed above in relation to the decreasing trends observed for the magnetic field intermittency with increasing energy ratios for $Re_\lambda > Re_{\lambda,c}$. Turbulence fields with larger length scales generally portray less intermittent effects. For

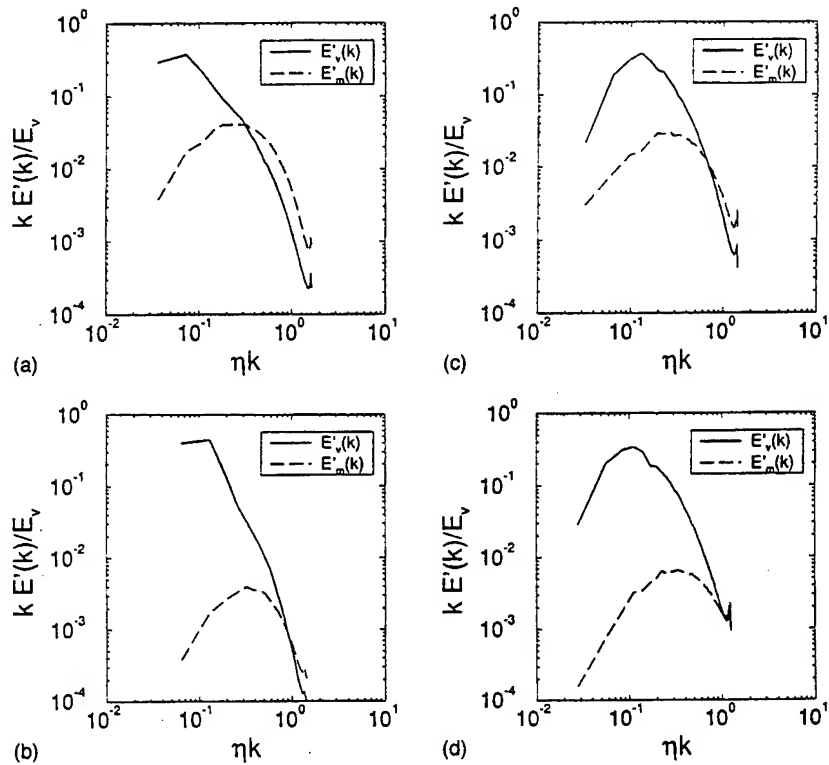


FIG. 10. Kinetic and magnetic energy spectra normalized by the mean turbulence energy: (a) IRun0, (b) IRun6, (c) SRun2, and (d) SRun1. The ISO results are time averaged and the SHR results are for the peak times.

example, passive scalar fields generally display asymptotic Gaussian statistics, but derivatives of the scalar are characterized by smaller length scales and portray significant departures from Gaussian.^{20,33} It is unknown whether the magnetic field intermittency will continue to decrease at larger Reynolds numbers (Fig. 5), and future simulations and/or experiments are needed to address this issue.

Another feature pertaining to energy spectra is found for ISO flows near the critical Reynolds number. The present results suggest that sustained dynamo action can occur in the absence of equipartition of high wave-number kinetic and magnetic energies. This is illustrated in Fig. 11 which depicts the normalized kinetic and magnetic energy spectra for the case IRun7. This is the lowest Reynolds number ISO simu-

lation for which a sustained dynamo action is observed. Notice that there is no equipartition of energy in this case; the magnetic energy spectrum appears to be “floating” nearly two decades beneath the kinetic spectrum. Any exchange of energy must be occurring through only very weak Alfvén waves. The simulation was conducted for more than 100 HD eddy turnover times and confirmed that the \mathbf{b} field is sustained. It may be possible for the equipartition to occur at very low energy values (at very high wave numbers). To capture the crossing point of the two spectra would require simulations with much higher resolution.

D. Structure and organization

This section is devoted to physical descriptions of coherency in 3-D nonhelical MHD turbulence. For this purpose, instantaneous fields from each of the cases IRun0 and SRun2 are considered for detailed investigation. The results are considered at time $t/\tau_e = 25$ for the ISO data and at time $Yt = 10$ for the SHR data. Other simulated results from each configuration are confirmed to be in accord with the results presented for these two cases. Figure 12 illustrates the small scale structure of the ISO turbulence field. In Fig. 12(a) the vorticity field is highlighted with vorticity vectors in only the regions where the local vorticity magnitude is within 10% of its maximum value. As in the HD flow field, the high amplitude vorticity regions tend to organize into tube structures having thickness of the order of the Kolmogorov scale and length of the order of the integral scale. Figure 12(b) depicts magnetic field vectors in only the regions where the local magnetic field amplitude is within 10% of its maximum

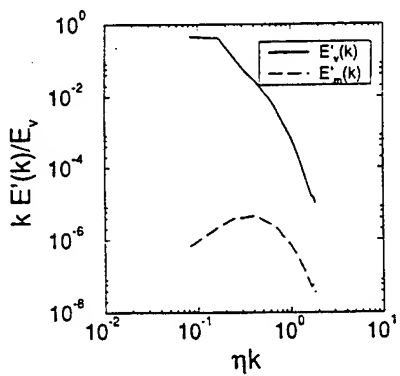


FIG. 11. Kinetic and magnetic energy spectra normalized by the mean turbulence energy for case IRun7.

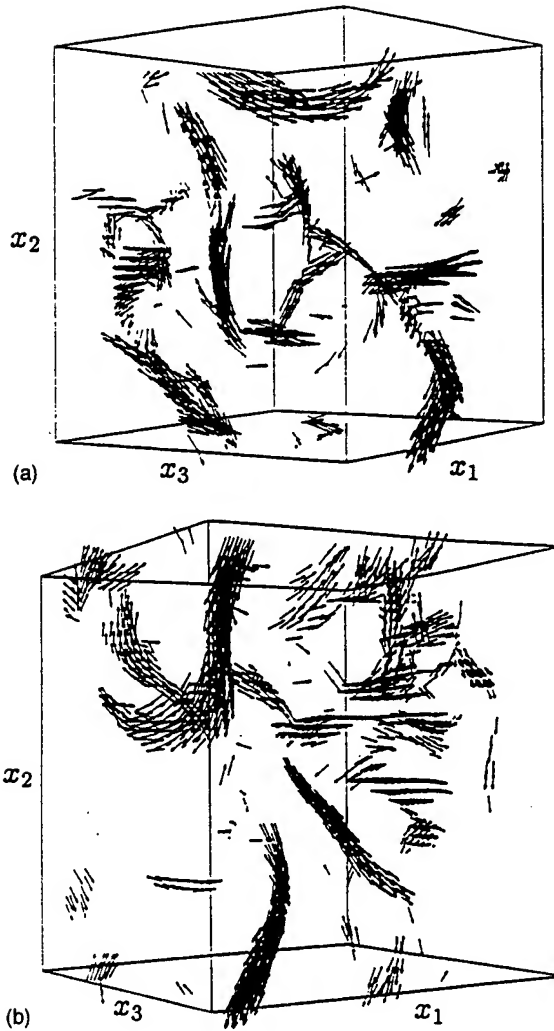


FIG. 12. Illustration of coherent structures in case IRun0 at time $t/\tau_e=25$ as depicted by vectors located in high amplitude regions: (a) vorticity vectors and (b) magnetic induction vectors.

value. The magnetic field also displays evidence of “tube-like” structures, hereinafter referred to as magnetic flux tubes. In contrast to the vorticity field, the magnetic field also shows a substantial tendency to align in “sheet-like” structures [the high amplitude induction regions at the upper right corner of Fig. 12(b) are confirmed with flow visualization as being sections of magnetic sheets]. Flow visualization shows that the regions of maximal current density are related more to the sheet structures than to the flux tubes. Both the vorticity and the induction fields are observed to be strongly intermittent. That is, the fields are concentrated in only a small fraction of the volume in physical space. No obvious correlation is observed between the two types of structures.

The vortical structure of homogeneous shear flows is known to be dominated by vortex tubes (aligned with the principal axis of the flow) which fold into the shape of a “horseshoe.” These structures are referred to as “hairpin” vortices.³⁰ Figure 13 shows the interaction of a typical hairpin vortex with a magnetic flux tube in the SHR flow. The structures are depicted with lines which are everywhere tangent to the vector of interest and which are concentrated only

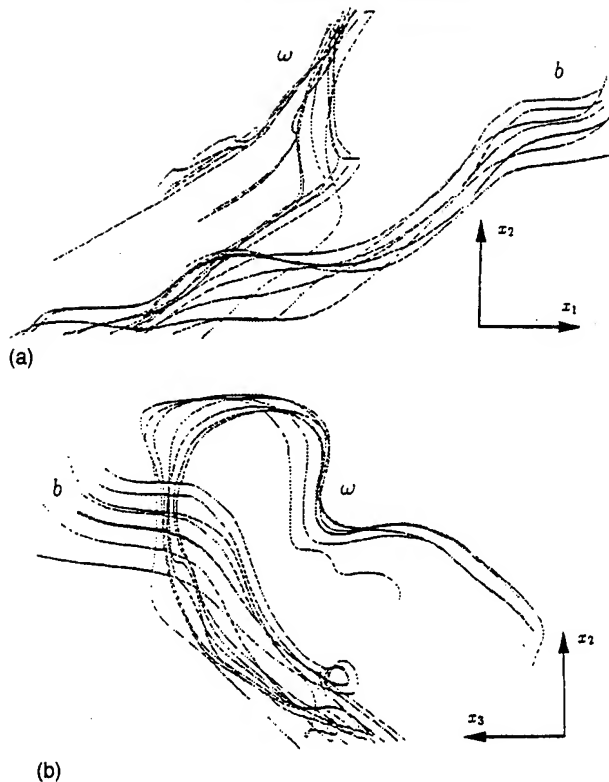


FIG. 13. Interaction of a vorticity hairpin vortex and a magnetic flux tube for case SRun1 at time $Yt=8$: (a) spanwise view, and (b) streamwise view.

in regions of relatively high amplitude vorticity or magnetic field, respectively. Flow visualizations provide no evidence of magnetic hairpins. The magnetic flux tubes in the SHR flow show a tendency to align along directions close to the principal axis (45° in the x_1 - x_2 plane). Both the vorticity and the magnetic tube structures are of approximately the same length and width as those observed in the ISO flow.

The preferential alignment of the vorticity and the magnetic field vectors in the SHR flow is quantified with the inclination angle [$\theta=\tan^{-1}(v_2/v_1)$ for any vector v_i] of these vectors in the x_1 - x_2 plane. Figure 14 shows the distribution of this angle (the PDF of θ multiplied by 360°) for the vorticity field and also for several of the electromagnetic fields. The angle $\theta=0$ indicates the direction of positive x_1 (streamwise), with positive angles representing counter-clockwise rotation about the x_3 axis. The HD vorticity results are in agreement with the previous analysis of Rogers and Moin.³⁰ That is, there is peak alignment of the vorticity with the principal axis (45°) with equal relative weights for both positive and negative vorticity. The effect of the magnetic field is to skew the vorticity alignment towards the x_1 axis. This is explained by the alignment of the Lorentz force which acts perpendicularly to the \mathbf{b} field. The magnetic field and the Lorentz force show preferred angles approximately equal to 20° and -80° , respectively. The net effect is to force the vorticity vectors towards the x_1 axis.

The electromagnetic structure of several flux tubes was investigated via flow visualization. In general, these tubes were observed to have width on the order of the Kolmogorov scale and length on the order of the integral scale. The flux

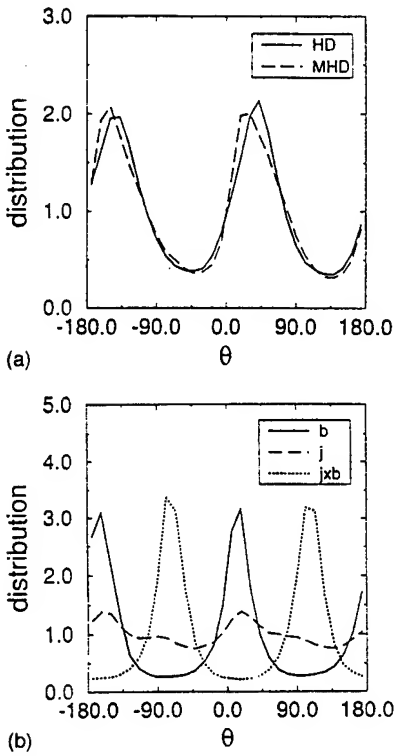


FIG. 14. Distribution of the inclination angle of the projection of vector fields in the x_1 - x_2 plane for case SRun1 at time $Y_t = 8$: (a) vorticity vector. (b) electromagnetic vectors.

tubes tend to repulse the local fluid by exerting a relatively strong Lorentz force on the fluid element radially away from themselves. This offers a possible explanation for the results of Fig. 4 which displays a large reduction in kinetic enstrophy for MHD turbulence, and may also explain the increase in turbulence length scales. Flux tubes forming in or near regions of large velocity gradients can act to “break up” these regions through the repulsive Lorentz action. This would have the effect of increasing the Kolmogorov scale and also decreasing the total kinetic enstrophy.

A more elaborate description of the small scale turbulence dynamics is achieved with the examination of the eigenvectors of the symmetric rate of strain tensor. Following the traditional notation, the eigenvalues are labeled as $\alpha \geq \beta \geq \gamma$, and the strain magnitude is denoted by S . In incompressible flows, $\alpha + \beta + \gamma = 0$, α is extensive, γ is compressive, and β has been shown to be typically extensive in HD turbulence (i.e., positive $\langle \beta \rangle$ values).^{34,35} The corresponding eigenvectors are denoted by e_α , e_β , and e_γ , respectively. The typically extensive nature of the second eigenvalue is confirmed by the present MHD results. Table V lists the mean, the skewness, and the flatness for β/β_{rms} . The values correspond to instantaneous data of ISO simulation IRun0, and to the peak time data of SHR simulations SRun0 and SRun2. The middle eigenvalue of the magnetic field strain tensor [$s_{ij}^{(m)} = (b_{i,j} + b_{j,i})/2$] is also included, and is denoted by β_m . The mean value for β remains positive; however, the magnitude is reduced for both of the MHD flows. This indicates a slight change in the small scale hydrodynamic structure of the MHD turbulence. In contrast to the

TABLE V. Statistics of the middle eigenvalue of the rate of strain tensors of both the velocity field (β) and the magnetic field (β_m), normalized by their respective standard deviations. IHD and SHD correspond, respectively, to HD results of IRun0 and SRun0 cases. IMHD and SMHD correspond, respectively, to MHD results of IRun0 and SRun2 cases.

	β (IHD)	β (SHD)	β (IMHD)	β (SMHD)	β_m (ISO)	β_m (SHR)
Mean	0.750	0.547	0.685	0.443	0.013	0.001
μ_3	1.17	0.838	1.31	1.41	0.030	0.046
μ_4	4.34	4.60	4.12	5.78	4.77	4.52

hydrodynamic field, β_m remains symmetrically distributed with near zero mean in both flows, and hence shows no tendency for either compressive or extensive character. This may be related to the lack of skewness for the longitudinal derivatives of the magnetic induction mentioned in Sec. III B, and also provides insight into the existence of both magnetic tube and sheet structures. Magnetic tube structures display two compressive magnetic strain eigenvectors ($\beta_m < 0$), whereas magnetic sheet structures are characterized by two extensive eigenvectors ($\beta_m > 0$).

Hereinafter, the analyses are limited to the IRun0 results, as the SHR results were observed to show similar trends. The PDF of the alignment of the vorticity vector with the electromagnetic fields is presented in Fig. 15. The magnetic field shows a strong tendency to align somewhat parallel to the vorticity vector. The vortex/flux tube interaction in Fig. 13 illustrates this effect, as the tails of the hairpin vortex are in the vicinity of the flux tube, where they run parallel to each other. The electric current running helically around the flux tubes would therefore be expected to show a preferred perpendicular alignment with the vorticity vector. However, Fig. 15 shows that no significant preferred alignment exists for these vectors. This can be explained in terms of the location of the strongest current magnitude within the flow field. As noted above, the strongest current regions are associated with the magnetic sheet structures which are correlated with the high strain regions of the flow, not the vorticity regions. This effect can be quantified by examining the statistics of the electromagnetic field conditioned on the second invariant of the deformation tensor:

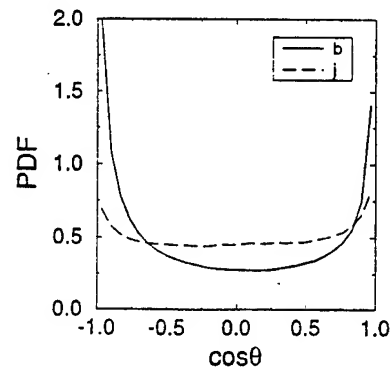


FIG. 15. PDF of the angle of alignment between the vorticity vector and the electromagnetic vectors. Case IRun0 at time $t/\tau_e = 25$.

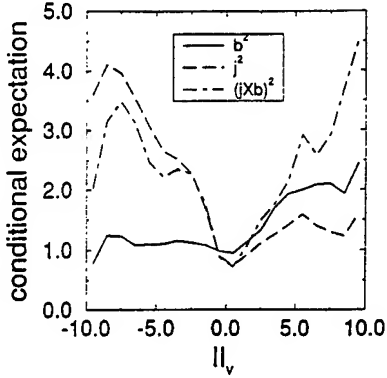


FIG. 16. Expected value of the squared magnitudes of the magnetic field, electric current, and the Lorentz force conditioned on the second invariant of the deformation tensor normalized by its standard deviation for simulation IRun0 at time $t/\tau_e=25$. The squared magnitudes are normalized by their expected values.

$$II_v = -\frac{1}{2} \frac{\partial u_i}{\partial x_j} \frac{\partial u_j}{\partial x_i} = -\frac{1}{2} \left(S^2 - \frac{1}{4} \omega_i \omega_i \right).$$

Therefore, the positive and negative values of II_v correspond to regions of high vorticity and high strain, respectively. Figure 16 presents the expectations of the squared magnitudes of the magnetic field, electric current, and the Lorentz force ($j \times b$), conditioned on the magnitude of the second invariant. The squared vector magnitudes are normalized by their mean values, and the second invariant is normalized by its standard deviation. Notice that there is a small tendency for the magnetic high amplitude regions to be located in regions of moderate to strong vorticity. However, these may only be relatively strong rotational fluid regions outside of the vortex tubes, as the flow visualization here (and that by Meneguzzi, Frisch, and Pouquet¹⁶) show no indication that these structures are correlated. Of more importance is the stronger correlation of the high amplitude current regions with the high strain regions of the flow. The current shows only moderate amplitudes in high vorticity regions, and hence no significant preferred alignment with the vorticity vector. The maximal regions of the Lorentz force are observed to be correlated with both high amplitude vorticity and high amplitude strain regions. Flow visualization also shows that regions of strong Lorentz force are associated with both the magnetic sheet structures (large strain) and the magnetic flux tubes (large vorticity).

The effects of the magnetic field on the hydrodynamics can be illustrated with the PDF of the alignment angle between the Lorentz force and various hydrodynamic vectors as presented in Fig. 17. In part (a) of the figure the entire field is considered, but in part (b) the angles are conditioned on only regions of the flow having a positive second invariant greater than three times its standard deviation. In this manner, the regions of predominantly vorticity tube structures are isolated. Note the change in the heights for the probabilities in the high vorticity regions. In agreement with the previously described parallel alignment of the b and ω_i vectors, the Lorentz force is typically perpendicular to the vorticity and parallel to the kinetic pressure gradient. When conditioned on the high vorticity regions, the probability for

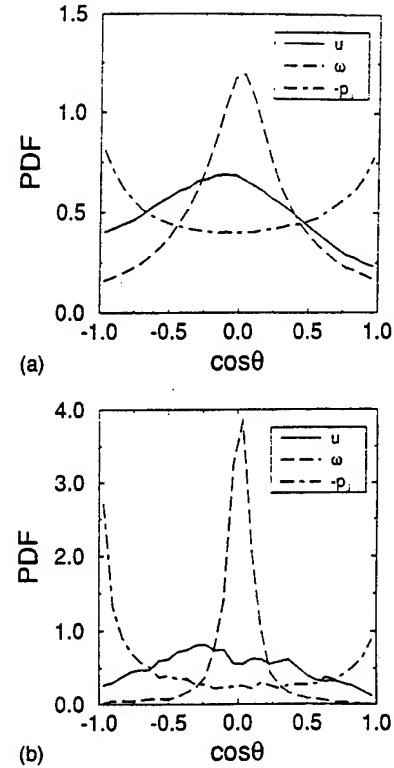


FIG. 17. PDF of the angle of alignment between the Lorentz force and the velocity, vorticity and negative of the kinetic pressure gradient: (a) the entire flow volume, (b) conditioned on regions where the second invariant is positive and larger than three times its standard deviation. Case IRun0 at time $t/\tau_e=25$.

these alignments becomes largely amplified. Also note that the PDF of the pressure gradient alignment in Fig. 17(b) is skewed towards antiparallel alignment. A phenomenological description of the vorticity tube structures can be made in which the low pressure vortical tubes are being broken up by the outward radial Lorentz force acting against the natural pressure gradient.

IV. SUMMARY AND CONCLUSIONS

Direct numerical simulations are conducted to study the small scale structure and dynamics of homogeneous nonhelical magnetohydrodynamic turbulence with unity magnetic Prandtl number. Both stationary isotropic and homogeneous shear flows are considered in both the presence and the absence of the magnetic field. The effects of the initial magnetic field conditions are examined and found to be somewhat insignificant for the stationary states of the isotropic flow. However, the homogeneous shear flow is significantly dependent on the initial conditions over the entire duration of the simulations. In particular, the initial length scale of the magnetic field is observed to influence the early time amplification of the field. This is due to a larger mean magnetic dissipation for initially small scale magnetic fields, and may result in an order of magnitude change in the ratio of magnetic to kinetic energy over the entire duration of the simulations.

Small scale dynamo action is observed in both flows. For the isotropic flow a critical Reynolds number of $Re_\lambda \approx 30$ is

found above which a stationary state is reached with a sustained magnetic field. For the range of parameters considered, the time averaged ratio of magnetic to kinetic energies scales nearly linearly with the Reynolds number. The homogeneous shear flow does not attain stationary states. However, monotonically increasing magnetic energies at late times indicate the presence of a dynamo effect. Although the magnetic energy is increasing, its ratio with the kinetic energy shows a decreasing trend. This is due to a larger time scale for the magnetic field response, as compared with the growth rate of the turbulence.

The simulation results reveal several modifications to the turbulence structure due to the presence of the magnetic field. In particular, in both flows the turbulence kinetic energy is decreased by the Lorentz force. However, except for very high amplitude initial magnetic fields in the shear flow simulations, the Taylor microscale Reynolds number is increased by the magnetic field. This occurs due to the enlargement of the hydrodynamic length scales. Also due to the magnetic field, the turbulence intermittency and the kinetic enstrophy are both observed to decrease, but the anisotropy is increased in shear flows. The induction is itself highly anisotropic in shear flows, and displays an off-diagonal magnetic Reynolds stress of opposite sign to the corresponding kinetic Reynolds stress.

Although the Reynolds numbers considered in the present simulations are not sufficiently large to produce discernible inertial ranges, many interesting features of the kinetic and magnetic energy spectra are portrayed. The kinetic energy spectra are shown to display increased relative high wave-number energy when a magnetic field is present. The crossing point of the normalized kinetic and magnetic energy spectra is observed to migrate towards the low wave numbers as the ratio of the magnetic energy to the kinetic energy is increased. Additionally, the wave number of the maximum kinetic energy increases with the increase of energy ratio.

The magnetic field is found to organize into both sheet- and tube-like structures. The regions of large magnetic field magnitude show a small correlation with the regions of moderate to large vorticity magnitude, and electric current structures are found to be correlated with the regions of large strain amplitude. The Lorentz force shows a strong tendency to align antiparallel with the pressure gradient force in the regions of strong vorticity. This has the effect of "breaking up" the turbulence structures and results in a decreased kinetic enstrophy. This structural description provides a physical interpretation of some of the above-mentioned phenomena.

ACKNOWLEDGMENTS

We are indebted to Dr. John Shebalin for many useful comments.

This work is part of an effort sponsored by the National Science Foundation under Grant No. CTS-9253488 and by the U.S. Office of Naval Research under Grant No. N00014-94-1-0667. Computational resources are provided by the School of Engineering and Applied Science Computing Center at SUNY—Buffalo and by the National Center for Supercomputing Applications at the University of Illinois at Urbana.

- ¹A. N. Kolmogorov, Dokl. Akad. Nauk SSSR. **30** (11), 301 (1941).
- ²D. Biskamp, *Nonlinear Magnetohydrodynamics* (Cambridge University Press, New York, 1993).
- ³G. K. Batchelor, Proc. R. Soc. London **201**, 405 (1950).
- ⁴J. H. Thomas, Phys. Fluids **11**, 1245 (1968).
- ⁵H. K. Moffatt, J. Fluid Mech. **53**, 385 (1972).
- ⁶A. Pouquet, U. Frisch, and J. Leorat, J. Fluid Mech. **77**, 321 (1976).
- ⁷D. Montgomery and T. Hatori, Plasma Phys. Controlled Fusion **26**, 717 (1984).
- ⁸W. H. Matthaeus, M. L. Goldstein, and S. R. Lantz, Phys. Fluids **29**, 1504 (1986).
- ⁹H. Chen and D. Montgomery, Plasma Phys. Controlled Fusion **29**, 205 (1987).
- ¹⁰J. Leorat, A. Pouquet, and U. Frisch, J. Fluid Mech. **104**, 419 (1981).
- ¹¹P. H. Roberts and T. H. Jensen, Phys. Fluids B **5**, 2657 (1993).
- ¹²P. Givi, Prog. Energy Combust. Sci. **15**, 1 (1989).
- ¹³P. Givi, in *Turbulent Reacting Flows*, edited by P. A. Libby and F. A. Williams (Academic, London, 1994), Chap. 8, pp. 475–572.
- ¹⁴A. Pouquet and G. S. Patterson, J. Fluid Mech. **85**, 305 (1978).
- ¹⁵P. A. Gillman and J. Miller, Astrophys. J. Suppl. **46**, 211 (1981).
- ¹⁶M. Meneguzzi, U. Frisch, and A. Pouquet, Phys. Rev. Lett. **47**, 1060 (1981).
- ¹⁷M. Meneguzzi and A. Pouquet, J. Fluid Mech. **205**, 297 (1989).
- ¹⁸D. Biskamp, H. Welter, and M. Walter, Phys. Fluids B **2**, 3024 (1990).
- ¹⁹U. Frisch, P. L. Sulem, and M. Nelkin, J. Fluid Mech. **87**, 719 (1978).
- ²⁰R. S. Miller, Ph.D. thesis, State University of New York at Buffalo, NY, 1995.
- ²¹A. Pouquet, P. L. Sulem, and M. Meneguzzi, Phys. Fluids **31**, 2635 (1988).
- ²²A. Orszag and C. M. Tang, J. Fluid Mech. **90**, 120 (1979).
- ²³S. Kida, S. Yanase, and J. Mizushima, Phys. Fluids A **3**, 457 (1991).
- ²⁴A. Nordlund, A. Brandenburg, R. L. Jennings, M. Rieutord, J. Ruokolainen, R. F. Stein, and I. Tuominen, Astrophys. J. **392**, 647 (1992).
- ²⁵A. Brandenburg, I. Procaccia, and D. Segel, Phys. Plasmas **2**, 1148 (1995).
- ²⁶J. V. Shebalin, W. H. Matthaeus, and D. Montgomery, J. Plasma Phys. **29**, 525 (1983).
- ²⁷S. Oughton, E. R. Priest, and W. H. Matthaeus, J. Fluid Mech. **280**, 95 (1994).
- ²⁸V. Eswaran, and S. B. Pope, Comput. Fluids **16**, 257 (1988).
- ²⁹R. S. Rogallo, *NASA Technical Memorandum 81315* (NASA Ames Research Center, Moffat Field, CA, 1981).
- ³⁰M. M. Rogers, and P. Moin, J. Fluid Mech. **176**, 33 (1987).
- ³¹Z. S. She, E. Jackson, and S. A. Orszag, Proc. R. Soc. London Ser. A **434**, 101 (1991).
- ³²D. Biskamp and U. Bremer, Phys. Rev. Lett. **72**, 3819 (1993).
- ³³F. Jaberi, R. Miller, C. Madnia, and P. Givi, J. Fluid Mech. **313**, 241 (1996).
- ³⁴R. M. Kerr, Phys. Rev. Lett. **59**, 783 (1987).
- ³⁵W. T. Ashurst, A. R. Kerstein, R. M. Kerr, and C. H. Gibson, Phys. Fluids **30**, 2343 (1987).

APPENDIX VII

Non-Gaussian Scalar Statistics in Homogeneous Turbulence

Non-Gaussian scalar statistics in homogeneous turbulence

By F. A. JABERI, R. S. MILLER, C. K. MADNIA
AND P. GIVI

Department of Mechanical and Aerospace Engineering, State University of New York at Buffalo,
Buffalo, NY 14260-4400, USA

(Received 1 November 1994 and in revised form 18 September 1995)

Results are presented of numerical simulations of passive scalar mixing in homogeneous, incompressible turbulent flows. These results are generated via the Linear Eddy Model (LEM) and Direct Numerical Simulation (DNS) of turbulent flows under a variety of different conditions. The nature of mixing and its response to the turbulence field is examined and the single-point probability density function (p.d.f.) of the scalar amplitude and the p.d.f.s of the scalar spatial-derivatives are constructed. It is shown that both Gaussian and exponential scalar p.d.f.s emerge depending on the parameters of the simulations and the initial conditions of the scalar field. Aided by the analyses of data, several reasons are identified for the non-Gaussian behaviour of the scalar amplitude. In particular, two mechanisms are identified for causing exponential p.d.f.s: (i) a non-uniform action of advection on the large and the small scalar scales, (ii) the nonlinear interaction of the scalar and the velocity fluctuations at small scales. In the absence of a constant non-zero mean scalar gradient, the behaviour of the scalar p.d.f. is very sensitive to the initial conditions. In the presence of this gradient, an exponential p.d.f. is not sustained regardless of initial conditions. The numerical results pertaining to the small-scale intermittency (non-Gaussian scalar derivatives) are in accord with laboratory experimental results. The statistics of the scalar derivatives and those of the velocity-scalar fluctuations are also in accord with laboratory measured results.

1. Introduction

It has been more than four decades since Hawthorne, Weddell & Hottel (1949) indicated the advantages of the probability density function (p.d.f.) method for statistical description of reacting turbulent flows. Since then, p.d.f. methods have been used rather extensively as witnessed by many review articles devoted to the topic (Toor 1975; Pope 1979; Libby & Williams 1980, 1994; O'Brien 1980; Pope 1985, 1990); for the latest review, see Dopazo (1994). The systematic means of determining the p.d.f. involves the solution of the transport equation governing its evolution. In this equation, however, the effects of molecular action do not appear in a closed form and can be described only by means of employing an external model. In many of the previous applications, this problem has been overcome through the use of the Coalescence/Dispersion (C/D) models. Examples are the early C/D prototype of Curl (1963), the Linear Mean Square Estimation (LMSE) theory of Dopazo & O'Brien (1976), and the closure of Janicka, Kolbe & Kollmann (1979) amongst others. While not all of these closures were originally presented in a C/D form, it is now

established that the majority of those in current use (including the three mentioned above) can be cast in a generalized C/D mould (Pope 1982; McMurtry & Givi 1989).

None of the C/D closures currently in use are regarded as physically plausible – the primary reason being that they are not capable of producing an asymptotic ‘Gaussian’ p.d.f. for a scalar field in homogeneous turbulent flows. Such a Gaussian asymptotic state has been observed in several laboratory (Miyawaki, Tsujikawa & Uraguchi 1974; Tavoularis & Corrsin 1981a) and direct numerical simulation (DNS) (Givi & McMurtry 1988; Eswaran & Pope 1988; McMurtry & Givi 1989) results; see Givi (1989) for a review. This ‘incapability’ of the C/D models has been a driving force for the development of other mixing closures capable of generating Gaussian statistics. Examples are the age-biasing scheme of Pope (1982), the Amplitude Mapping Closure (AMC) of Kraichnan (1989) and Chen, Chen & Kraichnan (1989) and the Johnson-Edgeworth Translation (JET) of Miller *et al.* (1993). These models exhibit one common feature: They all yield an approximate asymptotic Gaussian scalar p.d.f. in homogeneous turbulent flows.

The results of some of the more recent laboratory and numerical experiments, however, indicate the possibility of distributions other than Gaussian. The measurements of Heslot, Castaing & Libchaber (1987), Castaing *et al.* (1989) and Sano, Wu & Libchaber (1989) (known as the Chicago group) show that the temperature fluctuations in the convective core of a Rayleigh–Bérnard cell are Gaussian when the Rayleigh number (Ra) is less than a critical value, but become ‘exponential’ when the magnitude of Ra exceeds the critical value. The results of numerical simulations (Christie & Domaradzki 1993, 1994) and laboratory experiments (Solomon and Golub 1991) suggest that in addition to the Rayleigh number, the geometry of the cell and the magnitude of the Prandtl number also affect the statistics. Solomon (1990) shows that the temperature p.d.f. can be either Gaussian, exponential or a combination of the two throughout the convected core. Thoroddsen & Van Atta (1992) show that while the scalar derivative exhibits a strong exponential feature in stably stratified flows, the temperature fluctuations are governed by Gaussian statistics. The experiments of Jayesh & Warhaft (1991, 1992) reveal several characteristics of the p.d.f. of a passive temperature field in decaying homogeneous grid turbulence. For turbulent Reynolds numbers (based on the integral scale) $Re_l > 70$ they show that in the presence of a constant (non-zero) mean scalar gradient, the temperature p.d.f. is exponential, while for $Re_l < 70$ an approximate Gaussian p.d.f. is formed. These results are not in accord with those of earlier measurements of Tavoularis & Corrsin (1981a) who report a Gaussian scalar p.d.f. in the presence of a linear mean scalar profile in homogeneous shear flows for Reynolds numbers greater than 70. In the absence of the mean scalar gradient, Jayesh & Warhaft (1992) report a nearly Gaussian temperature p.d.f. regardless of the magnitude of the Reynolds number. Exponential scalar p.d.f.s are also reported in the experiments of Gollub *et al.* (1991) and Lane *et al.* (1993) conducted in a stirred flow with a constant mean scalar gradient and a near Gaussian velocity field. It is indicated, however, that by increasing the correlation length scale of the velocity field, the scalar statistics become Gaussian even at very large Reynolds numbers.

These recent experimental findings have motivated several analytical and computational investigations for the purpose of understanding the reasons for non-Gaussian scalar statistics. In an effort to explain the Chicago experiments, Yakhot (1989) modified an existing theory of passive scalar p.d.f.s (Sinai & Yakhot 1989) for the problem of Rayleigh–Bérnard convection. This formulation is based on the argument that the large-scale coherent vortex structures influence the hydrodynamic stability of the

thermal boundary layer, thus modifying the mechanism of turbulence production. Kimura & Kraichnan (1993) show that a nonlinear mean scalar profile and/or an 'active' scalar field can cause non-Gaussian statistics. The generated results for cases with a nonlinear mean scalar profile exhibit trends qualitatively similar to those in the Boussinesq convection experiments (Belmonte, Tilgner & Libchaber 1994; Siggia 1994). Pumir, Shraiman & Siggia (1991) and Holzer & Pumir (1993) propose a one-dimensional 'mean-field' phenomenological model based on which they argue that in the presence of a constant mean scalar gradient, non-Gaussian statistics emerge as an inherent property of random advection. Kerstein & McMurtry (1994b) argue that the exponential tails deduced from the mean-field theory are primarily due to the functional form of the advection process which is enacted by an 'additivity' assumption. They show that depending on the statistics of the advection field, a wide variety of scalar p.d.f.s (including Gaussian) can be generated. Using a two-dimensional model in which the velocity evolves under the Euler equation in a restricted band of wavenumbers, Holzer & Siggia (1994) show that exponential-like scalar p.d.f.s occur when the magnitude of the scalar dissipation is non-zero. Ching & Tu (1994) report results of two-dimensional simulations of a passive scalar advected by a solenoidal velocity field. Depending on the parameterization of the problem, the scalar p.d.f. may become non-Gaussian, even without the presence of the mean scalar gradient. Similar p.d.f.s are also observed in the large-eddy simulation results of Metais & Lesieur (1992). These observations indicate the need for more improved models for prediction of the scalar p.d.f. under different mixing scenarios (Jaberi & Givi 1995).

The phenomenon of small-scale 'intermittency', portrayed by non-Gaussian statistics of the derivative-field, has been the subject of widespread investigations in turbulence research since the original theory of Kolmogorov (1941). Although this theory remains the basis of nearly all turbulence research, it is an incomplete description of realistic turbulent flow in that it does not describe intermittency effects (Landau & Lifshitz 1959; Obukhov 1962; Kolmogorov 1962; Gurvich & Yaglom 1967; Monin & Yaglom 1975). Early experiments reveal that although the p.d.f. of the velocity field is Gaussian, the p.d.f. of velocity derivatives exhibit larger than Gaussian tails with departures increasing with the Reynolds number (Batchelor & Townsend 1949; Monin & Yaglom 1975; Yamamoto & Kambe 1991). These intermittent p.d.f.s are observed even for very low Reynolds number flows (Chen *et al.* 1993) and may occur in both the dissipation range and/or the inertial range of turbulence. The former is associated with non-Gaussian velocity derivatives. The latter is identified through the statistics of the two-point velocity difference (structure function) for inertial range separations and yields corrections to the $-5/3$ Kolmogorov energy spectrum scaling (Van Atta & Antonia 1980; Anselmet *et al.* 1984; Castaing, Gagne & Hopfinger 1990; Vincent & Meneguzzi 1991).

The results of recent DNS experiments suggest that the regions of strongest vorticity are organized in elongated thin tubes, with thickness and length on the order of the Kolmogorov scale and the integral scale, respectively (Kerr 1985; Hosokawa & Yamamoto 1989; Vincent & Meneguzzi 1991; Tanaka & Kida 1993). Jimenez *et al.* (1993) observe that these tubes are a natural feature of turbulence, and do not depend on the particular forcing scheme employed. She (1990) and She & Orszag (1991) develop a 'two-fluid' model of intermittency which incorporates the existence of these organized structures. This model is capable of capturing the statistical behaviour of both the inertial- and the dissipation-range intermittency (She, Jackson & Orszag 1991). Most investigations of turbulent scalar mixing are for flows with Schmidt numbers of order unity ($Sc \sim 1$) for which the scalar spectral regimes

are analogous to those of the velocity field†. In this case, the application of the Kolmogorov (1941) description to the scalar is also inadequate due to an inability to account for intermittency. In particular, while the scalar fluctuations typically portray Gaussian statistics (Antonia & Van Atta 1978; Givi & McMurtry 1988; Eswaran & Pope 1988; McMurtry & Givi 1989), scalar derivatives and differences are known to exhibit larger tails with stronger departures than observed in the velocity statistics (Van Atta & Chen 1970; Antonia *et al.* 1984; Castaing *et al.* 1990; Miller *et al.* 1995). As with the hydrodynamics, the scalar field is known to be dominated by organized structures characterized by regions of strong scalar-derivative magnitude. Ruetsch & Maxey (1991 & 1992) show that regions of large scalar gradients form ‘sheet-like’ structures which are found to occur in regions of persistent straining of the flow field. It has also been shown (Kerr 1985; Ashurst, Chen & Rogers 1987a; Ashurst *et al.* 1987b; Nomura & Elghobashi 1992; Miller 1995) that the scalar gradient vector tends to align parallel to both the pressure gradient and the most compressive eigenvector of the strain-rate tensor in these regions. Miller *et al.* (1995) extend the two-fluid description of She (1990) to account for the role of scalar sheets in the dissipation-range scalar intermittency. While the results obtained in this way portray some features of small-scale scalar intermittency, the phenomenon of the non-Gaussian scalar-amplitude p.d.f. remains an unresolved issue.

1.1. Objective

The objective of this work is to demonstrate that there are several factors which determine the outcome of scalar mixing in homogeneous turbulent flows. The message to be conveyed is to confirm that the p.d.f. of the scalar can adopt many different forms and that the Gaussian form as indicated by Givi & McMurtry (1988), Eswaran & Pope (1988) and McMurtry & Givi (1989) is only one of the many possible outcomes. In doing so, the phenomenon of scalar mixing is numerically simulated with the goal of identifying some of the means by which non-Gaussian statistics are generated. The hope is to provide the reasons for these statistics as observed in recent laboratory and numerical experiments. The analysis is based on two computational procedures: (i) the mechanistic Linear Eddy Model (LEM) of Kerstein (1988), and (ii) DNS. The reasoning for the use of the LEM is its relative low computational cost, allowing a large number of simulations. It also provides a means of simulating high Reynolds number flows, albeit in a phenomenological manner. In the context considered, as will be described in the next section, LEM simulations reveal many features of scalar mixing which, in turn, identify several cases to be considered subsequently by DNS. In both simulations, only the transport of a passive and conserved scalar variable is considered; the analyses pertaining to dynamically active and/or chemically reactive scalars are postponed for future work.

2. Linear eddy model simulation

Details of the LEM and its application in modelling of turbulent mixing and chemical reaction are described in several papers by Kerstein (1988, 1989, 1990, 1991); for a recent review see McMurtry, Menon & Kerstein (1993b). The prominent feature of the model in applications to turbulence simulations is its capacity to explicitly differentiate among the different physical processes of turbulent stirring

† Not including the extensive literature of chemical engineering devoted to liquid scalar mixing (Brodkey 1975), since small-scale intermittency is not discussed in this literature.

(convection) and molecular diffusion (and chemical reaction). This is achieved by a reduced ‘one-dimensional’ (linear) description of the scalar field which allows the resolution of all length scales even for flows with relatively large Reynolds numbers. The physical interpretation of the one-dimensional domain is dependent on the particular case under consideration (Kerstein 1992). Along the one-dimensional domain, the diffusion process is implemented deterministically by the solution of the appropriate diffusion equation. The manner by which turbulent convection is treated constitutes the primary feature of the model. This process is modelled by random ‘rearrangement’ (stirring) events of the scalar field along the domain. The rules by which these rearrangement processes occur are established such that the random displacements of fluid elements result in a diffusivity that is equal to the ‘turbulent diffusivity’ of the flow. The parameters which govern this process are λ , the frequency of stirring, and $f(\ell)$, the p.d.f. of eddy size (ℓ) of the segments of the flow which are to be rearranged. To determine explicit expressions for the size and frequency of rearrangement events, a particular rearrangement *mapping* must be chosen. Kerstein (1991) shows that the *triplet* map reflects several physical features which suggest its choice for high Reynolds number turbulence simulations. The stirring events induced by this mapping introduce a random walk of a marker particle on the linear domain. Based on high Reynolds number scaling laws, the diffusivity induced by all eddies up to some size l is assumed to scale as $D_T(l) \sim l^p$. The parameter p takes on the value $4/3$ for inertial-range turbulence, but can be treated as a variable to study other assumed scalings. Based on these scaling arguments, it can be shown that the following relations must be satisfied (Kerstein 1991):

$$f(\ell) = \frac{5}{3} \frac{\ell^{-8/3}}{\eta^{-5/3} - L_u^{-5/3}}, \quad \eta \leq \ell \leq L_u. \quad (1)$$

$$\lambda = \frac{54}{5} \frac{1}{L_u \tau_L} \left(\frac{L_u}{\eta} \right)^{5/3}. \quad (2)$$

Here, τ_L is the eddy turnover time. L_u is the integral scale and η is the Kolmogorov length scale. In this representation, the statistics of the velocity field are inputs to the model. The required model parameters which describe the turbulent field include the turbulent diffusivity (D_T), the integral velocity length scale (L_u), the Reynolds number (Re) and the Schmidt number (Sc). The relation between the model D_T and turbulent diffusivity is needed to relate the computational time to the physical time. The parameter L_u is defined as the largest allowable eddy for a given flow, and l represents the size of a ‘typical’ eddy. The LEM analogue of the Reynolds number is defined by $Re = (L_u/\eta)^{4/3}$. Equations (1) and (2) are based on scaling relations for high Reynolds number flows (Tennekes & Lumley 1972) and therefore the results are most applicable under this condition.

In the implementation of the model for the simulation of a three-dimensional homogeneous turbulent flow, the linear dimension is interpreted to be the time-varying space curve which is locally aligned with the prominent direction of the scalar gradient (Kerstein 1991). In the implementation of the triplet mapping (or any other mapping procedures), however, one must be careful about the magnitudes of the length scales involved in the simulations. For example, if the size of the whole computational domain (L_B) is small, the statistics are dependent on the mapping procedure. Moreover, the number of grid points employed for numerical discretization must be large enough to resolve the Kolmogorov scale sufficiently. Finally, the

Case	Initial condition for the scalar field	L_u	Re	Sc
LEM-1	Square wave, $L_\phi = 1$	1	90	0.7
LEM-2	Square wave, $L_\phi = 2$	1	90	0.7
LEM-3	Double square wave, $L_\phi = 1, 2$	1	90	0.7
LEM-4	Square wave, $L_\phi = 1$	3	90	0.7
LEM-5	Square wave, $L_\phi = 2$	3	90	0.7
LEM-6	Double square wave, $L_\phi = 1, 2$	3	90	0.7
LEM-7	Gaussian spectrum, $K_s = 2$	1	90	0.7
LEM-8	Gaussian spectrum, $K_s = 3$	1	90	0.7
LEM-9	Gaussian spectrum, $K_s = 8$	1	90	0.7
LEM-10	Gaussian spectrum, $K_s = 3$	2	90	0.7
LEM-11	Top-hat spectrum, $K_s = 2$	1	90	0.7
LEM-12	Top-hat spectrum, $K_s = 3$	1	90	0.7
LEM-13	Top-hat spectrum, $K_s = 8$	1	90	0.7
LEM-14	Double top-hat spectrum, $K_{s1} = 2, K_{s2} = 12$	1	90	0.7
LEM-15	Double top-hat spectrum, $K_{s1} = 8, K_{s2} = 12$	1	90	0.7
LEM-16	Double top-hat spectrum, $K_{s1} = 2, K_{s2} = 12$	2	90	0.7
LEM-17	Gaussian spectrum, $K_s = 20$	1	90	0.7
LEM-18	Gaussian spectrum, $K_s = 30$	1	90	0.7
LEM-19	Double square wave, $L_\phi = 1, 2$	1	50	0.7
LEM-20	Double square wave, $L_\phi = 5, 10$	5	900	0.7
LEM-21	Double square wave, $L_\phi = 1, 2$	1	90	0.05
LEM-22	Double square wave, $L_\phi = 1, 2$	3	90	0.05

TABLE 1. Conditions for the LEM simulations. For the cases denoted 'square wave', the initial scalar p.d.f. is an approximate double-delta function (equation (3)). For all the other cases, the initial p.d.f. is approximately Gaussian. In all the cases, $L_\phi = 1$ corresponds to 200 grid points. $K_s = 1$ corresponds to 1000 grid points. $L_u = 1$ corresponds to 200 grid points.

accuracy of the flow statistics is dependent on the number of grid points and the number of realizations employed for data sampling.

LEM results

The resolution requirement for the LEM simulations depends on the magnitudes of the model Reynolds number and the Schmidt number. As we shall see in the simulated results here, the outcome of mixing is strongly dependent on the length scales of the velocity and the scalar field. All the simulations are conducted within relatively large box sizes; typically, $N_c = L_B/L_u = O(100)$, where N_c denotes the number of 'cells' within the box. The number of grid points within each cell is determined in such a way to resolve the Kolmogorov length scale. McMurtry *et al.* (1993a) suggest that ≈ 6 grid points provide the sufficient resolution. For example, with $L_u = 1$ and $Re = 90$, with 200 grid points within each cell the desired accuracy is achieved. With this, there would be a total of $N = 200 \times N_c$ grid points within the whole domain. In addition, each simulation is repeated N_s times; thus the total number of samples for statistical analysis is $N_s \times N$. In most of the simulations, $N_c = 200$ is used. Simulations with smaller box sizes consisting of $N_c = 100$ cells yield almost identical results. In almost all the cases, the simulations are repeated $N_s = 100$ times. Therefore, the statistical information is gathered from 4×10^6 samples. The computer time to gather this many samples for $Re = 90$ simulations is about one hour on the Cray-YMP computer. While this is substantially less than that required for typical DNS (Givi 1994), it is not insignificant. Therefore, in some cases the magnitude of N_s was decreased but it was never less than 10. In order to mimic different mixing scenarios, a variety of different initial scalar

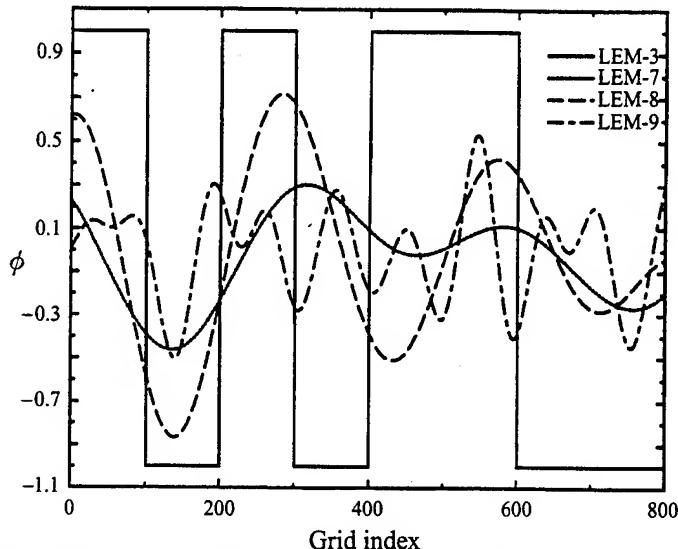


FIGURE 1. Initial distribution of the scalar for some of the LEM cases within a domain consisting of 800 grid points.

conditions are considered. All the cases considered are listed in table 1 and will be described in detail below. In all these cases, a stationary (non-decaying) hydrodynamic field is considered and its influence is modelled by the triplet mapping. The scalar field in all the cases is decaying. In addition to the initial distributions of the scalar field, the difference between the cases is due to the magnitudes of the hydrodynamic and the scalar length scales, the Schmidt number and the Reynolds number.

An objective of these LEM simulations (and also the DNS to be discussed in the next section) is to determine the time-evolution of the scalar statistics. There is no rigorous mathematical definition of the asymptotic time denoting the 'final' stage(s) of mixing (Kerstein & McMurtry 1994a). As mixing proceeds, the p.d.f. of the scalar field tends to form a delta function in the composition domain centred at the average value of the scalar, i.e. $P(\phi) \rightarrow \delta(\phi - \langle \phi \rangle)$; $\langle \phi \rangle$ denotes the ensemble-average value of the scalar variable ϕ with p.d.f. $P(\phi)$. At large times, the magnitude of the scalar variance σ^2 is significantly reduced ($\sigma^2 \rightarrow 0$ for a decaying scalar field) and the values of all constituents of the statistical ensemble are close to the mean scalar value. Here, the simulations are continued until the scalar variance decays to at least $O(10^{-3})$ of its initial value.

In the first set of simulations (LEM-1–LEM-3) the mixing progression from an initial condition corresponding to two scalar 'slabs' with alternating values of $\phi = \pm 1$ is considered. With this, the initial p.d.f. is composed of two delta functions:

$$P(\phi, t=0) = \frac{1}{2}\delta(\phi - 1) + \frac{1}{2}\delta(\phi + 1). \quad (3)$$

In LEM-1 and LEM-2, the initial field is composed of a 'square wave', with wavelengths $L_\phi = 1$ and $L_\phi = 2$, respectively. In LEM-3, the initial field is composed of a 'double square wave' with $L_\phi = 1, 2$. In all three cases, $L_u = 1$. Figure 1 shows the double square wave distribution within a supercell as produced in LEM-3. The single square wave distribution, as used in LEM-1, is the same as that shown within the first 400 grids on this figure and is repeated throughout the domain. Cases LEM-4–LEM-6 employ the same scalar initializations as in LEM-1–LEM-3, respectively, but with $L_u = 3$.

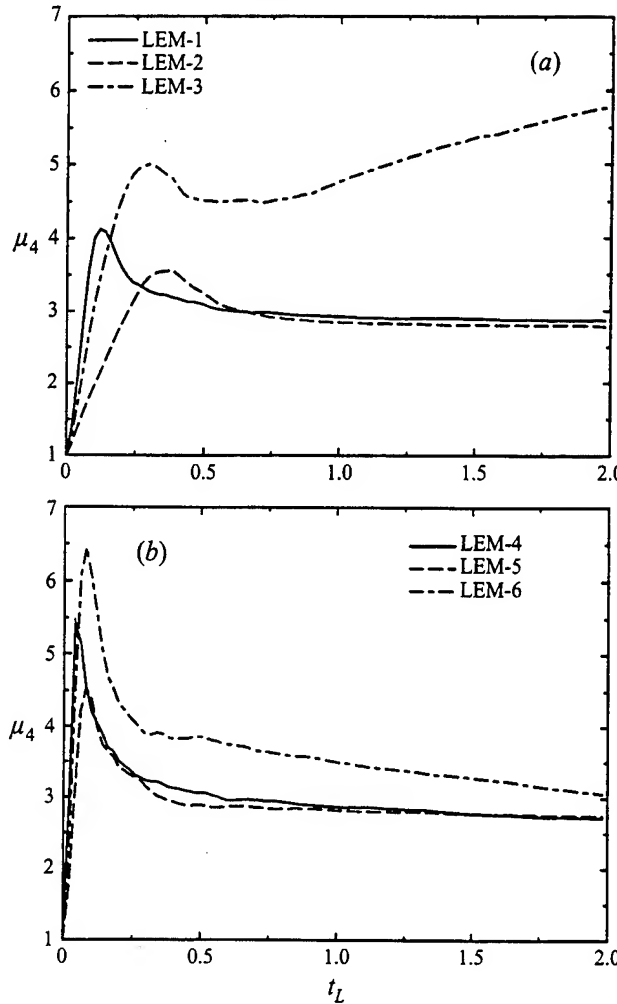


FIGURE 2. Temporal variation of the LEM-generated scalar kurtosis. The scalar field is initialized in the physical domain: (a) LEM-1 ($L_u = 1, L_\phi = 1$), LEM-2 ($L_u = 1, L_\phi = 2$), LEM-3 ($L_u = 1, L_\phi = 1, 2$); (b) LEM-4 ($L_u = 3, L_\phi = 1$), LEM-5 ($L_u = 3, L_\phi = 2$), LEM-6 ($L_u = 3, L_\phi = 1, 2$).

The temporal variations of the scalar kurtosis, μ_4 ($\mu_m = \langle \phi'^m \rangle / (\sigma^2)^{m/2}$, the prime denoting the deviation from the mean), in LEM-1-LEM-6 are shown in figure 2. A unit of time in these and all the subsequent figures pertaining to LEM simulations corresponds to one eddy turnover time, i.e. $t_L = t/\tau_L$. Figure 2(a) shows that in LEM-1 and LEM-2, after $t_L = 0.6$, the p.d.f.s adopt an approximate Gaussian distribution whereas in LEM-3 the p.d.f. exhibits tails broader than Gaussian. By increasing the hydrodynamic length scale (figure 2b) the behaviour in LEM-4 and LEM-5 show a similar trend. However, in LEM-6 the departure from Gaussian is significantly less than that in LEM-3. The p.d.f.s at $t_L = 2$ for these six cases are shown in figure 3, and the temporal variations of the correlation between the scalar and its rate of dissipation (ϵ_ϕ), defined by

$$\rho(t) = \frac{\langle \phi'^2 \epsilon_\phi \rangle}{\langle \phi'^2 \rangle \langle \epsilon_\phi \rangle} - 1 \quad (4)$$

are shown in figure 4. For a Gaussian distribution, ϕ and ϵ are statistically independent

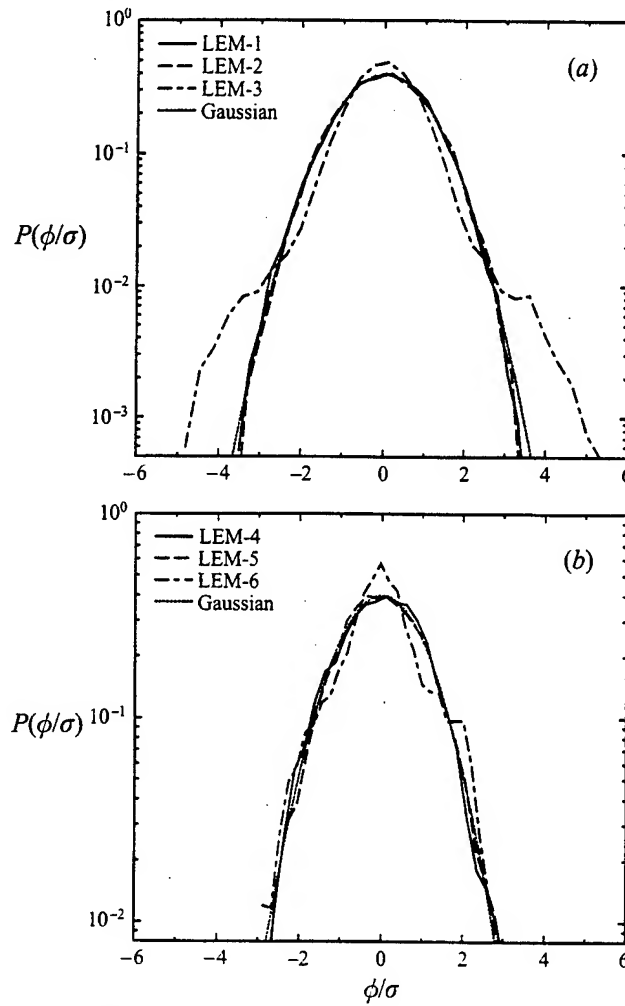


FIGURE 3. LEM-generated p.d.f.s of scalar at $t_L = 2$. LEM-1–LEM-6 as figure 2.

($\rho = 0$). Thus, the numerical values of ρ at large times provide an accurate measure of the deviation of the p.d.f. from Gaussian as observed in figure 3.

Figures 2–4 illustrate one reason for the non-Gaussian behaviour of the scalar p.d.f.. In all the cases with a single value for L_ϕ the p.d.f. is Gaussian after $t_L \approx 0.6$ regardless of the magnitude of L_u . In these cases, the influence of the hydrodynamic field as mimicked by the LEM is similar on all scalar blobs. Thus, the larger slabs of the scalar are broken as a result of triplet mapping, and mixing is completed by diffusion at small scales. The breakage of the scalar blobs is statistically the same in all the slabs even though the rate is different depending on the magnitude of L_ϕ . In this way, the mixing behaviour is similar to that in the laboratory experiments of Miyawaki *et al.* (1974) and Tavoularis & Corrsin (1981a) which do in fact suggest Gaussian p.d.f.s. The behaviour in LEM-3 is markedly different, primarily due to a ‘non-uniform’ influence of the hydrodynamic field. In this case with $L_u = 1$, the effect of stirring is more dominant in the slabs with $L_\phi = 1$ than those with $L_\phi = 2$. This means that the molecular mixing acts at different time levels for different L_ϕ values. Thus, the ‘local’ influence of mixing is not the same in square waves with different wavelengths. Consequently, at

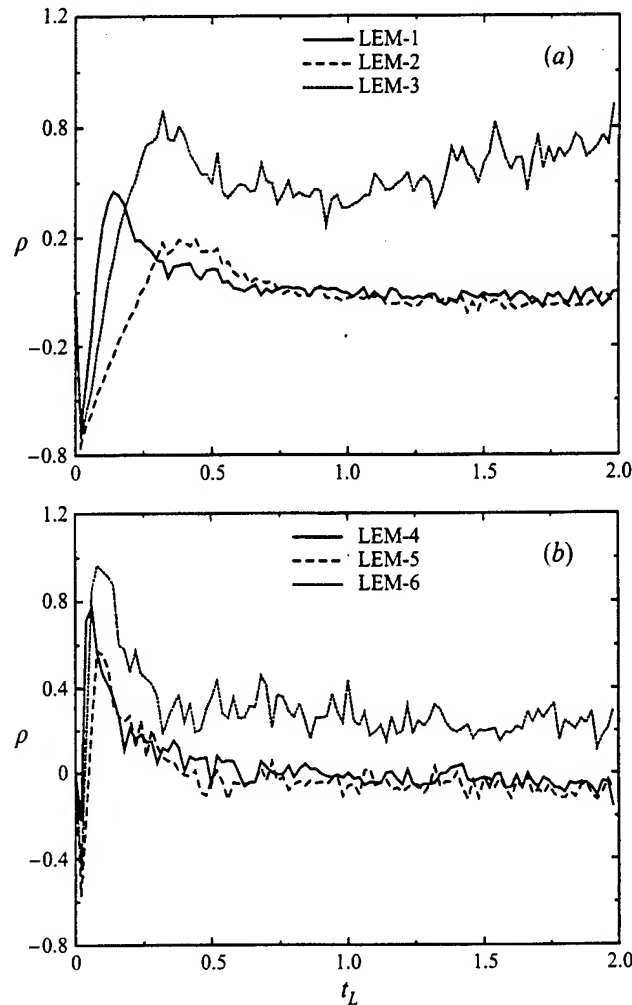


FIGURE 4. Temporal variation of LEM-generated ρ . LEM-1–LEM-6 as figure 2.

intermediate times the scalar fields are composed of ‘two fields’ whose combined weighted effects yield non-Gaussian statistics even if each of the two original fields are Gaussian. Although it is expected that a Gaussian p.d.f. would emerge if the computations are continued until very long times, the non-Gaussian behaviour does prevail for a long time. In this regard, it is important to indicate that at $t_L = 1$ the magnitude of the variance in LEM-3 ($\sigma^2 = 5.74 \times 10^{-4}$) is smaller than that in LEM-2 ($\sigma^2 = 5.96 \times 10^{-4}$). But the p.d.f. in LEM-2 is Gaussian and that in LEM-3 is exponential.

By increasing the magnitude of the velocity length scale $L_u = 3$, the departure from Gaussian becomes less significant. In this case (LEM-6), the influence of stirring is relatively more uniform (as compared with that in LEM-3) in all the scalar blobs. The reason is that now large scalar slabs rapidly follow the turbulence cascade (enacted by the triplet mapping) and the initial field is stirred uniformly before the molecular diffusion can significantly influence the p.d.f.. Thus, after the formation of exponential p.d.f.s at intermediate times, the p.d.f. at long times becomes closer to Gaussian. With the argument presented above it is plausible to expect the p.d.f. at long times in LEM-6 to be somewhere between those in LEM-3 and LEM-1.

It would be interesting to examine the evolution of the mixing from an initial Gaussian state. This is done in LEM-7-LEM-18. In these cases, the initialization procedure is similar to that used in the DNS of Eswaran & Pope (1988). It involves the specification of the scalar power spectrum with random magnitudes of the phase angles. This spectrum is specified within a subdomain (supercell) composed of 1000 grid points and the initial scalar field in each of the supercells is similar. For a box with 40 000 grids, there are 40 supercells each composed of 5 cells. The corresponding Fourier wavenumbers within each of the subdomains is between $-500 \leq K \leq 500$. The energy is distributed at low wavenumbers with the following functional forms:

(i) a Gaussian spectrum with a peak at K_s :

$$E_\phi(K, t = 0) = \frac{32}{3} \left(\frac{2}{\pi} \right)^{1/2} \frac{K^4}{K_s^5} \exp \left\{ -2 \left(\frac{K}{K_s} \right)^2 \right\}; \quad (5)$$

(ii) a top-hat spectrum centered at K_s with a width $\Delta K = \frac{1}{2}$,

$$E_\phi(K, 0) = \begin{cases} 1 & \text{if } K_s - \Delta K \leq K \leq K_s + \Delta K \\ 0 & \text{elsewhere;} \end{cases} \quad (6)$$

(iii) a double-hat spectrum with peaks centered at K_{s1}, K_{s2} with a width $\Delta K = \frac{1}{2}$,

$$E_\phi(K, 0) = \begin{cases} 1 & \text{if } K_{s1} - \Delta K \leq K \leq K_{s1} + \Delta K \text{ or } K_{s2} - \Delta K \leq K \leq K_{s2} + \Delta K \\ 0 & \text{elsewhere.} \end{cases} \quad (7)$$

The Gaussian spectrum with $K_s \geq 3$ generates a multi-scale initial scalar field, whereas the top-hat spectrum yields an approximate single length scale. Figure 1 provides a typical graphical visualization of the initial scalar distribution within a supercell as produced in LEM-7-LEM-9.

With an initial Gaussian scalar field, the combined influences of advection and diffusion can yield non-Gaussian scalar p.d.f.s (Kimura & Kraichnan 1993). This issue is considered here where the role of several parameters in causing exponential p.d.f.s is discussed. In figure 5 results are presented of the temporal variations of the kurtosis for LEM-7-LEM-10 with initial Gaussian scalar fields. In LEM-7 with $K_s = 2$ the scalar field is primarily composed of large uniform size slabs. Therefore all the slabs are broken into smaller ones almost simultaneously. As a result, the kurtosis increases slowly then returns to the Gaussian value of 3. By distributing the initial energy around $K_s = 3$ (LEM-8), a wider range of the initial scalar length scales are produced with some of the scalar slabs larger than L_u . The evolution of the scalar kurtosis in this case portrays a roughly similar trend as that in LEM-3 (or LEM-6). The initial degree of segregation is, however, different. In LEM-8 the p.d.f. becomes exponential with tails broader than Gaussian even at very long times. An increase to $K_s = 8$ (LEM-9) does not necessarily enhance the behaviour. Although in this case the initial scalar field is composed of blobs with multiple length scales, most of the length scales are smaller than L_u . Thus the 'flapping' induced by the velocity field is dominant only at initial times when the kurtosis is slightly increased before the p.d.f. returns to the Gaussian state. A similar behaviour is observed for $K_s = 3$ with $L_u = 2$ (LEM-10).

A similar qualitative kurtosis evolution is observed for the cases with the initial top-hat spectrum (LEM-11-LEM-13) as shown in figure 6. However, in none of these cases do exponential p.d.f.s persist. This is due to the relative uniformity of the initial length scale distribution of the scalar. Thus the behaviour in all these cases is similar to those with a square wave distribution (e.g. LEM-1, LEM-2). However,

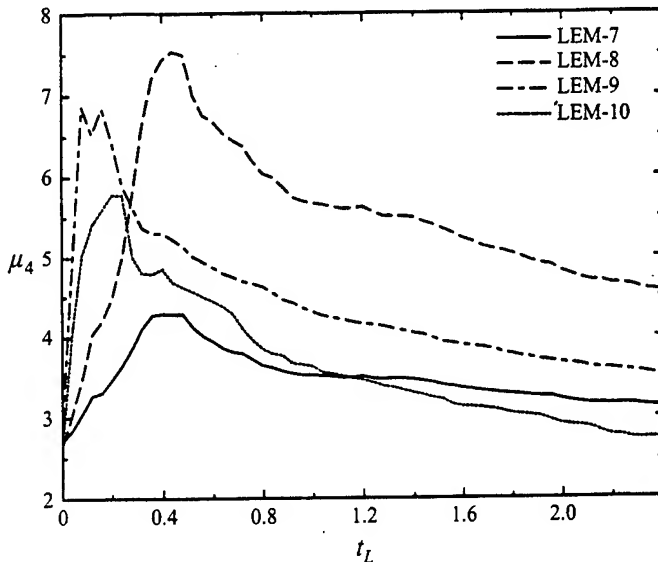


FIGURE 5. Temporal variation of the LEM-generated scalar kurtosis. The scalar field is initialized with a Gaussian spectrum: LEM-7 ($K_s = 2, L_u = 1$), LEM-8 ($K_s = 3, L_u = 1$), LEM-9 ($K_s = 8, L_u = 1$), LEM-10 ($K_s = 3, L_u = 2$),

when a double-hat spectrum is employed (LEM-14), a somewhat more profound non-Gaussian p.d.f. is observed. In this case, with $K_{s1} = 2, K_{s2} = 12$ the behaviour is similar to that in LEM-3 in which the approximate double length scale in the initial scalar field with $L_u = 1$ causes a persistent exponential p.d.f.. The increase of K_{s1} to 8 (LEM-15) or the increase of L_u to 2 (LEM-16) results in p.d.f.s closer to Gaussian. The reason for this behaviour is made clear by realizing that the conditions in LEM-15 and LEM-16 are 'effectively' similar to those in LEM-9 and LEM-10, respectively.

Another means of producing non-Gaussian behaviour is through the simultaneous interaction of velocity and scalar fluctuations at small scales. This issue will be discussed further in the next section where the DNS-generated results are discussed. At this point it suffices to present the results for LEM-17 and LEM-18. These correspond to mixing with an initial Gaussian spectrum but with $K_s = 20, 30$, respectively. In figure 7 the kurtosis evolutions for these cases are compared with that of LEM-9. This comparison indicates that by increasing the relative weight of the small scales the p.d.f.s develop flatter tails at early times. At long times, the kurtosis in LEM-17 ($K_s = 20$) is smaller than that in LEM-9. This is in accord with the trend shown in figure 5 for LEM-8 and LEM-9 which suggests that as K_s becomes larger the statistical behaviour becomes closer to Gaussian. However, by increasing K_s further to the value of 30, an increase in the kurtosis value is observed. Note that in this case, the initial length scale of the scalar field is much smaller than L_u . The triplet mapping implements velocity scales in the range $\eta \leq l \leq L_u$. The interactions of small scalar length scales with the velocity at small l values yield an overall non-Gaussian behaviour. It is noted that the departure from Gaussian as generated by the second mechanism is not very strong at long times.

Based on the results presented thus far, two scenarios are identified for causing non-Gaussian flat-tail scalar p.d.f.s. (i) When there is a separation of length scales in the initial condition of the scalar, and the dominant scale of advection is less than

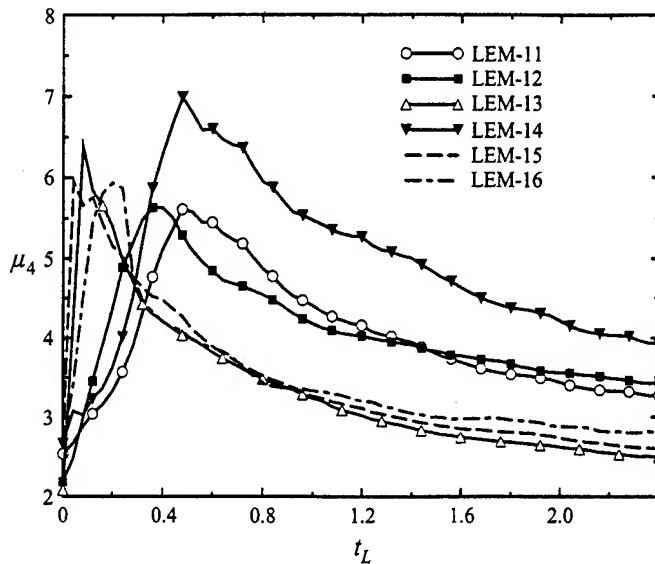


FIGURE 6. Temporal variation of the LEM-generated scalar kurtosis. The scalar field is initialized with a top-hat or a double-hat spectrum: LEM-11 ($K_s = 2$, $L_u = 1$), LEM-12 ($K_s = 3$, $L_u = 1$), LEM-13 ($K_s = 8$, $L_u = 1$), LEM-14 ($K_{s1} = 2$, $K_{s2} = 12$, $L_u = 1$), LEM-15 ($K_{s1} = 8$, $K_{s2} = 12$, $L_u = 1$), LEM-16 ($K_{s1} = 2$, $K_{s2} = 12$, $L_u = 2$),

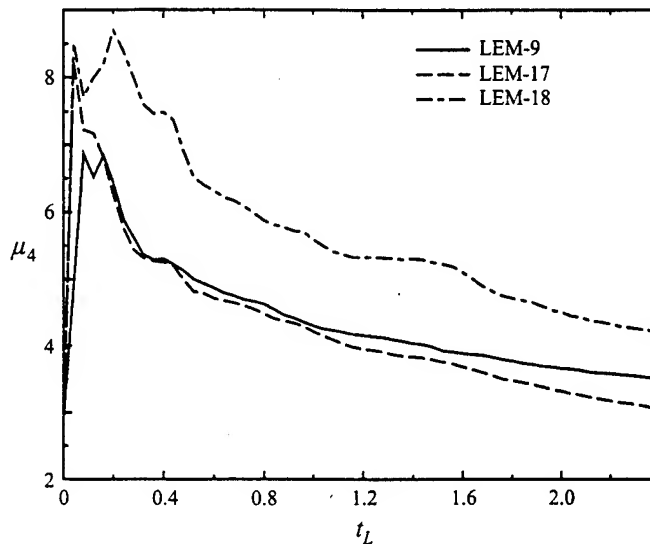


FIGURE 7. Temporal variation of the LEM-generated scalar kurtosis. The scalar field is initialized with a Gaussian spectrum: LEM-9 ($K_s = 8$, $L_u = 1$), LEM-17 ($K_s = 20$, $L_u = 1$), LEM-18 ($K_s = 30$, $L_u = 1$).

that of the scalar: in this case, the simultaneous action of advection and molecular diffusion causes the scalar to develop a non-Gaussian flat-tail p.d.f. (ii) When there is an increase of the initial weight of small scales: in this case, the decrease in the magnitude of the scalar gradient occurs faster by the action of molecular diffusion. While the advection tends to drive the scalar-gradient p.d.f. toward a non-Gaussian form, molecular diffusion acts to return it to Gaussian. With a combination of these two effects, the scalar tends to be correlated with its gradient, thus a non-Gaussian

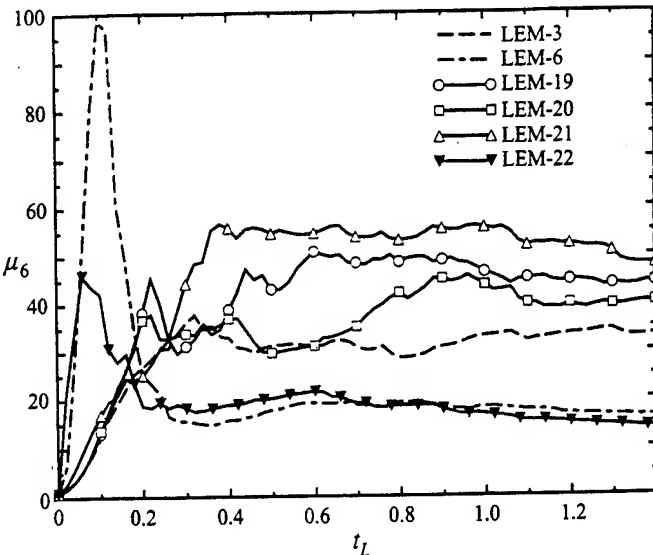


FIGURE 8. Temporal variation of the LEM-generated scalar superskewness. The scalar field is initialized in the physical domain as double square waves: LEM-3 ($Re = 90$, $Sc = 0.7$), LEM-6 ($Re = 90$, $Sc = 0.7$), LEM-19 ($Re = 50$, $Sc = 0.7$), LEM-20 ($Re = 900$, $Sc = 0.7$), LEM-21 ($L_u = 1$, $Re = 90$, $Sc = 0.05$), LEM-22 ($L_u = 3$, $Re = 90$, $Sc = 0.05$).

(usually flatter tail) p.d.f. develops. Note that the mechanism responsible for this non-Gaussian behaviour always exists. But when the initial weight of the small scales is large, the effects are more pronounced and are more clearly exhibited. In the cases considered here, the non-Gaussian behaviour generated by the first mechanism appears much stronger than that caused by the second route (compare, for example, LEM-18 with LEM-3).

At this point it is instructive to examine the influence of the model Reynolds number and the molecular Schmidt number on the outcome of mixing. While a thorough parametric study is not intended, cases LEM-19-LEM-22 provide some useful insight. In figure 8 results are presented of the temporal evolution of the scalar superskewness for the field initialized the same as in LEM-3 but with different values of the Reynolds and the Schmidt numbers. This figure shows that the overall influence of Re is not significant. This is to be expected, as in the context of the LEM the primary influence of the Reynolds number is on the variation of the velocity length scales participating in the rearrangement event. The influence of Sc is more intriguing. Figure 8 indicates that for the initial field composed of a double square wave with $L_u = 1$, a decrease in Sc yields a more pronounced exponential p.d.f. at long times, but it does not yield a noticeable influence when $L_u = 3$. The enhanced non-Gaussian behaviour at lower Sc values is not in accord with the expectation that the intermittency of the scalar derivative and the departure from Gaussian scalar p.d.f. increase with increasing Sc (Kerr 1985; McMurtry *et al.* 1993a). To explain the behaviour here, it is important to realize that in the absence of molecular diffusion the p.d.f. would not experience any changes. Therefore, as the magnitude of the molecular diffusion coefficient is increased, i.e. as Sc is decreased, the influence of molecular action on the p.d.f. becomes more pronounced. This influence is more noticeable when $L_u = 1$. In this case, the length scale of the velocity field is smaller than the largest scale of the scalar field. This velocity field influences the small scalar scales significantly but does not have a pronounced effect on the large scalar scales. As

Sc decreases, the difference between mixing of small-scale and of large-scale scalars becomes more significant. This yields a more exponential p.d.f. as demonstrated by the deviation of the results in LEM-21 from those in LEM-3. However, as the magnitude of the velocity length scale increases, the relative influence of advection (on the small- and the large-scale scalars) is similar and the p.d.f. at long times is not significantly modified. This is demonstrated by the similarity of the results in LEM-6 and LEM-22.

The results presented above can be better understood by considering the following physical scenario: consider two scalar blobs, one with a size smaller than the largest velocity eddy and the other blob larger than this eddy. As a result of advection, the small blob is almost immediately stirred by turbulence and follows the cascade down to small scales. The time scale of this process is the same as that of the turbulent diffusivity. In the same time period, the larger blob is only dispersed and 'waits' until its size becomes the same or smaller than that of the largest eddies. Then, it experiences a mixing similar to that felt by the smaller blob. Again, remember that molecular diffusion is only effective at small scales and the p.d.f. can only be changed with the presence of molecular diffusion. Therefore the p.d.f. corresponding to the small blob is now changed from an initial double delta to a mixed near-Gaussian form. The same would happen for the p.d.f. of the large blob but with a time lag. The weighted sum of the two statistics can behave in a variety of different forms depending on the weights of the two original blobs. At intermediate times, there will always be a combination of small and large scales as figure 8 does indicate strong non-Gaussian behaviour at intermediate times in all the cases. For the small blobs which are already stirred, molecular diffusion is more active and changes the p.d.f. more rapidly. During this change, the larger blobs wait until turbulence brings their sizes near to the active scales of molecular diffusion. Different statistics for different blobs imply, as indicated before, that the weighted sum of statistics exhibits stronger departure from Gaussian. Now if the size of the velocity eddy is larger than the largest of the scalar blobs, both blobs follow the turbulence cascade. During the time that molecular diffusion acts to change the p.d.f. from its double-delta form, the blobs are uniformly stirred by turbulence. Thus, the decrease of Sc would not have a significant influence on mixing at long times. In fact, if L_u is large enough it may even have an opposite effect. That is, as Sc decreases, the molecular diffusion can damp the rate of kurtosis and superskewness growth. Therefore, it is concluded that the role of Sc is very sensitive to both the initial scalar scale distribution and the initial extent of mixing. Further numerical simulations with large Schmidt numbers are required for a more elaborate investigation of this issue.

3. Direct numerical simulation

The results of the LEM simulations provide the guideline in our further, and somewhat more extensive, analysis of the problem via DNS. One of the early applications of DNS in the problem of turbulent scalar mixing and reaction is due to Hill (1979) and since then such simulations have provided a very useful and effective means of capturing some of the physical aspects of this complex phenomenon (Kerr 1983, 1985, 1990; Givi & McMurtry 1988; Eswaran & Pope 1988; Leonard & Hill 1988, 1991, 1992; McMurtry & Givi 1989; Metais & Lesieur 1992; Madnia, Frankel & Givi 1992; Frankel, Madnia & Givi 1993; Miller *et al.* 1993, 1995; Frankel 1993); a recent review is available (Givi 1994).

Our objective in the simulations conducted here is to analyse the statistical behaviour of passive scalars in three-dimensional, solenoidal, homogeneous and isotropic

velocity fields. All simulations are performed within a triply periodic box flow by means of a spectral-collocation numerical scheme employing Fourier basis functions (Givi & Madnia 1993). The hydrodynamic field is initialized by a random three-dimensional fluctuating velocity with zero mean and with a specified spectral density function. A wide-band von Kármán spectrum is imposed. The velocity field is then allowed to evolve according to the Navier-Stokes equations for more than 10 eddy turnover times to reach to a ‘self-similar’ condition. This is considered as the initial condition for the scalar mixing. Simulations are conducted with both ‘unforced’ and ‘forced’ hydrodynamic fields. In the former, the turbulence field is decaying whereas in the latter a steady turbulence field is established. The forcing scheme requires the energy in the low wavenumbers to remain constant. In this way the magnitudes of the turbulent length and velocity scales, and thus the magnitude of the Reynolds number, remain approximately constant throughout the evolution. Further details can be found in Givi (1989).

The transport of the scalar field is considered under two conditions: a zero mean scalar gradient and a constant (non-zero) mean scalar gradient.† In the former, the variance of the scalar field monotonically decreases as mixing proceeds; in the latter the mean scalar gradient forces the variance to reach an asymptotic value after a transient time. In this case, in order to maintain periodicity in all directions the scalar field ψ is decomposed into a mean and a fluctuating part as

$$\psi(\mathbf{x}, t) = \mathcal{A}y + \phi(\mathbf{x}, t). \quad (8)$$

Here ϕ denotes the mean-subtracted scalar value and \mathcal{A} is a constant denoting the magnitude of the mean scalar gradient. With this initialization the transport of the scalar fluctuation is governed by

$$\frac{\partial \phi}{\partial t} + \mathbf{V} \cdot \nabla \phi + \mathcal{A}v = \mathcal{D}_M \nabla^2 \phi, \quad (9)$$

where \mathbf{V} is the velocity field, v is the y -component of the velocity vector along which the scalar gradient is imposed, and \mathcal{D}_M is the molecular diffusion coefficient. This equation indicates that the mean scalar gradient acts like a ‘source’ term in the ϕ transport equation. It is the statistics of this field that are of importance. Moreover, when $\mathcal{A} \neq 0$, the statistics of the normalized variable ϕ/\mathcal{A} are expected to be similar at long times. This was verified numerically. All the cases considered are listed in tables 2 and 3. The simulations are conducted with the following three initialization schemes.

Scheme 1: The initial scalar field has a Gaussian p.d.f. and is specified in Fourier space. The amplitudes of the Fourier modes are selected based on a specified input energy spectrum. The weights of the real and the imaginary components of each Fourier mode are determined based on a random phase. With this, the initial scalar field adopts a Gaussian p.d.f. in the physical domain. The conditions in all the flows initialized in this manner are listed in table 2(a). Different forms of the initial scalar spectra are considered as indicated in the second column of table 2(a). In the cases with a double-hat spectrum, the parameter α is defined as

$$\alpha = \frac{E(K_{s1}, t=0)}{E(K_{s2}, t=0)}. \quad (10)$$

Scheme 2: The initial scalar field yields an approximate double-delta p.d.f.. The

† Hereinafter, a ‘constant’ mean scalar gradient implies a ‘non-zero’ gradient unless otherwise stated.

Case	Initial scalar spectra	\mathcal{A}	Turbulence	Re_λ	Sc
(a) DNS-1	Gaussian		Forced	58	0.5
DNS-2	Gaussian		Decaying	58 to 18	0.5
DNS-3	Gaussian		Forced	38	0.5
DNS-4	Gaussian		Decaying	38 to 13	0.5
DNS-5	Top-hat, $K_s = 1$		Forced	58	0.5
DNS-6	Top-hat, $K_s = 5$		Forced	58	0.5
DNS-7	Double-hat, $K_{s1} = 1, K_{s2} = 5, \alpha = 0.2$		Forced	58	0.5
DNS-8	Double-hat, $K_{s1} = 1, K_{s2} = 5, \alpha = 1$		Forced	58	0.5
(b) DNS-9	Top-hat, $K_s = 8$	0	Forced	58	0.5
DNS-10	Double-hat, $K_{s1} = 1, K_{s2} = 8, \alpha = 0.125$	0	Forced	58	0.5
DNS-11	Double-hat, $K_{s1} = 1, K_{s2} = 8, \alpha = 1$	0	Forced	58	0.5
DNS-12	Double-hat, $K_{s1} = 1, K_{s2} = 8, \alpha = 0.125$	0	Both	58 to 18	0.5
DNS-13	Double-hat, $K_{s1} = 1, K_{s2} = 8, \alpha = 1$	0.2	Forced	58	0.5
DNS-14	Top-hat, $K_s = 8$	0.5	Forced	58	0.5
DNS-15	Top-hat, $K_s = 1$	0.5	Forced	58	0.5
(c)	DNS-16 Square wave	0	Forced	58	0.5
DNS-17	Double square wave	0	Forced	58	0.5
DNS-18	Double square wave	0	Forced	58	0.05

TABLE 2. Conditions for 64^3 DNS. (a) Scheme 1 (with an initial Gaussian p.d.f.). Each of the simulations for DNS-1-DNS-4 are conducted under all of the following conditions: (I) $K_s = 8, \mathcal{A} = 0$, (II) $K_s = 4, \mathcal{A} = 0$, (III) $K_s = 1, \mathcal{A} = 0$, (IV) $K_s = 8, \mathcal{A} = 0.5$, (V) $K_s = 1, \mathcal{A} = 0.5$. In all the other simulations, $\mathcal{A} = 0$. (b) Scheme 2 (with an initial double-delta p.d.f.). In the case indicated 'both' in column 4 the flow is forced until $t_D = 3$. After this time, forcing is removed. (c) Scheme 3 (scalar field initialized in the physical domain).

scalar field is initialized in a more isotropic manner than that composed of square waves (Scheme 3). The procedure is essentially the same as that first proposed by Eswaran & Pope (1988). Again, the components of the Fourier scalar modes are specified by a random phase. These components are then transformed back into the physical space. The scalars with a negative amplitude are set to $\phi = -1$ and those with a positive value are set to $\phi = +1$. The numerical simulation of the field with this 'exact' double-delta distribution is not possible due to formation of very sharp gradients in the physical domain. This problem is overcome by transforming the scalar field into the Fourier domain and decreasing the relative weights at high wavenumbers. As a result, the physical values are no longer bounded by ± 1 (Eswaran & Pope 1988). This field is allowed to go through molecular diffusion to reduce the amplitude. In the simulations here the initial scalar values are bounded by ± 1.01 . Table 2(b) provides the list of all the parameters employed in DNS of flows initiated by this scheme.

Scheme 3: The scalar field is initialized in the physical domain in such a way as to yield a square wave in the y -direction (Givi & McMurtry 1988). The scalar slabs with $\phi = \pm 1$ values are similar to those shown in figure 1 for LEM-1. To avoid sharp gradients in DNS, the scalar slab interfaces are prescribed by an error function. The scalar values are constant in (x, z) -planes in each of the locations along the y -direction. The flow parameters for the simulations with this initialization are listed in table 2(c).

The simulations of the cases listed in table 2 are conducted in a domain discretized by 64^3 Fourier-collocation points. In a few cases, listed in table 3, some simulations with 128^3 collocation points are also conducted. In some of the cases, the simulations are repeated several (up to 10) times to ensure the reliability of the statistics; the

Case	Scheme	Initial scalar field	α	Turbulence	Re_λ	Sc
BDNS-1	3	Double square wave	0	Forced	80	0.5
BDNS-2	2	Double-hat, $K_{s1} = 1, K_{s2} = 8, \alpha = 0.125$	0	Forced	80	0.5
BDNS-3	1	Gaussian, $K_s = 8$	0.5	Forced	80	0.5

TABLE 3. Conditions for 128^3 DNS. For schemes 1 and 2 column 3 specifies the initial shapes of the spectral density function of the scalar. For scheme 3 column 3 specifies the initial scalar profile in the physical space.

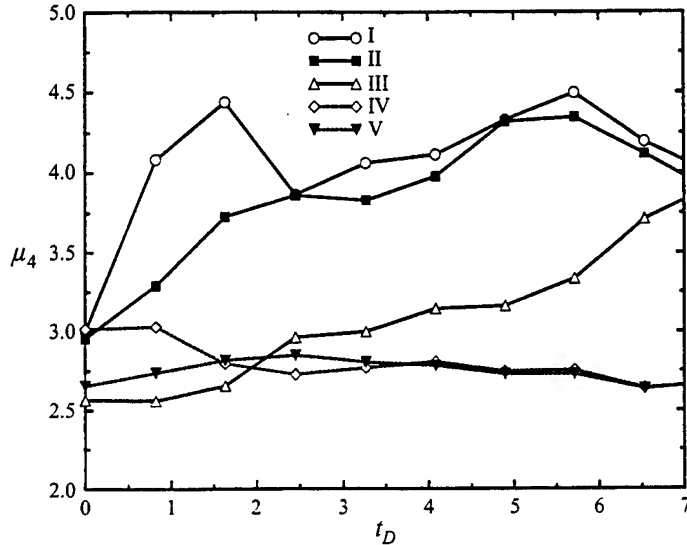


FIGURE 9. Temporal variation of the scalar kurtosis generated by DNS-1. Forced turbulence, $Re_\lambda = 58$, with an initial Gaussian spectrum and an initial Gaussian p.d.f. (Scheme 1): (I) $K_s = 8, \alpha = 0$, (II) $K_s = 4, \alpha = 0$, (III) $K_s = 1, \alpha = 0$, (IV) $K_s = 8, \alpha = 0.5$, (V) $K_s = 1, \alpha = 0.5$.

trends portrayed by the statistics are shown to remain similar. The definition of the other variables listed in tables 2 and 3 is clear. These variables indicate the presence ($\alpha \neq 0$), or the absence ($\alpha = 0$) of the mean scalar gradient, the dynamics of the velocity field (forced, decaying, or both), and the magnitudes of the Reynolds number based on the Taylor length scale (Re_λ) and the molecular Schmidt number (Sc).

DNS results

The 'time' t_D in the figures presented in this section denotes the time as normalized by the eddy turnover time of DNS. Since a variety of different conditions are considered, the magnitude of the eddy turnover time is not identical in all the simulations. In the cases with a decaying turbulence field, the initial eddy turnover time is used. It is important to indicate here that τ_L is an order of magnitude larger than τ_D (McMurtry *et al.* 1993a). In all of the cases described below, the field of velocity fluctuations exhibits a nearly Gaussian p.d.f.. The statistics of this field are not presented here; rather, the statistical behaviour of the scalar field is the subject of detailed discussions.

First, the mixing evolution from an initial Gaussian state (Scheme 1) is considered. As indicated in table 2(a), the difference between the cases is associated with the

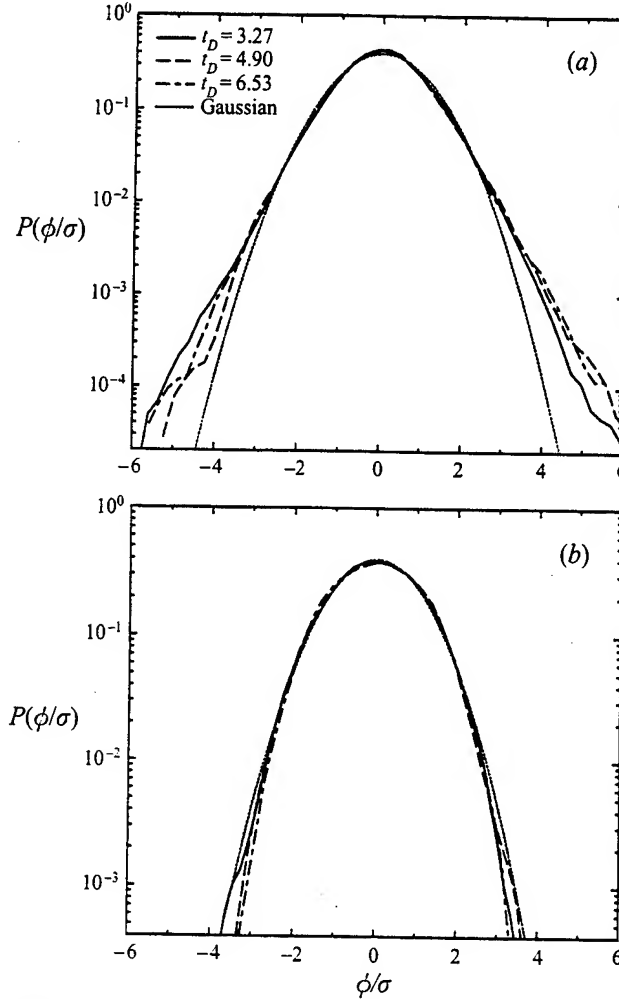


FIGURE 10. Normalized p.d.f.s of the scalar field at several time levels generated by DNS-1.
(a) case I: $K_s = 8$, $\alpha = 0$; (b) case IV: $K_s = 8$, $\alpha = 0.5$.

magnitudes of K_s and α . Each of the simulations for an initial Gaussian spectrum (DNS-1–DNS-4) is conducted under all of the following conditions: (I) $K_s = 8$, $\alpha = 0$; (II) $K_s = 4$, $\alpha = 0$; (III) $K_s = 1$, $\alpha = 0$; (IV) $K_s = 8$, $\alpha = 0.5$; (V) $K_s = 1$, $\alpha = 0.5$. In figure 9 the temporal evolution of the kurtosis for DNS-1, cases I–V is presented. To generalize the conclusions drawn from the scalars' kurtosis profiles, the variations of higher-order moments, the profiles of the p.d.f.s, the 'conditional expected dissipation' of the scalars, and the correlation between the scalar and its dissipation (equation (4)) are monitored in all the simulations. These statistics are useful for a quantitative description of the departure from Gaussian, especially at the tails of the p.d.f. (Sinai & Yakhhot 1989; Miller *et al.* 1993; Jaber, Miller & Givi 1995). However, with the exception of the p.d.f.s and some of the higher moments in some of the cases, these profiles are not shown. The results in figure 9 indicate that in I and II the p.d.f.s quickly develop exponential tails, whereas in IV and V they remain approximately Gaussian at all times. These are also observed in the p.d.f. profiles in figure 10 for cases I and IV. In III, the scalar field starts with

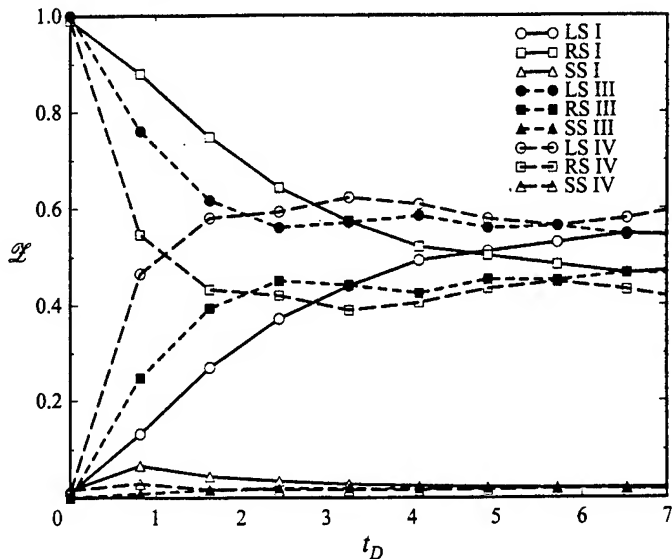


FIGURE 11. Temporal variation of the parameter \mathcal{Z} generated by DNS-1. I: $K_s = 8$, $\alpha = 0$, III: $K_s = 1$, $\alpha = 0$, IV: $K_s = 8$, $\alpha = 0.5$.

mostly large length scales. Thus, the statistics remain Gaussian for a long time. In the presence of a constant mean gradient, the kurtosis varies slightly (IV, V) regardless of initial conditions. As expected, after the initial transient time the statistics become identical in these two cases. The trends observed in the first three cases can be explained in view of the LEM results. The initial field in case I is mostly composed of small scalar scales; thus the behaviour is somewhat similar to that in LEM-18. That is, the second mechanism for non-Gaussian behaviour, as identified above is observed. In III, the initial scalar field is dominated by large scales; thus the tendency for non-Gaussian behaviour is very weak for a long time. In case II, the initial field is composed of both small and large scalar scales and yields a relatively strong non-Gaussian behaviour similar to that observed in LEM-8.

A useful means of characterizing the influence of mixing is by band-pass filtering of the DNS data. Here, the whole band of the scalar spectrum in the range $0 < k < 30$ is divided into regions $0 < k \leq 3$, $3 < k \leq 15$, $15 < k \leq 30$, and $30 < k \leq 30$. At the ranges of the Reynolds numbers considered, the separation of scales in the physical domain cannot be represented by a Fourier band-pass cutoff. Nevertheless, we refer to these regions as those pertaining to large scales (LS), intermediate scales (IMS), retained scales (RS) and small scales (SS), respectively. The temporal variation of the 'percentage of the scalar energy' is defined as

$$\mathcal{Z}(t) = \frac{\int_{K_l}^{K_u} E_\phi(K, t) dK}{\int_0^{K_{max}} E_\phi(K, t) dK}, \quad (11)$$

where K_l , K_u indicate the lower and the upper cutoff wavenumbers, respectively, and the denominator on the right-hand-side denotes the scalar variance. The corresponding \mathcal{Z} values for some of the representative cases of DNS-1 are shown in figure 11. This figure indicates that in all the cases (some not shown for clarity) only a very small portion, typically less than 2%, of the total energy is associated with SS. In case I,

the magnitude of \mathcal{L} associated with LS increases and that of RS decreases, until the two become very close at $t_D \approx 4$. A similar trend is observed in II (not shown) but the initial difference between the LS and the RS values of \mathcal{L} are understandably less. Therefore, it takes a shorter time for the two \mathcal{L} values to become equivalent. In III, the \mathcal{L} values for LS are significantly greater than those for RS at initial times. Therefore, the statistics are expected to be dictated primarily by LS. In IV, the initial evolution of \mathcal{L} values is similar to those in I. However, within a very short time LS values become larger than those corresponding to RS. The results for V (not shown) are in accord with those here: at small times the profiles are similar to those in III and after $t_D \approx 2$ they become almost identical to those in IV. A striking feature portrayed by these results is the independence of the results at long time from the variance ratios at the initial time. Figure 11 indicates that despite a noticeable difference in the initial allocation of variances pertaining to LS and RS, the long-time ratios of the variances are very close. In fact, with the two cases with a mean gradient the results are almost identical. The kurtosis values of the filtered data are presented in figure 12. Part (a) of this figure indicates that the p.d.f.s associated with LS are nearly Gaussian at all times in all the cases. The IMS-p.d.f.s (figure 12b) are flatter than Gaussian, but the departure from Gaussian is less when a mean gradient is imposed. In all the cases, the kurtosis values associated with SS are consistently high (figure 12c), indicating exponential p.d.f.s for SS. These results indicate that while non-Gaussian behaviour can be developed within the full and the intermediate scales, it is not an inherent property of large scales. This observation is very useful in our discussions below.

Contrary to that of the scalar, the p.d.f. of scalar derivatives exhibits a somewhat similar behaviour in all the cases. In figure 13, results are presented of the p.d.f. of $\partial\phi/\partial y$ where it is shown that in all the cases an intermittent behaviour is prevailed. Moreover, the statistics are expected to be different when a mean scalar gradient is imposed. The results in figure 13 show symmetric p.d.f.s for cases I-III, but skewed p.d.f.s for IV and V. It has been established that a scalar field embedded in a locally isotropic velocity field may not be locally isotropic (Budwig, Tavoularis & Corrsin 1985; Thoroddsen & Van Atta 1992; Tong & Warhaft 1994). This is typically measured by the skewness of the scalar-fluctuation derivatives since, by reflectional symmetry they should all vanish if the scalar field is locally isotropic. The asymmetry of the p.d.f. in figure 13 is consistent with the experimental measurements (Van Atta & Antonia 1980; Tavoularis & Corrsin 1981a; Budwig *et al.* 1985; Thoroddsen & Van Atta 1992) and recent simulated results (Holzer & Siggia 1994; Pumir 1994; Miller *et al.* 1995). The mechanism responsible for the skewness is due to the mean scalar gradient, even though the velocity field is isotropic. The p.d.f.s of the scalar dissipation (not shown) exhibit departure from a log-normal distribution with a considerable skewness, consistent with the results of previous computational and experimental investigations (Eswaran & Pope 1988; Andrews & Shivamoggi 1990; Vincent & Meneguzzi 1991; Jayesh & Warhaft 1992; Miller *et al.* 1995).

The temporal evolution of the scalar kurtosis in DNS-2 (for cases I-V) with an unforced hydrodynamic field is shown in figure 14. A comparison of this figure with figure 9 reveals the significance of forcing. In case I, a mild increase in the kurtosis suggests that a non-Gaussian p.d.f. for this case is due to the interaction of diffusion and advection at small scales which is weaker than that in the stationary field (DNS-1). In II, the magnitude of the kurtosis increases (similar to that in DNS-1(II)), but the tendency to return toward the Gaussian state is very weak and the field retains its non-Gaussian state even at long times. The decay of turbulence energy is the primary factor in retaining the non-Gaussian p.d.f.. Again, in the presence of the

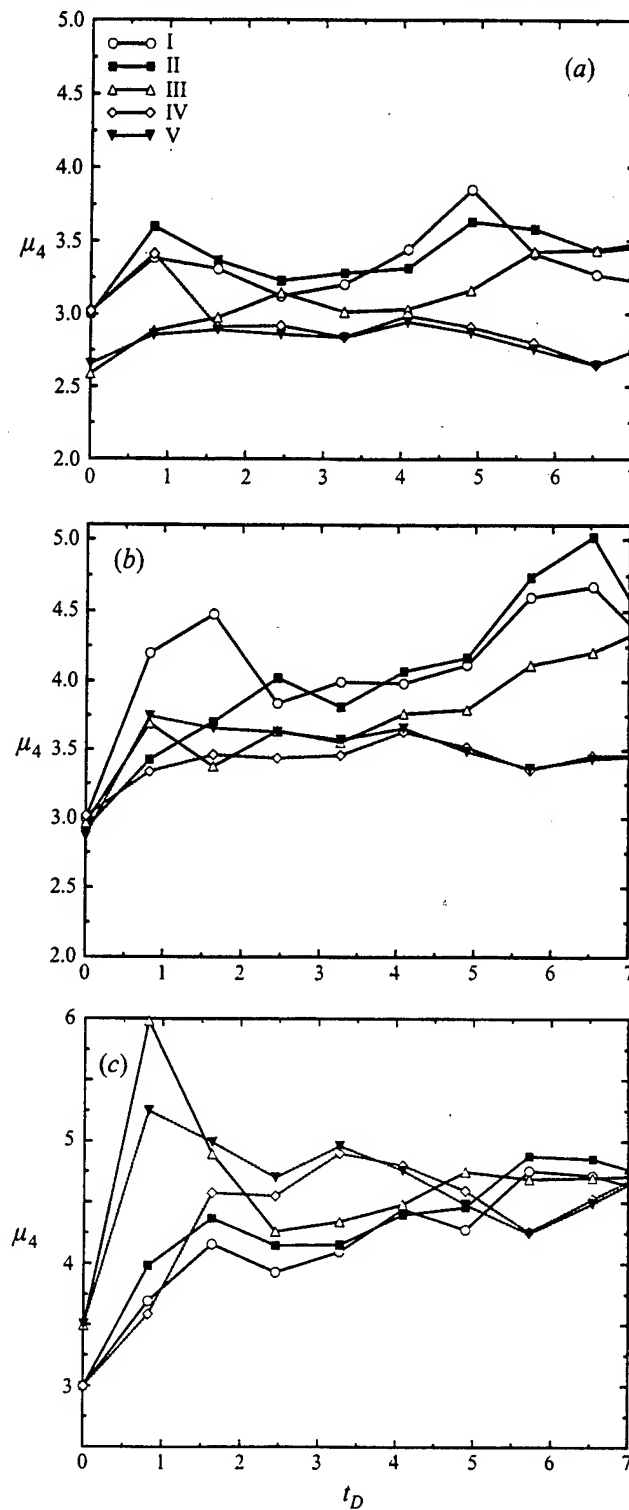


FIGURE 12. Temporal variation of the partitioned kurtosis generated by DNS-1. I: $K_s = 8$, $\alpha' = 0$, II: $K_s = 4$, $\alpha' = 0$, III: $K_s = 1$, $\alpha' = 0$, IV: $K_s = 8$, $\alpha' = 0.5$, V: $K_s = 1$, $\alpha' = 0.5$. (a) LS ($0 < K \leq 3$), (b) IMS ($3 < K \leq 15$), (c) SS ($15 < K \leq 30$).

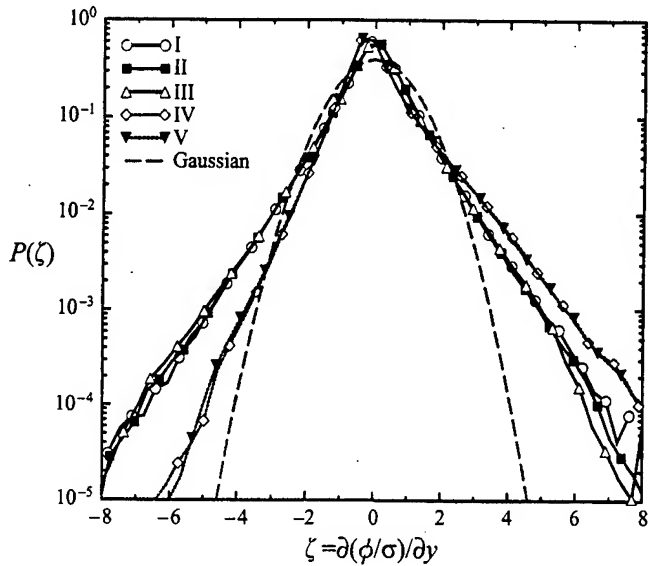


FIGURE 13. Normalized p.d.f.s of the scalar derivatives in the y -direction in DNS-1 at $t_D = 3$.

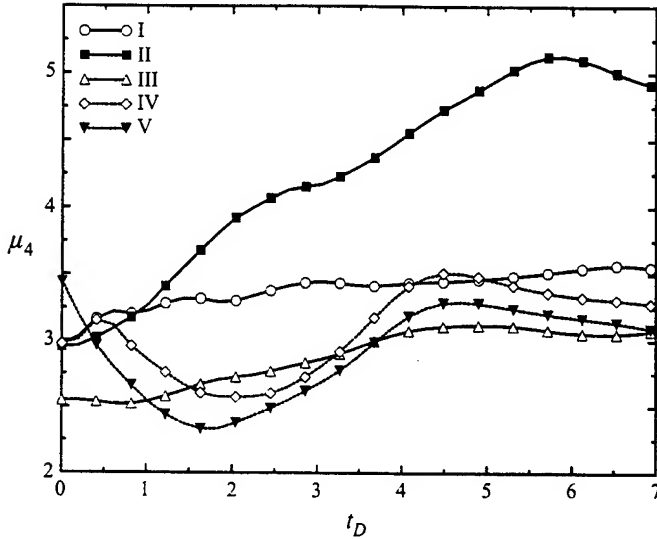


FIGURE 14. Temporal variation of the scalar kurtosis generated by DNS-2. Decaying turbulence, $Re_\lambda = 58$ to 18, with an initial Gaussian spectrum and an initial Gaussian p.d.f. (Scheme 1): (I) $K_s = 8$, $\alpha = 0$, (II) $K_s = 4$, $\alpha = 0$, (III) $K_s = 1$, $\alpha = 0$, (IV) $K_s = 8$, $\alpha = 0.5$, (V) $K_s = 1$, $\alpha = 0.5$.

mean gradient (cases IV and V) the statistics at long times are similar. However, it is noted that the extent of similarity is not the same as that in cases IV and V of DNS-1. This implies that in a decaying field with a mean scalar gradient, the effect of initial conditions can be more preserved than in a stationary field. This behaviour was consistently observed in all our other simulations and is useful in interpreting some of the experimental results, as will be discussed in the next section. The p.d.f.s of the y -derivative of the scalar (not shown) portray a trend similar to that in figure 13 indicating that skewed p.d.f.s are also formed in decaying (lower Re) flows.

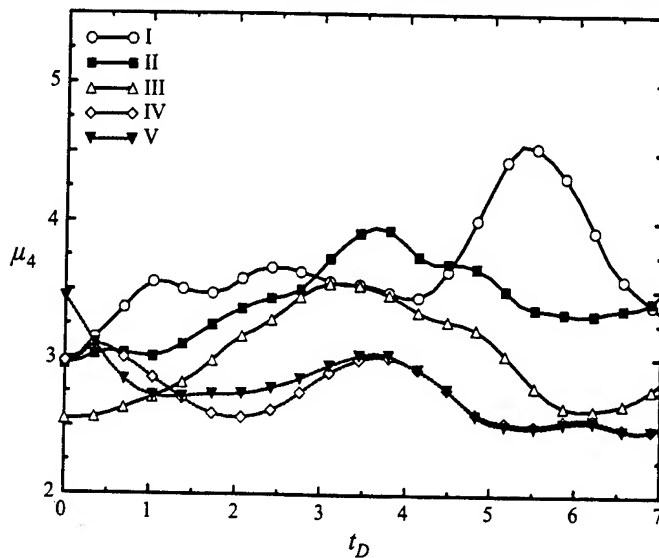


FIGURE 15. As figure 14 but generated by DNS-3. Forced turbulence, $Re_\lambda = 38$.

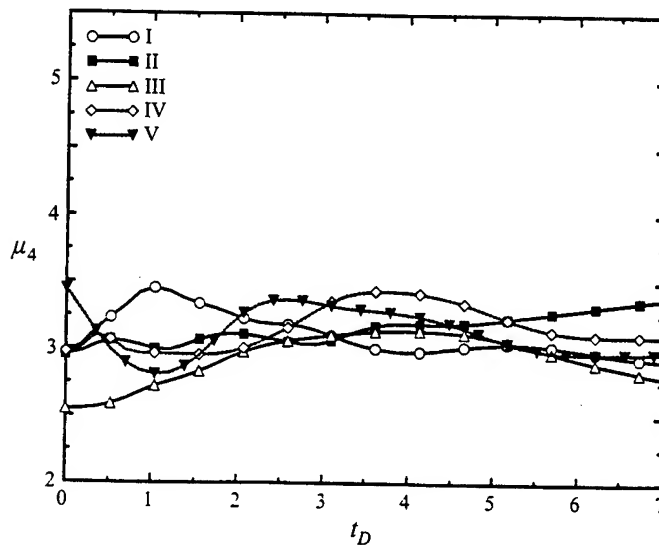


FIGURE 16. As figure 14 but generated by DNS-4. Decaying turbulence, $Re_\lambda = 38$ to 13.

A decrease in the magnitude of the Reynolds number is expected to yield a milder non-Gaussian behaviour. This is shown in figure 15 where results are presented for DNS-3. The Reynolds number in all the cases in DNS-3 is smaller than those in DNS-1. A comparison of this figure with figure 9 indicates that the initial growth rate of the scalar kurtosis is less when the Reynolds number is decreased. In case I, after a mild increase during four eddy turnover times, the kurtosis increases abruptly and then relaxes toward the Gaussian value. Again, in all the cases with the mean scalar gradient (cases IV and V) the scalar field remains Gaussian at all times. The influence of hydrodynamic forcing is more dominant at this lower Reynolds number, as the results for DNS-4 in figure 16 show that with a decaying turbulence field, no

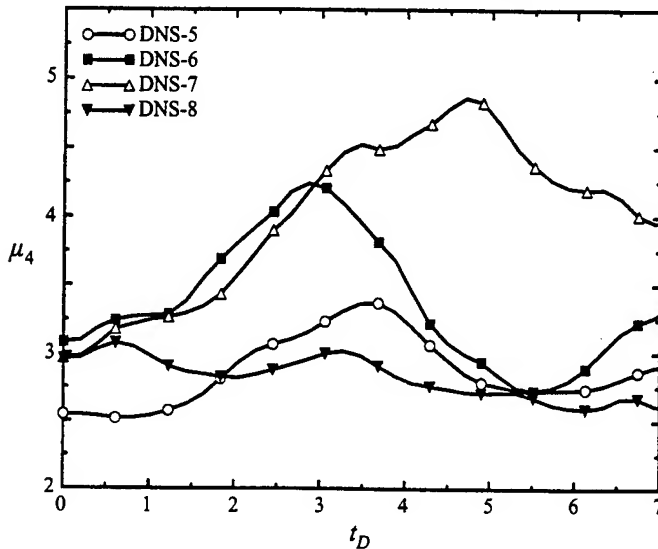


FIGURE 17. Temporal variation of the DNS-generated scalar kurtosis. Forced turbulence, $Re_\lambda = 58$. The scalar field is initialized with a top-hat or double-hat spectrum and an initial Gaussian p.d.f. (Scheme 1). DNS-5 ($K_s = 1$), DNS-6 ($K_s = 5$), DNS-7 ($K_{s1} = 1, K_{s2} = 5, \alpha = 0.2$), DNS-8 ($K_{s1} = 1, K_{s2} = 5, \alpha = 1$).

significant change is observed from the initial Gaussian scalar field (compare with figures 14 and 15).

Based on the results presented for DNS-1–DNS-4 it can be concluded that at moderate Reynolds numbers, the statistics of the scalar field with a zero mean scalar gradient are strongly dependent on the initial conditions. In the presence of a steady (forced) advection field, the scalar p.d.f. can change from an initial Gaussian to a highly non-Gaussian distribution depending on the initial weights of small- and large-scale scalars. If the turbulence field is allowed to decay, once a non-Gaussian p.d.f. develops it lasts longer. As the magnitude of the Reynolds number decreases it is still possible to develop non-Gaussian p.d.f.s although at a much later time. Now if, in addition, the turbulence field is allowed to decay, departure from the Gaussian state is further delayed (in our case it is never developed).

To further examine the effects of the initial scalar length scale distribution on the long-time statistics, the results for DNS-5–DNS-8 are considered in figure 17. In DNS-5 and DNS-6, the scalar field is initialized with a Gaussian scalar p.d.f. and a top-hat energy spectrum. The results for these two cases indicate that, in accord with the LEM results (LEM-9, LEM-18), by increasing the magnitude of K_s the kurtosis adopts higher values at intermediate times. By adding a small amount of energy at large scales the non-Gaussian behaviour can be significantly enhanced. This is witnessed in DNS-7 in which the initial field is similar to DNS-6 (with $K_{s2} = 5$) but with a relatively small energy ($\alpha = 0.2$) at $K_{s1} = 1$. In this case, the exponential behaviour is preserved throughout mixing. However, for large α values, e.g. DNS-8 in which the energy is distributed equally between wavenumbers 5 and 1, the growth of the kurtosis is significantly damped. In this case, the field is dominated by large scales and does not allow exponential p.d.f.s. The results for a case with $K_{s1} = 1, K_{s2} = 8$ show a similar behaviour, and thus are not shown. These observations are in accord with our earlier findings based on the LEM in that the presence of initial multi-length scalar scales results in departure from Gaussian if the initial energy is distributed

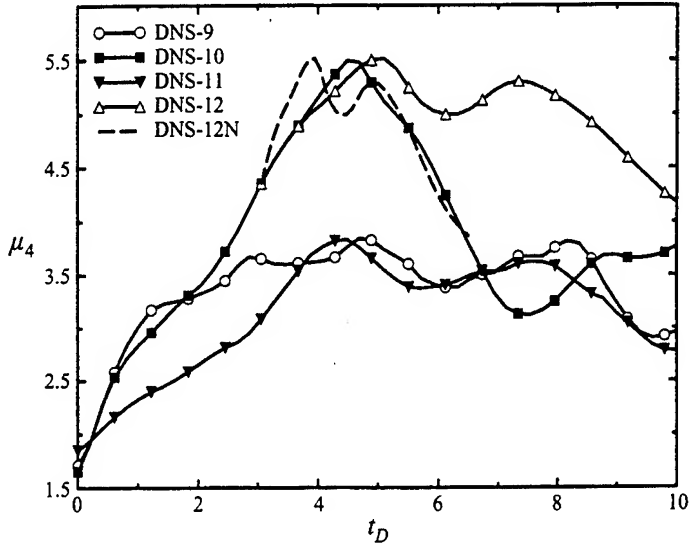


FIGURE 18. Temporal variation of the DNS-generated scalar kurtosis. The scalar field is initialized with a top-hat or double-hat spectrum and an initial double-delta p.d.f. (Scheme 2). DNS-9 ($K_{s1} = 8$), DNS-10 ($K_{s1} = 1$, $K_{s2} = 8$, $\alpha = 0.125$), DNS-11 ($K_{s1} = 1$, $K_{s2} = 8$, $\alpha = 1$), DNS-12 ($K_{s1} = 1$, $K_{s2} = 8$, $\alpha = 0.125$). All cases are with a forced turbulent field. The forcing is removed at $t_D = 3$ in DNS-12. The case DNS-12N is the same as DNS-12 but the time axis is normalized by the effective eddy turnover time.

'appropriately' and the field is not dominated by large scales. By 'appropriate' it is meant that there is some energy at large scalar scales, but its magnitude is smaller than that at other scales. It is not at present possible to predict *a priori* the response to a specific α value in the range specified without conducting DNS.

The results for the cases with an initial double-delta p.d.f. (Scheme 2) are discussed next. The evolution of the kurtosis in DNS-9–DNS-12 is shown in figure 18. This figure shows that in contrast to the case with an initial Gaussian p.d.f., when the magnitude of energy in the small scales is relatively large (DNS-9), the kurtosis at long times is not significantly larger than 3. This suggests that starting from an unmixed scalar field, the increase of small scales does not necessarily yield non-Gaussian behaviour. By increasing energy by 12.5% at large scales (DNS-10) the kurtosis grows significantly and the p.d.f. develops exponential tails. However, at $t_D \approx 4.5$ the kurtosis starts to decrease rapidly and adopts a near-Gaussian value at long times. The reason for this return to the Gaussian state is that in this case the dominant scalar length scale is comparable to the hydrodynamic length scale. So, the exponential nature of the p.d.f. is rapidly destroyed by the stirring process (similar to LEM-6). This is further assessed in DNS-12. The initialization in this case is similar to that in DNS-10, but at $t_D = 3$ the forcing of the hydrodynamic field is removed. In this case, interestingly, the kurtosis decays very slowly and the exponential nature of the p.d.f. is preserved for a longer time. As before, by increasing the energy at large scales (DNS-11) the growth of the kurtosis is damped and the p.d.f. remains close to Gaussian. A comparison of the results for cases DNS-10 and DNS-12 suggests that once an exponential p.d.f. is established it has less tendency to relax when the turbulent field is decaying. The difference between DNS-10 and DNS-12 can be roughly related to the difference in the magnitudes of the eddy turnover times due to the difference in the advection fields in the two simulations.

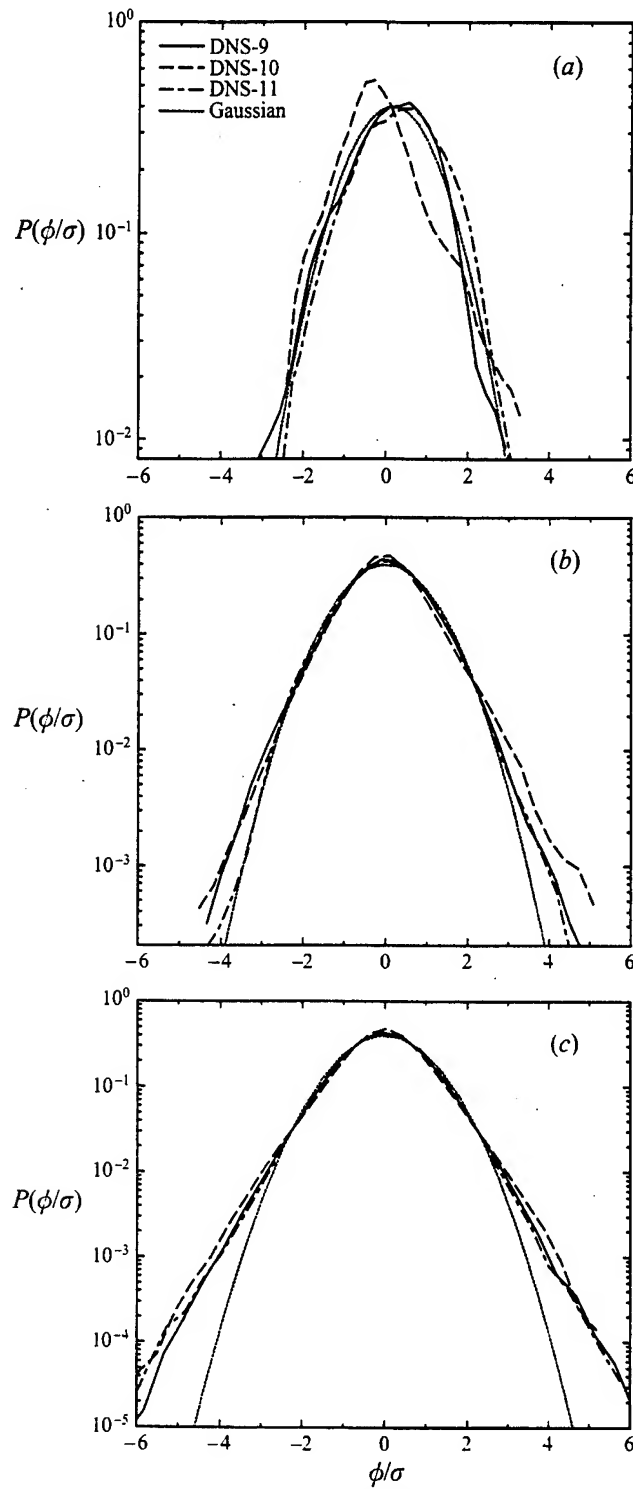


FIGURE 19. Normalized p.d.f.s of the bandpass-filtered scalar generated by DNS-9, DNS-10, and DNS-11 at $t_D = 4.286$. (a) LS: $0 < K \leq 3$, (b) IMS: $3 < K \leq 15$, (c) SS: $15 < K \leq 30$.

To show this, the time for DNS-12 is normalized by an 'effective' eddy turnover time which is the average of this time during the simulation after forcing is removed. The kurtosis results with the time axis scaled in this way are identified by DNS-12N in figure 18. Within the time duration of the simulation, the trend in kurtosis values in DNS-12N is close to that in DNS-10. However, the values are not identical. This is expected as the average of the eddy turnover time, as evaluated here, is not capable of reflecting the effects of the modified advection field. Nevertheless, all these results confirm that exponential p.d.f.s can be developed by adding an appropriate amount of large scales to the initial scalar field. It must be pointed out that the departure from Gaussian is not the explicit character of large scales. In figure 19 the p.d.f.s of filtered data are presented for cases DNS-9–DNS-11. Figure 19(a) indicates that the large scales, although somewhat asymmetric, are close to Gaussian. The IMS statistics, figure 19(b), do show long-tailed p.d.f.s with a small degree of asymmetry due to the distribution of the initial energy. The p.d.f.s for the scalar field in SS are similar and exponential in all the cases (figure 19c).

The variations of the kurtosis and the skewness values for DNS-13 are compared with those of DNS-11 in figure 20(a). In DNS-13 the initial scalar field, similar to DNS-11, is composed of a double-delta p.d.f. with significant energy at large scales. The results indicate that until $t_D \approx 12$, the statistics remain Gaussian in both cases. After this time, the kurtosis rises sharply in the case without a mean gradient (DNS-11), but there are no significant changes in the case with a mean gradient (DNS-13). The non-Gaussian behaviour in DNS-11 is the consequence of the presence of large initial scalar scales. It must be noted that this presence also results in skewed p.d.f.s in the simulations with a limited number of low-wavenumber modes. For the cases considered here, this is shown in figure 20(a) which in fact suggests large skewness values for DNS-11. Of course, if the calculations are repeated several times and statistics are gathered with a large number of realizations, the skewness would vanish but the kurtosis would not. However, the large scales do not cause skewed IMS p.d.f.s even those with flat-tail p.d.f.s. This is observed in figure 20(b) which shows that in DNS-11 and DNS-13 the p.d.f.s are fairly symmetric. Also, it is important to indicate that the behaviour shown in figure 20(a) for DNS-11 is not due to a numerical resolution problem. The normalized spectral density functions of the scalar (E_ϕ) and its dissipation (D_ϕ), shown in figure 20(c), are very similar in the two cases and are also similar to the corresponding spectra of the velocity field. The behaviour portrayed by DNS-11 and DNS-13 are also observed in two additional simulations (not shown here) in which the initial spectral density function obeys a power law of the form k^{-3} . For the case with $\alpha = 0$, the behaviour is similar to that in DNS-11, but with a negative skewness at long times. The results for $\alpha = 0.2$ are identical to those in DNS-13. All these results indicate that the presence of large scales is a strong source of non-Gaussian behaviour. This observation is very useful in interpreting some of the experimental results as discussed in the next section.

The non-Gaussian behaviour just described is not observed in the presence of a mean scalar gradient with the Scheme 2 initialization. The reason is that with such a

FIGURE 20. (a) Temporal variation of the DNS-generated scalar skewness and kurtosis. (b) p.d.f.s of the IMS ($3 < K \leq 15$) bandpass-filtered scalar at $t_D = 15.92$. (c) The spectral density functions at $t_D = 15.92$ of the velocity field $E_v(K)$, the scalar field $E_\phi(K)$, the dissipation of the velocity field $D_v(K)$ and the dissipation spectra of the scalar field $D_\phi(K)$. Forced turbulence, $Re_\lambda = 58$. The scalar field is initialized via Scheme 2 with an initial double-delta p.d.f. and with a double-hat spectrum, $K_{s1} = 1$, $K_{s2} = 8$, $\alpha = 1$. DNS-11 ($\alpha = 0$), DNS-13 ($\alpha = 0.2$).

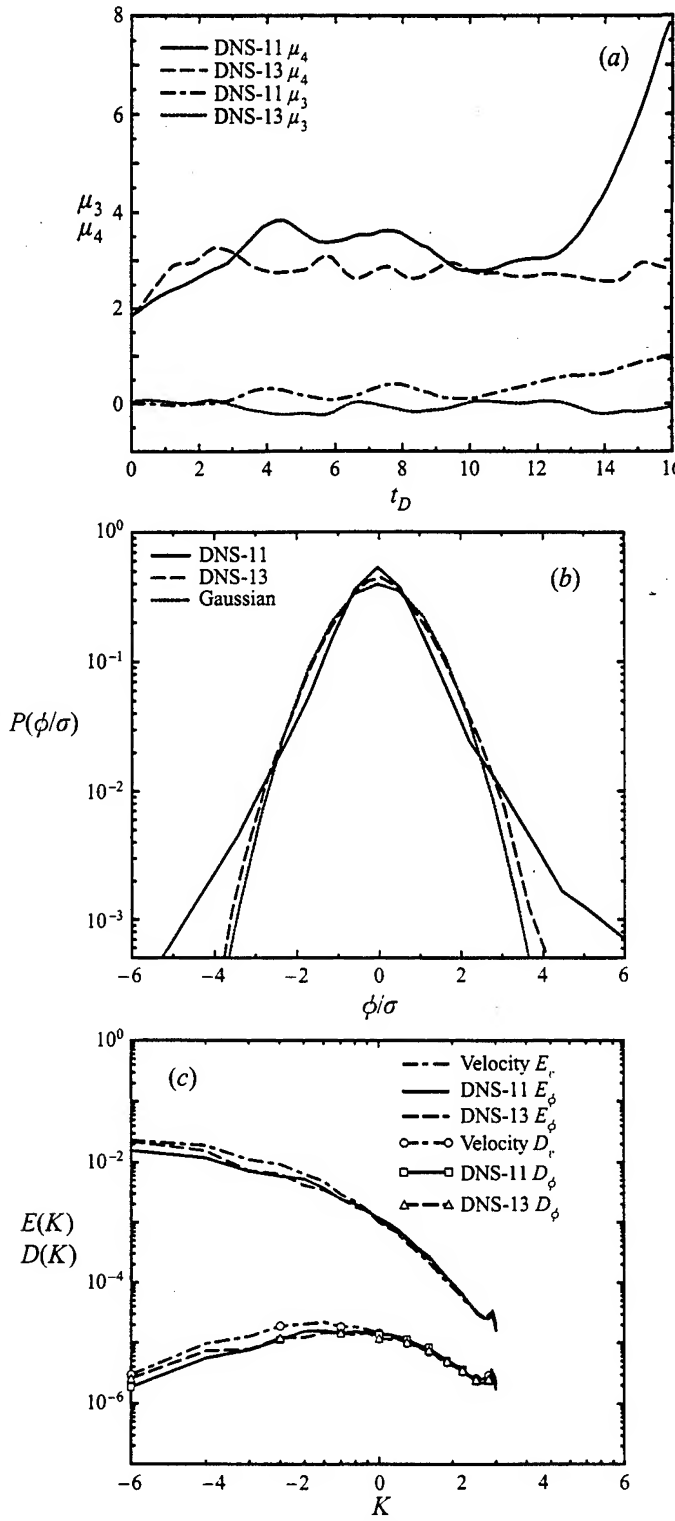


FIGURE 20. For caption see facing page.

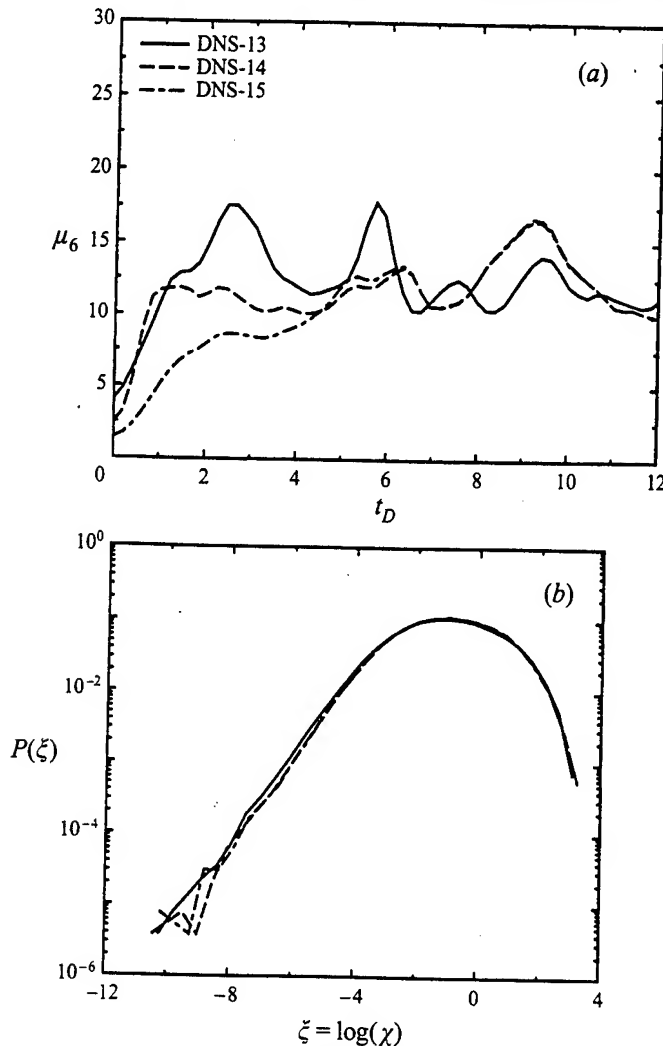


FIGURE 21. (a) Temporal variation of the DNS-generated scalar superskewness. (b) p.d.f.s of the scalar dissipation at $t_D = 12$. Forced turbulence, $Re_\lambda = 58$. The scalar field is initialized via Scheme 2 with an initial double-delta p.d.f. DNS-13 (double-hat spectrum, $K_{s1} = 1$, $K_{s2} = 8$, $\alpha = 1$, $\omega = 0.2$), DNS-14 (top-hat spectrum, $K_s = 8$, $\alpha = 0.5$). DNS-15 (top-hat spectrum, $K_s = 1$, $\alpha = 0.5$).

gradient, the long-time statistics are fairly independent of initial conditions and also independent of the amplitude of the scalar gradient. This is demonstrated by the results for DNS-13–DNS-15 in which both the initial scalar conditions and the magnitude of ω are varied. The results are given in figure 21(a) for the superskewness evolution and in figure 21(b) for the p.d.f.s of the scalar dissipation (χ) at $t_D = 12$. These figures demonstrate that the behaviour at long times is similar in all these cases (the spectral density functions are also similar, but are not shown). Of course, the independence from the initial conditions would be less pronounced in a decaying turbulence field.

In comparing the results generated by DNS with those via LEM one should keep in mind that the ratio of the length scale of the velocity to that of the scalar is an important parameter in the characterization of mixing. In DNS, these scales are limited by the computational domain (box size) at the upper bound. The same is also true in LEM but the scales can be imposed more independently of each other

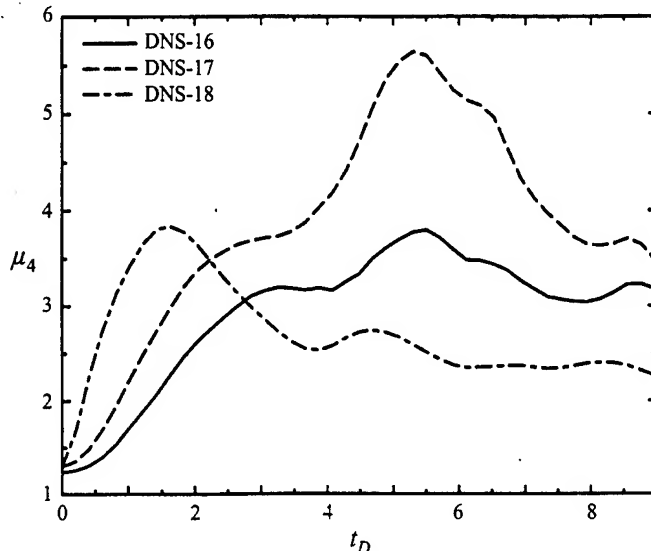


FIGURE 22. Temporal variation of the DNS-generated scalar kurtosis. Forced turbulence, $Re_\lambda = 58$. The scalar field is initialized via Scheme 3. DNS-16 (square wave, $Sc = 0.5$), DNS-17 (double square wave, $Sc = 0.5$), DNS-18 (double square wave, $Sc = 0.05$).

and with a higher degree of freedom in specifying the ranges. Here, it is shown that with the initialization of the scalar field in the form of square waves, trends similar to those depicted by LEM are observed. The simulations for $Sc = 0.5$ are labelled DNS-16 and DNS-17. For the former, a single square scalar wave (in the y -direction) is imposed. For the latter, a double square wave is imposed. Note that while the initial scalar profile in the y -direction is similar to that in the LEM initialization (figure 1), the initial scalar fields are not identical owing to the three-dimensionality of the DNS. The results in figure 22 show that after an initial transient time, the kurtosis remains close to 3 in DNS-16. But it increases in DNS-17 with a higher rate toward a larger value before decreasing to the near-Gaussian value at long times. This behaviour is similar to that observed in LEM-3; however, here the departure from Gaussian is not very significant since the dominant scale of the velocity is of the same order as that of the scalar (LEM-6).

The influence of the Schmidt number on the scalar p.d.f. is difficult to determine by DNS, as only a limited range of this parameter can be considered by direct simulations. However, some features are captured by a limited number of simulations and are discussed here. In DNS-18, the same initialization as DNS-17 is employed but with $Sc = 0.05$. The results in figure 22 indicate that by decreasing Sc the kurtosis grows faster initially, but then decreases and relaxes to a value less than 3. In these cases, the dominant scale of the velocity is of the same magnitude as that of the scalar. Thus the effect of Sc should be, and is, the same as that presented in figure 8 showing the difference between cases LEM-6 and LEM-22. Further extensive simulations with broader ranges of the length scales and the Schmidt number are required to generalize the influence of Sc on the scalar p.d.f. which (as shown in both the LEM and the DNS results) can be very complex. However, it seems that the effect of Sc on the scalar spatial-derivatives is somewhat less complex. In all the cases considered here it was observed that as Sc decreases, the intermittency of the scalar derivatives is less pronounced. This observation is consistent with previously established results (Kerr 1985).

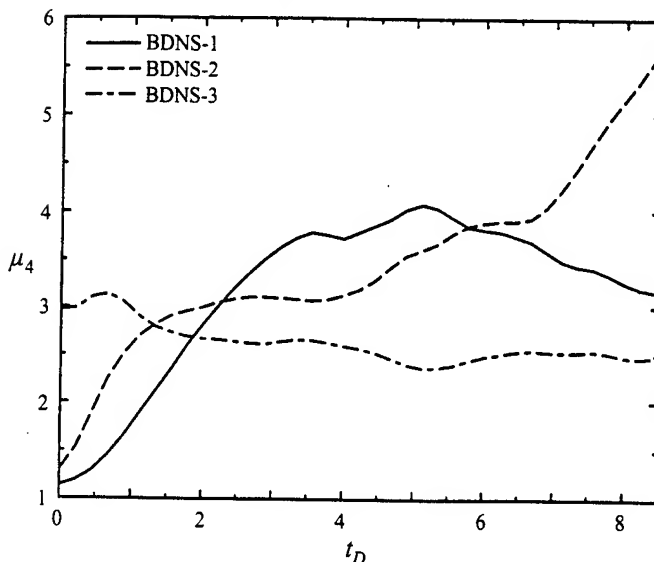


FIGURE 23. Temporal variation of the DNS-generated scalar kurtosis. Forced turbulence, $Re_\lambda = 80$. BDNS-1 (Scheme 3: double square wave, $\alpha' = 0$), BDNS-2 (Scheme 2: double-hat spectrum, $K_{s1} = 1$, $K_{s2} = 8$, $\alpha = 0.125$, $\alpha' = 0$). BDNS-3 (Scheme 1: Gaussian, $K_s = 8$, $\alpha' = 0.5$).

An important characteristic displayed in DNS results is the lack of an exponential p.d.f. in all the simulations with an imposed mean scalar gradient. This is consistent with the analysis of Kimura & Kraichnan (1993), but is not in accord with that suggested by Pumir *et al.* (1991), Jayesh & Warhaft (1992) and Holzer & Siggia (1994). To confirm this finding, and also to study mixing at larger Reynolds numbers here a few additional simulations are performed with a higher resolution (128^3 collocation points). The conditions for these simulations are listed in table 3. Cases BDNS-1, BDNS-2, and BDNS-3 are initialized in a manner similar to DNS-17, DNS-10 and DNS-1(IV), respectively, but with a larger magnitude of the Reynolds number. Figure 23 indicates that the behaviour of BDNS-1 is similar to that of DNS-17, but with less deviation from Gaussian at long times. This is expected since in these two cases (DNS-17, BDNS-1) the largest scales of the scalar and the velocity fields are nearly equal and the initial scalar field is composed of two large slabs. The increase in Re provides a better stirring of the unmixed initial scalar field. Thus the p.d.f. at long times would be closer to Gaussian. The evolution of the kurtosis for BDNS-2 does not exhibit the same trend since the long-time p.d.f. is exponential. In this case, the separation of initial scalar length scales is more clearly established and the large scales have a smaller weight. As indicated before, the presence of rare large scales (small α values) in the initial field is sufficient to cause non-Gaussian behaviour as shown here by large values of the kurtosis in BDNS-2. The results in BDNS-3 are nearly identical to those in DNS-1(IV, V) in which the kurtosis values remain near 3. This indicates that in the presence of a constant mean gradient, the p.d.f. remains close to Gaussian regardless of the value of the Reynolds number. It is useful to note that the magnitude of the Reynolds number based on the integral length scale (Re_I) here is twice the critical Re above which Jayesh & Warhaft (1992) suggest exponential p.d.f.s should prevail.

Finally, some of the present results are compared with available experimental data. A quantitative comparison is made here; further qualitative comparisons are made

Variable	DNS-3(IV)	TW94	TV92	BTC85
$\left\langle \left(\frac{\partial \phi}{\partial x} \right)^3 \right\rangle / \left\langle \left(\frac{\partial \phi}{\partial x} \right)^2 \right\rangle^{3/2}$	-0.09	<0.1	small	small
$\left\langle \left(\frac{\partial \phi}{\partial y} \right)^3 \right\rangle / \left\langle \left(\frac{\partial \phi}{\partial y} \right)^2 \right\rangle^{3/2}$	1.67	1.8	1.2	1.4
$\left\langle \left(\frac{\partial \phi}{\partial x} \right)^4 \right\rangle / \left\langle \left(\frac{\partial \phi}{\partial x} \right)^2 \right\rangle^2$	7.32	8.5	-	-
$\left\langle \left(\frac{\partial \phi}{\partial y} \right)^4 \right\rangle / \left\langle \left(\frac{\partial \phi}{\partial y} \right)^2 \right\rangle^2$	9.21	10.0	-	-
$\langle u\phi \rangle / (\langle \phi^2 \rangle \langle u^2 \rangle)^{1/2}$	-0.009	small	small	small
$\langle v\phi \rangle / (\langle \phi^2 \rangle \langle v^2 \rangle)^{1/2}$	-0.586	-0.7	-0.68	-0.65
$\langle (u\phi)^3 \rangle / (\langle \phi^2 \rangle \langle u^2 \rangle)^{3/2}$	-0.101	-	-	-
$\langle (v\phi)^3 \rangle / (\langle \phi^2 \rangle \langle v^2 \rangle)^{3/2}$	-2.398	-	-2.1	-
$\langle (u\phi)^4 \rangle / (\langle \phi^2 \rangle \langle u^2 \rangle)^2$	6.583	-	-	-
$\langle (v\phi)^4 \rangle / (\langle \phi^2 \rangle \langle v^2 \rangle)^2$	11.61	-	11.0	-

TABLE 4. Comparison between the present simulated results and experimental measurements for some of the variables for cases with a constant mean scalar gradient. In the experiments, $Re_s \approx 40$. TW94, TVA92 and BTC85 correspond to Tong & Warhaft (1994), Thoroddsen & Van Atta (1992) and Budwig *et al.* (1985), respectively.

in the next section. The experimental data considered are those provided by Budwig *et al.* (1985), Thoroddsen & Van Atta (1992) and Tong & Warhaft (1994). It must be indicated, however, that not all the conditions and the measured results are identical in these experiments. Moreover, some of the measured statistics are not invariable in each experiment and they are subject to change depending on the location of the measurements. In analysing the simulated results using such experiments, at least in the context considered here, it is more appropriate to make qualitative comparisons as done in the next section. Nevertheless, it is useful to examine the trends established numerically in the light of the laboratory data.

All our results indicate that intermittency of the scalar derivative in the x -direction (perpendicular to the direction of the mean scalar gradient) is enhanced as the Reynolds number increases. The same is true for the derivative in the y -direction (parallel to the mean gradient direction), but with higher skewness magnitudes. At the range considered the skewness does not seem to be noticeably dependent on Re . These results are consistent with recent results based on the experiments of Tong & Warhaft (1994) and the numerical results of Pumir (1994). Also, the simulated p.d.f.s of the velocity-scalar fluctuations ($u\phi$ and $v\phi$) are exponential with relatively high skewness values for $v\phi$. This is in accord with the experiments of Thoroddsen & Van Atta (1992). Table 4 provides a quantitative comparison between all the simulated and laboratory results. For this comparison, DNS-3(IV) is considered since in this case a mean scalar gradient is imposed in accord with the experiments, and the Reynolds number is close to that in the experiments of Thoroddsen & Van Atta (1992) and Tong & Warhaft (1994). The statistics in this table are generated via time averaging over several realizations, in addition to space averaging. This is justifiable since in the

presence of the mean scalar gradient, the field can be assumed quasi-stationary (or in a sense ergodic) at long times.

In accord with the experimental measurements, the numerical results show negligible skewness values for the scalar derivative and the scalar flux in the x -direction, but indicate significant skewness values for the y -derivative and the scalar flux in the y -direction. The simulated skewness and kurtosis values of the scalar gradients are close to those in the experiments of Tong & Warhaft (1994). With inclusion of data for BDNS-3 (with $Re_z = 80$) for the y -derivative skewness (1.59) and kurtosis (10.82), the numerical results indicate a relative independence of the skewness and Re_z , and a scaling of $Re^{0.21}$ for the kurtosis. These scalings are in accord with those suggested by Tong & Warhaft (1994). The experimental values for the mean flux $\langle v\phi \rangle$ are underestimated by DNS, but the simulated values of the skewness and the kurtosis of this flux compare well with the measurements (Thoroddsen & Van Atta 1992).

4. Further discussion

In the light of the numerical results generated, here an interpretation is provided of some of the features observed in recent laboratory and numerical experiments on scalar mixing in turbulent flows.

In the mixing experiments of Gollub *et al.* (1991) and Lane *et al.* (1993) of a flow between heated walls, the transition from a Gaussian to an exponential scalar p.d.f. is accompanied by a sharp increase in the effective diffusivity and a decrease in the magnitude of the mean scalar gradient within a region far from the boundary layers. Most of the temperature drop occurs in the boundary layer, and the interior mean temperature varies linearly from one side to the other. However, the magnitude of the mean temperature gradient in the interior regions varies nonlinearly with the Reynolds number. The steep decline of the magnitude of the mean gradient near the critical Re implies a substantial increase in the bulk thermal transport over a relatively narrow region near the wall. The sharp growth of the skewness of scalar fluctuations for Reynolds numbers greater than a critical value is also an important characteristic of this experiment. This skewness is preserved even when considering a large sample size and is not a consequence of limited statistical data or measurement errors. Lane *et al.* (1993) explain that the skewness may be generated by a weak large-scale flow drift which might be caused by flow instabilities at high Re . They also indicate that by increasing the correlation length scale of the velocity from 0.48 to 1.7 cm the scalar p.d.f. remains Gaussian even up to $Re = 8000$. The critical Re above which sudden changes occur in the bulk properties in this case is 1000. In several aspects, these results are in accord with our findings. Before the transition Re the statistics are mostly determined by the mean gradient. The unmixed large-scale plumes within the boundary layer are stable and do not mix with interior fluids. This means that the statistics are dictated by the interior linear (approximately) mean scalar profile where the fluids are well mixed. Therefore, the p.d.f. remains approximately Gaussian. As Re increases to its critical value, the large scales at the boundary become unstable and are engulfed within the interior regions of the flow. These are still large-scale structures and their combination with the mixed interior fluid results in skewed p.d.f.s with broad tails. This behaviour is observed in our LEM (cases LEM-3, LEM-8, LEM-14) and DNS (cases DNS-10, DNS-11, BDNS-2) results. The instability of large scales facilitates the transport of the energy-containing scales at the boundary into the interior region, resulting in the increase of the heat flux and the effective diffusivity. At the same time, the fluid within the interior region

is more vigorously mixed yielding a low value of the local mean scalar gradient. The fluid in this region is continuously fed by rare large scales, and the unmixed thermal plumes are convected from boundary flows and are stirred by the interior flow. If the feeding by the large scales is continuous, as it is in the experiments, the p.d.f. remains exponential. If there is no influx of large scales, then mixing is transient and a Gaussian p.d.f. is eventually observed. These observations are in accord with our simulations as we show that the presence of rare large scales yields exponential p.d.f.s. However, a linear mean scalar profile is not responsible for this behaviour as in all our simulations pertaining to this issue the magnitude of the mean gradient is zero. Note that the significant portion of the temperature difference occurs near the walls and a substantial amount of heat transfer is due to the bulk motion of the fluid. One cannot expect to have significant 'unmixed' regions with exponential p.d.f.s, and at the same time expect an increase in the heat transfer and the thermal diffusivity. Therefore, it may not necessarily be the mean scalar gradient that is causing non-Gaussian intermittency, but it is the bulk fluid motion which introduces the large-scale boundary fluids into the central region. Of course the quantitative outcome depends on the magnitudes of the length scales, Re and Sc , and also the geometry of the flow configuration.

In the experiments of Gollub *et al.* (1991) and Lane *et al.* (1993) it is also shown that weak large scales can cause skewed p.d.f.s, the degree of which is enhanced as Re increases. This behaviour is more pronounced when the largest length scale of the velocity is smaller than that of the scalar, and disappears when the velocity length scale increases. Moreover, with an increase of the velocity scale from a size smaller than the scalar scale to one larger, the p.d.f. changes from exponential to Gaussian. It has been suggested (Lane *et al.* 1993; Kimura & Kraichnan 1993) that this behaviour could be due to non-isotropy or non-homogeneity of the velocity field. This does not seem to be the case as the results of previous laboratory (Tavoularis & Corrsin 1981a) and numerical (Rogers, Moin & Reynolds 1986; Miller *et al.* 1995) experiments on non-isotropic shear flows show Gaussian scalar p.d.f.s even at large Reynolds numbers. In fact, the non-homogeneity in the experiments of Lane *et al.* (1993) is more significant when Re is less than the critical value, i.e. when the p.d.f. is Gaussian. In DNS-11 we show that by an increase of the initial scalar energy at low wavenumbers, the presence of large scales causes skewed p.d.f.s. But this is not due to the presence of the mean scalar gradient. This skewness is expected to vanish if a large number of realizations are considered.

Notwithstanding the 'active' role of scalars, the behaviour discussed above is also observed in the convection experiments. In the Rayleigh-Bernard experiments of Solomon & Gollub (1991), the temperature p.d.f. is Gaussian or exponential if the Rayleigh number is below or above the transition value (Ra_t). For $Ra < Ra_t$, the presence of thermal plumes is detected. These plumes remain attached to the wall from which they erupt, but span the layer all the way to the opposite wall without breaking. In the more energetic state, when $Ra > Ra_t$, the plumes are broken apart by turbulence resulting in a flow dominated by disconnected and freely convecting fluid blobs (thermals). In the 'soft turbulence' regime ($Ra < Ra_t$), the influence of thermal plumes on the temperature p.d.f. is negligible. They only contribute to the mean transport across the cell and do not significantly affect the temperature fluctuations. In the hard turbulence regime ($Ra > Ra_t$), the breaking of large scales contributes to the scalar fluctuations throughout the cell including the central mixing core. In this regime, Zocchi, Moses & Libchaber (1991) indicate that most of the temperature drop occurs near the boundary plates and the bulk of the interior fluid is at constant

temperature. The experiments of the Chicago group indicate a Gaussian p.d.f. in the soft turbulence regime and an exponential p.d.f. in the hard turbulence regime. Our results, however, imply that it is not only the magnitude of Ra_t , that determines the p.d.f.; the influence of the thermal plumes is also important and should be considered. In other words, hard-soft turbulence regions may not necessarily be associated with exponential-Gaussian p.d.f.s. Rather, it is the distribution of the scalar length scales and their relation to the velocity length scales that are important in determining the p.d.f.. Note that the size of the plumes and their eruption are controlled by the aspect ratio of the cell and the magnitude of Ra . As the plumes grow and break, they interact with the fluid within the core. In the core, therefore, the p.d.f. is governed by a weighted sum of the statistics of the incoming unmixed flow with that of the well-mixed original core fluid. As we show in DNS-10 and BDNS-2 this can cause non-Gaussian behaviour in accord with that observed experimentally. In this regard, our results are consistent with those obtained by Christie & Domaradzki (1993, 1994) as they indicate that at a fixed Ra , both Gaussian and exponential p.d.f.s can be generated by varying the cell aspect ratio. Our arguments are also in accord with Solomon & Gollub (1991) who indicate that the scalar p.d.f. is chiefly controlled by the coherency of thermal plumes.

The stratified thermal convection experiments of Thoroddsen & Van Atta (1992) provide further evidence in support of our physical arguments. The inherent stability of the flow in this low- Re experiment is sufficient to keep the p.d.f. Gaussian, even with an imposed mean scalar gradient. Gaussian p.d.f.s are observed in all the cases considered in this experiment, consistent with all the results portrayed here for DNS-1(IV), DNS-13, BDNS-3. Further experiments at large Reynolds numbers would be very valuable in generalizing the conclusions drawn from these simulations.

The experimental results of Jayesh & Warhaft (1992) on passive scalar mixing in decaying grid-generated turbulence indicate the presence of both Gaussian and exponential scalar p.d.f.s. They suggest that in the presence of a constant mean scalar gradient, after a complex initial evolution the p.d.f. adopts an exponential form if the Reynolds number based on the integral flow scale (Re_I) is larger than a critical value ($Re_c \approx 70$). In the absence of the mean gradient, the p.d.f. is skewed but approximately Gaussian. The results of earlier experiments of Tavoularis & Corrsin (1981a) in turbulent shear flows with a constant mean scalar gradient suggest Gaussian p.d.f.s even for Reynolds numbers much larger than Re_c of Jayesh & Warhaft (1992). It seems unlikely that the non-isotropic nature of shear turbulence is responsible for the deviation from Gaussian as witnessed in the experiments of Lane *et al.* (1993) and the convection experiments of Heslot *et al.* (1987). In all the cases considered in our DNS of flows with a constant mean gradient, the p.d.f. is Gaussian regardless of the initial conditions and the magnitude of the Reynolds number. This is consistent with the experimental findings of Tavoularis & Corrsin (1981a), DNS results of Rogers, Mansour & Reynolds (1989) and recent analyses of Kimura & Kraichnan (1993), but not in accord with the numerical results of Holzer & Siggia (1994). We also show that once non-Gaussian statistics are formed they tend to exist longer in a decaying turbulent flow than in a forced stationary flow. This is especially true when there are large-scale scalar fluctuations that cannot be stirred by small-velocity eddies, even in the presence of a constant mean gradient. It appears that this condition is present in the experiments of Jayesh & Warhaft (1992).

One notable difference between the experiments of Jayesh & Warhaft (1992) and Tavoularis & Corrsin (1981a) is the ratio of the length scales of the scalar to the velocity. In Jayesh & Warhaft (1992) for the case with a mean gradient this

ratio is greater than unity, but in Tavoularis & Corrsin (1981a) it is smaller than unity. Thus our results in the cases with a mean scalar gradient are expected to be consistent with those of Tavoularis & Corrsin (1981b). The analysis of Kimura & Kraichnan (1993) shows that a nonlinear or a piecewise linear mean scalar profile can cause significant non-Gaussian behaviour. In our DNS, a perfectly linear mean scalar profile for the whole domain is imposed; therefore, the length scales of scalar fluctuations are determined by the forcing function due to the mean gradient in (9). This does not appear to be the case in the experiments since the mean scalar profile, even if perfectly linear, does not extend over the entire domain. Thus it is possible that the effect of initial (inlet) conditions are preserved in governing the consequent statistics. Furthermore, in the presence of the mean gradient in Jayesh & Warhaft's (1992) experiments, the large scalar scales evaluated based on the peak of the scalar spectrum (l_θ) remain larger than the velocity integral scale along the tunnel. From the measured temperature spectrum it can be deduced that scalar scales up to 70 times larger than l_θ are present. For example, it is shown that scalar scales larger than $7l_\theta$ contribute to 8% of the total scalar variance. In our simulations we show that this amount of large scales is sufficient to create significant departure from Gaussian especially when $l_u < l_\theta$. Despite their contribution in developing exponential-tail p.d.f.s, these large scales do not necessarily portray non-Gaussian behaviour themselves. In fact, if these scales are filtered out, the p.d.f. of the retained field exhibits a strong exponential behaviour. This is observed in our results presented in figure 19(b).

In the absence of the mean gradient, the reported results in Jayesh & Warhaft (1992) correspond to the case where the scalar length scale is smaller than that of the velocity. For this case, based on our LEM (cases LEM-6, LEM-10, LEM-16) and DNS (cases DNS-5, DNS-16) results, we expect the scalar p.d.f. to be near Gaussian. As indicated by Warhaft & Lumley (1978) in grid-generated turbulence experiments it is not clear how to change the thermal length scales (by grid heating) without affecting the velocity field. This is an important issue awaiting further investigations, especially by laboratory experiments.

5. Concluding remarks

The results of our numerical experiments reveal the intricate physics of scalar mixing and the complex role played by the combined influences of advection and molecular diffusion in turbulent flows. The primary observation made here is to verify that the long-time p.d.f. of a passive scalar in homogeneous turbulent flows is not necessarily Gaussian (or of any other particular form), and the fate of mixing is dependent on several factors. The objective of this work is to identify some of the causes for non-Gaussian behaviour of the scalar field and to determine the influence of several flow parameters in governing the scalar statistics. Aided by the analyses of the numerically generated data, an attempt is made to interpret the results provided in several recent laboratory experiments. With this interpretation, it is easy to see that there are many more possibilities (than those discussed here) for generating non-Gaussian p.d.f.s. However, there are several conclusions that can be drawn from the simulated results. These conclusions are itemized here, with the caveat that they are established in the range of parameters, resolution, and within the time durations considered in the present simulations:

- (i) Two mechanisms are identified for causing exponential p.d.f.s of the scalar amplitude due to the concurrent actions of advection and diffusion. (1) A non-uniform

action of advection on the large and the small scalar scales: for this, the dominant scale of advection should be smaller than that of the scalar and the weight of the large scalar scales should be 'appropriately' imposed. By 'appropriate' it is meant that there is some energy at large scalar scales, but its magnitude is smaller than that at other scales. (2) The nonlinear interaction of the scalar and the velocity fluctuations at small scales: in this case, the scalar tends to be correlated with the scalar gradient due to the smoothing effect of molecular diffusion on the scalar gradient. This correlation leads to a weak non-Gaussian behaviour and can be enhanced by increasing the weight of small scalar scales.

(ii) Although the presence of an appropriate amount of large scalar scales is a source of non-Gaussian behaviour, the p.d.f.s of the large scales themselves are not necessarily exponential.

(iii) In the absence of a mean scalar gradient, i.e. a decaying scalar field, the p.d.f. is very sensitive to the initial conditions. In the presence of this gradient, non-Gaussian behaviour is not sustained regardless of initial conditions.

(iv) The statistical behaviour is different in a stationary turbulence field from that in a decaying field. Once non-Gaussian behaviour is developed, it has a tendency to survive for a longer time in a decaying field.

(v) Contrary to its role in the scalar-derivative p.d.f.s, the Schmidt number exhibits a rather complex influence on the p.d.f.s of the scalar amplitude. In most of the cases considered, non-Gaussian behaviour becomes more pronounced as the magnitude of the Schmidt number is increased. However, an opposite behaviour can be observed under the first criterion (noted above). Further laboratory and numerical experiments with large Sc values are required to investigate this issue.

(vi) It is suggested that the non-Gaussian behaviour observed in recent laboratory experiments on passive scalar mixing may not be necessarily due to the presence of a linear mean scalar profile. It is argued that the initial/boundary conditions, and/or the nonlinearity of the mean scalar profile could be the cause of this behaviour.

(vii) It is suggested that the non-Gaussian behaviour observed in recent convection laboratory experiments may not be necessarily due the presence of a hard-turbulence regime. It is the dynamics of the thermal plumes that could be the cause.

(viii) The simulated results pertaining to small-scale intermittency are in accord with laboratory experimental results. The DNS generated statistics of the scalar derivatives and the velocity-scalar fluctuations are also in agreement with laboratory measurements.

A challenging next step would be the analysis of mixing for active scalars and/or chemically reactive flows (Libby & Williams 1994) in both homogeneous and non-homogeneous flows.

We are grateful to Drs Alan Kerstein and Patrick McMurtry for many helpful discussions. This work is sponsored by the Office of Naval Research under Grant N00014-94-1-0667 and by the National Science Foundation under Grant CTS-9253488. Computational resources are provided by the SEAS Computing Center at SUNY-Buffalo and by the NCSA at the University of Illinois at Urbana.

REFERENCES

ANDREWS, L. C. & SHIVAMOGGI, B. K. 1990 The gamma distribution as a model for temperature dissipation in intermittent turbulence. *Phys. Fluids A* **2**, 105–110.

ANSELMET, F., GAGNE, Y., HOPFINGER, E. J. & ANTONIA, R. A. 1984 High-order velocity structure functions in turbulent shear flows. *J. Fluid Mech.* **140**, 63–89.

ANTONIA, R. A., HOPFINGER, E. J., GAGNE, Y. & ANSELMET, F. 1984 Temperature structure functions in turbulent shear flows. *Phys. Rev. A* **30**, 2704–2707.

ANTONIA, R. A. & VAN ATTA, C. W. 1978 Structure functions of temperature fluctuations in turbulent shear flows. *J. Fluid Mech.* **84**, 561–580.

ASHURST, W. T., CHEN, J.-Y. & ROGERS, M. M. 1987a Pressure gradient alignment with strain rate and scalar gradient in simulated Navier-Stokes turbulence. *Phys. Fluids* **30**, 3293–3294.

ASHURST, W. T., KERSTEIN, A. R., KERR, R. M. & GIBSON, C. H. 1987b Alignment of vorticity and scalar gradient with strain rate in simulated Navier-Stokes turbulence. *Phys. Fluids* **30**, 2343–2353.

BATCHELOR, G. K. & TOWNSEND, A. A. 1949 The nature of turbulence motion at large wave numbers. *Proc. R. Soc. Lond. A* **199**, 534–550.

BELMONTE, A., TILGNER, A. & LIBCHABER, A. 1994 Temperature and velocity boundary layers in turbulent convection. *Phys. Rev. E* **50**, 269–279.

BRODKEY, R. S. (ed.) 1975 *Turbulence in Mixing Operations*. Academic.

BUDWIG, R., TAVOURARIS, S. & CORRSIN, S. 1985 Temperature fluctuations and heat flux in grid-generated isotropic turbulence with streamwise and transverse mean-temperature gradients. *J. Fluid Mech.* **153**, 441–460.

CASTAING, B., GAGNE, Y. & HOPFINGER, E. J. 1990 Velocity probability density functions of high Reynolds number turbulence. *Physica D* **46**, 177–200.

CASTAING, B., GUNARATNE, G., HESLOT, F., KADANOFF, L., LIBCHABER, A., THOMAE, S., WU, X. Z., ZALESKI, S. & ZANETTI, G. 1989 Scaling of hard thermal turbulence in Rayleigh-Bernard convection. *J. Fluid Mech.* **204**, 1–30.

CHEN, H., CHEN, S. & KRAICHNAN, R. H. 1989 Probability distribution of a stochastically advected scalar field. *Phys. Rev. Lett.* **63**, 2657–2660.

CHEN, S., DOOLEN, G., HERRING, J. R., KRAICHNAN, R. H., ORSZAG, S. A. & SHE, Z. S. 1993 Far-dissipation range of turbulence. *Phys. Rev. Lett.* **70**, 3051–3054.

CHING, E. S. C. & TU, Y. 1994 Passive scalar fluctuations with and without a mean gradient: A numerical study. *Phys. Rev. E* **49**, 1278–1282.

CHRISTIE, S. L. & DOMARADZKI, J. A. 1993 Numerical evidence for the nonuniversality of the soft/hard turbulence classification for thermal convection. *Phys. Fluids A* **5**, 412–421.

CHRISTIE, S. L. & DOMARADZKI, J. A. 1994 Scale dependence of the statistical character of turbulent fluctuations in thermal convection. *Phys. Fluids* **6**, 1848–1855.

CURL, R. L. 1963 Dispersed phase mixing: I. Theory and effects in simple reactors. *AIChE J.* **9**, 175–181.

DOPAZO, C. 1994 Recent developments in p.d.f. methods. In *Turbulent Reacting Flows* (ed. P. A. Libby & F. A. Williams), pp. 375–474. Academic.

DOPAZO, C. & O'BRIEN, E. E. 1976 Statistical treatment of non-isothermal chemical reactions in turbulence. *Combust. Sci. Tech.* **13**, 99–112.

ESWARAN, V. & POPE, S. B. 1988 Direct numerical simulations of the turbulent mixing of a passive scalar. *Phys. Fluids* **31**, 506–520.

FRANKEL, S. H. 1993 Probabilistic and deterministic description of turbulent flows with nonpremixed reactants. PhD thesis. Department of Mechanical and Aerospace Engineering, State University of New York at Buffalo, Buffalo, NY.

FRANKEL, S. H., MADNIA, C. K. & GIVI, P. 1993 Comparative assessment of closures for turbulent reacting flows. *AIChE J.* **39**, 899–903.

GIVI, P. 1989 Model free simulations of turbulent reactive flows. *Prog. Energy Combust. Sci.* **15**, 1–107.

GIVI, P. 1994 Spectral and random vortex methods in turbulent reacting flows. In *Turbulent Reacting Flows* (ed. P. A. Libby & F. A. Williams), pp. 475–572. Academic.

GIVI, P. & MADNIA, C. K. 1993 Spectral methods in combustion. In *Numerical Modeling in Combustion* (ed. T. J. Chung), pp. 409–452. Taylor & Francis.

GIVI, P. & McMURTRY, P. A. 1988 Non-premixed reaction in homogeneous turbulence: Direct numerical simulations. *AIChE J.* **34**, 1039–1042.

GOLLUB, J. P., CLARKE, J., GHARIB, M., LANE, B. & MESQUITA, O. N. 1991 Fluctuations and transport in a stirred fluid with a mean gradient. *Phys. Rev. Lett.* **67**, 3507–3510.

GURVICH, A. S. & YAGLOM, A. M. 1967 Breakdown of eddies and probability distributions for small-scale turbulence. *Phys. Fluids Suppl.* **10**, S59–S65.

HAWTHORNE, W. R., WEDELL, D. S. & HOTTEL, H. C. 1949 Mixing and combustion in turbulent gas jets. In *3rd Symp. on Combustion, Flames and Explosion Phenomena*, pp. 266–288. The Combustion Institute, Pittsburgh, PA.

HESLOT, F., CASTAING, B. & LIBCHABER, A. 1987 Transitions to turbulence in helium gas. *Phys. Rev. A* **36**, 5870–5873.

HILL, J. C. 1979 Simulation of chemical reaction in a turbulent flow. In *Proc. Second R. F. Ruth Chemical Engineering Research Symposium*, pp. 27–53. Ames, Iowa.

HOLZER, M. & PUMIR, A. 1993 Simple models of non-Gaussian statistics for a turbulently advected passive scalar. *Phys. Rev. E* **47**, 202–219.

HOLZER, M. & SIGGIA, E. D. 1994 Turbulent mixing of a passive scalar. *Phys. Fluids* **6**, 1820–1837.

HOSOKAWA, I. & YAMAMOTO, K. 1989 Fine structure of a directly simulated isotropic turbulence. *J. Phys. Soc. Japan* **58**, 20–23.

JABERI, F. A. & GIVI, P. 1995 Inter-layer diffusion model of scalar mixing in homogeneous turbulence. *Combust. Sci. Tech.* **104**, 249–272.

JABERI, F. A., MILLER, R. S. & GIVI, P. 1995 Conditional statistics in turbulent scalar mixing and reaction. *AIChE J.*, In press.

JANICKA, J., KOLBE, W. & KOLLMANN, W. 1979 Closure of the transport equation for the probability density function of turbulent scalar field. *J. Nonequil. Thermodyn.* **4**, 47–66.

JAYESH & WARHAFT, Z. 1991 Probability distribution of a passive scalar in grid-generated turbulence. *Phys. Rev. Lett.* **67**, 3503–3506.

JAYESH & WARHAFT, Z. 1992 Probability distribution, conditional dissipation, and transport of passive temperature fluctuations in grid-generated turbulence. *Phys. Fluids A* **4**, 2292–2307.

JIMENEZ, J., WRAY, A. A., SAFFMAN, P. G. & ROGALLO, R. S. 1993 The structure of intense vorticity in isotropic turbulence. *J. Fluid Mech.* **255**, 65–90.

KERR, R. M. 1983 High-order derivative correlations and the alignment of small-scale structures in isotropic numerical turbulence. *NASA TM* 84407.

KERR, R. M. 1985 High-order derivative correlations and the alignment of small-scale structures in isotropic numerical turbulence. *J. Fluid Mech.* **153**, 31–58.

KERR, R. M. 1990 Velocity, scalar and transfer spectra in numerical turbulence. *J. Fluid Mech.* **211**, 309–332.

KERSTEIN, A. R. 1988 A linear eddy model of turbulent scalar transport and mixing. *Combust. Sci. Tech.* **60**, 391–421.

KERSTEIN, A. R. 1989 Linear eddy modelling of turbulent transport. II: Applications to shear layer mixing. *Combust. Flame* **75**, 397–413.

KERSTEIN, A. R. 1990 Linear eddy modelling of turbulent transport. Part 3. Mixing and differential molecular diffusion in round jets. *J. Fluid. Mech.* **216**, 411–435.

KERSTEIN, A. R. 1991 Linear-eddy modelling of turbulent transport. Part 6. Microstructure of diffusive scalar mixing fields. *J. Fluid Mech.* **231**, 361–394.

KERSTEIN, A. R. 1992 Linear-eddy modelling of turbulent transport. Part 7. Finite-rate chemistry and multi-stream mixing. *J. Fluid Mech.* **240**, 289–313.

KERSTEIN, A. R. & McMURTRY, P. A. 1994a Low wave number statistics of randomly advected passive scalars. *Phys. Rev. E* **50**, 2057–2063.

KERSTEIN, A. R. & McMURTRY, P. A. 1994b Mean-field theories of random advection. *Phys. Rev. E* **49**, 474–482.

KIMURA, Y. & KRAICHNAN, R. H. 1993 Statistics of an advected passive scalar. *Phys. Fluids A* **5**, 2264–2277.

KOLMOGOROV, A. N. 1941 The local structure of turbulence in incompressible viscous fluid for large Reynolds numbers. *Dokl. Akad. Nauk SSSR* **30**, 301–305.

KOLMOGOROV, A. N. 1962 A refinement of previous hypotheses concerning the local structure of turbulence in a viscous incompressible fluid at high Reynolds number. *J. Fluid Mech.* **13**, 82–85.

KRAICHNAN, R. H. 1989 Closures for probability distributions. *Bull. Am. Phys. Soc.* **34**, 2298.

LANDAU, L. D. & LIFSHITZ, E. M. 1959 *Fluid Mechanics*. Pergamon.

LANE, B. R., MESQUITA, O. N., MEYERS, S. R. & GOLLUB, J. P. 1993 Probability distributions and thermal transport in a turbulent grid flow. *Phys. Fluids A* **5**, 2255–2263.

LEONARD, A. D. & HILL, J. C. 1988 Direct numerical simulation of turbulent flows with chemical reaction. *J. Sci. Comput.* **3**, 25–43.

LEONARD, A. D. & HILL, J. C. 1991 Scalar dissipation and mixing in turbulent reacting flows. *Phys. Fluids A* **3**, 1286–1299.

LEONARD, A. D. & HILL, J. C. 1992 Mixing and chemical reaction in sheared and nonsheared homogeneous turbulence. *Fluid Dyn. Res.* **10**, 273–297.

LIBBY, P. A. & WILLIAMS, F. A. (ed.) 1980 *Turbulent Reacting Flows*. Topics in Applied Physics, vol. 44. Springer.

LIBBY, P. A. & WILLIAMS, F. A. (ed.) 1994 *Turbulent Reacting Flows*. Academic.

MADNIA, C. K., FRANKEL, S. H. & GIVI, P. 1992 Reactant conversion in homogeneous turbulence: Mathematical modeling, computational validations and practical applications. *Theoret. Comput. Fluid Dyn.* **4**, 79–93.

McMURTRY, P. A., GANSUZE, T. C., KERSTEIN, A. R. & KRUEGER, S. K. 1993a Linear eddy simulations of mixing in a homogeneous turbulent flow. *Phys. Fluids A* **5**, 1023–1034.

McMURTRY, P. A. & GIVI, P. 1989 Direct numerical simulations of mixing and reaction in a nonpremixed homogeneous turbulent flow. *Combust. Flame* **77**, 171–185.

McMURTRY, P. A., MENON, S. & KERSTEIN, A. R. 1993b Linear eddy modeling of turbulent combustion. *Energy & Fuels* **7**, 817–826.

METAIS, O. & LESIEUR, M. 1992 Spectral large-eddy simulation of isotropic and stably stratified turbulence. *J. Fluid Mech.* **239**, 157–194.

MILLER, R. S. 1995 Passive scalar, magnetic field, and solid particle transport in homogeneous turbulence. PhD thesis, Department of Mechanical and Aerospace Engineering, State University of New York at Buffalo, Buffalo, NY.

MILLER, R. S., FRANKEL, S. H., MADNIA, C. K. & GIVI, P. 1993 Johnson-Edgeworth translation for probability modeling of binary scalar mixing in turbulent flows. *Combust. Sci. & Tech.* **91**, 21–52.

MILLER, R. S., JABERI, F. A., MADNIA, C. K. & GIVI, P. 1995 The structure and small-scale intermittency of passive scalars in homogeneous turbulence. *J. Sci. Comput.* **10**, 151–180.

MIYAWAKI, O., TSUIKAWA, H. & Uraguchi, Y. 1974 Turbulent mixing in multi-nozzle injector tubular mixers. *J. Chem. Engng Japan* **7**, 52–74.

MONIN, A. S. & YAGLOM, A. M. 1975 *Statistical Fluid Mechanics*, Vol. 2. MIT Press.

NOMURA, K. K. & ELGHOBASHI, S. E. 1992 Mixing characteristics of an inhomogeneous scalar in isotropic and homogeneous sheared turbulence. *Phys. Fluids A* **4**, 606–625.

O'BRIEN, E. E. 1980 The probability density function (p.d.f.) approach to reacting turbulent flows. In *Turbulent Reacting Flows* (ed. P. A. Libby & F. A. Williams), pp. 185–218. Springer.

OBUKHOV, A. M. 1962 Some specific features of atmospheric turbulence. *J. Fluid Mech.* **13**, 77–81.

POPE, S. B. 1979 The statistical theory of turbulent flames. *Phil. Trans. R Soc. Lond. A* **291**, 529–568.

POPE, S. B. 1982 An improved turbulent mixing model. *Combust. Sci. Tech.* **28**, 131–145.

POPE, S. B. 1985 p.d.f. methods for turbulent reactive flows. *Prog. Energy Combust. Sci.* **11**, 119–192.

POPE, S. B. 1990 Computations of turbulent combustion: Progress and challenges. In *Proc. 23rd Symp. (Intl) on Combustion*, pp. 591–612. The Combustion Institute, Pittsburgh, PA.

PUMIR, A. 1994 A numerical study of the mixing of a passive scalar in three dimensions in the presence of a mean gradient. *Phys. Fluids* **6**, 2118–2132.

PUMIR, A., SHRAIMAN, B. & SIGGIA, E. D. 1991 Exponential tails and random advection. *Phys. Rev. Lett.* **3**, 2838–2840.

ROGERS, M. M., MANSOUR, N. N. & REYNOLDS, W. C. 1989 An algebraic model for the turbulent flux of a passive scalar. *J. Fluid Mech.* **203**, 77–101.

ROGERS, M. M., MOIN, P. & REYNOLDS, W. C. 1986 The structure and modeling of the hydrodynamic and passive scalar fields in homogeneous turbulent shear flow. Department of Mechanical Engineering TF-25, Stanford University, Stanford, CA.

RUETSCH, G. R. & MAXEY, M. R. 1991 Small-scale features of vorticity and passive scalar fields in homogeneous-isotropic turbulence. *Phys. Fluids A* **3**, 1587–1597.

RUETSCH, G. R. & MAXEY, M. R. 1992 The evolution of small-scale structures in homogeneous-isotropic turbulence. *Phys. Fluids A* **4**, 2747–2760.

SANO, M., WU, X. Z. & LIBCHABER, A. 1989 Turbulence in helium gas free convection. *Phys. Rev. A* **40**, 6421–6430.

SHE, Z. S. 1990 Physical model of intermittency in turbulence: Near dissipation range non-Gaussian statistics. *Phys. Rev. Lett.* **66**, 600–603.

SHE, Z. S., JACKSON, E. & ORSZAG, S. A. 1991 Structure and dynamics of homogeneous turbulence: Models and simulations. *Proc. R. Soc. Lond. A* **434**, 101–124.

SHE, Z. S. & ORSZAG, S. A. 1991 Physical model of intermittency in turbulence: Inertial-range non-Gaussian statistics. *Phys. Rev. Lett.* **66**, 1701–1704.

SIGGIA, E. D. 1994 High Rayleigh number convection. *Ann. Rev. Fluid Mech.* **26**, 137–168.

SINAI, Y. G. & YAKHOT, V. 1989 Limiting probability distributions of a passive scalar in a random velocity field. *Phys. Rev. Lett.* **63**, 1962–1964.

SOLOMON, T. H. 1990 Transport and boundary layers in Rayleigh-Bernard convection. PhD thesis, Department of Physics, University of Pennsylvania, Philadelphia.

SOLOMON, T. H. & GOLLUB, J. P. 1991 Thermal boundary layers and heat flux in turbulent convection: The role of recirculating flows. *Phys. Rev. A* **43**, 6683–6693.

TANAKA, M. & KIDA, S. 1993 Characterization of vortex tubes and sheets. *Phys. Fluids A* **5**, 2079–2082.

TAVOULARIS, S. & CORRSIN, S. 1981a Experiments in nearly homogenous turbulent shear flow with a uniform mean temperature gradient. Part 1. *J. Fluid Mech.* **104**, 311–347.

TAVOULARIS, S. & CORRSIN, S. 1981b Experiments in nearly homogenous turbulent shear flow with a uniform mean temperature gradient. Part 2. The fine structure. *J. Fluid Mech.* **104**, 349–367.

TENNEKES, H. & LUMLEY, J. L. 1972 *A First Course in Turbulence*. MIT Press.

THORODDSEN, S. T. & VAN ATTA, C. W. 1992 Exponential tails and skewness of density-gradient probability density functions in stably stratified turbulence. *J. Fluid Mech.* **244**, 547–566.

TONG, C. & WARhaft, Z. 1994 On passive scalar derivative statistics in grid turbulence. *Phys. Fluids* **6**, 2165–2176.

TOOR, H. L. 1975 The non-premixed reaction: $A + B \rightarrow \text{Products}$. In *Turbulence in Mixing Operations* (ed. R. S. Brodsky), pp. 123–166. Academic.

VAN ATTA, C. W. & ANTONIA, R. A. 1980 Reynolds number dependence of skewness and flatness factors of turbulent velocity derivatives. *Phys. Fluids* **23**, 252–257.

VAN ATTA, C. W. & CHEN, W. Y. 1970 Structure functions of turbulence in the atmospheric boundary layer over the ocean. *J. Fluid Mech.* **44**, 145–159.

VINCENT, A. & MENEGUZZI, M. 1991 The spatial structure and statistical properties of homogeneous turbulence. *J. Fluid Mech.* **225**, 1–20.

WARhaft, Z. & LUMLEY, J. L. 1978 An experimental study of the decay of temperature fluctuations in grid-generated turbulence. *J. Fluid Mech.* **88**, 659–684.

YAKHOT, V. 1989 Probability distributions in high Rayleigh number Bernard convection. *Phys. Rev. Lett.* **63**, 1965–1967.

YAMAMOTO, K. & KAMBE, T. 1991 Gaussian and near exponential probability distributions of turbulence obtained from a numerical simulation. *Fluid Dyn. Res.* **8**, 65–72.

ZOCCHI, G., MOSES, E. & LIBCHABER, A. 1991 Coherent structures in turbulent convection: An experimental study. *Physica A* **166**, 387–407.

APPENDIX VIII

Conditional Expected Dissipation & Diffusion in Turbulent Scalar Mixing and Reaction

TRANSPORT PHENOMENA IN COMBUSTION

Proceedings of the Eighth International Symposium on
Transport Phenomena in Combustion (ISTP-VIII) held in
San Francisco, California, July 16-20, 1995
Organized under the Auspices of the Pacific Center of
Thermal-Fluids Engineering

VOLUME 2

Edited by

S. H. Chan

Department of Mechanical Engineering
University of Wisconsin-Milwaukee
Milwaukee, Wisconsin USA



Taylor & Francis

CONDITIONAL EXPECTED DISSIPATION & DIFFUSION IN TURBULENT SCALAR MIXING AND REACTION

Farhad A. Jaber, Richard S. Miller and Peyman Givi
Department of Mechanical and Aerospace Engineering
State University of New York at Buffalo
Buffalo, NY 14260-4400, U.S.A.

ABSTRACT

Analytical expressions are obtained for the conditional expected dissipation and the conditional expected diffusion of a passive scalar contaminant in homogeneous turbulent flows by means of several turbulence closures. It is shown that if the single-point probability density function (PDF) of the scalar is represented by the family of exponential distributions, the conditional expected dissipation varies significantly depending on the exponent of the PDF. However, the conditional expected diffusion remains identical. For those members with tails broader than gaussian, the conditional expected dissipation is concave up and for tails narrower than gaussian it is concave down. This is proved mathematically without resorting to asymptotic analysis (of the final stages of mixing) as conducted previously. For all cases, the conditional expected diffusion adopts a linear profile consistent with the linear mean square estimation (LMSE) theory. The similarity of the conditional diffusion field is explained in the context of the "lamellar" theory of turbulent mixing. The mathematical results are in accord with previous results generated by Direct Numerical Simulation (DNS), and are further validated here by comparison with data obtained via the Linear Eddy Model (LEM) of mixing. It is suggested that the behavior of the conditional expected diffusion at the scalar bounds has a significant influence on the evolution of the PDF.

INTRODUCTION

Mathematical modelling of the conditional expected scalar dissipation and the conditional expected scalar diffusion is of crucial interest in the statistical description of turbulent mixing [1, 2]. In turbulent combustion the behavior of the conditional expected dissipation is of primary importance for describing the rate of reactant conversion in flows with non-equilibrium chemistry. This is particularly the case in diffusion flames, as the rate of reactant conversion is related to the expected dissipation of an appropriately defined mixture frac-

tion [1, 3, 4]. In more recent theories of non-premixed turbulent flames also, it is shown that the success in decoupling the effects of turbulence from those of chemistry is dependent on the model used to describe the conditional expected dissipation. For example, in the laminar diffusion flamelet model [5–7], the flamelet library is parameterized with the magnitude of the expected dissipation of the mixture fraction. In the conditional moment method [8] the evaluation of the conditional statistics of reacting variables requires knowledge of the conditional expected dissipation of the mixture fraction. These conditional statistics appear as unclosed terms in the transport equation describing the evolution of the single-point probability density function (PDF) of the scalar field. In fact, the problem encountered in combustion modeling is the same as that in single point PDF modeling [9]. This closure problem in the single-point PDF description remains an unresolved issue despite the extent of efforts devoted to it within the past several years; see Ref. [10] for a recent review.

In turbulence modeling, a strategy which has proven useful is to determine the PDF first by other means, and then extract the information pertaining to conditional statistics. This procedure was not feasible before when Coalescence/Dispersion (C/D) type closures were typically utilized [11]. This is problematic from a modeling standpoint since the known drawbacks of C/D closures cannot be removed. However, the development of three recent mixing models; namely the Amplitude Mapping Closure (AMC) of Kratchman [12, 13], the Johnson-Edgeworth 'Translation (JET)' of Miller *et al.* [14], and the Linear Eddy Model (LEM) of Kerstein [15, 16], have encouraged such *a priori* approach. In fact the approach has proven extremely useful in that many subtle features of the models are clearly demonstrated [14, 17–20]. As an example, the drawbacks of the AMC and the JET could only be demonstrated by examining the conditional statistics, as described in detail in Ref. [14].

Our intention in this work is to provide a formal mathematical framework by which the properties of the conditional statistics are identified. For that, we first evaluate the conditional expected dissipation and the conditional expected diffusion for the general family of the exponential scalar PDFs. This family is considered since it includes the gaussian PDF, which is frequently utilized in turbulent combustion modeling (see e.g. Refs. [1, 2]), and also includes PDFs with tails broader than and narrower than gaussian. Some of the features portrayed by this mathematical development are then explained in the framework of the lamellar theory of mixing. Finally, all the results are compared with numerical data obtained by the LEM.

EVOLUTION OF THE PDF

In an incompressible homogeneous turbulent flow, the evolution of the PDF of a conserved Fickian scalar variable, $\phi(\mathbf{x}, t)$, denoted by $P(\phi, t)$, is governed

by [10]:

$$\frac{\partial P}{\partial t} + \frac{\partial^2}{\partial \phi^2} (E\{\xi^2|\phi\} P) = 0, \quad \phi_t \leq \phi \leq \phi_u \quad (1)$$

where $\xi^2 = \kappa \nabla \phi \cdot \nabla \phi$, κ is the molecular diffusion coefficient and $E\{\xi^2|\phi\}$ is the expected value of the scalar dissipation conditioned (denoted by the vertical bar) on the scalar value, ϕ . Equation (1) can alternatively be expressed as:

$$\frac{\partial P}{\partial t} + \frac{\partial}{\partial \phi} (E\{\zeta|\phi\} P) = 0, \quad (2)$$

where $\zeta = \kappa \nabla^2 \phi$, and $E\{\zeta|\phi\}$ denotes the conditional expected value of the scalar diffusion. At the single-point level neither of the conditional statistics are known nor are their unconditional expected values including the expected value of total dissipation, ϵ :

$$\epsilon(t) = \int_{\phi_t}^{\phi_u} P(\phi, t) E\{\xi^2|\phi\} d\phi. \quad (3)$$

In deriving Eq. (1), use has been made of:

$$\frac{\partial (E\{\zeta|\phi\} P)}{\partial \phi} = \frac{\partial^2 (E\{\xi^2|\phi\} P)}{\partial \phi^2}. \quad (4)$$

Equation (4) can be solved analytically for the PDF. With the condition:

$$\int_{\phi_t}^{\phi_u} E\{\zeta|\phi\} P(\phi, t) d\phi = 0, \quad (5)$$

the solution of Eq. (4) is:

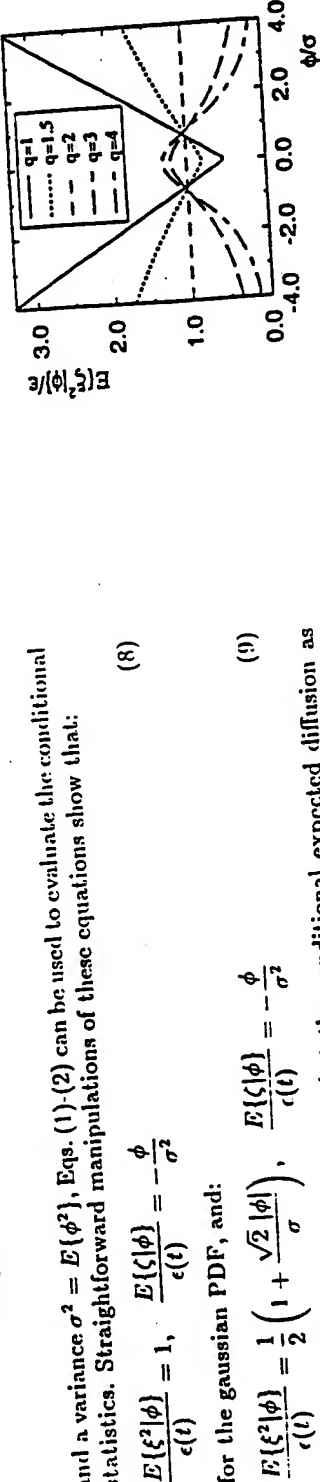
$$P(\phi, t) = \frac{C_1}{E\{\xi^2|\phi\}} \exp \left(\int_{\phi_t}^{\phi} \frac{E\{\zeta|\psi\}}{E\{\xi^2|\psi\}} d\psi \right), \quad (6)$$

where the constant C_1 is obtained by the constraint $\int_{\phi_t}^{\phi_u} P(\phi, t) d\phi = 1$. This equation, providing an explicit relation between the PDF and the conditional expected diffusion & dissipation, is the same as that derived in Ref. [19]. However, it is not necessary here to assume a stationary field and Eq. (6) is valid regardless of the homogeneous field being stationary or decaying.

Given the PDF it is possible to determine the conditional statistics [14]. The family of exponential PDFs are very useful in analyzing the problem of scalar mixing [17, 20, 22]. These PDFs are expressed as:

$$P(\phi) = C(K, q) \exp \left(-\frac{|\phi - \phi_0|^q}{K} \right), \quad -\infty = \phi_t \leq \phi \leq \phi_u = \infty, \quad (7)$$

where $q = 2$ corresponds to a gaussian PDF, and $q = 1$ implies a Laplace (double exponential) density. Considering PDFs with a mean $\phi_0 = E\{\phi\} = 0$



and a variance $\sigma^2 = E\{\phi^2\}$, Eqs. (1)-(2) can be used to evaluate the conditional statistics. Straightforward manipulations of these equations show that:

$$\frac{E\{\xi^2|\phi\}}{E\{\xi|\phi\}} = 1, \quad \frac{E\{\zeta|\phi\}}{\epsilon(t)} = -\frac{\phi}{\sigma^2} \quad (8)$$

for the gaussian PDF, and:

$$E\{\xi^2|\phi\} = \frac{1}{2} \left(1 + \frac{\sqrt{2} |\phi|}{\sigma} \right), \quad \frac{E\{\zeta|\phi\}}{\epsilon(t)} = -\frac{\phi}{\sigma^2} \quad (9)$$

for the Laplace PDF. It is noted that the conditional expected diffusion as predicted by these two densities are identical and are the same as that of the Least Mean Square Estimation (LMSE) model [23]. Based on this observation, we propose that for all the other members of the family of exponential PDF's, the linear profile is applicable. This proposal is plausible provided that:

$$\frac{1}{C} \frac{\partial C}{\partial t} = \frac{\epsilon}{\sigma^2}, \quad \frac{1}{K} \frac{\partial K}{\partial t} = -\frac{\epsilon q}{\sigma^2}. \quad (10)$$

Straightforward manipulation of Eq. (7) shows that:

$$K(\sigma, q) = M(q)\sigma^q, \quad C(\sigma, q) = N(q)\sigma^{-1}, \quad (11)$$

where $M(q)$ and $N(q)$ are known functions of q . Due to the nature of Eq. (11), it is easily verified that Eq. (10) is valid regardless of the magnitude of q . The difference between members of the families of PDF's is exhibited by considering the conditional expected dissipation. This is facilitated by making use of Eqs. (1)-(3). The final results after significant manipulations yield [24]:

$$\frac{E\{\xi^2|\phi\}}{\epsilon} = \frac{K \frac{q}{\gamma}}{q \sigma^2} \left\{ \Gamma\left(\frac{2}{q}\right) - \gamma\left(\frac{2}{q}, \frac{|\phi|^q}{K}\right) \right\} \exp\left(\frac{|\phi|^q}{K}\right) \quad (12)$$

where Γ and γ denote the Gamma function and the incomplete Gamma function, respectively. With the identity:

$$\Gamma(1+n) - \gamma(1+n, z) = n! \exp(-z) \sum_{k=0}^{n-1} \frac{z^k}{k!}, \quad n = 0, 1, 2, \dots \quad (13)$$

the corresponding analytical relations for the gaussian density and the Laplace density are exactly recovered for $q = 2$ and $q = 1$, respectively. For other values of q , Eq. (12) can be evaluated only by numerical means.¹ The profiles of the conditional expected dissipation are shown in Fig. 1. This figure clearly shows that if the PDF exhibits tails broader than gaussian ($q < 2$), the normalized conditional dissipation portrays a "bowl" shaped curve (concave up) near the mean scalar value. For PDF's with tails narrower than gaussian ($q > 2$), the conditional dissipation adopts a "bell" shaped (concave down) curve. For $q =$

Figure 1. The conditional expected dissipation of the scalar normalized by the total dissipation for several members of the exponential PDF.

2, the profile is a straight line $E\{\xi^2|\phi\} = \epsilon$. Only in this case, i.e. a gaussian PDF, is the conditional scalar dissipation independent of the scalar value. The relation between the nature of the conditional dissipation and the broadness (narrowness) of the PDF at its tails was first proved in Ref. [20], and later utilized in Ref. [18] to point out the drawbacks of AMG. However, the relation was established based on a speculation on the asymptotic behavior of scalar mixing in stationary turbulence. Here, Eq. (12) is a direct mathematical demonstration of this relation and is very convenient when assessing the results obtained by other closures.

THE LAMELLAR DESCRIPTION

Some features of the conditional expected diffusion can be explained in the context of the lamellar theory of mixing [25]. According to this theory, a major part of scalar diffusion in turbulent flows occurs in a system of layer-like striation, or lamellae. Each of these lamellae have a thickness ($2h$) which in general is a function of space and time, i.e. $h = h(x, t)$. The rate of stretching and folding of the lamellar structures is governed by turbulent eddies. In accordance with the physics of the problem, the lamellar theory indicates that mixing with the mechanisms: molecular diffusion and turbulent evolution is governed by two mechanisms: molecular diffusion and turbulent advection. The former occurs primarily at small scales, whereas the latter is a multi-scale phenomenon. For thin diffusion zones and sufficiently steep scalar gradients across the scalar interfaces, the diffusion process takes place in a direction approximately normal to the interface, which is also observed to be mostly aligned with the most compressive principal strain rate [26]. We represent this direction by y which is bounded by striation thickness, h , that is $-h \leq y \leq h$. This thickness is defined as a positive random variable which has a frequency denoted by the Striation Thickness Distribution (STD) [25]

¹For $q = 4$ and $q \rightarrow \infty$ the results can be expressed, respectively, in terms of Error functions and the exponential integral, both of which still require numerical evaluations.

and Case 3 ($L_A/L = 2$). For a full description of the model implementation we refer to Ref. [34], as all the LEM results are extracted from this reference.

The PDF results as obtained by the LEM are shown in Fig. 2. The general trend is somewhat similar in all cases in that the PDF evolves from an initial binary state to an asymptotic distribution centered around the mean value. The difference between the cases is most pronounced at the intermediate stages of mixing. The form of the PDF at $\sigma = 0.13$ is shown in the figure, where the results are also compared with the gaussian, Laplace, and AMC [3, 35] generated distributions. In all the cases the PDFs are parameterized with the same normalized variance as generated by the LEM since none of the single-point closures are capable of providing the evolution of $\sigma(t)$. Figure 2 indicates that the forms of the PDF as generated by AMC and LEM show better agreement for $L_A/L = 2$. For $L_A/L = 1/2$, the LEM generated PDFs are closer to the Laplace distribution. The results of the conditional statistics are presented in Figs. 3-4. For the AMC, the mathematical relations for the binary scalar mixing with $\phi_1, \phi_2 = -1, 1$, and $E[\phi] = 0$ are derived in Ref. [14] and are given as:

$$\frac{E[\xi^2 \phi]}{\epsilon(t)} = \left[\frac{1 + \sin(\frac{\pi}{2} \mathcal{G})}{1 - \sin(\frac{\pi}{2} \mathcal{G})} \right] \exp \left\{ -2 [\text{erf}^{-1}(\phi)]^2 \right\}, \quad (19)$$

$$\frac{E[\zeta \phi]}{\epsilon(t)} = \left[\frac{-\sqrt{\pi}}{\sin(\frac{\pi}{2} \mathcal{G})} \sqrt{\frac{1 + \sin(\frac{\pi}{2} \mathcal{G})}{1 - \sin(\frac{\pi}{2} \mathcal{G})}} \right] \exp \left\{ -[\text{erf}^{-1}(\phi)]^2 \right\} \text{erf}^{-1}(\phi), \quad (20)$$

where $\mathcal{G} = \sigma^2(t)/\sigma^2(0)$. The initial conditional expected dissipation as predicted by LEM is similar in all cases and the curves are all bell-shaped (not shown here). However, the difference between all the cases is revealed at later stages of mixing. The results for $\sigma = 0.13$ are compared with those corresponding to a Laplace PDF and the AMC generated solution in Fig. 3. Note that the normalized conditional dissipation corresponding to the gaussian distribution is a straight line at unity. The LEM generated results show that both bell- and basin-shaped distributions are obtained. For cases with PDFs close to the Laplace distribution, the results are close to first of Eq. (9) near the mean value. For those cases in which the PDFs are close to those of AMC, the curves show a bell-shape distribution. Also, consistent with the analyses pertaining to Eq. (12), if the tails of the PDFs are broader than gaussian (Fig. 2(a)) the conditional expected dissipation curve is basin shaped (Fig. 3(a)). If the skirt of the PDF is less extended than gaussian (Fig. 2(c)), the conditional dissipation is more bell-shaped (Fig. 3(c)).

The profiles for the conditional expected diffusion are shown in Fig. 4. In this case, the LMSE results are identical to those provided by all members of the exponential PDF's. A particular feature observed in this figure is the similarity of all models near the mean value of the scalar. This similarity which has also been observed in previous DNS [14, 28] is embedded in Eq. (17). To demonstrate the significance of this observation, we consider the following two distributions within the lamellae with a STD with unbounded support:

$$\phi = \text{erf}\left(\frac{\psi}{\sqrt{2}\Sigma}\right), \quad \phi = \tanh\left(\frac{\psi}{\Sigma}\right) \quad (21)$$

where $\Sigma = \Sigma(\sigma(t))$ and cannot be described in the context of single-point description. A direct use of Eq. (17) yields:

$$E[\zeta \phi] = -\frac{2}{\sqrt{\pi}\Sigma} \frac{d\Sigma}{dt} \exp \left\{ -[\text{erf}^{-1}(\phi)]^2 \right\} \text{erf}^{-1}(\phi), \quad (22)$$

for the first of Eq. (21), and

$$E[\zeta \phi] = -\frac{1}{\Sigma} \frac{d\Sigma}{dt} \tanh^{-1}(\phi)(1 - \phi^2) \quad (23)$$

for the second of Eq. (21). Note that the functional form of these equations are identical, respectively, to those obtained by LEM (Eq. (20)), and the Logistic-Normal density of JEP [14]. This is interesting considering the fact that the form of STD is not utilized in deriving these relations. For the conditional

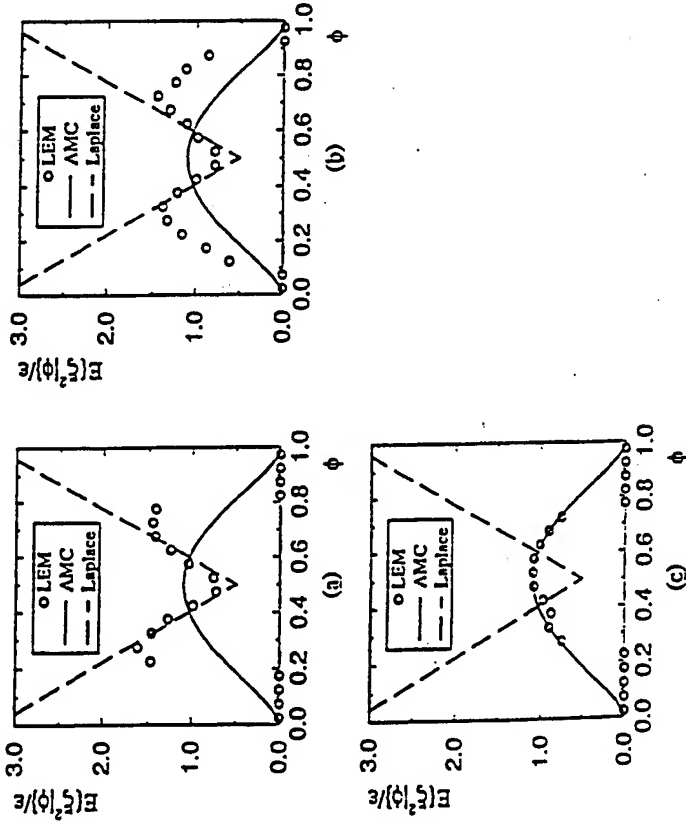


Figure 3. The conditional expected value of the scalar dissipation predicted by the LEM at $\sigma = 0.13$ and its comparison with the other closures. (a) Case 1, (b) Case 2, (c) Case 3.

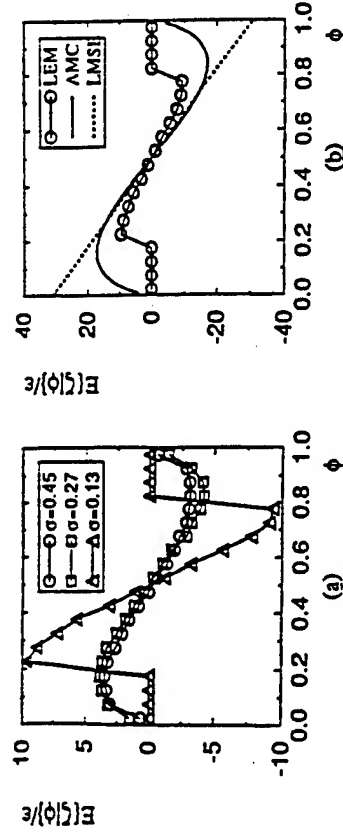


Figure 4. The conditional expected value of the scalar diffusion. (a) Case 1 at several σ values, (b) Case 1 at $\sigma = 0.13$ and its comparisons with the results of AMC and LMSE.

expected dissipation, however, the knowledge of STD is required. The AMC results, Eq. (19) can be obtained only by further assumption of a Rayleigh STD which implies a gaussian $G(y)$.

The behavior described above is also observed for non-symmetric PDFs. However, it is not possible to present the results in a closed analytical form in terms of the variance; thus numerical integration is required. These results show that the asymmetry of the PDF is exhibited through the profiles of the conditional expected diffusion. But for the AMC, the conditional expected dissipation is always symmetric regardless of the magnitude of $E\{\phi\}$. This is non-physical as demonstrated in several DNS studies [34].

The uniqueness of the conditional expected diffusion for all the members of the family of exponential distributions, and its similarity for the closures considered here indicates that a major influence of this diffusion is through its behavior near the scalar bounds. For the exponential family, the PDF is defined within an unbounded support and the model obviously cannot account for the variations of these bounds in the composition domain. Moreover, the primary reason for the drawbacks of the AMC and JET is due to a lack of capability of the models to account for the boundary encroachment as mixing proceeds [14]. Since there are no mechanisms to account for domain shrinkage, these closures yield the behavior near the scalar bounds as shown in Fig. 4(b). In the lamellar description, this can be cured through the description of STD [24]. For the AMC and JET, currently there is no procedure by which the problem can be overcome in a robust manner.

CONCLUSION

A mathematical description is provided of the correlation between the condi-

tional expected dissipation and the single point probability density function of passive scalars in homogeneous turbulent flows. By considering the general family of exponential PDFs it is shown that for PDFs with tails broader than gaussian, the conditional dissipation portrays a basin shape; and for those with a skirt less extended than gaussian, the conditional dissipation is bell-shaped. This is further assessed by analyzing the results obtained by the Linear Eddy Model (LEM) under several mixing conditions. It is also proved that all members of the family of exponential PDFs have an identical conditional expected diffusion. The role of the conditional expected diffusion is explained in the context of LEM with those of other recent mixing closures (AMC and JET), the results of LEM with the same conditional scalar diffusion near the mean value of the scalar. The primary role of the conditional diffusion is through its behavior near the scalar bounds in the composition domain. This is in accord with results obtained previously by Direct Numerical Simulations (DNS). In the lamellar theory, the boundary evolution is controlled by the Striation Thickness Distribution (STD).

ACKNOWLEDGEMENTS

This work is sponsored by the Office of Naval Research under Grant N00014-94-1-0677 and by the National Science Foundation under Grant CTS-9253488. Computational resources are provided by NSF through NCSA at the University of Illinois.

REFERENCES

- Libby, P. A. and Williams, F. A., Eds., *Turbulent Reacting Flows*, volume 44 of *Topics in Applied Physics*, Springer-Verlag, Heidelberg, 1980.
- Elfersberg, E. and Peters, N., *Proceedings of 22nd Symp. (Int.) on Combustion*, pp. 693-700, The Combustion Institute, Pittsburgh, PA, 1988.
- Williams, F. A., *Combustion Theory*, The Benjamin/Cummings Publishing Company, Menlo Park, CA, 2nd edition, 1985.
- Libby, R. W., In Libby and Williams [1], chapter 3.
- Peters, N., *Proceedings of 21st Symp. (Int.) on Combustion*, pp. 1231-1250, The Combustion Institute, Pittsburgh, PA, 1986.
- Peters, N., *Prog. Energy Combust. Sci.* 10, pp. 319-339 (1984).
- Libby, P. A. and Williams, F. A., Eds., *Turbulent Reacting Flows*, Academic Press, London, UK, 1994.
- Libby, R. W., Phys. Fluids A. 5, pp. 436-444 (1993).
- Janicka, J. and Peters, N., *Proceedings of 19th Symp. (Int.) on Combustion*, pp. 367-374, The Combustion Institute, Pittsburgh, PA, 1982.
- Dopazo, C., In Libby and Williams [1], chapter 7.
- Pope, S. B., *Combust. Sci. and Tech.* 28, pp. 131-145 (1982).
- Chen, H., Chen, S., and Krichman, R. H., *Phys. Rev. Lett.* 63, pp. 2657-2660 (1989).
- Pope, S. H., *Theoret. Comput. Fluid Dynamics* 2, pp. 255-270 (1991).

14. Miller, R. S., Frankel, S. H., Madnia, C. K., and Givi, P., *Combust. Sci. and Tech.*, **91**, pp. 21-52 (1993).
15. Kerstein, A. R., *Combust. Sci. and Tech.*, **80**, pp. 391-421 (1988).
16. Kerstein, A. R., *J. Fluid Mech.*, **231**, pp. 361-394 (1991).
17. Yakhut, V., Orazag, S. A., Balachandar, S., Jackson, E., She, Z.-S., and Sirovich, L., *J. Sci. Comput.*, **5**, pp. 199-221 (1990).
18. Gao, F., *Phys. Fluids A*, **3**, pp. 2438-2444 (1991).
19. Pope, S. B. and Ching, E. S. C., *Phys. Fluids A*, **5**, pp. 1529-1531 (1993).
20. Sunai, Y. G. and Yakhut, V., *Phys. Rev. Lett.*, **63**, pp. 1962-1964 (1989).
21. Bockhorn, H., *Proceedings of the 22nd Symp. (Int.) on Combustion*, pp. 605-604, The Combustion Institute, Pittsburgh, PA, 1988.
22. Jayesh and Warhaft, Z., *Phys. Fluids A*, **4**, pp. 2292-2307 (1992).
23. O'Brien, E. E., In Libby and Williams [1], chapter 5.
24. Jabeij, F. A., Ph.D. Thesis, Department of Mechanical and Aerospace Engineering, State University of New York at Buffalo, Buffalo, NY, 1995, In preparation.
25. Ottino, J. M., *The Kinematics of Mixing: Stretching, Chaos, and Transport*, Cambridge University Press, Cambridge, U.K., 1989.
26. Ashurst, W. T., Kerstein, A. R., Kerr, R. M., and Gilson, C. H., *Phys. Fluids*, **30**, pp. 2343-2353 (1987).
27. Kerstein, A. R., *Phys. Fluids A*, **27**, pp. 2819-2827 (1991).
28. Leonard, A. D. and Hill, J. C., *Phys. Fluids A*, **3**, pp. 1286-1299 (1991).
29. Eswaran, V. and Pope, S. B., *Phys. Fluids*, **31**, pp. 506-520 (1988).
30. Givi, P., In Libby and Williams [7], chapter 8.
31. Givi, P., *Prog. Energy Combust. Sci.*, **15**, pp. 1-107 (1989).
32. Kimura, Y. and Krachman, R. A., *Phys. Fluids A*, **5**, pp. 2264-2277 (1993).
33. McMurry, P. A., Menon, S., and Kerstein, A. R., *Energy & Fuels*, **7**, pp. 817-826 (1993).
34. Frankel, S. H., Ph.D. Thesis, Department of Mechanical and Aerospace Engineering, State University of New York at Buffalo, Buffalo, NY, 1993.
35. Jiang, T.-L., Gao, F., and Givi, P., *Phys. Fluids A*, **4**, pp. 1028-1035 (1992).

APPENDIX IX

Conditional Statistics in Turbulent Scalar Mixing and Reaction

Conditional Statistics in Turbulent Scalar Mixing and Reaction

F. A. Jaber, R. S. Miller, and P. Givi

Dept. of Mechanical and Aerospace Engineering, State University of New York at Buffalo, Buffalo, NY 14260

For more than 30 years, the pioneering hypothesis of Toor (1962) has been utilized for statistical modeling of turbulent reacting flows with nonpremixed reactants. According to this hypothesis, in a chemical reaction of the type "Fuel + Oxidizer → Products" in homogeneous isothermal flows with stoichiometric and (initially) nonpremixed reactants, the temporal decay rate of the "unmixedness" (reactants' covariance) is independent of chemistry and can be related to the standard deviation of the "mixture fraction." This mixture fraction (also referred to as the Shvab-Zeldovich variable (Libby and Williams, 1980)) is a conserved scalar which portrays the mixing behavior of the system under nonreacting but otherwise identical flow conditions (Brodkey, 1975; Toor, 1975). Denoting the concentration of one of the reactants, say fuel by \mathcal{F} , and the mixture fraction by ϕ , Toor (1962) shows that in the limit of infinitely fast chemistry

$$\frac{E\{\mathcal{F}(t)\}}{E\{\mathcal{F}(t')\}} = \frac{\sigma(t)}{\sigma(t')}, \quad (1)$$

where $E\{\cdot\}$ denotes the expectation (ensemble-mean value) and $\sigma^2(t)$ is the variance of the mixture fraction. This mixture fraction, considered a random variable, is defined within the lower and upper bounds: $\phi \in [\phi_l, \phi_u]$. In a spatially homogeneous turbulent flow the statistics are generated by realization and/or space-sampling, thus the decay of the mixture fraction variance and the rate of reactant conversion depend only on time (t).

Determination of the statistics of reacting scalars from those of the mixture fraction continues to be a very challenging issue. Dutta and Tarbell (1989), Frankel et al. (1993), and Frankel (1993) discuss comparative assessments of several turbulence closures for this purpose. In Toor's results portrayed by Eq. 1 the primary assumption is that the probability density function (pdf) of the mixture fraction is Gaussian, and remains Gaussian throughout mixing. In this note we show that Eq. 1 is valid under a less restrictive condition, and that the Gaussian pdf is one special case which satisfies this gen-

eral condition. This proof is provided by considering the transport equation governing the evolution of the mixture fraction pdf. With this equation, several other important features of scalar mixing are also identified.

The lefthand side of Eq. 1 is determined directly by the pdf of the mixture fraction. By defining $\phi = 0$ as the reaction surface (the flame sheet), we have (Libby and Williams, 1980): $E\{\mathcal{F}(t)\} = \int_0^{\phi_u} \phi P(\phi, t) d\phi$, where P denotes the pdf of ϕ . With the transformation $[\phi, t] \rightarrow [y = \phi/\sigma(t), \sigma(t)]$, Eq. 1 is expressed as

$$\frac{E\{\mathcal{F}(t)\}}{\sigma(t)} = \int_0^{y_u = [\phi_u/\sigma(t)]} y P[y, \sigma(t)] dy. \quad (2)$$

In order for Eq. 1 to be valid, two conditions must be satisfied: (1) the pdf in the integrand of Eq. 2 must be time-invariant, i.e., $P[y, \sigma(t)] = P(y)$; and (2) the upper limit of the integral must be time-invariant. Here we demonstrate that both of these conditions are satisfied when the "conditional expected diffusion" of the mixture fraction is "linear" in the composition space. For this demonstration, we consider the transport equation for the pdf of ϕ in spatially homogeneous turbulent flows (O'Brien, 1980; Pope, 1985; Dopazo, 1994)

$$\frac{\partial P}{\partial t} + \frac{\partial}{\partial \phi} (E\{\zeta|\phi\}P) = 0. \quad (3)$$

Assuming that the molecular diffusion is governed by the Fick's law, $\zeta = \kappa \nabla^2 \phi$, κ is the molecular diffusion coefficient. The term $E\{\zeta|\phi\}$ denotes the expectation of the scalar diffusion conditioned (denoted by the vertical bar) on the scalar value ϕ . Equation 3 is alternatively expressed as (O'Brien, 1980; Pope, 1985)

$$\frac{\partial P}{\partial t} + \frac{\partial^2}{\partial \phi^2} (E\{\xi^2|\phi\}P) = 0, \quad (4)$$

with $\xi^2 = \kappa \nabla \phi \cdot \nabla \phi$ and $E\{\xi^2|\phi\}$ denoting the conditional expectation of the scalar dissipation. At the level of single-point closure, neither of these conditional expectations are known,

Current address of R. S. Miller: Applied Technologies Section, Jet Propulsion Laboratory, 4800 Oak Grove Drive, Pasadena, CA 91109.

nor is the unconditional expectation of scalar dissipation, $E\{\xi^2\} = \int_{\phi_0}^{\phi_u} P(\phi, t) E\{\xi^2|\phi\} d\phi$. Given the pdf it is possible to determine these conditional expectations (Miller et al., 1993). First, we consider the general family of "exponential pdfs" since this family includes the Gaussian distribution as assumed by Toor, and it also includes other distributions which have been observed in more recent laboratory and numerical experiments (Castaing et al., 1989; Kerstein, 1991; Gollub et al., 1991; Pumir et al., 1991; Jayesh and Warhaft, 1992; Metais and Lesieur, 1992; Lane et al., 1993; Kimura and Kraichnan, 1993)

$$P(\phi, \sigma(t)) = C(\sigma(t), q) \exp\left(-\frac{|\phi - \phi_0|^q}{K[\sigma(t), q]}\right), \quad \phi \in [\phi_l, \phi_u] \equiv [-\infty, \infty], \quad (5)$$

where q is a constant parameter; $q = 2$ corresponds to Gaussian and $q = 1$ implies the Laplace (double exponential) density. Considering distributions with the mean $\phi_0 = E\{\phi\} = 0$ and the variance $\sigma^2 = E\{\phi^2\}$, manipulation of Eqs. 3-4 in the format outlined by Miller et al. (1993) yields

$$\frac{E\{\xi^2|\phi\}}{E\{\xi^2\}} = 1, \quad \frac{E\{\zeta|\phi\}}{E\{\xi^2\}} = -\frac{\phi}{\sigma^2} \quad (6)$$

for the Gaussian density, and

$$\frac{E\{\xi^2|\phi\}}{E\{\xi^2\}} = \frac{1}{2} \left(1 + \frac{\sqrt{2}|\phi|}{\sigma}\right), \quad \frac{E\{\zeta|\phi\}}{E\{\xi^2\}} = -\frac{\phi}{\sigma^2} \quad (7)$$

for the Laplace pdf. It is noted that the conditional expectations of diffusion as predicted by these two densities are identical, and are linear in the compositional domain in accord with the least mean-square estimation (LMSE) model (Dopazo, 1994; O'Brien, 1980). Based on this observation, we propose that for all the other members of the family of exponential pdfs, the linear profile is applicable. This proposal is plausible provided that

$$\frac{1}{C} \frac{\partial C}{\partial t} = \frac{E\{\xi^2\}}{\sigma^2}, \quad \frac{1}{K} \frac{\partial K}{\partial t} = -\frac{qE\{\xi^2\}}{\sigma^2}. \quad (8)$$

Manipulation of Eq. 5 shows that $K(\sigma, q) = M(q)\sigma^q$ and $C(\sigma, q) = N(q)\sigma^{-1}$, where $M(q)$ and $N(q)$ are known functions of q . Thus, it is easily verified that Eq. 8 is indeed valid regardless of the magnitude of q .

The general condition under which the conditional expected diffusion is linear for any pdf has been established by Valiño et al. (1994). By considering the characteristic of Eq. 3, they show that with a linear conditional expected diffusion, the pdf of the variable y is time-invariant. Here, we provide a direct means of establishing this condition by substituting the second of Eq. 6 into Eq. 3. Denoting the Fourier transform of the pdf by \tilde{P}

$$P(\phi, t) = \frac{1}{\sqrt{2\pi}} \int_{-\infty}^{\infty} \tilde{P}(\Omega, t) \exp(j\Omega\phi) d\Omega, \quad j = \sqrt{-1} \quad (9)$$

we have

$$\frac{\partial \tilde{P}}{\partial t} + \frac{\Omega E\{\xi^2\}}{\sigma^2} \frac{\partial \tilde{P}}{\partial \Omega} = 0. \quad (10)$$

This differential equation has the trial solution

$$\tilde{P}(\Omega, t) = \tilde{f}[\Omega \exp\{h(\sigma, t)t\}], \quad (11)$$

where the function \tilde{f} depends on the initial condition $P(\phi, 0)$. With $\sigma(d\sigma/dt) = -E\{\xi^2\}$, this trial solution satisfies Eq. 3 with $h(\sigma, t) = (1/t)\ln[\sigma(t)]$. Thus the unique solution of Eq. 10 is

$$\tilde{P}(\Omega, t) = \tilde{f}[\Omega \sigma(t)]. \quad (12)$$

This solution shows that the transformation $[\phi, t] \rightarrow [y, \sigma(t)]$ is very convenient in portraying the nature of pdf evolution when the conditional expected diffusion is linear. With this transformation Eq. 3 yields

$$P[y, \sigma(t)] = G(y) \quad \text{only,} \quad (13)$$

where the function G is determined by the initial condition and remains the same through mixing. Equation 13 means that for a linear conditional expected diffusion, the pdf of the scalar variable adopts a "self-similar" form in the sense that the pdf of the variable normalized by its standard deviation is time-invariant. This does not imply a "stationary field" as $P(\phi, t)$ can be time-dependent. This self-similarity is, in fact, noticed in direct numerical simulation results (Miller et al., 1993) in which the linearity of the conditional scalar diffusion field is also corroborated. It must be noted that in using the linear conditional diffusion field in LMSE, O'Brien (1980) points to permanency of the initial shape of the pdf when the parameter $\beta = [E\{\xi^2\}(t)]/\sigma^2(t)$ is constant. The mathematical procedure adopted here provides a direct means of determining the functional form of the parameter y , as undisguised by Eq. 12. Valiño et al. (1994) and Sinai and Yakhot (1989) suggest this functional form *a priori* by the inspection of numerical simulation data.

Now we consider condition (2) pertaining to the limits of $[y_l(t), y_u(t)] = [\phi_l/\sigma(t), \phi_u/\sigma(t)]$. For a pdf with an "unbounded support" $[y_l, y_u] \equiv [-\infty, \infty]$ condition (2) is satisfied. For the Gaussian pdf, obviously an unbounded support is implied by Toor. For a pdf within a "bounded domain," mixing is accompanied by the migration of the scalar bounds in the composition space as shown by Miller et al. (1993). Notwithstanding the randomness of the scalar bounds, Miller et al. (1993) also show

$$\frac{d\phi_u}{dt} = -\frac{d\phi_l}{dt} = E\{\zeta|\phi_u\} = -E\{\zeta|\phi_l\}. \quad (14)$$

With a linear conditional expected diffusion in Eq. 14 we have

$$\frac{\phi_u(t)}{\sigma(t)} = -\frac{\phi_l(t)}{\sigma(t)} = \text{Constant} = \frac{\phi_u(0)}{\sigma(0)} = C. \quad (15)$$

Equations 13 and 15 indicate that the linearity of the conditional expected diffusion satisfies both conditions (1) and (2); and thus imply the validity of Eq. 1. The Gaussian pdf is one special case which satisfies these conditions, but there are other distributions and/or mixing closures which portray a similar behavior (Givi, 1989). Considering the (approximate) linearity of the conditional diffusion field in several recent numerical and laboratory experiments (Miller et al., 1993; Pope and Ching, 1993; Leonard and Hill, 1991; Kailasanath et al., 1993) in which the pdf is not necessarily Gaussian, it is plausible to assume that Toor's results would be applicable for modeling of equivalent reacting systems. Of course, this would be true if the conditional diffusion remains linear at all times: It is well-established that for initially "segregated" reactants with the initial pdf composed of an exact double-delta function, the assumption is not generally plausible when $t' \rightarrow 0$, $t \neq t'$ (Kosály, 1987; Givi and McMurtry, 1988; Madnia et al., 1992; Frankel et al., 1993) unless the pdf remains double-delta at all times. The transformation of the double-delta pdf to Gaussian (or other) distributions is accompanied by a nonlinear conditional expected diffusion (Miller et al., 1993).

At this point, it is instructive to note that with the same linear conditional diffusion, the conditional expected dissipation can vary depending on the initial form of the pdf. It is useful to note that the self-similarity of the pdf also implies the self-similarity of the conditional dissipation. With the requirements (Miller et al., 1993) $P(\phi_l, t)E\{\xi^2|\phi_l\} = P(\phi_u, t)E\{\xi^2|\phi_u\} = 0$, Eq. 4 gives

$$\frac{E\{\xi^2|y\}}{E\{\xi^2\}} = \frac{-\int_{-C}^y y' P(y') dy'}{P(y)}. \quad (16)$$

The righthand side of Eq. 16, while time-invariant, does depend on the pdf. For the exponential family, for example, Eqs. 3-4 yield, after significant manipulations (Jaberi, 1996)

$$\frac{E\{\xi^2|\phi\}}{E\{\xi^2\}} = \frac{K^{2q}}{q\sigma^2} \left\{ \Gamma\left(\frac{2}{q}\right) - \gamma\left(\frac{2}{q}, \frac{|\phi|^q}{K}\right) \right\} \exp\left(\frac{|\phi|^q}{K}\right), \quad (17)$$

where Γ and γ denote the gamma function and the incomplete gamma function, respectively. With the identity

$$\Gamma(1+n) - \gamma(1+n, z) = n! \exp(-z) \sum_{k=0}^n \frac{z^k}{k!}, \quad n = 0, 1, \dots \quad (18)$$

the corresponding algebraic relations for the Gaussian density and the Laplace density, Eqs. 6 and 7 are exactly recovered for $q = 2$ and $q = 1$, respectively. For other values of q , Eq. 17 can be evaluated only by numerical means (for $q = 4$ and $q \rightarrow \infty$ the results can be expressed, respectively, in terms of the error function and the exponential integral, both of which still require numerical evaluation). Note that for the Gaussian member ($q = 2$) an analytical expression for the conditional expected dissipation has been previously obtained (Gao, 1991). The results based on Eq. 17 in Figure 1 confirm that if the pdf exhibits tails broader than Gaussian

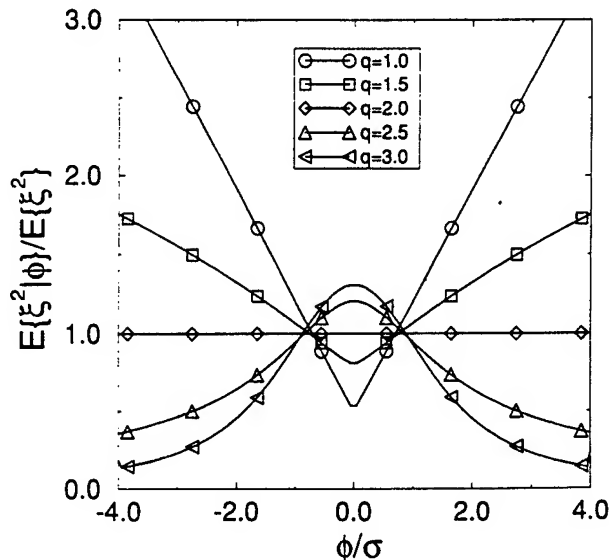


Figure 1. Normalized conditional expected dissipation of the scalar for several members of the exponential pdf.

($q < 2$), the normalized conditional dissipation portrays a "basin" shaped curve (concave up) near the mean scalar value. For pdfs with tails narrower than Gaussian ($q > 2$), the conditional dissipation is "bell" shaped (concave down). For $q = 2$, the profile is a straight line $E\{\xi^2|\phi\} = E\{\xi^2\}$. Only in this case is the conditional scalar dissipation independent of the scalar value (Gao, 1991), for which Eq. 1 was derived by Toor. The relation between the conditional dissipation and broadness (narrowness) of the pdf at its tails was first derived by Sinai and Yakhot (1989) based on a speculation on the asymptotic behavior of scalar mixing in stationary turbulence. Here, Eq. 17 illustrates this relation directly and is very convenient for assessing the results obtained by other closures.

Acknowledgment

We are indebted to Professor H. L. Toor for providing valuable comments on the first draft of this article. This work is part of an effort sponsored by the office of Naval Research under grant N00014-94-1-0677.

Notation

- C = constant
- $E[\cdot]$ = conditional expectation
- P = PDF
- y = normalized scalar variable: $y = \phi/\sigma(t)$

Greek letters

- γ = incomplete gamma function
- Γ = gamma function
- ζ = scalar diffusion
- κ = diffusion coefficient
- ξ^2 = scalar dissipation
- σ = standard deviation of the mixture fraction
- ϕ = composition domain

Superscripts

- l = lower limit in the composition space
- u = upper limit in the composition space

Literature Cited

Brodkey, R. S., ed., *Turbulence in Mixing Operation*, Academic Press, New York (1975).

Castaing, B., G. Gunaratne, F. Heslot, L. Kadanoff, A. Libchaber, S. Thomae, X. Z. Wu, S. Zaleski, and G. Zanetti, "Scaling of Hard Thermal Turbulence in Rayleigh-Bernard Convection," *J. Fluid Mech.*, **204**, 1 (1989).

Dopazo, C., "Recent Developments in pdf Methods," *Turbulent Reacting Flows*, Chap. 7, P. A. Libby and F. A. Williams, eds., Academic Press, London, pp. 375-474 (1994).

Dutta, A., and J. M. Tarbell, "Closure Models for Turbulent Reacting Flows," *AICHE J.*, **35**, 2013 (1989).

Frankel, S. H., C. K. Madnia, and P. Givi, "Comparative Assessment of Closures for Turbulent Reacting Flows," *AICHE J.*, **39**, 899 (1993).

Frankel, S. H., "Probabilistic and Deterministic Description of Turbulent Flows with Nonpremixed Reactants," PhD Thesis, Dept. of Mechanical and Aerospace Engineering, State Univ. of New York at Buffalo (1993).

Gao, F., "Mapping Closure and Non-Gaussianity of the Scalar Probability Density Functions in Isotropic Turbulence," *Phys. Fluids A*, **3**, 2438 (1991).

Givi, P., and P. A. McMurtry, "Non-Premixed Reaction in Homogeneous Turbulence: Direct Numerical Simulations," *AICHE J.*, **34**, 1039 (1988).

Givi, P., "Model Free Simulations of Turbulent Reactive Flows," *Prog. Energy Combust. Sci.*, **15**, 1 (1989).

Gollub, J. P., J. Clarke, M. Gharib, B. Lane, and O. N. Mesquita, "Fluctuations and Transport in a Stirred Fluid with a Mean Gradient," *Phys. Rev. Lett.*, **67**, 3507 (1991).

Jaberi, F. A., "Mixing and Reaction in Homogeneous Turbulence," PhD Thesis, Dept. of Mechanical and Aerospace Engineering, State Univ. of New York at Buffalo (1996).

Jayesh and Z. Warhaft, "Probability Distribution, Conditional Dissipation, and Transport of Passive Temperature Fluctuations in Grid-Generated Turbulence," *Phys. Fluids A*, **4**, 2292 (1992).

Kailasanath, P., K. R. Sreenivasan, and J. R. Saylor, "Conditional Scalar Dissipation Rates in Turbulent Wakes, Jets, and Boundary Layers," *Phys. Fluids A*, **5**, 3207 (1993).

Kerstein, A. R., "Linear-Eddy Modeling of Turbulent Transport. Part 6. Microstructure of Diffusive Scalar Mixing Fields," *J. Fluid Mech.*, **231**, 361 (1991).

Kimura, Y., and R. H. Kraichnan, "Statistics of an Advecte Passive Scalar," *Phys. Fluids A*, **5**, 2264 (1993).

Kosály, G., "Non-Premixed Simple Reaction in Homogeneous Turbulence," *AICHE J.*, **33**, 1998 (1987).

Lane, B. R., O. N. Mesquita, S. R. Meyers, and J. P. Gollub, "Probability Distributions and Thermal Transport in a Turbulent Grid Flow," *Phys. Fluids A*, **5**, 2255 (1993).

Leonard, A. D., and J. C. Hill, "Scalar Dissipation and Mixing in Turbulent Reacting Flows," *Phys. Fluids A*, **3**, 1286 (1991).

Libby, P. A., and F. A. Williams, eds., *Turbulent Reacting Flows. Topics in Applied Physics*, Vol. 44, Springer-Verlag, Heidelberg (1980).

Madnia, C. K., S. H. Frankel, and P. Givi, "Reactant Conversion in Homogeneous Turbulence: Mathematical Modeling, Computational Validations and Practical Applications," *Theoret. Comput. Fluid Dynamics*, **4**, 79 (1992).

Metais, O., and M. Lesieur, "Spectral Large-Eddy Simulation of Isotropic and Stably Stratified Turbulence," *J. Fluid Mech.*, **239**, 157 (1992).

Miller, R. S., S. H. Frankel, C. K. Madnia, and P. Givi, "Johnson-Edgeworth Translation for Probability Modeling of Binary Scalar Mixing in Turbulent Flows," *Combust. Sci. and Tech.*, **91**, 21 (1993).

O'Brien, E. E., "The Probability Density Function (PDF) Approach to Reacting Turbulent Flows," in *Libby and Williams*, Chap. 5, p. 185 (1980).

Pope, S. B., and E. S. C. Ching, "Stationary Probability Density Functions: An Exact Result," *Phys. Fluids A*, **5**, 1529 (1993).

Pope, S. B., "PDF Methods for Turbulent Reactive Flows," *Prog. Energy Combust. Sci.*, **11**, 119 (1985).

Pumir, A., B. Shraiman, and E. D. Siggia, "Exponential Tails and Random Advection," *Phys. Rev. Lett.*, **3**, 2838 (1991).

Sinai, Y. G., and V. Yakhot, "Limiting Probability Distributions of a Passive Scalar in a Random Velocity Field," *Phys. Rev. Lett.*, **63**, 1962 (1989).

Toor, H. L., "Mass Transfer in Dilute Turbulent and Nonturbulent Systems with Rapid Irreversible Reactions and Equal Diffusivities," *AICHE J.*, **8**, 70 (1962).

Toor, H. L., "The Non-Premixed Reaction: $A + B \rightarrow Products$," in Brodkey, pp. 123-166 (1975).

Valiño, L., C. Dopazo, and J. Ros, "Quasistationary Probability Density Functions in the Turbulent Mixing of a Scalar Field," *Phys. Rev. Lett.*, **72**, 3518 (1994).

Manuscript received Jan. 11, 1995, and revision received July 10, 1995.

APPENDIX X

Inter-Layer Diffusion Model of Scalar Mixing in Homogeneous Turbulence

Inter-Layer Diffusion Model of Scalar Mixing in Homogeneous Turbulence

F. A. JABERI and P. GIVI *Department of Mechanical and Aerospace
Engineering, State University of New York at Buffalo, Buffalo, NY 14260-4400*

(Received March 31, 1994; in final form December 27, 1994)

ABSTRACT—A field-parametrized model termed the *Inter-Layer Diffusion Model* (ILDM) is developed and is implemented for the probabilistic description of scalar mixing in homogeneous turbulent flows. The essential element of the model is based on the lamellar theory of mixing in the context developed by Kerstein (1991a), and proposes that there are two coupled mechanisms by which the mixing process is described. These mechanisms are due to: (1) local events and (2) integrated global events. The mathematical formalities by which the closure is invoked are described and it is shown that the conditional expected diffusion of the scalar field depicted by the model depends more directly on the local events. With the manipulation of each of these two mechanisms, several families of scalar probability density functions (pdf's) are generated. These families include some of the distributions generated by other mixing closures. The similarity of local events imply the similarity of the conditional expected diffusion as generated via these models. The global events manifest themselves by the evolution of the conditional expected dissipation, and also the boundedness of the composition domain. While the pdf's generated in this way are very different, their applications for modeling of mixing limited reactions do not yield significantly different results.

Key Words: Turbulent mixing, lamellar model, homogeneous turbulence, reacting flows

1 INTRODUCTION

Description of scalar mixing continues to be a challenging task in mathematical modeling of turbulent flows (Brodkey, 1975; Kerstein, 1991b; Ottino, 1989; Dopazo, 1994). Within this past decade alone, several strategies have been devised and implemented for a variety of applications. Examples are the approaches based on scalar probability density function (pdf) via modeled transport equations (Pope, 1985; Chen *et al.*, 1989; Madnia *et al.*, 1992; Miller *et al.*, 1993; Givi, 1989; Dopazo, 1994), assumed pdf methods (Bockhorn, 1988; Frankel *et al.*, 1993), and other procedures such as the Linear Eddy Model (LEM) (Kerstein, 1988; Kerstein, 1991b; Kerstein, 1992), the Fokker-Plank equation (Fox, 1992), spectral closures (Larcheveque and Lesieur, 1981; Frankel *et al.*, 1992) and lamellar structures (Ottino, 1989; Kerstein, 1991a), amongst others. Due to the complexity of the subject, the extent of success of these closures has been appraised only in a limited context. In some cases, the performance of the models has been assessed by comparison with data generated by direct numerical simulations (DNS) (Givi, 1994). However, because of the limitations of DNS the generality of the conclusions drawn by such comparisons cannot be guaranteed without caution. Also, the extent of data obtained by laboratory experiments is not very significant; it has been only recently that substantiated data, useful for modeling purposes, have been generated (Jayesh and Warhaft, 1992; Kailasanath *et al.*, 1993). However, the challenges associated with the problem are well-recognized, warranting continued work on the subject.

A standard test case that has proven useful in the contributions cited above, is the problem of passive scalar mixing from an initial binary state in homogeneous-isotropic turbulence (Givi and McMurtry, 1988; Eswaran and Pope, 1988; McMurtry and Givi, 1989; Madnia *et al.*, 1992; Miller *et al.*, 1993; Frankel *et al.*, 1993; Frankel *et al.*, 1992; Jiang *et al.*, 1992; Metais and Lesieur, 1992; Kimura and Kraichnan, 1993). In this setting, the problem of mixing is isolated from other competing physical mechanisms. It also provides a relatively simple condition to configure in both laboratory and numerical experiments. In this context, turbulent mixing involves two physical mechanisms: turbulent convection and molecular diffusion. The first is a mechanical "stirring" process which results in the stretching of intermaterial area of the scalar. Mixing induced by such stirring is completed at small scales by the molecular action through diffusion of substances across intermaterial surface areas. The results of recent laboratory experiments (Southerland and Dahm, 1993) and numerical simulations (Ruetsch and Maxey, 1992) suggest that a major part of scalar diffusion occurs in a system of *layer-like striation, or lamellae*. Each of these lamellae have a thickness ($2w$) which in general is a function of space and time, $w = w(\vec{x}, t)$. The rate of stretching and folding of the lamellar structures is governed by turbulent eddies. Development of a physical model which can accurately portray the mechanisms of lamellar stretching as well as the distribution of these lamellae are the subject of current research (Ottino, 1989; Muzzio and Ottino, 1989b; Muzzio and Ottino, 1989a; Sokolov and Blumen, 1991a; Sokolov and Blumen, 1991b).

The lamellar description has proven useful in depicting the kinematics of turbulent mixing and also in reproducing the results obtained by other closures. For example, Kerstein (1991a) shows that with particular specifications of the scalar profile within each lamellae and the pdf of lamellae thickness, the family of pdf's generated by the Amplitude Mapping Closure (AMC) (Kraichnan, 1989; Chen *et al.*, 1989) are obtained. Fox (1992) employs the lamellar theory and provides an evolution equation for the joint pdf of the scalar and its gradient based on the stochastic Fokker-Planck equation. The unknown coefficients of this equation are pre-specified to provide the evolution of the pdf. With this method, the statistical behavior at the asymptotic stage must be known *a priori*, since the parameters of the model are adjusted to yield this behavior.

Our purpose in this work is to further examine the lamellar theory and to investigate some of its features for statistical modeling of mixing in turbulent flows. The formalities on which the model is based are discussed in a mathematical context with an explicit description of the assumptions made in its simplifications for the present applications. A feature of the model is its capability in explaining the reasoning for the success (or lack thereof) of other recent turbulent mixing closures. This is facilitated by comparative assessments of the *conditional expected dissipation* and the *conditional expected diffusion* of the scalar field as predicted by the model. However, as will be shown, a wide variety of solutions emerge. In the context considered, a specific selection cannot be made. Neither is such a selection recommended without further knowledge of the turbulent field, as many of these solutions are justifiable on physical grounds. In fact, in a complicated turbulent mixing problem a combination of these cases may exist. The behavior of the conditional statistics as predicted by the model is very useful in depicting many subtle features of turbulent mixing which are not realized via previous closures.

2 PROBABILITY MODELING AND THE LAMELLAR DESCRIPTION

With the assumption of Fickian diffusion, the transport equation for a passive scalar variable, $\phi(\vec{x}, t)$ in a homogeneous incompressible turbulent flow is expressed by:

$$\frac{\partial \phi}{\partial t} + \vec{U} \cdot \nabla \phi = \mathcal{D}_{\infty} \nabla^2 \phi, \quad (1)$$

where $\vec{U}(\vec{x}, t)$ and \mathcal{D}_{∞} denote the velocity vector and the molecular diffusion coefficient, respectively. Using standard methods (Pope, 1985) the evolution equation for the single-point pdf, $P(\phi(\vec{x}, t))$ of the scalar is expressed by:

$$\frac{\partial P}{\partial t} + \frac{\partial(DP)}{\partial \phi} = 0, \quad \phi_l \leq \phi \leq \phi_u, \quad (2)$$

or alternatively by:

$$\frac{\partial P}{\partial t} + \frac{\partial^2(EP)}{\partial \phi^2} = 0. \quad (3)$$

In these equations, ϕ_l, ϕ_u denote the scalar bounds, D represents the expected value of the scalar diffusion conditioned on the scalar value, ϕ , and E denotes the expected value of scalar dissipation conditioned on ϕ . Neither of these conditional statistics are known, nor are the unconditional expected values including the expected scalar dissipation $\varepsilon(t) = \int_{\phi_l}^{\phi_u} E(\phi, t) P(\phi, t) d\phi$. This describes the closure problem inherent in a statistical description at the single-point level.

Equation (1) indicates that mixing evolution is governed by two mechanisms: molecular diffusion and turbulent advection. The former occurs primarily at small scales whereas the latter is a multi-scale phenomenon. For thin diffusion zones and sufficiently steep scalar gradients across the scalar interfaces, the diffusion process takes place in a direction approximately normal to the interface and can be treated as unidirectional. We represent this direction by y which is bounded by *striation thickness*, w , that is $-w \leq y \leq w$. This thickness is defined as a positive random variable which has a frequency defined by the *Striation Thickness Distribution* (STD) (Muzzio and Ottino, 1989b; Ottino, 1989) $h(w)$. The pdf of the scalar, conditioned on the lamellae thickness is denoted by $g(\phi|w)$ and is given by its definition:

$$g(\phi|w) = \begin{cases} \frac{1}{2w} \left| \frac{\partial y}{\partial \phi} \right| & \text{if } -w \leq y \leq w \\ 0 & \text{elsewhere} \end{cases} \quad (4)$$

The scalar pdf is thus determined by:

$$P(\phi, t) = \int_{|y|}^{\infty} f(w) g(\phi|w) dw. \quad (5)$$

where $f(w)dw$ is the probability of the event that the scalar falls within the domain $[w, w + dw]$. Therefore:

$$f(w) = \frac{wh(w)}{\int_0^x wh(w)dw}. \quad (6)$$

With the use of Equations (4), (5), (6) we have (Kerstein, 1991a):

$$P(\phi(y, t), t) = \left| \frac{\hat{c}y}{\hat{c}\phi} \right| G(|y|), \quad (7)$$

where $| |$ indicates the absolute value, and

$$G(y) = \frac{1 - C(y)}{2\langle w \rangle}, \quad (8)$$

with $C(w)$ denoting the cumulative distribution function (CDF) of w . Embedded in this derivation are the assumptions that $\hat{c}y/\hat{c}\phi$ is independent of the lamellae thickness distribution (Kerstein, 1991a; Fox, 1992). This relation which was first obtained by Kerstein (1991a) yields a variety of pdf families depending on the STD and the scalar profile within the lamellae. The first term on RHS of Equation (7) is governed primarily by the molecular diffusion. The second term represents the role of the STD and manifest the influences of stirring. It is useful to think of the first term as a representation of local events, and consider the second term as the influence of global events. These two are not independent and each of them is influenced by the other.

3 CONDITIONAL STATISTICS

Given the scalar pdf, Equations (2) and (3) can be used to determine the conditional expected diffusion and the conditional expected dissipation of the scalar field. The conditional expected diffusion is determined by using Equations (2), (3) and (7). Implementation of the mathematical procedure detailed by Miller *et al.* (1993) yields:

$$D(\phi(y, t), t) = -\frac{1}{\left| \frac{\hat{c}y}{\hat{c}\phi} \right| G(|y|)} \frac{\hat{c} \left(\int_{y_l}^y G(|y|) dy \right)}{\partial y} \frac{\hat{c}y}{\partial t}, \quad (9)$$

where $y = y(\phi, t)$, and y_l denotes the value of y corresponding to ϕ_l . Now with the assumption that the scalar distribution is monotonic within the lamellae and also assuming that y_l is fixed, the conditional expected diffusion simplifies to the form:

$$D(\phi(y, t), t) = -\left(\frac{\hat{c}y}{\hat{c}\phi} \right)^{-1} \left(\frac{\hat{c}y}{\partial t} \right). \quad (10)$$

This relation exhibits an important feature. It indicates that D is not "directly" dependent on the STD and is chiefly governed by the transient scalar evolution within

the lamellae. Therefore, if the scalar distribution within the lamellar structures is the same – even approximately – the conditional expected diffusion protracts a similar behavior. With this view, it is not surprising that the majority of pdf closures and data obtained by DNS and laboratory experiments yield similar conditional diffusion fields (Miller *et al.*, 1993; Pope and Ching, 1993; Leonard and Hill, 1991; Kailasanath *et al.*, 1993). The conditional expected dissipation is determined by using Equations (3) and (7):

$$E(\phi(y, t), t) = -\frac{1}{\left|\frac{\partial y}{\partial \phi}\right| G(|y|)} \int_{y_1}^y G(|y|) \left|\frac{\partial \phi}{\partial y}\right| \frac{\partial y}{\partial t} dy. \quad (11)$$

4 ILDM

The specification of a self-similar scalar distribution within the inter-material domain alleviates the formulation of the mixing problem in that the “exact” spatial variation of the scalar field is not considered. Instead, this variation is governed by the STD. Thus, two closure problems are involved: (1) specification of the time-variant domains and accounting for their stretching, and (2) determination of the scalar transport in each of these domains. Clearly, the first closure is to determine $h(w)$, and the second one deals with the specification of scalar distribution within the lamellae. In the absence of a velocity field, one expects that the STD retains its initial form and the scalar profile evolves according to a pure diffusion equation. In a turbulent flow, however, the STD is influenced by turbulent stirring and the scalar distribution is governed by a convection-diffusion transport equation expressed in a frame of reference attached to the moving material element. This transport is governed by Equation (1) with the velocity vector replaced by a relative velocity vector ($\vec{U} = \vec{U}_{rel}$) (Ottino, 1989). In the context of the lamellar theory, as indicated before, it is assumed that the transport occurs in one principal direction. By expressing Equation (1) in 1-D along the direction aligned with the local gradient of scalar, we have:

$$\frac{\partial \phi}{\partial t} + V_{rel} \frac{\partial \phi}{\partial y} = \mathcal{D}_{\infty} \frac{\partial^2 \phi}{\partial y^2}. \quad (12)$$

Here, V_{rel} is time-space dependent and denotes the effects of the relative velocity field \vec{U}_{rel} in the direction of principal scalar transport. Ottino (1989) suggests that in a small size material region, the relative velocity can be approximated by a linear profile $V_{rel} = \alpha(y, t)y$, where $-\alpha(y, t)$ is the surface area stretch function and is governed by hydrodynamics. Ottino (1989) also suggests that in chaotic flows, α is on average constant. Therefore, by a change of variable, \mathcal{D}_{∞} can be set equal to unity. Equation (12), together with a striation thickness pdf constitutes the basis of what we term the *Inter-Layer Diffusion Model* (ILDM). With this model, turbulent mixing is modeled in terms of two coupled mechanisms: (1) Those associated with local events, and (2) those of the global events. The local events are described by the modeled form of the transport equation within the inter-layer material (Eq. (12)), and the global influences are exhibited through the specification of $h(w)$. In the ILDM, the effect of large eddies is

implicitly subtracted from that of all the other eddies. That is, in a frame of reference moving with large eddies (those much larger than the scalar size), the remaining eddies determine the evolution of the STD and the dispersion of the scalar within the lamellae. The (indirect) dependency of the conditional expected diffusion on the striation thickness is governed by the transport within the normalized fixed region. For a linear velocity distribution the influence of STD is effectively manipulated by adjusting the diffusion coefficient. This is well understood since the molecular diffusion is a fluid property with a fixed length scale and turbulent diffusion is a flow phenomenon involving the whole spectrum of length scales. By normalizing with its thickness, each lamellae can be effectively treated with a fixed size and a modified diffusion coefficient. In the form presented, a "specific" striation thickness distribution cannot be suggested. However, it is argued that different physical scenarios observed in either DNS, or laboratory measurements, or obtained by means of other mixing closures can be expressed in terms of the model.

5 OTHER CLOSURES

For clarity of the discussions below, a brief summary is provided of the AMC and the LEM mixing closures. The basic element of the AMC involves the mapping of the scalar field (ϕ) into a stationary Gaussian field ϕ_0 , $-\infty < \phi_0 < \infty$ by the mapping $\phi = \chi(\phi_0, t)$. The mapping function is governed by (Chen *et al.*, 1989):

$$\frac{\partial \chi}{\partial t} + \phi_0 \frac{\partial \chi}{\partial \phi_0} = \frac{\hat{\epsilon}^2 \chi}{\partial \phi_0^2}. \quad (13)$$

Here, t denotes a "normalized time" whose relation with the physical time cannot be determined in the context of a single-point description. For an initial binary state with the pdf composed of two delta functions at $\phi = \pm 1$, the solution of Equation (13) is of the form (Pope, 1991; Madnia *et al.*, 1992):

$$\phi = \chi(\phi_0, t) = \text{erf}(d\phi_0 + c), \quad (14)$$

where $d = (1/\sqrt{2}\tau)$, $c = -\phi^* \sqrt{1+\tau^2}/\sqrt{2}\tau$, and $\tau(t) = \sqrt{\exp(2t) - 1}$, and $\phi^* = -\sqrt{2}\text{erf}^{-1}(\langle \phi \rangle)$ is a measure of the initial asymmetry of the pdf. This mapping yields:

$$P(\phi, t) = \frac{\tau}{2} \exp \left([\text{erf}^{-1}(\phi)]^2 - \tau^2 \left[\text{erf}^{-1}(\phi) + \frac{\phi^* \sqrt{1+\tau^2}}{\sqrt{2}\tau} \right]^2 \right), \quad (15)$$

$$D(\phi, t) = \frac{2}{\tau \sqrt{\pi}} \frac{\hat{\epsilon} \tau}{\hat{\epsilon} t} \left(\frac{\tau}{\sqrt{1+\tau^2}} \text{erf}^{-1}(\langle \phi \rangle) - \text{erf}^{-1}(\phi) \right) \exp[-(\text{erf}^{-1}(\phi))^2], \quad (16)$$

$$E(\phi, t) = \frac{2}{\pi \tau (1+\tau^2)} \frac{\hat{\epsilon} \tau}{\hat{\epsilon} t} \exp(-2[\text{erf}^{-1}(\phi)]^2). \quad (17)$$

Equations (16) and (17) for non-symmetric pdf's were first derived by Frankel (1993). An equivalent form of Equation (17) for symmetric pdf's was first derived by Gao (1991).

The primary feature of the LEM is its treatment of the mixing phenomenon in one direction. This one-dimensional description allows the resolution of *all* length scales even for flows with relatively large Reynolds and Peclet numbers. This is facilitated by differentiating between turbulent stirring (convection) and molecular diffusion (and chemical reaction). The physical interpretation of the one-dimensional domain is dependent on the particular case under consideration (see McMurtry *et al.*, 1993b, for a recent review). Along the one-dimensional domain, the diffusion (and the chemical reaction) process is implemented deterministically by the solution of the appropriate molecular transport equation(s). The manner by which turbulent convection is treated constitutes the primary feature of the LEM. This is modeled by random rearrangement (stirring) events of the scalar field along the domain. The rules by which these rearrangement processes occur are established in such a way that the random displacements of fluid elements mimic the effects of a turbulent diffusivity. The application of this model in interpreting the results obtained by DNS data and those based on the lamellar theory has been useful (McMurtry *et al.*, 1993a; Cremer *et al.*, 1992). This warrants further investigation of the model and its capabilities.

Both of these models can be compared with the ILDM. In the AMC, the evolution equation for mapping, Equation (13) is analogous to Equation (12) with $\phi \equiv \chi(\phi_0, t)$, $\phi_0 \equiv xy$. Also, for an initial binary state, the initial condition for Equation (12) is similar to that of the AMC. Therefore the solutions of these two equations are similar (of error-function type (Eq. (14)). For a linear velocity field, the effect of the STD can be absorbed into the diffusion coefficient. In the AMC this coefficient is embedded within the normalized time. Kerstein (1991a) shows that with the further assumption of a Rayleigh density for $h(w)$, the two models become identical. This assumption implies a Gaussian pdf for $G(|y|)$ which yields an asymptotic Gaussian-like (but not exactly Gaussian) density for the scalar pdf. Note that this asymptotic behavior is not very sensitive to the distributions within the lamellae and can be obtained for other members of the family of the pdf's generated by the Johnson Edgeworth Translation (JET) (Miller *et al.*, 1993).

It can be argued that the LEM provides a means of mimicking Equation (12) with a random stirring mechanism to simulate the influence of advection. Kerstein (1991b) suggests that this simulation is to be conducted by means of a random triplet stirring. In this way, the effects of all eddies are taken into account by equating the implied "effective diffusivity" to the "turbulent diffusivity". This is enacted in a one-dimensional representation of the system, regardless of the configuration. In the ILDM, the linear effects of the largest eddies are implicitly subtracted from those of the remaining ones. These remaining effects are modeled into two parts: (1) the dispersion effects are captured by solving the scalar transport equation (Eq. (12)) between two interfaces, and (2) the distribution of these interfaces due to stirring are modeled. In other words, the LEM considers the whole scalar field in a fixed size domain and simulates its evolution in a probabilistic manner. In a homogeneous flow, the whole domain is considered for statistical analysis. In the ILDM, the integration is over all lamellae and is dependent on the configuration of intermaterial structures.

6 PDF GENERATION

In the context of the ILDM, several families of scalar pdf's are generated. In the format considered here, it is not possible to prescribe $h(w)$ *a priori*; its exact specification depends on the evolution of the length scales of the hydrodynamic and the scalar fields. Therefore, the contribution of this term is modeled. The other modeling assumption involves the behavior of the advection term in Equation (12). In this section, the family of pdf's generated by the manipulations of these two terms is presented, together with a discussion of their relations with other closures. The conditional expected dissipation and the conditional expected diffusion associated with each of these pdf's are calculated since these conditional statistics provide significant insight pertaining to mixing phenomenon (Miller *et al.*, 1993; Jayesh and Warhaft, 1992; Pope and Ching, 1993; Kailasanath *et al.*, 1993; Sinai and Yakhot, 1989). Both symmetric and non-symmetric pdf's are considered and all the results are compared with data obtained by DNS. These data are taken from homogeneous turbulence simulations of Madnia *et al.* (1992); Miller *et al.* (1993); Frankel *et al.* (1993) and are compared with model results at the same values of the scalar variance. With this comparison, it is not implied that these DNS data provide an absolute standard for model validation, as various other mixing conditions have been generated by DNS (Metais and Lesieur, 1992; Kimura and Kraichnan, 1993; Jaber, 1995). Rather, the results here are intended to promote more future DNS (or laboratory experiments) with the aim of capturing some of the trends predicted here.

6.1 Error-Function Distribution within the Lamella

For an initial binary state, one solution of Equation (12) is of the form:

$$\phi = \operatorname{erf}\left(\frac{y}{\sqrt{2}\tau} + c'\right), \quad (18)$$

where similar to those in AMC (Eq. (14)), τ and c' are functions of time. Substituting this equation into Equations (7), (8), (10) and (11) yields:

$$P(\phi(y)) = \sqrt{\frac{\pi}{2}} \tau \exp\left[\left(\frac{y}{\sqrt{2}\tau} + c'\right)^2\right] G(|y|), \quad (19)$$

$$D(\phi(y)) = \frac{-2}{\sqrt{\pi}\tau} \left(\frac{y}{\sqrt{2}\tau} \frac{d\tau}{dt} - \tau \frac{dc'}{dt} \right) \exp\left[-\left(\frac{y}{\sqrt{2}\tau} + c'\right)^2\right]. \quad (20)$$

$$E(\phi(y)) = \frac{-2\sqrt{2}}{\pi\tau^2} \frac{\exp\left[-\left(\frac{y}{\sqrt{2}\tau} + c'\right)^2\right]}{G(|y|)} \left(\frac{1}{\sqrt{2}\tau} \frac{d\tau}{dt} \int_{y_1}^y y G(|y|) \exp\left[-\left(\frac{y}{\sqrt{2}\tau} + c'\right)^2\right] dy \right. \\ \left. - \tau \frac{dc'}{dt} \int_{y_1}^y G(|y|) \exp\left[-\left(\frac{y}{\sqrt{2}\tau} + c'\right)^2\right] dy \right). \quad (21)$$

In these equations, the variable c' is determined implicitly (Jaberi, 1995) by knowing the average value of the scalar $\langle \phi \rangle$ which is time invariant. An important feature of Equation (20) is that the conditional expected diffusion obtained here is similar to that generated by the AMC (Eq. (16)).

Exponential STD:

The exponential STD is given by:

$$h(w) = \beta(n+1)w^n \exp(-\beta w^{n+1}), \quad (22)$$

where $\beta = [\sqrt{2/\pi} \Gamma(n+2/n+1)]^{n+1}$ and Γ denotes the gamma function. Using this STD, the scalar pdf adopts the form:

$$P((\phi(y))) = \frac{\tau}{2} \exp \left[\left(\frac{y}{\sqrt{2}\tau} + c' \right)^2 - \beta |y|^{n+1} \right]. \quad (23)$$

As indicated by Kerstein (1991a) for the special case of the Rayleigh distribution ($n = 1$), the generated pdf is the same as that obtained by the AMC (Eq. 15) and the conditional expected diffusion is expressed by Equation (20). In general, the analytical expressions for the conditional expected dissipation are somewhat complex (Jaberi (1995) provides the analytical expressions for some of the cases). For the Rayleigh distribution, integration of Equation (21) is straightforward:

$$\begin{aligned} E(\phi(y)) &= \frac{(d\tau/dt)}{\pi \tau^3 A} \exp(-[(A+D)y^2 + 2By + 2c'^2]) + \sqrt{\frac{1}{\pi A}} \frac{1}{\tau^3} \\ &\quad \left[\frac{d\tau}{dt} \left(\frac{B}{2A} + \frac{dc'}{dt} \right) \right] \left[1 - \text{erf} \left(\frac{2Ay+B}{2\sqrt{A}} \right) \right] \exp \left(\frac{B^2}{4A} - (Dy^2 + By + c'^2) \right]. \end{aligned} \quad (24)$$

Here, $A = (1/2)(1/\tau^2 + 1)$, $B = \sqrt{2}c'/\tau$, and $D = (1/2)(1/\tau^2 - 1)$. As expected, Equation (24) is the same as Equation (17). The family of pdf's generated (Eq. 23) is characterized by the counter-balance of the two terms in the exponential term. The positive term exhibits the influence of scalar gradient and is minimum around $\phi = 0$. The negative term denotes the STD effect and is maximum near the mean scalar value. The influence of the STD on the scalar pdf becomes more dominant as n decreases and/or τ increases. The statistical results generated for $n = 0, 1, 3$ are presented in Figures 1–2. These results are for a symmetric pdf within $[-1, 1]$, i.e. $\langle \phi \rangle = 0$. As anticipated, the parameter n has a strong influence on the pdf and on the conditional expected dissipation, as Figure 1(b) is markedly different from the self-similar bell shaped for $n = 1$ for the pdf's shown in Figure 2(a) (Gao, 1991; Jiang *et al.*, 1992). The influence of the parameter on the conditional expected diffusion is not significant and all the results resemble that shown in Figure 1(c). For a system composed of randomly distributed lamellae thickness, Sokolov and Blumen (1991a); Sokolov and Blumen (1991b) suggest that in the absence of stretching the STD is close to a gamma function. This corresponds to $n = 0$. In this case, the pdf's have non-negligible values at the scalar bounds and exhibit the characteristics of an exponential-tail pdf (Fig. 1(a)). This indicates that even for an error-function scalar distribution within the lamellae, it is possible to have long-tail pdf's. From a physical standpoint this corresponds to a case

where there are noticeable slabs of materials with long intermaterial distances. In these slabs, the molecular diffusion process with large characteristics time scales is unable to mix the scalar sufficiently, thus unmixed regions prevail. This results in a concave up, basin-shaped profile for the conditional expected dissipation near the mean scalar

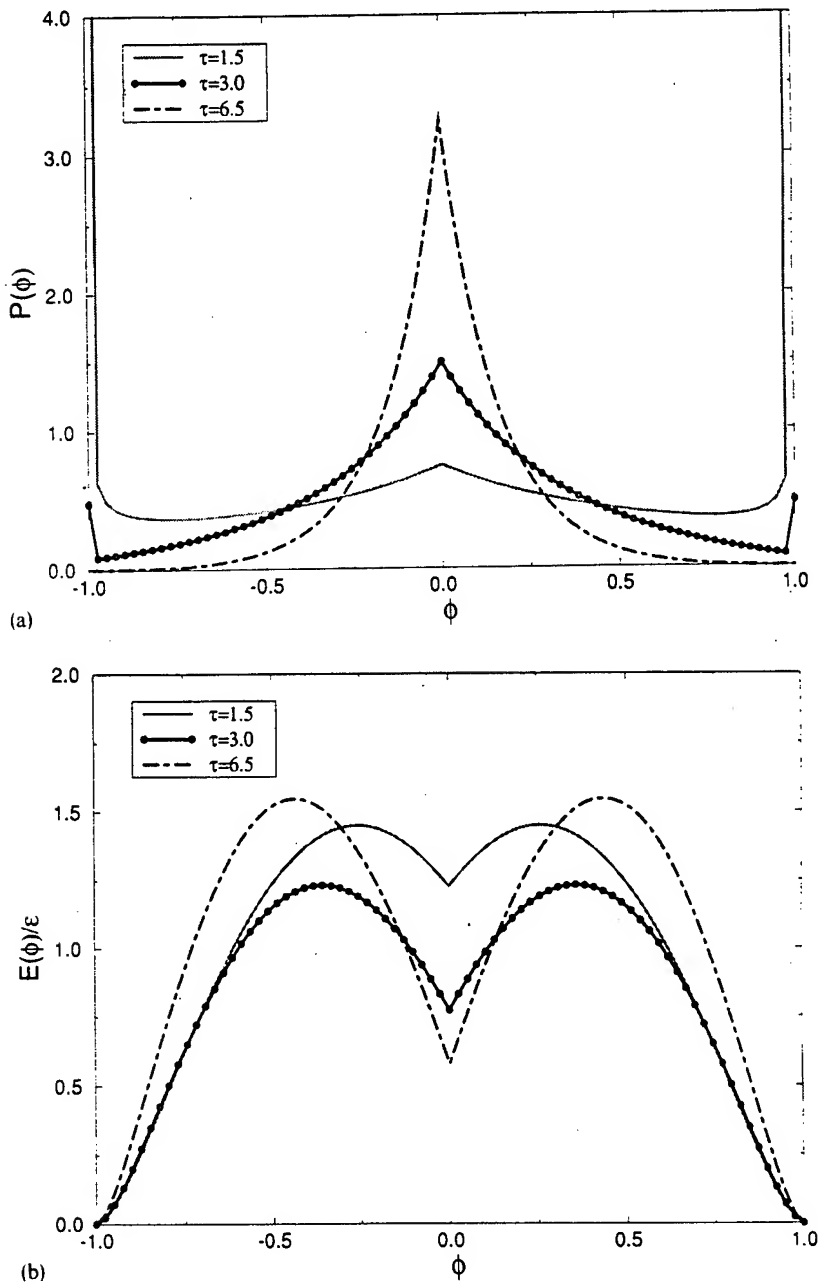


FIGURE 1 Statistical results based on an exponential STD. $n = 0$, $\langle \phi \rangle = 0$. (a) PDF. (b) Normalized conditional expected dissipation. (c) Normalized conditional expected diffusion.

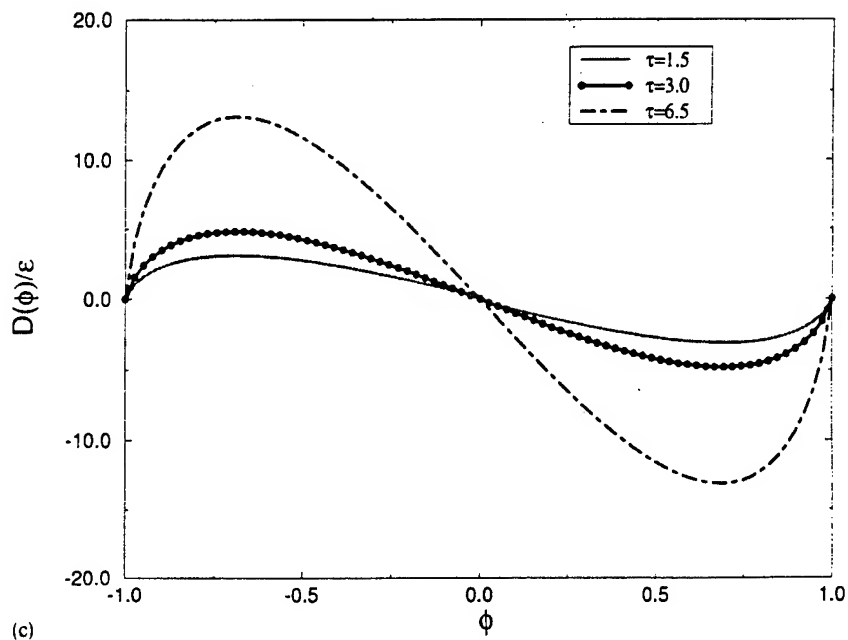


FIGURE 1 (Continued.)

value (Fig. 1(b)). The existence of two maximum and one minimum in these curves is a logical consequence of tendency of the conditional expected dissipation to be zero at its bounds (Miller *et al.*, 1993; Jaber, 1995). Note that the scalar is always bounded within the same domain. That is the conditional expected dissipation is anchored at $\phi = \pm 1$. This is due to the unboundedness of the STD. The results for $n = 3$ suggest that the pdf is somewhat uniform near the mean scalar value, but has sharp gradients in the composition domain. This is understandable since as the magnitude of n increases, the STD approaches a delta function and the pdf portrays a double-delta like distribution. This behavior is similar to the pdf evolution corresponding to a uniform STD which is presented below.

Other STD's:

Here, the model predictions based on the Rayleigh STD are compared with those generated by several bounded STD's to capture some of the important physics as discussed by Miller *et al.* (1993). For the purpose of demonstration three STD's are considered: Uniform striation thickness, constant STD and a linear STD. The extension for STD's defined by higher order polynomials is straightforward. The physical justifications for choosing these distributions are provided *posteriori* by the generated pdf's and the conditional statistics as shown in Figures 3-4. For all the cases, it is possible to express the statistics analytically (Jaber, 1995). For example for the uniform

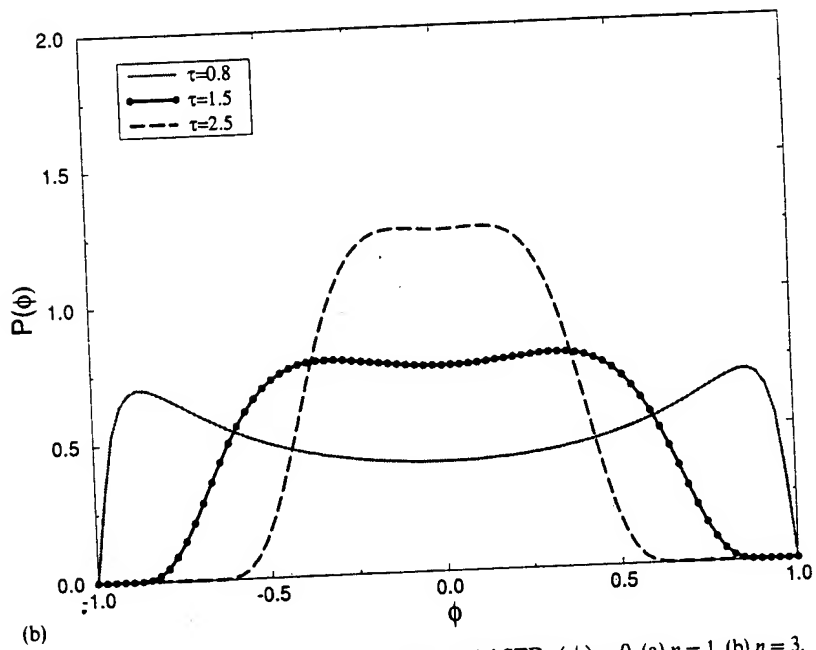
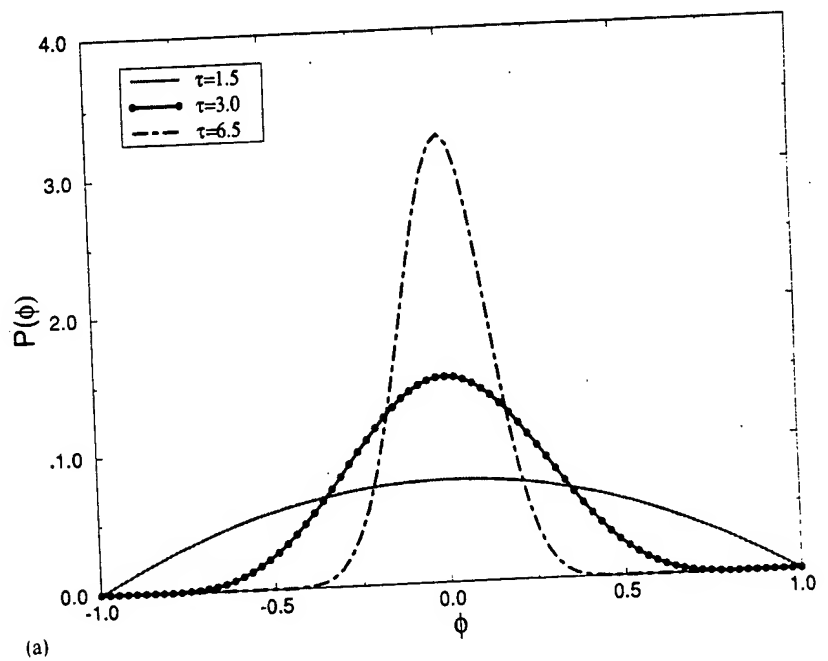


FIGURE 2 PDF results based on an exponential STD. $\langle \phi \rangle = 0$. (a) $n = 1$, (b) $n = 3$.

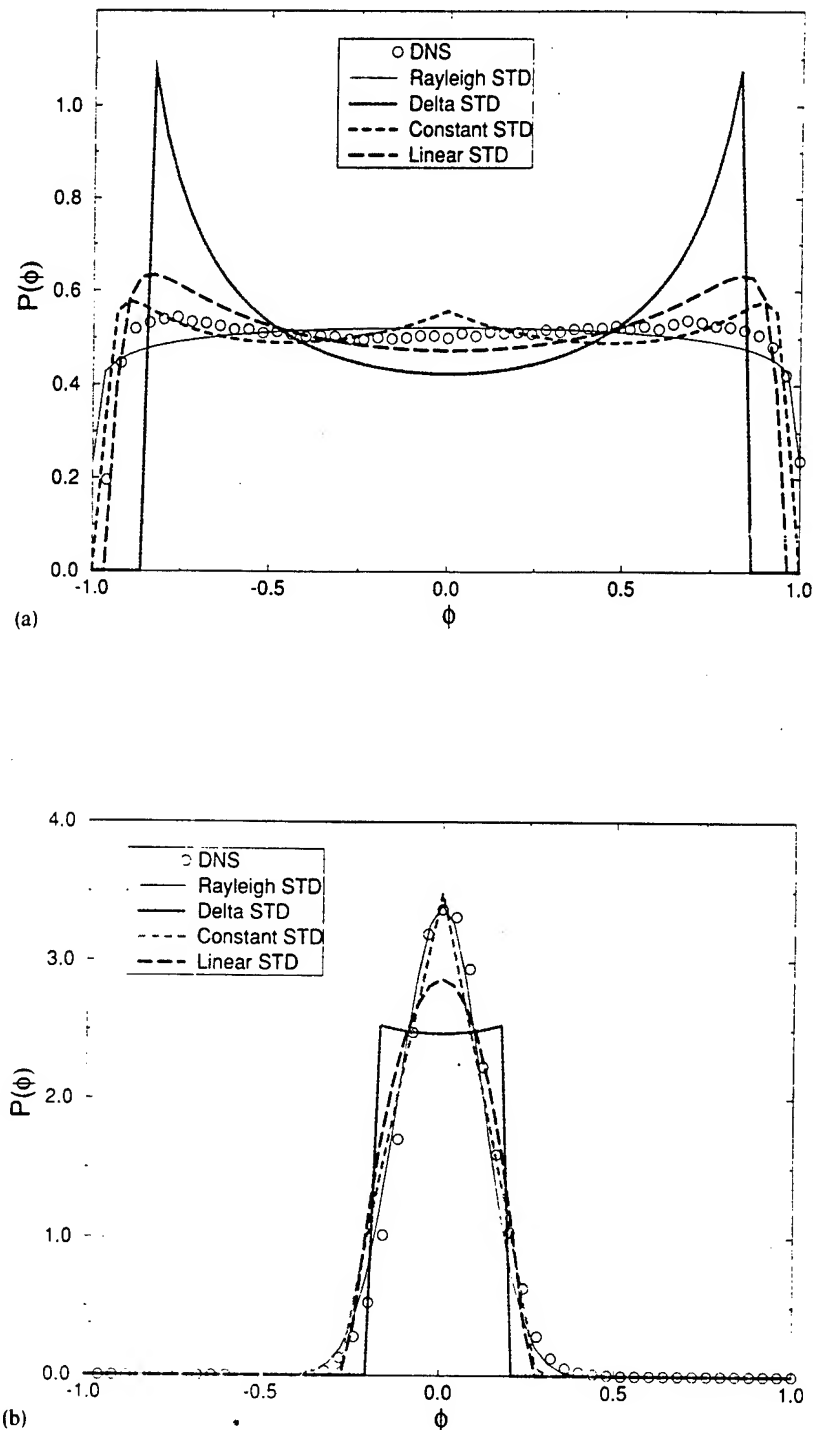


FIGURE 3 Comparison amongst the PDF's generated via various closures and with DNS. $\langle \phi \rangle = 0$. (a) $\sigma^2 = 0.3175$. (b) $\sigma^2 = 0.01346$.

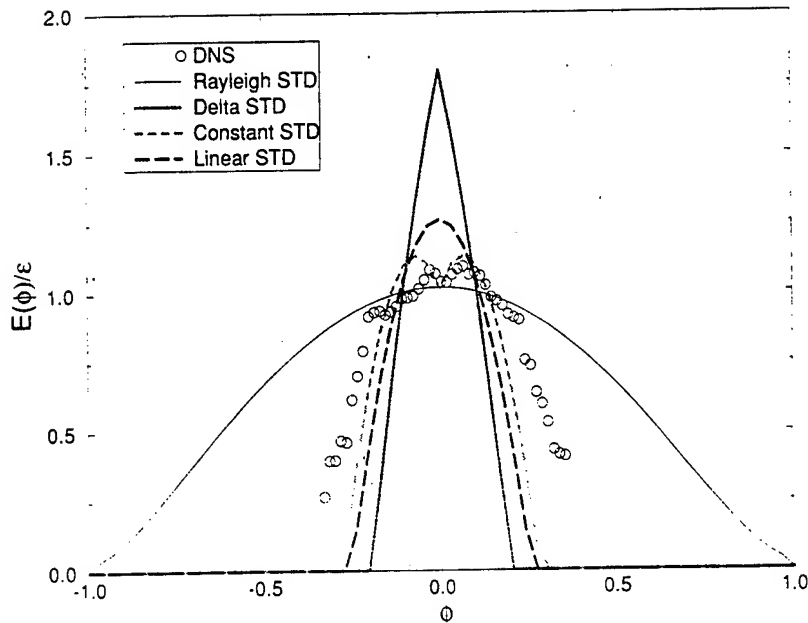


FIGURE 4 Comparison amongst the conditional expected dissipation generated via various closures and with DNS at $\sigma^2 = 0.01346$.

striation thickness ($w = w^*$), we have $h(w) = \delta(w - w^*)$. This yields:

$$G(|y|) = \begin{cases} \frac{1}{2w^*} & \text{if } -w^* \leq y \leq w^*; \\ 0 & \text{elsewhere} \end{cases}$$

and:

$$P(\phi(y)) = \begin{cases} \sqrt{\frac{\pi}{2}} \frac{\tau}{2w^*} \exp\left(\left(\frac{y}{\sqrt{2}\tau} + c'\right)^2\right) & \text{if } -w^* \leq y \leq w^*; \\ 0 & \text{elsewhere,} \end{cases} \quad (25)$$

$$E(\phi(y)) = \frac{2}{\pi} \exp\left(-\frac{3}{2}s^2\right) \left(\frac{1}{\tau} \frac{dt}{dt} D_{-2}(\sqrt{2}s) - \left(\frac{1}{\tau^2} \frac{dt}{dt} y - \sqrt{2} \frac{dc'}{dt} \right) D_{-1}(\sqrt{2}s) \right) \quad (26)$$

Here, D_v denote the parabolic cylinder function of order v (Abramowitz and Stegun, 1972), and $s = (y/\sqrt{2}\tau) + c' = \operatorname{erf}^{-1}(\phi)$. For a constant STD, $h(w)$ is given by:

$$h(w) = \begin{cases} \frac{1}{w_u} & \text{if } 0 \leq w \leq w_u; \\ 0 & \text{otherwise.} \end{cases} \quad (27)$$

where, w_u is a constant. The linear STD is defined by:

$$h(w) = \begin{cases} \frac{2w}{w_u^2} & \text{if } 0 \leq w \leq w_u; \\ 0 & \text{otherwise.} \end{cases} \quad (28)$$

The explicit analytical expressions for the pdf and the conditional statistics as generated by Equations (27)–(28) are somewhat complex and are not given here; they are available in Jaber (1995). The final results are shown in Figures 3–4 and show that with these bounded STD's, mixing is accompanied by the encroachment of the boundaries in the composition domain. The effect of this boundary migration is more pronounced in the profiles of the conditional statistics at large times in Figures 4–5 (the profiles at initial times are similar and are not shown). This behavior is consistent with the results portrayed by the DNS data and does point to the drawbacks of the AMC (Miller *et al.*, 1993) and/or other closures with an effective unbounded STD. The pdf's generated by the delta STD are composed of two marching peaks and asymptotically form a single peak at the mean scalar value. This evolution is somewhat similar to that of the Linear Mean Square Estimation (LMSE) (Dopazo and O'Brien, 1976) and is similar to that obtained from the solution of for the case of pure diffusion with an initial double delta distribution (Fox, 1992). This type of pdf evolution characterizes mixing problems with

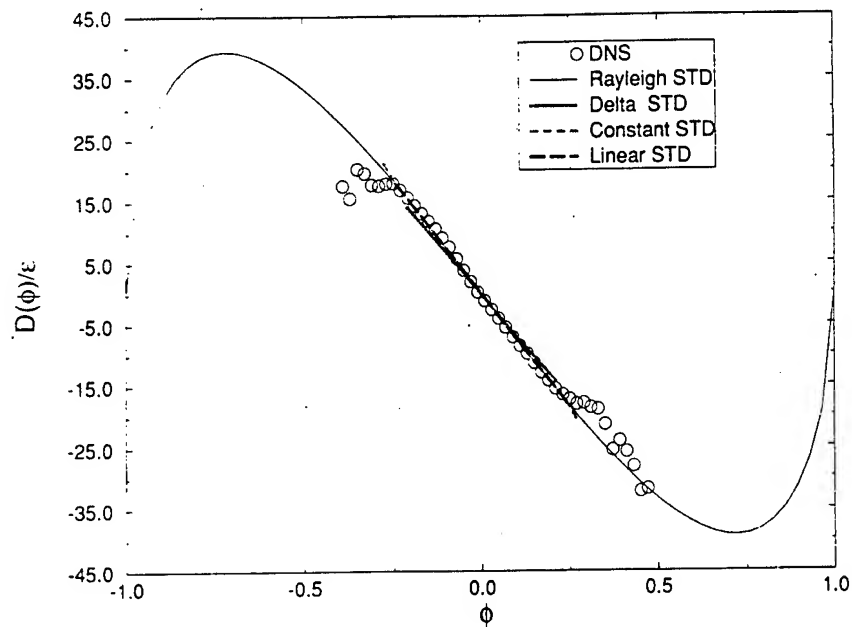


FIGURE 5 Comparison amongst the conditional expected diffusion generated via various closures and with DNS at $\sigma^2 = 0.01346$.

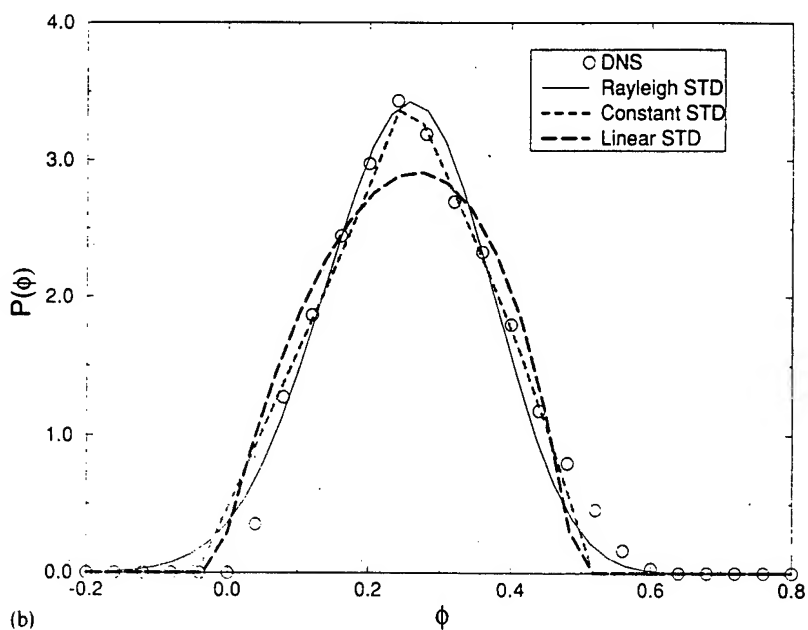
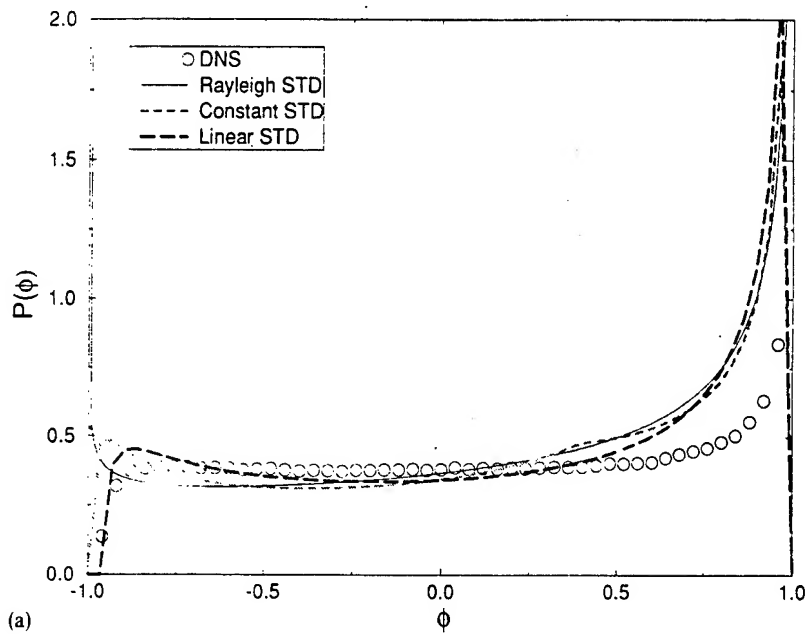


FIGURE 6 Comparison amongst the PDF's generated via various closures and with DNS. $\langle \phi \rangle = 0.25$. (a) $\sigma^2 = 0.39$, (b) $\sigma^2 = 0.13$.

small velocity effects and corresponds to the scalar evolution in a flow dominated by small scales. The physical reasoning for this behavior is that small velocity length scales do not produce a substantial large scale mixing and their influence is exhibited only through enhanced diffusion. Similar results have been obtained via the LEM (Cremer *et al.*, 1992; Frankel, 1993). With a constant STD and a linear STD, the pdf evolution is somewhat more similar to that given by the Rayleigh STD and also by the JET (Miller *et al.*, 1993). The trimodal nature of the pdf at early times as produced by the constant STD has not been observed in available DNS but has been captured by the LEM (McMurtry *et al.*, 1993a) None of the pdf's generated in this way yield an asymptotic exact Gaussian state as exhibited by the profiles of the conditional expected dissipation.

The difference between the closures is better exhibited by the results for the non-symmetric case. A comparison of all the closures is made in Figures 6–8 for $\langle \phi \rangle = 0.25$. The procedure for producing these results is identical to that for the symmetric pdf. However, the numerical means of evaluating the constant c' is somewhat more involved. Here, the evaluation is made by an iterative procedure but in some of the cases it is possible to provide explicit analytical expression for this parameter (Jaberi, 1995). The pdf's as produced by all the closure are relatively similar and asymptotically tend to be concentrated near the mean scalar value. However, the difference between the closures is most obvious in the profiles of the conditional statistics at late times. It is noted that the conditional expected dissipation for $n = 1$ (AMC) always yields a symmetric profile regardless of the extent of asymmetry in the

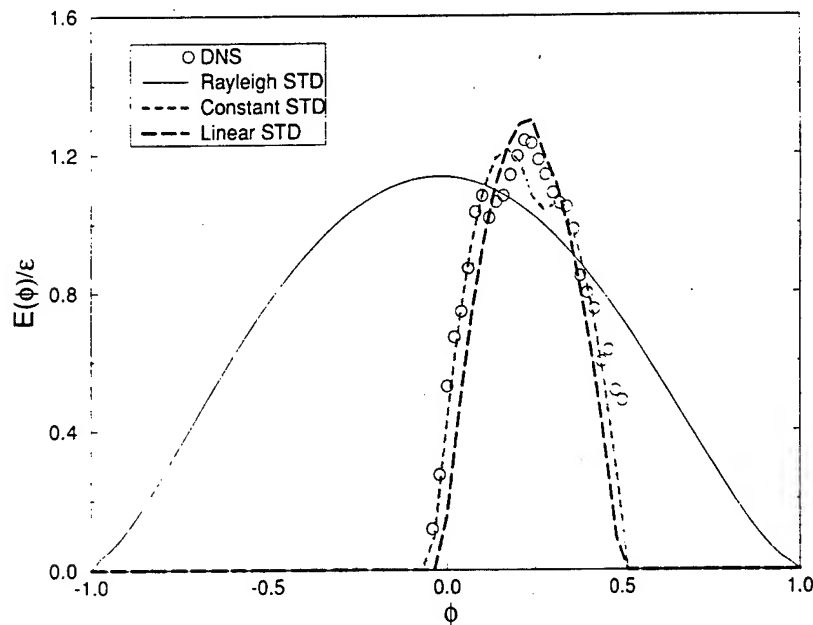


FIGURE 7 Comparison amongst the conditional expected dissipation generated via various closures and with DNS. $\langle \phi \rangle = 0.25$, $\sigma^2 = 0.13$.

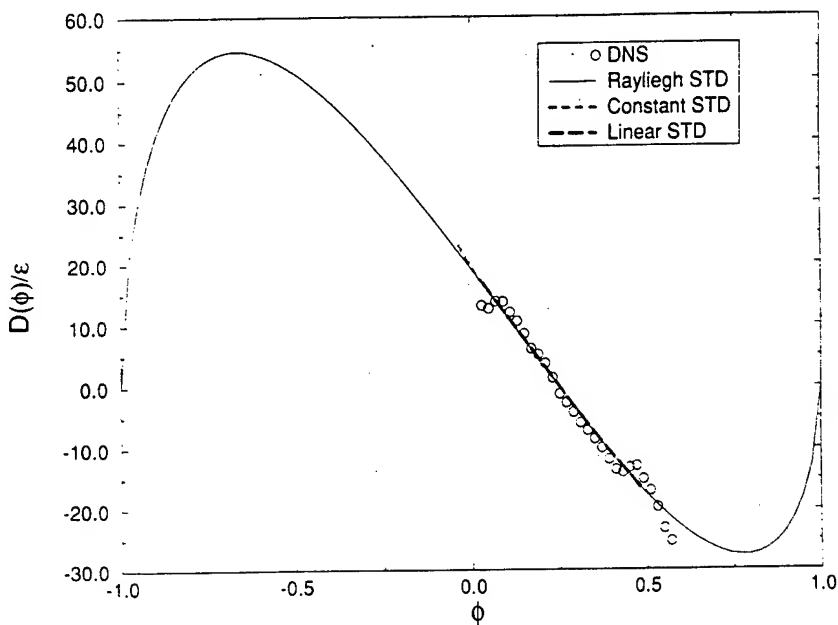


FIGURE 8 Comparison amongst the conditional expected diffusion generated via various closures and with DNS. $\langle \phi \rangle = 0.25$, $\sigma^2 = 0.13$.

pdf (Fig. 7). The rigorous mathematical reasoning for this behavior is given by Frankel (1993). The distributions produced by other models do not portray this behavior. As indicated in Figure 7, the results for all cases with a finite STD bounds are close to DNS data. The conditional diffusion (Fig. 8) for $n = 1$ does portray the non-symmetric nature of mixing, but is still always anchored at the bounds of the composition domain. This trend is not observed for the cases with bounded STD's and the results are in a better agreement with DNS data.

6.2 Effects of Scalar Distribution within the Lamellae

There are other scalar profiles which satisfy Equation (12). The solution of this equation depends primarily on the velocity field. Several simple velocity fields are considered along with a Rayleigh STD. The scalar profiles are obtained by the spectral-collocation solution of Equation (12) within a fixed physical domain (normalized by w). For a pure diffusion transport within the lamellae, *i.e.* $V_{\text{rel}} = 0$ the generated pdf is Gaussian-like as expected (not shown). For a linear velocity profile ($V_{\text{rel}} = \alpha y$) the results exhibit similar trends as those governed by the AMC. By varying the magnitude of α the counter-balance between the convection and the diffusion in Equation (12) changes but the general behavior of the scalar pdf remains the same. Therefore, the primary difference is through the time scale of the pdf evolution. For a constant velocity profile, the results show a significant departure from those of the AMC. This is shown in Figure 9 for the conditional expected dissipation implying an

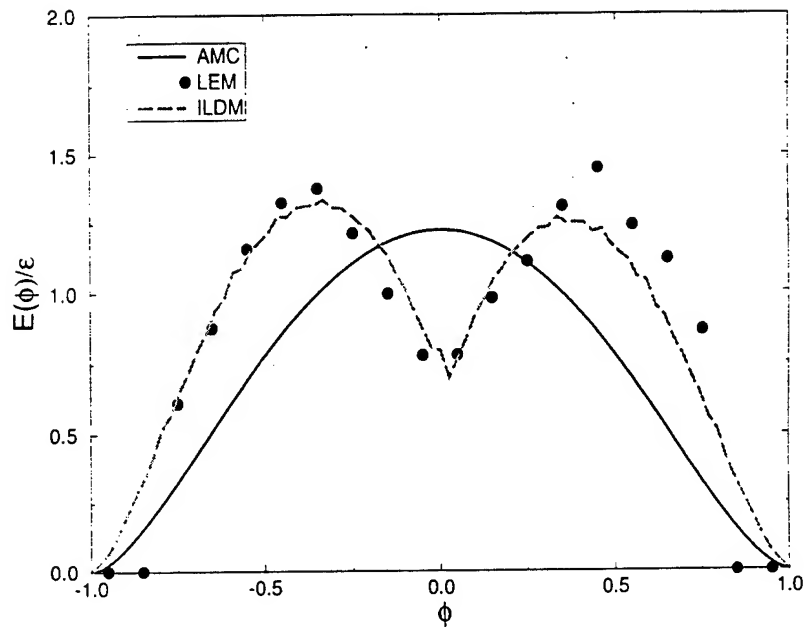


FIGURE 9 Comparison of ILDM prediction of the normalized conditional dissipation based on a Rayleigh STD and a constant inter-layer velocity profile with the results based on the AMC and the LEM. $\langle \phi \rangle = 0$.

exponential type pdf with a significant magnitude of the pdf at the bounds. The results for this case are also compared with those based on AMC and LEM. The exponential nature of the pdf which cannot be generated by the AMC is captured by the LEM. This is shown by the basin shape structure of the conditional dissipation profile. This structure is similar to that in Figure 1(b) and imply pdf tails close to a Laplace (double exponential) distribution. An increase in the amplitude of the velocity results in a faster evolution of the pdf towards the mean value. An asymptotic exponential scalar distribution has not been observed in most previous numerical simulations (Eswaran and Pope, 1988; Leonard and Hill, 1991; Givi and McMurtry, 1988; McMurtry and Givi, 1989; Miller *et al.*, 1993), the exceptions are those in LES results of Metais and Lesieur (1992) and in recent DNS results of Kimura and Kraichnan (1993), Jaberi (1995).

The limited results presented here¹ reveal the dominant influence of the velocity field on the evolution of the pdf. In a turbulent flow field with a wide spectrum of eddy sizes, the influence of the turbulent advection is more complex. Motivated by these results, the assessment of the role of velocity field by DNS is strongly recommended. However, due to the small range of the Reynolds number that can be considered by DNS, such an assessment could be very difficult – but is currently under way. In the meantime, other

¹ Further results with bounded STD's and with different velocity fields are available (Jaberi, 1995).

approaches by which the effects of convection in Equation (12) can be examined, should be followed. For example, the LEM provides one means of doing exactly so.

7 APPLICATIONS FOR MODELING OF REACTING FLOWS

One of the most important applications of pdf closure is due their use for modeling of turbulent combustion (Pope, 1985). The results generated here can be used directly for modeling of *mixing controlled* homogeneous chemically reacting systems. Namely, in determining the limiting rate of reactant conversion in a simple chemistry of the type $\mathcal{F} + \mathcal{O} \rightarrow \text{Products}$. In this system the statistics of the reacting field can be related to those of an appropriately defined mixture fraction (Williams, 1985). This mixture fraction is a conserved scalar variable, similar to the variable ϕ considered above. The ensemble-mean values of the mass fractions of the reacting species are the most important physical variables from a practical standpoint. Therefore, it is useful to examine the differences between the pdf's in predicting the rate of mean reactants' decay. For unity mass fractions for the free stream fuel and oxidizer, the conserved scalar variable is defined as $\phi = F - O$, where F and O denote the mass fractions of the fuel and the oxidizer, respectively. Nonpremixed reactants imply an initial binary state for the variable ϕ . Therefore, the initial pdf of ϕ is composed of two delta functions at $\phi = \pm 1$. If the reactants are introduced in stoichiometric proportions, $\langle \phi \rangle = 0$ and non unity equivalence ratios imply non-zero values for the mean mixture fraction. In fuel-rich mixtures, $\langle \phi \rangle > 0$. With the AMC, Madnia *et al.* (1992) have analytically integrated the pdf for the evaluation of the mean reactants mass fractions. In non-stoichiometric mixture, the final results are in the form of definite integrals of the parabolic cylinder functions. In stoichiometric mixtures, the results simplify considerably and are directly related to the mixture fraction:

$$\frac{\langle F \rangle(t)}{\langle F \rangle(0)} = \frac{\langle O \rangle(t)}{\langle O \rangle(0)} = \frac{2}{\pi} \arcsin \left(\sqrt{\sin \left[\frac{\pi I_s}{2} \right]} \right). \quad (29)$$

I_s denotes the "intensity of segregation" (Brodkey, 1975). For non-stoichiometric mixtures and for other probability distributions generated here, analytical solutions are not possible and the results can be obtained only by integrating the pdf numerically. The final results for some sample cases are presented in Figures 10 and 11; the behavior for other cases are similar (Jaberi, 1995). For the stoichiometric case, obviously both reactants decay at the same rate (Fig. 10). For the fuel-rich mixture, the oxidizer is depleted faster and there is a surplus of fuel left at the final stages of mixing ($I_s \approx 0$). In all the cases considered, the results indicate that there is not a substantial difference between the closure prediction. Based on these observations, the analytical relations of Madnia *et al.* (1992) are recommended for predicting the limiting rate of mean reactant conversion in both homogeneous and non-homogeneous mixtures, at least until the development of more accurate closures.

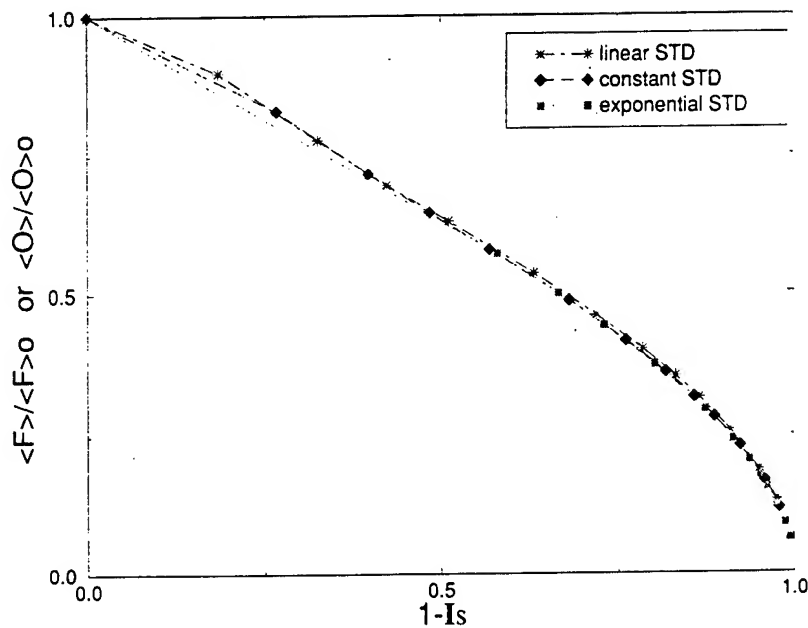


FIGURE 10 Decay of mean reactants' concentration in a stoichiometric mixture as predicted by the ILDM with several different STD's.

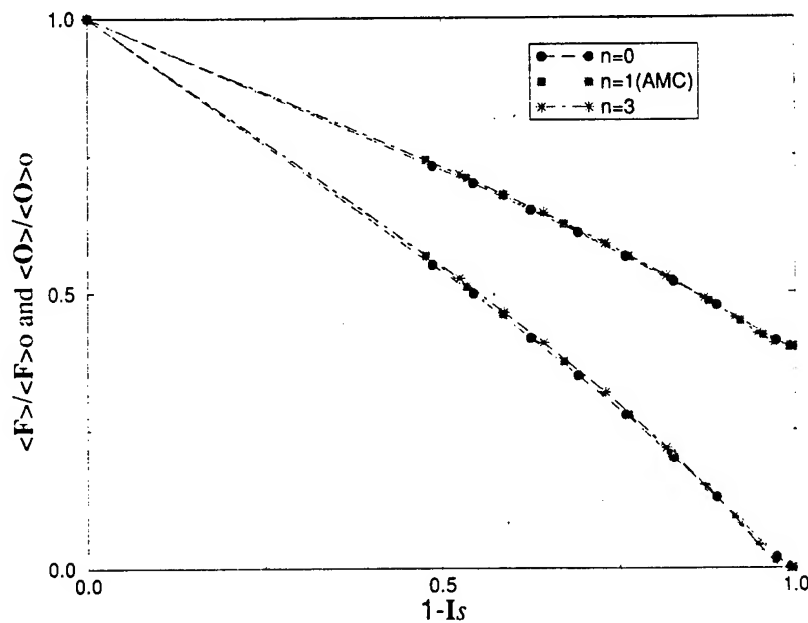


FIGURE 11 Decay of mean reactants' concentration in a fuel-rich mixture as predicted by the ILDM with an exponential STD.

8 SUMMARY

It is shown that the lamellar theory provides a simple means of "mimicking" several scalar mixing scenarios in homogeneous turbulent flows. The model described here is an extension of that first proposed by Kerstein (1991a) and suggests that there are two mechanisms by which the mixing process is described. These mechanisms are due to: (1) local events and (2) global events. The local effects are described by the distribution of the scalar within the lamellae, and the global effects are exhibited by the statistical distribution of the striation thickness. The properties of the model are assessed with the examinations of the conditional statistics of the scalar field. It is shown that the difference between the closures is exhibited in the profiles of the Probability Density Function (pdf) of the scalar and the conditional expected value of the scalar dissipation. However, all the cases yield approximately similar profiles for the conditional expected diffusion of the scalar. This behavior is mathematically justified and explains the similarity of the conditional diffusion as observed in recent contributions (Miller *et al.*, 1993; Pope and Ching, 1993; Leonard and Hill, 1991; Kailasanath *et al.*, 1993). The primary influence of the conditional diffusion is shown to be through its behavior at the bounds in the composition domain. It is also shown that with the manipulations of each of the two primary mechanisms, many different pdf's can be generated. Some of these pdf's have been observed in previous DNS studies and some have been captured by other mixing closures. However, some of the cases considered here are yet to be observed (via DNS, experiments, other closures, etc.). It is claimed that this does not necessarily imply the non-physical character of the mixing scenario in these cases. Rather, it indicates the need for further test cases to be considered in future simulations and experiments. In these efforts, one must be careful in identifying the roles of the velocity and scalar length scales as these scales may lead to different asymptotic behaviors. In this regard an assessment of the model by means of DNS in the format recently reported by Kimura and Kraichnan (1993) and by the LEM in the context proposed by Cremer *et al.* (1992) is useful. Also, the flexibility of the model may offer an assistance to other closures which are based on *a priori* knowledge of the statistical evolution. Finally, it is shown that while the pdf's generated by the model are different, their application for determining the limiting rate of mean reactant conversion in mixing limited non-premixed turbulent flows do not yield significantly different results. Thus, the closed form expression obtained via one of the models is recommended for all the other cases.

ACKNOWLEDGEMENTS

This work is part of an effort sponsored by the Office of Naval Research under Grant N00014-94-1-0677, and by the National Science Foundation under Grant CTS-9253488.

REFERENCES

Abramowitz, M. and Stegun, I. A. (1972). *Handbook of Mathematical Functions and Formulas, Graphs, and Mathematical Tables*. Government Printing Office, Washington, D.C.
Bockhorn, H. (1988). Finite chemical reaction rate and local equilibrium effects in turbulent hydrogen-air diffusion flames. In *Proceedings of the 22nd Symp. (Int.) on Combustion*, The Combustion Institute pp. 665-664, Pittsburgh, PA.

Brodkey, R. S., editor. (1975). *Turbulence in Mixing Operation*. Academic Press, New York, NY.

Chen, H., Chen, S. and Kraichnan, R. H. (1989). Probability distribution of a stochastically advected scalar field. *Phys. Rev. Lett.*, **63**, 2657–2660.

Cremer, M. A., McMurtry, P. A. and Kerstein, A. R. (1992). Effects of turbulence length-scale distribution on scalar mixing in homogeneous turbulent flow. *Bull. Amer. Phys. Soc.*, **37**, 1805.

Dopazo, C. (1994). Recent developments in pdf methods. In Libby and Williams (1994), chapter 7, pp. 375–474.

Dopazo, C. and O'Brien, E. E. (1976). Statistical treatment of non-isothermal chemical reaction in turbulence. *Combust. Sci. and Tech.*, **13**, 99–112.

Eswaran, V. and Pope, S. B. (1988). Direct numerical simulations of the turbulent mixing of a passive scalar. *Phys. Fluids*, **31**, 506–520.

Fox, R. O. (1992). The Fokker-Planck closure for turbulent molecular mixing: Passive scalars. *Phys. Fluids*, **A 4**, 1230–1244.

Frankel, S. H. (1993). *Probabilistic and Deterministic Description of Turbulent Flows with Nonpremixed Reactants*. Ph.D. Thesis, Department of Mechanical and Aerospace Engineering, State University of New York at Buffalo, Buffalo, NY.

Frankel, S. H., Jiang, T.-L. and Givi, P. (1992). Modeling of isotropic reacting turbulence by a hybrid Mapping-EDQNM closure. *AIChE J.*, **38**, 535–543.

Frankel, S. H., Madnia, C. K. and Givi, P. (1993). Comparative assessment of closures for turbulent reacting flows. *AIChE J.*, **39**, 899–903.

Gao, F. (1991). Mapping closure and non-Gaussianity of the scalar probability density functions in isotropic turbulence. *Phys. Fluids A*, **3**, 2438–2444.

Givi, P. (1989). Model free simulations of turbulent reactive flows. *Prog. Energy Combust. Sci.*, **15**, 1–107.

Givi, P. (1994). Spectral and random vortex methods in turbulent reacting flows. In Libby and Williams (1994), chapter 8, pp. 475–572.

Givi, P. and McMurtry, P. A. (1988). Non-premixed reaction in homogeneous turbulence: Direct numerical simulations. *AIChE J.*, **34**, 1039–1042.

Jaberi, F. A. (1995). Ph.D. Thesis, Department of Mechanical and Aerospace Engineering, State University of New York at Buffalo, Buffalo, NY. In preparation.

Jayesh and Warhaft, Z. (1992). Probability distribution, conditional dissipation, and transport of passive temperature fluctuations in grid-generated turbulence. *Phys. Fluids A*, **4**, 2292–2307.

Jiang, T.-L., Gao, F. and Givi, P. (1992). Binary and trinary scalar mixing by Fickian diffusion-Some mapping closure results. *Phys. Fluids A*, **4**, 1028–1035.

Kailasanath, P., Sreenivasan, K. R. and Saylor, J. R. (1993). Conditional scalar dissipation rates in turbulent wakes, jets, and boundary layers. *Phys. Fluids A*, **5**, 3207–3215.

Kerstein, A. R. (1988). A linear eddy model of turbulent scalar transport and mixing. *Combust. Sci. and Tech.*, **60**, 391–421.

Kerstein, A. R. (1991a). Flapping model of scalar mixing in turbulence. *Phys. Fluids A*, **27**, 2819–2827.

Kerstein, A. R. (1991b). Linear-eddy modeling of turbulent transport. Part 6. Microstructure of diffusive scalar mixing fields. *J. Fluid Mech.*, **231**, 361–394.

Kerstein, A. R. (1992). Linear-eddy modeling of turbulent transport. Part 7. Finite-rate chemistry and multi-stream mixing. *J. Fluid Mech.*, **240**, 289–313.

Kimura, Y. and Kraichnan, R. H. (1993). Statistics of an advected passive scalar. *Phys. Fluids A*, **5**, 2264–2277.

Kraichnan, R. H. (1989). Closures for probability distribution. *Bull. Amer. Phys. Soc.*, **34**, 2298.

Larcheveque, M. and Lesieur, M. (1981). The applications of eddy-damped Markovian closures to the problem of dispersion of particle pairs. *J. Mech.*, **20**, 113.

Leonard, A. D. and Hill, J. C. (1991). Scalar dissipation and mixing in turbulent reacting flows. *Phys. Fluids A*, **3**, 1286–1299.

Libby, P. A. and Williams, F. A., editors. (1994). *Turbulent Reacting Flows*. Academic Press, London, UK.

Madnia, C. K., Frankel, S. H. and Givi, P. (1992). Reactant conversion in homogeneous turbulence: Mathematical modeling, computational validations and practical applications. *Theoret. Comput. Fluid Dynamics*, **4**, 79–93.

McMurtry, P. A. and Givi, P. (1989). Direct numerical simulations of mixing and reaction in a nonpremixed homogeneous turbulent flow. *Combust. Flame*, **77**, 171–185.

McMurtry, P. A., Gansauge, T. C., Kerstein, A. R. and Krueger, S. K. (1993a). Linear eddy simulations of mixing in a homogeneous turbulent flow. *Phys. Fluids A*, **5**, 1023–1034.

McMurtry, P. A., Menon, S. and Kerstein, A. R. (1993b). Linear eddy modeling of turbulent combustion. *Energy & Fuels*, **7**, 817–826. Proceedings of 7th Annual Technical Conference of ACERC.

Metais, O. and Lesieur, M. (1992). Spectral large-eddy simulation of isotropic and stably stratified turbulence. *J. Fluid Mech.*, **239**, 157–194.

Miller, R. S., Frankel, S. H., Madnia, C. K. and Givi, P. (1993). Johnson-Edgeworth translation for probability modeling of binary scalar mixing in turbulent flows. *Combust. Sci. and Tech.*, **91**, 21-52.

Muzzio, F. J. and Ottino, J. M. (1989a). Dynamics of a lamellar system with diffusion and reaction: Scaling analysis and global kinetics. *Phys. Rev., A* **40**, 7182-7192.

Muzzio, F. J. and Ottino, J. M. (1989b). Evolution of a lamellar system with diffusion and reaction: A scaling approach. *Phys. Rev. Lett.*, **63**, 47-50.

Ottino, J. M. (1989). *The Kinematics of Mixing: Stretching, Chaos, and Transport*. Cambridge University Press, Cambridge, U.K.

Pope, S. B. (1985). PDF methods for turbulent reactive flows. *Prog. Energy Combust. Sci.*, **11**, 119-192.

Pope, S. B. (1991). Mapping closures for turbulent mixing and reaction. *Theoret. Comput. Fluid Dynamics*, **2**, 255-270.

Pope, S. B. and Ching, E. S. C. (1993). Stationary probability density functions: An exact result. *Phys. Fluids, A* **5**, 1529-1531.

Ruetsch, G. R. and Maxey, M. R. (1992). The evolution of small-scale structures in homogeneous-isotropic turbulence. *Phys. Fluids, A* **4**, 2747-2760.

Sinai, Y. G. and Yakhot, V. (1989). Limiting probability distributions of a passive scalar in a random velocity field. *Phys. Rev. Lett.*, **63**, 1962-1964.

Sokolov, I. M. and Blumen, a. (1991a). Diffusion-controlled reactions in lamellar systems. *Phys. Rev., A* **43**, 2714-2719.

Sokolov, I. M. and Blumen, A. (1991b). Distribution of striation thickness in reacting lamellar systems. *Phys. Rev., A* **43**, 6546-6549.

Southerland, K. B. and Dahm, W. J. A. (1993). Striation thickness distribution in turbulent flows. *Bull. Amer. Phys. Soc.*, **38**, 2205.

Williams, F. A. (1985). *Combustion Theory*. The Benjamin/Cummings Publishing Company, Menlo Park, CA, 2nd edition.